
**Title 40 CFR Part 191
Subparts B and C
Compliance Recertification
Application
for the
Waste Isolation Pilot Plant

Appendix PA-2009
Performance Assessment**



**United States Department of Energy
Waste Isolation Pilot Plant**

**Carlsbad Field Office
Carlsbad, New Mexico**

Appendix PA-2009
Performance Assessment

Table of Contents

PA-1.0 Introduction PA-1

PA-2.0 Overview and Conceptual Structure of the PA PA-4

 PA-2.1 Overview of Performance Assessment..... PA-4

 PA-2.1.1 Changes in the CRA-2009 PA PA-5

 PA-2.1.2 Conceptual Basis for PA..... PA-6

 PA-2.1.3 Undisturbed Repository Performance..... PA-7

 PA-2.1.4 Disturbed Repository Performance..... PA-9

 PA-2.1.5 Compliance Demonstration Method..... PA-15

 PA-2.1.6 Results of the PA PA-16

 PA-2.2 Conceptual Structure of the PA..... PA-17

 PA-2.2.1 Regulatory Requirements PA-18

 PA-2.2.2 Probabilistic Characterization of Different Futures..... PA-20

 PA-2.2.3 Estimation of Releases..... PA-21

 PA-2.2.4 Probabilistic Characterization of Parameter Uncertainty PA-24

 PA-2.3 PA Methodology PA-27

 PA-2.3.1 Identification and Screening of FEPs PA-27

 PA-2.3.2 Scenario Development and Selection PA-28

 PA-2.3.3 Calculation of Scenario Consequences..... PA-37

PA-3.0 Probabilistic Characterization of Futures PA-39

 PA-3.1 Probability Space..... PA-40

 PA-3.2 AICs and PICs PA-40

 PA-3.3 Drilling Intrusion PA-40

 PA-3.4 Penetration of Excavated/Nonexcavated Area PA-41

 PA-3.5 Drilling Location PA-42

 PA-3.6 Penetration of Pressurized Brine PA-43

 PA-3.7 Plugging Pattern PA-43

 PA-3.8 Activity Level..... PA-43

 PA-3.9 Mining Time..... PA-44

 PA-3.10 Scenarios and Scenario Probabilities..... PA-45

 PA-3.11 CCDF Construction..... PA-47

PA-4.0 Estimation of Releases PA-48

 PA-4.1 Results for Specific Futures..... PA-48

 PA-4.2 Two-Phase Flow: BRAGFLO PA-50

 PA-4.2.1 Mathematical Description..... PA-50

 PA-4.2.2 Initial Conditions PA-65

 PA-4.2.3 Creep Closure of Repository PA-67

 PA-4.2.4 Fracturing of MBs and DRZ..... PA-67

 PA-4.2.5 Gas Generation PA-69

 PA-4.2.6 Capillary Action in the Waste..... PA-75

 PA-4.2.7 Shaft Treatment PA-76

 PA-4.2.8 Option D Panel Closures PA-77

 PA-4.2.9 Borehole Model PA-80

PA-4.2.10 Castile Brine Reservoir.....	PA-81
PA-4.2.11 Numerical Solution.....	PA-82
PA-4.2.12 Gas and Brine Flow across Specified Boundaries.....	PA-85
PA-4.2.13 Additional Information.....	PA-86
PA-4.3 Radionuclide Transport in the Salado: NUTS.....	PA-86
PA-4.3.1 Mathematical Description.....	PA-88
PA-4.3.2 Calculation of Maximum Concentration $S_T(Br, Ox, El)$	PA-91
PA-4.3.3 Radionuclides Transported.....	PA-93
PA-4.3.4 NUTS Tracer Calculations.....	PA-96
PA-4.3.5 NUTS Transport Calculations.....	PA-97
PA-4.3.6 Numerical Solution.....	PA-97
PA-4.3.7 Additional Information.....	PA-100
PA-4.4 Radionuclide Transport in the Salado: PANEL.....	PA-101
PA-4.4.1 Mathematical Description.....	PA-101
PA-4.4.2 Numerical Solution.....	PA-102
PA-4.4.3 Implementation in PA.....	PA-103
PA-4.4.4 Additional Information.....	PA-103
PA-4.5 Cuttings and Cavings to Surface: CUTTINGS_S.....	PA-103
PA-4.5.1 Cuttings.....	PA-104
PA-4.5.2 Cavings.....	PA-104
PA-4.5.3 Additional Information.....	PA-111
PA-4.6 Spallings to Surface: DRSPALL and CUTTINGS_S.....	PA-111
PA-4.6.1 Summary of Assumptions.....	PA-111
PA-4.6.2 Conceptual Model.....	PA-112
PA-4.6.3 Numerical Model.....	PA-124
PA-4.6.4 Implementation.....	PA-129
PA-4.6.5 Additional Information.....	PA-130
PA-4.7 DBR to Surface: BRAGFLO.....	PA-130
PA-4.7.1 Overview of Conceptual Model.....	PA-130
PA-4.7.2 Linkage to Two-Phase Flow Calculation.....	PA-132
PA-4.7.3 Conceptual Representation for Flow Rate $rDBR(t)$	PA-134
PA-4.7.4 Determination of Productivity Index J_p	PA-135
PA-4.7.5 Determination of Waste Panel Pressure $p_w(t)$ and DBR.....	PA-137
PA-4.7.6 Boundary Value Pressure p_{wf}	PA-138
PA-4.7.7 Boundary Value Pressure p_{wE1}	PA-145
PA-4.7.8 End of DBR.....	PA-150
PA-4.7.9 Numerical Solution.....	PA-151
PA-4.7.10 Additional Information.....	PA-153
PA-4.8 Groundwater Flow in the Culebra Dolomite.....	PA-153
PA-4.8.1 Mathematical Description.....	PA-154
PA-4.8.2 Implementation.....	PA-155
PA-4.8.3 Computational Grids and Boundary Value Conditions.....	PA-158
PA-4.8.4 Numerical Solution.....	PA-160
PA-4.8.5 Additional Information.....	PA-160
PA-4.9 Radionuclide Transport in the Culebra Dolomite.....	PA-160
PA-4.9.1 Mathematical Description.....	PA-162

PA-4.9.2 Numerical Solution	PA-170
PA-4.9.3 Additional Information	PA-174
PA-5.0 Probabilistic Characterization of Subjective Uncertainty	PA-176
PA-5.1 Probability Space	PA-176
PA-5.2 Variables Included for Subjective Uncertainty	PA-177
PA-5.3 Variable Distributions	PA-177
PA-5.4 Correlations and Dependencies	PA-178
PA-5.5 Separation of Aleatory and Epistemic Uncertainty	PA-180
PA-6.0 Computational Procedures.....	PA-181
PA-6.1 Sampling Procedures	PA-181
PA-6.2 Sample Size for Incorporation of Subjective Uncertainty.....	PA-182
PA-6.3 Statistical Confidence on Mean CCDF	PA-182
PA-6.4 Generation of Latin Hypercube Samples.....	PA-183
PA-6.5 Generation of Individual Futures.....	PA-185
PA-6.6 Construction of CCDFs	PA-186
PA-6.7 Mechanistic Calculations.....	PA-188
PA-6.7.1 BRAGFLO Calculations.....	PA-188
PA-6.7.2 NUTS Calculations	PA-189
PA-6.7.3 PANEL Calculations	PA-190
PA-6.7.4 DRSPALL Calculations.....	PA-191
PA-6.7.5 CUTTINGS_S Calculations	PA-191
PA-6.7.6 BRAGFLO Calculations for DBR Volumes	PA-192
PA-6.7.7 MODFLOW Calculations.....	PA-192
PA-6.7.8 SECOTP2D Calculations.....	PA-193
PA-6.8 Computation of Releases.....	PA-193
PA-6.8.1 Undisturbed Releases.....	PA-194
PA-6.8.2 Direct Releases	PA-194
PA-6.8.3 Radionuclide Transport Through the Culebra	PA-196
PA-6.8.4 Determining Initial Conditions for Direct and Transport Releases	PA-197
PA-6.8.5 CCDF Construction	PA-199
PA-6.9 Sensitivity Analysis	PA-200
PA-6.9.1 Scatterplots	PA-201
PA-6.9.2 Regression Analysis.....	PA-202
PA-6.9.3 Stepwise Regression Analysis	PA-203
PA-7.0 Results for the Undisturbed Repository	PA-204
PA-7.1 Salado Flow	PA-204
PA-7.1.1 Pressure in the Repository	PA-204
PA-7.1.2 Brine Saturation in the Waste	PA-205
PA-7.1.3 Brine Flow Out of the Repository	PA-208
PA-7.2 Radionuclide Transport	PA-209
PA-7.2.1 Radionuclide Transport to the Culebra.....	PA-210
PA-7.2.2 Radionuclide Transport to the Land Withdrawal Boundary.....	PA-210

PA-8.0 Results for a Disturbed Repository..... PA-212

 PA-8.1 Drilling Scenarios PA-212

 PA-8.2 Mining Scenarios PA-213

 PA-8.3 Salado Flow PA-213

 PA-8.3.1 Pressure in the Repository PA-213

 PA-8.3.2 Brine Saturation PA-215

 PA-8.3.3 Brine Flow out of the Repository PA-219

 PA-8.4 Radionuclide Transport PA-224

 PA-8.4.1 Radionuclide Source Term PA-224

 PA-8.4.2 Transport through MBs and Shaft PA-226

 PA-8.4.3 Transport to the Culebra PA-226

 PA-8.4.4 Transport Through the Culebra PA-229

 PA-8.5 Direct Releases PA-231

 PA-8.5.1 Cuttings and Cavings PA-231

 PA-8.5.2 Spallings PA-232

 PA-8.5.3 DBRs..... PA-235

PA-9.0 Normalized Releases PA-237

 PA-9.1 Cuttings and Cavings..... PA-237

 PA-9.2 Spallings PA-238

 PA-9.3 Direct Brine PA-238

 PA-9.4 Groundwater Transport PA-240

 PA-9.5 Total Normalized Releases..... PA-241

PA-10.0 References PA-247

List of Figures

Figure PA-1. Overall Mean CCDFs for Total Normalized Releases: CRA-2009 PA and CRA-2004 PABC PA-16

Figure PA-2. Computational Models Used in PA..... PA-23

Figure PA-3. Construction of the CCDF Specified in 40 CFR Part 191 Subpart B PA-23

Figure PA-4. Distribution of CCDFs Resulting from Possible Values for the Sampled Parameters PA-25

Figure PA-5. Example Mean Probability of Release and the Confidence Limits on the Mean from CRA-2009 PA..... PA-26

Figure PA-6. Example CCDF Distribution From CRA-2009 PA (Replicate 1)..... PA-26

Figure PA-7. Logic Diagram for Scenario Analysis PA-29

Figure PA-8. Conceptual Release Pathways for the UP Scenario PA-30

Figure PA-9. Conceptual Release Pathways for the Disturbed Repository M Scenario..... PA-32

Figure PA-10. Conceptual Release Pathways for the Disturbed Repository Deep Drilling E2 Scenario..... PA-34

Figure PA-11. Conceptual Release Pathways for the Disturbed Repository Deep Drilling E1 Scenario..... PA-35

Figure PA-12. Conceptual Release Pathways for the Disturbed Repository Deep Drilling E1E2 Scenario PA-36

Figure PA-13. CDF for Time Between Drilling Intrusions PA-41

Figure PA-14. Discretized Locations for Drilling Intrusions..... PA-42

Figure PA-15. Computational Grid Used in BRAGFLO for PA PA-54

Figure PA-16. Definition of Element Depth in BRAGFLO Grid PA-55

Figure PA-17. Identification of Individual Cells in BRAGFLO Grid PA-56

Figure PA-18. Schematic View of the Simplified Shaft Model..... PA-78

Figure PA-19. Schematic Side View of Option D Panel Closure..... PA-78

Figure PA-20. Representation of Option D Panel Closures in the BRAGFLO Grid..... PA-79

Figure PA-21. Selecting Radionuclides for the Release Pathways Conceptualized by
PA PA-94

Figure PA-22. Detail of Rotary Drill String Adjacent to Drill Bit..... PA-106

Figure PA-23. Schematic Diagram of the Flow Geometry Prior to Repository
Penetration..... PA-112

Figure PA-24. Schematic Diagram of the Flow Geometry After Repository
Penetration..... PA-113

Figure PA-25. Effective Wellbore Flow Geometry Before Bit Penetration PA-113

Figure PA-26. Effective Wellbore Flow Geometry After Bit Penetration..... PA-114

Figure PA-27. Finite-Difference Zoning for Wellbore PA-125

Figure PA-28. DBR Grid Used in PA PA-131

Figure PA-29. Assignment of Initial Conditions for DBR Calculation PA-133

Figure PA-30. Borehole Representation Used for Poettmann-Carpenter Correlation PA-140

Figure PA-31. Areas of Potash Mining in the McNutt Potash Zone..... PA-157

Figure PA-32. Modeling Domain for Groundwater Flow (MODFLOW) and
Radionuclide Transport (SECOTP2D) in the Culebra PA-158

Figure PA-33. Boundary Conditions Used for Simulations of Brine Flow in the
Culebra PA-159

Figure PA-34. Finite-Difference Grid Showing Cell Index Numbering Convention
Used by MODFLOW PA-161

Figure PA-35. Parallel-Plate, Dual-Porosity Conceptualization..... PA-162

Figure PA-36. Schematic of Finite-Volume Staggered Mesh Showing Internal and
Ghost Cells PA-171

Figure PA-37. Illustration of Stretched Grid Used for Matrix Domain Discretization..... PA-173

Figure PA-38. Correlation Between S_HALITE:PRMX_LOG and
S_HALITE:COMP_RCK..... PA-179

Figure PA-39. Correlation between CASTILLER:PRMX_LOG and
CASTILLER:COMP_RCK..... PA-179

Figure PA-40. Dependency between WAS_AREA:GRATMICI and
WAS_AREA:GRATMICH..... PA-180

Figure PA-41. Logic Diagram for Determining the Intrusion Type PA-199

Figure PA-42. Processing of Input Data to Produce CCDFs PA-201

Figure PA-43. Pressure in the Waste Panel Region, Replicate R1, Scenario S1,
CRA-2009 PA PA-205

Figure PA-44. Primary Correlations of Pressure in the Waste Panel Region with
Uncertain Parameters, Replicate R1, Scenario S1, CRA-2009 PA..... PA-206

Figure PA-45. Brine Saturation in the Waste Panel Region, Replicate R1, Scenario
S1, CRA-2009 PA PA-207

Figure PA-46. Primary Correlations of Brine Saturation in the Waste Panel Region with Uncertain Parameters, Replicate R1, Scenario S1, CRA-2009 PA..... PA-207

Figure PA-47. Brine Flow Away From the Repository, Replicate R1, Scenario S1, CRA-2009 PA PA-208

Figure PA-48. Brine Flow via All MBs Across the LWB, Replicate R1, Scenario S1, CRA-2009 PA PA-209

Figure PA-49. Primary Correlations of Total Cumulative Brine Flow Away from the Repository with Uncertain Parameters, Replicate R1, Scenario S1, CRA-2009 PA PA-210

Figure PA-50. Pressure in the Waste Panel Region for Replicate R1, Scenario S2, CRA-2009 PA PA-214

Figure PA-51. Pressure in the Waste Panel Region for Replicate R1, Scenario S4, CRA-2009 PA PA-214

Figure PA-52. Primary Correlations of Pressure in the Waste Panel Region with Uncertain Parameters, Replicate R1, Scenario S2, CRA-2009 PA..... PA-216

Figure PA-53. Primary Correlations of Pressure in the Waste Panel Region with Uncertain Parameters, Replicate R1, Scenario S4, CRA-2009 PA..... PA-216

Figure PA-54. Brine Saturation in the Waste Panel Region for Replicate R1, Scenario S2, CRA-2009 PA PA-217

Figure PA-55. Brine Saturation in the Waste Panel Region for Replicate R1, Scenario S4, CRA-2009 PA PA-218

Figure PA-56. Primary Correlations of Brine Saturation in the Waste Panel Region with Uncertain Parameters, Replicate R1, Scenario S2, CRA-2009 PA..... PA-218

Figure PA-57. Primary Correlations of Brine Saturation in the Waste Panel Region with Uncertain Parameters, Replicate R1, Scenario S4, CRA-2009 PA..... PA-219

Figure PA-58. Total Cumulative Brine Outflow in Replicate R1, Scenario S2, CRA-2009 PA PA-220

Figure PA-59. Brine Flow via All MBs Across the LWB in Replicate R1, Scenario S2, CRA-2009 PA PA-221

Figure PA-60. Total Cumulative Brine Outflow in Replicate R1, Scenario S4, CRA-2009 PA PA-221

Figure PA-61. Brine Flow via All MBs Across the LWB in Replicate R1, Scenario S4, CRA-2009 PA PA-222

Figure PA-62. Primary Correlations of Cumulative Brine Flow Away from the Repository with Uncertain Parameters, Replicate R1, Scenario S2, CRA-2009 PA PA-223

Figure PA-63. Primary Correlations of Cumulative Brine Flow Away from the Repository with Uncertain Parameters, Replicate R1, Scenario S4, CRA-2009 PA PA-223

Figure PA-64. Total Mobilized Concentrations in Salado Brine, Replicate R1, CRA-2009 PA PA-225

Figure PA-65. Total Mobilized Concentrations in Castile Brine, Replicate R1, CRA-2009 PA PA-225

Figure PA-66. Cumulative Normalized Release to the Culebra, Scenario S2, CRA-2009 PA PA-227

Figure PA-67. Cumulative Normalized Release to the Culebra, Scenario S3, CRA-2009 PA PA-227

Figure PA-68. Cumulative Normalized Release to the Culebra, Scenario S4, CRA-2009 PA PA-228

Figure PA-69. Cumulative Normalized Release to the Culebra, Scenario S5, CRA-2009 PA PA-228

Figure PA-70. Cumulative Normalized Release to the Culebra, Replicate R1, Scenario S6, CRA-2009 PA PA-229

Figure PA-71. Scatterplot of Waste Particle Diameter Versus Spallings Volume, CRA-2009 PA PA-232

Figure PA-72. Scatterplot of Waste Permeability Versus Spallings Volume, CRA-2009 PA PA-233

Figure PA-73. Sensitivity of DBR Volumes to Pressure and Mobile Brine Saturation, Replicate R1, Scenario S2, Lower Panel, CRA-2009 PA PA-236

Figure PA-74. Overall Mean CCDFs for Cuttings and Cavings Releases: CRA-2009 PA and CRA-2004 PABC PA-238

Figure PA-75. Overall Mean CCDFs for Spallings Releases: CRA-2009 PA and CRA 2004 PABC PA-239

Figure PA-76. Overall Mean CCDFs for DBRs: CRA-2009 PA and CRA-2004 PABC..... PA-239

Figure PA-77. Mean CCDFs for Releases from the Culebra for Replicate R2: CRA-2009 PA and CRA-2004 PABC..... PA-241

Figure PA-78. The Preponderance and Distribution of Zeros Can Control the Regression PA-242

Figure PA-79. Total Normalized Releases, Replicates R1, R2, and R3, CRA-2009 PA PA-242

Figure PA-80. Confidence Interval on Overall Mean CCDF for Total Normalized Releases, CRA-2009 PA PA-243

Figure PA-81. Mean CCDFs for Components of Total Normalized Releases, Replicate R1, CRA-2009 PA..... PA-244

Figure PA-82. Mean CCDFs for Components of Total Normalized Releases, Replicate R2, CRA-2009 PA..... PA-244

Figure PA-83. Mean CCDFs for Components of Total Normalized Releases, Replicate R3, CRA-2009 PA..... PA-245

Figure PA-84. Overall Mean CCDFs for Total Normalized Releases: CRA-2009 PA and CRA-2004 PABC PA-245

List of Tables

Table PA-1. WIPP Project Changes and Cross References..... PA-5

Table PA-2. Release Limits for the Containment Requirements..... PA-19

Table PA-3. Parameter Values Used in Representation of Two-Phase Flow PA-57

Table PA-4. Models for Relative Permeability and Capillary Pressure in Two-Phase Flow PA-63

Table PA-5. Initial Conditions in the Rustler PA-66

Table PA-6.	Probabilities for Biodegradation of Different Organic Materials (WAS_AREA:PROBDEG) in the CRA-2009 PA and the CRA-2004 PA	PA-72
Table PA-7.	Permeabilities for Drilling Intrusions Through the Repository.....	PA-81
Table PA-8.	Boundary Value Conditions for P_g and P_b	PA-83
Table PA-9.	Auxiliary Dirichlet Conditions for S_g and P_b	PA-83
Table PA-10.	Calculated Values for Dissolved Solubility	PA-92
Table PA-11.	Scale Factor $SF_{Hum}(Br, Ox, El)$ Used in Definition of $S_{Hum}(Br, Ox, El)$	PA-93
Table PA-12.	Scale Factor $SF_{Mic}(Ox, El)$ and Upper Bound $UB_{Mic}(Ox, El)$ (mol/L) Used in Definition of $S_{Mic}(Br, Ox, El)$	PA-93
Table PA-13.	Combination of Radionuclides for Transport.....	PA-96
Table PA-14.	Initial and Boundary Conditions for $C_{bl}(x, y, t)$ and $C_{sl}(x, y, t)$	PA-98
Table PA-15.	Uncertain Parameters in the DRSPALL Calculations.....	PA-129
Table PA-16.	Initial Porosity in the DBR Calculation	PA-135
Table PA-17.	Boundary Conditions for p_b and S_g in DBR Calculations.....	PA-139
Table PA-18.	Radionuclide Culebra Transport Diffusion Coefficients.....	PA-163
Table PA-19.	Variables Representing Epistemic Uncertainty in the CRA-2009 PA	PA-164
Table PA-20.	Sampled Parameters Added Since the CRA-2004 PA	PA-177
Table PA-21.	Sampled Parameters Removed Since the CRA-2004 PA	PA-177
Table PA-22.	Correlation Observed Between Variables S_HALITE:PRMX_LOG and S_HALITE:COMP_RCK in Replicate 1	PA-184
Table PA-23.	Correlation Observed Between Variables CASTILER:PRMX_LOG and CASTILER:COMP_RCK in Replicate 1	PA-184
Table PA-24.	Algorithm to Generate a Single Future	PA-185
Table PA-25.	BRAGFLO Scenarios in the CRA-2009 PA	PA-188
Table PA-26.	NUTS Release Calculations in the CRA-2009 PA	PA-190
Table PA-27.	CUTTINGS_S Release Calculations in the CRA-2009 PA	PA-191
Table PA-28.	MODFLOW Scenarios in the CRA-2009 PA	PA-193
Table PA-29.	SECOTP2D Scenarios in the CRA-2004 PA	PA-193
Table PA-30.	Number of Realizations with Radionuclide Transport to the LWB Under Partial-Mining Conditions.....	PA-230
Table PA-31.	Number of Realizations with Radionuclide Transport to the LWB Under Full-Mining Conditions.....	PA-231
Table PA-32.	CRA-2009 PA Cuttings and Cavings Area Statistics.....	PA-232
Table PA-33.	CRA-2009 PA Spallings Volume Statistics	PA-234
Table PA-34.	CRA-2009 PA DBR Volume Statistics.....	PA-235
Table PA-35.	CRA-2009 PA and CRA-2004 PABC Statistics on the Overall Mean for Total Normalized Releases in EPA Units at Probabilities of 0.1 and 0.001	PA-246

Acronyms and Abbreviations

%	percent
AIC	active institutional control
An	actinide
BRAGFLO	BRine And Gas FLOW computer code
C	Celsius
CCA	Compliance Certification Application
CCDF	complementary cumulative distribution function
CDF	cumulative distribution function
CFR	Code of Federal Regulations
CH-TRU	contact-handled transuranic
Ci	curies
CL	Confidence Limit
CPR	cellulosic, plastic, and rubber
CRA	Compliance Recertification Application
DBR	direct brine release
DDZ	drilling damaged zone
DOE	U.S. Department of Energy
DP	disturbed repository performance
DRZ	disturbed rock zone
E	deep drilling scenario
EPA	U.S. Environmental Protection Agency
ERDA	U.S. Energy Research and Development Administration
FEP	feature, event, and process
FMT	Fracture-Matrix Transport
FVW	fraction of excavated repository volume occupied by waste
gal	gallon
GWB	Generic Weep Brine
in	inch
J	Joule
K	Kelvin
K_d	distribution coefficient

kg	kilogram
km	kilometer
km ²	square kilometers
L	liter
LHS	Latin hypercube sampling
LWB	land withdrawal boundary
M	mining scenario
m	meter
m ²	square meters
m ³	cubic meters
MB	marker bed
ME	mining and drilling scenario
mi	miles
mol	mole
MPa	megapascal
MTHM	metric tons of heavy metal
MWd	megawatt-days
N	Newton
Pa	Pascal
PA	performance assessment
PABC	performance assessment baseline calculation
PAVT	Performance Assessment Verification Test
PCC	partial correlation coefficient
PCS	panel closure system
PDE	partial differential equation
PDF	probability distribution function
PIC	passive institutional control
PRCC	partial rank correlation coefficient
RH-TRU	remote-handled transuranic
RKS	Redlich-Kwong-Soave
RoR	Rest of Repository
s	second

s ²	seconds squared
SCF/d	standard cubic feet per day
SMC	Salado Mass Concrete
SNL	Sandia National Laboratories
SRC	standardized regression coefficient
T field	transmissivity field
TRU	transuranic
TVD	Total Variation Diminishing
UP	undisturbed repository performance
WIPP	Waste Isolation Pilot Plant
yr	year

Elements and Chemical Compounds

Al	aluminum
Am	americium
C	carbon
C ₆ H ₁₀ O ₅	generic formula for CPR
Ca	calcium
CH ₄	methane
Cm	curium
CO ₂	carbon dioxide
Cr	chromium
Cs	cesium
Fe	iron
H ₂	hydrogen gas
H ₂ O	water
H ₂ S	hydrogen sulfide
I	iodine
Mg	magnesium
Mg(OH) ₂	brucite
Mg ₅ (CO ₃) ₄ (OH) ₂ ·4H ₂ O	hydromagnesite (5424)

MgO	magnesium oxide, or periclase
Mn	manganese
Ni	nickel
NO ₃ ⁻	nitrate
Np	neptunium
Pb	lead
Pm	promethium
Pu	plutonium
Ra	radium
Sn	tin
SO ₄	sulfate
SO ₄ ²⁻	sulfate ion
Sr	strontium
Tc	technetium
Th	thorium
U	uranium
V	vanadium

1 PA-1.0 Introduction

2 This appendix presents the mathematical models used to evaluate performance of the Waste
3 Isolation Pilot Plant (WIPP) disposal system and the results of these models for the 2009
4 Compliance Recertification Application (CRA-2009) Performance Assessment (PA). The term
5 PA signifies an analysis that (1) identifies the processes and events that might affect the disposal
6 system; (2) examines the effects of these processes and events on the performance of the disposal
7 system; and (3) estimates the cumulative releases of radionuclides, considering the associated
8 uncertainties, caused by all significant processes and events (40 CFR § 191.12 [U.S.
9 Environmental Protection Agency 1993]). PA is designed to address three primary questions
10 about the WIPP:

11 Q1: What processes and events that might affect the disposal system could take place at the
12 WIPP site over the next 10,000 years?

13 Q2: How likely are the various processes and events that might affect the disposal system to
14 take place at the WIPP site over the next 10,000 years?

15 Q3: What are the consequences of the various processes and events that might affect the
16 disposal system that could take place at the WIPP site over the next 10,000 years?

17 In addition, accounting for uncertainty in the parameters of the PA models leads to a further
18 question:

19 Q4: How much confidence should be placed in answers to the first three questions?

20 These questions give rise to a methodology for quantifying the probability distribution of
21 possible radionuclide releases from the WIPP repository over the next 10,000 years and
22 characterizing the uncertainty in that distribution due to imperfect knowledge about the
23 parameters contained in the models used to predict releases. The containment requirements of 40
24 CFR § 191.13 require this probabilistic methodology.

25 This appendix is organized as follows: Section PA-2.0 gives an overview and describes the
26 overall conceptual structure of the CRA-2009 PA. The WIPP PA is designed to address the
27 requirements of section 191.13, and thus involves three basic entities: (1) a probabilistic
28 characterization of different futures that could occur at the WIPP site over the next 10,000 years,
29 (2) models for both the physical processes that take place at the WIPP site and the estimation of
30 potential radionuclide releases that may be associated with these processes, and (3) a
31 probabilistic characterization of the uncertainty in the models and parameters that underlies the
32 WIPP PA. Section PA-2.0 is supplemented by Appendix SCR-2009, which documents the
33 results of the screening process for features, events, and processes (FEPs) that are retained in the
34 conceptual models of repository performance.

35 Section PA-3.0 describes the probabilistic characterization of different futures. This
36 characterization plays an important role in the construction of the complementary cumulative
37 distribution function (CCDF) specified in section 191.13. Regulatory guidance and extensive
38 review of the WIPP site identified exploratory drilling for natural resources and the mining of

1 potash as the only significant disruptions at the WIPP site with the potential to affect
2 radionuclide releases to the accessible environment. Section PA-3.0 summarizes the stochastic
3 variables that represent future drilling and mining events in the PA. The results of the PA for
4 CRA-2009, as documented in Section PA-7.0, Section PA-8.0, and Section PA-9.0 of this
5 appendix, confirm that direct releases from drilling intrusions are the major contributors to
6 radionuclide releases to the accessible environment.

7 Section PA-4.0 presents the mathematical models for both the physical processes that take place
8 at the WIPP and the estimation of potential radionuclide releases. The mathematical models
9 implement the conceptual models as prescribed in 40 CFR § 194.23 (2004), and permit the
10 construction of the CCDF specified in section 191.13. Models presented in Section PA-4.0
11 include two-phase (i.e., gas and brine) flow in the vicinity of the repository; radionuclide
12 transport in the Salado Formation (hereafter referred to as the Salado); releases to the surface at
13 the time of a drilling intrusion due to cuttings, cavings, spallings, and direct brine releases
14 (DBRs); brine flow in the Culebra Dolomite Member of the Rustler Formation (hereafter
15 referred to as the Culebra); and radionuclide transport in the Culebra. Section PA-4.0 is
16 supplemented by Appendices MASS-2009, TFIELD-2009, and PORSURF-2009. Appendix
17 MASS-2009 discusses the modeling assumptions used in the WIPP PA. Appendix TFIELD-
18 2009 discusses the generation of the transmissivity fields (T fields) used to model groundwater
19 flow in the Culebra. Appendix PORSURF-2009 presents results from modeling the effects of
20 excavated region closure, waste consolidation, and gas generation in the repository.

21 Section PA-5.0 discusses the probabilistic characterization of parameter uncertainty, and
22 summarizes the uncertain variables incorporated into the CRA-2009 PA, the distributions
23 assigned to these variables, and the correlations between variables. Section PA-5.0 is
24 supplemented by Fox (2008) and Appendix SOTERM-2009. Fox (2008) catalogs the full set of
25 parameters used in the CRA-2009 PA, previously referred to as the CCA Appendix PAR and the
26 CRA-2004, Appendix PA, Attachment PAR. Appendix SOTERM-2009 describes the actinide
27 (An) source term for the WIPP performance calculations, including the mobile concentrations of
28 actinides that may be released from the repository in brine.

29 Section PA-6.0 summarizes the computational procedures used in the CRA-2009 PA, including
30 sampling techniques (i.e., random and Latin hypercube sampling (LHS)); sample size, statistical
31 confidence for mean CCDF, generation of sample, generation of individual futures, construction
32 of CCDFs, calculations performed with the models discussed in Section PA-4.0, construction of
33 releases for each future, and the sensitivity analysis techniques in use.

34 Section PA-7.0 presents the results of the PA for an undisturbed repository. Releases from the
35 undisturbed repository are determined by radionuclide transport in brine flowing from the
36 repository to the land withdrawal boundary (LWB) through the marker beds (MBs) or shafts.
37 Releases in the undisturbed scenario are used to demonstrate compliance with the individual and
38 groundwater protection requirements in 40 CFR Part 191 (40 CFR § 194.51 and 40 CFR
39 § 194.52).

40 Section PA-8.0 presents PA results for a disturbed repository. As will be discussed in Section
41 PA-2.3.1, the only future events and processes in the analysis of disturbed repository
42 performance are those associated with mining and deep drilling. Release mechanisms include

1 direct releases at the time of the intrusion via cuttings, cavings, spillings, and DBR, and long-
2 term releases via radionuclide transport up abandoned boreholes to the Culebra and thence to the
3 LWB.

4 Section PA-9.0 presents the set of CCDFs resulting from the CRA-2009 PA. This material
5 supplements 40 CFR § 194.34, which demonstrates compliance with the containment
6 requirements of section 191.13. Section PA-9.0 presents the most significant output variables
7 from the PA models, accompanied by sensitivity analyses to determine which subjectively
8 uncertain parameters are most influential in the uncertainty of PA results.

9 The overall structure of the CRA-2009 PA does not differ from that presented in the first WIPP
10 Compliance Certification Application (CCA) (U.S. Department of Energy 1996), the CRA-2004
11 (U.S. Department of Energy 2004) or the CRA-2004 Performance Assessment Baseline
12 Calculation (PABC) (Leigh et al. 2005). This recertification application appendix follows the
13 approach used by Helton et al. (1998) to document the mathematical models used in the CCA PA
14 and the results of that analysis. Much of the content of this appendix derives from Helton et al.
15 (1998); these authors' contributions are gratefully acknowledged.

1 **PA-2.0 Overview and Conceptual Structure of the PA**

2 Because of the amount and complexity of the material presented in Appendix PA-2009, an
3 introductory summary is provided below, followed by detailed discussions of the topics in the
4 remainder of this section, which is organized as follows:

5 Section PA-2.1 – Overview of PA and the results

6 Section PA-2.2 – The conceptual structure of the PA used to evaluate compliance with the
7 containment requirements

8 Section PA-2.3 – The overall methodology used to develop FEPs, the screening methodology
9 applied to the FEPs, the results of the screening process, and the development
10 of the scenarios considered in the system-level consequence analysis

11 The U.S. Department of Energy (DOE) continues to use the same PA methodology as in the
12 CCA and CRA-2004 because changes that have been made since the U.S. Environmental
13 Protection Agency (EPA) certified WIPP do not impact PA methodology. A corresponding
14 detailed presentation for the CRA-2004 PA methodology is provided in the CRA-2004, Chapter
15 6.0, Section 6.1, and a detailed presentation for the CRA-2004 PABC implementation is
16 provided in Leigh et al. (2005). A corresponding detailed presentation for the CCA PA
17 methodology is provided in Helton et al. (1998, Section 2).

18 **PA-2.1 Overview of Performance Assessment**

19 A demonstration of future repository performance was required by the disposal standards in Part
20 191. The EPA required a PA to demonstrate that potential cumulative releases of radionuclides
21 to the accessible environment over a 10,000-year period after disposal are less than specified
22 limits based on the nature of the materials disposed (section 191.13). The PA is to determine the
23 effects of all significant processes and events that may affect the disposal system, consider the
24 associated uncertainties of the processes and events, and estimate the probable cumulative
25 releases of radionuclides.

26 A PA was included in the CCA. This was the first demonstration of compliance by the DOE
27 with the EPA's disposal standards. The EPA required a verification PA based on the CCA PA
28 that included revised parameters and distributions. This PA was termed the CCA Performance
29 Assessment Verification Test (PAVT) (Trovoto 1997). The EPA based the original certification
30 of the WIPP on the information in the CCA and the results of the CCA PAVT (U.S.
31 Environmental Protection Agency 1998a). The CCA PAVT is documented in Sandia National
32 Laboratories (SNL) 1997 and U.S. Department of Energy 1997.

33 The WIPP is required to be recertified every five years after first waste receipt (Public Law
34 02-579). A revised PA was included in the first recertification application in 2004. This PA is
35 termed the CRA-2004 PA, and is documented in the CRA-2004, Chapter 6.0. The EPA again
36 required a verification PA using revised modeling assumptions and parameters (Cotsworth
37 2005). This PA was termed the CRA-2004 PABC and was documented in Leigh et al. (2005).

1 As part of the five-year recertification cycle, a PA is included in the CRA-2009. The CRA-2009
 2 PA is a culmination of the previous PAs and is not significantly different from the CRA-2004
 3 PABC, as the methodologies, conceptual models, and assumptions have not changed. Updates to
 4 parameters and improvements to computer codes are incorporated in the CRA-2009.

5 **PA-2.1.1 Changes in the CRA-2009 PA**

6 A list of changes to PA since the CRA-2004 and citations for where they are discussed is shown
 7 in Table PA-1. In addition to the changes discussed in Table PA-1, the terminology used to
 8 describe uncertainty has been updated to reflect the usage now prevalent in the risk assessment
 9 literature. Previously, uncertainty in model parameters was referred to as “subjective
 10 uncertainty,” and that due to stochastic processes was referred to as “stochastic uncertainty.” In
 11 the years since these terms were first employed, these concepts have matured, and the term
 12 “epistemic uncertainty” is now used to describe uncertainty from lack of knowledge, while the
 13 term “aleatory uncertainty” now describes uncertainty due to natural variability, e.g. uncertainty
 14 arising from future events whose occurrence can be defined in terms of probabilities. In this text,
 15 the terms epistemic uncertainty and aleatory uncertainty are used in place of the terms subjective
 16 uncertainty and stochastic uncertainty, respectively.

17 **Table PA-1. WIPP Project Changes and Cross References**

WIPP Project Change	Cross Reference
CRA-2004 to CRA-2004 PABC Changes^a	
Inventory Information	Leigh, Trone, and Fox 2005
An Solubility Values	Garner and Leigh 2005
An Solubility Uncertainty Ranges	Garner and Leigh 2005
Microbial Gas Generation Model	Nemer and Stein 2005
Culebra T Fields Mining Modification	Lowry and Kanney 2005
Anhydrite Material Parameters	Vugrin et al. 2005
SPALL Model Parameters	Vugrin 2005
CRA-2004 PABC to CRA-2009 Changes^b	
DBR Maximum Duration Parameter	Kirkes 2007
Conditional Relationship Between Humid and Inundated Cellulosic, Plastic, or Rubber (CPR) Degradation Rates	Kirchner 2008a
BRAGFLO Code Improvements	Nemer and Clayton 2008
Capillary Pressure and Relative Permeability Model	Nemer and Clayton 2008
Drilling Rate	Clayton 2008a
Parameter Error Corrections <ul style="list-style-type: none"> • Emplaced CPR • Halite/Disturbed Rock Zone (DRZ) Parameter • Fraction of Repository Occupied by Waste • NUTS and DBR Calculation Input Files 	Nemer 2007a, Ismail 2007a, Dunagan 2007, Ismail 2007b, Clayton 2007

^a See Leigh et al. 2005 for additional discussion of these changes and their implementation in the CRA-2004 PABC.

^b See Clayton et al. 2008 for additional discussions of these changes and their implementation in the CRA-2009 PA.

1 From this assessment, the DOE has demonstrated that the WIPP continues to comply with the
2 containment requirements of section 191.13. The containment requirements are stringent and
3 state that the DOE must demonstrate a reasonable expectation that the probabilities of
4 cumulative radionuclide releases from the disposal system during the 10,000 years following
5 closure will fall below specified limits. The PA analyses supporting this determination must be
6 quantitative and consider uncertainties caused by all significant processes and events that may
7 affect the disposal system, including future inadvertent human intrusion into the repository. A
8 quantitative PA is conducted using a series of loosely coupled computer models in which
9 epistemic parameter uncertainties are addressed by a stratified Monte Carlo sampling procedure
10 on selected input parameters, and uncertainties related to future intrusion events are addressed
11 using simple random sampling.

12 As required by regulation, results of the PA are displayed as CCDFs showing the probability that
13 cumulative radionuclide releases from the disposal system will exceed the values calculated for
14 scenarios considered in the analysis. These CCDFs are calculated using reasonable and, in some
15 cases, conservative conceptual models based on the scientific understanding of the disposal
16 system's behavior. Parameters used in these models are derived from experimental data, field
17 observations, and relevant technical literature. Changes to the CCA and CRA-2004 parameters
18 and models since the original certification have been incorporated into the CRA-2009 PA
19 (Clayton 2008a). The overall mean CCDF continues to lie entirely below the specified limits,
20 and the WIPP therefore continues to be in compliance with the containment requirements of 40
21 CFR Part 191 Subpart B (see Section PA-2.1.6). Sensitivity analysis of results shows that the
22 location of the mean CCDF is dominated by radionuclide releases that could occur on the surface
23 during an inadvertent penetration of the repository by a future drilling operation (Section PA-
24 9.0). Releases of radionuclides to the accessible environment from transport in groundwater
25 through the shaft seal systems and the subsurface geology are negligible, with or without human
26 intrusion, and do not significantly contribute to the mean CCDF. No releases are predicted to
27 occur at the ground surface in the absence of human intrusion. The natural and engineered barrier
28 systems of the WIPP provide robust and effective containment of transuranic (TRU) waste, even
29 if the repository is penetrated by multiple boreholes.

30 **PA-2.1.2 Conceptual Basis for PA**

31 The foundations of PA are a thorough understanding of the disposal system and the possible
32 future interactions of the repository, waste, and surrounding geology. The DOE's confidence in
33 the results of PA is based in part on the strength of the original research done during site
34 characterization, experimental results used to develop and confirm parameters and models, and
35 robustness of the facility design.

36 The progression of compliance applications document these aspects of PA leading up to the
37 CRA-2009 PA (i.e., the CCA, the CCA PAVT [Sandia National Laboratories 1997 and U.S.
38 Department of Energy 1997], the CRA-2004 PA, and the CRA-2004 PABC [Leigh et al. 2005]).

39 The interactions of the repository and waste with the geologic system, and the response of the
40 disposal system to possible future inadvertent human intrusion, are described in Section PA-
41 2.1.4.

1 **PA-2.1.3 Undisturbed Repository Performance**

2 An evaluation of undisturbed repository performance, which is defined to exclude human
3 intrusion and unlikely disruptive natural events, is required by regulation (see 40 CFR § 191.15
4 and 40 CFR § 191.24). Evaluations of past and present natural geologic processes in the region
5 indicate that none has the potential to breach the repository within 10,000 years (see the CCA,
6 Appendix SCR, Section SCR.1). Disposal system behavior is dominated by the coupled
7 processes of rock deformation surrounding the excavation, fluid flow, and waste degradation.
8 Each of these processes can be described independently, but the extent to which they occur is
9 affected by the others.

10 Rock deformation immediately around the repository begins as soon as excavation creates a
11 disturbance in the stress field. Stress relief results in some degree of brittle fracturing and the
12 formation of a DRZ, which surrounds excavations in all deep mines including the WIPP
13 repository. For the WIPP, the DRZ is characterized by an increase in permeability and porosity,
14 and it may ultimately extend a few meters (m) from the excavated region. Salt will also deform
15 by creep processes resulting from deviatoric stress, causing the salt to move inward and fill
16 voids. Salt creep will continue until deviatoric stress is dissipated and the system is once again at
17 stress equilibrium (see the CRA-2004, Chapter 6.0, Section 6.4.3.1).

18 The ability of salt to creep, thereby healing fractures and filling porosity, is one of its
19 fundamental advantages as a medium for geologic disposal of radioactive waste, and one reason
20 it was recommended by the National Academy of Sciences (see the CCA, Chapter 1.0, Section
21 1.3). Salt creep provides the mechanism for crushed salt compaction in the shaft seal system,
22 yielding properties approaching those of intact salt within 200 years (see the CCA, Appendix
23 SEAL, Appendix D, Section D5.2). Salt creep will also cause the DRZ surrounding the shaft to
24 heal rapidly around the concrete components of the seal system. In the absence of elevated gas
25 pressure in the repository, salt creep would also substantially compact the waste and heal the
26 DRZ around the disposal region. Fluid pressures can become large enough through the
27 combined effect of salt creep reducing pore volumes, and gas generation from waste degradation
28 processes, to maintain significant porosity (greater than 20%) within the disposal room
29 throughout the performance period (see also the CRA-2004, Chapter 6.0, Section 6.4.3).

30 Characterization of the Salado indicates that fluid flow from the far field does not occur on time
31 scales of interest in the absence of an artificially imposed hydraulic gradient (see the CRA-2004,
32 Chapter 2.0, Section 2.1.3.4 for a description of Salado investigations). This lack of fluid flow is
33 the second fundamental reason for choosing salt as a medium for geologic disposal of radioactive
34 waste. Lack of fluid flow is a result of the extremely low permeability of evaporite rocks that
35 make up the Salado. Excavating the repository has disturbed the natural hydraulic gradient and
36 rock properties, resulting in fluid flow. Small quantities of interstitial brine present in the Salado
37 move toward regions of low hydraulic potential, and brine seeps are observed in the underground
38 repository. The slow flow of brine from halite into more permeable anhydrite MBs, and then
39 through the DRZ into the repository, is expected to continue as long as the hydraulic potential
40 within the repository is below that of the far field. The repository environment will also include
41 gas, so the fluid flow must be modeled as a two-phase process. Initially, the gaseous phase will
42 consist primarily of air trapped at the time of closure, although other gases may form from waste
43 degradation. In the PA, the gaseous phase pressure will rise due to creep closure, gas generation,

1 and brine inflow, creating the potential for flow from the excavated region (see also the
2 CRA-2004, Chapter 6.0, Section 6.4.3.2).

3 An understanding of waste degradation processes indicates that the gaseous phase in fluid flow
4 and the repository's pressure history will be far more important than if the initial air were the
5 only gas present. Waste degradation can generate significant additional gas by two processes
6 (see also the CRA-2004, Chapter 6.0, Section 6.4.3.3 for historical perspective, and Leigh et al.
7 2005, Section 2.3 and Section 2.4 for changes):

- 8 1. The generation of hydrogen (H_2) gas by anoxic corrosion of steels, other iron (Fe)-based
9 alloys, and aluminum (Al) and Al-based alloys
- 10 2. The generation of carbon dioxide (CO_2), hydrogen sulfide (H_2S), and methane (CH_4) by
11 anaerobic microbial consumption of waste containing CPR materials

12 Coupling these gas-generation reactions to fluid-flow and salt-creep processes is complex. Gas
13 generation will increase fluid pressure in the repository, thereby decreasing the hydraulic
14 gradient and deviatoric stress between the far field and the excavated region and inhibiting the
15 processes of brine inflow and salt creep. Anoxic corrosion will also consume brine as it breaks
16 down water to oxidize steels and other Fe-based alloys and release H_2 . Thus, corrosion has the
17 potential to be a self-limiting process, in that as it consumes all water in contact with steels and
18 other Fe-based alloys, it will cease. Microbial reactions also require water, either in brine or the
19 gaseous phase. It is assumed that microbial reactions will result in neither the consumption nor
20 production of water.

21 The total volume of gas generated by corrosion and microbial consumption may be sufficient to
22 result in repository pressures that approach lithostatic. Sustained pressures above lithostatic are
23 not physically reasonable within the disposal system, because the more brittle anhydrite layers
24 are expected to fracture if sufficient gas is present. The conceptual model implemented in the
25 PA causes anhydrite MB permeability and porosity to increase rapidly as pore pressure
26 approaches and exceeds lithostatic. This conceptual model for pressure-dependent fracturing
27 approximates the hydraulic effect of pressure-induced fracturing and allows gas and brine to
28 move more freely within the MBs at higher pressures (see the CRA-2004, Chapter 6.0, Section
29 6.4.5.2).

30 Overall, the behavior of the undisturbed disposal system will result in extremely effective
31 isolation of the radioactive waste. Concrete, clay, and asphalt components of the shaft seal
32 system will provide an immediate and effective barrier to fluid flow through the shafts, isolating
33 the repository until salt creep has consolidated the compacted crushed salt components and
34 permanently sealed the shafts. Around the shafts, the DRZ in halite layers will heal rapidly
35 because the presence of the solid material within the shafts will provide rigid resistance to creep.
36 The DRZ around the shaft, therefore, will not provide a continuous pathway for fluid flow (see
37 the CRA-2004, Chapter 6.0, Section 6.4.4). Similarly, the panel closure will rigidly resist creep,
38 leading to a build-up of compressive stress which in turn will cause a rapid elimination of the
39 DRZ locally. In PA, it is conservatively assumed that the DRZ does not heal around either the
40 disposal region or the operations and experimental regions, and pathways for fluid flow may
41 exist indefinitely to the overlying and underlying anhydrite layers (e.g., MB 139 and Anhydrites

1 A and B). Some quantity of brine will be present in the repository under most conditions and
2 may contain actinides mobilized as both dissolved and colloidal species. Gas generation by
3 corrosion and microbial degradation is expected to occur, and will result in elevated pressures
4 within the repository. These pressures will not significantly exceed lithostatic because the more
5 brittle anhydrite layers will fracture and provide a pathway for gas to leave the repository.
6 Fracturing due to high gas pressures may enhance gas and brine migration from the repository,
7 but gas transport will not contribute to the release of actinides from the disposal system. Brine
8 flowing out of the waste disposal region through anhydrite layers may transport actinides as
9 dissolved and colloidal species. However, the quantity of actinides that may reach the accessible
10 environment boundary through the interbeds during undisturbed repository performance is
11 insignificant and has no effect on the compliance determination. No migration of radionuclides
12 is expected to occur vertically through the Salado (see Section PA-7.0, and Ismail and Garner
13 2008).

14 **PA-2.1.4 Disturbed Repository Performance**

15 The WIPP PA is required by the performance standards to consider scenarios that include
16 intrusions into the repository by inadvertent and intermittent drilling for resources. The
17 probability of these intrusions is based on a future drilling rate. This rate was calculated using the
18 method outlined in Section 33, which analyzes the past record of drilling events in the Delaware
19 Basin. Active institutional controls (AICs) are assumed to prevent intrusion during the first 100
20 years after closure (40 CFR § 194.41). Passive institutional controls (PICs) were assumed in the
21 CCA to effectively reduce the drilling rate by two orders of magnitude for the 600-year period
22 following 100 years of active control. However, in certifying the WIPP, the EPA denied credit
23 for the effectiveness of passive controls for 600 years (U.S. Environmental Protection Agency
24 1998a). Although the CRA-2009 PA does not include a reduced drilling intrusion rate to account
25 for PICs, future PAs may do so. Future drilling practices are assumed to be the same as current
26 practice, also consistent with regulatory criteria. These practices include the type and rate of
27 drilling, emplacement of casing in boreholes, and the procedures implemented when boreholes
28 are plugged and abandoned (see 40 CFR § 194.33).

29 Human intrusion by drilling may cause releases from the disposal system through five
30 mechanisms:

- 31 1. Cuttings, which include material intersected by the rotary drilling bit
- 32 2. Cavings, which include material eroded from the borehole wall during drilling
- 33 3. Spallings, which include solid material carried into the borehole during rapid
34 depressurization of the waste disposal region
- 35 4. DBRs, which include contaminated brine that may flow to the surface during drilling
- 36 5. Long-term brine releases, which include the contaminated brine that may flow through a
37 borehole after it is abandoned

1 The first four mechanisms immediately follow an intrusion event and are collectively referred to
2 as direct releases. The accessible environment boundary for these releases is the ground surface.
3 The fifth mechanism, An transport by long-term groundwater flow, begins when concrete plugs
4 are assumed to degrade in an abandoned borehole and may continue throughout the regulatory
5 period. The accessible environment boundary for these releases is the lateral subsurface limit of
6 the controlled area (CRA-2004, Chapter 6.0, Section 6.0.2.3).

7 Repository conditions prior to intrusion will be the same as those for undisturbed repository
8 performance, and all processes active in undisturbed repository performance will continue to
9 occur following intrusion. Because an intrusion provides a pathway for radionuclides to reach
10 the ground surface and enter the geological units above the Salado, additional processes will
11 occur that don't in the undisturbed repository performance. These processes include the
12 mobilization of radionuclides as dissolved and colloidal species in repository brine and
13 groundwater flow, and subsequent An transport in the overlying units. Flow and transport in the
14 Culebra are of particular interest because it is the most transmissive unit above the repository.
15 Thus, the Culebra is a potential pathway for lateral migration of contaminated brine in the event
16 of a drilling intrusion accompanied by significant flow up the intrusion borehole (see the
17 CRA-2004, Chapter 6.0, Section 6.4.6.2).

18 **PA-2.1.4.1 Cuttings and Cavings**

19 In a rotary drilling operation, the volume of material brought to the surface as cuttings is
20 calculated as the cylinder defined by the thickness of the unit and the diameter of the drill bit.
21 The quantity of radionuclides released as cuttings is therefore a function of the activity of the
22 intersected waste and the diameter of the intruding drill bit. The DOE uses a constant value of
23 0.31115 m (12.25 inches [in]), consistent with bits currently used at the WIPP depth in the
24 Delaware Basin (see the CRA-2004, Chapter 6.0, Section 6.4.12.5). The intersected waste
25 activity may vary depending on the type of waste intersected. The DOE considers random
26 penetrations into remote-handled (RH) transuranic (TRU) (RH-TRU) waste and each of the 690
27 different waste streams (Leigh, Trone, and Fox 2005, Section 4.4) identified for contact-handled
28 (CH) transuranic (TRU) (CH-TRU) waste (569 and 693 waste streams were used in the CCA and
29 the CRA-2004, respectively; see the CRA-2004, Chapter 6.0, Section 6.0.2.3.1).

30 The volume of particulate material eroded from the borehole wall by the drilling fluids and
31 brought to the surface as cavings may be affected by the drill bit diameter, effective shear
32 resistance of the intruded material, speed of the drill bit, viscosity of the drilling fluid and rate at
33 which it is circulated in the borehole, and other properties related to the drilling process. The
34 most important of these parameters, after drill bit diameter, is the effective shear resistance of the
35 intruded material (Leigh et al. 2005, Section 7.2). In the absence of data describing the
36 reasonable and realistic future properties of degraded waste and magnesium oxide (MgO)
37 backfill, the DOE used conservative parameter values based on the properties of fine-grained
38 sediment. Other properties are assigned fixed values consistent with current practice. The
39 quantity of radionuclides released as cavings depends on the volume of eroded material and its
40 activity, which is treated in the same manner as the activity of cuttings (see also Section PA-4.5
41 and Section PA-6.8.2.1).

1 **PA-2.1.4.2 Spallings**

2 Unlike releases from cuttings and cavings, which occur with every modeled borehole intrusion,
3 spalling releases will occur only if pressure in the waste-disposal region exceeds the hydrostatic
4 pressure in the borehole. At lower pressures, below about 8 megapascals (MPa), fluid in the
5 waste-disposal region will not flow toward the borehole. At higher pressures, gas flow toward
6 the borehole may be sufficiently rapid to cause additional solid material to enter the borehole. If
7 spalling occurs, the volume of spalled material will be affected by the physical properties of the
8 waste, such as its tensile strength and particle diameter. The DOE based the parameter values
9 used in the PA on reasonable and conservative assumptions. Since the CCA, a revised
10 conceptual model for the spallings phenomena has been developed (see the CRA-2004,
11 Appendix PA, Section PA-4.6 and Appendix PA, Attachment MASS, Section MASS-16.1.3).
12 Model development, execution, and sensitivity studies necessitated implementing parameter
13 values pertaining to waste characteristics, drilling practices, and physics of the process. The
14 parameter range for particle size was derived by expert elicitation (Carlsbad Area Office
15 Technical Assistance Contractor [CTAC] 1997).

16 The quantity of radionuclides released as spalled material depends on the volume of spalled
17 waste and its activity. Because spalling may occur at a greater distance from the borehole than
18 cuttings and cavings, spalled waste is assumed to have the volume-averaged activity of CH-TRU
19 waste, rather than the sampled activities of individual waste streams. The low permeability of
20 the region surrounding the RH-TRU waste means it is isolated from the spallings process and
21 does not contribute to the volume or activity of spalled material (see also Section PA-4.6 and
22 Section PA-6.8.2.2 for more description of the spallings model).

23 **PA-2.1.4.3 Direct Brine Flow**

24 Radionuclides may be released to the accessible environment if repository brine enters the
25 borehole during drilling and flows to the ground surface. The quantity of radionuclides released
26 by direct brine flow depends on the volume of brine reaching the ground surface and the
27 concentration of radionuclides contained in the brine. As with spallings, DBRs will not occur if
28 repository pressure is below the hydrostatic pressure in the borehole. At higher repository
29 pressures, mobile brine present in the repository will flow toward the borehole. If the volume of
30 brine flowing from the repository into the borehole is small, it will not affect the drilling
31 operation, and flow may continue until the driller reaches the base of the evaporite section and
32 installs casing in the borehole (see also Section PA-4.7 and Section PA-6.8.2.3).

33 **PA-2.1.4.4 Mobilization of Actinides in Repository Brine**

34 Actinides may be mobilized in repository brine in two principal ways:

- 35 1. As dissolved species
- 36 2. As colloidal species

37 The solubilities of actinides depend on their oxidation states, with the more reduced forms (for
38 example, III and IV oxidation states) being less soluble than the oxidized forms (V and VI).

1 Conditions within the repository will be strongly reducing because of large quantities of metallic
2 Fe in the steel containers and the waste, and—in the case of plutonium (Pu)—only the lower-
3 solubility oxidation states (Pu(III) and Pu(IV)) will persist. Microbial activity will also help
4 create reducing conditions. Solubilities also vary with pH. The DOE is therefore emplacing
5 MgO in the waste-disposal region to ensure conditions that reduce uncertainty and establish low
6 An solubilities. MgO consumes CO₂ and buffers pH, lowering An solubilities in WIPP brines
7 (see Appendix SOTERM-2009 and Appendix MgO-2009). Solubilities in the PA are based on
8 the chemistry of brines that might be present in the waste-disposal region, reactions of these
9 brines with the MgO engineered barrier, and strongly reducing conditions produced by anoxic
10 corrosion of steels and other Fe-based alloys.

11 The waste contains organic ligands that could increase An solubilities by forming complexes
12 with dissolved An species. However, these organic ligands also form complexes with other
13 dissolved metals, such as magnesium (Mg), calcium (Ca), Fe, lead (Pb), vanadium (V),
14 chromium (Cr), manganese (Mn), and nickel (Ni), that will be present in repository brines due to
15 corrosion of steels and other Fe-based alloys. The CRA-2009 PA speciation and solubility
16 calculations include the effect of organic ligands but not the beneficial effect of competition with
17 Fe, Pb, V, Cr, Mn, and Ni. (Appendix SOTERM-2009, Section SOTERM-2.3.6 and Section
18 SOTERM-4.6, and Brush and Xiong 2005).

19 Colloidal transport of actinides has been examined, and four types of colloids have been
20 determined to represent the possible behavior at the WIPP. These include microbial colloids,
21 humic substances, An intrinsic colloids, and mineral fragments. Concentrations of An mobilized
22 as these colloidal forms are included in the estimates of total An concentrations used in PA
23 (Appendix SOTERM-2009, Section SOTERM-3.8.1 and Section SOTERM-4.7, and Garner and
24 Leigh 2005).

25 **PA-2.1.4.5 Long-Term Brine Flow up an Intrusion Borehole**

26 Long-term releases to the ground surface or groundwater in the Rustler Formation (hereafter
27 referred to as the Rustler) or overlying units may occur after the borehole has been plugged and
28 abandoned. In keeping with regulatory criteria, borehole plugs are assumed to have properties
29 consistent with current practice in the basin. Thus, boreholes are assumed to have concrete plugs
30 emplaced at various locations. Initially, concrete plugs effectively limit fluid flow in the
31 borehole. However, under most circumstances, these plugs cannot be expected to remain fully
32 effective indefinitely. For the purposes of PA, discontinuous borehole plugs above the
33 repository are assumed to degrade 200 years after emplacement. From then on, the borehole is
34 assumed to fill with a silty-sand-like material containing degraded concrete, corrosion products
35 from degraded casing, and material that sloughs into the hole from the walls. Of six possible
36 plugged borehole configurations in the Delaware Basin, three are considered either likely or
37 adequately representative of other possible configurations; one configuration (a two-plug
38 configuration) is explicitly modeled in the flow and transport model (see Section PA-3.7 and
39 Appendix MASS-2009, Section MASS-16.3).

40 If sufficient brine is available in the repository, and if pressure in the repository is higher than in
41 the overlying units, brine may flow up the borehole following plug degradation. In principle,
42 this brine could flow into any permeable unit or to the ground surface if repository pressure were

1 high enough. For modeling purposes, brine is allowed to flow only into the higher-permeability
2 units and to the surface. Lower-permeability anhydrite and mudstone layers in the Rustler are
3 treated as if they were impermeable to simplify the analysis while maximizing the amount of
4 flow into units where it could potentially contribute to disposal system releases. Model results
5 indicate that essentially all flow occurs into the Culebra, which has been recognized since the
6 early stages of site characterization as the most transmissive unit above the repository and the
7 most likely pathway for subsurface transport (see also the CRA-2004, Chapter 2.0, Section
8 2.2.1.4.1.2).

9 **PA-2.1.4.6 Groundwater Flow in the Culebra**

10 Site characterization activities in the units above the Salado have focused on the Culebra. These
11 activities have shown that the direction of groundwater flow in the Culebra varies somewhat
12 regionally, but in the area that overlies the repository, flow is southward. These characterization
13 and modeling activities conducted in the units above the Salado confirm that the Culebra is the
14 most transmissive unit above the Salado. The Culebra is the unit into which actinides are likely
15 to be introduced from long-term flow up an abandoned borehole. Regional variation in the
16 Culebra's groundwater flow direction is influenced by the transmissivity observed, as well as the
17 lateral (facies) changes in the lithology of the Culebra in the groundwater basin where the WIPP
18 is located. Site characterization activities have provided no evidence of karst groundwater
19 systems in the controlled area, although groundwater flow in the Culebra is affected by the
20 presence of fractures, fracture fillings, and vuggy pore features (see Appendix HYDRO-2009
21 and the CRA-2004, Chapter 2.0, Section 2.1.3.5). Other laboratory and field activities have
22 focused on the behavior of dissolved and colloidal actinides in the Culebra.

23 Basin-scale regional modeling of three-dimensional groundwater flow in the units above the
24 Salado demonstrates that it is appropriate, for the purposes of estimating radionuclide transport,
25 to conceptualize the Culebra as a two-dimensional confined aquifer (see the CRA-2004, Chapter
26 2.0, Section 2.2.1.1). Uncertainty in the flow field is incorporated by using 100 different
27 geostatistically based T fields, each of which is consistent with available head and transmissivity
28 data (Appendix PA-2009, Appendix TFIELD-2009).

29 Groundwater flow in the Culebra is modeled as a steady-state process, but two mechanisms
30 considered in the PA could affect flow in the future. Potash mining in the McNutt Potash Zone
31 (hereafter referred to as the McNutt) of the Salado, which occurs now in the Delaware Basin
32 outside the controlled area and may continue in the future, could affect flow in the Culebra if
33 subsidence over mined areas causes fracturing or other changes in rock properties (see the
34 CRA-2004, Chapter 6.0, Section 6.3.2.3). Climatic changes during the next 10,000 years may
35 also affect groundwater flow by altering recharge to the Culebra (see the CRA-2004, Chapter
36 6.0, Section 6.4.9 and the CCA, Appendix CLI).

37 Consistent with regulatory criteria of 40 CFR § 194.32, mining outside the controlled area is
38 assumed to occur in the near future, and mining within the controlled area is assumed to occur
39 with a probability of 1 in 100 per century (adjusted for the effectiveness of AICs during the first
40 100 years after closure). Consistent with regulatory guidance, the effects of mine subsidence are
41 incorporated in PA by increasing the transmissivity of the Culebra over the areas identified as
42 mineable by a factor sampled from a uniform distribution between 1 and 1000 (U.S.

1 Environmental Protection Agency 1996a, p. 5229). T fields used in PA are therefore adjusted
2 and steady-state flow fields calculated accordingly; once for mining that occurs only outside the
3 controlled area, and once for mining that occurs both inside and outside the controlled area
4 (Appendix TFIELD-2009, Section 9.0). Mining outside the controlled area is considered in both
5 undisturbed and disturbed repository performance.

6 The extent to which the climate will change during the next 10,000 years and how such a change
7 will affect groundwater flow in the Culebra are uncertain. Regional three-dimensional modeling
8 of groundwater flow in the units above the Salado indicates that flow velocities in the Culebra
9 may increase by a factor of 1 to 2.25 for reasonably possible future climates (see the CCA,
10 Appendix CLI). This uncertainty is incorporated in PA by scaling the calculated steady-state
11 specific discharge within the Culebra by a sampled parameter within this range.

12 **PA-2.1.4.7 Actinide Transport in the Culebra**

13 Field tests have shown that the Culebra is best characterized as a double-porosity medium for
14 estimating contaminant transport in groundwater (see the CRA-2004, Chapter 2.0, Section
15 2.2.1.4.1.2 and Appendix HYDRO-2009). Groundwater flow and advective transport of
16 dissolved or colloidal species and particles occurs primarily in a small fraction of the rock's total
17 porosity and corresponds to the porosity of open and interconnected fractures and vugs.
18 Diffusion and slower advective flow occur in the remainder of the porosity, which is associated
19 with the low-permeability dolomite matrix. Transported species, including actinides (if present),
20 will diffuse into this porosity.

21 Diffusion from the advective porosity into the dolomite matrix will retard An transport through
22 two mechanisms. Physical retardation occurs simply because actinides that diffuse into the
23 matrix are no longer transported with the flowing groundwater. Transport is interrupted until
24 they diffuse back into the advective porosity. In situ tracer tests have demonstrated this
25 phenomenon. Chemical retardation also occurs within the matrix as actinides are sorbed onto
26 dolomite grains. The relationship between sorbed and liquid concentrations is assumed to be
27 linear and reversible. The distribution coefficients (K_{ds}) that characterize the extent to which
28 actinides will sorb on dolomite were based on experimental data (see the CRA-2004, Chapter
29 6.0, Section 6.4.6.2).

30 **PA-2.1.4.8 Intrusion Scenarios**

31 Human intrusion scenarios evaluated in the PA include both single intrusion events and
32 combinations of multiple boreholes. Two different types of boreholes are considered: those that
33 penetrate a pressurized brine reservoir in the underlying Castile Formation (hereafter referred to
34 as the Castile), and those that do not.

35 The presence of a brine reservoir under the repository is speculative, but on the basis of current
36 information cannot be ruled out. A pressurized brine reservoir was encountered at the WIPP-12
37 borehole within the controlled area to the north of the disposal region, and other pressurized
38 brine reservoirs associated with regions of deformation in the Castile have been encountered
39 elsewhere in the Delaware Basin (see the CRA-2004, Chapter 2.0, Section 2.2.1.2.2). Based on a
40 geostatistical analysis of the geophysical data of brine encounters in the region, the DOE

1 estimates that there is a 0.08 probability that a random borehole penetrating waste in the WIPP
2 will also penetrate an underlying brine reservoir (see the CCA, Appendix MASS, Attachment
3 18-6). Upon their review of the CCA, the EPA determined that the DOE should treat this
4 probability as uncertain, ranging from 0.01 to 0.60 in the CCA PAVT. The EPA also required
5 the DOE to modify the assumptions concerning Castile properties to increase the brine reservoir
6 volumes (U.S. Environmental Protection Agency 1998b; *Technical Support Document for*
7 *194.23: Parameter Justification Report*, Section 5). The EPA determined that changing the rock
8 compressibility and porosity of the Castile effectively modified the sampled brine reservoir
9 volume to include the possibility of larger brine reservoir volumes like those encountered by the
10 WIPP-12 borehole.

11 The primary consequence of penetrating a pressurized reservoir is to provide an additional
12 source of brine beyond that which might flow into the repository from the Salado. Direct
13 releases at the ground surface resulting from the first repository intrusion would be unaffected by
14 additional Castile brine, even if it flowed to the surface, because brine moving straight up a
15 borehole will not significantly mix with waste. However, the presence of Castile brine could
16 significantly increase radionuclide releases in two ways. First, the volume of contaminated brine
17 that could flow to the surface may be greater for a second or subsequent intrusion into a
18 repository that has already been connected by a previous borehole to a Castile reservoir. Second,
19 the volume of contaminated brine that may flow up an abandoned borehole after plug
20 degradation may be greater for combinations of two or more boreholes that intrude the same
21 panel if one of the boreholes penetrates a pressurized reservoir. Both processes are modeled in
22 PA.

23 **PA-2.1.5 Compliance Demonstration Method**

24 The DOE's approach to demonstrating continued compliance is the PA, which is based on the
25 criteria indicated in section 194.34. The PA process comprehensively considers the FEPs
26 relevant to disposal system performance (see Appendix SCR-2009). Those FEPs shown by
27 screening analyses to potentially affect performance are included in quantitative calculations
28 using a system of loosely coupled computer models to describe the interaction of the repository
29 with the natural system, both with and without human intrusion. Uncertainty in parameter values
30 is incorporated in the analysis by a Monte Carlo approach, in which multiple simulations (or
31 realizations) are completed using sampled values for the imprecisely known input parameters
32 (see the CRA-2004, Chapter 6.0, Section 6.1.5). Distribution functions characterize the state of
33 knowledge for these parameters, and each realization of the modeling system uses a different set
34 of sampled input values. A sample size of 300 results in 300 different values of each parameter.
35 Thus, there are 300 different sets (vectors) of input parameter values. These 300 vectors were
36 divided among 3 replicates. Quality assurance activities demonstrate that the parameters,
37 software, and analysis used in PA were the result of a rigorous process conducted under
38 controlled conditions (40 CFR § 194.22).

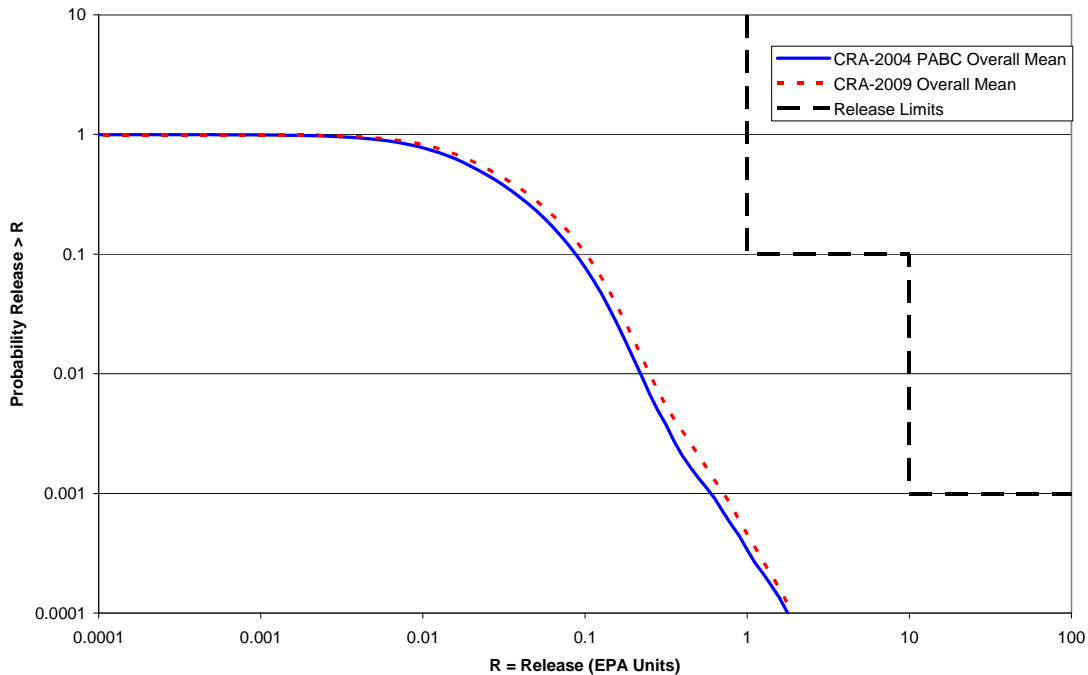
39 Of the FEPs considered, exploratory drilling for natural resources was identified as the only
40 disruption with sufficient likelihood and consequence of impacting releases from the repository.
41 For each vector of parameters values, 10,000 possible futures (realizations) are simulated, where
42 a single future is defined as a series of intrusion events that occur randomly in space and time
43 (Section PA-2.2). Each of these futures is assumed to have an equal probability of occurring;

1 hence a probability of 0.0001. Cumulative radionuclide releases from the disposal system are
 2 calculated for each future, and CCDFs are constructed by sorting the releases from smallest to
 3 largest and then summing the probabilities across the future. Mean CCDFs were then computed
 4 for the three replicates of sampled parameters (Section PA-2.2).

5 **PA-2.1.6 Results of the PA**

6 This section summarizes the results of the CRA-2009 PA and demonstrates that the WIPP
 7 continues to comply with the quantitative containment requirements in 40 CFR § 191.13(a). The
 8 CRA-2009 PA is different than the original certification PA in the CCA and the PA in the
 9 CRA-2004 PABC because it includes additional information, changes, and new data required by
 10 40 CFR § 194.15 recertification application requirements. Table PA-1 details the changes and
 11 new information included in this PA.

12 The results of the CRA-2009 PA demonstrate that the repository continues to comply with the
 13 disposal standards. The key metric for regulatory compliance is the mean CCDF. Figure PA-1,
 14 which compares the overall mean CCDF for the CRA-2009 PA to the overall mean CCDF for
 15 the CRA-2004 PABC, demonstrates two key points. First, the overall mean CCDF lies entirely
 16 below the limits specified in section 191.13(a). Thus, the WIPP is in compliance with the
 17 containment requirements of Part 191. Second, for any probability, the expected releases in the
 18 CRA-2009 PA are only slightly higher than those in the CRA-2004 PABC, primarily because of
 19 the increased drilling rate.



20
 21 **Figure PA-1. Overall Mean CCDFs for Total Normalized Releases: CRA-2009 PA and**
 22 **CRA-2004 PABC**

23 Detailed results of the CRA-2009 PA are contained in Section PA-9.0, which describes
 24 sensitivity analyses conducted as the final step in the Monte Carlo analysis. These sensitivity

1 analyses indicate the relative importance of each sampled parameter in terms of its contribution
2 to uncertainty in estimating disposal system performance. Analyses also examine the sensitivity
3 of intermediate performance measures to the sampled parameters. Examples of such
4 intermediate performance measures include the quantity of radionuclides released to the
5 accessible environment by any one mechanism (for example, cuttings or DBRs), and other model
6 results that describe conditions of interest, such as disposal region pressure.

7 Section PA-9.0 presents CCDF distributions for each replication of the analysis, mean CCDFs,
8 and an overall mean CCDF with the 95% confidence interval estimated from the 3 independent
9 mean distributions. All 300 individual CCDFs, as well as the overall mean CCDF determined
10 from the 3 replicates, lie entirely below and to the left of the limits specified in section 191.13(a)
11 (see Figure PA-79). Thus, the WIPP continues to comply with the containment requirements of
12 Part 191. Comparing the results of the 3 replicates indicates that the sample size of 100 in each
13 replicate is sufficient to generate a stable distribution of outcomes (see Figure PA-80). Within
14 the region of regulatory interest (that is, at probabilities greater than $10^{-3}/10^4$ year [yr]), the
15 mean CCDFs from each replicate are essentially indistinguishable from the overall mean.

16 As discussed in Section PA-9.1, Section PA-9.2, and Section PA-9.3, examining the normalized
17 releases from cuttings and cavings, spallings, and DBRs provides insight into the relative
18 importance of each release mode's contribution to the mean CCDF's location and the
19 compliance determination. Releases from cuttings and cavings dominate the mean CCDF at high
20 probabilities, while DBRs dominate the mean CCDF at low probabilities. Spallings are less
21 important and have very little effect on the location of the mean. Subsurface releases from
22 groundwater transport are less than 10^{-6} EPA units and make no contribution to the mean
23 CCDF's location.

24 Uncertainties characterized in the natural system and the interaction of waste with the disposal
25 system environment show little variation between the location of the mean CCDFs of the three
26 replicates, providing additional confidence in the compliance determination. The natural and
27 engineered barrier systems of the WIPP provide robust and effective containment of TRU waste
28 even if the repository is penetrated by multiple borehole intrusions.

29 **PA-2.2 Conceptual Structure of the PA**

30 This section outlines the conceptual structure of the WIPP PA. First, a discussion of the
31 regulatory requirements is given. The requirements of section 191.13 and section 194.34
32 (summarized in Section PA-2.2.1) lead to the identification of three main PA components:

- 33 1. A probabilistic characterization of the likelihood for different futures to occur at the WIPP
34 site over the next 10,000 years
- 35 2. A procedure for estimating the radionuclide releases to the accessible environment
36 associated with each possible future that could occur at the WIPP site over the next 10,000
37 years
- 38 3. A probabilistic characterization of the uncertainty in the parameters used to estimate
39 potential releases

1 The probabilistic methods employed in WIPP PA give rise to the CCDF specified in section
2 191.13(a) and the distributions specified by 40 CFR § 194.34(b).

3 **PA-2.2.1 Regulatory Requirements**

4 The methodology employed in PA derives from the EPA's standard for the geologic disposal of
5 radioactive waste, Environmental Radiation Protection Standards for the Management and
6 Disposal of Spent Nuclear Fuel, High-Level and Transuranic Radioactive Wastes (Part 191)
7 (U.S. Environmental Protection Agency 1993), which is divided into three subparts. 40 CFR
8 Part 191 Subpart A applies to a disposal facility prior to decommissioning and establishes
9 standards for the annual radiation doses to members of the public from waste management and
10 storage operations. Part 191 Subpart B applies after decommissioning and sets probabilistic
11 limits on cumulative releases of radionuclides to the accessible environment for 10,000 years
12 (section 191.13) and assurance requirements to provide confidence that section 191.13 will be
13 met (40 CFR § 191.14). Part 191 Subpart B also sets limits on radiation doses to members of the
14 public in the accessible environment for 10,000 years of undisturbed repository performance
15 (section 191.15). 40 CFR Part 191 Subpart C limits radioactive contamination of groundwater
16 for 10,000 years after disposal (section 191.24). In this recertification application, the DOE must
17 demonstrate a reasonable expectation that the WIPP will continue to comply with the
18 requirements of Part 191 Subparts B and C.

19 The following is the central requirement in Part 191 Subpart B, and the primary determinant of
20 the PA methodology (U.S. Environmental Protection Agency 1985, p. 38086).

21 § 191.13 Containment Requirements:

22 (a) Disposal systems for spent nuclear fuel or high-level or transuranic radioactive wastes shall be
23 designed to provide a reasonable expectation, based upon performance assessments, that
24 cumulative releases of radionuclides to the accessible environment for 10,000 years after disposal
25 from all significant processes and events that may affect the disposal system shall:

26 (1) Have a likelihood of less than one chance in 10 of exceeding the quantities calculated
27 according to Table 1 (Appendix A); and

28 (2) Have a likelihood of less than one chance in 1,000 of exceeding ten times the quantities
29 calculated according to Table 1 (Appendix A).

30 (b) Performance assessments need not provide complete assurance that the requirements of
31 191.13(a) will be met. Because of the long time period involved and the nature of the events and
32 processes of interest, there will inevitably be substantial uncertainties in projecting disposal
33 system performance. Proof of the future performance of a disposal system is not to be had in the
34 ordinary sense of the word in situations that deal with much shorter time frames. Instead, what is
35 required is a reasonable expectation, on the basis of the record before the implementing agency,
36 that compliance with 191.13(a) will be achieved.

37 Section 191.13(a) refers to "quantities calculated according to Table 1 (Appendix A)," which
38 means a normalized radionuclide release to the accessible environment based on the type of
39 waste being disposed, the initial waste inventory, and the size of release that may occur (U.S.
40 Environmental Protection Agency 1985, Appendix A). Table 1 of Appendix A specifies
41 allowable releases (i.e., release limits) for individual radionuclides and is reproduced as Table

1 PA-2. The WIPP is a repository for TRU waste, which is defined as “waste containing more
 2 than 100 nanocuries of alpha-emitting TRU isotopes, with half-lives greater than twenty years,
 3 per gram of waste” (U.S. Environmental Protection Agency 1985, p. 38084). The normalized
 4 release R for TRU waste is defined by

$$5 \quad R = \sum_i \left(\frac{Q_i}{L_i} \right) \left(\frac{1 \times 10^6 \text{ Ci}}{C} \right) \quad (\text{PA.1})$$

6 where Q_i is the cumulative release of radionuclide i to the accessible environment during the
 7 10,000-year period following closure of the repository (curies [Ci]), L_i is the release limit for
 8 radionuclide i given in Table PA-2 (Ci), and C is the amount of TRU waste emplaced in the
 9 repository (Ci). In the CRA-2009 PA, $C = 2.32 \times 10^6$ Ci (Leigh and Trone 2005, Section 3).
 10 Further, “accessible environment” means (1) the atmosphere, (2) land surfaces, (3) surface
 11 waters, (4) oceans, and (5) all of the lithosphere beyond the controlled area. “Controlled area”
 12 means (1) a surface location, to be identified by PICs, that encompasses no more than 100 square
 13 kilometers (km²) and extends horizontally no more than 5 kilometers (km) in any direction from
 14 the outer boundary of the original radioactive waste’s location in a disposal system, and (2) the
 15 subsurface underlying such a location (section 191.12).

16 PAs are the basis for addressing the containment requirements. To help clarify the intent of Part
 17 191, the EPA promulgated 40 CFR Part 194 (2004), Criteria for the Certification and

18 **Table PA-2. Release Limits for the Containment Requirements (U.S. Environmental**
 19 **Protection Agency 1985, Appendix A, Table 1)**

Radionuclide	Release Limit L_i per 1000 MTHM ^a or Other Unit of Waste ^b
Americium-241 or -243	100
Carbon-14	100
Cesium-135 or -137	1,000
Iodine-129	100
Neptunium-237	100
Pu-238, -239, -240, or -242	100
Radium-226	100
Strontium-90	1,000
Technetium-99	10,000
Thorium (Th) -230 or -232	10
Tin-126	1,000
Uranium (U) -233, -234, -235, -236, or -238	100
Any other alpha-emitting radionuclide with a half-life greater than 20 years	100
Any other radionuclide with a half-life greater than 20 years that does not emit alpha particles	1,000

a Metric tons of heavy metal (MTHM) exposed to a burnup between 25,000 megawatt-days (MWd) per metric ton of heavy metal (MWd/MTHM) and 40,000 MWd/MTHM.

b An amount of TRU wastes containing one million Ci of alpha-emitting TRU radionuclides with half-lives greater than 20 years.

1 Recertification of the Waste Isolation Pilot Plant’s Compliance with the Part 191 Disposal
2 Regulations. There, an elaboration on the intent of section 191.13 is prescribed.

3 § 194.34 Results of performance assessments.

4 (a) The results of performance assessments shall be assembled into “complementary, cumulative
5 distributions functions” (CCDFs) that represent the probability of exceeding various levels of
6 cumulative release caused by all significant processes and events.

7 (b) Probability distributions for uncertain disposal system parameter values used in performance
8 assessments shall be developed and documented in any compliance application.

9 (c) Computational techniques, which draw random samples from across the entire range of the
10 probability distributions developed pursuant to paragraph (b) of this section, shall be used in
11 generating CCDFs and shall be documented in any compliance application.

12 (d) The number of CCDFs generated shall be large enough such that, at cumulative releases of 1
13 and 10, the maximum CCDF generated exceeds the 99th percentile of the population of CCDFs
14 with at least a 0.95 probability.

15 (e) Any compliance application shall display the full range of CCDFs generated.

16 (f) Any compliance application shall provide information which demonstrates that there is at least
17 a 95% level of statistical confidence that the mean of the population of CCDFs meets the
18 containment requirements of § 191.13 of this chapter.

19 The DOE’s methodology for PA uses information about the disposal system and waste to
20 evaluate performance over the 10,000-year regulatory time period. To accomplish this task, the
21 FEPs with potential to affect the future of the WIPP are first defined (Section PA-2.3.1). Next,
22 scenarios that describe potential future conditions in the WIPP are formed from logical
23 groupings of retained FEPs (Section PA-2.3.2). The scenario development process results in a
24 probabilistic characterization for the likelihood of different futures that could occur at the WIPP
25 (Section PA-2.2.2). Using the retained FEPs, models are developed to estimate the radionuclide
26 releases from the repository (Section PA-2.2.3). Finally, uncertainty in model parameters is
27 characterized probabilistically (Section PA-2.2.4).

28 **PA-2.2.2 Probabilistic Characterization of Different Futures**

29 As discussed in Section PA-2.3.1, the CCA PA scenario development process for the WIPP
30 identified exploratory drilling for natural resources as the only disruption with sufficient
31 likelihood and consequence of impacting releases from the repository (see the CCA, Appendix
32 SCR). In addition, Part 194 specifies that the occurrence of mining within the LWB must be
33 included in the PA. This has not changed for the CRA-2009 PA. As a result, the projection of
34 releases over the 10,000 years following closure of the WIPP is driven by the nature and timing
35 of intrusion events.

36 The collection of all possible futures \mathbf{x}_{st} forms the basis for the probability space $(\mathcal{S}_{st}, \mathbb{S}_{st}, p_{st})$
37 characterizing aleatory uncertainty, where $\mathcal{S}_{st} = \{\mathbf{x}_{st} : \mathbf{x}_{st} \text{ is a possible future of the WIPP}\}$, \mathbb{S}_{st} is
38 a suitably restricted collection of sets of futures, called “scenarios” (Section PA-3.10), and p_{st} is

1 a probability measure for the elements of \mathcal{S}_{st} . A possible future, $\mathbf{x}_{st,i}$, is thus characterized by
 2 the collection of intrusion events that occur in that future:

$$3 \quad \mathbf{x}_{st,i} = \left[\underbrace{(t_1, e_1, l_1, b_1, p_1, \mathbf{a}_1)}_{1^{\text{st}} \text{ intrusion}}, \underbrace{(t_2, e_2, l_2, b_2, p_2, \mathbf{a}_2)}_{2^{\text{nd}} \text{ intrusion}}, \dots, \underbrace{(t_n, e_n, l_n, b_n, p_n, \mathbf{a}_n)}_{n^{\text{th}} \text{ intrusion}}, t_{\min} \right] \quad (\text{PA.2})$$

4 where

- 5 n is the number of drilling intrusions
 6 t_j is the time (year) of the j^{th} intrusion
 7 l_j designates the location of the j^{th} intrusion
 8 e_j designates the penetration of an excavated or nonexcavated area by the j^{th} intrusion
 9 b_j designates whether or not the j^{th} intrusion penetrates pressurized brine in the Castile
 10 Formation
 11 p_j designates the plugging procedure used with the j^{th} intrusion (i.e., continuous plug, two
 12 discrete plugs, three discrete plugs)
 13 \mathbf{a}_j designates the type of waste penetrated by the j^{th} intrusion (i.e., no waste, CH-TRU
 14 waste, RH-TRU waste, and, for CH-TRU waste, the waste streams encountered)
 15 t_{\min} is the time at which potash mining occurs within the LWB

16 The subscript st indicates that aleatory (i.e., stochastic) uncertainty is being considered; the
 17 letters st are retained for historical context. The subscript i indicates that the future \mathbf{x}_{st} is one of
 18 many sample elements from \mathcal{S}_{st} .

19 The probabilistic characterization of n , t_j , l_j , and e_j is based on the assumption that drilling
 20 intrusions will occur randomly in time and space at a constant average rate (i.e., follow a Poisson
 21 process); the probabilistic characterization of b_j derives from assessed properties of brine
 22 pockets; the probabilistic characterization of \mathbf{a}_j derives from the volumes of waste emplaced in
 23 the WIPP in relation to the volume of the repository; and the probabilistic characterization of p_j
 24 derives from current drilling practices in the sedimentary basin (i.e., the Delaware Basin) in
 25 which the WIPP is located. A vector notation is used for \mathbf{a}_j because it is possible for a given
 26 drilling intrusion to miss the waste or to penetrate different waste types (CH-TRU and RH-TRU)
 27 as well as to encounter different waste streams in the CH-TRU waste. Further, the probabilistic
 28 characterization for t_{\min} follows from the criteria in Part 194 that the occurrence of potash
 29 mining within the LWB should be assumed to occur randomly in time (i.e., follow a Poisson
 30 process with a rate constant of $\lambda_m = 10^{-4} \text{ yr}^{-1}$), with all commercially viable potash reserves
 31 within the LWB extracted at time t_{\min} . In practice, the probability measure p_{st} is defined by
 32 specifying probability distributions for each component of \mathbf{x}_{st} , as discussed further in Section
 33 PA-3.0.

34 PA-2.2.3 Estimation of Releases

35 Based on the retained FEPs (Section PA-2.3.1), release mechanisms include direct transport of
 36 material to the surface at the time of a drilling intrusion (i.e., cuttings, spallings, and brine flow)
 37 and release subsequent to a drilling intrusion due to brine flow up a borehole with a degraded

1 plug (i.e., groundwater transport). The quantities of releases are determined by the state of the
 2 repository through time, which is determined by the type, timing, and sequence of prior intrusion
 3 events. For example, pressure in the repository is an important determinant of spillings, and the
 4 amount of pressure depends on whether the drilling events that have occurred penetrated brine
 5 pockets and how long prior to the current drilling event the repository was inundated.

6 Computational models for estimating releases were developed using the retained FEPs; these
 7 models are summarized in Figure PA-2. These computational models implement the conceptual
 8 models representing the repository system as described in section 194.23 and the mathematical
 9 models for physical processes presented in Section PA-4.0. Most of the computational models
 10 involve the numerical solution of partial differential equations (PDEs) used to represent
 11 processes such as material deformation, fluid flow, and radionuclide transport.

12 The collection of computation models can be represented abstractly as a function $f(\mathbf{x}_{st}|\mathbf{v}_{su})$,
 13 which quantifies the release that could result from the occurrence of a specific future \mathbf{x}_{st} and a
 14 specific set of values for model parameters \mathbf{v}_{su} . Because the future of the WIPP is unknown, the
 15 values of $f(\mathbf{x}_{st}|\mathbf{v}_{su})$ are uncertain. Thus, the probability space $(\mathcal{S}_{st}, \mathbb{S}_{st}, p_{st})$, together with the
 16 function $f(\mathbf{x}_{st}|\mathbf{v}_{su})$, give rise to the CCDF specified in section 191.13(a), as illustrated in Figure
 17 PA-3. The CCDF represents the probability that a release from the repository greater than R will
 18 be observed, where R is a point on the abscissa (x-axis) of the graph (Figure PA-3).

19 Formally, the CCDF depicted in Figure PA-3 results from an integration over the probability
 20 space $(\mathcal{S}_{st}, \mathbb{S}_{st}, p_{st})$:

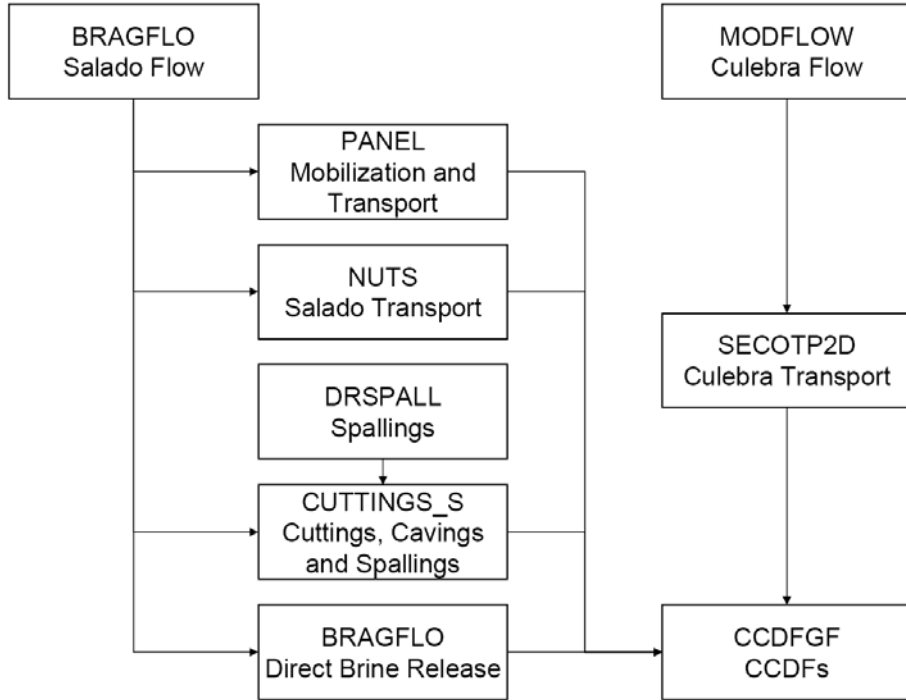
$$21 \quad \text{prob}(rel > R|\mathbf{v}_{su}) = \int_{\mathcal{S}_{st}} \delta_R(f(\mathbf{x}_{st}|\mathbf{v}_{su})) d_{st}(\mathbf{x}_{st}|\mathbf{v}_{su}) dV_{st} \quad (\text{PA.3})$$

22 where $\delta_R(f(\mathbf{x}_{st}|\mathbf{v}_{su})) = 1$ if $f(\mathbf{x}_{st}|\mathbf{v}_{su}) > R$, $\delta_R(f(\mathbf{x}_{st}|\mathbf{v}_{su})) = 0$ if $f(\mathbf{x}_{st}|\mathbf{v}_{su}) \leq R$, and $d_{st}(\mathbf{x}_{st}|\mathbf{v}_{su})$ is the
 23 probability density function associated with the probability space $(\mathcal{S}_{st}, \mathbb{S}_{st}, p_{st})$. In practice, the
 24 integral in Equation (PA.3) is evaluated by a Monte Carlo technique, where a random sample
 25 $\mathbf{x}_{st,i}$, $i = 1, nR$, is generated from \mathcal{S}_{st} consistent with the probability distribution p_{st} . Using this
 26 random sample, Equation (PA.3) is numerically evaluated as

$$27 \quad \text{prob}(rel > R|\mathbf{v}_{su}) = \int_{\mathcal{S}_{st}} \delta_R(f(\mathbf{x}_{st}|\mathbf{v}_{su})) d_{st}(\mathbf{x}_{st}|\mathbf{v}_{su}) dV_{st} \quad (\text{PA.4})$$

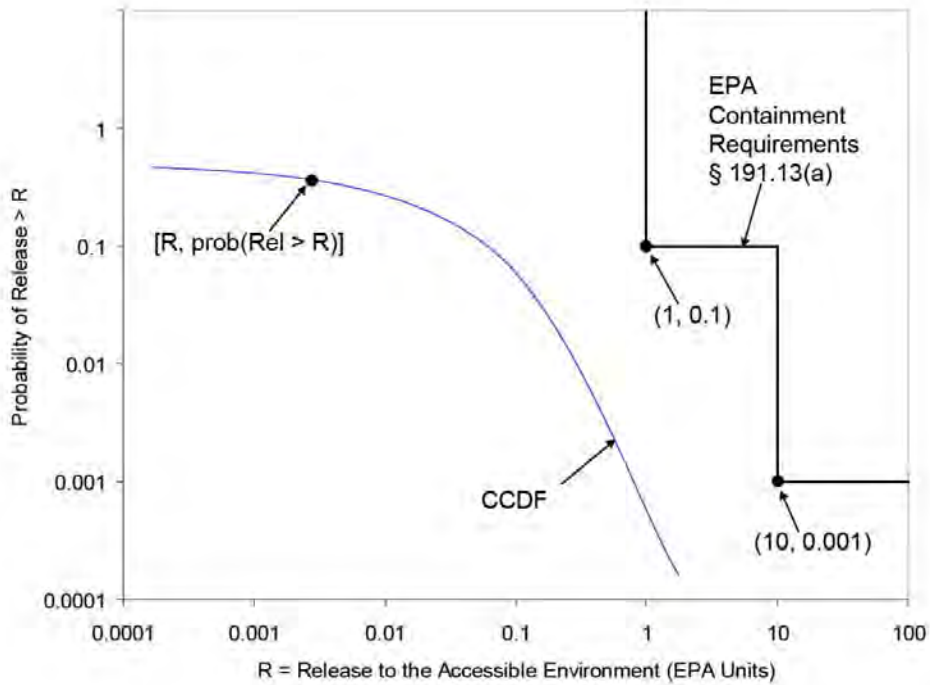
$$\cong \sum_{j=1}^{nR} \delta_R(f(\mathbf{x}_{st,j}|\mathbf{v}_{su})) / nR$$

28 The models in Figure PA-2 are too complex to permit a closed-form evaluation of the integral in
 29 Equation (PA.4) that defines the CCDF specified in Part 191. In WIPP PA, these probability
 30 distribution functions (PDFs) are constructed using Monte Carlo simulation to sample the entire
 31 possible set of release outcomes. As long as the sampling is conducted properly and a sufficient
 32 number of samples is collected, the PDF of the sample should successfully approximate the PDF
 33 of the sample “universe” of all possible releases.



1
2

Figure PA-2. Computational Models Used in PA



3
4

Figure PA-3. Construction of the CCDF Specified in 40 CFR Part 191 Subpart B

1 In PA, the number of samples nR used to construct a CCDF is 10,000. However, the models in
 2 Figure PA-2 are also too computationally intensive to permit their evaluation for each of these
 3 10,000 futures. Due to this constraint, the models in Figure PA-2 are evaluated for a relatively
 4 small number of specific scenarios, and the results of these evaluations are used to construct
 5 CCDFs. The representative scenarios are labeled E0, E1, E2, and E1E2, and are defined in
 6 Section PA-3.10; the procedure for constructing a CCDF from these scenarios is described in
 7 Section PA-6.0.

8 **PA-2.2.4 Probabilistic Characterization of Parameter Uncertainty**

9 If the parameters used in the process-level models of Figure PA-2 were precisely known and if
 10 the models could accurately predict the future behavior of the repository, the evaluation of
 11 repository performance alone would be sufficient to answer the first three questions related to
 12 repository performance. However, the models do not perfectly represent the dynamics of the
 13 system and their parameters are not precisely known. Therefore, it is necessary to estimate the
 14 confidence one has in the CCDFs being constructed. The confidence in the CCDFs is established
 15 using Monte Carlo methods to evaluate how the uncertainty in the model parameters impacts the
 16 CCDFs or releases. The probabilistic characterization of the uncertainty in the model parameters
 17 is the outcome of the data development effort for the WIPP (summarized in Section 8.0 in Fox
 18 2008).

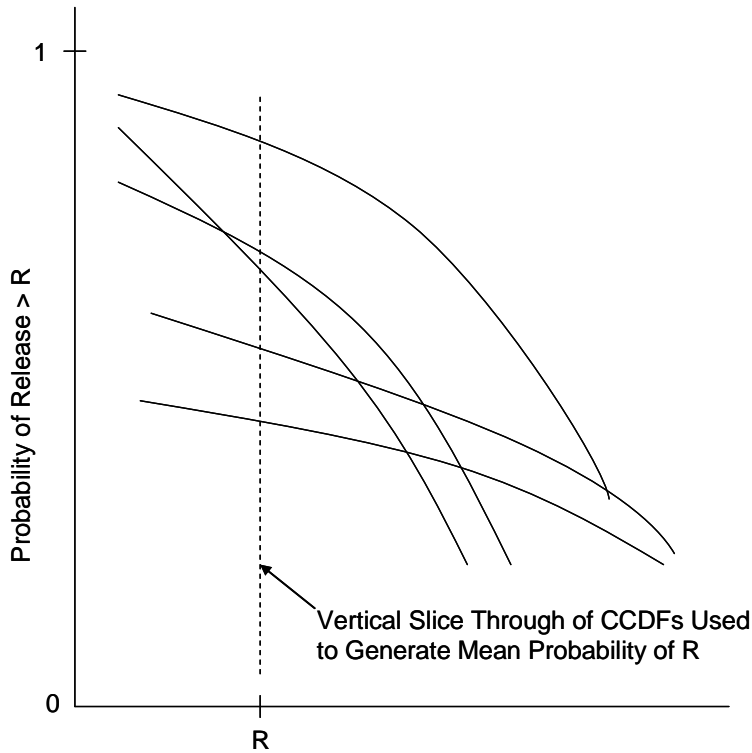
19 Formally, uncertainty in the parameters that underlie the WIPP PA can be characterized by a
 20 second probability space $(\mathcal{S}_{su}, \mathbb{S}_{su}, p_{su})$, where the sample space \mathcal{S}_{su} is defined by

$$21 \quad \mathcal{S}_{su} = \{\mathbf{v}_{su}: \mathbf{v}_{su} \text{ is a sampled vector of parameter values}\} \quad (\text{PA.5})$$

22 The subscript su indicates that epistemic (i.e., subjective) uncertainty is being considered; the
 23 letters su are retained for historical context. An element $\mathbf{v}_{su} \in \mathcal{S}_{su}$ is a vector $\mathbf{v}_{su} = v_{su,1}, v_{su,2},$
 24 $\dots, v_{su,N}$ of length N , where each element $v_{su,k}$ is an uncertain parameter used in the models to
 25 estimate releases. In practice, the probability measure p_{su} is defined by specifying probability
 26 distributions for each element of \mathbf{v}_{su} , discussed further in Section PA-5.0.

27 If the actual value for \mathbf{v}_{su} were known, the CCDF resulting from evaluation of Equation (PA.4)
 28 could be determined with certainty and compared with the criteria specified in Part 191.
 29 However, given the complexity of the WIPP site, the 10,000-year period under consideration,
 30 and the state of knowledge about the natural and engineered system, values for \mathbf{v}_{su} are not
 31 known with certainty. Rather, the uncertainty in \mathbf{v}_{su} is characterized probabilistically, as
 32 described above, leading to a distribution of CCDFs (Figure PA-4) with each CCDF resulting
 33 from one of many vectors of values of \mathbf{v}_{su} . The uncertainty associated with the parameters is
 34 termed epistemic uncertainty, and has been referred to in WIPP PA documentation as subjective
 35 uncertainty.

36 WIPP PA uses a Monte Carlo procedure for evaluating the effects of epistemic uncertainty on
 37 releases. The procedure involves sampling the distributions assigned to the uncertain parameters
 38 and generating a CCDF of releases based on the results of the process-level models generated
 39 using those parameters values. By repeating this process many times, a distribution of the



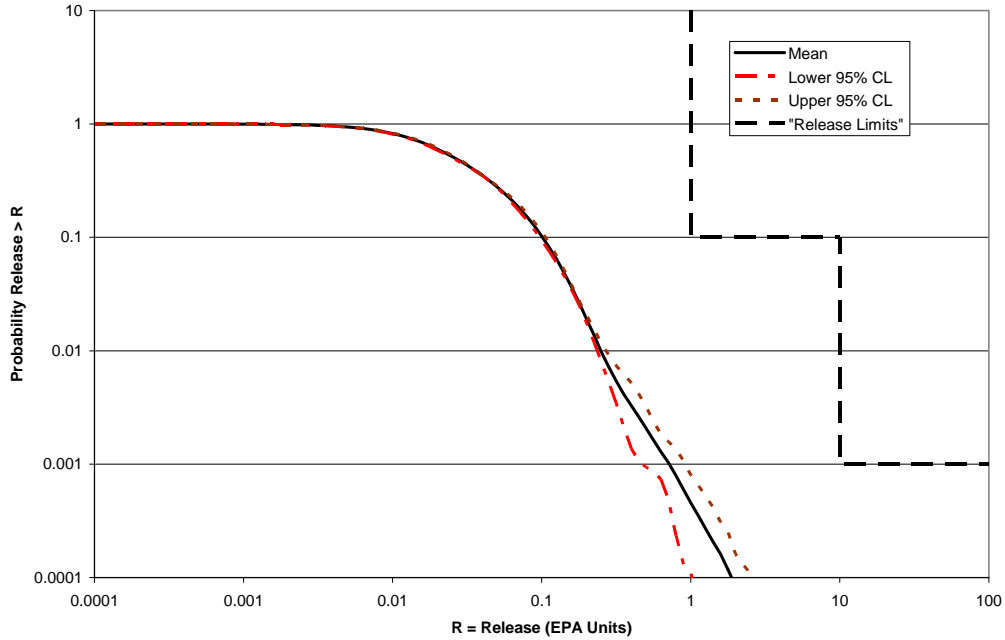
R = Release to Accessible Environment (EPA Units)

Figure PA-4. Distribution of CCDFs Resulting from Possible Values for the Sampled Parameters

CCDFs can be constructed. The requirements of section 191.13 are evaluated, in part, using the mean probability of release. The overall mean probability curve is created by averaging across the CCDFs for releases, i.e., averaging the CCDFs across vertical slices (Figure PA-4) (a formal definition is provided in Helton et al. 1998). In addition, confidence limits on the mean are computed using standard t-statistics (Figure PA-5). The proximity of these curves to the boundary line in Figure PA-3 indicates the confidence with which Part 191 will be met. Confidence is also established by examining the distribution of the CCDFs in relation to the release limits (Figure PA-6).

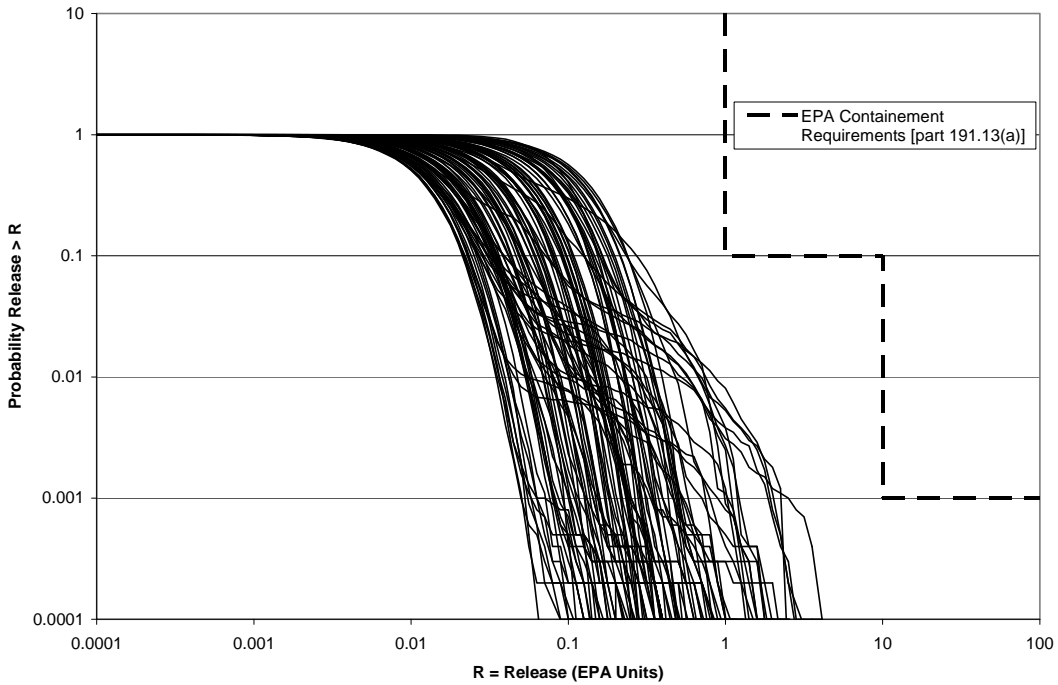
WIPP PA uses a stratified sampling design called LHS (McKay, Beckman, and Conover 1979) to generate a sample $\mathbf{v}_{su}, i = 1, \dots, nLHS$, from \mathcal{S}_{su} consistent with the probability distribution p_{su} . LHS is an efficient scheme for sampling the range of a distribution using a relatively small sample. Based on order statistics, the sample size of $nLHS = 300$ replicates would provide coverage of 99% of the CCDF distribution with a confidence of 95%.

In Part 194, the EPA decided that the statistical portion of the determination of compliance with Part 191 will be based on the sample mean. The LHS sample sizes should be demonstrated operationally to improve (reduce the size of) the confidence interval for the estimated mean. The underlying principle is to show convergence of the mean (U.S. Environmental Protection Agency 1996b, p. 8-41).



1

2 **Figure PA-5. Example Mean Probability of Release and the Confidence Limits on the**
 3 **Mean from CRA-2009 PA**



4

5 **Figure PA-6. Example CCDF Distribution From CRA-2009 PA (Replicate 1)**

1 The DOE has chosen to demonstrate repeatability of the mean and to address the associated
2 criteria of Part 194 using an operational approach of multiple replication, as proposed by Iman
3 (1982). The complete set of PA calculations was repeated three times with all aspects of the
4 analysis identical except for the random seed used to initiate the LHS procedure. Thus, PA
5 results are available for 3 replicates, each based on an independent set of 100 LHS vectors drawn
6 from identical distributions for imprecisely known parameters and propagated through an
7 identical modeling system. This technique of multiple replication allows the adequacy of the
8 sample size chosen in the Monte Carlo analysis to be evaluated and provides a suitable measure
9 of confidence in the mean CCDF estimation used to demonstrate compliance with section
10 191.13(a).

11 **PA-2.3 PA Methodology**

12 This section addresses scenarios formed from FEPs that were retained for PA calculations, and
13 introduces the specification of scenarios for consequence analysis.

14 **PA-2.3.1 Identification and Screening of FEPs**

15 The EPA has provided criteria concerning the scope of PAs in 40 CFR § 194.32. In particular,
16 criteria relating to the identification of potential processes and events that may affect disposal
17 system performance are provided in 40 CFR § 194.32(e), which states

18 Any compliance application(s) shall include information which:

19 (1) Identifies all potential processes, events or sequences and combinations of processes and
20 events that may occur during the regulatory time frame and may affect the disposal system;

21 (2) Identifies the processes, events or sequences and combinations of processes and events
22 included in performance assessments; and

23 (3) Documents why any processes, events or sequences and combinations of processes and events
24 identified pursuant to paragraph (e)(1) of this section were not included in performance
25 assessment results provided in any compliance application.

26 Section 32 of this application fulfills these criteria by documenting the DOE's identification,
27 screening, and screening results of all potential processes and events consistent with the criteria
28 specified in section 194.32(e).

29 The first two steps in scenario development involve identifying and screening FEPs that are
30 potentially relevant to the performance of the disposal system. The CRA-2004, Chapter 6.0,
31 Section 6.2 discusses the development of a comprehensive initial FEPs set used in the CCA, the
32 methodology and criteria used for screening, the method used to reassess the CCA FEPs for the
33 CRA-2004, and a summary of the FEPs retained for scenario development. Changes to FEPs
34 since the CRA-2004 are outlined in Section 32 and Appendix SCR-2009 of this application.

35 The original FEPs generation and screening were documented in the CCA, and the resulting
36 FEPs list became the FEPs compliance baseline. The baseline contained 237 FEPs and was
37 documented the CCA, Appendix SCR. The EPA compliance review of FEPs was documented in
38 EPA's Technical Support Document 194.32: Scope of PA (U.S. Environmental Protection

1 Agency 1998c). The EPA numbered each FEP with a different scheme than the DOE used for
2 the CCA. The DOE has since adopted the EPA's numbering scheme.

3 **PA-2.3.2 Scenario Development and Selection**

4 Logic diagrams illustrate the formation of scenarios for consequence analysis from combinations
5 of events that remain after FEP screening (Cranwell et al. 1990) (Figure PA-7). Each scenario
6 shown in Figure PA-7 is defined by a combination of occurrence and nonoccurrence for all
7 potentially disruptive events. Disruptive events are defined as those that create new pathways or
8 significantly alter existing pathways for fluid flow and, potentially, radionuclide transport within
9 the disposal system. Each of these scenarios also contains a set of features and nondisruptive
10 events and processes that remain after FEP screening. As shown in Figure PA-7, undisturbed
11 repository performance (UP) and disturbed repository performance (DP) scenarios are
12 considered in consequence modeling for the WIPP PA. The UP scenario is used for compliance
13 assessments (40 CFR § 194.54 and 40 CFR § 194.55). Important aspects of UP and DP
14 scenarios are summarized in this section.

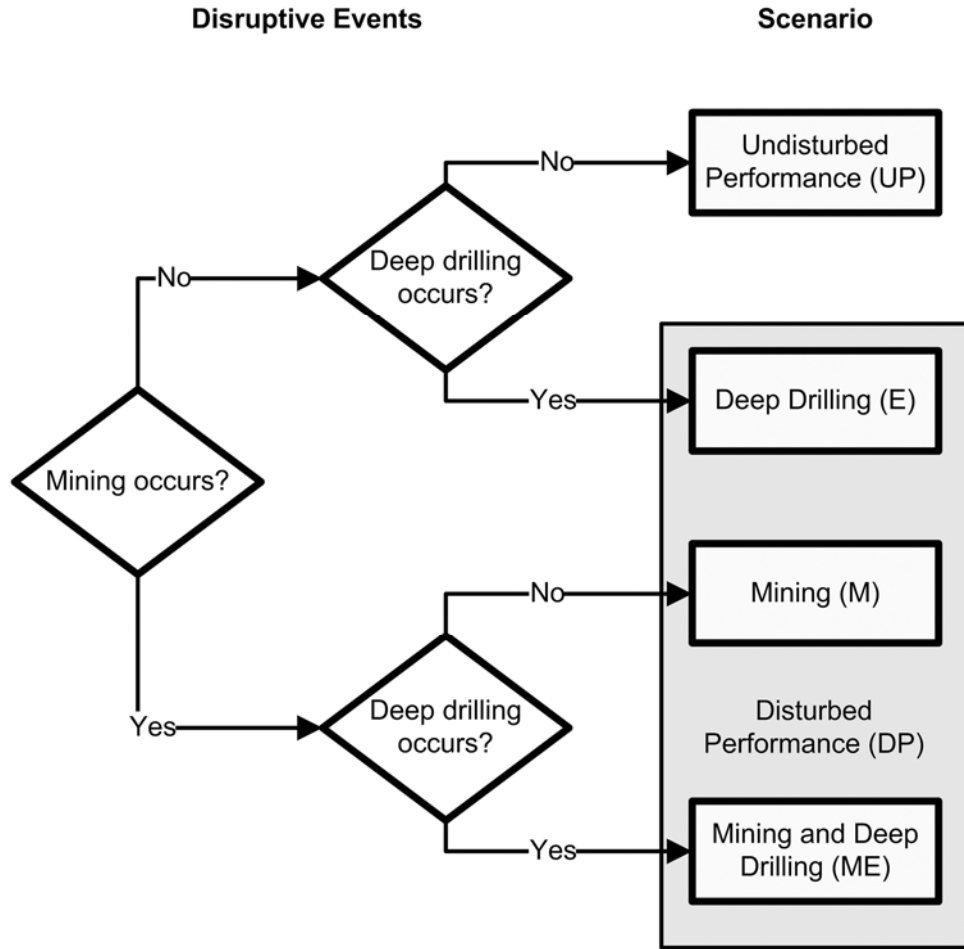
15 **PA-2.3.2.1 Undisturbed Repository Performance**

16 The UP scenario is defined in 40 CFR § 191.12 to mean “the predicted behavior of a disposal
17 system, including consideration of the uncertainties in predicted behavior, if the disposal system
18 is not disrupted by human intrusion or the occurrence of unlikely natural events.” For
19 compliance assessments with respect to the Individual and Groundwater Protection
20 Requirements (section 191.15; Appendix IGP-2009), it is only necessary to consider the UP
21 scenario. The UP scenario is also considered with DP scenario for PA with respect to the
22 containment requirements (section 191.13).

23 No potentially disruptive natural events and processes are likely to occur during the regulatory
24 time frame. Therefore, all naturally occurring events and processes retained for scenario
25 construction are nondisruptive and are considered part of the UP scenario. Mining outside the
26 LWB is assumed at the end of AIC for all scenarios. The M scenario involves future mining
27 within the controlled area. The disturbed repository E scenario involves at least one deep drilling
28 event that intersects the waste disposal region. The M scenario and the E scenario may both
29 occur in the future. The DOE calls a future in which both of these events occur the ME scenario.
30 More detailed descriptions are found in Section PA-2.3.2.2.

31 The only natural features and waste- and repository-induced FEPs retained after screening that
32 are excluded in the UP scenario, but included in the DP scenario, are those directly associated
33 with the potential effects of future deep drilling within the controlled area. Among the most
34 significant FEPs that will affect the UP scenario within the disposal system are excavation-
35 induced fracturing, gas generation, salt creep, and MgO in the disposal rooms.

- 36 • The repository excavation and consequent changes in the rock stress field surrounding the
37 excavated opening will create a DRZ immediately adjacent to excavated openings. The
38 DRZ will exhibit mechanical and hydrological properties different than those of the intact
39 rock.



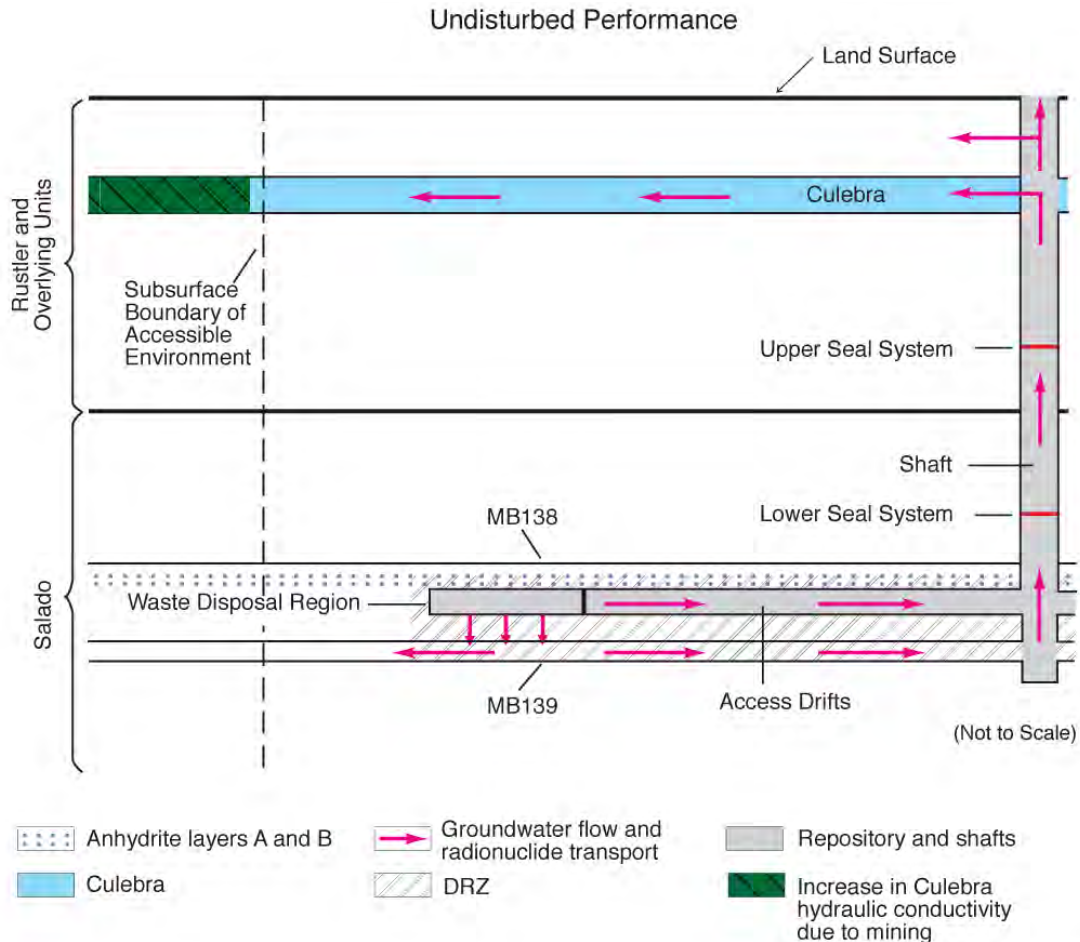
1
2

Figure PA-7. Logic Diagram for Scenario Analysis

- 3
- Organic material in the waste may degrade because of microbial activity, and brine will corrode metals in the waste and waste containers, with concomitant generation of gases. Gas generation may result in pressures sufficient to both maintain or develop fractures and change the fluid flow pattern around the waste disposal region.
- 4
- 5
- 6
- 7
- At the repository depth, salt creep will tend to heal fractures and reduce the permeability of the DRZ and the crushed salt component of the long-term shaft seals to near that of the host rock salt.
- 8
- 9
- 10
- The MgO engineered barrier emplaced in the disposal rooms will react with CO₂ and maintain mildly alkaline conditions. Metal corrosion in the waste and waste containers will maintain reducing conditions. These effects will maintain low radionuclide solubility.
- 11
- 12
- 13
- 14 Radionuclides can become mobile as a result of waste dissolution and colloid generation following brine flow into the disposal rooms. Colloids may be generated from the waste
- 15 following brine flow into the disposal rooms. Colloids may be generated from the waste
- 16 (humics, mineral fragments, and An intrinsic colloids) or from other sources (humics, mineral
- 17 fragments, and microbes).

1 Conceptually, there are several pathways for radionuclide transport within the undisturbed
 2 disposal system that may result in releases to the accessible environment (Figure PA-8).
 3 Contaminated brine may migrate away from the waste-disposal panels if pressure within the
 4 panels is elevated by gas generated from corrosion or microbial consumption. Radionuclide
 5 transport may occur laterally, through the anhydrite interbeds toward the subsurface boundary of
 6 the accessible environment in the Salado, or through access drifts or anhydrite interbeds to the
 7 base of the shafts. In the latter case, if the pressure gradient between the panels and overlying
 8 strata is sufficient, contaminated brine may migrate up the shafts. As a result, radionuclides may
 9 be transported directly to the ground surface, or laterally away from the shafts through permeable
 10 strata such as the Culebra, toward the subsurface boundary of the accessible environment. These
 11 conceptual pathways are shown in Figure PA-8.

12 The modeling system described in Section PA-4.0 includes potential radionuclide transport along
 13 other pathways, such as migration through Salado halite. However, the natural properties of the
 14 undisturbed system make radionuclide transport to the accessible environment via these other
 15 pathways unlikely.



16
17

Figure PA-8. Conceptual Release Pathways for the UP Scenario

CCA-009-2

1 **PA-2.3.2.2 Disturbed Repository Performance**

2 Assessments for compliance with section 191.13 need to consider the potential effects of future
3 disruptive natural and human-initiated events and processes on the performance of the disposal
4 system. No potentially disruptive natural events and processes are considered sufficiently likely
5 to require inclusion in analyses of either the UP or DP scenario. The only future human-initiated
6 events and processes retained after FEP screening are those associated with mining and deep
7 drilling (but not the subsequent use of a borehole) within the controlled area or LWB when
8 institutional controls cannot be assumed to eliminate the possibility of such activities (Section
9 PA-3.2 and the CRA-2004, Chapter 6.0, Section 6.4.12.1). In total, 21 disturbed repository FEPs
10 associated with future mining and deep drilling have been identified. These FEPs were assigned
11 a screening designator of the DP scenario.

12 For evaluating the consequences of disturbed repository performance, the DOE has defined the
13 mining scenario (M), the deep drilling scenario (E), and a mining and drilling scenario (ME).
14 These scenarios are described in the following sections.

15 **PA-2.3.2.2.1 Disturbed Repository M Scenario**

16 The M scenario involves future mining within the controlled area. Consistent with the criteria
17 stated by the EPA in 40 CFR § 194.32(b) for PA calculations, the effects of potential future
18 mining within the controlled area are limited to changes in hydraulic conductivity of the Culebra
19 that result from subsidence (as described in Section PA-3.9).

20 Radionuclide transport may be affected in the M scenario if a head gradient between the waste-
21 disposal panels and the Culebra causes brine contaminated with radionuclides to move from the
22 waste-disposal panels to the base of the shafts and up to the Culebra. The changes in the Culebra
23 T field may affect the rate and direction of radionuclide transport within the Culebra. Features of
24 the M scenario are illustrated in Figure PA-9.

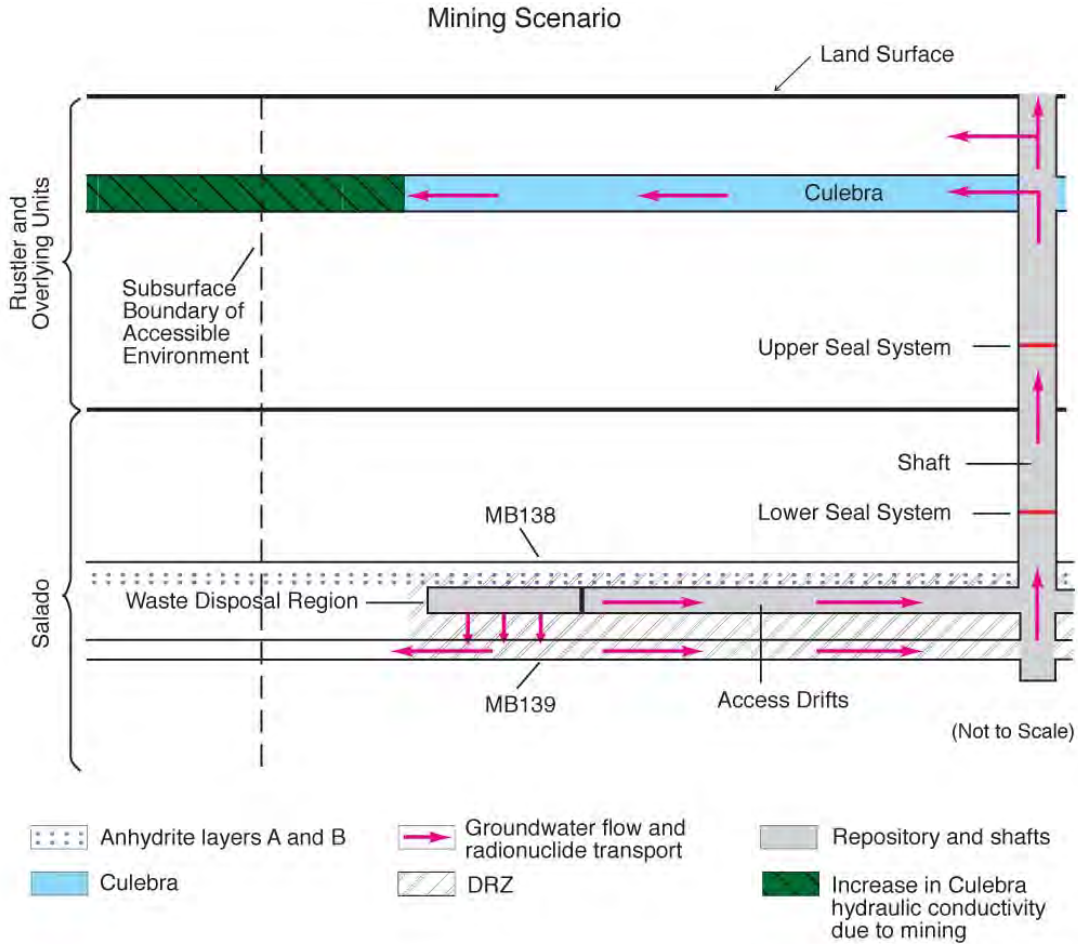
25 The three disturbed repository FEPs labeled M in the CRA-2004, Chapter 6.0, Table 6-9 are
26 related to the occurrence and effects of future mining. The modeling system used for the M
27 scenario is similar to that developed for the UP scenario, but with a modified Culebra T field in
28 the controlled area to account for the mining effects.

29 **PA-2.3.2.2.2 Disturbed Repository E Scenario**

30 The disturbed repository E scenario involves at least one deep drilling event that intersects the
31 waste disposal region. The EPA provides criteria for analyzing the consequences of future
32 drilling events in PA in 40 CFR § 194.33(c).

33 Performance assessments shall document that in analyzing the consequences of drilling events, the
34 Department assumed that:

35 (1) Future drilling practices and technology will remain consistent with practices in the Delaware
36 Basin at the time a compliance application is prepared. Such future drilling practices shall
37 include, but shall not be limited to: the types and amounts of drilling fluids; borehole depths,
38 diameters, and seals; and the fraction of such boreholes that are sealed by humans; and



CCA-119-2

Figure PA-9. Conceptual Release Pathways for the Disturbed Repository M Scenario

(2) Natural processes will degrade or otherwise affect the capability of boreholes to transmit fluids over the regulatory time frame.

Consistent with these criteria, there are several pathways for radionuclides to reach the accessible environment in the E scenario. Before any deep drilling intersects the waste, potential release pathways are identical to those in the undisturbed repository scenario.

If a borehole intersects the waste in the disposal rooms, releases to the accessible environment may occur as material entrained in the circulating drilling fluid is brought to the surface. Particulate waste brought to the surface may include cuttings, cavings, and spillings. Cuttings are the materials cut by the drill bit as it passes through waste. Cavings are the materials eroded by the drilling fluid in the annulus around the drill bit. Spallings are the materials forced into the circulating drilling fluid if there is sufficient pressure in the waste disposal panels. During drilling, contaminated brine may flow up the borehole and reach the surface, depending on fluid pressure within the waste disposal panels.

When abandoned, the borehole is assumed to be plugged in a manner consistent with current practices in the Delaware Basin as prescribed in 40 CFR § 194.33(c)(1). An abandoned intrusion

1 borehole with degraded casing and/or plugs may provide a pathway for fluid flow and
2 contaminant transport from the intersected waste panel to the ground surface if the fluid pressure
3 within the panel is sufficiently greater than hydrostatic. Additionally, if brine flows through the
4 borehole to overlying units, such as the Culebra, it may carry dissolved and colloidal actinides
5 that can be transported laterally to the accessible environment by natural groundwater flow in the
6 overlying units.

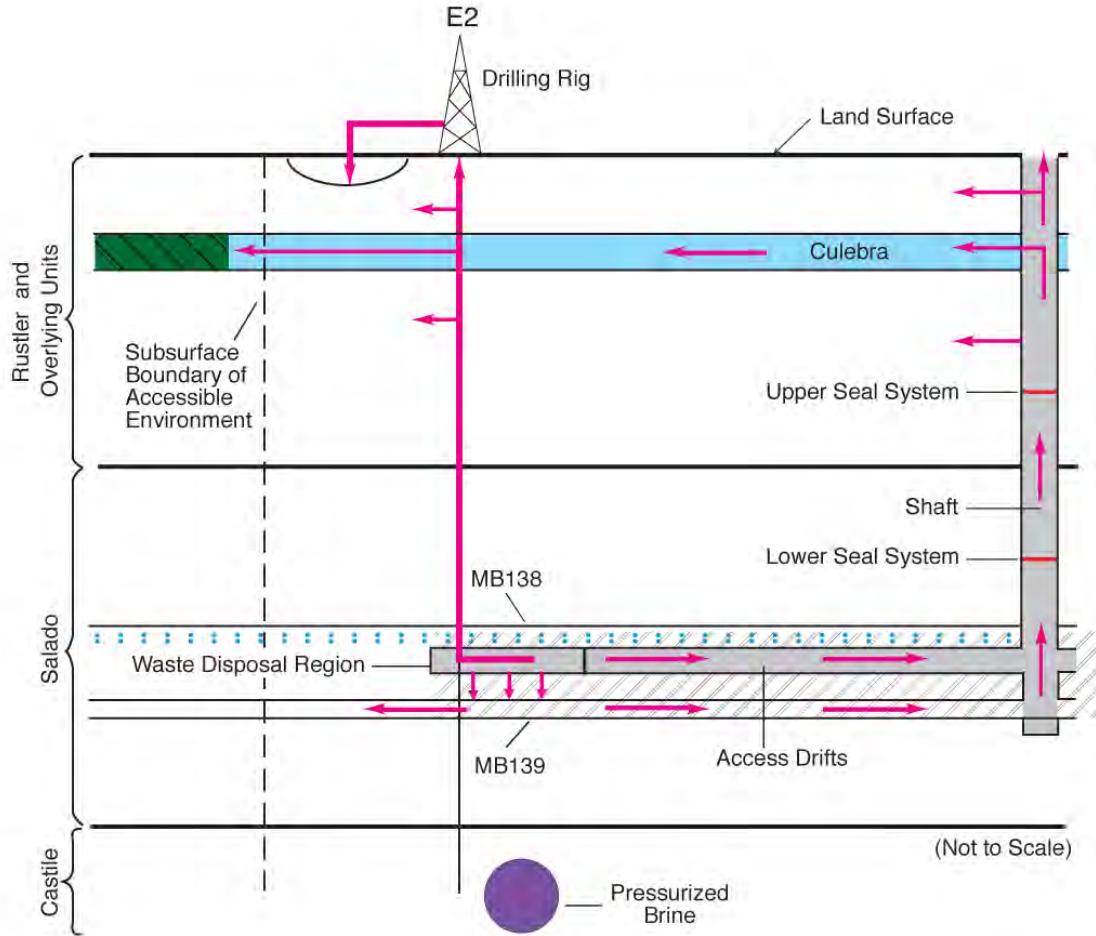
7 Alternatively, the units intersected by an intrusion borehole may provide sources for brine flow
8 to a waste panel during or after drilling. For example, in the northern Delaware Basin, the
9 Castile, which underlies the Salado, contains isolated volumes of brine at fluid pressures greater
10 than hydrostatic (as discussed in the CRA-2004, Chapter 2.0, Section 2.2.1.2.2). The WIPP-12
11 penetration of one of these reservoirs provided data on one brine reservoir within the controlled
12 area. The location and properties of brine reservoirs cannot be reliably predicted; thus, the
13 possibility of a deep borehole penetrating both a waste panel and a brine reservoir is accounted
14 for in consequence analysis of the WIPP, as discussed in the CRA-2004, Chapter 6.0, Section
15 6.4.8. Such a borehole could provide a connection for brine flow from the Castile to the waste
16 panel, thus increasing fluid pressure and brine volume in the waste panel.

17 A borehole that is drilled through a disposal room pillar, but does not intersect waste, could also
18 penetrate the brine reservoir underlying the waste disposal region. Such an event would, to some
19 extent, depressurize the brine reservoir, and thus would affect the consequences of any
20 subsequent reservoir intersections. The PA does not take credit for possible brine reservoir
21 depressurization.







22 The DOE has distinguished two types of deep drilling events by whether or not the borehole
23 intersects a Castile brine reservoir. A borehole that intersects a waste disposal panel and
24 penetrates a Castile brine reservoir is designated an E1 event. A borehole that intersects a waste
25 panel but does not penetrate a Castile brine reservoir is designated an E2 event. The
26 consequences of deep drilling intrusions depend not only on the type of a drilling event, but on
27 whether the repository was penetrated by an earlier E2 event or flooded due to an earlier E1
28 event. The PA also does not take credit for depressurization of brine reservoirs from multiple
29 drilling intrusions. These scenarios are described in order of increasing complexity in the
30 following sections.

31 **PA-2.3.2.2.3 The E2 Scenario**

32 The E2 scenario is the simplest scenario for inadvertent human intrusion into a waste disposal
33 panel. In this scenario, a panel is penetrated by a drill bit; cuttings, cavings, spallings, and brine
34 flow releases may occur; and brine flow may occur in the borehole after it is plugged and
35 abandoned. Sources for brine that may contribute to long-term flow up the abandoned borehole
36 are the Salado or, under certain conditions, the units above the Salado. An E2 scenario may
37 involve more than one E2 drilling event, although the flow and transport model configuration
38 developed for the E2 scenario evaluates the consequences of futures that have only one E2 event.
39 Features of the E2 scenario are illustrated in Figure PA-10.



Note: Borehole penetrates waste and does not penetrate pressurized brine in the underlying Castile. Arrows indicate hypothetical direction of groundwater flow and radionuclide transport.

-  Anhydrite layers A and B
-  Groundwater flow and radionuclide transport
-  Repository and shafts
-  Culebra
-  DRZ
-  Increase in Culebra hydraulic conductivity due to mining

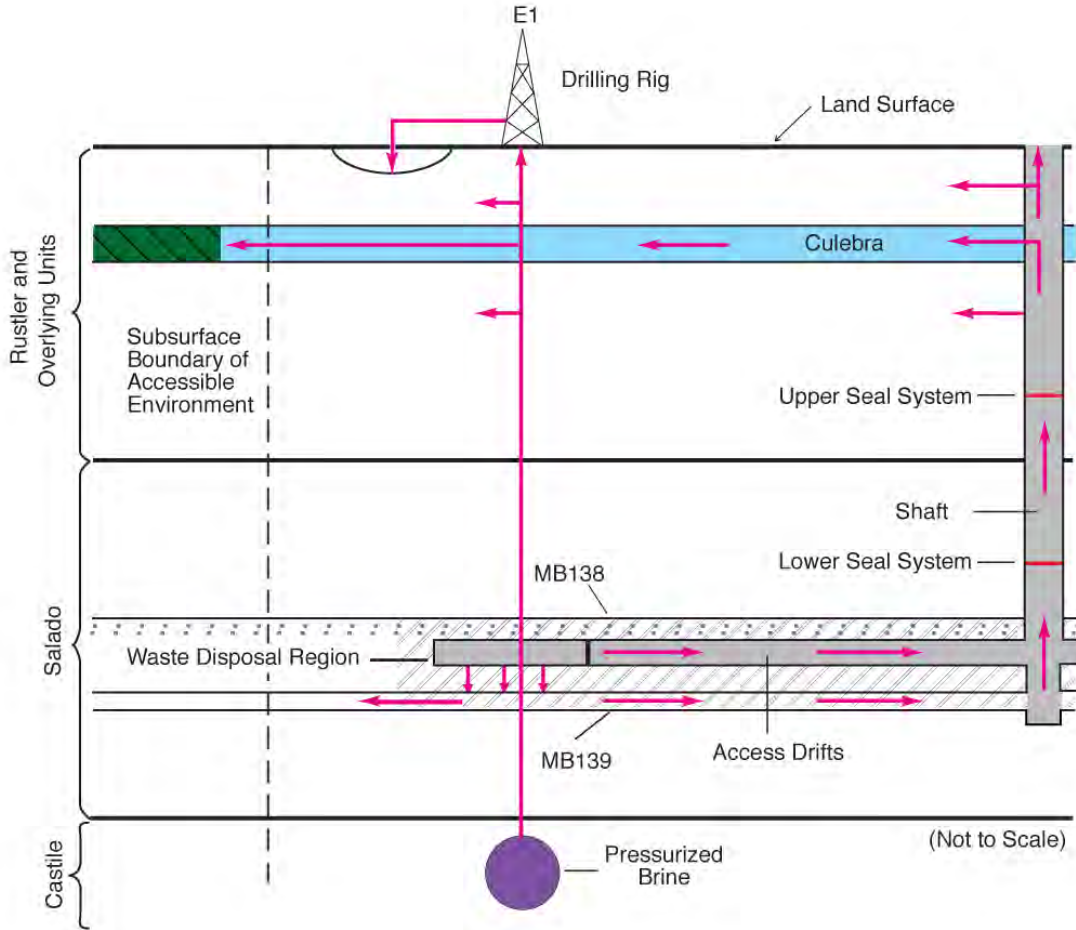
CCA-011-2

1
2 **Figure PA-10. Conceptual Release Pathways for the Disturbed Repository Deep Drilling**
3 **E2 Scenario**

4 **PA-2.3.2.2.4 The E1 Scenario**

5 Any scenario with exactly one inadvertent penetration of a waste panel that also penetrates a
6 Castile brine reservoir is called E1. Features of this scenario are illustrated in Figure PA-11.

7 Sources of brine in the E1 scenario are the brine reservoir, the Salado, and, under certain
8 conditions, the units above the Salado. However, the brine reservoir is conceptually the
9 dominant source of brine in this scenario. The flow and transport model configuration developed
10 for the E1 scenario evaluates the consequences of futures that have only one E1 event.



Note: Borehole penetrates waste and pressurized brine in the underlying Castile Formation. Arrows indicate hypothetical direction of groundwater flow and radionuclide transport.

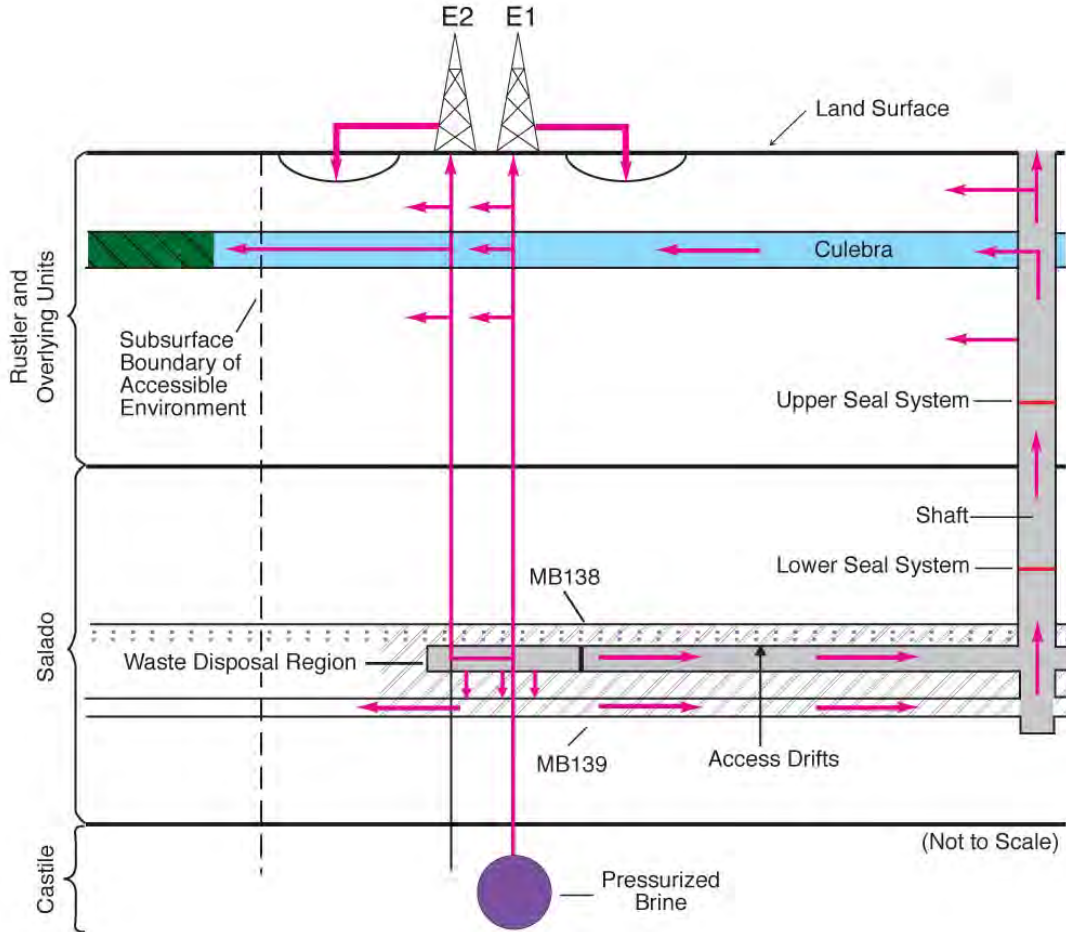
- Anhydrite layers A and B
- Culebra
- Groundwater flow and radionuclide transport
- DRZ
- Repository and shafts
- Increase in Culebra hydraulic conductivity due to mining

CCA-010-2

1
2 **Figure PA-11. Conceptual Release Pathways for the Disturbed Repository Deep Drilling**
3 **E1 Scenario**

4 **PA-2.3.2.2.5 The E1E2 Scenario**

5 The E1E2 scenario is defined as all futures with multiple penetrations of a waste panel of which
6 at least one intrusion is an E1. One example of this scenario, with a single E1 event and a single
7 E2 event penetrating the same panel, is illustrated in Figure PA-12. However, the E1E2 scenario
8 can include many possible combinations of intrusion times, locations, and types of event (E1 or
9 E2). The sources of brine in this scenario are those listed for the E1 scenario, and multiple E1
10 sources may be present. The E1E2 scenario has a potential flow path not present in the E1 or E2
11 scenarios: flow from an E1 borehole through the waste to another borehole. This flow path has
12 the potential to (1) bring large quantities of brine in direct contact with waste and (2) provide a



Note: Example shown includes only two boreholes, both of which penetrate waste and one of which penetrates pressurized brine in the underlying Castile. Pathways are similar for examples containing multiple boreholes. Arrows indicate hypothetical direction of groundwater flow and radionuclide transport.

- Anhydrite layers A and B
- Culebra
- Groundwater flow and radionuclide transport
- DRZ
- Repository and shafts
- Increase in Culebra hydraulic conductivity due to mining

CCA-012-2

1
 2 **Figure PA-12. Conceptual Release Pathways for the Disturbed Repository Deep Drilling**
 3 **E1E2 Scenario**

4 less restrictive path for this brine to flow to the units above the Salado (via multiple boreholes)
 5 compared to either the individual E1 or E2 scenarios. It is both the presence of brine reservoirs
 6 and the potential for flow through the waste to other boreholes that make this scenario different
 7 from combinations of E2 boreholes in terms of potential consequences. Estimates from flow and
 8 transport modeling are used to determine the extent of flow between boreholes and whether
 9 modeled combinations of E1 and E2 boreholes at specific locations in the repository should be
 10 treated as E1E2 scenarios or as independent E1 and E2 scenarios in the consequence analysis.

1 **PA-2.3.2.3 Disturbed Repository ME Scenario**

2 The M scenario and the E scenario may both occur in the future. The DOE calls a future in
3 which both of these events occur the ME scenario. The occurrence of both mining and deep
4 drilling do not create processes beyond those already described separately for the M and E
5 scenarios. For example, the occurrence of mining does not influence any of the interactions
6 between deep boreholes and the repository or brine reservoirs, nor does the occurrence of drilling
7 impact the effects of mining on Culebra hydrogeology.

8 **PA-2.3.2.4 Scenarios Retained for Consequence Analysis**

9 The scenarios described in Section PA-2.3.2.1, Section PA-2.3.2.2, and Section PA-2.3.2.3 have
10 been retained for consequence analysis to determine compliance with the containment
11 requirements in section 191.13. The modeling systems used to evaluate the consequences of
12 these undisturbed and disturbed scenarios are discussed in Section PA-2.3.3.

13 **PA-2.3.3 Calculation of Scenario Consequences**

14 Calculating scenario consequences requires quantitative modeling. This section discusses the
15 conceptual and computational models and some parameter values used to estimate the
16 consequence of the scenarios described in Section PA-2.3.2. Additional discussion of conceptual
17 models and modeling assumptions is provided in Section PA-4.0. Additional descriptions of
18 sampled parameter values are included in Fox (2008).

19 A single modeling system was used to represent the disposal system and calculate the CCDFs.
20 The modeling system, however, can be conveniently described in terms of various submodels,
21 with each describing a part of the overall system. The models used in the WIPP PA, as in other
22 complex analyses, exist at four different levels.

- 23 1. **Conceptual models** are a set of qualitative assumptions that describe a system or subsystem
24 for a given purpose. At a minimum, these assumptions concern the geometry and
25 dimensionality of the system, initial and boundary conditions, time dependence, and the
26 nature of the relevant physical and chemical processes. The assumptions should be
27 consistent with one another and with existing information within the context of the given
28 purpose.
- 29 2. **Mathematical models** represent the processes at the site. The conceptual models provide
30 the context within which these mathematical models must operate, and define the processes
31 they must characterize. The mathematical models are predictive in the sense that, once
32 provided with the known or assumed properties of the system and possible perturbations to
33 the system, they predict the response of the system. The processes represented by these
34 mathematical models include fluid flow, mechanical deformation, radionuclide transport in
35 groundwater, and removal of waste through intruding boreholes.
- 36 3. **Numerical models** are developed to approximate mathematical model solutions because
37 most mathematical models do not have closed-form solutions.

1 4. The complexity of the system requires computer codes to solve the numerical models. The
2 implementation of the numerical model in the computer code with specific initial and
3 boundary conditions and parameter values is generally referred to as the *computational*
4 *model*.

5 Data are descriptors of the physical system being considered, normally obtained by experiment
6 or observation. Parameters are values necessary in mathematical, numerical, or computational
7 models. The distinction between data and parameters can be subtle. Parameters are distinct from
8 data, however, for three reasons: (1) Data may be evaluated, statistically or otherwise, to
9 generate model parameters to account for uncertainty in data. (2) Some parameters have no
10 relation to the physical system, such as the parameters in a numerical model to determine when
11 an iterative solution scheme has converged. (3) Many model parameters are applied at a
12 different scale than one directly observed or measured in the physical system. The distinction
13 between data and parameter values is described further in Fox (2008) and Tierney (1990), where
14 distribution derivations for specific parameters are given. The interpretation and scaling of
15 experimental and field data are discussed in Fox (2008) for individual and sampled parameters,
16 as appropriate.

1 **PA-3.0 Probabilistic Characterization of Futures**

2 The PA for the WIPP identifies uncertainty in parameters and uncertainty in future events as
3 distinctly different entities and requires sampling to be conducted in two dimensions. One
4 dimension focuses on characterizing the uncertainty in terms of the probability that various
5 possible futures will occur at the WIPP site over the next 10,000 years. The other dimension
6 characterizes the uncertainty due to lack of knowledge about the precise values of model
7 parameters appropriate for the WIPP repository. Each dimension of the analysis is characterized
8 by a probability space. Monte Carlo methods are used with the WIPP PA modeling system to
9 sample each of the two probability spaces.

10 Characterizing the probability distribution for the first dimension of the PA depends on
11 identifying the kinds of events that could impact releases from the repository over the next
12 10,000 years. Screening analyses of possible future events concluded that the only significant
13 events with the potential to affect radionuclide releases to the accessible environment are drilling
14 and mining within the LWB (Appendix SCR-2009, Section SCR-5.0). Consequently, modeling
15 the future states of the repository focuses on representing the occurrences and effects of these
16 two events. CCDFGF uses stochastic processes to simulate intrusion events by drilling and the
17 occurrence of mining for natural resources. CCDFGF assembles the results from the
18 deterministic models and selects the most appropriate scenario data provided by these models to
19 use as the simulation of a 10,000-year future progresses. Ten thousand potential futures are
20 simulated and used to create distributions of potential releases, and then compiled into a single
21 CCDF of potential releases.

22 WIPP PA is required not only to estimate the likelihood of future releases, but to establish
23 confidence in those estimates. Confidence is established using the second dimension of the
24 analysis, which is based on the evaluation of uncertainty in the values of some of the parameters
25 of the deterministic models. This uncertainty is assumed to represent a lack of knowledge about
26 the true values of the parameters, and is labeled epistemic uncertainty. Epistemic uncertainty can
27 be viewed as the representation of potential systematic errors in the results. The impact of
28 epistemic uncertainty on the results is determined by generating 300 sets of parameter values
29 using a stratified random sampling design, LHS, and then running the deterministic models and
30 CCDFGF with each set of sampled parameters. Thus, 300 CCDFs are generated by CCDFGF.
31 One set of parameters is often referred to as a vector. The 300 simulations are organized as 3
32 replicates of 100 vectors each. Because the uncertainty assigned to the parameters represents a
33 lack of knowledge, this epistemic uncertainty could theoretically be reduced by collecting data to
34 improve knowledge about the parameters. Epistemic uncertainty is represented in the
35 projections of potential releases from the repository by the variability among the 300 CCDFs.

36 The WIPP PA modeling system consists of a set of loosely coupled deterministic models
37 (BRAGFLO, PANEL, NUTS, SECOTP2D, and CUTTINGS_S) that provide scenario-specific
38 results to the code CCDFGF (Figure PA-2). CCDFGF is, in contrast, a stochastic simulation
39 model used to simulate potential futures of repository performance where drilling and mining
40 intrusions can impact the state of the repository and produce release events. CCDFGF
41 implements intrusions as stochastic events, thus incorporating the aleatory uncertainty associated
42 with projections of future events. This section describes how aleatory uncertainty is
43 implemented in PA. Epistemic uncertainty is discussed in Section PA-6.0.

1 **PA-3.1 Probability Space**

2 As discussed in Section PA-2.2.2, aleatory uncertainty is defined by the possible futures $\mathbf{x}_{st,i}$
3 conditional on the set i of parameters used in Equation (PA.2). Section PA-3.2, Section PA-3.3,
4 Section PA-3.4, Section PA-3.5, Section PA-3.6, Section PA-3.7, Section PA-3.8, and Section
5 PA-3.9 describe the individual components t_j , e_j , l_j , b_j , p_j , \mathbf{a}_j , and t_{min} of $\mathbf{x}_{st,i}$ and their associated
6 probability distributions. The concept of a scenario as a subset of the sample space of $\mathbf{x}_{st,i}$ is
7 discussed in Section PA-3.10. The procedure used to sample the individual elements $\mathbf{x}_{st,i}$ is
8 described in Section PA-6.5.

9 **PA-3.2 AICs and PICs**

10 AICs and PICs will be implemented at the WIPP site to deter human activity detrimental to
11 repository performance. AICs and PICs are described in detail in the CRA-2004, Chapter 7.0
12 and in appendices referenced in Chapter 7.0. In this section, the impact of AICs and PICs on PA
13 is described.

14 AICs will be implemented at the WIPP after final facility closure to control site access and
15 ensure that activities detrimental to disposal system performance do not occur within the
16 controlled area. The AICs will preclude human intrusion in the disposal system. A 100-year
17 limit on the effectiveness of AICs in PA is established in 40 CFR § 191.14(a). Because of the
18 regulatory restrictions and the nature of the AICs that will be implemented, PA assumes there are
19 no inadvertent human intrusions or mining in the controlled area for 100 years following
20 repository closure.

21 PICs are designed to deter inadvertent human intrusion into the disposal system. Only minimal
22 assumptions were made about the nature of future society when designing the PICs to comply
23 with the assurance requirements. The preamble to Part 194 limits any credit for PICs in
24 deterring human intrusion to 700 years after disposal (U.S. Environmental Protection Agency
25 1996a p. 5231). Although the DOE originally took credit for PICs in the CCA PA, but has not
26 taken credit since. Not including PICs is a conservative implementation, as no credit is taken for
27 a beneficial process.

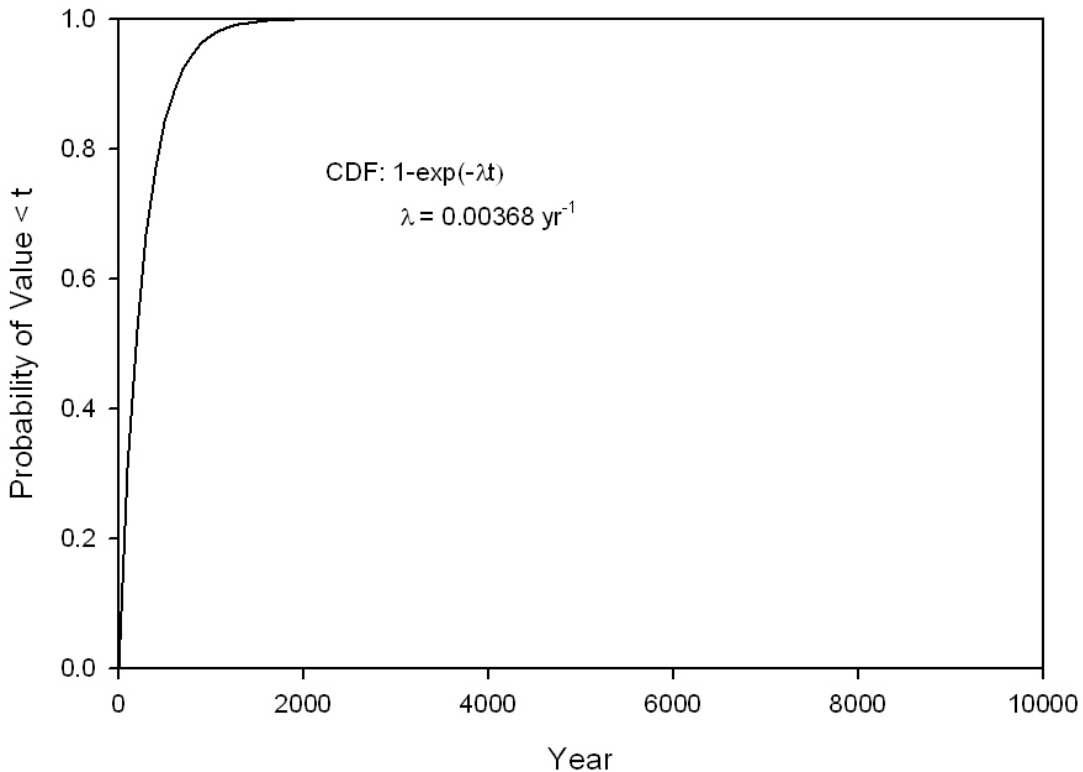
28 **PA-3.3 Drilling Intrusion**

29 As described in Section PA-2.3.2.2, drilling intrusions in PA are assumed to occur randomly in
30 time and space following a Poisson process. Specifically, the drilling rate considered within the
31 area marked by a berm as part of the system for PICs (Fox 2008, Table 46) is 5.85×10^{-3}
32 intrusions per square kilometer per year (km^2/yr). AICs are assumed to prevent any drilling
33 intrusions for the first 100 years after the decommissioning of the WIPP (Section PA-3.2). In the
34 computational implementation of PA, it is convenient to represent the Poisson process for
35 drilling intrusions by its corresponding rate term $\lambda_d(t)$ for intrusions into the area marked by the
36 berm. Specifically,

$$\lambda_d(t) = \begin{cases} 0 & 0 \leq t < 100 \text{ yr} \\ (0.6285 \text{ km}^2)(5.85 \times 10^{-3} \text{ km}^{-2} \text{ yr}^{-1}) = 3.68 \times 10^{-3} \text{ yr}^{-1} & 100 \leq t \leq 10,000 \text{ yr} \end{cases} \quad (\text{PA.6})$$

2 where 0.6285 km² is the area enclosed by the berm (Fox 2008, Table 45) and *t* is elapsed time
 3 since decommissioning the WIPP.

4 The function $\lambda_d(t)$ defines the parameter of the exponential distribution that gives rise to the
 5 times of intrusions, t_j of Equation (PA.2). In the computational implementation of the analysis,
 6 the exponential distribution is sampled to define the times between successive drilling intrusions
 7 (Figure PA-13, Section PA-6.5). A key assumption of the exponential distribution is that events
 8 are independent of each other, so the occurrence of one has no effect on the occurrence of the
 9 next event. The process giving rise to such events is sometimes called a Poisson process because
 10 the distribution of such events over a fixed interval of time is a Poisson distribution. Due to the
 11 10,000-year regulatory period specified in section 191.13, t_j is assumed to be bounded above by
 12 10,000 years in the definition of $\mathbf{x}_{st,i}$. Further, t_j is bounded below by 100 years as defined in
 13 Equation (PA.6).



14
 15 **Figure PA-13. CDF for Time Between Drilling Intrusions**

16 **PA-3.4 Penetration of Excavated/Nonexcavated Area**

17 The variable e_j is a designator for whether or not the j^{th} drilling intrusion penetrates an
 18 excavated, waste-filled area of the repository: $e_j = 0$ or 1 implies penetration of nonexcavated or

1 excavated area, respectively. The corresponding probabilities $P[e_j = 0]$ and $P[e_j = 1]$ for $e_j = 0$
 2 and $e_j = 1$ are

3
$$pEx_1 = P[e_j = 1] = 0.1273 \text{ km}^2 / 0.6285 \text{ km}^2 = 0.203 \tag{PA.7}$$

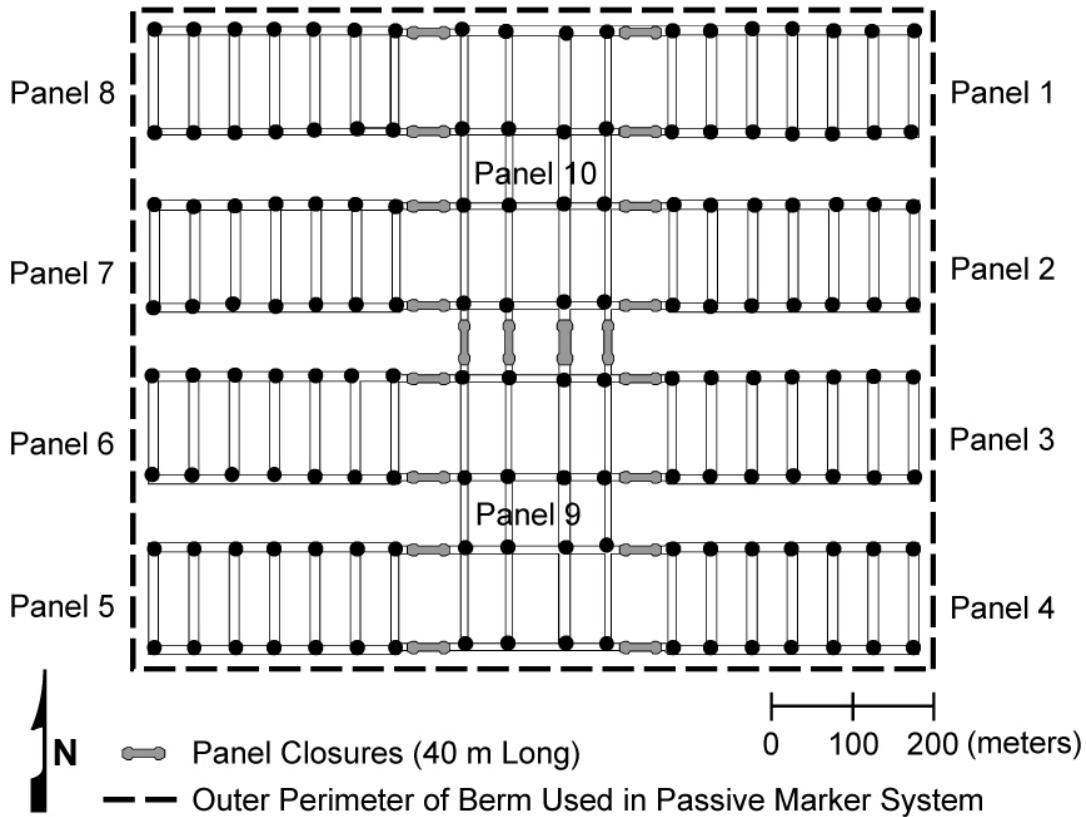
4
$$pEx_0 = P[e_j = 0] = 1 - pEx_1 = 0.797 \tag{PA.8}$$

5 where 0.1273 km^2 and 0.6285 km^2 are the excavated area of the repository and the area of the
 6 berm, respectively (Fox 2008, Table 45).

7 **PA-3.5 Drilling Location**

8 Locations of drilling intrusions through the excavated, waste-filled area of the repository are
 9 discretized to the 144 locations in Figure PA-14. Assuming that a drilling intrusion occurs
 10 within the excavated area, it is assumed to be equally likely to occur at each of these 144
 11 locations. Thus, the probability pL_k that drilling intrusion j will occur at location l_k , $k = 1, 2, \dots,$
 12 144 in Figure PA-14 is

13
$$pL_{k;k=1,2,3} = P[k = 1] = P[k = 2] = \dots = P[k = 144] = 1/144 = 6.94 \times 10^{-3} \tag{PA.9}$$



14 **Figure PA-14. Discretized Locations for Drilling Intrusions**

1 **PA-3.6 Penetration of Pressurized Brine**

2 The conceptual models for the Castile include the possibility that pressurized brine reservoirs
 3 underlie the repository (Section PA-4.2.10). The variable b_j is a designator for whether or not
 4 the j^{th} drilling intrusion penetrates pressurized brine, where $b_j = 0$ signifies nonpenetration and b_j
 5 = 1 signifies penetration of pressurized brine. In PA, the probability $pB_1 = P[b_j = 1]$ is sampled
 6 from a uniform distribution ranging from 0.01 to 0.60 (see GLOBAL:PBRINE in Table PA-19).

7 **PA-3.7 Plugging Pattern**

8 Three borehole plugging patterns, p_k , are considered in PA: (1) p_1 , a full concrete plug through
 9 the Salado to the Bell Canyon Formation (hereafter referred to as Bell Canyon), (2) p_2 , a two-
 10 plug configuration with concrete plugs at the Rustler/Salado interface and the Castile/Bell
 11 Canyon interface, and (3) p_3 , a three-plug configuration with concrete plugs at the Rustler/
 12 Salado, Salado/Castile, and Castile/Bell Canyon interfaces. The probability that a given drilling
 13 intrusion will be sealed with plugging pattern p_k , $k = 1, 2, 3$, is given by pPL_k , where $pPL_1 = P[k$
 14 = 1] = 0.015, $pPL_2 = P[k = 2] = 0.696$, $pPL_3 = P[k = 3] = 0.289$ (Fox 2008, Table 46).

15 **PA-3.8 Activity Level**

16 The waste intended for disposal at the WIPP is represented by 767 distinct waste streams, with
 17 690 of these waste streams designated as CH-TRU waste and 77 designated as RH-TRU waste
 18 (Leigh, Trone and Fox 2005, Section 4.4). For the CRA-2009 PA, the 77 separate RH-TRU
 19 waste streams are represented by a single, combined RH-TRU waste stream. The activity levels
 20 for the waste streams are given in Fox (2008, Table 48 and Table 49). Each waste container
 21 emplaced in the repository contains waste from a single CH-TRU waste stream. Waste packaged
 22 in 55-gallon (gal) drums is stacked 3 drums high within the repository. Although waste in other
 23 packages (e.g., standard waste boxes, 10-drum overpacks, etc.) may not be stacked 3 high, PA
 24 assumes that each drilling intrusion into CH-TRU waste intersects 3 different waste streams. In
 25 contrast, all RH-TRU waste is represented by a single waste stream, and so each drilling
 26 intrusion through RH-TRU waste is assumed to intersect this single waste stream. Appendix
 27 MASS-2009, Section MASS-21.0 examines the sensitivity of PA results to the assumption that
 28 three waste streams are intersected by each drilling intrusion into CH-TRU waste.

29 The vector \mathbf{a}_j characterizes the type of waste penetrated by the j^{th} drilling intrusion. Specifically,

30
$$\mathbf{a}_j = 0 \text{ if } e_j = 0 \tag{PA.10}$$

31 (i.e., if the i^{th} drilling intrusion does not penetrate an excavated area of the repository);

32
$$\mathbf{a}_j = 1 \text{ if } e_j = 1 \text{ and RH-TRU is penetrated} \tag{PA.11}$$

33
$$\mathbf{a}_j = [iCH_{j1}, iCH_{j2}, iCH_{j3}] \text{ if } e_j = 1 \text{ and CH-TRU is penetrated} \tag{PA.12}$$

1 where iCH_{j1} , iCH_{j2} , and iCH_{j3} are integer designators for the CH-TRU waste streams intersected
 2 by the j^{th} drilling intrusion (i.e., each of iCH_{j1} , iCH_{j2} , and iCH_{j3} is an integer between 1 and
 3 690).

4 Whether the j^{th} intrusion penetrates a nonexcavated or excavated area is determined by the
 5 probabilities pE_0 and pE_1 discussed in Section PA-3.4. The type of waste penetrated is
 6 determined by the probabilities pCH and pRH . The excavated area used for disposal of CH-TRU
 7 waste (aCH) is 1.115×10^5 square meters (m^2) and the area used for disposal of RH-TRU waste
 8 (aRH) is $1.576 \times 10^4 m^2$ (Fox 2008, Table 45), for a total disposal area of $aEX = aCH + aRH =$
 9 $1.273 \times 10^5 m^2$. Given that the j^{th} intrusion penetrates an excavated area, the probabilities pCH
 10 and pRH of penetrating CH-TRU and RH-TRU waste are given by

11
$$pCH = P[\text{CH waste area penetrated}] = aCH / aEX = (1.115 \times 10^5 m^2) / (1.273 \times 10^5 m^2) = 0.876$$

 12 (PA.13)

13
$$pRH = P[\text{RH waste area penetrated}] = aRH / aEX = (1.576 \times 10^4 m^2) / (1.273 \times 10^5 m^2) = 0.124$$

 14 (PA.14)

15 As indicated in this section, the probabilistic characterization of \mathbf{a}_j depends on a number of
 16 individual probabilities. Specifically, pEx_0 and pEx_1 determine whether a nonexcavated or
 17 excavated area is penetrated (Section PA-3.5); pCH and pRH determine whether CH-TRU or
 18 RH-TRU waste is encountered, given penetration of an excavated area; and the individual waste
 19 stream probabilities in Fox (2008, Table 48 and Table 49), determine the specific waste streams
 20 iCH_{j1} , iCH_{j2} , and iCH_{j3} encountered given a penetration of CH-TRU waste. The probability of
 21 encountering a particular CH-TRU waste stream is computed as the ratio of the volume of that
 22 waste stream to the volume of CH-TRU waste.

23 **PA-3.9 Mining Time**

24 Full mining of known potash reserves within the LWB is assumed to occur at time t_{min} . The
 25 occurrence of mining within the LWB in the absence of institutional controls is specified as
 26 following a Poisson process with a rate of $\lambda_m = 1 \times 10^{-4} \text{ yr}^{-1}$ (Fox 2008, Table 46). However,
 27 this rate can be reduced by AICs and PICs. Specifically, AICs are assumed to result in no
 28 possibility of mining for the first 100 years after decommissioning of the WIPP. In PA, PICs do
 29 not affect the mining rate. Thus, the mining rate $\lambda_m(t)$ is

30
$$\lambda_m(t) = 0 \text{ yr}^{-1} \quad \text{for } 0 \leq t < 100 \text{ yrs} \quad (\text{PA.15})$$

31
$$\lambda_m(t) = 1 \times 10^{-4} \text{ yr}^{-1} \quad \text{for } 100 \leq t \leq 10,000 \text{ yrs} \quad (\text{PA.16})$$

32 where t is the elapsed time since decommissioning of the WIPP.

33 In the computational implementation of the analysis, $\lambda_m(t)$ is used to define the distribution of
 34 time to mining. The use of $\lambda_m(t)$ to characterize t_{min} is analogous to the use of λ_d to

1 characterize the t_j , except that only one mining event is assumed to occur (i.e., $\mathbf{x}_{st,i}$ contains only
 2 one value for t_{min}) in order to be consistent with guidance given in Part 194 that mining within
 3 the LWB should be assumed to remove all economically viable potash reserves. Due to the
 4 10,000-year regulatory period specified in section 191.13, t_{min} is assumed to be bounded above
 5 by 10,000 years in the definition of $\mathbf{x}_{st,i}$.

6 **PA-3.10 Scenarios and Scenario Probabilities**

7 A scenario is a subset of the sample space for aleatory uncertainty. The underlying goal of
 8 scenario definition is to define the state of repository conditions prior to and following intrusion
 9 events. Scenarios are specific cases of inputs or system states that are selected to cover the range
 10 of possible cases. Given the complexity of the futures $\mathbf{x}_{st,i}$ (see Equation (PA.2)), many different
 11 scenarios can be defined. The computational complexity of the function $f(\mathbf{x}_{st,i}|\mathbf{v}_{su})$ in Section
 12 PA-2.2.3 limits evaluation to only a few intrusion scenarios. As presented in Section PA-2.3.2,
 13 PA considers four fundamental intrusion scenarios:

14 E0 = no drilling intrusion through an excavated area of the repository

15 E1 = a drilling intrusion through an excavated area of the repository that penetrates
 16 pressurized brine in the Castile

17 E2 = a drilling intrusion through an excavated area of the repository that does not
 18 penetrate pressurized brine in the Castile

19 E1E2 = two or more previous intrusions, at least one of which is an E1 intrusion

20 These definitions of intrusion scenarios capture the most important events impacting the state of
 21 the repository: whether or not the repository is inundated by the penetration of a brine pocket,
 22 and whether or not there exists a possible route of release upward via a borehole. The state of the
 23 repository is also designated as E0, E1, E2, or E1E2. Scenarios for some of the process-level
 24 models consist of a single intrusion scenario occurring at specific times. CCDFGF is used to
 25 simulate multiple intrusions over 10,000 years.

26 If only the intrusion scenarios controlled the state of the repository, then the state would be
 27 defined by the sequence of drilling events alone. However, CCDFGF also considers the impact
 28 of plugging pattern on boreholes. A borehole with a full plugging pattern that penetrates the
 29 waste area is also assumed to have no impact, and leaves the repository in its previous state,
 30 including the undisturbed state (see Section PA-6.8.4.1 and Figure PA-41 for more details).
 31 Thus, an E2 intrusion event into an E0 repository will result in an E0 state if a full plugging
 32 pattern is used, or an E2 state otherwise. An E1 intrusion subsequent to an E2 intrusion will
 33 leave the repository in an E1E2 state, where it will remain, regardless of subsequent intrusions.
 34 It is therefore important to distinguish between the type of intrusion, listed above, and the state of
 35 the repository.

36 The probability that no excavated area will be penetrated during the 10,000-year interval can be
 37 computed using a distribution of the number of penetration events and the probability that a

1 drilling event will penetrate the excavated area. For the Poisson distribution of drilling events,
 2 the probability of there being n events in the 10,000-year history is

$$3 \quad \frac{e^{-\lambda_d \times 9900} (\lambda_d \times 9900)^n}{n!} \text{ for } n = 1, 2, 3, \dots \quad (\text{PA.17})$$

4 where λ_d is the mean drilling rate per year in the period following the period of AICs, 9,900 is
 5 the number of years in which drilling can occur after the institutional control period of 100 years,
 6 and n is the number of drilling events. The probability of having n events all within the
 7 nonexcavated area is pEx_0^n , or specifically 0.797^n . Thus, the probability of having only events
 8 in the nonexcavated area over 10,000 years, i.e., having no drilling intrusions into the excavated
 9 area, is just the sum across all n of the products of the probability of having exactly n drilling
 10 events and the probability that all n events penetrate the unexcavated area:

$$11 \quad \sum_{n=0}^{\infty} \frac{e^{-\lambda_d \times 9900} (\lambda_d \times 9900)^n}{n!} pEx_0^n = e^{-\lambda_d \times 9900 \times pEx_1} \quad (\text{PA.18})$$

12 The calculated probability becomes

$$13 \quad \exp(-0.203 \times 3.68 \times 10^{-3} \times (10000 - 100)) = 6.1 \times 10^{-4} \quad (\text{PA.19})$$

14 This probability is the lower bound on the probability of the repository being in an E0 state,
 15 given that it does not include the consideration of the plugging pattern.

16 The probability of a single E1, E2, or E1E2 intrusion over 10,000 years is relatively small.
 17 Assuming that pB_1 takes on its mean value of 0.305 (see Section PA-3.6), and ignoring the
 18 impact of the plugging pattern, for a constant rate of drilling, λ_d , these equations are

$$19 \quad e^{-pEx_1 \lambda_d \times 9900} (pEx_1 \lambda_d \times 9900) pB_1 = 1.4 \times 10^{-3} \quad (\text{PA.20})$$

20 and

$$21 \quad e^{-pEx_1 \lambda_d \times 9900} (pEx_1 \lambda_d \times 9900) pB_0 = 3.2 \times 10^{-3} \quad (\text{PA.21})$$

22 respectively, where $(pEx_1 \times \lambda_d)$ represents the annual rate of drilling into the excavated region of
 23 the repository which is multiplied by 9900 to give the rate per 9,900 years. The probability of an
 24 intrusion into the excavated area is subsequently multiplied by the probability of hitting or
 25 missing a brine pocket. In this form, it can be seen that the term for the probability for intrusion
 26 is equivalent to the PDF of the Poisson distribution for $n = 1$:

$$27 \quad f(n) = \frac{e^{-\lambda} \lambda^n}{n!} \quad (\text{PA.22})$$

1 The expressions defining the probability of being in the E0 state after 10,000 years and of having
2 a single E1 or E2 intrusion event after 10,000 years are relatively simple because the scenarios
3 E0, E1, and E2 are relatively simple. The scenario E1E2 is more complex and, as a result,
4 computing its probability is also more complex. Closed-form formulas for the probabilities of
5 quite complex scenarios can be derived, but they are very complicated and involve large
6 numbers of iterated integrals (Helton 1993). These probabilities of single E1 and E2 intrusions
7 are relevant to the scenarios used by the process-level models.

8 **PA-3.11 CCDF Construction**

9 CCDFGF simulates histories that can have many intrusion events (WIPP Performance
10 Assessment 2003a). The process-level models evaluate the releases at a small number of
11 specific times for each of the four intrusion scenarios. Releases from the repository are
12 calculated using results from these fundamental scenarios (Section PA-6.7 and Section PA-6.8).
13 Releases for an arbitrary future are estimated from the results of these fundamental scenarios
14 (Section PA-6.8); these releases are used to construct CCDFs by Equation (PA.4).

15 Previous WIPP PAs have used the Monte Carlo approach to construct the CCDF indicated in
16 Equation (PA.4). The Monte Carlo approach generates releases for 10,000 possible futures.
17 CCDFs are constructed by treating the 10,000 releases values as order statistics; each release is
18 assigned a probability of 1×10^{-4} , and the CCDF can be constructed by plotting the complement
19 of the sum of the probabilities ordered by the release value. The CRA-2009 PA uses the same
20 approach as the CRA-2004 PA.

1 PA-4.0 Estimation of Releases

2 This section describes how releases to the accessible environment are estimated for a particular
3 future in PA.

4 PA-4.1 Results for Specific Futures

5 The function $f(\mathbf{x}_{st,i})$ estimates the radionuclide releases to the accessible environment associated
6 with each of the possible futures ($\mathbf{x}_{st,i}$) that could occur at the WIPP site over the next 10,000
7 years. In practice, $f(\mathbf{x}_{st,i})$ is quite complex and is constructed by the models implemented in
8 computer programs used to simulate important processes and releases at the WIPP. In the
9 context of these models, $f(\mathbf{x}_{st,i})$ has the form

$$\begin{aligned}
 f(\mathbf{x}_{st,i}) = & f_C(\mathbf{x}_{st,i}) + f_{SP}[\mathbf{x}_{st,i}, f_B(\mathbf{x}_{st,i})] + f_{DBR}[\mathbf{x}_{st,i}, f_B(\mathbf{x}_{st,i})] \\
 & + f_{MB}[\mathbf{x}_{st,i}, f_B(\mathbf{x}_{st,i})] + f_{DL}[\mathbf{x}_{st,i}, f_B(\mathbf{x}_{st,i})] + f_S[\mathbf{x}_{st,i}, f_B(\mathbf{x}_{st,i})] \quad (\text{PA.23}) \\
 & + f_{ST}[f_{MF}(\mathbf{x}_{st,0}), f_{NP}[\mathbf{x}_{st,i}, f_B(\mathbf{x}_{st,i})]]
 \end{aligned}$$

11 where

- 12 $\mathbf{x}_{st,i}$ ~ particular future under consideration
 13 $\mathbf{x}_{st,0}$ ~ future involving no drilling intrusions but a mining event at the same
 14 time t_{min} as in x_{st}
 15 $f_C(\mathbf{x}_{st,i})$ ~ cuttings and cavings release to accessible environment for $\mathbf{x}_{st,i}$
 16 calculated with CUTTINGS_S
 17 $f_B(\mathbf{x}_{st,i})$ ~ two-phase flow in and around the repository calculated for $\mathbf{x}_{st,i}$ with
 18 BRAGFLO; in practice, $f_B(\mathbf{x}_{st,i})$ is a vector containing a large amount
 19 of information, including pressure and brine saturation in various
 20 geologic members
 21 $f_{SP}[\mathbf{x}_{st,i}, f_B(\mathbf{x}_{st,i})]$ ~ spillings release to accessible environment for $\mathbf{x}_{st,i}$ calculated with the
 22 spillings model contained in DRSPALL and CUTTINGS_S; this
 23 calculation requires repository conditions calculated by $f_B(\mathbf{x}_{st,i})$ as
 24 input
 25 $f_{DBR}[\mathbf{x}_{st,i}, f_B(\mathbf{x}_{st,i})]$ ~ DBR to accessible environment for $\mathbf{x}_{st,i}$ also calculated with
 26 BRAGFLO; this calculation requires repository conditions calculated
 27 by $f_B(\mathbf{x}_{st,i})$ as input
 28 $f_{MB}[\mathbf{x}_{st,i}, f_B(\mathbf{x}_{st,i})]$ ~ release through anhydrite MBs to accessible environment for $\mathbf{x}_{st,i}$
 29 calculated with NUTS; this calculation requires flows in and around
 30 the repository calculated by $f_B(\mathbf{x}_{st,i})$ as input

- 1 $f_{DL}[\mathbf{x}_{st,i}, f_B(\mathbf{x}_{st,i})]$ ~ release through Dewey Lake to accessible environment for $\mathbf{x}_{st,i}$
2 calculated with NUTS; this calculation requires flows in and around
3 the repository calculated by $f_B(\mathbf{x}_{st,i})$ as input
- 4 $f_S[\mathbf{x}_{st,i}, f_B(\mathbf{x}_{st,i})]$ ~ release to land surface due to brine flow up a plugged borehole for $\mathbf{x}_{st,i}$
5 calculated with NUTS; this calculation requires flows in and around
6 the repository calculated by $f_B(\mathbf{x}_{st,i})$ as input
- 7 $f_{MF}(\mathbf{x}_{st,0})$ ~ flow field in the Culebra calculated for $\mathbf{x}_{st,0}$ with MODFLOW; $\mathbf{x}_{st,0}$ is
8 used as an argument to f_{MF} because drilling intrusions are assumed to
9 cause no perturbations to the flow field in the Culebra
- 10 $f_{NP}[\mathbf{x}_{st,i}, f_B(\mathbf{x}_{st,i})]$ ~ release to Culebra for $\mathbf{x}_{st,i}$ calculated with NUTS or PANEL as
11 appropriate; this calculation requires flows in and around the
12 repository calculated by $f_B(\mathbf{x}_{st,i})$ as input
- 13 $f_{ST}[f_{MF}(\mathbf{x}_{st,0}), f_{NP}[\mathbf{x}_{st,i}, f_B(\mathbf{x}_{st,i})]]$ ~ groundwater transport release through Culebra to
14 accessible environment calculated with SECOTP2D. This calculation
15 requires MODFLOW results (i.e., $f_{MF}(\mathbf{x}_{st,i})$) and NUTS or PANEL
16 results (i.e., $f_{NP}[\mathbf{x}_{st,i}, f_B(\mathbf{x}_{st,i})]$) as input

17 The remainder of this section describes the mathematical structure of the mechanistic models
18 that underlie the component functions of $f(\mathbf{x}_{st,i})$ in Equation (PA.23).

19 The Monte Carlo CCDF construction procedure, implemented in the code CCDFGF (WIPP
20 Performance Assessment 2003a), uses a sample of size $nS = 10,000$ in PA. The individual
21 programs that estimate releases do not run fast enough to allow this many evaluations of f . As a
22 result, a two-step procedure is being used to evaluate f in calculating the summation in Equation
23 (PA.23). First, f and its component functions are evaluated with the procedures (i.e., models)
24 described in this section for a group of preselected futures. Second, values of $f(\mathbf{x}_{st})$ for the
25 randomly selected futures $\mathbf{x}_{st,i}$ used in the numerical evaluation of the summation in Equation
26 (PA.23) are then constructed from results obtained in the first step. These constructions are
27 described in Section PA-6.7 and Section PA-6.8, and produce the evaluations of $f(\mathbf{x}_{st})$ that are
28 actually used in Equation (PA.23).

29 For notational simplicity, the functions on the right-hand side of Equation (PA.23) will typically
30 be written with only \mathbf{x}_{st} as an argument (e.g., $f_{SP}(\mathbf{x}_{st})$ will be used instead of $f_{SP}[\mathbf{x}_{st}, f_B(\mathbf{x}_{st})]$).
31 However, the underlying dependency on the other arguments will still be present.

32 The major topics considered in this chapter are two-phase flow in the vicinity of the repository as
33 modeled by BRAGFLO (i.e., f_B) (Section PA-4.2), radionuclide transport in the vicinity of the
34 repository as modeled by NUTS (i.e., $f_{MB}, f_{DL}, f_S, f_{NP}$) (Section PA-4.3), radionuclide transport
35 in the vicinity of the repository as modeled by PANEL (i.e., f_{NP}) (Section PA-4.4), cuttings and
36 cavings releases to the surface as modeled by CUTTINGS_S (i.e., f_C) (Section PA-4.5), spillings
37 releases to the surface as modeled by DRSPALL and CUTTINGS_S (i.e., f_{SP}) (Section PA-4.6),

1 DBRs to the surface as modeled by BRAGFLO (i.e., f_{DBR}) (Section PA-4.7), brine flow in the
 2 Culebra as modeled by MODFLOW (i.e., f_{MF}) (Section PA-4.8), and radionuclide transport in
 3 the Culebra as modeled by SECOTP2D (i.e., f_{ST}) (Section PA-4.9).

4 PA-4.2 Two-Phase Flow: BRAGFLO

5 Quantifying the effects of gas and brine flow on radionuclide transport from the repository
 6 requires a two-phase (brine and gas) flow code. The two-phase flow code BRAGFLO is used to
 7 simulate gas and brine flow in and around the repository (Nemer 2007b and 2007c).
 8 Additionally, the BRAGFLO code incorporates the effects of disposal room consolidation and
 9 closure, gas generation, and rock fracturing in response to gas pressure. This section describes
 10 the mathematical models on which BRAGFLO is based, the representation of the repository in
 11 the model, and the numerical techniques employed in the solution.

12 PA-4.2.1 Mathematical Description

13 Two-phase flow in the vicinity of the repository is represented by the following system of two
 14 conservation equations, two constraint equations, and three equations of state:

15 Gas Conservation

$$16 \quad \nabla \cdot \left[\frac{\alpha \rho_g K_g k_{rg}}{\mu_g} (\nabla P_g + \rho_g g \nabla h) \right] + \alpha q_g + \alpha q_{rg} = \alpha \frac{\partial (\phi \rho_g S_g)}{\partial t} \quad (\text{PA.24})$$

17 Brine Conservation

$$18 \quad \nabla \cdot \left[\frac{\alpha \rho_b K k_{rb}}{\mu_b} (\nabla P_b + \rho_b g \nabla h) \right] + \alpha q_b + \alpha q_{rb} = \alpha \frac{\partial (\phi \rho_b S_b)}{\partial t} \quad (\text{PA.25})$$

19 Saturation Constraint

$$20 \quad S_g + S_b = 1 \quad (\text{PA.26})$$

21 Capillary Pressure Constraint

$$22 \quad P_c = P_g - P_b = P_c(S_b) \quad (\text{PA.27})$$

23 Gas Density

$$24 \quad \rho_g \text{ (determined by Redlich-Kwong-Soave (RKS) equation of state; see Equation (PA.51))} \\ 25 \quad (\text{PA.28})$$

26 Brine Density

$$27 \quad \rho_b = \rho_{b0} \exp \left[c_b (P_b - P_{b0}) \right] \quad (\text{PA.29})$$

1 Formation Porosity

$$2 \quad \phi = \phi_0 \exp \left[c_\phi (P_b - P_{b0}) \right] \quad (\text{PA.30})$$

3 where

4 g = acceleration due to gravity (meters per second squared [m])5 h = vertical distance from a reference location (m)6 k_{rl} = relative permeability (dimensionless) to fluid l , $l = b$ (brine), g (gas)7 P_c = capillary pressure in Pascals (Pa)8 P_l = pressure of fluid l (Pa)9 q_{rl} = rate of production (or consumption, if negative) of fluid l due to chemical reaction
10 (kilograms per cubic meter per seconds [kg/m³/s])11 q_l = rate of injection (or removal, if negative) of fluid l (kg/m³/s)12 S_l = saturation of fluid l (dimensionless)13 t = time (s)14 α = geometry factor (m)15 ρ_l = density of fluid l (kg/m³)16 μ_l = viscosity of fluid l (Pa s)17 ϕ = porosity (dimensionless)18 ϕ_0 = reference (i.e., initial) porosity (dimensionless)19 P_{b0} = reference (i.e., initial) brine pressure (Pa), constant in Equation (PA.29) and spatially
20 variable in Equation (PA.30)21 ρ_0 = reference (i.e., initial) brine density (kg/m³)22 c_ϕ = pore compressibility (Pa⁻¹)23 c_b = brine compressibility (Pa⁻¹)24 K = permeability of the material (m²), isotropic for PA (Howarth and Christian-Frear
25 1997)26 For the brine transport Equation (PA.25), the intrinsic permeability of the material is used. For
27 the gas transport Equation (PA.24), the permeability K is modified to account for the
28 Klinkenberg effect (Klinkenberg 1941). Specifically,

$$29 \quad K_g = K \left(\frac{1 + bK^a}{P_g} \right) \quad (\text{PA.31})$$

30 where a and b are gas and formation-dependent constants. Values of $a = -0.3410$ and $b = 0.2710$
31 were determined from data obtained for MB 139 (Christian-Frear 1996), with these values used
32 for all regions in Figure PA-15.33 The conservation equations are valid in one (i.e., $\nabla = [\partial/\partial x]$), two (i.e., $\nabla = [\partial/\partial x, \partial/\partial y]$), and
34 three (i.e., $\nabla = [\partial/\partial x, \partial/\partial y, \partial/\partial z]$) dimensions. In PA, the preceding system of equations is used

1 to model two-phase fluid flow within the two-dimensional region shown in Figure PA-15. The
2 details of this system are now discussed.

3 The α term in Equation (PA.24) and Equation (PA.25) is a dimension-dependent geometry factor
4 and is specified by

$$\begin{aligned} 5 \quad \alpha &= \text{area normal to flow direction in one-dimensional flow (i.e., } \Delta y \Delta z; \text{ units = m}^2\text{)} \\ 6 \quad &= \text{thickness normal to flow plane in two-dimensional flow (i.e., } \Delta z; \text{ units = m)} \\ 7 \quad &= 1 \text{ in three-dimensional flow (dimensionless)} \end{aligned} \quad (\text{PA.32})$$

8 PA uses a two-dimensional geometry to compute two-phase flow in the vicinity of the
9 repository, and as a result, α is the thickness of the modeled region (i.e., Δz) normal to the flow
10 plane (Figure PA-15). Due to the use of the two-dimensional grid in Figure PA-15, α is spatially
11 dependent, with the values used for α defined in the column labeled “ Δz .” Specifically, α
12 increases with distance away from the repository edge in both directions to incorporate the
13 increasing pore volume through which fluid flow occurs. The method used in PA, called
14 rectangular flaring, is illustrated in Figure PA-16 and ensures that the total volume surrounding
15 the repository is conserved in the numerical grid. The equations and method used to determine α
16 for the grid shown in Figure PA-15 are described in detail by Stein (2002).

17 The h term in Equation (PA.24) and Equation (PA.25) defines vertical distance from a reference
18 point. In PA, this reference point is taken to be the center of MB 139 at the location of the shaft
19 (i.e., $(x_{ref}, y_{ref}) = (23664.9 \text{ m}, 378.685 \text{ m})$, which is the center of cell 1266 in Figure PA-17).
20 Specifically, h is defined by

$$21 \quad h(x, y) = (x - x_{ref}) \sin \theta + (y - y_{ref}) \cos \theta \quad (\text{PA.33})$$

22 where θ is the inclination of the formation in which the point (x, y) is located. In PA, the Salado
23 is modeled as having an inclination of 1 degree from north to south, and all other formations are
24 modeled as being horizontal. Thus, $\theta = 1$ degree for points within the Salado, and $\theta = 0$ degrees
25 otherwise. Treating the Salado as an inclined formation and treating the Castile, Castile brine
26 reservoir, Rustler, and overlying units as horizontal creates discontinuities in the grid at the lower
27 and upper boundaries of the Salado. However, this treatment does not create a computational
28 problem, since the Salado is isolated from vertical flow; its upper boundary adjoins the
29 impermeable Los Medaños Member (formerly referred to as the Unnamed Member) at the base
30 of the Rustler, and its lower boundary adjoins the impermeable Castile.

31 In the solution of Equations (PA.24) through (PA.30), S_b and S_g are functions of location and
32 time. Thus, P_c , k_{rb} , and k_{rg} are functions of the form $P_c(x, y, t)$, $k_{rb}(x, y, t)$, and $k_{rg}(x, y, t)$. In
33 the computational implementation of the solution of the preceding equations, flow of phase l out
34 of a computational cell (Figure PA-17) cannot occur when $S_l(x, y, t) \leq S_{lr}(x, y, t)$, where S_{lr}
35 denotes the residual saturation for phase l . The values used for S_{lr} , $l = b, g$ are summarized in
36 Table PA-3.

1 Values for ϕ_0 and c_ϕ (Equation (PA.30)) are also given in Table PA-3. Initial porosity ϕ_0 for the
 2 DRZ is a function of the uncertain parameter for initial halite porosity ϕ_{0H} (HALPOR; see Table
 3 PA-19) and is given by Martell (1996a) and Bean et al. (1996), Section 4):

$$4 \quad \phi_0 = \phi_{0H} + 0.0029 \quad (\text{PA.34})$$

5 Initial porosity ϕ_0 of the Castile brine reservoir is calculated from the uncertain sampled
 6 parameter for the bulk Castile rock compressibility (BPCOMP; see Table PA-19), according to
 7 the following relationship:

$$8 \quad \phi_0 = \frac{BPCOMP}{1.0860 \times 10^{-10}} \quad (\text{PA.35})$$

9 where 1.0860×10^{-10} is a scaling constant that ensures that the productivity ratio, PR , remains
 10 constant at $2.0 \times 10^{-3} \text{ m}^3/\text{Pa}$. The productivity ratio PR is computed by

$$11 \quad PR = V \frac{BPCOMP}{\phi_0} \quad (\text{PA.36})$$

12 where V is the volume of the grid block representing the Castile brine reservoir in Figure PA-15.
 13 Because of this relationship, the initial porosity of the brine reservoir ranges from 0.1842 to
 14 0.9208. This range of porosity is not meant to represent an actual reservoir, but rather allows a
 15 reservoir to supply a volume of brine to the repository in the event of an E1 intrusion consistent
 16 with observed brine flows in the Delaware Basin.

17 The compressibility c_ϕ in Equation (PA.30) and Table PA-3 is pore compressibility.
 18 Compressibility is treated as uncertain for Salado anhydrite, Salado halite, and regions of
 19 pressurized brine in the Castile. However, the sampled value for each of these variables
 20 corresponds to bulk compressibility rather than to the pore compressibility actually used in the
 21 calculation. Assuming all of the change in volume during compression occurs in the pore
 22 volume, the conversion from bulk compressibility c_r to pore compressibility c_ϕ is approximated
 23 by

$$24 \quad C_\phi = \frac{C_r}{\phi_0} \quad (\text{PA.37})$$

25 where ϕ_0 is the initial porosity in the region under consideration.

26 The primary model used in PA for capillary pressure P_c and relative permeability k_{rl} is a
 27 modification of the Brooks-Corey model (Brooks and Corey 1964). In this model, P_c , k_{rb} , and
 28 k_{rg} are defined by

$$29 \quad P_c = P_t(k) / S_{e2}^{1/\lambda} \quad (\text{PA.38})$$

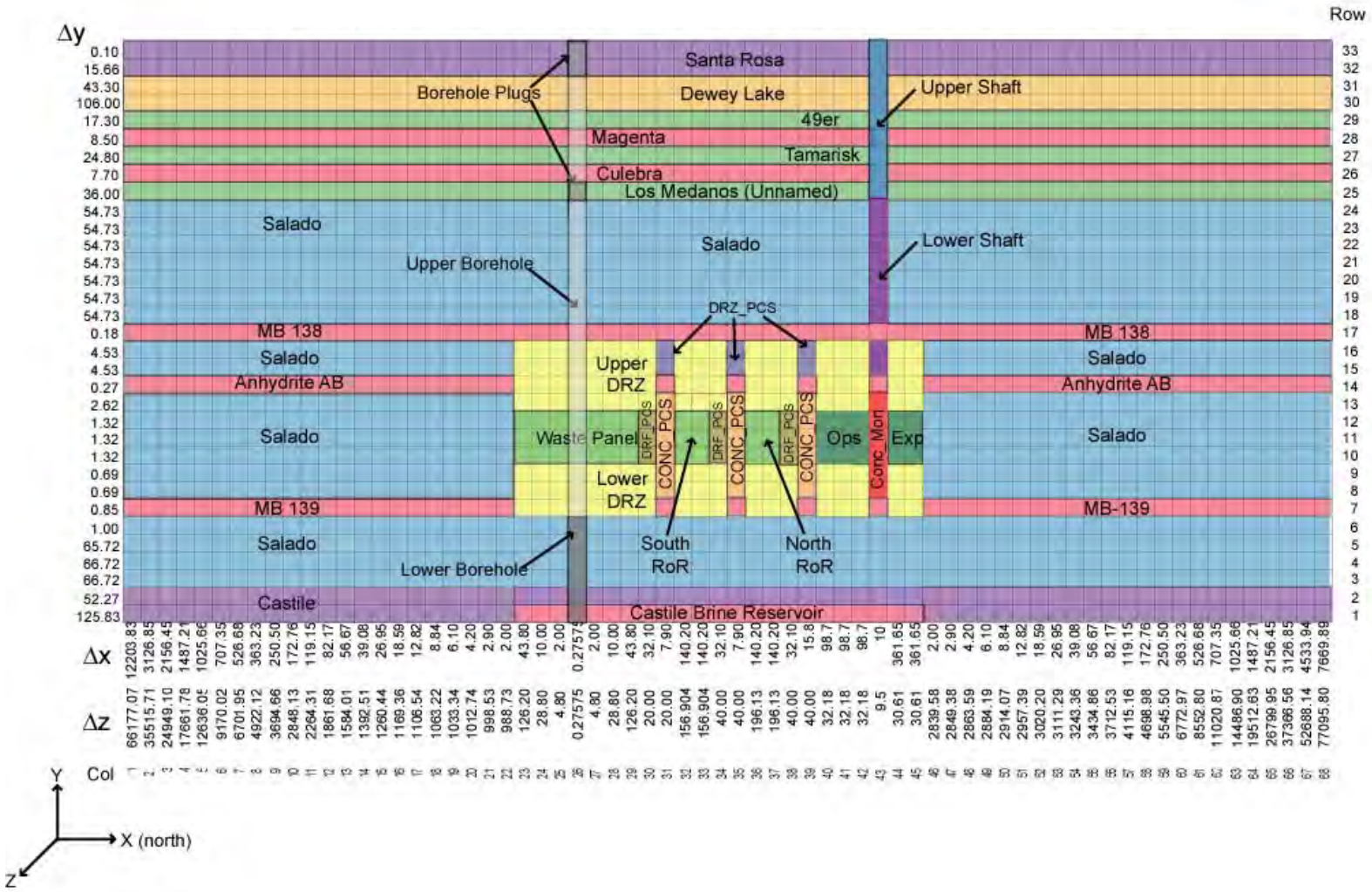
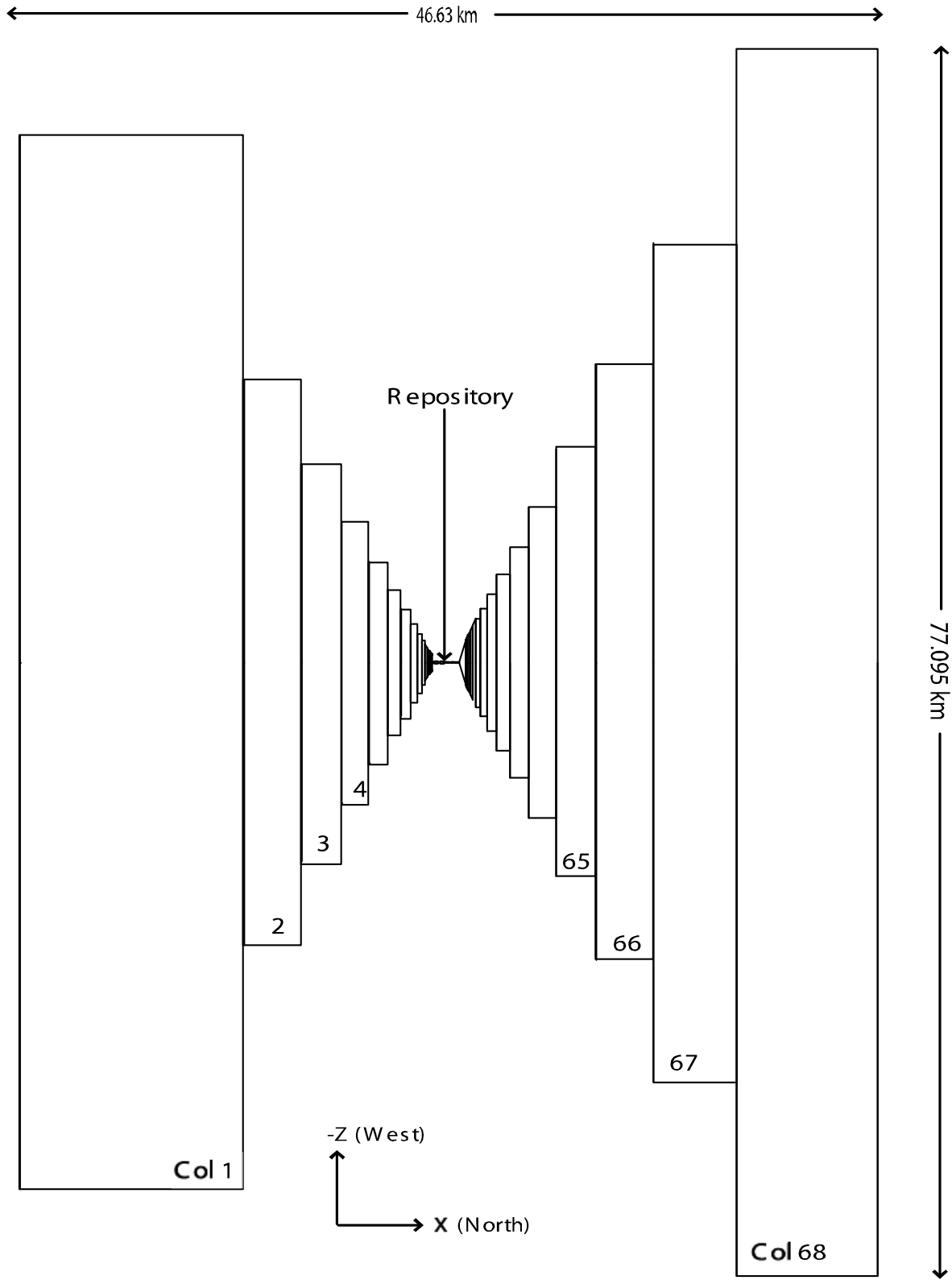


Figure PA-15. Computational Grid Used in BRAGFLO for PA



1
2

Figure PA-16. Definition of Element Depth in BRAGFLO Grid

Table with 34 columns and 155 rows of numerical data, representing individual cells in a BRAGFLO Grid. The values are integers ranging from 1 to 1550, with some cells containing 0 or blank space.

Figure PA-17. Identification of Individual Cells in BRAGFLO Grid

Table PA-3. Parameter Values Used in Representation of Two-Phase Flow

Region	Material	Material Description	Brooks-Corey Pore Distribution (PORE_DIS) ^a	Threshold Pressure Linear Parameter (PCT_A) ^a	Threshold Pressure Exponential Parameter (PCT_EXP) ^a	Residual Brine Saturation (SAT_RBRN) ^a	Residual Gas Saturation (SAT_RGAS) ^a	Porosity (POROSITY) ^a	Pore Compressibility ^a	Intrinsic Permeability (PRMX_LOG) ^a
			λ	a	η	S_{br}	S_{gr}	ϕ_0	$c\phi, \text{Pa}^{-1}$	k, m^2
Salado	S_HALITE	Undisturbed halite	0.7	0.56	-0.346	0.3	0.2	HALPOR ^b	f(HALCOMP) ^{b,d}	10 ^x , x = HALPRM ^b
DRZ	DRZ_0	DRZ, -5 to 0 years	0.7	0.0	0.0	0.0	0.0	f(HALPOR) ^{b,c}	f(HALCOMP) ^{b,d}	1.0 × 10 ⁻¹⁷
	DRZ_1	DRZ, 0 to 10,000 years	0.7	0.0	0.0	0.0	0.0	f(HALPOR) ^{b,c}	f(HALCOMP) ^{b,d}	10 ^x , x = DRZPRM ^b
MB 138	S_MB138	Anhydrite MB in Salado	ANHBCEXP ^b	0.26	-0.348	ANRBSAT ^b	ANRGSSAT ^b	0.011	f(ANHCOMP) ^{b,d}	10 ^x , x = ANHPRM ^b
Anhydrite AB	S_ANH_AB	Anhydrite layers A and B in Salado	ANHBCEXP ^b	0.26	-0.348	ANRBSAT ^b	ANRGSSAT ^b	0.011	f(ANHCOMP) ^{b,d}	10 ^x , x = ANHPRM ^b
MB 139	S_MB139	Anhydrite MB in Salado	ANHBCEXP ^b	0.26	-0.348	ANRBSAT ^b	ANRGSSAT ^b	0.011	f(ANHCOMP) ^{b,d}	10 ^x , x = ANHPRM ^b
Waste Panel	CAVITY_1	Single waste panel, -5 to 0 years	NA ^e	NA ^e	NA ^e	0.0	0.0	1.0	0.0	1.0 × 10 ⁻¹⁰
—	WAS_AREA	Single waste panel, 0 to 10,000 years	2.89	0.0	0.0	WRBRNSAT ^b	WRGSSAT ^b	0.848 ^f	0.0	2.4 × 10 ⁻¹³
Rest of Repository (RoR)	CAVITY_2	RoR, -5 to 0 years	NA ^e	NA ^e	NA ^e	0.0	0.0	1.0	0.0	1.0 × 10 ⁻¹⁰
—	REPOSIT	RoR, 0 to 10,000 years	2.89	0.0	0.0	WRBRNSAT ^b	WRGSSAT ^b	0.848 ^f	0.0	2.4 × 10 ⁻¹³
Ops and Exp	CAVITY_3	Operations area, -5 to 0 years	NA ^e	NA ^e	NA ^e	0.0	0.0	1.0	0.0	1.0 × 10 ⁻¹⁰
—	OPS_AREA	Operations area, 0 to 10,000 years	NA ^e	NA ^e	NA ^e	0.0	0.0	0.18	0.0	1.0 × 10 ⁻¹¹
Exp	CAVITY_3	Experimental area, -5 to 0 years	NA ^e	NA ^e	NA ^e	0.0	0.0	1.0	0.0	1.0 × 10 ⁻¹⁰

a Parenthetical parameter names are property names for the corresponding material, as indicated in.

b Uncertain variable; see Table PA-19.

c See Equation (PA.34).

d See Equation (PA.37); ϕ_0 can also be defined by an uncertain variable.

e These materials are using relative permeability model = 11; see Table PA-4.

f Initial value of porosity ϕ_0 ; porosity changes dynamically to account for creep closure (see Section PA-4.2.3).

g See Equation (PA.35).

Table PA-3. Parameter Values Used in Representation of Two-Phase Flow (Continued)

Region	Material	Material Description	Brooks-Corey Pore Distribution (PORE_DIS) ^a λ	Threshold Pressure Linear Parameter (PCT_A) ^a a	Threshold Pressure Exponential Parameter (PCT_EXP) ^a η	Residual Brine Saturation (SAT_RBRN) ^a S_{br}	Residual Gas Saturation (SAT_RGAS) ^a S_{gr}	Porosity (POROSITY) ^a ϕ_0	Pore Compressibility ^a $c\phi, \text{Pa}^{-1}$	Intrinsic Permeability (PRMX_LOG) ^a k, m^2
—	EXP_AREA	Experimental area, 0 to 10,000 years	NA ^e	NA ^e	NA ^e	0.0	0.0	0.18	0.0	1.0×10^{-11}
Castile	IMPERM_Z	Castile	0.7	0.0	0.0	0.0	0.0	0.005	0.0	1.0×10^{-35}
Castile Brine Reservoir	CASTILER	Brine Reservoir in Castile	0.7	0.56	-0.346	0.2	0.2	f(BPCOMP) ^{b,g}	f(BPCOMP) ^{b,d}	$10^x, x = \text{BPPRM}^b$
Culebra	CULEBRA	Culebra Member of Rustler	0.6436	0.26	-0.348	0.08363	0.07711	0.151	6.622517×10^{-10}	7.72681×10^{-14}
Magenta	MAGENTA	Magenta Member of Rustler	0.6436	0.26	-0.348	0.08363	0.07711	0.138	1.915942×10^{-9}	6.309576×10^{-16}
Dewey Lake	DEWYLAK	Dewey Lake Redbeds	0.6436	0.0	0.0	0.08363	0.07711	0.143	6.993007×10^{-8}	5.011881×10^{-17}
Santa Rosa	SANTAROS	Santa Rosa Formation	0.6436	0.0	0.0	0.08363	0.07711	0.175	5.714286×10^{-8}	1.0×10^{-10}
Los Medaños	UNNAMED	Los Medaños Member of Rustler	0.7	0.0	0.0	0.2	0.2	0.181	0.0	1.0×10^{-35}
Tamarisk	TAMARISK	Tamarisk Member of Rustler	0.7	0.0	0.0	0.2	0.2	0.064	0.0	1.0×10^{-35}
Forty-niner	FORTYNIN	Forty-niner Member of Rustler	0.7	0.0	0.0	0.2	0.2	0.082	0.0	1.0×10^{-35}
DRZ_PCS	DRZ_0	DRZ, -5 to 0 years	0.7	0.0	0.0	0.0	0.0	f(HALPOR) ^{b,c}	f(HALCOMP) ^{b,d}	1.0×10^{-17}
DRZ_PCS	DRZ_PCS	DRZ above the panel closures, 0 to 10,000 years	0.7	0.0	0.0	0.0	0.0	f(HALPOR) ^{b,c}	f(HALCOMP) ^{b,d}	$10^x, x = \text{DRZPCPRM}^b$

a Parenthetical parameter names are property names for the corresponding material, as indicated in Table PA-19.

b Uncertain variable; see Table PA-19.

c See Equation (PA.34).

d See Equation (PA.37); ϕ_0 can also be defined by an uncertain variable.

e These materials are using relative permeability model = 11; see Table PA-4.

f Initial value of porosity ϕ_0 ; porosity changes dynamically to account for creep closure (see Section PA-4.2.3).

g See Equation (PA.35).

Table PA-3. Parameter Values Used in Representation of Two-Phase Flow (Continued)

Region	Material	Material Description	Brooks-Corey Pore Distribution (PORE_DIS) ^a λ	Threshold Pressure Linear Parameter (PCT_A) ^a a	Threshold Pressure Exponential Parameter (PCT_EXP) ^a η	Residual Brine Saturation (SAT_RBRN) ^a S_{br}	Residual Gas Saturation (SAT_RGAS) ^a S_{gr}	Porosity (POROSITY) ^a ϕ_0	Pore Compressibility ^a $c\phi, \text{Pa}^{-1}$	Intrinsic Permeability (PRMX_LOG) ^a k, m^2
CONC_PCS	CAVITY_4	Concrete portion of panel closures, -5 to 0 years	NA ^e	NA ^e	NA ^e	0.0	0.0	1.0	0.0	1.0×10^{-10}
—	CONC_PCS	Concrete portion of panel closures, 0 to 10,000 years	CONBCEXP ^b	0.0	0.0	CONBRNBRN ^b	CONGSSAT ^b	0.05	1.2×10^{-9}	$10^x, x = \text{CONPRM}^b$
DRF_PCS	CAVITY_4	Drift adjacent to panel closures, -5 to 0 years	NA ^e	NA ^e	NA ^e	0.0	0.0	1.0	0.0	1.0×10^{-10}
—	DRF_PCS	Drift adjacent to panel closures, 0 to 10,000 years	2.89	0.0	0.0	WRBRNBRN ^b	WRGSSAT ^b	0.848 ^f	0.0	2.4×10^{-13}
CONC_MON	CAVITY_4	Concrete monolith portion of shaft seals, -5 to 0 years	NA ^e	NA ^e	NA ^e	0.0	0.0	1.0	0.0	1.0×10^{-10}
—	CONC_MON	Concrete monolith portion of shaft seals, 0 to 10,000 years	0.94	0.0	0.0	SHURBRN ^b	SHURGAS ^b	0.05	1.2×10^{-9}	1.0×10^{-14}
Upper Shaft	CAVITY_4	Upper portion of shaft seals, -5 to 0 years	NA ^e	NA ^e	NA ^e	0.0	0.0	1.0	0.0	1.0×10^{-10}
—	SHFTU	Upper portion of shaft seals, 0 to 10,000 years	CONBCEXP ^b	0.0	0.0	SHURBRN ^b	SHURGAS ^b	0.005	2.05×10^{-8}	$10^x, x = \text{SHUPRM}^b$

a Parenthetical parameter names are property names for the corresponding material, as indicated in Table PA-19.

b Uncertain variable; see Table PA-19.

c See Equation (PA.34).

d See Equation (PA.37); ϕ_0 can also be defined by an uncertain variable.

e These materials are using relative permeability model = 11; see Table PA-4.

f Initial value of porosity ϕ_0 ; porosity changes dynamically to account for creep closure (see Section PA-4.2.3).

g See Equation (PA.35).

Table PA-3. Parameter Values Used in Representation of Two-Phase Flow (Continued)

Region	Material	Material Description	Brooks-Corey Pore Distribution (PORE_DIS) ^a λ	Threshold Pressure Linear Parameter (PCT_A) ^a a	Threshold Pressure Exponential Parameter (PCT_EXP) ^a η	Residual Brine Saturation (SAT_RBRN) ^a S_{br}	Residual Gas Saturation (SAT_RGAS) ^a S_{gr}	Porosity (POROSITY) ^a ϕ_0	Pore Compressibility ^a $c\phi, \text{Pa}^{-1}$	Intrinsic Permeability (PRMX_LOG) ^a k, m^2
Lower Shaft	CAVITY_4	Lower portion of shaft seals, -5 to 0 years	NA ^e	NA ^e	NA ^e	0.0	0.0	1.0	0.0	1.0×10^{-10}
—	SHFTL_T1	Lower portion of shaft seals, 0 to 200 years	CONBCEXP ^b	0.0	0.0	SHURBRN ^b	SHURGAS ^b	0.005	4.28×10^{-9}	$10^x, x = \text{SHLPRM1}^b$
—	SHFTL_T2	Lower portion of shaft seals, 200 to 10,000 years	CONBCEXP ^b	0.0	0.0	SHURBRN ^b	SHURGAS ^b	0.005	4.28×10^{-9}	$10^x, x = \text{SHLPRM2}^b$
Borehole plugs	CONC_PLG	Concrete borehole plug, before plug degradation	0.94	0.0	0.0	0.0	0.0	0.32	1.1875×10^{-9}	$10^x, x = \text{PLGPRM}^b$
—	BH_SAND	Borehole after plug degradation, 200 years after intrusion	0.94	0.0	0.0	0.0	0.0	0.32	0.0	$10^x, x = \text{BHPRM}^b$
Upper Borehole	BH_OPEN	Borehole above repository before plug degradation	0.7	0.0	0.0	0.0	0.0	0.32	0.0	1.0×10^{-9}
—	BH_SAND	Borehole after plug degradation, 200 years after intrusion	0.94	0.0	0.0	0.0	0.0	0.32	0.0	$10^x, x = \text{BHPRM}^b$
Lower Borehole	BH_OPEN	Borehole below repository before creep closure	0.7	0.0	0.0	0.0	0.0	0.32	0.0	1.0×10^{-9}
—	BH_CREEP	Borehole below repository after creep closure, 1,000 years after intrusion	0.94	0.0	0.0	0.0	0.0	0.32	0.0	$10^x/10, x = \text{BHPRM}^d$

a Parenthetical parameter names are property names for the corresponding material, as indicated in Table PA-19.

b Uncertain variable; see Table PA-19.

c See Equation (PA.34).

d See Equation (PA.37); ϕ_0 can also be defined by an uncertain variable.

e These materials are using relative permeability model = 11; see Table PA-4.

f Initial value of porosity ϕ_0 ; porosity changes dynamically to account for creep closure (see Section PA-4.2.3).

g See Equation (PA.35).

1
$$k_{rb} = S_{e1}^{(2+3\lambda)/\lambda} \quad (\text{PA.39})$$

2
$$k_{rg} = (1 - S_{e2})^2 \left(1 - S_{e2}^{(2+\lambda)/\lambda}\right) \quad (\text{PA.40})$$

3 where

4 λ = pore distribution parameter (dimensionless)

5 $P_t(k)$ = capillary threshold pressure (Pa) as a function of intrinsic permeability k (Webb
6 1992)

7
$$= ak^\eta \quad (\text{PA.41})$$

8 S_{e1} = effective brine saturation (dimensionless) without correction for residual gas
9 saturation

10
$$= (S_b - S_{br}) / (1 - S_{br}) \quad (\text{PA.42})$$

11 S_{e2} = effective brine saturation (dimensionless) with correction for residual gas saturation

12
$$= (S_b - S_{br}) / (1 - S_{gr} - S_{br}) \quad (\text{PA.43})$$

13 The values used for λ , a , η , S_{br} , S_{gr} , and k are summarized in Table PA-3. The statement that
14 the Brooks-Corey model is in use means that P_c , k_{rb} , and k_{rg} are defined by Equation (PA.38)
15 through Equation (PA.40).

16 In the anhydrite MBs, either the Brooks-Corey model or the van Genuchten-Parker model is used
17 as determined by the subjectively uncertain parameter ANHBCVGP (see Table PA-19). A linear
18 model is used to represent two-phase flow in an open borehole (i.e., for the first 200 years after a
19 drilling intrusion for boreholes with two-plug or three-plug configurations, in the open cavities
20 [CAVITY_1, . . . , CAVITY_4], and for the experimental and operations areas). This is discussed
21 further below.

22 In the van Genuchten-Parker model, P_c , k_{rb} , and k_{rg} are defined by (van Genuchten 1978)

23
$$P_c = P_{VGP} \left(S_{e2}^{-1/m} - 1 \right)^{1-m} \quad (\text{PA.44})$$

24
$$k_{rb} = S_{e1}^{1/2} \left[1 - \left(1 - S_{e1}^{1/m} \right)^m \right]^2 \quad (\text{PA.45})$$

25
$$k_{rg} = (1 - S_{e2})^{1/2} \left(1 - S_{e2}^{1/m} \right)^{2m} \quad (\text{PA.46})$$

1 where $m = \lambda/(1 + \lambda)$ and the capillary pressure parameter P_{VGP} is determined by requiring that
 2 the capillary pressures defined in Equation (PA.38) and Equation (PA.44) are equal at an
 3 effective brine saturation of $S_{e2} = 0.5$ (Webb 1992). The van Genuchten-Parker model is only
 4 used for the anhydrite MBs in the Salado and uses the same values for λ , S_{br} , and S_{gr} as the
 5 Brooks-Corey model (Table PA-3).

6 In the linear model used for the open borehole (RELP_MOD = 5), P_c , k_{rb} , and k_{rg} are defined by

7
$$P_c = 0, k_{rb} = S_{e1}, k_{rg} = 1 - S_{e1} \quad (\text{PA.47})$$

8 Another linear model (RELP_MOD = 11) is used for the open cavities (CAVITY_1, . . . ,
 9 CAVITY_4) for the -5 to 0 year portion of the simulation (see Section PA-4.2.2) and the
 10 experimental and operations areas (t = 0 to 10,000 years) which, in PA, are modeled without a
 11 time-dependent creep closure:

12
$$k_{rl} = 0 \quad \text{for} \quad S_l < S_{lr} \quad (\text{PA.48})$$

13
$$k_{rl} = \frac{(S_l - S_{lr})}{tol} \quad \text{for} \quad S_{lr} \leq S_l \leq S_{lr} + tol \quad (\text{PA.49})$$

14
$$k_{rl} = 1 \quad \text{for} \quad S_l > S_{lr} + tol \quad (\text{PA.50})$$

15 where $l =$ gas or brine and tol is a tolerance (slope) over which the relative permeability changes
 16 linearly from 0 to 1. In PA, $tol = 1 \times 10^{-2}$ (dimensionless). Thus, the relative permeabilities are
 17 ~ 1 for saturations away from residual saturation.

18 Capillary pressure P_c for both the van Genuchten-Parker and Brooks-Corey models becomes
 19 unbounded as brine saturation S_b approaches the residual brine saturation, S_{br} . To avoid
 20 unbounded values, P_c is capped at 1×10^8 Pa in selected regions (Table PA-4).

21 Gas density is computed using the RKS equation of state, with the gas assumed to be pure H₂.
 22 For a pure gas, the RKS equation of state has the form (Walas 1985, pp. 43–54)

23
$$P_g = \frac{RT}{V - b} - \frac{a\alpha}{V(V + b)} \quad (\text{PA.51})$$

24 where

25 $R =$ gas constant = 8.31451 Joules (J) mole (mol)⁻¹ K⁻¹

26 $T =$ temperature (K) = 300.15 K (= 30 °C; 81 °F)

27 $V =$ molar volume (m³ mol⁻¹)

28 $a = 0.42747 R^2 T_{crit}^2 / P_{crit}$

29 $b = 0.08664 RT_{crit} / P_{crit}$

1 **Table PA-4. Models for Relative Permeability and Capillary Pressure in Two-Phase Flow**

Material	Relative Permeability ^a (RELP_MOD)	Capillary Pressure ^b (CAP_MOD)	Material	Relative Permeability ^a (RELP_MOD)	Capillary Pressure ^b (CAP_MOD)
S_HALITE	4	2	WAS_AREA	12	1
DRZ_0	4	1	DRZ_1	4	1
S_MB139	ANHBCVGP ^c	2	DRZ_PCS	Sampled	1
S_ANH_AB	ANHBCVGP ^c	2	CONC_PCS	4	2
S_MB138	ANHBCVGP ^c	2	UNNAMED	4	1
CAVITY_1	11	1	TAMARISK	4	1
CAVITY_2	11	1	FORTYNIN	4	1
CAVITY_3	11	1	DRF_PCS	12	1
CAVITY_4	11	1	REPOSIT	12	1
IMPERM_Z	4	1	CONC_MON	4	2
CASTILER	4	2	SHFTU	4	1
OPS_AREA	11	1	SHFTL_T1	4	1
EXP_AREA	11	1	SHFTL_T2	4	1
CULEBRA	4	2	CONC_PLG	4	1
MAGENTA	4	2	BH_OPEN	5	1
DEWYLAKE	4	2	BH_SAND	4	1
SANTAROS	4	1	BH_CREEP	4	1

^a Relative permeability model, where 4 = Brooks-Corey model given by Equation (PA.38) through Equation (PA.40), 5 = linear model given by Equation (PA.47), 11 = linear model given by Equation (PA.48) through Equation (PA.50), 12 = modified Brooks-Corey model to account for cutoff saturation (Nemer 2007c), and ANHBCVGP ~ use of Brooks-Corey or van Genuchten-Parker model treated as a subjective uncertainty.

^b Capillary pressure model, where 1 = capillary pressure is unbounded, 2 = P_c bounded above by 1×10^8 Pa as S_b approaches S_{br} .

^c See ANHBCVGP in Table PA-19.

2

$$3 \quad \alpha = \left[1 + (0.48508 + 1.55171\omega - 0.15613\omega^2)(1 - T_r^{0.5}) \right]^2$$

$$4 \quad \approx 1.202 \exp(-0.30288T_r) \text{ for H}_2 \text{ (Graboski and Daubert 1979)}$$

5 T_{crit} = critical temperature (K)

6 P_{crit} = critical pressure (Pa)

7 $T_r = T / T_{crit}$ = reduced temperature

8 ω = acentric factor

9 = 0 for H₂ (Graboski and Daubert 1979)

10 In order to account for quantum effects in H₂, effective critical temperature and pressure values
 11 of $T_{crit} = 43.6$ K and $P_{crit} = 2.047 \times 10^6$ Pa are used instead of the true values for these
 12 properties (Prausnitz 1969). Equation (PA.51) is solved for molar volume V . The gas density ρ_g
 13 then is given by

$$1 \quad \rho_g = \frac{M_{w,H_2}}{V} \quad (\text{PA.52})$$

2 where M_{w,H_2} is the molecular weight of H_2 (i.e., 2.01588×10^{-3} kg/mol; see Weast 1969, p.
3 B-26).

4 Brine density ρ_b is defined by Equation (PA.29), with $\rho_{b0} = 1230.0$ kg/m³ at a pressure of $P_{b0} =$
5 1.0132×10^5 Pa and $c_b = 2.5 \times 10^{-10}$ Pa⁻¹ (Roberts 1996). Porosity, ϕ , is used as defined by
6 Equation (PA.30) with two exceptions: in the repository (see Section PA-4.2.3) and in the DRZ
7 and MBs subsequent to fracturing (see Section PA-4.2.4). The values of ϕ_0 and c_ϕ used in
8 conjunction with Equation (PA.30) are listed in Table PA-3. The reference pressure P_{b0} in
9 Equation (PA.30) is spatially variable and corresponds to the initial pressures $P_b(x, y, -5)$ (here,
10 -5 means at time equal to -5 years; see Section PA-4.2.2). The gas and brine viscosities μ_l , $l = g,$
11 b in Equation (PA.24) and Equation (PA.25) were assumed to have values of $\mu_g = 8.93 \times 10^{-6}$
12 Pa s (H2:VISCO; see Vargaftik 1975) and $\mu_b = 2.1 \times 10^{-3}$ Pa s (BRINESAL:VISCO; see
13 McTigue 1993).

14 The terms q_g , q_{rg} , q_b , and q_{rb} in Equation (PA.24) and Equation (PA.25) relate to well injection
15 or removal (i.e., q_g , q_b) and reaction, production, or consumption (i.e., q_{rg} , q_{rb}) of gas and brine,
16 with positive signs corresponding to injection or production and negative signs corresponding to
17 removal or consumption. In the long-term Salado flow calculations, no injection or removal of
18 gas or brine is calculated using q_g and q_b . Thus, q_g and q_b are equal to zero. That is, after an
19 intrusion, the borehole is treated as a porous media, rather than a point source or sink of brine
20 and gas. Furthermore, the mass and pressure lost to a DBR during the intrusion is conservatively
21 ignored in the BRAGFLO calculations. In the DBR calculations discussed in Section PA-4.7, q_g
22 and q_b are used to describe injection and production wells in the DBR grid.

23 In PA, no gas consumption occurs through the term q_{rg} (see below), and gas production has the
24 potential to occur (due to corrosion of steel or microbial degradation of CPR materials) only in
25 the waste disposal regions of the repository (i.e., Waste Panel, South RoR, and North RoR in
26 Figure PA-15). Thus,

$$27 \quad q_{rg} \geq 0 \text{ in waste disposal regions of Figure PA-15}$$

$$28 \quad = 0 \text{ elsewhere} \quad (\text{PA.53})$$

29 Gas consumption occurs due to the reaction of CO_2 with MgO in the waste panels, and
30 potentially from the sulfidation of steel. This gas consumption is not modeled using q_{rg} , but is
31 accounted for by reducing the gas generation rate q_{rg} , as discussed in Section PA-4.2.5. Finally,
32 no brine production occurs, and brine consumption has the potential to occur (due to the
33 consumption of brine during steel corrosion) only in the waste disposal regions of the repository.
34 Thus,

$$\begin{aligned}
 1 \quad & q_{rb} \leq 0 \text{ in waste disposal regions of Figure PA-15} \\
 2 \quad & = 0 \text{ elsewhere} \tag{PA.54}
 \end{aligned}$$

3 More detail on the definition of q_{rg} and q_{rb} is provided in Section PA-4.2.5.

4 **PA-4.2.2 Initial Conditions**

5 In each two-phase flow simulation, a short period of time representing disposal operations is
 6 simulated. This period of time is called the start-up period, and covers 5 years from $t = -5$ years
 7 to 0 years, corresponding to the amount of time a typical panel is expected to be open during
 8 disposal operations. All grid locations require initial brine pressure and gas saturation at the
 9 beginning of the simulation ($t = -5$ years).

10 The Rustler and overlying units (except in the shaft) are modeled as horizontal with spatially
 11 constant initial pressure in each layer (see Figure PA-15). Table PA-5 lists the initial brine
 12 pressure, P_b , and gas saturation, S_g , for the Rustler.

13 The Salado (Mesh Rows 3–24 in Figure PA-15) is assumed to dip uniformly $\theta = 1$ degree
 14 downward from north to south (right to left in Figure PA-15). Except in the repository
 15 excavations and the shaft, brine is initially assumed (i.e., at -5 years) to be in hydrostatic
 16 equilibrium relative to an uncertain initial pressure $P_{b,ref}$ (SALPRES; see Table PA-19) at a
 17 reference point located at shaft center at the elevation of the midpoint of MB 139, which is the
 18 center of Cell 1266 in Figure PA-17. This gives rise to the condition

$$19 \quad P_b(x, y, -5) = P_{b,ref} + \frac{1}{c_b} \ln \left[\frac{\rho_b(x, y, -5)}{\rho_{b0}} \right] \tag{PA.55}$$

$$20 \quad \rho_b(x, y, -5) = \frac{1}{g c_b \left[y_e - \Phi(x_{ref}, y_{ref}, -5) + \frac{1}{g c_b \rho_{b0}} \right]} \tag{PA.56}$$

$$21 \quad \Phi(x_{ref}, y_{ref}, -5) = y_{ref} + \frac{1}{g c_b} \left[\frac{1}{\rho_{b0}} - \frac{1}{\rho_b(x_{ref}, y_{ref}, -5)} \right] \tag{PA.57}$$

$$22 \quad \rho_b(x_{ref}, y_{ref}, -5) = \rho_{b0} \exp \left[-c_b (P_{b,ref} - P_{b0}) \right] \tag{PA.58}$$

$$23 \quad y_e = y_{ref} + h(x, y) \tag{PA.59}$$

1

Table PA-5. Initial Conditions in the Rustler

Name	Mesh Row (Figure PA-15)	$P^b(x, y, -5)$, Pa	$S^g(x, y, -5)$
Santa Rosa ^c	33	1.013250×10^5	$1 - S_b = 0.916$ ($S_b = \text{SANTAROS:SAT_IBRN}$) ^a
Santa Rosa ^c	32	1.013250×10^5	$1 - S_b = 0.916$ ($S_b = \text{SANTAROS:SAT_IBRN}$) ^a
Dewey Lake ^c	31	1.013250×10^5	$1 - S_b = 0.916$ ($S_b = \text{SANTAROS:SAT_USAT}$) ^a
Dewey Lake ^c	30	7.355092×10^5	$1 - S_b = 0.916$ ($S_b = \text{SANTAROS:SAT_USAT}$) ^a
Forty-niner ^c	29	1.47328×10^6	0 ^b
Magenta	28	9.465×10^5 (MAGENTA:PRESSURE)	0 ^b
Tamarisk ^c	27	1.82709×10^6	0 ^b
Culebra	26	9.141×10^5 (CULEBRA:PRESSURE)	0 ^b
Los Medaños ^c	25	2.28346×10^6	0 ^b

^a The names in parenthesis are parameters in the WIPP PA Parameter Database.

^b The Rustler is assumed to be fully saturated. This initial condition is set in the program ICSET. See Nemer and Clayton (2008, Section 3.2).

^c These pressures are calculated in the ALGEBRA1 step analogously to Equation (PA.55) below, using the brine density of 1220 kg/m³. See subsequent discussion taking $\theta = 0$ and the reference point (x_{ref}, y_{ref}) at the top of the Dewey Lake. See the ALGEBRA input file ALG1_BF_CRA09.INP in library LIBCRA09_BF, class CRA09-1 on the WIPP PA cluster for details. See Nemer and Clayton (2008, Section 4.1.7) for details on the ALGEBRA1 step.

2

3 where

4 $h(x, y)$ is defined in Equation (PA.33)

5 $\rho_{b0} = 1220 \text{ kg/m}^3$ (BRINESAL:DNSFLUID)

6 $c_b = 3.1 \times 10^{-10} \text{ Pa}^{-1}$ (BRINESAL:COMPRES)

7 $g = 9.80665 \text{ m/s}^2$

8 $P_{b,ref} = 1.01325 \times 10^5 \text{ Pa}$ (BRINESAL:REF_PRES)

9 $P_{b0} =$ sampled far-field pressure in the undisturbed halite (S_HALITE:PRESSURE)

10 In the Salado, initial gas saturation $S_g(x, y, -5) = 0$ (see Nemer and Clayton 2008, Section 4.1.6).

11 The Castile (Mesh Rows 1 and 2) is modeled as horizontal, and initial brine pressure is spatially
 12 constant within each layer (no dip), except that the brine reservoir is treated as a different
 13 material from rest of Castile and has a different initial pressure which is a sampled parameter.
 14 Specifically, outside the brine reservoir, pressure is calculated using Equation (PA.55) above
 15 with no dip ($\theta = 0$) in the ALGEBRA1 step. Within the reservoir, $P_b(x, y, -5) = BPINTPRS$, the
 16 uncertain initial pressure in the reservoir (see Table PA-19). Initial gas saturation $S_g(x, y, -5) =$
 17 0.

1 Within the shaft (areas Upper Shaft, Lower Shaft, and CONC_MON) and panel closures (areas
2 CONC_PCS and DRF_PCS), $P_b(x, y, -5) = 1.01325 \times 10^5$ Pa and $S_g(x, y, -5) = 0$. Within the
3 excavated areas (Waste Panel, South RoR, and North RoR, Ops and Exp), $P_b(x, y, -5) = 1.01325$
4 $\times 10^5$ Pa and $S_g(x, y, -5) = 0$.

5 At the end of the initial five-year start-up period and the beginning of the regulatory period ($t = 0$
6 years), brine pressure and gas saturation are reset in the shaft, panel closures, and excavated
7 areas. In the shaft (areas Upper Shaft, Lower Shaft, and CONC_MON) and panel closures (areas
8 CONC_PCS and DRF_PCS), $P_b(x, y, 0) = 1.01325 \times 10^5$ Pa and $S_g(x, y, 0) = 1 \times 10^{-7}$ (see
9 CONC_MON:SAT_IBRN). In the waste disposal regions (areas Waste Panel, South RoR, and
10 North RoR), $P_b(x, y, 0) = 1.01325 \times 10^5$ Pa and $S_g(x, y, 0) = 0.985$ (see
11 WAS_AREA:SAT_IBRN). In the other excavated areas, $P_b(x, y, 0) = 1.01325 \times 10^5$ Pa and
12 $S_g(x, y, 0) = 1.0$.

13 **PA-4.2.3 Creep Closure of Repository**

14 Salt creep occurs naturally in the Salado halite in response to deviatoric stress. Inward creep of
15 rock is generally referred to as creep closure. Creep closure of excavated regions begins
16 immediately from excavation-induced deviatoric stress. If the rooms were empty, closure would
17 proceed to the point where the void volume created by the excavation would be eliminated as the
18 surrounding formation returned to a uniform stress state. In the waste disposal region, inward
19 creep of salt causes consolidation of the waste, and this waste consolidation continues until
20 loading in the surrounding rock is uniform, at which point salt creep and waste consolidation
21 ceases. The amount of waste consolidation that occurs and the time it takes to consolidate are
22 governed by the waste properties (e.g., waste strength, modulus, etc.), the surrounding rock
23 properties, the dimensions and location of the room, and relative quantities of brine and gas
24 present.

25 The porosity of the waste disposal regions and neighboring access drifts (i.e., Waste Panel, South
26 RoR, North RoR, and DRF_PCS in Figure PA-15) is assumed to change through time due to
27 creep closure of the halite surrounding the excavations. The equations on which BRAGFLO is
28 based do not incorporate this type of deformation. Therefore, the changes in repository porosity
29 due to halite deformation are modeled in a separate analysis with the geomechanical program
30 SANTOS, which implements a quasi-static, large-deformation, finite-element procedure (Stone
31 1997). Interpolation procedures are then used with the SANTOS results to define porosity (ϕ)
32 within the repository as a function of time, pressure, and gas generation rate.

33 For more information on the generation of the porosity surface for BRAGFLO in PA, see
34 Appendix PORSURF-2009.

35 **PA-4.2.4 Fracturing of MBs and DRZ**

36 Fracturing within the anhydrite MBs (i.e., regions MB 138, Anhydrite AB, and MB 139 in
37 Figure PA-15) and in the DRZ (region DRZ in Figure PA-15) is assumed to occur at pressures
38 slightly above lithostatic pressure, and is implemented through a pressure-dependent

1 compressibility $c_r(P_b)$ (Mendenhall and Gerstle 1995). Specifically, MB fracturing begins at a
 2 brine pressure of

$$3 \quad P_{bi} = P_{b0} + \Delta P_i \quad (\text{PA.60})$$

4 where P_{bi} and P_{b0} are spatially dependent (i.e., $P_{b0} = P(x, y, 0)$) as in Section PA-4.2.2) and ΔP_i
 5 $= 2 \times 10^5$ Pa (see S_MB138:PI_DELTA in Fox 2008, Table 30)

6 Fracturing ceases at a pressure of

$$7 \quad P_{ba} = P_{b0} + \Delta P_a \quad (\text{PA.61})$$

8 and a fully fractured porosity of

$$9 \quad \phi(P_{ba}) = \phi_a = \phi_0 + \Delta \phi_a \quad (\text{PA.62})$$

10 where $\Delta P_a = 3.8 \times 10^6$ Pa (see S_MB138:PF_DELTA in Fox 2008, Table 30), ϕ_0 is spatially
 11 dependent (Table PA-3), and $\Delta \phi_a = 0.04, 0.24,$ and 0.04 for anhydrite materials S_MB138,
 12 S_ANH_AB, and S_MB139, respectively (see S_MB138:DPHIMAX in Fox 2008, Table 30).

13 Once fractured, compressibility c_r becomes a linear function

$$14 \quad c_r(P_b) = c_r + \left(\frac{P_b - P_{bi}}{P_{ba} - P_{bi}} \right) (c_{ra} - c_r) \quad (\text{PA.63})$$

15 of brine pressure for $P_{bi} \leq P_b \leq P_{ba}$, with c_{ra} defined so that the solution ϕ of

$$16 \quad \frac{d\phi}{dP_b} = c_{ra}(P_b)\phi, \quad \text{where } \phi(P_{bi}) = \phi_0 \exp[c_r(P_{bi} - P_{b0})] \quad (\text{PA.64})$$

17 satisfies $\phi(P_{ba}) = \phi_a$; specifically, c_{ra} is given by

$$18 \quad c_{ra} = c_r \left[1 - \frac{2(P_{ba} - P_{b0})}{P_{ba} - P_{bi}} \right] + \left[\frac{2}{P_{ba} - P_{bi}} \right] \ln \left(\frac{\phi_a}{\phi_0} \right) \quad (\text{PA.65})$$

19 The permeability $k_f(P_b)$ of fractured material at brine pressure P_b is related to the permeability of
 20 unfractured material at brine pressure P_{bi} by

$$21 \quad k_f(P_b) = \left[\frac{\phi(P_b)}{\phi(P_{bi})} \right]^n k \quad (\text{PA.66})$$

1 where k is the permeability of unfractured material (i.e., at P_{bi}) and n is defined so that $k_f(P_{ba}) =$
 2 $1 \times 10^{-9} \text{ m}^2$ (i.e., n is a function of k , which is an uncertain input to the analysis; see ANHPRM
 3 in Table PA-19). When fracturing occurs, $k_f(P_b)$ is used instead of k in the definition of the
 4 permeability for the fractured areas of the anhydrite MBs.

5 Fracturing is also modeled in the DRZ region in Figure PA-15. The fracture model
 6 implementation is the same as for the anhydrite materials. In this case, fracturing would be in
 7 halite rather than anhydrite, but because of the limited extent of the DRZ and the proximity of
 8 the nearby interbeds, this representation was deemed acceptable by the Salado Flow Peer Review
 9 panel (Caporuscio, Gibbons, and Oswald 2003).

10 PA-4.2.5 Gas Generation

11 Gas production is assumed to result from anoxic corrosion of steel and the microbial degradation
 12 of CPR materials. Thus, the gas generation rate q_{rg} in Equation (PA.24) is of the form

$$13 \quad q_{rg} = q_{rgc} + q_{rgm} \quad (\text{PA.67})$$

14 where q_{rgc} is the rate of gas production per unit volume of waste ($\text{kg}/\text{m}^3/\text{s}$) due to anoxic
 15 corrosion of Fe-base metals, and q_{rgm} is the rate of gas production per unit volume of waste
 16 ($\text{kg}/\text{m}^3/\text{s}$) due to microbial degradation of CPR materials. Furthermore, q_{rb} in Equation (PA.25)
 17 is used to describe the consumption of brine during the corrosion process.

18 Gas generation takes place only within the waste disposal regions (i.e., Waste Panel, South RoR,
 19 and North RoR in Figure PA-15) and all the generated gas is assumed to have the same
 20 properties as H_2 (see discussion in Appendix MASS-2009, Section MASS-3.2). In PA, the
 21 consumable materials are assumed to be homogeneously distributed throughout the waste
 22 disposal regions (i.e., the concentration of Fe-base metals and CPR materials in the waste is not
 23 spatially dependent). A separate analysis examined the potential effects on PA results of
 24 spatially varying Fe-base metal and CPR material concentrations, and concluded that PA results
 25 are not affected by representing these materials with spatially varying concentrations (see
 26 Appendix MASS-2009, Section MASS-21.0).

27 The rates q_{rgc} , q_{rb} , and q_{rgm} ($\text{kg}/\text{m}^3/\text{s}$) are defined by

28 gas generation by corrosion

$$29 \quad q_{rgc} = (R_{ci}S_{b,eff} + R_{ch}S_g^*)D_s\rho_{Fe}X_c(\text{H}_2|\text{Fe})M_{\text{H}_2} \quad (\text{PA.68})$$

30 brine consumption by corrosion

$$31 \quad q_{rb} = (q_{rgc}/M_{\text{H}_2})X_c(\text{H}_2\text{O}|\text{H}_2)M_{\text{H}_2\text{O}} \quad (\text{PA.69})$$

32 and microbial gas generation

$$q_{rgm} = (R_{mi}S_{b,eff} + R_{mh}S_g^*)D_c y(H_2|C)M_{H_2} B_{fc} \quad (PA.70)$$

2 where

3 D_s = surface area concentration of steel in the repository (m² surface area steel/
4 m³ disposal volume)

5 D_c = mass concentration of cellulose in the repository (kg biodegradable
6 material/m³ disposal volume)

7 M_{H_2} = molecular weight of H₂ (kg H₂/mol H₂)

8 M_{H_2O} = molecular weight of water (H₂O) (kg H₂O/mol H₂O)

9 R_{ci} = corrosion rate under inundated conditions (m/s)

10 R_{ch} = corrosion rate under humid conditions (m/s)

11 R_{mi} = rate of cellulose biodegradation under inundated conditions (mol
12 C₆H₁₀O₅/kg C₆H₁₀O₅/s)

13 R_{mh} = rate of cellulose biodegradation under humid conditions (mol C₆H₁₀O₅/kg
14 C₆H₁₀O₅/s)

15 $S_{b,eff}$ = effective brine saturation due to capillary action in the waste materials (see
16 Equation (PA.90) in Section PA-4.2.6)

$$S_g^* = \begin{cases} 1 - S_{b,eff} & \text{if } S_{b,eff} > 0 \\ 0 & \text{if } S_{b,eff} = 0 \end{cases}$$

18 $X_c(H_2|Fe)$ = stoichiometric coefficient for gas generation due to corrosion of steel, i.e.,
19 moles of H₂ produced by the corrosion of 1 mole of Fe (mol H₂/mol Fe)

20 $X_c(H_2O|H_2)$ = stoichiometric coefficient for brine consumption due to corrosion of steel,
21 i.e., moles of H₂O consumed per mole of H₂ generated by corrosion (mol
22 H₂O/mol H₂)

23 $y(H_2|C)$ = average stoichiometric factor for microbial degradation of cellulose, i.e.,
24 the moles of H₂ generated per mole of carbon consumed by microbial
25 action (mol H₂/mol C)

26 ρ_{Fe} = molar density of steel (mol/m³)

1 B_{fc} = parameter (WAS_AREA:BIOGENFC; discussed in detail later in this
 2 section) uniformly sampled from 0 to 1, used to account for the
 3 uncertainty in whether microbial gas generation could be realized in the
 4 WIPP at experimentally measured rates.

5 The products $R_{ci} D_s \rho_{Fe} X_c$, $R_{ch} D_s \rho_{Fe} X_c$, $R_{mi} D_c y$, and R_{mh} in Equation (PA.68) and Equation
 6 (PA.70) define constant rates of gas generation (mol/m³/s) that continue until the associated
 7 substrate (i.e., steel or cellulose) is exhausted (i.e., zero order kinetics are assumed). The terms
 8 $S_{b,eff}$ and S_g^* in Equation (PA.68) and Equation (PA.70), which are functions of location and
 9 time, correct for the amount of substrate exposed to inundated and humid conditions,
 10 respectively. All the corrosion and microbial action is assumed to cease when no brine is
 11 present, which is the reason that 0 replaces $S_g = 1$ in the definition of S_g^* . In PA, $R_{ch} = 0$ and R_{ci} ,
 12 R_{mh} , and R_{mi} are defined by uncertain variables (see WGRCOR, WGRMICH, WGRMICI in
 13 Table PA-19). However, R_{mh} is now sampled based on the sampled value of R_{mi} : see Nemer and
 14 Clayton (2008, Section 5.1.3). Further, $M_{H_2} = 2.02 \times 10^{-3}$ kg/mol (Lide 1991, pp. 1-7, 1-8),
 15 $M_{H_2O} = 1.80 \times 10^{-2}$ kg/mol (Lide 1991, pp. 1-7, 1-8), $\rho_{Fe} = 1.41 \times 10^5$ mol/m³ (Telander and
 16 Westerman 1993), and D_s , D_c , $X_c(H_2O|H_2)$, $X_c(H_2|Fe)$, and $y(H_2|C)$ are discussed below.

17 The concentration D_s in Equation (PA.68) is defined by

$$18 \quad D_s = A_d n_d / V_R \quad (\text{PA.71})$$

19 where

20 A_d = surface area of steel associated with a waste disposal drum (m²/drum)

21 V_R = initial volume of a single room in the repository (m³)

22 n_d = ideal number of waste drums that can be close-packed into a single room

23 In PA, $A_d = 6$ m²/drum (REFCON:ASDRUM), $V_R = 3,644$ m³ (REFCON:VROOM), and $n_d =$
 24 6804 drums (REFCON:DRROOM).

25 The biodegradable materials to be disposed at the WIPP consist of cellulosic materials, plastics,
 26 and rubbers. Cellulosics have been demonstrated experimentally to be the most biodegradable of
 27 these materials (Francis, Gillow, and Giles 1997). The occurrence of significant microbial gas
 28 generation in the repository will depend on whether (1) microbes capable of consuming the
 29 emplaced organic materials will be present and active, (2) sufficient electron acceptors will be
 30 present and available, and (3) enough nutrients will be present and available.

31 During the CRA-2004 PABC, the EPA (Cotsworth 2005) indicated that the probability that
 32 microbial gas generation could occur (WMICDFLG) should be set equal to 1 in PA calculations.
 33 In the CRA-2004, the probability that microbial gas generation could occur was assigned a value
 34 of 0.5. To comply with the EPA's letter, in the CRA-2004 PABC and the CRA-2009 PA the
 35 parameter WMICDFLG was changed so that the probability that microbial gas generation could
 36 occur was set to 1 while preserving the previous probability distribution on whether CPR could
 37 be degraded. This is summarized in Table PA-6, and is discussed further in Nemer and Stein
 38

1 **Table PA-6. Probabilities for Biodegradation of Different Organic Materials**
 2 **(WAS_AREA:PROBDEG) in the CRA-2009 PA and the CRA-2004 PA**

WAS_AREA:PROBDEG	Meaning	Probability CRA-2004	Probability CRA-2009
0	No microbial degradation can occur	0.5	0.0
1	Biodegradation of only cellulose can occur	0.25	0.75
2	Biodegradation of CPR materials can occur	0.25	0.25

3
 4 (2005, Section 5.4). Because there are significant uncertainties in whether the experimentally
 5 observed gas-generation rates could be realized in the WIPP repository, during the CRA-2004
 6 PABC the EPA agreed to allow the DOE to multiply the sampled microbial rates by a parameter
 7 (WAS_AREA:BIOGENFC) uniformly sampled from 0 to 1. This is discussed further in Nemer,
 8 Stein, and Zelinski (2005, Section 4.2.2).

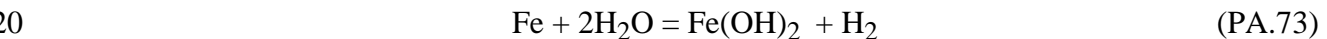
9 In cases where biodegradation of rubbers and plastics occur, rubbers and plastics are converted
 10 to an equivalent quantity of cellulose based on their carbon equivalence (Wang and Brush
 11 1996a). This produces the density calculation

$$D_c = \begin{cases} m_{cel} / V_R & \text{for biodegradation of cellulose only} \\ (m_{cel} + m_r + 1.7m_p) / V_R & \text{for biodegradation of CPR materials} \end{cases} \quad (\text{PA.72})$$

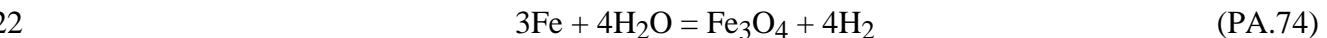
12
 13 where m_{cel} is the mass of cellulose (kg), m_r is the mass of rubbers (kg), and m_p is the mass
 14 of plastics (kg).

15 In the CRA-2009 PA, the emplacement materials (cellulose and plastic) have been added to m_{cel}
 16 and m_p . This is discussed further in Nemer and Clayton (2008, Section 5.1.1). Density values
 17 for CPR materials can be found in Fox (2008, Table 34).

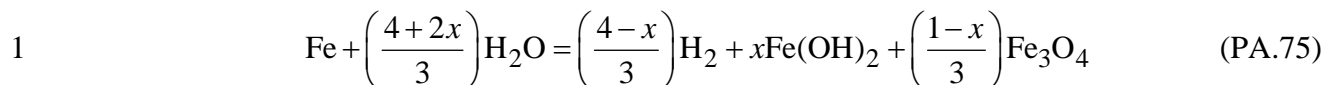
18 The most plausible corrosion reactions after closure of the WIPP are believed to be (Wang and
 19 Brush 1996a)



21 and



23 When normalized to 1 mole of Fe and linearly weighted by the factors x and $1-x$ ($0 \leq x \leq 1$), the
 24 two preceding reactions become



2 where x and $1-x$ are the fractions of Fe consumed in the reactions in Equation (PA.73) and
 3 Equation (PA.74), respectively. Although magnetite (Fe_3O_4) has been observed to form on Fe as
 4 a corrosion product in low-Mg anoxic brines at elevated temperatures (Telander and Westerman
 5 1997) and in oxic brine (Haberman and Frydrych 1988), there is no evidence that it will form at
 6 WIPP repository temperatures. If Fe_3O_4 were to form, H_2 would be produced (on a molar basis)
 7 in excess of the amount of Fe consumed. However, anoxic corrosion experiments (Telander and
 8 Westerman 1993) did not indicate the production of H_2 in excess of the amount of Fe consumed.
 9 Therefore, the stoichiometric factor x in Reaction (PA.75) is set to 1.0 (i.e., $x = 1$), which implies
 10 that Reaction (PA.73) represents corrosion. Thus, the stoichiometric factor for corrosion is

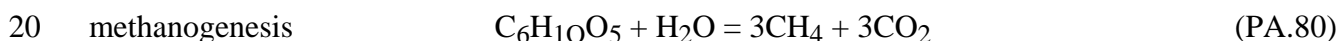
$$11 \quad X_c(\text{H}_2|\text{Fe}) = (4-x)/3 = 1 \text{ mol/mol} \quad (\text{PA.76})$$

12 which implies that one mole of H_2 is produced for each mole of Fe consumed, and the
 13 stoichiometric factor for brine consumption is

$$14 \quad X_c(\text{H}_2\text{O}|\text{H}_2) = (4+2x)/3 = 2 \text{ mol/mol} \quad (\text{PA.77})$$

15 which implies that two moles of H_2O are consumed for each mole of H_2 produced.

16 The most plausible biodegradation reactions after closure of the WIPP are believed to be (Wang
 17 and Brush 1996a)

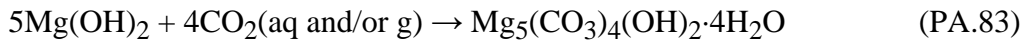
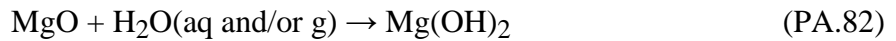


21 Accumulation of CO_2 produced by the above reactions could decrease pH and add carbonate to
 22 increase An solubility in the repository (Wang and Brush 1996b).

23 However, in the CRA-2004 PABC, the EPA (Cotsworth 2005) directed the DOE to remove
 24 methanogenesis (Equation (PA.80)) from PA. The EPA cited the presence of calcium sulfate as
 25 gypsum and anhydrite in the bedded salt surrounding the repository as possible sources of
 26 sulfate. These sources of sulfate would, if accessible, promote sulfate reduction (Equation
 27 (PA.82)), which is energetically and kinetically favored over methanogenesis. In response, the
 28 DOE removed methanogenesis from PA. Additionally, the DOE removed Fe sulfidation from
 29 PA as a gas-consuming reaction because sulfidation of steel produces one mole of H_2 for every
 30 mole of H_2S consumed,

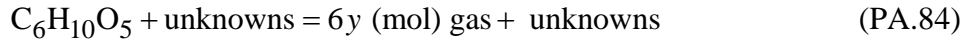


1 This and the removal of methanogenesis are discussed fully in Nemer and Zelinski (2005).
 2 To provide added assurance of WIPP performance, a sufficient amount of MgO is added to the
 3 repository to remove CO₂ (Bynum et al. 1997). MgO in polypropylene “supersacks” is
 4 emplaced on top of the three-layer waste stacks to create conditions that reduce An solubilities in
 5 the repository (see Appendix MgO-2009 and Appendix SOTERM-2009, Section SOTERM-2.3).
 6 If brine flows into the repository, MgO will react with water in brine and in the gaseous phase to
 7 produce brucite (Mg[OH]₂). MgO will react with essentially all of the CO₂ that could be
 8 produced by complete microbial consumption of the CPR materials in the waste, and will create
 9 hydromagnesite with the composition Mg₅(CO₃)₄(OH)₂·4H₂O (Appendix MgO-2009; Appendix
 10 SOTERM-2009, Section SOTERM-2.0). The most important MgO hydration and carbonation
 11 reactions that will occur in the WIPP are



14 In these equations, “aq and/or g” indicates that the H₂O or CO₂ that reacts with MgO and/or
 15 brucite could be present in the aqueous phase (brine) and/or the gaseous phase. The removal of
 16 CO₂ by MgO is not explicitly modeled as a separate reaction in PA. Rather, the effect of CO₂
 17 consumption is accounted for by modifying the stoichiometry of Reaction (PA.78), Reaction
 18 (PA.79), and Reaction (PA.80) to remove the CO₂ from the mass of gas produced by microbial
 19 action.

20 The average stoichiometry of Reaction (PA.78), Reaction (PA.79), and Reaction (PA.80), is



22 where the average stoichiometric factor *y* in Reaction (PA.84) represents the number of moles of
 23 gas produced and retained in the repository from each mole of carbon consumed. This factor *y*
 24 depends on the extent of the individual biodegradation pathways in Reaction (PA.84), and the
 25 consumption of CO₂ by MgO. A range of values for *y* is estimated by considering the maximum
 26 mass of gas that can be produced from consumption of cellulosics (*M_{cel}*) and Fe-base metals
 27 (*M_{Fe}*), and is derived as follows (Wang and Brush 1996b). Estimates of the maximum quantities
 28 *M_{cel}* and *M_{Fe}* (mol) of cellulosics (i.e., C₆H₁₀O₅) and steels that can be potentially consumed in
 29 10,000 years are given by

$$30 \quad M_{cel} = \min \left\{ \frac{6000m_{cel}}{162}, 3.2 \times 10^{11} R_m m_{cel} \right\} \quad (\text{PA.85})$$

$$31 \quad M_{Fe} = \min \left\{ \frac{1000m_{Fe}}{56}, 4.4 \times 10^{16} R_{ci} A_d n_d \right\} \quad (\text{PA.86})$$

32 where *m_{cel}* and *m_{Fe}* are the masses (kg) of cellulosics (see Equation (PA.72) for definition) and
 33 steels initially present in the repository. The mass of cellulosics that can be consumed is

1 determined by the uncertain parameter WMICDFLG (see Table PA-19). The mass of steels m_{Fe}
 2 = 5.16×10^7 kg; this value is calculated as

$$3 \quad V_{CH} (\rho_{WCH} + \rho_{CCH}) + V_{RH} (\rho_{WRH} + \rho_{CRH}) \quad (\text{PA.87})$$

4 where V_{CH} and V_{RH} are the volumes of CH-TRU and RH-TRU waste, ρ_{WCH} and ρ_{WRH} are the
 5 Fe densities in CH-TRU and RH-TRU waste, and ρ_{CCH} and ρ_{CRH} are the Fe densities of the
 6 containers of CH-TRU and RH-TRU waste (see Fox 2008, Table 34). The terms $6000 m_{cel}/162$
 7 and $1000 m_{Fe}/56$ in Equation (PA.85) and Equation (PA.86) equal the inventories in moles of
 8 cellulose and steel, respectively. The terms $3.2 \times 10^{11} R_m m_{cel}$ and $4.4 \times 10^{16} R_{ci} A_d n_d$ equal
 9 the maximum amounts of cellulose and steel that could be consumed over 10,000 years. In
 10 Equation (PA.85), $R_m = \max\{R_{mh}, R_{mi}\}$, where R_{mh} and R_{mi} are defined by uncertain variables
 11 (see WGRMICH and WGRMICI in Table PA-19, respectively), and $3.2 \times 10^{11} = (3.15569 \times 10^7$
 12 s/yr) (10^4 yr). In Equation (PA.86), $A_d n_d$ is the total surface area of all drums (m^2) and the factor
 13 $4.4 \times 10^{16} = (3.15569 \times 10^7$ s/yr) (10^4 yr) (1.41×10^5 mol/ m^3), where $\rho_{Fe} = 1.41 \times 10^5$ mol/ m^3
 14 (see Equation (PA.72)) (Telander and Westerman 1993), converts the corrosion rate from m/s to
 15 mol/ m^2 /s.

16 A range of possible values for the average stoichiometric factor y in Reaction (PA.84) can be
 17 obtained by considering individual biodegradation pathways involving M_{cel} and accounting for
 18 the removal of CO_2 by the MgO.

19 In the absence of methanogenesis and steel sulfidation, y from Equation (PA.84) becomes

$$20 \quad y = \frac{\left[\frac{2.4}{4.8} M_{NO_3} + \frac{1}{2} \left(M_{cel} - \frac{6}{4.8} M_{NO_3} \right) \right]}{M_{cel}} \quad (\text{PA.88})$$

$$21 \quad M_{NO_3} = \min \left\{ M_{NO_3}^0, \frac{4}{5} M_{cel} \right\} \quad (\text{PA.89})$$

22 where $M_{NO_3}^0$ is the quantity of NO_3^- (mols) initially present in the repository. Specifically,
 23 $M_{NO_3}^0 = 4.31 \times 10^7$ mol (Fox 2008, Table 39).

24 **PA-4.2.6 Capillary Action in the Waste**

25 Capillary action (wicking) is the ability of a material to carry a fluid by capillary forces above
 26 the level it would normally seek in response to gravity. In the current analysis, this phenomena
 27 is accounted for by defining an effective saturation given by

$$S_{b,eff} = \begin{cases} S_b - S_{min} + S_{wick} \left(1 - \text{Exp} \left(200\alpha \left(\text{Max} (S_b - S_{min}, 0) \right)^2 \right) \right) & \text{if } 0 < S_b \leq 1 - S_{wick} + S_{min} \\ 0 & \text{if } S_b \leq S_{min} \\ 1 & \text{if } S_b > 1 - S_{wick} + S_{min} \end{cases} \quad (\text{PA.90})$$

where

$S_{b,eff}$ = effective brine saturation

S_b = brine saturation

S_{wick} = wicking saturation

S_{min} = minimum brine saturation at which code can run in the waste-filled areas

α = smoothing parameter = -1000

The effective saturation given by Equation (PA.90) differs from that in the CRA-2004 PA in that $S_{b,eff}$ now approaches zero as S_b approaches a small value S_{min} . In simulations where Fe corrosion dried out the repository, the time required to complete the simulation could be quite long. In order to speed up the code and increase robustness, the parameter S_{min} was added. For PA, $S_{min} = 0.015$, which was small enough to not affect the results, while greatly reducing run time. This is explained fully in Nemer and Clayton (2008, Section 5.2.2).

The effective saturation is used on a grid block basis within all waste regions (Waste Panel, South RoR, and North RoR in Figure PA-15). The wicking saturation, S_{wick} , is treated as an uncertain variable (see WASTWICK in Table PA-19). The effective brine saturation $S_{b,eff}$ is currently used only to calculate the corrosion of steel (Equation (PA.68)) and the microbial degradation of cellulose (Equation (PA.70)), and does not directly affect the two-phase flow calculations indicated.

PA-4.2.7 Shaft Treatment

The WIPP excavation includes four shafts that connect the repository region to the surface: the air intake shaft, salt handling shaft, waste handling shaft, and exhaust shaft. In PA, these four shafts are modeled as a single shaft. The rationale for this modeling treatment is set forth in SNL (Sandia National Laboratories 1992, Volume 5, Section 2.3).

The shaft seal model included in the PA grid (Column 43 in Figure PA-15) is the simplified shaft model used in the CRA-2004 PA and the CRA-2004 PABC. The simplified shaft seal model used in PA is described by Stein and Zelinski (2003) and is briefly discussed below; this model was approved by the Salado Flow Peer Review Panel (Caporuscio, Gibbons, and Oswald 2003).

The planned design of the shaft seals involves numerous materials, including earth, crushed salt, clay, asphalt, and Salado Mass Concrete (SMC) (see the CCA, Appendix SEAL). The design is intended to control both short-term and long-term fluid flow through the Salado portion of the

1 shafts. For the CCA PA, each material in the shaft seal was represented in the BRAGFLO grid.
2 Analysis of the flow results from the CCA PA and the subsequent CCA PAVT (Sandia National
3 Laboratories 1997 and U.S. Department of Energy 1997) indicated that no significant flows of
4 brine or gas occurred in the shaft during the 10,000-year regulatory period. As a result of these
5 analyses, a simplified shaft seal model was developed for the CRA-2004 PA.

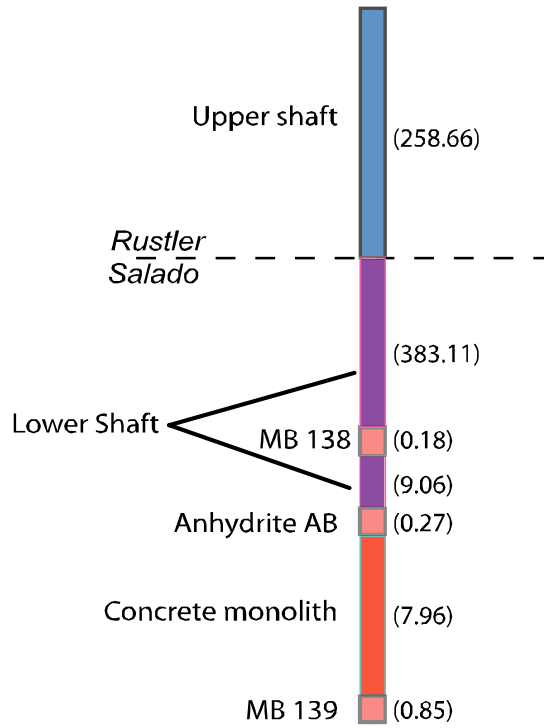
6 A conceptual representation of the simplified shaft seal system used in PA is shown in Figure
7 PA-18. The simplified model divides the shaft into three sections: an upper section (shaft seal
8 above the Salado), a lower section (within the Salado), and a concrete monolith section within
9 the repository horizon. A detailed discussion of how the material properties were assigned for
10 the simplified shaft seal model is included in James and Stein (2003). The permeability value
11 used to represent the upper and lower sections is defined as the harmonic mean of the component
12 materials' permeability in the detailed shaft seal model (including permeability adjustments
13 made for the DRZ assumed to surround the lower shaft seal section within the Salado). Porosity
14 is defined as the thickness-weighted mean porosity of the component materials. Other material
15 properties are described in James and Stein (2003).

16 The lower section of the shaft experiences a change in material properties at 200 years. This
17 change simulates the consolidation of seal materials within the Salado and significantly
18 decreases permeability. This time was chosen as a conservative overestimate of the amount of
19 time expected for this section of the shaft to become consolidated. The concrete monolith
20 section of the shaft is unchanged from the CCA PA and is represented as being highly permeable
21 for 10,000 years to ensure that fluids can access the north end (operations and experimental
22 areas) in the model. In three thin regions at the stratigraphic position of the anhydrite MBs, the
23 shaft seal is modeled as MB material (Figure PA-18). This model feature is included so that
24 fluids flowing in the DRZ and MB fractures can access the interbeds to the north of the
25 repository "around" the shaft seals. Because these layers are so thin, they have virtually no
26 effect on the effective permeability of the shaft seal itself.

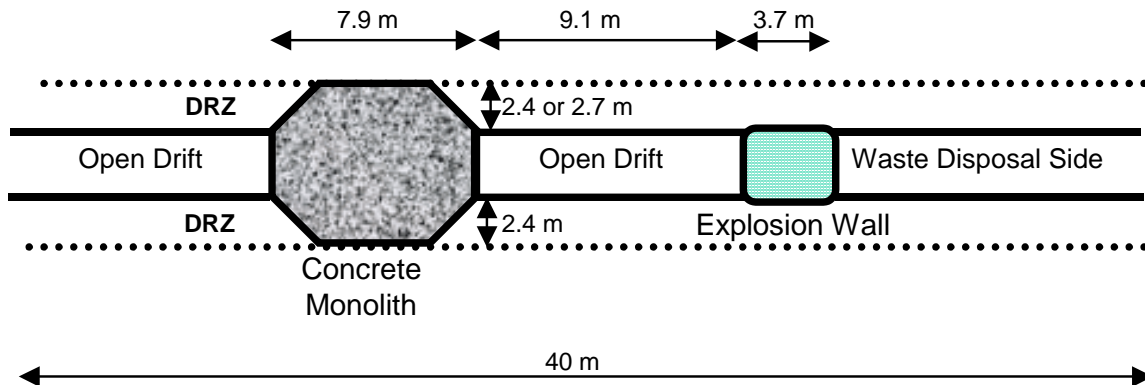
27 The simplified shaft model was tested in the AP-106 analysis (Stein and Zelinski 2003), which
28 supports the Salado Flow Peer Review (Caporuscio, Gibbons, and Oswald 2003). The results of
29 the AP-106 analysis demonstrate that vertical brine flow through the simplified shaft model is
30 comparable to brine flows seen through the detailed shaft model used in the CCA PA and
31 subsequent CCA PAVT calculations.

32 **PA-4.2.8 Option D Panel Closures**

33 PA includes panel closures models that represent the Option D panel closure design (see the
34 CRA-2004, Chapter 6.0, Section 6.4.3), which are unchanged from the CRA-2004. Option D
35 closures (Figure PA-19) are designed to allow minimal fluid flow between panels. PA explicitly
36 represents selected Option D panel closures in the computational grid using a model approved by
37 the Salado Flow Peer Review Panel (Caporuscio, Gibbons, and Oswald 2003). The Option D
38 panel closure design has several components: an SMC monolith, which extends into the DRZ in
39 all directions; an empty drift section; and a block and mortar explosion wall (Figure PA-19).
40 Each set of panel closures are represented in the BRAGFLO grid by 4 materials in 13 grid cells
41 (Figure PA-20):



1
2 **Figure PA-18. Schematic View of the Simplified Shaft Model (numbers on right indicate**
3 **dimensions in meters)**



4
5 **Figure PA-19. Schematic Side View of Option D Panel Closure**

- 6
- Six cells of panel closure concrete (area CONC_PCS, material CONC_PCS)
- 7
- One cell above and one cell below the concrete material consisting of MB anhydrite
- 8
- (areas MB 139 and Anhydrite AB, materials S_MB139 and S_ANH_AB, respectively)
- 9
- Two cells of healed DRZ above Anhydrite AB and the panel closure system (PCS) (area
- 10
- DRZ_PCS, material DRZ_PCS)
- 11
- Three cells of empty drift and explosion wall (area DRF_PCS, material DRF_PCS)

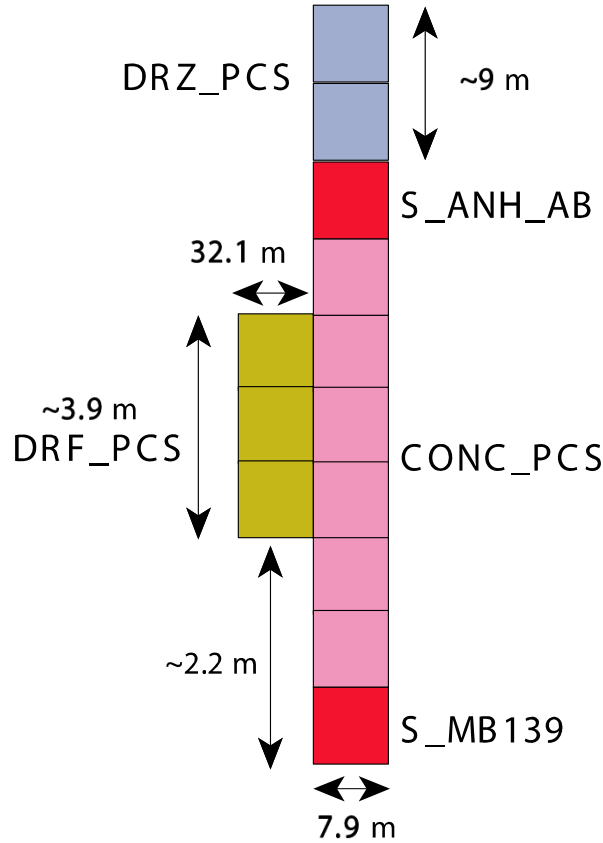


Figure PA-20. Representation of Option D Panel Closures in the BRAGFLO Grid

Properties for the materials making up the panel closure system are listed in Table PA-3.

PA-4.2.8.1 Panel Closure Concrete

The Option D panel closure design requires the use of a salt-saturated concrete, identified as SMC, as specified for the shaft seal system. The design of the shaft seal system and the properties of SMC are described in the CCA, Appendix SEAL. The BRAGFLO grid incorporates the material CONC_PCS, which is assigned the material properties of undegraded SMC and is used to represent the concrete portion of the Option D panel closure system (Figure PA-15). A double-thickness concrete segment represents the northernmost set of panel closures (between the north RoR and the operations area). This feature represents the two sets of panel closures in series that will be emplaced between the waste-filled repository and the shaft.

PA-4.2.8.2 Panel Closure Abutment with MBs

In the BRAGFLO grid, regions where the Option D panel closures intersect the MBs are represented as blocks of MB material (Figure PA-15). This representation is warranted for two reasons:

1. The MB material has a very similar permeability distribution (10^{-21} to $10^{-17.1}$ m²) to the concrete portion of the Option D panel closures ($10^{-20.699}$ to 10^{-17} m²), and thus, assigning

1 this material as anhydrite MB in the model has essentially the same effect as calling it
2 concrete, as long as pressures are below the fracture initiation pressure.

3 2. In the case of high pressures, it is expected that fracturing may occur in the anhydrite MBs
4 and flow could go “around” the panel closures and out of the two-dimensional plane
5 considered in the model grid. In this case, the flow would be through the MB material,
6 which incorporates a fracture model, as described above.

7 **PA-4.2.8.3 DRZ Above the Panel Closure**

8 After constructing the concrete portion of the panel closure, the salt surrounding the monolith
9 will be subjected to compressive stresses, which will facilitate the rapid healing of disturbed
10 halite. The rounded configuration of the monolith creates a situation very favorable for concrete
11 durability: high compressive stresses and low stress differences. In turn, the compressive
12 stresses developed within the salt will quickly heal any damage caused by construction
13 excavation, thereby eliminating the DRZ along this portion of the panel closure. The
14 permeability of the salt immediately above and below the rigid concrete monolith component of
15 Option D will approach the intrinsic permeability of the undisturbed Salado halite.

16 To represent the DRZ above the monoliths, PA uses the material DRZ_PCS in the BRAGFLO
17 grid (Figure PA-15). The values assigned to DRZ_PCS are the same as those used for the DRZ
18 above the excavated areas (material DRZ_1, see Table PA-3), except for the properties
19 PRMX_LOG, PRMY_LOG, and PRMZ_LOG, the logarithms of permeability in the x, y, and z
20 directions, respectively. These permeability values are assigned the same distributions used for
21 the material CONC_PCS. In this instance, the values are based on the nature of the model setup,
22 not directly on experimental data (although the general range of the distribution agrees with
23 experimental observations of healed salt). The use of these permeabilities ensures that any fluid
24 flow is equally probable through or around the Option D panel closures, and represents the range
25 of uncertainty that exists in the performance of the panel closure system.

26 **PA-4.2.8.4 Empty Drift and Explosion Wall Materials**

27 The DRF_PCS is the material representing the empty drift and explosion wall. For simplicity,
28 this material is assumed to have hydrologic properties equivalent to the material representing the
29 waste panel and is used for the three sets of panel closures represented in the grid (Figure PA-
30 15). The creep closure model is applied to this material to be consistent with the neighboring
31 materials. The assignment of a high permeability to this region for the PA calculations, which
32 contains the explosion wall, is justified because the explosion wall is not designed to withstand
33 the stresses imposed by creep closure beyond the operational period and will be highly
34 permeable following rapid room closure.

35 **PA-4.2.9 Borehole Model**

36 The major disruptive event in PA is the penetration of the repository by a drilling intrusion. In
37 the undisturbed scenario (see Section PA-6.7.1), these blocks have the material properties of the
38 neighboring stratigraphic or excavated modeling unit, and there is no designation in the borehole
39 grid except for the reduced lateral dimensions of this particular column of grid blocks.

1 In the scenarios simulating drilling disturbance, these cells start out with the same material
 2 properties as in the undisturbed scenario, but at the time of intrusion, the borehole grid blocks are
 3 reassigned to borehole material properties. The drilling intrusion is modeled by modifying the
 4 permeability of the grid blocks in Column 26 of Figure PA-15 (values listed in Table PA-7).
 5 Furthermore, the drilling intrusion is assumed to produce a borehole with a diameter of 12.25 in.
 6 (0.31 m) (Vaughn 1996, Howard 1996), borehole fill is assumed to be incompressible, capillary
 7 effects are ignored, residual gas and brine saturations are set to zero, and porosity is set to 0.32
 8 (see materials CONC_PLG, BH_OPEN, BH_SAND, and BH_CREEP in Table PA-3). When a
 9 borehole that penetrates pressurized brine in the Castile is simulated (i.e., an E1 intrusion), the
 10 permeability modifications indicated in Table PA-7 extend from the ground surface (i.e., Grid
 11 Cell 2155 in Figure PA-17) to the base of the pressurized brine (i.e., Grid Cell 2225 in Figure
 12 PA-17). When a borehole that does not penetrate pressurized brine in the Castile is under
 13 consideration (i.e., an E2 intrusion), the permeability modifications indicated in Table PA-7 stop
 14 at the bottom of the lower DRZ (i.e., Grid Cell 1111 in Figure PA-17).

15 **PA-4.2.10 Castile Brine Reservoir**

16 High-pressure Castile brine was encountered in several WIPP-area boreholes, including the
 17 WIPP-12 borehole within the controlled area and the ERDA-6 borehole northeast of the site.
 18 Consequently, the conceptual model for the Castile includes the possibility that brine reservoirs
 19 underlie the repository. The E1 and E1E2 scenarios include borehole penetration of both the
 20 repository and a brine reservoir in the Castile.

21 Unless a borehole penetrates both the repository and a brine reservoir in the Castile, the Castile is
 22 conceptually unimportant to PA because of its expected low permeability. Two regions are
 23 specified in the disposal system geometry of the Castile horizon: the Castile (Rows 1 and 2 in
 24

25 **Table PA-7. Permeabilities for Drilling Intrusions Through the Repository**

Time After Intrusion	Assigned Permeabilities
0–200 years	Concrete plugs are assumed to be emplaced at the Santa Rosa (i.e., a surface plug with a length of 15.76 m; corresponds to Grid Cells 2113, 2155 in Figure PA-17) and the Los Medaños Member of the Rustler (i.e., a plug at the top of the Salado with a length of 36 m; corresponds to Grid Cell 1644 in Figure PA-17). Concrete plugs are assumed to have a permeability log-uniformly sampled between 10^{-19} m^2 to 10^{-17} m^2 (see material CONC_PLG in Table PA-4). The open portions of the borehole are assumed to have a permeability of $1 \times 10^{-9} \text{ m}^2$.
200–1200 years	Concrete plugs are assumed to fail after 200 years (U.S. Department of Energy 1995). An entire borehole is assigned a permeability typical of silty sand log-uniformly sampled between $10^{-16.3} \text{ m}^2$ and 10^{-11} m^2 (see parameter BHPRM in and material BH_SAND in Table PA-4).
> 1200 years	Permeability of borehole reduced by one order of magnitude in the Salado beneath the repository due to creep closure of borehole (Thompson et al. 1996) (i.e., $k = 10^x/10$, $x = \text{BHPRM}$, in Grid Cells 2225, 1576, 26, 94, 162, 230 of Figure PA-17). No changes are made within and above the lower DRZ (see material BH_CREEP in Table PA-4).

26

1 Figure PA-15) and a reservoir (Row 1, Columns 23 to 45 in Figure PA-15). The Castile region
2 has an extremely low permeability, which prevents it from participating in fluid flow processes.

3 It is unknown whether a brine reservoir exists below the repository. As a result, the conceptual
4 model for the brine reservoirs is somewhat different from those for known major properties of
5 the natural barrier system, such as stratigraphy. The principal difference is that a reasonable
6 treatment of the uncertainty of the existence of a brine reservoir requires assumptions about the
7 spatial distribution of such reservoir and the probability of intersection (see Attachment MASS-
8 2009, Section MASS.18.1). A range of probabilities for a borehole hitting a brine reservoir is
9 used (see Section PA-3.6).

10 In addition to the stochastic uncertainty in the location and hence in the probability of
11 intersecting reservoirs, there is also uncertainty in the properties of reservoirs. The manner in
12 which brine reservoirs would behave if penetrated is captured by parameter ranges and is
13 incorporated in the BRAGFLO calculations of disposal system performance. The conceptual
14 model for the behavior of such a brine reservoir is discussed below. The properties specified for
15 brine reservoirs are pressure, permeability, compressibility, and porosity, and are sampled from
16 parameter ranges (see Table PA-19).

17 Where they exist, Castile brine reservoirs in the northern Delaware Basin are believed to be
18 fractured systems, with high-angle fractures spaced widely enough that a borehole can penetrate
19 through a volume of rock containing a brine reservoir without intersecting any fractures, and
20 therefore not producing brine. Castile brine reservoirs occur in the upper portion of the Castile
21 (Popielak et al. 1983). Appreciable volumes of brine have been produced from several reservoirs
22 in the Delaware Basin, but there is little direct information on the areal extent of the reservoirs or
23 the existence of the interconnection between them. Data from WIPP-12 and ERDA-6 indicate
24 that fractures have a variety of apertures and permeabilities, and they deplete at different rates.
25 Brine occurrences in the Castile behave as reservoirs; that is, they are bounded systems.

26 **PA-4.2.11 Numerical Solution**

27 Determining gas and brine flow in the vicinity of the repository requires solving the two
28 nonlinear PDEs in Equation (PA.24) through Equation (PA.30) on the computational domain in
29 Figure PA-15, along with evaluating appropriate auxiliary conditions. The actual unknown
30 functions in this solution are P_b and S_g , although the constraint conditions also give rise to values
31 for P_g and S_b . As two dimensions in space and one dimension in time are in use, P_b , P_g , S_b , and
32 S_g are functions of the form $P_b(x, y, t)$, $P_g(x, y, t)$, $S_b(x, y, t)$, and $S_g(x, y, t)$.

33 Solving Equation (PA.24) through Equation (PA.30) requires both initial value and boundary
34 value conditions for P_b and S_g . The initial value conditions for P_b and S_g are given in Section
35 PA-4.2.2. As indicated there, the calculation starts at time $t = -5$ years, with a possible resetting
36 of values at $t = 0$ years, which corresponds to final waste emplacement and sealing of the
37 repository. The boundary conditions are such that no brine or gas moves across the exterior grid
38 boundary (Table PA-8). This Neumann-type boundary condition is maintained for all time.
39 Further, BRAGFLO allows the user to maintain a specified pressure and/or saturation at any grid
40

1 **Table PA-8. Boundary Value Conditions for P_g and P_b**

Boundaries below (Row 1, $y = 0$ m) and above (Row 33, $y = 1039$ m) system for $0 \leq x \leq 46630$ m (Columns 1-68) and $-5 \text{ yr} \leq t$. Below, j refers to the unit normal vector in the positive y direction.	
$(\nabla P_g + \rho_g g \nabla h) \Big _{(x,y,t)} \cdot \mathbf{j} = 0 \text{ Pa} / \text{m}$	No gas flow condition
$(\nabla P_b + \rho_b g \nabla h) \Big _{(x,y,t)} \cdot \mathbf{j} = 0 \text{ Pa} / \text{m}$	No brine flow condition
Boundaries at left (Column 1, $x = 0$ m) and right (Column 68, $x = 46630$ m) of system for $0 \leq y \leq 1039$ m (Rows 1-33) and $-5 \text{ yr} \leq t$. Below, i refers to the unit normal vector in the positive x direction.	
$(\nabla P_g + \rho_g g \nabla h) \Big _{(x,y,t)} \cdot \mathbf{i} = 0 \text{ Pa} / \text{m}$	No gas flow condition
$(\nabla P_b + \rho_b g \nabla h) \Big _{(x,y,t)} \cdot \mathbf{i} = 0 \text{ Pa} / \text{m}$	No brine flow condition

2
 3 block. This is not a boundary condition and is not required to close the problem. This feature is
 4 used to specify Dirichlet-type conditions at the surface grid blocks (Columns 1-68, Row 33,
 5 Figure PA-15) and at the far-field locations in the Culebra and Magenta (Columns 1 and 68, Row
 6 26, and Columns 1 and 68, Row 28, Figure PA-15). These auxiliary conditions are summarized
 7 in **Error! Not a valid bookmark self-reference.**

8 A fully implicit finite-difference procedure is used to solve Equation (PA.24) through Equation
 9 (PA.30). The associated discretization of the gas mass balance equation is given by

$$\begin{aligned}
 & \frac{1}{\Delta x_i} \left\{ \frac{1}{x_{i+1} - x_i} \left[\frac{\alpha \rho_g k_x k_{rg}}{\mu_g} \right]_{i+1/2,j}^{n+1} \left(\Phi_{g_{i+1,j}}^{x-} - \Phi_{g_{i,j}}^{x+} \right)^{n+1} \right. \\
 & \left. - \frac{1}{x_i - x_{i-1}} \left[\frac{\alpha \rho_g k_x k_{rg}}{\mu_g} \right]_{i-1/2,j}^{n+1} \left(\Phi_{g_{i,j}}^{x-} - \Phi_{g_{i-1,j}}^{x+} \right)^{n+1} \right\} \\
 & + \frac{1}{\Delta y_j} \left\{ \frac{1}{y_{j+1} - y_j} \left[\frac{\alpha \rho_g k_y k_{rg}}{\mu_g} \right]_{i,j+1/2}^{n+1} \left(\Phi_{g_{i,j+1}}^{y-} - \Phi_{g_{i,j}}^{y+} \right)^{n+1} \right. \\
 & \left. - \frac{1}{y_j - y_{j-1}} \left[\frac{\alpha \rho_g k_y k_{rg}}{\mu_g} \right]_{i,j-1/2}^{n+1} \left(\Phi_{g_{i,j}}^{y-} - \Phi_{g_{i,j-1}}^{y+} \right)^{n+1} \right\}
 \end{aligned}$$

1 **Table PA-9. Auxiliary Dirichlet Conditions for S_g and P_b**

Surface Grid Blocks	
$S_g(i, j, t) = 0.08363$	Columns 1–42, 44–68, Row 33, $-5 \text{ yr} \leq t$ Saturation is not forced at the shaft cell on the surface because its saturation is reset to 1.0 at $t = 0 \text{ yr}$.
$P_b(i, j, t) = 1.01 \times 10^5 \text{ Pa}$	Columns 1–68, row 33, $-5 \text{ yr} \leq t$
Culebra and Magenta Far Field	
$P_b(i, 26, t) = 9.14 \times 10^5 \text{ Pa}$	$i = 1 \text{ and } 68, j = 26, -5 \text{ yr} \leq t$ (Culebra)
$P_b(i, 28, t) = 9.47 \times 10^5 \text{ Pa}$	$i = 1 \text{ and } 68, j = 28, -5 \text{ yr} \leq t$ (Magenta)

2

3
$$+\alpha_{i,j}q_{g_{i,j}}^{n+1} + \alpha_{i,j}q_{rg_{i,j}}^{n+1} - \frac{(\alpha\phi\rho_g S_g)_{i,j}^{n+1} - (\alpha\phi\rho_g S_g)_{i,j}^n}{\Delta t} = 0 \quad (\text{PA.91})$$

4 where Φ represents the phase potentials given by

5
$$\Phi_{g_{i,j}}^{x+} = P_{g_{i,j}} + \rho_{g_{i+1/2,j}} g h_{i,j}, \quad \Phi_{g_{i,j}}^{x-} = P_{g_{i,j}} + \rho_{g_{i-1/2,j}} g h_{i,j}$$

6 and

7
$$\Phi_{g_{i,j}}^{y+} = P_{g_{i,j}} + \rho_{g_{i,j+1/2}} g h_{i,j}, \quad \Phi_{g_{i,j}}^{y-} = P_{g_{i,j}} + \rho_{g_{i,j-1/2}} g h_{i,j}$$

8 the subscripts are defined by

- 9 i = x-direction grid index
 10 j = y-direction grid index
 11 $i \pm 1/2$ = x-direction grid block interface
 12 $j \pm 1/2$ = y-direction grid block interface
 13 x_i = grid block center in the x-coordinate direction (m)
 14 y_j = grid block center in the y-coordinate direction (m)
 15 Δx_i = grid block length in the x-coordinate direction (m)
 16 Δy_j = grid block length in the y-coordinate direction (m)

17 the superscripts are defined by

- 18 n = index in the time discretization, known solution time level
 19 $n+1$ = index in the time discretization, unknown solution time level

20 and the interblock densities are defined by

$$1 \quad \rho_{g_{i+1/2,j}} = \frac{\Delta x_{i+1,j}}{\Delta x_{i,j} + \Delta x_{i+1,j}} \rho_{g_{i,j}} + \frac{\Delta x_{i,j}}{\Delta x_{i,j} + \Delta x_{i+1,j}} \rho_{g_{i+1,j}}$$

$$2 \quad \rho_{g_{i-1/2,j}} = \frac{\Delta x_{i,j}}{\Delta x_{i-1,j} + \Delta x_{i,j}} \rho_{g_{i-1,j}} + \frac{\Delta x_{i-1,j}}{\Delta x_{i-1,j} + \Delta x_{i,j}} \rho_{g_{i,j}}$$

$$3 \quad \rho_{g_{i,j+1/2}} = \frac{\Delta y_{i,j+1}}{\Delta y_{i,j} + \Delta y_{i,j+1}} \rho_{g_{i,j}} + \frac{\Delta y_{i,j}}{\Delta y_{i,j} + \Delta y_{i,j+1}} \rho_{g_{i,j+1}}$$

$$4 \quad \rho_{g_{i,j-1/2}} = \frac{\Delta y_{i,j}}{\Delta y_{i,j-1} + \Delta y_{i,j}} \rho_{g_{i,j-1}} + \frac{\Delta y_{i,j-1}}{\Delta y_{i,j-1} + \Delta y_{i,j}} \rho_{g_{i,j}}$$

5 The interface values of k_{rg} in Equation (PA.91) are evaluated using upstream weighted values
 6 (i.e., the relative permeabilities at each grid block interface are defined to be the relative
 7 permeabilities at the center of the adjacent grid block with the highest potential). Further,
 8 interface values for $\alpha \rho_g k_x / \mu_g$ and $\alpha \rho_g k_y / \mu_g$ are obtained by harmonic averaging of adjacent grid
 9 block values for these expressions. Currently all materials are isotropic, i.e. $k_x = k_y = k_z$.

10 The discretization of the brine mass balance equation is obtained by replacing the subscript for
 11 gas, g , by the subscript for brine, b . As a reminder, P_g and S_b are replaced in the numerical
 12 implementation with the substitutions indicated by Equation (PA.27) and Equation (PA.26),
 13 respectively. Wells are not used in the conceptual model for long-term Salado flow calculations,
 14 but they are used for DBR calculations. Thus, for long-term Salado flow calculations, the terms
 15 q_g and q_b are zero. For long-term Salado flow calculations, the wellbore is not treated by a well
 16 model, but rather is explicitly modeled within the grid as a distinct material region (i.e., Upper
 17 Borehole and Lower Borehole in Figure PA-15).

18 The resultant coupled system of nonlinear brine and gas mass balance equations is integrated in
 19 time using the Newton-Raphson method with upstream weighting of the relative permeabilities,
 20 as previously indicated. The primary unknowns at each computational cell center are brine
 21 pressure and gas saturation.

22 **PA-4.2.12 Gas and Brine Flow across Specified Boundaries**

23 The Darcy velocity vectors $v_g(x, y, t)$ and $v_b(x, y, t)$ for gas and brine flow ($m^3/m^2/s = m/s$) are
 24 defined by the expressions

$$25 \quad v_g(x, y, t) = k k_{rg} (\nabla P_g + \rho_g g \nabla h) / \mu_g \quad (\text{PA.92})$$

26 and

$$27 \quad v_b(x, y, t) = k k_{rb} (\nabla P_b + \rho_b g \nabla h) / \mu_b \quad (\text{PA.93})$$

1 Values for v_g and v_b are obtained and saved as the numerical solution of Equation (PA.24)
 2 through Equation (PA.30) is carried out. Cumulative flows of gas, $C_g(t, B)$, and brine, $C_b(t, B)$,
 3 from time 0 to time t across an arbitrary boundary B in the domain of (Figure PA-15) is then
 4 given by

$$5 \quad C_l(t, B) = \int_0^t \left[\int_B \alpha(x, y) \mathbf{v}_l(x, y, t) \cdot \mathbf{n}(x, y) ds \right] dt \quad (\text{PA.94})$$

6 for $l = g, b$, where $\alpha(x, y)$ is the geometry factor defined in Equation (PA.32), $n(x, y)$ is an
 7 outward-pointing unit normal vector, and $\int_B ds$ denotes a line integral. As an example, B could
 8 correspond to the boundary of the waste disposal regions in Figure PA-15. The integrals
 9 defining $C_g(t, B)$ and $C_b(t, B)$ are evaluated using the Darcy velocities defined by Equation
 10 (PA.92) and Equation (PA.93). Due to the dependence of gas volume on pressure, $C_g(t, B)$ is
 11 typically calculated in moles or cubic meters at standard temperature and pressure, which
 12 requires an appropriate change of units for v_g in Equation (PA.95).

13 **PA-4.2.13 Additional Information**

14 Additional information on BRAGFLO and its use in the CRA-2009 PA can be found in the
 15 BRAGFLO user's manual (Nemer 2007c), the BRAGFLO design document (Nemer 2007b) and
 16 the analysis package for the Salado flow calculations in the CRA-2009 PA (Nemer and Clayton
 17 2008).

18 **PA-4.3 Radionuclide Transport in the Salado: NUTS**

19 The NUTS code is used to model radionuclide transport in the Salado. NUTS models
 20 radionuclide transport within all regions for which BRAGFLO computes brine and gas flow, and
 21 for each realization uses as input the corresponding BRAGFLO velocity field, pressures,
 22 porosities, saturations, and other model parameters, including, for example, the geometrical grid,
 23 residual saturation, material map, and compressibility. Of the radionuclides that are transported
 24 vertically due to an intrusion or up shaft, it is assumed that the lateral radionuclide transport is in
 25 the most transmissive unit, the Culebra. Therefore, the radionuclide transport through the Dewey
 26 Lake to the accessible environment (f_{DL} in Equation [PA.33]) and to the land surface due to
 27 long-term flow (f_S in Equation [PA.33]) are set to zero for consistency.

28 The PA uses NUTS in two different modes. First, the code is used in a computationally fast
 29 *screening* mode to identify those BRAGFLO realizations for which it is unnecessary to do full
 30 transport calculations because the amount of contaminated brine that reaches the Culebra or the
 31 LWB within the Salado is insufficient to significantly contribute to the total integrated release of
 32 radionuclides from the disposal system. For the remaining realizations, which have the
 33 possibility of consequential release, a more computationally intensive calculation of each
 34 radionuclide's full transport is performed (see Section PA-6.7.2).

1 This section describes the model used to compute radionuclide transport in the Salado for E0,
2 E1, and E2 scenarios (defined in Section PA-2.3.2). The model for transport in the E1E2
3 scenario, which is computed using the PANEL code, is described in Section PA-4.4.

4 NUTS models radionuclide transport by advection (see Attachment MASS-2009, Section
5 MASS-13.5). NUTS disregards sorptive and other retarding effects throughout the entire flow
6 region. Physically, some degree of retardation must occur at locations within the repository and
7 the geologic media; it is therefore conservative to ignore retardation processes. NUTS also
8 ignores reaction-rate aspects of dissolution and colloid formation processes, and mobilization is
9 assumed to occur instantaneously. Neither molecular nor mechanical dispersion is modeled in
10 NUTS. These processes are assumed to be insignificant compared to advection, as discussed
11 further in Attachment MASS-2009, Section MASS-13.5.

12 Colloidal actinides are subject to retardation by chemical interaction between colloids and solid
13 surfaces and by clogging of small pore throats (i.e., by sieving). There will be some interaction
14 of colloids with solid surfaces in the anhydrite interbeds. Given the low permeability of intact
15 interbeds, it is likely that pore apertures will be small and some sieving will occur. However,
16 colloidal particles, if not retarded, are transported slightly more rapidly than the average velocity
17 of the bulk liquid flow. Because the effects on transport of slightly increased average pore
18 velocity and retarded interactions with solid surfaces and sieving offset one another, the DOE
19 assumes residual effects of these opposing processes will be either small or beneficial, and does
20 not incorporate them when modeling An transport in the Salado interbeds.

21 If brine in the repository moves into interbeds, it is likely that mineral precipitation reactions will
22 occur. Precipitated minerals may contain actinides as trace constituents. Furthermore, colloidal-
23 sized precipitates will behave like mineral-fragment colloids, which are destabilized by brines,
24 quickly agglomerating and settling by gravity. The beneficial effects of precipitation and
25 coprecipitation are neglected in PA.

26 Fractures, channeling, and viscous fingering may also impact transport in Salado interbeds,
27 which contain natural fractures. Because of the low permeability of unfractured anhydrite, most
28 fluid flow in interbeds will occur in fractures. Even though some properties of naturally
29 fractured interbeds are characterized by in situ tests, other uncertainty exists in the characteristics
30 of the fracture network that may be created with high gas pressure in the repository. The PA
31 modeling system accounts for the possible effects on porosity and permeability of fracturing by
32 using a fracturing model (see Section PA-4.2.4). The processes and effects associated with
33 fracture dilation or fracture propagation not already captured by the PA fracture model are
34 negligible (see the CCA, Appendix MASS, Section MASS.13.3 and Appendix MASS
35 Attachment 13.2). Of those processes not already incorporated, channeling has the greatest
36 potential effect.

37 Channeling is the movement of fluid through the larger-aperture sections of a fracture network
38 with locally high permeabilities. It could locally enhance An transport. However, it is assumed
39 that the effects of channeled flow in existing or altered fractures will be negligible for the length
40 and time scales associated with the disposal system. The DOE believes this assumption is
41 reasonable because processes are likely to occur that limit the effectiveness of channels or the
42 dispersion of actinides in them. First, if gas is present in the fracture network, it will be present

1 as a nonwetting phase and will occupy the portions of the fracture network with relatively large
 2 apertures, where the highest local permeabilities will exist. The presence of gas thus removes
 3 the most rapid transport pathways from the contaminated brine and decreases the impact of
 4 channeling. Second, brine penetrating the Salado from the repository is likely to be completely
 5 miscible with in situ brine. Because of miscibility, diffusion or other local mixing processes will
 6 probably broaden fingers (reduce concentration gradients) until the propagating fingers are
 7 indistinguishable from the advancing front.

8 Gas will likely penetrate the liquid-saturated interbeds as a fingered front, rather than a uniform
 9 front. Fingers form when there is a difference in viscosity between the invading fluid (gas) and
 10 the resident fluid (liquid brine), and because of channeling effects. This process does not affect
 11 An transport, however, because actinides of interest are transported only in the liquid phase,
 12 which will not displace gas in the relatively high-permeability regions due to capillary effects.

13 **PA-4.3.1 Mathematical Description**

14 The following system of PDEs is used to model radionuclide transport in the Salado:

15
$$-\nabla \cdot \alpha \mathbf{v}_b C_{bl} + \alpha S_l = \alpha \frac{\partial}{\partial t} (\phi S_b C_{bl}) + (\alpha \phi S_b C_{bl}) \lambda_l - \alpha \phi S_b \sum_{p \in P(l)} C_{bp} \lambda_p \quad (\text{PA.95})$$

16
$$-S_l = \frac{\partial}{\partial t} (C_{sl}) + C_{sl} \lambda_l - \sum_{p \in P(l)} C_{sp} \lambda_p \quad (\text{PA.96})$$

17 for $l = 1, 2, \dots, n_R$, where

- 18 \mathbf{v}_b = Darcy velocity vector ($\text{m}^3/\text{m}^2/\text{s} = \text{m}/\text{s}$) for brine (supplied by BRAGFLO from solution
 19 of Equation (PA.93))
- 20 C_{bl} = concentration (kg/m^3) of radionuclide l in brine
- 21 C_{sl} = concentration (kg/m^3) of radionuclide l in solid phase (i.e., not in brine), with
 22 concentration defined with respect to total (i.e., bulk) formation volume (only used in
 23 repository; see Figure PA-15)
- 24 S_l = linkage term ($\text{kg}/\text{m}^3/\text{s}$) due to dissolution/precipitation between radionuclide l in brine
 25 and in solid phase (see Equation (PA.97))
- 26 ϕ = porosity (supplied by BRAGFLO from solution of Equation (PA.24) through Equation
 27 (PA.30))
- 28 S_b = brine saturation (supplied by BRAGFLO from solution of Equation (PA.24) through
 29 Equation (PA.30))
- 30 λ_l = decay constant (s^{-1}) for radionuclide l
- 31 $P(l) = \{p: \text{radionuclide } p \text{ is a parent of radionuclide } l\}$
- 32 n_R = number of radionuclides,

33 and α is the dimension-dependent geometry factor in Equation (PA.32). PA uses a two-
 34 dimensional representation for fluid flow and radionuclide transport in the vicinity of the

1 repository, with α defined by the element depths in Figure PA-15. Although omitted for brevity,
 2 the terms α , \mathbf{v}_b , C_{bl} , C_{sl} , S_l , S_b , and ϕ are functions $\alpha(x, y)$, $\mathbf{v}_b(x, y, t)$, $C_{bl}(x, y, t)$, $C_{sl}(x, y, t)$,
 3 $S_l(x, y, t)$, $S_b(x, y, t)$, and $\phi(x, y, t)$ of time t and the spatial variables x and y . Equation (PA.95)
 4 and Equation (PA.96) are defined and solved on the same computational grid (Figure PA-15)
 5 used by BRAGFLO for the solution of Equation (PA.24) through Equation (PA.30).

6 Radionuclides are assumed to be present in both brine (Equation (PA.95)) and in an immobile
 7 solid phase (Equation (PA.96)), although radionuclide transport takes place only by brine flow
 8 (Equation (PA.95)). The maximum radionuclide concentration is assumed to equilibrate
 9 instantly for each element (Section PA-4.3.2). Then each individual radionuclide equilibrates
 10 between the brine and solid phases based on the maximum concentration of its associated
 11 element and the mole fractions of other isotopes included in the calculation. The linkage
 12 between the brine and solid phases in Equation (PA.95) and Equation (PA.96) is accomplished
 13 by the term S_l , where

$$14 \quad S_l = \begin{cases} \delta(\tau - t) \text{Dif}(S_T, C_{b,El(l)}) MF_{sl} & \text{if } 0 \leq \text{Dif}(S_T, C_{b,El(l)}) \leq \frac{C_{s,El(l)}}{\phi S_b} \text{ and } 0 < S_b \\ \delta(\tau - t) \left[\frac{C_{s,El(l)}}{\phi S_b} \right] MF_{sl} & \text{if } 0 \leq \frac{C_{s,El(l)}}{\phi S_b} < \text{Dif}(S_T, C_{b,El(l)}) \text{ and } 0 < S_b \\ \delta(\tau - t) \text{Dif}(S_T, C_{b,El(l)}) MF_{bl} & \text{if } \text{Dif}(S_T, C_{b,El(l)}) < 0 \text{ and } 0 < S_b \\ 0 & \text{otherwise} \end{cases} \quad (PA.97)$$

16 where

17 $S_T [Br(t), Ox(l), El(l)]$ = maximum concentration (kg/m³) of element $El(l)$ in oxidation
 18 state $Ox(l)$ in brine type $Br(t)$, where $El(l)$ denotes the element of
 19 which radionuclide l is an isotope, $Ox(l)$ denotes the oxidation
 20 state in which element $El(l)$ is present, and $Br(t)$ denotes the type
 21 of brine present in the repository at time t (see Section PA-4.3.2
 22 for definition of $S_T [Br(t), Ox(l), El(l)]$).

23 $C_{p,El(l)}$ = concentration (kg/m³) of element $El(l)$ in brine ($p = b$) or solid (p
 24 = s), which is equal to the sum of concentrations of radionuclides
 25 that are isotopes of same element as radionuclide l , where $k \in$
 26 $El(l)$ only if k is an isotope of element $El(l)$:

$$27 \quad C_{p,El(l)} = \sum_{k \in El(l)} C_{p,k} \quad (PA.98)$$

1 $Dif(S_T, C_{b,El(l)})$ = difference (kg/m³) between maximum concentration of element
 2 $El(l)$ in brine and existing concentration of element $El(l)$ in brine

3
$$Dif(S_T, C_{b,El(l)}) = S_T [Br(t), Ox(l), El(l)] - C_{b,El(l)} \quad (PA.99)$$

4 MF_{pl} = mole fraction of radionuclide l in phase p , where $p = b$ (brine) or
 5 $p = s$ (solid)

6
$$MF_{pl} = C_{pl}CM_l / \sum_{k \in El(l)} C_{pk}CM_k \quad (PA.100)$$

7 CM_l = conversion factor (mol/kg) from kilograms to moles for
 8 radionuclide l

9 $\delta(\tau - t)$ = Dirac delta function (s⁻¹) ($\delta(\tau - t) = 0$ if $\tau \neq t$ and

10
$$\int_{-\infty}^{\infty} \delta(\tau - t) d\tau = 1$$
)

11 In the CCA and the CRA-2004, the function S_T had an additional parameter, Mi , representing the
 12 presence or absence of microbial activity. However, during preparations for the CRA-2004
 13 PABC, the EPA directed the DOE to change the probability of microbial activity to 1.0
 14 (Cotsworth 2005). The DOE therefore revised the probability distribution so that all vectors
 15 would have the possibility for microbial degradation of cellulose, while retaining the percentage
 16 of vectors showing microbial degradation of rubbers and plastic at 0.25 (Nemer 2005). This, in
 17 effect, sets Mi equal to “Yes” for all vectors. Mi is therefore suppressed as an argument of S_T in
 18 the remainder of this section.

19 The terms S_l , S_b , $C_{p,El(l)}$, MF_{pl} , and ϕ are functions of time t and the spatial variables x and y ,
 20 although the dependencies are omitted for brevity. The Dirac delta function, $\delta(\tau - t)$, appears in
 21 Equation (PA.97) to indicate that the adjustments to concentration are implemented
 22 instantaneously within the numerical solution of Equation (PA.95) and Equation (PA.96)
 23 whenever a concentration imbalance is observed.

24 The velocity vector \mathbf{v}_b in Equation (PA.95) and Equation (PA.96) is defined in Equation (PA.93)
 25 and is obtained from the numerical solution of Equation (PA.24) through Equation (PA.30). If B
 26 denotes an arbitrary boundary (e.g., the LWB) in the domain of Equation (PA.95) and Equation
 27 (PA.96) (as shown in Figure PA-15), the cumulative transport of $C_l(t, B)$ of radionuclide l from
 28 time 0 to time t across B is given by

29
$$C_l(t, B) = \int_0^t \left[\int_B \mathbf{v}_b(x, y, t) C_l(x, y, t) \alpha(x, y) \cdot \mathbf{n}(x, y) ds \right] dt \quad (PA.101)$$

1 where $\mathbf{n}(x, y)$ is an outward-pointing unit normal vector and $\int_B ds$ denotes a line integral over
 2 B .

3 Equation (PA.95) and Equation (PA.96) models advective radionuclide transport due to the
 4 velocity vector \mathbf{v}_b . Although the effects of solubility limits are considered, no chemical or
 5 physical retardation is included in the model. Molecular diffusion is not included in the model,
 6 because the radionuclides under consideration have molecular diffusion coefficients on the order
 7 of 10^{-10} m²/s, and thus can be expected to move only approximately 10 m over 10,000 years due
 8 to molecular diffusion. Mechanical dispersion is also omitted in NUTS, as the uniform initial
 9 radionuclide concentrations assumed within the repository and the use of time-integrated releases
 10 in assessing compliance with section 191.13 mean that mechanical dispersion will have
 11 negligible impact on overall performance.

12 **PA-4.3.2 Calculation of Maximum Concentration $S_T(Br, Ox, El)$**

13 A maximum concentration $S_T(Br, Ox, El)$ (mol/liter [L]) is calculated for each brine type ($Br \in$
 14 {Salado, Castile}), oxidation state ($Ox \in \{III, IV, V, VI\}$), and element ($El \in \{Am, Pu, U, Th\}$).
 15 The maximum concentration is given by

16
$$S_T(Br, Ox, El) = S_D(Br, Ox) + S_C(Br, Ox, El) \quad (PA.102)$$

17 where $S_D(Br, Ox)$ is the dissolved solubility (mol/L) and $S_C(Br, Ox, El)$ is the concentration
 18 (mol/L) of the element sorbed to colloids.

19 The dissolved solubility $S_D(Br, Ox)$ is given by

20
$$S_D(Br, Ox) = S_{FMT}(Br, Ox) \times 10^{UF(Ox)} \quad (PA.103)$$

21 where

22 $S_{FMT}(Br, Ox)$ = dissolved solubility (mol/L) calculated by Fracture-Matrix Transport (FMT)
 23 model (WIPP Performance Assessment 1998a) for brine type Br and oxidation
 24 state Ox
 25 $UF(Ox)$ = logarithm (base 10) of uncertainty factor for solubilities calculated by FMT
 26 expressed as a function of oxidation state Ox

27 Table PA-10 lists the calculated values of $S_{FMT}(Br, Ox)$; details of the calculation are provided
 28 in Appendix SOTERM-2009 and Brush (2005). The uncertainty factors $UF(Ox)$ are determined
 29 by the uncertain parameters WSOLVAR3 for the III oxidation state and WSOLVAR4 for the IV
 30 oxidation state; definitions of these parameters are provided in Table PA-19, and further details
 31 regarding the calculation of the solubilities is given in Appendix SOTERM-2009, Section
 32 SOTERM-5.1.3.

1 **Table PA-10. Calculated Values for Dissolved Solubility (see Appendix SOTERM-2009,**
 2 **Table SOTERM-16)**

Brine	Oxidation State			
	III	IV	V	VI ^a
Salado	3.87×10^{-7}	5.64×10^{-8}	3.55×10^{-6}	1.0×10^{-3}
Castile	2.88×10^{-7}	6.79×10^{-8}	8.24×10^{-7}	1.0×10^{-3}

^a Values for the VI solubilities were mandated by the EPA (U.S. Environmental Protection Agency 2005).

3

4 The concentration (mol/L) of the element sorbed to colloids $S_C(Br, Ox, El)$ is given by

5
$$S_C(Br, Ox, El) = S_{Hum}(Br, Ox, El) + S_{Mic}(Br, Ox, El) + S_{Act}(El) + S_{Mn} \quad (PA.104)$$

6 where

7 $S_{Hum}(Br, Ox, El)$ = solubility (concentration expressed in mol/L) in brine type Br of
 8 element El in oxidation state Ox resulting from humic colloid
 9 formation

10
$$= \min\{SF_{Hum}(Br, Ox, El) \times S_D(Br, Ox), UB_{Hum}\}$$

11 $SF_{Hum}(Br, Ox, El)$ = scale factor used as a multiplier on $S_D(Br, Ox)$ in definition of

12 $S_{Hum}(Br, Ox, El)$ (see $UB_{Mic}(Ox, El)$ = upper bound
 13 on solubility (concentration expressed in mol/L) of element El in
 14 oxidation state Ox resulting from microbial colloid formation (see
 15 Table PA-12)

16 Table PA-11)

17 UB_{Hum} = upper bound on solubility (concentration expressed in mol/L) of
 18 individual An elements resulting from humic colloid formation

19
$$= 1.1 \times 10^{-5} \text{ mol/L}$$

20 $S_{Mic}(Br, Ox, El)$ = solubility (concentration expressed in mol/L) in brine type Br of
 21 element El in oxidation state Ox resulting from microbial colloid
 22 formation

23
$$= \min\{SF_{Mic}(Ox, El) \times S_D(Br, Ox), UB_{Mic}(Ox, El)\}$$

24 $SF_{Mic}(Ox, El)$ = scale factor used as multiplier on $S_D(Br, Ox)$ in definition of $S_{Mic}(Br,$
 25 $Ox, El)$ (see Table PA-12)

$UB_{Mic}(Ox, El)$ = upper bound on solubility (concentration expressed in mol/L) of element El in oxidation state Ox resulting from microbial colloid formation (see Table PA-12)

Table PA-11. Scale Factor $SF_{Hum}(Br, Ox, El)$ Used in Definition of $S_{Hum}(Br, Ox, El)$ (see Appendix SOTERM-2009, Table SOTERM-21)

Brine	Element (Oxidation State)							
	Am(III)	Pu(III)	Pu(IV)	U(IV)	Th(IV)	Np(IV)	Np(V)	U(VI)
Salado	0.19	0.19	6.3	6.3	6.3	6.3	9.1×10^{-4}	0.12
Castile	WPHUMOX3 ^a	WPHUMOX3 ^a	6.3	6.3	6.3	6.3	7.4×10^{-3}	0.51

^a See Table PA-19.

Table PA-12. Scale Factor $SF_{Mic}(Ox, El)$ and Upper Bound $UB_{Mic}(Ox, El)$ (mol/L) Used in Definition of $S_{Mic}(Br, Ox, El)$ (see Appendix SOTERM-2009, Table SOTERM-21)

Parameter	Element (Oxidation State)							
	Am(III)	Pu(III)	Pu(IV)	U(IV)	Th(IV)	Np(IV)	Np(V)	U(VI)
$SF_{Mic}(Ox, El)$	3.6	0.3	0.3	0.0021	3.1	12.0	12.0	0.0021
$UB_{Mic}(Ox, El)$	1	6.8×10^{-5}	6.8×10^{-5}	0.0021	0.0019	0.0027	0.0027	0.0021

$S_{Act}(El)$ = solubility (concentration in mol/L) of element El resulting from An intrinsic colloid formation

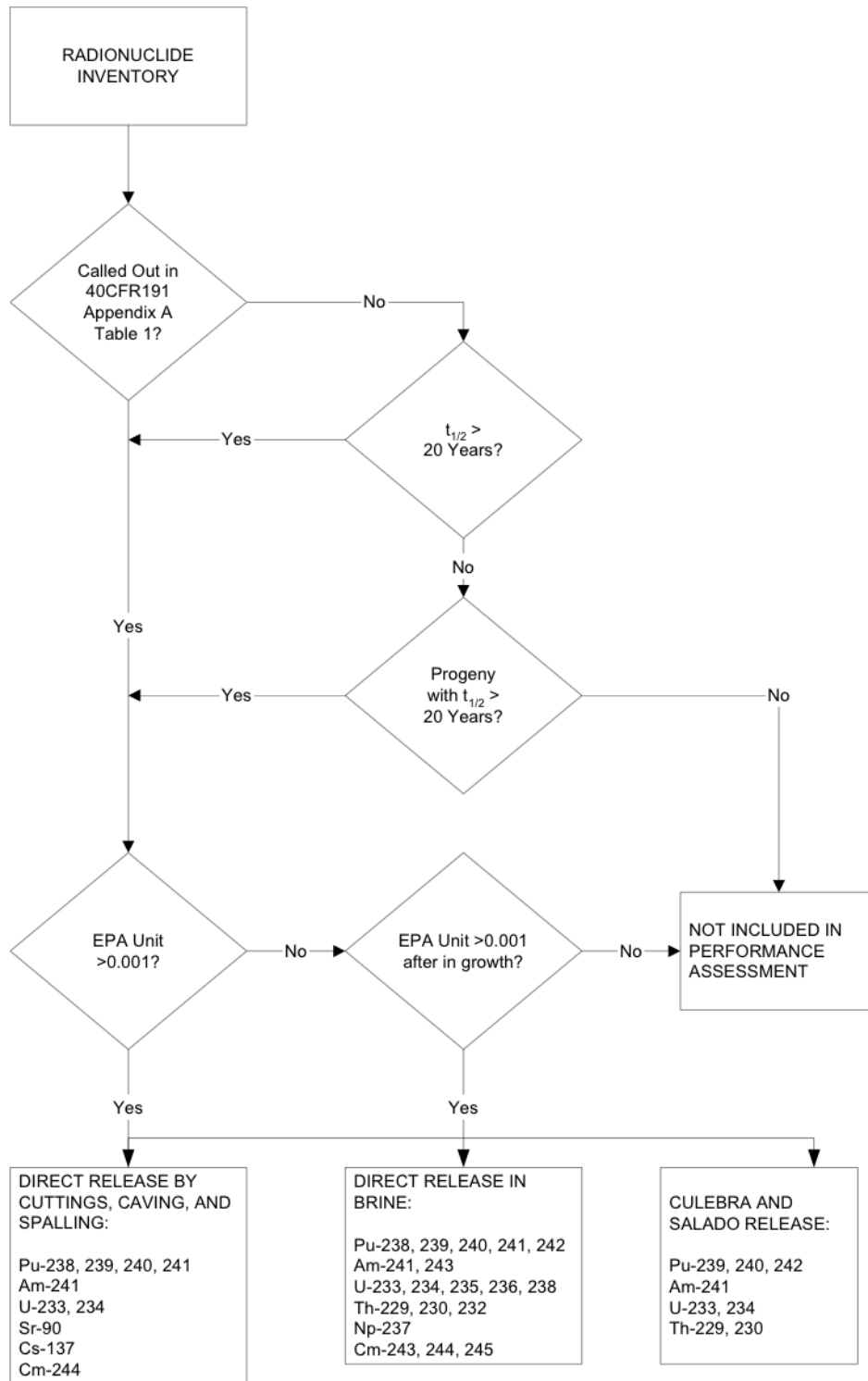
$$= \begin{cases} 1 \times 10^{-9} \text{ mol/L} & \text{if } El = \text{Pu} \\ 0 \text{ mol/L} & \text{otherwise} \end{cases}$$

S_{Mn} = solubility (concentration in mol/L) of individual An element resulting from mineral fragment colloid formation

$$= 2.6 \times 10^{-8} \text{ mol/L}$$

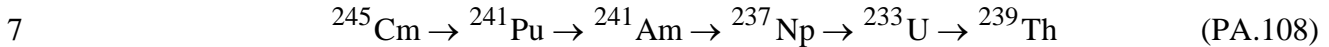
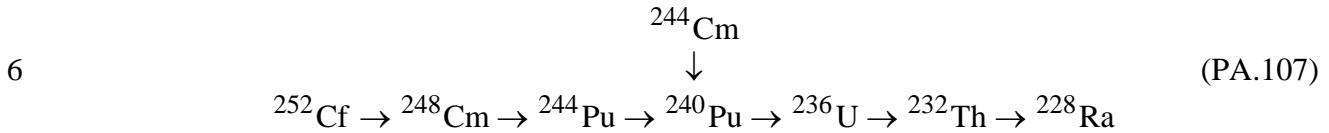
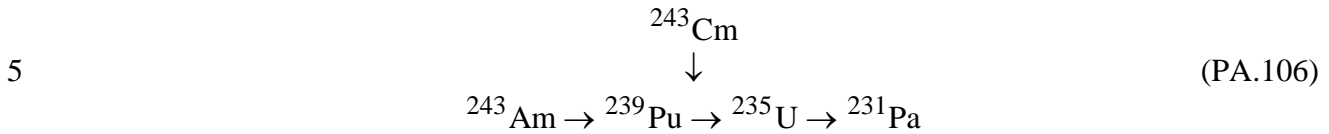
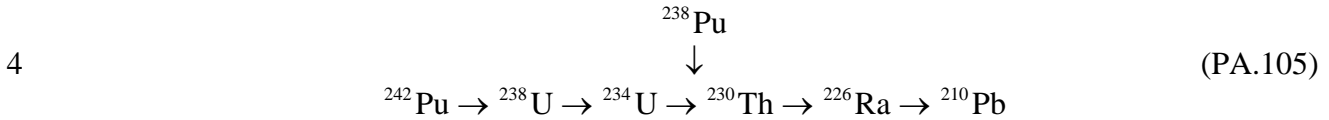
PA-4.3.3 Radionuclides Transported

Since the solution of Equation (PA.95) and Equation (PA.96) for this many radionuclides and decay chains would be very time-consuming, the number of radionuclides for direct inclusion in the analysis was reduced using the algorithm shown in Figure PA-21. The CRA-2009 PA uses the same reduction algorithm as the CCA PA (see the CCA, Appendix WCA); the algorithm was found to be acceptable in the CCA review (U.S. Environmental Protection Agency 1998a, Section 4.6.1.1).



1
2 **Figure PA-21. Selecting Radionuclides for the Release Pathways Conceptualized by PA**

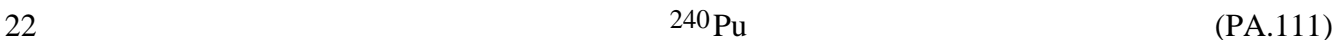
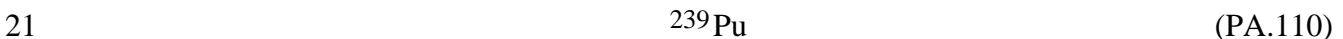
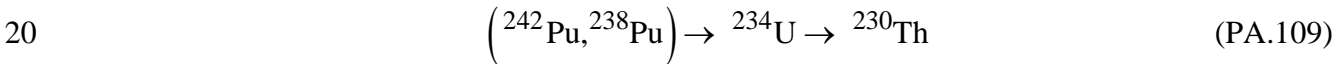
1 Using Figure PA-21, the number of radionuclides considered was reduced from 135 to a total of
 2 29 included in the decay calculations carried out by the PANEL code (Garner and Leigh 2005).
 3 These radionuclides belong to the following decay chains:



8 Radionuclides considered in the decay calculations that do not belong to one of the decay chains
 9 listed above are ${}^{147}\text{Pm}$, ${}^{137}\text{Cs}$, and ${}^{90}\text{Sr}$. In addition, some intermediates with extremely short
 10 half-lives, such as ${}^{240}\text{U}$, were omitted from the decay chains.

11 Further simplification of the decay chains is possible based on the total inventories. Releases of
 12 radionuclides whose inventories total less than one EPA unit are essentially insignificant, as any
 13 release that transports essentially all of a given species outside the LWB will be dominated by
 14 the releases of other species with much larger inventories. In addition, ${}^{137}\text{Cs}$ and ${}^{90}\text{Sr}$ can be
 15 omitted because their concentrations drop to below 1 EPA unit within 150 years, which makes it
 16 improbable that a significant release of these radionuclides will occur. Isotopes such as ${}^{241}\text{Pu}$,
 17 whose decay could affect the inventory of measurable isotopes, were reinstated.

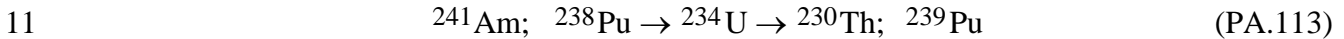
18 After the reduction of radionuclides outlined in Figure PA-21 and the above paragraph, the
 19 following 10 radionuclides remained from the decay chains shown above:



24 ${}^{238}\text{Pu}$ does not significantly affect transport calculations because of its short half-life (87.8
 25 years). The remaining nine radionuclides were then further reduced by combining those with
 26 similar decay and transport properties. In particular, ${}^{234}\text{U}$, ${}^{230}\text{Th}$, and ${}^{239}\text{Pu}$ were used as
 27 surrogates for the groups $\{ {}^{234}\text{U}, {}^{233}\text{U} \}$, $\{ {}^{230}\text{Th}, {}^{229}\text{Th} \}$, and $\{ {}^{242}\text{Pu}, {}^{240}\text{Pu}, {}^{239}\text{Pu} \}$, with the

1 initial inventories of ^{234}U , ^{230}Th , and ^{239}Pu being increased to account for the additional
 2 radionuclide(s) in each group.

3 In increasing the initial inventories, the individual radionuclides were combined on either a mole
 4 or curie basis (i.e., moles added and then converted back to curies, or curies added directly). In
 5 each case, the method that maximized the combined inventory was used; thus, ^{233}U was added to
 6 ^{234}U , ^{240}Pu to ^{239}Pu , and ^{229}Th to ^{230}Th by curies, while ^{242}Pu was added to ^{239}Pu by moles. In
 7 addition, ^{241}Pu was added to ^{241}Am by moles because ^{241}Pu has a half-life of 14 years and will
 8 quickly decay to ^{241}Am , and neglect of this ingrowth would underestimate the ^{241}Am inventory
 9 by about 4% (Table PA-13). The outcome of this process was the following set of five
 10 radionuclides in three simplified decay chains:



12 which were then used with Equation (PA.95) and Equation (PA.96) for transport in the vicinity
 13 of the repository. As ^{238}Pu does not significantly affect transport calculations, only the
 14 remaining four radionuclides are used in the Culebra transport calculations (Section PA-4.9).
 15 These radionuclides account for 99% of the EPA units in the waste after 2,000 years (Garner and
 16 Leigh 2005), and hence will dominate any releases by transport.

17 **Table PA-13. Combination of Radionuclides for Transport**

Combination	Isotope Initial Values	Combination Procedure	Combined Inventory
$^{233}\text{U} \rightarrow ^{234}\text{U}$	$1.23 \times 10^3 \text{ Ci } ^{233}\text{U}$ $3.44 \times 10^2 \text{ Ci } ^{234}\text{U}$	$1.23 \times 10^3 \text{ Ci } ^{233}\text{U}$ $\rightarrow 1.23 \times 10^3 \text{ Ci } ^{234}\text{U}$	$1.57 \times 10^3 \text{ Ci } ^{234}\text{U}$
$^{242}\text{Pu} \rightarrow ^{239}\text{Pu}$	$1.27 \times 10^1 \text{ Ci } ^{242}\text{Pu}$	$1.27 \times 10^1 \text{ Ci } ^{242}\text{Pu}$ $= 1.32 \times 10^1 \text{ moles } ^{242}\text{Pu}$ $\rightarrow 1.32 \times 10^1 \text{ moles } ^{239}\text{Pu}$ $= 1.98 \times 10^2 \text{ Ci } ^{239}\text{Pu}$	$6.78 \times 10^5 \text{ Ci } ^{239}\text{Pu}$
$^{240}\text{Pu} \rightarrow ^{239}\text{Pu}$	$9.55 \times 10^4 \text{ Ci } ^{240}\text{Pu}$ $5.82 \times 10^5 \text{ Ci } ^{239}\text{Pu}$	$9.55 \times 10^4 \text{ Ci } ^{240}\text{Pu}$ $\rightarrow 9.55 \times 10^4 \text{ Ci } ^{239}\text{Pu}$	
$^{229}\text{Th} \rightarrow ^{230}\text{Th}$	$5.21 \times 10^0 \text{ Ci } ^{229}\text{Th}$ $1.80 \times 10^{-1} \text{ Ci } ^{230}\text{Th}$	$5.21 \times 10^0 \text{ Ci } ^{229}\text{Th}$ $\rightarrow 5.21 \times 10^0 \text{ Ci } ^{230}\text{Th}$	$5.39 \times 10^0 \text{ Ci } ^{230}\text{Th}$
$^{241}\text{Pu} \rightarrow ^{241}\text{Am}$	$4.48 \times 10^5 \text{ Ci } ^{241}\text{Pu}$ $5.18 \times 10^5 \text{ Ci } ^{241}\text{Am}$	$5.38 \times 10^5 \text{ Ci } ^{241}\text{Pu}$ $= 1.79 \times 10^1 \text{ moles } ^{241}\text{Pu}$ $\rightarrow 1.79 \times 10^1 \text{ moles } ^{241}\text{Am}$ $= 1.50 \times 10^4 \text{ Ci } ^{241}\text{Am}$	$5.33 \times 10^5 \text{ Ci } ^{241}\text{Am}$

18

19 **PA-4.3.4 NUTS Tracer Calculations**

20 All BRAGFLO realizations are first evaluated using NUTS in a screening mode to identify those
 21 realizations for which a significant release of radionuclides to the LWB cannot occur. The
 22 screening simulations consider an infinitely soluble, nondecaying, nondispersive, and nonsorbing
 23 species as a tracer element. The tracer is given a unit concentration in all waste disposal areas of
 24 1 kg/m^3 . If the amount of tracer that reaches the selected boundaries (the top of the Salado and

1 the LWB within the Salado) does not exceed a cumulative mass of 10^{-7} kg within 10,000 years,
 2 it is assumed there is no consequential release to these boundaries. If the cumulative mass
 3 outside the boundaries within 10,000 years exceeds 10^{-7} kg, a complete transport analysis is
 4 conducted. The value of 10^{-7} kg is selected because, regardless of the isotopic composition of
 5 the release, it corresponds to a normalized release less than 10^{-6} EPA units, the smallest release
 6 displayed in CCDF construction (Stockman 1996). The largest normalized release would be
 7 9.98×10^{-7} EPA units, corresponding to 10^{-7} kg of ^{241}Am if the release was entirely ^{241}Am .

8 **PA-4.3.5 NUTS Transport Calculations**

9 For BRAGFLO realizations with greater than 10^{-7} kg reaching the boundaries in the tracer
 10 calculations, NUTS models the transport of five different radionuclide species (^{241}Am , ^{239}Pu ,
 11 ^{238}Pu , ^{234}U , and ^{230}Th). These radionuclides represent a larger number of radionuclides: as
 12 discussed in Section PA-4.3.3, radionuclides were grouped together based on similarities, such as
 13 isotopes of the same element and those with similar half-lives, to simplify the calculations. For
 14 transport purposes, solubilities are lumped to represent both dissolved and colloidal forms.
 15 These groupings simplify and expedite calculations.

16 **PA-4.3.6 Numerical Solution**

17 Equation (PA.95) and Equation (PA.96) are numerically solved by the NUTS program (WIPP
 18 Performance Assessment 1997a) on the same computational grid (Figure PA-15) used by
 19 BRAGFLO for the solution of Equation (PA.24), Equation (PA.25), Equation (PA.26), Equation
 20 (PA.27), Equation (PA.28), Equation (PA.29), and Equation (PA.30). In the solution procedure,
 21 Equation (PA.95) and Equation (PA.96) are numerically solved with $S_l = 0$ for each time step,
 22 with the instantaneous updating of concentrations indicated in Equation (PA.97) and the
 23 appropriate modification to C_{sl} in Equation (PA.96) taking place after the time step. The
 24 solution is carried out for the five radionuclides indicated in Equation (PA.113).

25 The initial value and boundary value conditions used with Equation (PA.95) and Equation
 26 (PA.96) are given in Table PA-14. At time $t = 0$ (corresponding to the year 2033), the total
 27 inventory of each radionuclide is assumed to be in brine; the solubility constraints associated
 28 with Equation (PA.97) then immediately adjust the values for $C_{bl}(x, y, t)$ and $C_{sl}(x, y, t)$ for
 29 consistency with the constraints imposed by $S_T(\text{Br}, \text{Ox}, \text{El})$ and available radionuclide inventory.

30 The n_R PDEs in Equation (PA.95) and Equation (PA.96) are discretized in two dimensions and
 31 then developed into a linear system of algebraic equations for numerical implementation. The
 32 following conventions are used in the representation of each discretized equation:

- 33 • The subscript b is dropped from C_{bl} , so that the unknown function is represented by C_l .
- 34 • A superscript n denotes time t_n , with the assumption that the solution C_l is known at time
 35 t_n and is to be propagated to time t_{n+1} .
- 36 • The grid indices are i in the x-direction and j in the y-direction, and are the same as the
 37 BRAGFLO grid indices.

1 **Table PA-14. Initial and Boundary Conditions for $C_{bl}(x, y, t)$ and $C_{sl}(x, y, t)$**

Initial Conditions for $C_{bl}(x, y, t)$ and $C_{sl}(x, y, t)$	
$C_{bl}(x, y, t)$	$= A_l(0)/V_b(0)$ if (x, y) is a point in the repository (i.e., areas Waste Panel, South RoR and North RoR, in Figure PA-15), where $A_l(0)$ is the amount (kg) of radionuclide l present at time $t = 0$ (Table PA-13) and $V_b(0)$ is the amount (m^3) of brine in repository at time $t = 0$ (from solution of Equation (PA.24) through Equation (PA.30) with BRAGFLO) for all (x, y) . $= 0$ otherwise.
$C_{sl}(x, y, t)$	$= 0$ if (x, y) is a point in the repository.
Boundary Conditions for $C_{bl}(x, y, t)$	
$f_l(B, t)$	$= \int_B \mathbf{v}_b(x, y, t) C_{bl}(x, y, t) \alpha(x, y) \cdot \mathbf{n}(x, y) ds$, where B is any subset of the outer boundary of the computational grid in Figure PA-15, $f_l(B, t)$ is the flux (kg/s) at time t of radionuclide l across B , $\mathbf{v}_b(x, y, t)$ is the Darcy velocity ($m^3/m^2/s$) of brine at (x, y) on B and is obtained from the solution of Equation (PA.24) through Equation (PA.30) by BRAGFLO, $\mathbf{n}(x, y)$ denotes an outward-pointing unit normal vector, and $\int_B ds$ denotes a line integral along B .

- 2
- 3
- Fractional indices refer to quantities evaluated at grid block interfaces.
 - Each time step by NUTS is equal to 20 BRAGFLO time steps because BRAGFLO stores results (here, v_b , ϕ , and S_b) every 20 time steps.

6 The following finite-difference discretization is used for the l^{th} equation in each grid block (i, j) :

$$q_{b,i+1/2,j}^{n+1} C_{l,i+1/2,j}^{n+1} - q_{b,i-1/2,j}^{n+1} C_{l,i-1/2,j}^{n+1} + q_{b,i,j+1/2}^{n+1} C_{l,i,j+1/2}^{n+1} - q_{b,i,j-1/2}^{n+1} C_{l,i,j-1/2}^{n+1} =$$

7

$$\frac{V_{R,i,j}}{\Delta t} \left[\left\{ \phi_{i,j} S_{b,i,j} C_{l,i,j} \right\}^{n+1} - \left\{ \phi_{i,j} S_{b,i,j} C_{l,i,j} \right\}^n \right] \tag{PA.114}$$

$$+ V_{R,i,j} \left\{ \phi_{i,j} S_{b,i,j} C_{l,i,j} \right\}^{n+1} \lambda_l - V_{R,i,j} \left(\phi_{i,j} S_{b,i,j} \right)^{n+1} \sum_{p \in P(l)} C_{p,i,j}^{n+1} \lambda_p$$

8 where q_b is the grid block interfacial brine flow rate (m^3/s) and V_R is the grid block volume (m^3).
 9 The quantity q_b is based on v_b and α in Equation (PA.95) and Equation (PA.96), and the
 10 quantity V_R is based on grid block dimensions (Figure PA-15) and α .

11 The interfacial values of concentration in Equation (PA.114) are discretized using the one-point
 12 upstream weighting method (Aziz and Settari 1979), which results in

$$\begin{aligned}
 & q_{b,i+1/2,j}^{n+1} \left(\omega_{i+1} C_{l,i,j}^{n+1} + (1 - \omega_{i+1}) C_{l,i+1,j}^{n+1} \right) - q_{b,i-1/2,j}^{n+1} \left(\omega_i C_{l,i-1,j}^{n+1} + (1 - \omega_i) C_{l,i,j}^{n+1} \right) \\
 & + q_{b,i,j+1/2}^{n+1} \left(\omega_{j+1} C_{l,i,j}^{n+1} + (1 - \omega_{j+1}) C_{l,i,j+1}^{n+1} \right) - q_{b,i,j-1/2}^{n+1} \left(\omega_j C_{b,i,j-1}^{n+1} + (1 - \omega_j) C_{l,i,j}^{n+1} \right) = \\
 & \frac{V_{R,i,j}}{\Delta t} \left[\left\{ \phi_{i,j} S_{b,i,j} C_{l,i,j} \right\}^{n+1} - \left\{ \phi_{i,j} S_{b,i,j} C_{l,i,j} \right\}^n \right] + V_{R,i,j} \left\{ \phi_{i,j} S_{b,i,j} C_{l,i,j} \right\}^{n+1} \lambda_l \\
 & - V_{R,i,j} \left(\phi_{i,j} S_{b,i,j} \right)^{n+1} \sum_{p \in P(l)} C_{p,i,j}^{n+1} \lambda_p
 \end{aligned} \tag{PA.115}$$

1

2 where ω derives from the upstream weighting for flow between adjacent grid blocks and is
3 defined by

4

$$\omega_i = \begin{cases} 1 & \text{if flow is from grid block } (i-1, j) \text{ to grid block } (i, j) \\ 0 & \text{otherwise} \end{cases}$$

5

$$\omega_j = \begin{cases} 1 & \text{if flow is from grid block } (i, j-1) \text{ to grid block } (i, j) \\ 0 & \text{otherwise} \end{cases}$$

6 By collecting similar terms, Equation (PA.115) can be represented by the linear equation

7

$$AC_{l,i,j-1}^{n+1} + BC_{l,i-1,j}^{n+1} + DC_{l,i,j}^{n+1} + EC_{l,i+1,j}^{n+1} + FC_{l,i,j+1}^{n+1} = R_{l,i,j} \tag{PA.116}$$

8 where

9

$$\begin{aligned}
 A &= -\omega_j q_{b,i,j-1/2}^{n+1} & B &= -\omega_j q_{b,i-1/2,j}^{n+1} \\
 E &= (1 - \omega_{i+1}) q_{b,i+1/2,j}^{n+1} & F &= (1 - \omega_{j+1}) q_{b,i,j+1/2}^{n+1}
 \end{aligned}$$

10

$$\begin{aligned}
 D &= -(1 - \omega_j) q_{b,i,j-1/2}^{n+1} - (1 - \omega_i) q_{b,i-1/2,j}^{n+1} + \omega_{j+1} q_{b,i,j+1/2}^{n+1} + \omega_{i+1} q_{b,i+1/2,j}^{n+1} \\
 & - \left(\frac{V_{R,i,j}}{\Delta t} - V_{R,i,j} \lambda_l \right) \left\{ \phi_{i,j} S_{b,i,j} \right\}^{n+1}
 \end{aligned}$$

11

$$R_{l,i,j} = -\frac{V_{R,i,j}}{\Delta t} \left\{ \phi_{i,j} S_{b,i,j} C_{l,i,j} \right\}^n - V_{R,i,j} \left(\phi_{i,j} S_{b,i,j} \right)^{n+1} \sum_{p \in P(l)} C_{p,i,j}^{n+1} \lambda_p$$

12 Given the form of Equation (PA.116), the solution of Equation (PA.95) and Equation (PA.96)
13 has now been reduced to the solution of $n_R \times n_G$ linear algebraic equations in $n_R \times n_G$ unknowns,
14 where n_R is the number of equations for each grid block (i.e., the number of radionuclides) and
15 n_G is the number of grid blocks into which the spatial domain is discretized (Figure PA-15).

16 The system of PDEs in Equation (PA.95) and Equation (PA.96) is strongly coupled because of
17 the contribution from parental decay to the equation governing the immediate daughter.

1 Consequently, a sequential method is used to solve for the radionuclide concentrations by
 2 starting at the top of a decay chain and working down from parent to daughter. This implies that
 3 when solving Equation (PA.116) for the l^{th} isotope concentration, all parent concentrations
 4 occurring in the right-hand-side term R are known. The system of equations is then linear in the
 5 concentrations of the l^{th} isotope. As a result, solving Equation (PA.95) and Equation (PA.96) is
 6 reduced from the solution of one algebraic equation at each time step with $n_R \times n_G$ unknowns to
 7 the solution of n_R algebraic equations each with n_G unknowns at each time step, which can result
 8 in a significant computational savings.

9 The matrix resulting from one-point upstream weighting has the following structural form for a
 10 3×3 system of grid blocks, and a similar structure for a larger number of grid blocks:

	1	2	3	4	5	6	7	8	9
1	X	X	0	X					
2	X	X	X	0	X				
3	0	X	X	0	0	X			
4	X	0	0	X	X	0	X		
5		X	0	X	X	X	0	X	
6			X	0	X	X	0	0	X
7				X	0	0	X	X	0
8					X	0	X	X	X
9						X	0	X	X

11
 12 where X designates possible nonzero matrix entries, and 0 designates zero entries within the
 13 banded structure. All entries outside of the banded structure are zero. Because of this structure, a
 14 banded direct elimination solver (Aziz and Settari 1979, Section 8.2.1) is used to solve the linear
 15 system for each radionuclide. The bandwidth is minimized by first indexing equations in the
 16 coordinate direction with the minimum number of grid blocks. The coefficient matrix is stored
 17 in this banded structure, and all infill coefficients calculated during the elimination procedure are
 18 contained within the band structure. Therefore, for the matrix system in two dimensions, a
 19 pentadiagonal matrix of dimension $I_{BW} \times n_G$ is inverted instead of a full $n_G \times n_G$ matrix, where
 20 I_{BW} is the bandwidth.

21 The numerical implementation of Equation (PA.96) enters the solution process through updates
 22 to the radionuclide concentrations in Equation (PA.115) between each time step, as indicated in
 23 Equation (PA.97). The numerical solution of Equation (PA.95) and Equation (PA.96) also
 24 generates the concentrations required to integrate numerically evaluating the integral that defines
 25 $C_l(t, B)$ in Equation (PA.101).

26 **PA-4.3.7 Additional Information**

27 Additional information on NUTS and its use in WIPP PA can be found in the NUTS users
 28 manual (WIPP Performance Assessment 1997a) and in the analysis package of Salado transport

1 calculations for the CRA-2009 PA (Ismail and Garner 2008). Furthermore, additional
 2 information on dissolved and colloidal actinides is given in Appendix SOTERM-2009.

3 **PA-4.4 Radionuclide Transport in the Salado: PANEL**

4 This section describes the model used to compute radionuclide transport in the Salado for the
 5 E1E2 scenario. The model for transport in E0, E1, and E2 scenarios is described in Section PA-
 6 4.3.

7 **PA-4.4.1 Mathematical Description**

8 A relatively simple mixed-cell model is used for radionuclide transport in the vicinity of the
 9 repository after an E1E2 intrusion, when connecting flow between two drilling intrusions into the
 10 same waste panel is assumed to take place. With this model, the amount of radionuclide l
 11 contained in a waste panel is represented by

12
$$\frac{dA_l}{dt} = -r_b C_{bl} - \lambda_l A_l + \sum_{p \in P(l)} \lambda_p A_p \quad (\text{PA.117})$$

13 where

14 $A_l(t)$ = amount (mol) of radionuclide l in waste panel at time t

15 $C_{bl}(t)$ = concentration (mol/m³) of radionuclide l in brine in waste panel at time t (Equation
 16 (PA.118) and Equation (PA.119))

17 $r_b(t)$ = rate (m³/s) at which brine flows out of the repository at time t (supplied by
 18 BRAGFLO from solution of Equation (PA.93))

19 and λ_l and $P(l)$ are defined in conjunction with Equation (PA.95) and Equation (PA.96).

20 The brine concentration C_{bl} in Equation (PA.117) is defined by

21
$$C_{bl}(t) = S_T [Br, Ox, El] MF_l(t) \quad \text{if } S_T [Br(t), Ox, El] \leq \sum_{k \in El(l)} A_k(t) / V_b(t) \quad (\text{PA.118})$$

22
$$= A_l(t) / V_b(t) \quad \text{if } \sum_{k \in El(l)} A_k(t) / V_b(t) < S_T [Br, Ox, El] \quad (\text{PA.119})$$

23 where

24 $MF_l(t)$ = mole fraction of radionuclide l in waste panel at time t

$$1 \qquad \qquad \qquad = \frac{A_l(t)}{\sum_{k \in El(l)} A_k(t)} \qquad \qquad \qquad (PA.120)$$

2 $V_b(t)$ = volume (m³) of brine in waste panel at time t (supplied by BRAGFLO from
 3 solution of Equation (PA.24), Equation (PA.25), Equation (PA.26), Equation
 4 (PA.27), Equation (PA.28), Equation (PA.29), and Equation (PA.30))

5 and $S_T[Br, Ox, El]$ is supplied by Equation (PA.102).

6 For Equation (PA.118) and Equation (PA.119), $S_T[Br, Ox, El]$ must be expressed in units of
 7 mol/L. In other words, $C_{bl}(t)$ is defined to be the maximum concentration (S_T in Equation
 8 (PA.102)) if there is sufficient radionuclide inventory in the waste panel to generate this
 9 concentration (Equation (PA.118)); otherwise, $C_{bl}(t)$ is defined by the concentration that results
 10 when all the relevant element in the waste panel is placed in solution (Equation (PA.119)). The
 11 dissolved and colloidal An equilibrate instantly for each element.

12 Given r_b and C_{bl} , evaluation of the integral

$$13 \qquad \qquad \qquad R_l(t) = \int_0^t C_{bl}(\tau) r_b(\tau) d\tau \qquad \qquad \qquad (PA.121)$$

14 provides the cumulative release $R_l(t)$ of radionuclide l from the waste panel through time t .

15 **PA-4.4.2 Numerical Solution**

16 Equation (PA.117) is numerically evaluated by the PANEL model (WIPP Performance
 17 Assessment 1998b) using a discretization based on time steps of 50 years or less. Specifically,
 18 Equation (PA.117) is evaluated with the approximation

$$19 \qquad \qquad \qquad A_l(t_{n+1}) = A_l(t_n) - \left[\int_{t_n}^{t_{n+1}} r_b(\tau) d\tau \right] C_{bl}(t_n) - A_l(t_n) \exp(-\lambda_l \Delta t) + G_l(t_n, t_{n+1})$$

20 (PA.122)

21 where

22 $G_l(t_n, t_{n+1})$ = gain in radionuclide l due to the decay of precursor radionuclides between t_n

23 and t_{n+1} (see Equation (PA.123)), $\Delta t = t_{n+1} - t_n = 50 \text{ yr}$.

24 As the solution progresses, values for $C_{bl}(t_n)$ are updated in consistency with Equation (PA.118)
 25 and Equation (PA.119), and the products $r_b(t_n)C_{bl}(t_n)$ are accumulated to provide an
 26 approximation to R_l in Equation (PA.121).

1 The term $G_l(t_n, t_{n+1})$ in Equation (PA.122) is evaluated with the Bateman equations (Bateman
 2 1910), with PANEL programmed to handle decay chains of up to five (four decay daughters for
 3 a given radionuclide). As a single example, if radionuclide l is the third radionuclide in a decay
 4 chain (i.e., $l = 3$) and the two preceding radionuclides in the decay chain are designated by $l = 1$
 5 and $l = 2$, then

$$G_3(t_n, t_{n+1}) = \frac{\lambda_2 A_2(t_n)}{(\lambda_3 - \lambda_2)} [\exp(-\lambda_2 \Delta t) - \exp(-\lambda_3 \Delta t)]$$

$$+ \lambda_1 \lambda_2 A_1(t_n) \left\{ \frac{\exp(-\lambda_1 \Delta t)}{(\lambda_2 - \lambda_1)(\lambda_3 - \lambda_1)} + \frac{\exp(-\lambda_2 \Delta t)}{(\lambda_3 - \lambda_2)(\lambda_1 - \lambda_2)} + \frac{\exp(-\lambda_3 \Delta t)}{(\lambda_1 - \lambda_3)(\lambda_2 - \lambda_3)} \right\} \quad (\text{PA.123})$$

7 in Equation (PA.122).

8 **PA-4.4.3 Implementation in PA**

9 The preceding model is used in two ways in PA. First, Equation (PA.121) estimates releases to
 10 the Culebra associated with E1E2 intrusion scenarios (see Section PA-6.7.3). Second, the
 11 radionuclide concentrations are computed using the minimum brine volume for a significant
 12 release to estimate DBRs (see Section PA-6.8.2.3). The calculation of the minimum brine
 13 volume used in the CRA-2009 PA is found in Stein (2005). The calculated concentrations are the
 14 S_l term indicated in Equation (PA.97) which are used in the NUTS calculations discussed in
 15 Section PA-4.3.

16 For E1E2 intrusions, the initial amount A_l of radionuclide l is the inventory of the decayed
 17 isotope at the time of the E1 intrusion. PANEL calculates the inventory of each of the 29
 18 radioisotopes throughout the regulatory period. The initial concentration C_{bl} of radionuclide l is
 19 computed by Equation (PA.117), Equation (PA.118), and Equation (PA.119). For the DBR
 20 calculations, the initial amount A_l of radionuclide l is the inventory of the isotope at the time of
 21 repository closure.

22 **PA-4.4.4 Additional Information**

23 Additional information on PANEL and its use in the CRA-2009 PA calculations can be found in
 24 the PANEL user's manual (WIPP Performance Assessment 2003b), the analysis package for
 25 PANEL calculations (Garner and Leigh 2005), and the analysis package for Salado transport
 26 calculations in the CRA-2009 PA (Ismail and Garner 2008).

27 **PA-4.5 Cuttings and Cavings to Surface: CUTTINGS_S**

28 Cuttings are waste solids contained in the cylindrical volume created by the cutting action of the
 29 drill bit passing through the waste, while cavings are additional waste solids eroded from the
 30 borehole by the upward-flowing drilling fluid within the borehole. The releases associated with
 31 these processes are computed within the CUTTINGS_S code (WIPP Performance Assessment
 32 2003c). The mathematical representations used for cuttings and cavings are described in this
 33 section.

1 **PA-4.5.1 Cuttings**

2 The uncompacted volume of cuttings removed and transported to the surface in the drilling fluid,
3 V_{cut} , is given by

$$4 \quad V_{cut} = AH_i = \pi D^2 H_i / 4 \quad (\text{PA.124})$$

5 where A is the drill bit area (m^2), H_i is the initial (or uncompacted) repository height (3.96 m),
6 and D is the drill-bit diameter (0.31115 m) (Fox 2008, Table 13). For drilling intrusions through
7 RH-TRU waste, $H_i = 0.509$ m is used (Fox 2008, Table 45).

8 **PA-4.5.2 Cavings**

9 The cavings component of the direct surface release is caused by the shearing action of the
10 drilling fluid on the waste as it flows up the borehole annulus. Like the cuttings release, the
11 cavings release is assumed to be independent of the conditions that exist in the repository during
12 a drilling intrusion.

13 The final diameter of the borehole depends on the diameter of the drillbit and on the extent to
14 which the actual borehole diameter exceeds the drill-bit diameter. Although a number of factors
15 affect erosion within a borehole (Chambre Syndicale de la Recherche et de la Production du
16 Petrole et du Gaz Naturel 1982), the most important is the fluid shear stress on the borehole wall
17 (i.e., the shearing force per unit area, N/m^2) resulting from circulating drilling fluids (Darley
18 1969, Walker and Holman 1971). As a result, PA estimates cavings removal with a model based
19 on the effect of shear stress on the borehole diameter. In particular, the borehole diameter is
20 assumed to grow until the shear stress on the borehole wall is equal to the shear strength of the
21 waste, which is the limit below which waste erosion ceases.

22 The final eroded diameter D_f (m) of the borehole through the waste determines the total volume
23 V (m^3) of uncompacted waste removed to the surface by circulating drilling fluid. Specifically,

$$24 \quad V = V_{cut} + V_{cav} = \pi D_f^2 H_i / 4 \quad (\text{PA.125})$$

25 where V_{cav} is the volume (m^3) of waste removed as cavings.

26 Most borehole erosion is believed to occur in the vicinity of the drill collar (Figure PA-22)
27 because of decreased flow area and consequent increased mud velocity (Rechard, Iuzzolino, and
28 Sandha 1990, Letters 1a and 1b, App. A). An important determinant of the extent of this erosion
29 is whether the flow of the drilling fluid in the vicinity of the collar is laminar or turbulent. PA
30 uses Reynolds numbers to distinguish between the occurrence of laminar flow and turbulent
31 flow. The Reynolds number is the ratio between inertial and viscous (or shear) forces in a fluid,
32 and can be expressed as (Fox and McDonald 1985)

$$33 \quad \text{Re} = \frac{\rho_f D_e v}{\eta} \quad (\text{PA.126})$$

1 where Re is the Reynolds number (dimensionless), ρ_f is the fluid density (kg/m^3), D_e is the
 2 equivalent diameter (m), $v = \|\mathbf{v}\|$ is the fluid speed (m s^{-1}), and η is the fluid viscosity (kg m^{-1}
 3 s^{-1}).

4 Typically, ρ_f , v , and η are averages over a control volume with an equivalent diameter of D_e ,
 5 where $\rho_f = 1.21 \times 10^3 \text{ kg/m}^3$ (Fox 2008, Table 13), $v = 0.7089 \text{ m s}^{-1}$ (based on 40 gal/min/in of
 6 drill diameter) (Berglund 1992), and $D_e = 2(R - R_i)$, as shown in Figure PA-22. The diameter of
 7 the drill collar (i.e., $2R_i$ in Figure PA-22) is 8.0 in = 0.2032 m (Ismail 2008). The determination
 8 of η is discussed below. PA assumes that Reynolds numbers less than 2100 are associated with
 9 laminar flow, while Reynolds numbers greater than 2100 are associated with turbulent flow
 10 (Walker 1976).

11 Drilling fluids are modeled as non-Newtonian, which means that the viscosity η is a function of
 12 the shear rate within the fluid (i.e., the rate at which the fluid velocity changes normal to the flow
 13 direction, m/s/m). PA uses a model proposed by Oldroyd (1958) to estimate the viscosity of
 14 drilling fluids. As discussed in the *Drilling Mud and Cement Slurry Rheology Manual* (Chambre
 15 Syndicale de la Recherche et de la Production du Petrole et du Gaz Naturel 1982), the Oldroyd
 16 model leads to the following expression for the Reynolds number associated with the helical
 17 flow of a drilling fluid within an annulus:

$$18 \quad Re = \frac{0.8165 \rho_f D_e v}{\eta_\infty} \quad (\text{PA.127})$$

19 where ρ_f , D_e , and v are defined as in Equation (PA.126), and η_∞ is the asymptotic value for the
 20 derivative of the shear stress (τ , $\text{kg m}^{-1} \text{ s}^{-2}$) with respect to the shear rate (Γ , s^{-1}) obtained as
 21 the shear rate increases (i.e., $\eta_\infty = d\tau / d\Gamma$ as $\Gamma \rightarrow \infty$). PA uses Equation (PA.127) to determine
 22 whether drilling fluids in the area of the drill collar are undergoing laminar or turbulent flow.

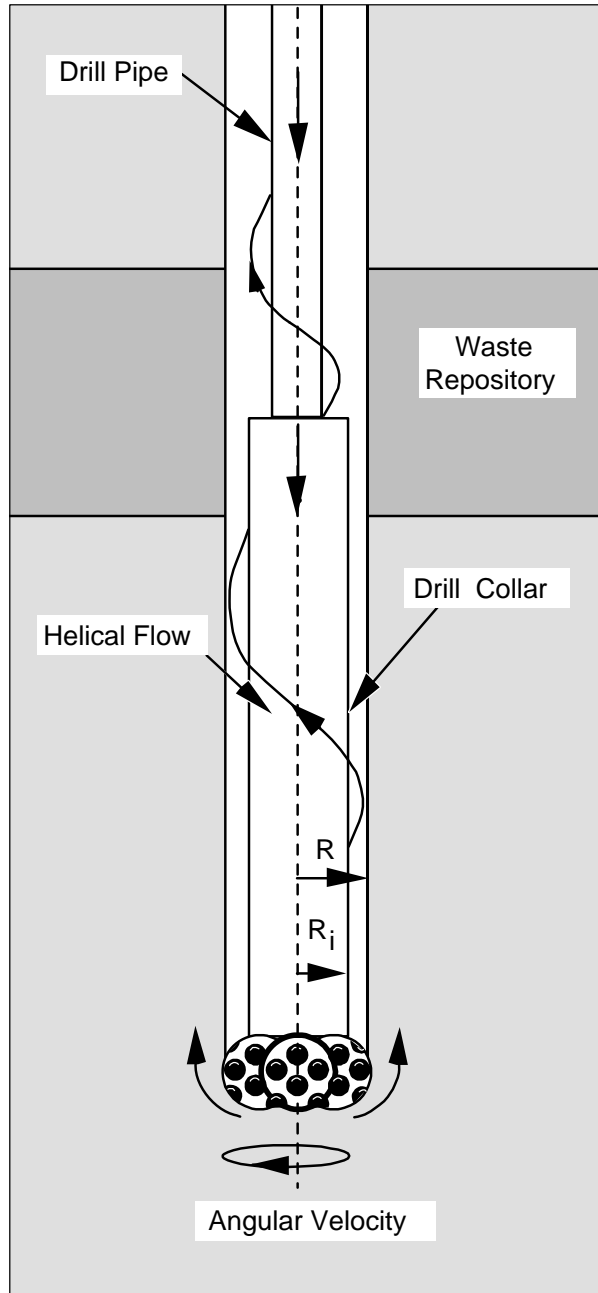
23 The Oldroyd model assumes that the shear stress τ is related to the shear rate Γ through the
 24 relationship

$$25 \quad \tau = \eta_0 \left(\frac{1 + \sigma_2 \Gamma^2}{1 + \sigma_1 \Gamma^2} \right) \Gamma \quad (\text{PA.128})$$

26 where η_0 is the asymptotic value of the viscosity ($\text{kg m}^{-1} \text{ s}^{-1}$) that results as the shear rate Γ
 27 approaches zero, and σ_1 and σ_2 are constants (s^2). The expression leads to

$$28 \quad \eta_\infty = \eta_0 \left(\frac{\sigma_2}{\sigma_1} \right) \quad (\text{PA.129})$$

29 PA uses values of $\eta_0 = 1.834 \times 10^{-2} \text{ kg m}^{-1} \text{ s}^{-1}$, $\sigma_1 = 1.082 \times 10^{-6} \text{ s}^2$, and $\sigma_2 = 5.410 \times 10^{-7} \text{ s}^2$
 30 (Berglund 1996), from which viscosity in the limit of infinite shear rate is found to be $\eta_\infty =$



1
2

Figure PA-22. Detail of Rotary Drill String Adjacent to Drill Bit

3 $9.17 \times 10^{-3} \text{ kg m}^{-1} \text{ s}^{-1}$. The quantity η_{∞} is comparable to the plastic viscosity of the fluid
4 (Chambre Syndicale de la Recherche et de la Production du Petrole et du Gaz Naturel 1982).

5 As previously indicated, different models are used to determine the eroded diameter D_f of a
6 borehole depending on whether flow in the vicinity of the drill collar is laminar or turbulent. The
7 model for borehole erosion in the presence of laminar flow is described next, and then the model
8 for borehole erosion in the presence of turbulent flow is described.

1 PA-4.5.2.1 Laminar Flow Model

2 As shown by Savins and Wallick (1966), the shear stresses associated with the laminar helical
3 flow of a non-Newtonian fluid, as a function of the normalized radius, r , can be expressed as

$$4 \quad \tau(R, r) = \sqrt{\left(\frac{C}{r^2}\right)^2 + \left[\frac{RJ}{2r}(r^2 - \lambda^2)\right]^2} \quad (\text{PA.130})$$

5 for $R_i/R \leq r \leq 1$, where R_i and R are the inner and outer radii within which the flow occurs, as
6 indicated in Figure PA-22; $\tau(R, \rho)$ is the shear stress ($\text{kg m}^{-1} \text{s}^{-2}$) at a radial distance ΔR beyond
7 the inner boundary (i.e., at $r = (R_i + \Delta R)/R$); and the variables C , J , and λ depend on R and
8 satisfy conditions Equation (PA.132) through Equation (PA.134) indicated below. The shear
9 stress at the outer radius R is given by

$$10 \quad \tau(R, 1) = \sqrt{C^2 + \left[\frac{RJ}{2}(1 - \lambda^2)\right]^2} \quad (\text{PA.131})$$

11 As previously indicated, the borehole radius R is assumed to increase as a result of erosional
12 processes until a value of R is reached at which $\tau(R, 1)$ is equal to the shear strength of the
13 waste. In PA, the shear strength of the waste is treated as an uncertain parameter (see
14 WTAUFAIL in Table PA-19). Computationally, determining the eroded borehole diameter R
15 associated with a particular value of the waste shear strength requires repeated evaluation of
16 $\tau(R, 1)$, as indicated in Equation (PA.131), until a value of R is determined for which $\tau(R, 1)$
17 equals the shear strength.

18 The quantities C , J , and λ must satisfy the following three conditions (Savins and Wallick 1966)
19 for Equation (PA.131) to be valid:

$$20 \quad \int_{R_i/R}^1 \left(\frac{x^2 - \lambda^2}{\eta x}\right) dx = 0 \quad (\text{PA.132})$$

$$21 \quad C \int_{R_i/R}^1 \frac{dx}{\eta x^3} = \Delta\Omega \quad (\text{PA.133})$$

$$22 \quad J \int_{R_i/R}^1 \left(\frac{(R_i/R)^2 - x^2}{\eta x}\right) \left(\frac{x^2 - \lambda^2}{\eta x}\right) dx = -\frac{2Q}{\pi R^4} \quad (\text{PA.134})$$

23 where η , the drilling fluid viscosity ($\text{kg m}^{-1} \text{s}^{-1}$), is a function of R and ρ ; $\Delta\Omega$ is the drill string
24 angular velocity (rad s^{-1}); and Q is the drilling fluid flow rate ($\text{m}^3 \text{s}^{-1}$).

1 The viscosity η in Equation (PA.132) through Equation (PA.134) is introduced into the analysis
 2 by assuming that the drilling fluid follows the Oldroyd model for shear stress in Equation
 3 (PA.128). By definition of the viscosity η ,

$$4 \quad \tau = \eta\Gamma \quad (\text{PA.135})$$

5 and from Equation (PA.128)

$$6 \quad \Gamma^2 = \frac{\eta - \eta_0}{\eta_0\sigma_2 - \eta\sigma_1} \quad (\text{PA.136})$$

7 thus the expression in Equation (PA.130) can be reformulated as

$$8 \quad \frac{\eta^2(\eta - \eta_0)^2}{(\eta_0\sigma_2 - \eta\sigma_1)^2} = \left(\frac{C}{r^2}\right)^2 + \left[\frac{RJ}{2r}(r^2 - \lambda^2)\right]^2 \quad (\text{PA.137})$$

9 As discussed by Savins and Wallick (1966) and Berglund (1992), the expressions in Equation
 10 (PA.132) through Equation (PA.134) and Equation (PA.136) can be numerically evaluated to
 11 obtain C , J , and λ for use in Equation (PA.130) and Equation (PA.131). In PA, the drill string
 12 angular velocity $\Delta\Omega$ is treated as an uncertain parameter (see DOMECA in Table PA-19), and

$$13 \quad Q = v(\pi R^2 - \pi R_i^2) \quad (\text{PA.138})$$

14 where $v = 0.7089 \text{ m s}^{-1}$ as used in Equation (PA.126), and η_0 , σ_1 , and σ_2 are defined as in
 15 Equation (PA.128) and Equation (PA.129).

16 PA-4.5.2.2 Turbulent Flow Model

17 The model for borehole erosion in the presence of turbulent flow is now described. Unlike the
 18 theoretically derived relationship for erosion in the presence of laminar flow, the model for
 19 borehole erosion in the presence of turbulent flow is empirical. In particular, pressure loss for
 20 axial flow in an annulus under turbulent flow conditions can be approximated by (Chambre
 21 Syndicale de la Recherche et de la Production du Petrole et du Gaz Naturel 1982)

$$22 \quad \Delta P = \frac{2fL\rho_f v^2}{0.8165D_e} \quad (\text{PA.139})$$

23 where ΔP is the pressure change (Pa), f is the Fanning friction factor (dimensionless), L is the
 24 distance (m) over which pressure change ΔP occurs, and ρ_f , v , and D_e are defined in Equation
 25 (PA.126).

26 For turbulent pipe flow, f is empirically related to the Reynolds number Re defined in Equation
 27 (PA.126) by (Whittaker 1985)

$$\frac{1}{\sqrt{f}} = -4 \log_{10} \left(\frac{\varepsilon}{3.72D} + \frac{1.255}{\text{Re} \sqrt{f}} \right) \quad (\text{PA.140})$$

where D is the inside diameter (m) of the pipe and ε is a “roughness term” equal to the average depth (m) of pipe wall irregularities. In the absence of a similar equation for flow in an annulus, Equation (PA.140) is used in PA to define f for use in Equation (PA.139), with D replaced by the effective diameter $D_e = 2(R - R_i)$ and ε equal to the average depth of irregularities in the waste-borehole interface. In the present analysis, $\varepsilon = 0.025$ m (Fox 2008, Table 34), which exceeds the value often selected in calculations involving very rough concrete or riveted steel piping (Streeter 1958).

The pressure change ΔP in Equation (PA.139) and the corresponding shear stress τ at the walls of the annulus are approximately related by

$$(\Delta P) \pi (R^2 - R_i^2) = 2\pi L \tau (R + R_i) \quad (\text{PA.141})$$

where $\pi(R^2 - R_i^2)$ is the cross-sectional area of the annulus (see Figure PA-22) and $2\pi L(R + R_i)$ is the total surface area of the annulus. Rearranging Equation (PA.139) and using the relationship in Equation (PA.135) yields

$$\tau(R) = \frac{f \rho_f v^2}{2(0.8165)} \quad (\text{PA.142})$$

which was used in the 1991 and 1992 WIPP PAs to define the shear stress at the surface of a borehole of radius R . The radius R enters into Equation (PA.132) through Equation (PA.134) through the use of $D = 2(R - R_i)$ in the definition of f in Equation (PA.140). As with laminar flow, the borehole radius R is assumed to increase until a value of $\tau(R)$ is reached that equals the sample value for the shear strength of the waste (i.e., the uncertain parameter WTAUFAIL in Table PA-19). Computationally, the eroded borehole diameter is determined by solving Equation (PA.142) for R under the assumption that $\tau(R)$ equals the assumed shear strength of the waste.

For the CRA-2004 PA, a slight modification to the definition of τ in Equation (PA.142) was made to account for drill string rotation when fluid flow in the vicinity of the drill collars is turbulent (Abdul Khader and Rao 1974; Bilgen, Boulos, and Akgungor 1973). Specifically, an axial flow velocity correction factor (i.e., a rotation factor), F_r , was introduced into the definition of τ . The correction factor F_r is defined by

$$F_r = v_{2100} / v \quad (\text{PA.143})$$

where v_{2100} is the norm of the flow velocity required for the eroded diameters to be the same for turbulent and laminar flow at a Reynolds number of $\text{Re} = 2100$, and is obtained by solving

1
$$\tau_{fail} = \frac{f\rho_f v_{2100}^2}{2(0.8165)} \quad (\text{PA.144})$$

2 for v_{2100} with D in the definition of f in Equation (PA.140) assigned the final diameter value that
 3 results for laminar flow at a Reynolds number of $Re = 2100$ (that is, the D in $D_e = 2(R - R_i) = D$
 4 $- 2R_i$ obtained from Equation (PA.127) with $Re = 2100$). The modified definition of τ is

5
$$\tau(R) = \frac{f\rho_f (F_r v)^2}{2(0.8165)} \quad (\text{PA.145})$$

6 and results in turbulent and laminar flow with the same eroded diameter at a Reynolds number of
 7 2100, where PA assumes that the transition between turbulent and laminar flow takes place.

8 **PA-4.5.2.3 Calculation of R_f**

9 The following algorithm was used to determine the final eroded radius R_f of a borehole and
 10 incorporates a possible transition from turbulent to laminar fluid flow within a borehole:

11 Step 1. Use Equation (PA.127) to determine an initial Reynolds number Re , with R initially set
 12 to the drill-bit radius, $R_0 = 0.31115$ m (Fox 2008, Table 13).

13 Step 2. If $Re < 2100$, the flow is laminar and the procedure in Section PA-4.5.2.1 is used to
 14 determine R_f . Because any increase in the borehole diameter will cause the Reynolds
 15 number to decrease, the flow will remain laminar and there is no need to consider the
 16 possibility of turbulent flow as the borehole diameter increases, with the result that R_f
 17 determined in this step is the final eroded radius of the borehole.

18 Step 3. If $Re \geq 2100$, then the flow is turbulent, and the procedure discussed in Section PA-
 19 4.5.2.2 is used to determine R_f . Once R_f is determined, the associated Reynolds number
 20 Re is recalculated using Equation (PA.127) and $R = R_f$. If the recalculated $Re > 2100$, a
 21 transition from turbulent to laminar flow cannot take place, and the final eroded radius is
 22 R_f determined in this step. If not, go to Step 4.

23 Step 4. If the Reynolds number Re with the new R_f in Step 3 satisfies the inequality $Re \leq 2100$,
 24 a transition from turbulent to laminar flow is assumed to have taken place. In this case,
 25 R_f is recalculated assuming laminar flow, with the outer borehole radius R initially
 26 defined to be the radius associated with $Re = 2100$. In particular, the initial value for R is
 27 given by the radius at which the transition from laminar to turbulent flow takes place:

28
$$R = R_i + \frac{2100\eta_\infty}{2(0.8165)v\rho} \quad (\text{PA.146})$$

29 which is obtained from Equation (PA.127) by solving for R with $Re = 2100$. A new
 30 value for R_f is then calculated with the procedure discussed in Section PA-4.5.2.1 for

1 laminar flow, with this value of R_f replacing the value from Step 3 as the final eroded
2 diameter of the borehole.

3 Step 5. Once R_f is known, the amount of waste removed to the surface is determined using
4 Equation (PA.125) with $D_f = 2R_f$.

5 **PA-4.5.3 Additional Information**

6 Additional information on CUTTINGS_S and its use in the CRA-2004 PA to determine cuttings
7 and cavings releases can be found in the CUTTINGS_S user's manual (WIPP Performance
8 Assessment 2003c) and in the analysis package for cuttings and cavings releases (Ismail 2008).

9 **PA-4.6 Spallings to Surface: DRSPALL and CUTTINGS_S**

10 Spallings are waste solids introduced into a borehole by the movement of waste-generated gas
11 towards the lower-pressure borehole. In engineering literature, the term "spalling" describes the
12 dynamic fracture of a solid material, such as rock or metal (Antoun et al. 2003). In WIPP PA,
13 the spallings model describes a series of processes, including tensile failure of solid waste,
14 fluidization of failed material, entrainment into the wellbore flow, and transport up the wellbore
15 to the land surface. Spallings releases could occur when pressure differences between the
16 repository and the wellbore cause solid stresses in the waste exceeding the waste material
17 strength and gas velocities sufficient to mobilize failed waste material.

18 The spallings model is described in the following sections. Presented first are the primary
19 modeling assumptions used to build the conceptual model. Next, the mathematical model and its
20 numerical implementation in the computer code DRSPALL are described. Finally,
21 implementation of the spallings model in WIPP PA by means of the code CUTTINGS_S is
22 discussed.

23 **PA-4.6.1 Summary of Assumptions**

24 Assumptions underlying the spallings model include the future state of the waste, specifications
25 of drilling equipment, and the driller's actions at the time of intrusion. Consistent with the other
26 PA models, the spallings model assumes massive degradation of the emplaced waste through
27 mechanical compaction, corrosion, and biodegradation. Waste is modeled as a homogeneous,
28 isotropic, weakly consolidated material with uniform particle size and shape. The rationale for
29 selecting the spallings model material properties is addressed in detail by Hansen et al. (1997)
30 and Hansen, Pfeifle, and Lord (2003).

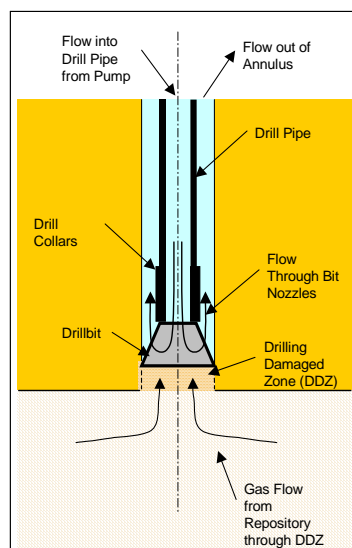
31 Drilling equipment specifications, such as bit diameter and drilling mud density, are based on
32 surveys of drillers in the Delaware Basin (Hansen, Pfeifle, and Lord 2003). Assumptions about
33 the driller's actions during the intrusion are conservative. Typically, the drilling mud density is
34 controlled to maintain a slightly "overbalanced" condition so that the mud pressure is always
35 slightly higher than the fluid pressures in the formation. If the borehole suddenly passes through
36 a high-pressure zone, the well can quickly become "underbalanced," with a resulting fluid
37 pressure gradient driving formation fluids into the wellbore. This situation is known as a *kick*
38 and is of great concern to drillers because a violent kick can lead to a blowout of mud, gas, and

1 oil from the wellbore, leading to equipment damage and worker injury. Standard drilling
 2 practice is to watch diligently for kicks. The first indicator of a kick is typically an increase in
 3 mud return rate, leading to an increase in mud pit volume (Frigaard and Humphries 1997).
 4 Downhole monitors detect whether the kick is air, H₂S, or brine. If the kick fluid is air, the
 5 standard procedure is to stop drilling and continue pumping mud in order to circulate the air
 6 pocket out. If the mud return rate continues to grow after drilling has stopped and the driller
 7 believes that the kick is sufficiently large to cause damage, the well may be shut in by closing the
 8 blowout preventer. Once shut in, the well pressure may be bled off slowly and mud weight
 9 eventually increased and circulated to offset the higher formation pressure before drilling
 10 continues. The spallings model simulates an underbalanced system in which a gas kick is
 11 assured, and the kick proceeds with no intervention from the drill operation. Therefore, drilling
 12 and pumping continue during the entire blowout event.

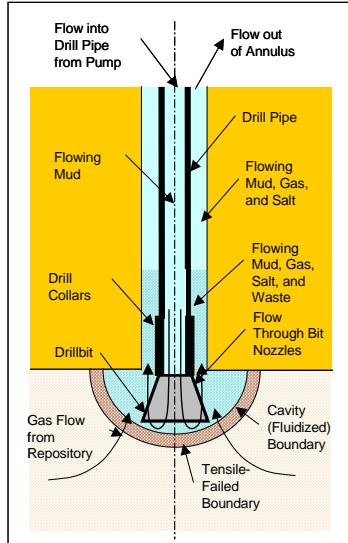
13 PA-4.6.2 Conceptual Model

14 The spallings model calculates transient repository and wellbore fluid flow before, during, and
 15 after a drilling intrusion. To simplify the calculations, both the wellbore and the repository are
 16 modeled by one-dimensional geometries. The wellbore assumes a compressible Newtonian fluid
 17 consisting of a mixture of mud, gas, salt, and waste solids; viscosity of the mixture varies with
 18 the fraction of waste solids in the flow. In the repository, flow is viscous, isothermal,
 19 compressible single-phase (gas) flow in a porous medium.

20 The wellbore and repository flows are coupled by a cylinder of porous media before penetration,
 21 and by a cavity representing the bottom of the borehole after penetration. Schematic diagrams of
 22 the flow geometry prior to and after penetration are shown in Figure PA-23 and Figure PA-24,
 23 respectively. The drill bit moves downward as a function of time, removing salt or waste
 24 material. After penetration, waste solids freed by drilling, tensile failure, and associated
 25 fluidization may enter the wellbore flow stream at the cavity forming the repository-wellbore
 26 boundary.



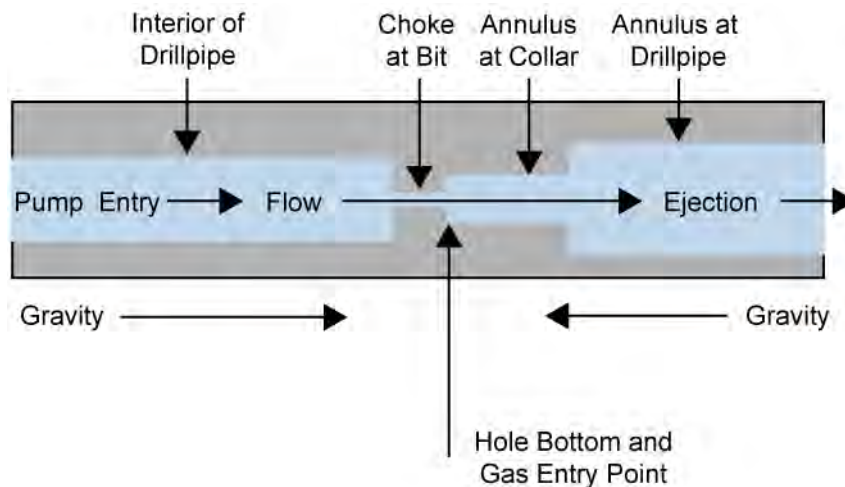
27
 28 **Figure PA-23. Schematic Diagram of the Flow Geometry Prior to Repository Penetration**



1
2 **Figure PA-24. Schematic Diagram of the Flow Geometry After Repository Penetration**

3 **PA-4.6.2.1 Wellbore Flow Model**

4 Flow in the well is modeled as a one-dimensional pipe flow with cross-sectional areas
 5 corresponding to the appropriate flow area at a given position in the well, as shown in Figure
 6 PA-25 and Figure PA-26. This model is conceptually similar to that proposed by Podio and
 7 Yang (1986) for use in the oil and gas industry. Drilling mud is added at the wellbore entrance
 8 by the pump. Flow through the drill bit is treated as a choke with cross-sectional area
 9 appropriate for the bit nozzle area. At the annulus output to the surface, the mixture is ejected at
 10 a constant atmospheric pressure. The gravitational body force acts in its appropriate direction
 11 based on position before or after the bit.



12
13 **Figure PA-25. Effective Wellbore Flow Geometry Before Bit Penetration**

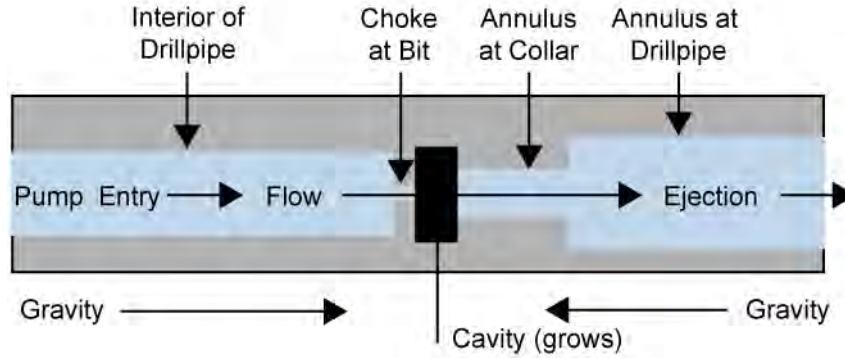


Figure PA-26. Effective Wellbore Flow Geometry After Bit Penetration

Prior to drill bit penetration into the repository, gas from the repository can flow through drilling-damaged salt into the well. After penetration, the cavity at the bottom of the wellbore couples the wellbore flow and the repository flow models; gas and waste material can exit the repository domain into the cavity. The cavity radius increases as waste materials are moved into the wellbore.

The system of equations representing flow in the wellbore consists of four equations for mass conservation, one for each phase (salt, waste, mud, and gas); one equation for conservation of total momentum; two equations relating gas and mud density to pressure; the definition of density for the fluid mixture; and one constraint imposed by the fixed volume of the wellbore. The conservation of mass and momentum is described by

$$\frac{\partial}{\partial t}(\rho_q V_q) + \frac{\partial}{\partial z}(\rho_q V_q u) = S_q \quad (\text{PA.147})$$

$$\frac{\partial}{\partial t}(\rho V u) + \frac{\partial}{\partial z}(\rho V u^2) = -V \left(\frac{\partial P}{\partial z} - \rho g + F \right) + S_{mom} \quad (\text{PA.148})$$

where

- q = phase (w for waste, s for salt, m for mud, and g for gas)
- V_q = volume (m^3) of phase q
- V = total volume (m^3)
- ρ_q = density (kg/m^3) of phase q , constant for salt and waste (2,180 and 2,650 kg/m^3 , respectively) and pressure-dependent for gas and mud (see Equation (PA.149) and Equation (PA.150))
- ρ = density of fluid mixture (kg/m^3) determined by Equation (PA.151)
- u = velocity (m/s) of fluid mixture in wellbore
- t = time (s)
- z = distance (m) from inlet at top of well
- S_q = rate of mass (kg/s) in phase q entering and exiting wellbore domain at position z (Equation (PA.162))

- 1 S_{mom} = rate of momentum (kg m/s²) entering and exiting wellbore domain at position z
 2 (Equation (PA.165))
 3 P = pressure (Pa) at position z
 4 g = standard gravity (9.8067 kg/m/s²)
 5 F = friction loss using pipe flow model (kg/m²/s²) determined by Equation (PA.153)

6 Gas is treated as isothermal and ideal, so the pressure and density are related by Boyle's law:

$$7 \quad \frac{\rho}{\rho_{g,0}} = \frac{P}{P_{atm}} \quad (\text{PA.149})$$

8 where $\rho_{g,0}$ is the density of H₂ gas at atmospheric pressure and 298 K (8.24182×10^{-2} kg/m³).

9 The mud is assumed to be a compressible fluid, so

$$10 \quad \rho_m = \rho_{m,0} [1 + c_m (P - P_{atm})] \quad (\text{PA.150})$$

11 where $\rho_{m,0}$ is the density of the mud at atmospheric pressure (1,210 kg/m³) and c_m is the
 12 compressibility of the mud (3.1×10^{-10} Pa⁻¹).

13 The density of the fluid mixture is determined from the densities and volumes occupied by the
 14 phases:

$$15 \quad \rho = \frac{\rho_g V_g + \rho_m V_m + \rho_s V_s + \rho_w V_w}{V} \quad (\text{PA.151})$$

16 The volume of each phase is constrained by the fixed total volume of the wellbore:

$$17 \quad V = V_g + V_m + V_s + V_w \quad (\text{PA.152})$$

18 The friction loss is a standard formulation for pipe flow (Fox and McDonald 1985), where the
 19 head loss per unit length is given as

$$20 \quad F = \frac{\Delta P}{L} = \frac{f \rho u^2}{2d_h} \quad (\text{PA.153})$$

21 where the hydraulic diameter d_h is given by

$$22 \quad d_h = \frac{4A}{\pi(D_i + D_o)} \quad (\text{PA.154})$$

23 In PA, $D_o = 0.31115$ m throughout the domain. From the bit to the top of the collar, $D_i =$
 24 0.2032 m; above the collar, $D_i = 0.1143$ m. The area A is calculated as the area of the annulus
 25 between the outer and inner radii:

1
$$A = \frac{\pi}{4} (D_o^2 - D_i^2) \quad (\text{PA.155})$$

2 Thus, $d_h = 0.108$ m from the bit to the top of the collar, and $d_h = 0.197$ m above the collar.

3 The Darcy friction factor f in Equation (PA.153) is determined by the method of Colebrook (Fox
4 and MacDonald 1985). In the laminar regime, which is assumed to be characterized by
5 Reynolds numbers below 2100 (Walker 1976),

6
$$f = \frac{64}{\text{Re}} \quad (\text{PA.156})$$

7 and in the turbulent regime ($\text{Re} > 2100$)

8
$$\frac{1}{\sqrt{f}} = -2.0 \log_{10} \left(\frac{\varepsilon}{3.72 d_h} + \frac{2.51}{\text{Re} \sqrt{f}} \right) \quad (\text{PA.157})$$

9 where $\text{Re} = \frac{u \rho d_h}{\eta}$ is the Reynolds number of the mixture, and η is the viscosity calculated in
10 Equation (PA.158), below. As the wellbore mixture becomes particle-laden, the viscosity of the
11 mixture is determined from an empirical relationship developed for proppant slurry flows in
12 channels for the oil and gas industry (Barree and Conway 1995). Viscosity is computed by an
13 approximate slurry formula based on the volume fraction of waste solids:

14
$$\eta = \eta_0 \left(1 - \frac{w}{w_{\max}} \right)^s \quad (\text{PA.158})$$

15 where η_0 is a base mixture viscosity (9.17×10^{-3} Pa s), $w = V_w/V$ is the current volume fraction
16 of waste solids, w_{\max} is an empirically determined maximal volume fraction above which flow is
17 choked (0.615), and s is an empirically determined constant (-1.5) (Hansen, Pfeifle, and Lord
18 2003).

19 **PA-4.6.2.1.1 Wellbore Initial Conditions**

20 Initial conditions in the wellbore approximate mixture flow conditions just prior to waste
21 penetration. The wellbore is assumed to contain only mud and salt. Initial conditions for the
22 pressure, fluid density, volume fractions of mud and salt, and the mixture velocity are set by the
23 following algorithm:

24 Step 1. Set pressure in the wellbore to hydrostatic: $P(z) = P_{\text{atm}} - \rho_m g z$.

25 Step 2. Set mud density using Equation (PA.150).

- 1 Step 3. Set mixture velocity: $u(z) = R_m/A(z)$, where R_m is the volume flow rate of the
 2 pump (0.0202 m³/s), and $A(z)$ is the cross-sectional area of the wellbore.
- 3 Step 4. Set volume of salt in each cell: $V_{s,i} = R_{drill}A_{bit}\Delta z_i/u_i$, where R_{drill} is the rate of
 4 drilling (0.004445 m/s), $A_{bit} = \pi d_{bit}^2 / 4$ is the area of the bottom of the
 5 wellbore, and d_{bit} is the diameter of the bit (0.31115 m).
- 6 Step 5. Set volume fraction of mud in each cell: $V_{m,i} = V_i - V_{s,i}$.
- 7 Step 6. Recalculate mixture density using Equation (PA.151), assuming no waste or gas
 8 in the wellbore.

9 The initial conditions set by this algorithm approximate a solution to the wellbore flow (Equation
 10 (PA.147) and Equation (PA.148)) for constant flow of mud and salt in the well. The
 11 approximation rapidly converges to a solution for wellbore flow if steady-state conditions are
 12 maintained (WIPP Performance Assessment 2003d).

13 PA-4.6.2.1.2 Wellbore Boundary Conditions

14 For simplicity, DRSPALL does not model flow of mud down the pipe to the bit. Mass can enter
 15 the wellbore below the drill bit and exit at the wellbore outlet. Below the bit, mud, salt, gas, and
 16 waste can enter the wellbore. PA assumes a constant volume of mud flow down the drilling
 17 pipe; therefore, the source term for mud, $S_{m,in}$, is set by the volumetric flow rate of the pump R_m
 18 (0.0202 m³/s) and the density of the mud at the bottom of the wellbore:

$$19 \quad S_{m,in} = \rho_m R_m \quad (\text{PA.159})$$

20 Until the drill bit penetrates the repository, salt enters the wellbore at a constant rate:

$$21 \quad S_{s,in} = \rho_s R_{drill} A_{bit} \quad (\text{PA.160})$$

22 Additional mass enters the wellbore by gas flow from the repository ($S_{gas,in}$) and spalling of
 23 waste material ($S_{w,in}$); these mass sources are discussed in Section PA-4.6.2.3. The outlet of the
 24 wellbore is set to atmospheric pressure. Mass exiting the wellbore is determined from the
 25 mixture velocity, the area of the outlet A_{out} (0.066 m²), and the density and volume fraction of
 26 each phase at the outlet of the wellbore:

$$27 \quad S_{q,out} = \rho u_{out} A_{out} \frac{V_q}{V} \quad (\text{PA.161})$$

28 Finally, the net change in mass and momentum for phase q is

$$29 \quad S_q = S_{q,in} - S_{q,out} \quad (\text{PA.162})$$

1
$$S_{mom,in} = \frac{\rho_{0,m}}{A_p} R_{mudpump} \quad (\text{PA.163})$$

2 The outlet of the wellbore is set to atmospheric pressure. Momentum exiting the wellbore is
 3 determined from the fluid velocity and the area of the outlet A_{out} (0.066 m^2):

4
$$S_{mom,out} = -\rho A_{out} u_{out}^2 \quad (\text{PA.164})$$

5 No momentum is added by mass flow into the wellbore from the repository; thus

6
$$S_{mom} = S_{mom,in} - S_{mom,out} \quad (\text{PA.165})$$

7 **PA-4.6.2.2 Repository Flow Model**

8 The repository is modeled as a radially symmetric domain. A spherical coordinate system is
 9 used for this presentation and for most DRSPALL calculations. In a few circumstances,
 10 cylindrical coordinates are used in PA calculations, where spall volumes are large enough that
 11 spherical coordinates are not representative of the physical process (Lord, Rudeen, and Hansen
 12 2003). Cylindrical coordinates are also available; the design document for DRSPALL (WIPP
 13 Performance Assessment 2003e) provides details on implementing the repository flow model in
 14 cylindrical coordinates.

15 Flow in the repository is transient, compressible, viscous, and single-phase (gas) flow in a porous
 16 medium. Gas is treated as isothermal and ideal. The equations governing flow in the repository
 17 are the equation of state for ideal gases (written in the form of Boyle's law for an ideal gas at
 18 constant temperature), conservation of mass, and Darcy's law with the Forchheimer correction
 19 (Aronson 1986, Whitaker 1996):

20
$$\frac{\rho_g}{\rho_{g,0}} = \frac{P}{P_{atm}} \quad (\text{PA.166})$$

21
$$\phi \frac{\partial \rho_g}{\partial t} + \nabla \cdot (\rho_g u) = 0 \quad (\text{PA.167})$$

22
$$\nabla P = -\frac{\eta_g}{k} (1 + F) u \quad (\text{PA.168})$$

23 where

- 24 P = pressure in pore space (Pa)
- 25 ρ_g = density of gas (kg/m^3)
- 26 u = velocity of gas in pore space (m/s)
- 27 ϕ = porosity of the solid (unitless)
- 28 η_g = gas viscosity ($8.934 \times 10^{-6} \text{ Pa s}$)

1 k = permeability of waste solid (m^2)
 2 F = Forchheimer correction (unitless)

3 The Forchheimer correction is included in Equation (PA.168) to account for inertia in the
 4 flowing gas, which becomes important at high gas velocities (Ruth and Ma 1992). When the
 5 Forchheimer coefficient is zero, Equation (PA.168) reduces to Darcy's law. A derivation of
 6 Equation (PA.168) from the Navier-Stokes equations is given by Whitaker (1996); the derivation
 7 suggests that F is a linear function of gas velocity for a wide range of Reynolds numbers.

8 In PA, the Forchheimer correction takes the form

$$9 \quad F = \beta_{nd} \rho u \quad (\text{PA.169})$$

10 where β_{nd} is the non-Darcy coefficient, which depends on material properties such as the
 11 tortuosity and area of internal flow channels, and is empirically determined (Belhaj et al. 2003).
 12 DRSPALL uses a value from Li et al. (2001) that measured high-velocity nitrogen flow through
 13 porous sandstone wafers, giving the result

$$14 \quad \beta_{nd} = \frac{1.15 \times 10^{-6}}{k\phi} \quad (\text{PA.170})$$

15 Equation (PA.166) through Equation (PA.168) combines into a single equation for pressure in
 16 the porous solid:

$$17 \quad \frac{\partial P}{\partial t} = \frac{k'}{2\phi\eta_g} \nabla^2 P^2 + \frac{1}{2\phi\eta_g} \nabla P^2 \cdot \nabla k' \quad (\text{PA.171})$$

18 where

$$19 \quad k' = \frac{k}{1+F} = \frac{k}{1+\beta_{nd}\rho u} \quad (\text{PA.172})$$

20 and the Laplacian operator in a radially symmetric coordinate system is given by

$$21 \quad \nabla^2 = \frac{1}{r^{n-1}} \frac{\partial}{\partial r} \left(r^{n-1} \frac{\partial}{\partial r} \right) \quad (\text{PA.173})$$

22 where $n = 2$ and $n = 3$ for polar and spherical coordinates, respectively.

23 In DRSPALL, the permeability of the waste solid is a subjectively uncertain parameter that is
 24 constant for waste material that has not failed and fluidized. In a region of waste that has failed,
 25 the permeability increases as the waste fluidizes by a factor of $1 + F_f$, where F_f is the fraction of
 26 failed material that has fluidized and is based on the fluidization relaxation time. This
 27 approximately accounts for the material bulking as it fluidizes.

1 Initial pressure in the repository is set to a constant value P_{ff} . A no-flow boundary condition is
 2 imposed at the outer boundary ($r = R$):

$$3 \qquad \qquad \qquad \nabla P(R) = 0 \qquad \qquad \qquad \text{(PA.174)}$$

4 At the inner boundary ($r = r_{cav}$), the pressure is specified as $P(r_{cav},t) = P_{cav}(t)$, where $P_{cav}(t)$ is
 5 defined in the next section. The cavity radius r_{cav} increases as drilling progresses and waste
 6 material fails and moves into the wellbore; calculation of r_{cav} is described in Section PA-
 7 4.6.2.3.3.

8 **PA-4.6.2.3 Wellbore to Repository Coupling**

9 Prior to penetration, a cylinder of altered-permeability salt material with diameter equal to the
 10 drill bit is assumed to connect the bottom of the wellbore to the repository. At the junction of the
 11 repository and this cylinder of salt, a small, artificial cavity is used to determine the boundary
 12 pressure for repository flow. After penetration, the cavity merges with the bottom of the
 13 wellbore to connect the wellbore to the repository.

14 **PA-4.6.2.3.1 Flow Prior to Penetration**

15 The cylinder of salt connecting the wellbore to the repository is referred to as the DDZ in Figure
 16 PA-23. The permeability of the DDZ, k_{DDZ} , is $1 \times 10^{-14} \text{ m}^2$. The spillings model starts with the
 17 bit 0.15 m above the repository; the bit advances at a rate of $R_{drill} = 0.004445 \text{ m/s}$.

18 To couple the repository to the DDZ, the model uses an artificial pseudo-cavity in the small
 19 hemispherical region of the repository below the wellbore with the same surface area as the
 20 bottom of the wellbore (Figure PA-26). The pseudo-cavity is a numerical device that smoothes
 21 the discontinuities in pressure and flow that would otherwise occur upon bit penetration of the
 22 repository. The pseudo-cavity contains only gas, and is initially at repository pressure. The
 23 mass of gas in the cavity m_{cav} is given by

$$24 \qquad \qquad \qquad \frac{dm_{cav}}{dt} = S_{rep} - S_{g,in} \qquad \qquad \qquad \text{(PA.175)}$$

25 where

26 S_{rep} = gas flow from repository into pseudo-cavity (kg/s); see Equation (PA.176)
 27 $S_{g,in}$ = gas flow from pseudo-cavity through DDZ into wellbore (kg/s); see Equation
 28 (PA.177)

29 Flow from the repository into the pseudo-cavity is given by

$$30 \qquad \qquad \qquad S_{rep} = \rho_{g,rep} u_{rep} \phi A_{cav} \qquad \qquad \qquad \text{(PA.176)}$$

31 where

- 1 $\rho_{g,rep}$ = gas density in repository at cavity surface (kg/m³) = $\rho_g(r_{cav})$
 2 u_{rep} = gas velocity (m/s) in repository at cavity surface = $u(r_{cav})$
 3 ϕ = porosity of waste (unitless)
 4 A_{cav} = surface area of hemispherical part of the cavity (m²)
 5 = $\pi d_{bit}^2 / 4$, where d_{bit} is the diameter of the bit (m)

6 Flow out of the pseudo-cavity through the DDZ and into the wellbore is modeled as steady-state
 7 using Darcy's Law:

8
$$S_{g,in} = \frac{k_{DDZ} \pi M_w}{2 \eta_g RTL} \left(\frac{d_{bit}}{2} \right)^2 (P_{cav}^2 - P_{BH}^2) \quad (\text{PA.177})$$

9 where

- 10 η_g = viscosity of H₂ gas (8.934 × 10⁻⁶ Pa s)
 11 M_w = molecular weight of H₂ gas (0.00202 kg / mol)
 12 R = ideal gas constant (8.314 J/mol K)
 13 T = repository temperature (constant at 300 K (27 °C; 80 °F))
 14 L = length (m) of DDZ (from bottom of borehole to top of repository)
 15 P_{cav} = pressure in pseudo-cavity (Pa)
 16 P_{BH} = pressure at bottom of wellbore (Pa)

17 A justification for using this steady-state equation is provided in the design document for
 18 DRSPALL (WIPP Performance Assessment 2003e). The pseudo-cavity is initially filled with
 19 gas at a pressure of P_{ff} . The boundary pressure on the well side (P_{BH}) is the pressure
 20 immediately below the bit, determined by Equation (PA.147) and Equation (PA.148). The
 21 pressure in the pseudo-cavity (P_{cav}) is determined by the ideal gas law:

22
$$P_{cav} = \frac{m_{cav} R_0 T}{V_{cav}} \quad (\text{PA.178})$$

23 where m_{cav} is the number of moles of gas in the cavity and the cavity volume V_{cav} is given by

24
$$V_{cav} = \frac{\pi d_{bit}^3}{24\sqrt{2}} \quad (\text{PA.179})$$

25 In PA, the drilling rate into the ground is assumed constant at 0.004445 m/s; thus $L = L_i -$
 26 $0.004445t$ until $L = 0$, at which time the bit penetrates the waste. The term L_i is the distance from
 27 the bit to the waste at the start of calculation (0.15 m).

1 **PA-4.6.2.3.2 Flow After Penetration**

2 After waste penetration, the bottom of the wellbore is modeled as a hemispherical cavity in the
 3 repository, the radius of which grows as drilling progresses and as material fails and moves into
 4 the cavity. Gas, drilling mud, and waste are assumed to thoroughly mix in this cavity; the
 5 resulting mixture flows around the drill collars and then up the annulus between the wellbore and
 6 the drill string. Gas flow from the repository into the cavity is given by Equation (PA.176);
 7 however, A_{cav} is now dependent on the increasing radius of the cavity (see Section PA-
 8 4.6.2.3.3). Mudflow into the cavity from the wellbore is given by Equation (PA.159). Waste
 9 flow into the cavity is possible if the waste fails and fluidizes; these mechanisms are discussed in
 10 Section PA-4.6.2.3.4 and Section PA-4.6.2.3.5. Pressure in the cavity is equal to that at the
 11 bottom of the wellbore, and is computed by Equation (PA.178).

12 **PA-4.6.2.3.3 Cavity Volume After Penetration**

13 The cylindrical cavity of increasing depth created by drilling is mapped to a hemispherical
 14 volume at the bottom of the wellbore to form the cavity. This mapping maintains equal surface
 15 areas in order to preserve the gas flux from the repository to the wellbore. The cavity radius
 16 from drilling is thus

17
$$r_{drill} = \sqrt{\frac{d_{bit}^2 + 4d_{bit}\Delta H}{8}} \quad (\text{PA.180})$$

18 where ΔH is the depth of the drilled cylinder. In PA, the drilling rate into the ground is assumed
 19 constant at 0.004445 m/s; thus $\Delta H = 0.004445t$ until $\Delta H = H$, the height of compacted waste (m).
 20 Since the initial height of the repository is 3.96 m, H is computed from the porosity ϕ by
 21 $H = 3.96(1 - \phi_0) / (1 - \phi)$, where ϕ_0 is the initial porosity of a waste-filled room.

22 The cavity radius r_{cav} is increased by the radius of failed and fluidized material r_{fluid} , which is
 23 the depth to which fluidization has occurred beyond the drilled radius. That is,

24
$$r_{cav} = r_{drill} + r_{fluid} \quad (\text{PA.181})$$

25 **PA-4.6.2.3.4 Waste Failure**

26 Gas flow from the waste creates a pressure gradient within the waste, which induces elastic
 27 stresses in addition to the far-field confining stress. These stresses may lead to tensile failure of
 28 the waste material, an assumed prerequisite to spallings releases. While the fluid calculations
 29 using Equation (PA.166) through Equation (PA.168) are fully transient, the elastic stress
 30 calculations are assumed to be quasi-static (i.e., sound-speed phenomena in the solid are
 31 ignored). Elastic effective stresses are (Timoshenko and Goodier 1970)

32
$$\sigma_r(r) = \sigma_{sr}(r) + \sigma_{ff} \left(1 - \left(\frac{r_{cav}}{r} \right)^3 \right) + P(r_{cav}) \left(\frac{r_{cav}}{r} \right)^3 - \beta P(r) \quad (\text{PA.182})$$

$$\sigma_{\theta}(r) = \sigma_{s\theta}(r) + \sigma_{ff} \left[1 + \frac{1}{2} \left(\frac{r_{cav}}{r} \right)^2 \right] - \frac{P(r_{cav})}{2} \left(\frac{r_{cav}}{r} \right)^3 - \beta P(r) \quad (\text{PA.183})$$

where β is Biot's constant (assumed here to be 1.0) and σ_{ff} is the confining far-field stress (assumed constant at 14.8 MPa).

The flow-related radial and tangential stresses (σ_{sr} and $\sigma_{s\theta}$, respectively) are computed by equations analogous to differential thermal expansion (Timoshenko and Goodier 1970):

$$\sigma_{sr}(r) = \frac{2\beta}{r^3} \left(\frac{1-2\nu}{1-\nu} \right) \int_{r_{cav}}^r (P(s) - P_{ff}) s^2 ds \quad (\text{PA.184})$$

$$\sigma_{s\theta}(r) = -\beta \left(\frac{1-2\nu}{1-\nu} \right) \left(\frac{1}{r^3} \int_{r_{cav}}^r (P(s) - P_{ff}) s^2 ds - (P(r) - P_{ff}) \right) \quad (\text{PA.185})$$

where P_{ff} is the initial repository pressure and ν is Poisson's ratio (0.38).

Since stresses are calculated as quasi-static, an initial stress reduction caused by an instantaneous pressure drop at the cavity face propagates instantaneously through the waste. The result of calculating Equation (PA.182) can be an instantaneous early-time tensile failure of the entire repository if the boundary pressure is allowed to change suddenly. This is nonphysical and merely a result of the quasi-static stress assumption, combined with the true transient pore pressure and flow-related stress equations. To prevent this nonphysical behavior, tensile failure propagation is limited by a tensile failure velocity (1000 m/s; see Hansen et al. 1997). This limit has no quantitative effect on results, other than to prevent nonphysical tensile failure.

At the cavity face, Equation (PA.182) and Equation (PA.184) evaluate to zero, consistent with the quasi-static stress assumption. This implies that the waste immediately at the cavity face cannot experience tensile failure; however, tensile failure may occur at some distance into the waste material. Consequently, the radial effective stress σ_r is averaged from the cavity boundary into the waste over a characteristic length L_t (0.02 m). If this average radial stress $\bar{\sigma}_r$ is tensile and its magnitude exceeds the material tensile strength ($|\bar{\sigma}_r| > \text{TENSLSTR}$), the waste is no longer capable of supporting radial stress and fails, permitting fluidization. The waste tensile strength is an uncertain parameter in the analysis (see TENSLSTR in Table PA-15).

Equation (PA.183) and Equation (PA.185) evaluate shear stresses in the waste. DRSPALL does not use the waste shear stresses to calculate waste failure for spall releases. These stresses are included in this discussion for completeness.

PA-4.6.2.3.5 Waste Fluidization

Failed waste material is assumed to be disaggregated, but not in motion; it remains as a porous, bedded material lining the cavity face, and is treated as a continuous part of the repository from the perspective of the porous flow calculations. The bedded material may be mobilized and enter the wellbore if the gas velocity in the failed material (see Equation (PA.168)) exceeds a

1 minimum fluidization velocity, U_f . The minimum fluidization velocity is determined by solving
 2 the following quadratic equation (Cherimisinoff and Cherimisinoff 1984, Ergun 1952)

$$3 \quad \frac{1.75 \left(\frac{d_p U_f \rho_g}{\eta_g} \right)^2}{a \phi^3} + 150 \left(\frac{1 - \phi}{a^2 \phi^3} \right) \left(\frac{d_p U_f \rho_g}{\eta_g} \right) = \frac{d_p^3 \rho_g (\rho_w - \rho_g) g}{\eta_g^2} \quad (\text{PA.186})$$

4 where

5 a = particle shape factor (unitless)

6 d_p = particle diameter (m)

7 Fluidization occurs in the failed material to the depth at which gas velocity does not exceed the
 8 fluidization velocity; this depth is denoted by r_{fluid} and is used to determine cavity radius
 9 (Section PA-4.6.2.3.3). If fluidization occurs, the gas and waste particles mix into the cavity at
 10 the bottom of the wellbore. Because this mixing cannot be instantaneous, which would be
 11 nonphysical (much as allowing instantaneous tensile failure propagation would be nonphysical),
 12 a small artificial relaxation time, equal to the cavity radius r_{cav} divided by the superficial gas
 13 velocity $u(r_{cav})$, is imposed upon the mixing phenomenon. The fluidized material is released
 14 into the cavity uniformly over the relaxation time.

15 **PA-4.6.3 Numerical Model**

16 The numerical model implements the conceptual and mathematical models described above
 17 (Section PA-4.6.2). Both the wellbore and the repository domain calculations use time-marching
 18 finite differences. These are part of a single computational loop and therefore use the same time
 19 step. The differencing schemes for the wellbore and repository calculations are similar, but not
 20 identical.

21 **PA-4.6.3.1 Numerical Method—Wellbore**

22 The wellbore is zoned for finite differencing, as illustrated in Figure PA-27, which shows zones,
 23 zone indices, grid boundaries, volumes, and interface areas. The method is Eulerian: zone
 24 boundaries are fixed, and fluid flows across the interfaces by advection. Quantities are zone-
 25 centered and integration is explicit in time.

26 To reduce computation time, an iterative scheme is employed to update the wellbore flow
 27 solution. The finite-difference scheme first solves Equation (PA.147) and Equation (PA.148) for
 28 the mass of each phase in each grid cell and the momentum in each grid cell.

29 The updated solution to Equation (PA.147) and Equation (PA.148) is then used to compute the
 30 volume of each phase, the pressure, and the mixture velocity in each grid cell.

31 All of the materials (mud, salt, gas, and waste) are assumed to move together as a mixture.
 32 Because fluid moves through the cell boundaries, the calculation requires a value for the flow
 33 through each cell boundary during a time step. These values are obtained by averaging the fluid
 34 velocities at the zone centers, given by

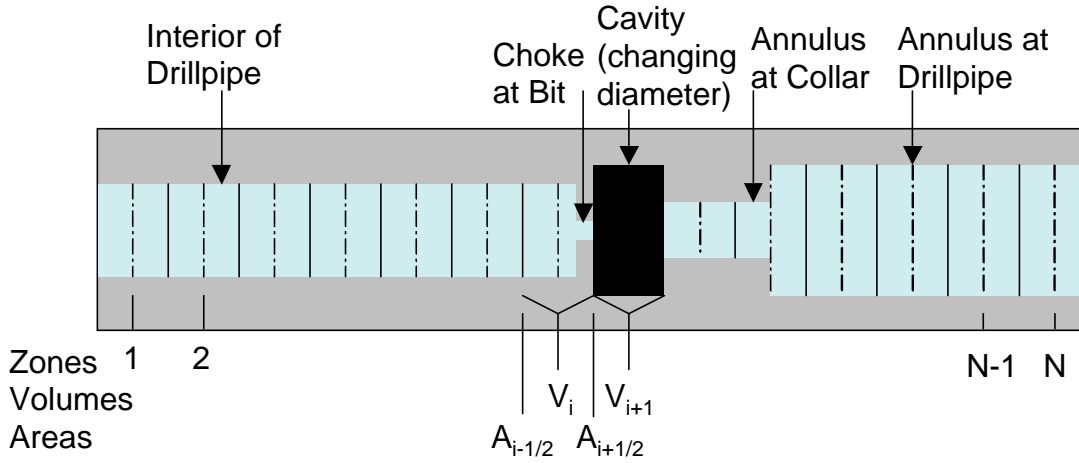


Figure PA-27. Finite-Difference Zoning for Wellbore

$$u_{i+1/2} = \frac{1}{2} (u_{i+1}^{n-1} + u_i^{n-1}) \quad (\text{PA.187})$$

The mass transport equation, prior to any volume change, becomes

$$V_i \rho_i^* = V_i \rho_i^{n-1} - (A_{i+1/2} \rho_{i+1/2}^{n-1} u_{i+1/2} - A_{i-1/2} \rho_{i-1/2}^{n-1} u_{i-1/2}) \Delta t + S_{m,i} \Delta t \quad (\text{PA.188})$$

Here, the source terms $S_{m,i}$ correspond to material entering or exiting at the pump, cavity, and surface. The “upwind” zone-centered densities are used for the interfaces values, $\rho_{i+1/2}^{n-1}$ and $\rho_{i-1/2}^{n-1}$.

Finally, any changed volumes are incorporated and numerical mass diffusion is added for stability:

$$V_i \rho_i^n = V_i \rho_i^* + \Delta z_i s \sum_{q \in \{w, m, s, g\}} \zeta_q D_{i,q} \quad (\text{PA.189})$$

where

$$D_{i,q} = \left[A_{i+1/2} \left((\rho f_q)_{i+1}^{n-1} - (\rho f_q)_i^{n-1} \right) - A_{i-1/2} \left((\rho f_q)_i^{n-1} - (\rho f_q)_{i-1}^{n-1} \right) \right]$$

and ζ_q is the diffusion coefficient for phase q . The density ρf_q for phase q being diffused is calculated from the mixture density, ρ , and the mass fraction, f_q , of phase q in the referenced cell ($f_q = \rho V_{q,i} / \rho V_i$). The numerical diffusion coefficient ζ_q is chosen empirically for stability. Separate diffusion coefficients could be used for the different materials (mud, gas, etc.); however, sufficient stability is obtained by diffusing only mud and salt using the same coefficient ($\zeta_m = \zeta_s = 0.0001$ and $\zeta_w = \zeta_g = 0$).

1 Momentum is differenced as

$$\begin{aligned}
 V_i (\rho u)_i^* &= V_i (\rho u)_i^{n-1} - \Delta t \left(A_{i+1/2} (\rho u)_{i+1/2}^{n-1} u_{i+1/2} - A_{i-1/2} (\rho u)_{i-1/2}^{n-1} u_{i-1/2} \right) \\
 &- V_i \Delta t \left(\frac{P_{i+1}^{n-1} - P_{i-1}^{n-1}}{2\Delta z} - \rho_i^{n-1} g + F_i^{n-1} \right) + S_{mom,i} \Delta t
 \end{aligned}
 \tag{PA.190}$$

3 where the dissipation term F_i^{n-1} is obtained from Equation (PA.153) and is constrained by

$$|F_i^{n-1}| \leq \left| \frac{P_{i+1}^{n-1} - P_{i-1}^{n-1}}{2\Delta z} - \rho_i^{n-1} g \right|
 \tag{PA.191}$$

5 and the sign of F_i^{n-1} is chosen to oppose flow. Finally, numerical momentum diffusion is added
6 without distinguishing between phases in the mixture (ρ is the mixture density):

$$V_i (\rho u)_i^n = V_i (\rho u)_i^* - \zeta_p \Delta x_i \left[A_{i+1/2} \left((\rho u)_{i+1}^{n-1} - (\rho u)_i^{n-1} \right) - A_{i-1/2} \left((\rho u)_i^{n-1} - (\rho u)_{i-1}^{n-1} \right) \right]
 \tag{PA.192}$$

9 In PA, $\zeta_p = 0.01$.

10 Equation (PA.150), Equation (PA.151), and Equation (PA.152) comprise a simultaneous system
11 of equations for the volumes of gas and mud and the pressure in the wellbore. The volumes of
12 salt and waste are known, since they are considered incompressible. Equation (PA.150) and
13 Equation (PA.151) combine into a quadratic equation for gas volume:

$$aV_g^2 + bV_g - c = 0
 \tag{PA.193}$$

15 where

$$a = 1 - c_m P_{atm},$$

$$b = c_m P_{atm} V_{g,0} - aV^* + V_{m,0},$$

$$16 \quad c = V^* c_m P_{atm} V_{g,0},$$

$$V_{g,0} = m_g / \rho_{g,0},$$

$$V_{m,0} = m_m / \rho_{m,0},$$

$$17 \quad V^* = V_m + V_g = V - V_s - V_w$$

18 The volume of the mud phase follows from Equation (PA.150) and the pressure from Equation
19 (PA.149). Once the mixture density in each cell (ρ_i) is updated by Equation (PA.151), the
20 mixture velocity in each cell (u_i) is computed by

1
$$u_i = \frac{(\rho u)_i}{\rho_i} \tag{PA.194}$$

2 where the quantity ρu is determined by Equation (PA.192).

3 **PA-4.6.3.2 Numerical Method—Repository**

4 The time integration method for the repository flow is implicit, with spatial derivatives
 5 determined after the time increment. This method requires the inversion of a matrix for the
 6 entire repository, which is usually straightforward. The implicit scheme is unconditionally
 7 stable. However, it is still necessary to use small time steps to ensure gradient accuracy.

8 The numerical method follows Press et al. (1989). For simplicity, the equations are presented for
 9 constant zone size, although DRSPALL implements difference equations that allow for a
 10 variable zone size. Near the cavity, a small, constant zone size is used, and then zones are
 11 allowed to grow geometrically as the outer boundary is approached. This procedure greatly
 12 increases computational efficiency without sacrificing accuracy in the region of interest.

13 For an isothermal ideal gas, the pseudopressure ψ is defined as

14
$$\psi = \frac{P^2}{\eta} \tag{PA.195}$$

15 Using Equation (PA.195), Equation (PA.171) is expanded to

16
$$\frac{\partial \psi}{\partial t} = D(\psi) \left[\frac{\partial^2 \psi}{\partial r^2} + \frac{(m-1)}{r} \frac{\partial \psi}{\partial r} + \frac{1}{k'} \frac{\partial k'}{\partial r} \frac{\partial \psi}{\partial r} \right] \tag{PA.196}$$

17 where $D(\psi) = \frac{k'}{\phi} \sqrt{\frac{\psi}{\eta}} = \frac{k'P}{\phi\eta}$; Equation (PA.196) is then converted to a difference equation by

18 treating $D(\psi)$ as constant over a zone, using its zone-centered value at the current time D_j^n :

19
$$\frac{\psi_j^{n+1} - \psi_j^n}{\Delta t} = \frac{D_j^n}{\Delta r} \left[\frac{\psi_{j+1}^{n+1} - 2\psi_j^{n+1} + \psi_{j-1}^{n+1}}{\Delta r} + \frac{(m-1)(\psi_{j+1}^{n+1} - \psi_{j-1}^{n+1})}{2r_j} \right. \\ \left. + \frac{(k'_{j+1}{}^{n+1} - k'_{j-1}{}^{n+1})(\psi_{j+1}^{n+1} - \psi_{j-1}^{n+1})}{4k'\Delta r} \right] \tag{PA.197}$$

20 Collecting similar terms in ψ leads to a tridiagonal system:

21
$$-\alpha_1 \psi_{j-1}^{n+1} + (1 + 2\alpha) \psi_j^{n+1} - \alpha_2 \psi_{j+1}^{n+1} = \psi_j^n, j = 1, 2, \dots \tag{PA.198}$$

1 where

$$2 \quad \alpha = \frac{D_j^n \Delta t}{(\Delta r)^2}$$

$$3 \quad \alpha_1 = \left(\frac{D_j^n}{\Delta r} \right) \left(\frac{1}{\Delta r} - \frac{(m-1)}{2r_j} - \frac{k'_{i+1}{}^{n+1} - k'_{i-1}{}^{n+1}}{4k' \Delta r} \right) \Delta t$$

$$4 \quad \alpha_2 = \left(\frac{D_j^n}{\Delta r} \right) \left(\frac{1}{\Delta r} + \frac{(m-1)}{2r_j} + \frac{k'_{i+1}{}^{n+1} - k'_{i-1}{}^{n+1}}{4k' \Delta r} \right) \Delta t$$

5 Equation (PA.198) may be solved by simplified LU decomposition, as presented in Press et al.
6 (1989).

7 The boundary condition at the inner radius is implemented by noting that for $i = 1$ (the first intact
8 or nonfluidized cell), ψ_{i-1} is the cavity pseudopressure, which is known, and therefore can be
9 moved to the right-hand side of Equation (PA.198):

$$10 \quad (1 + 2\alpha)\psi_1^{n+1} - \alpha_2\psi_2^{n+1} = \psi_1^n + \alpha_1\psi_{cav}^{n+1} \quad (\text{PA.199})$$

11 The far-field boundary condition is a zero gradient, which is implemented by setting
12 $\psi_{j+1}^{n+1} = \psi_j^{n+1}$ in Equation (PA.199), recognizing that $1 + 2\alpha = 1 + \alpha_1 + \alpha_2$ and rearranging, which
13 gives

$$14 \quad -\alpha_1\psi_{j-1}^{n+1} + (1 + \alpha_1)\psi_j^{n+1} = \psi_j^n \quad (\text{PA.200})$$

15 where j is the index of the last computational cell.

16 PA-4.6.3.3 Numerical Method—Wellbore to Repository Coupling

17 The term u_{rep} , appearing in Equation (PA.176), is the gas velocity in the repository at the waste-
18 cavity interface and is determined from the pressure gradient inside the waste. DRSPALL uses
19 the pressure (P_1) at the center of the first numerical zone in the waste to determine u_{rep} :

$$20 \quad u_{rep} = \frac{k(P_1 - P_{cav})}{\eta_g \phi \Delta r} \quad (\text{PA.201})$$

1 **PA-4.6.4 Implementation**

2 During development of the spallings model, a total of five parameters were determined to be
 3 both uncertain and potentially significant to model results (Hansen, Pfeifle, and Lord 2003; Lord
 4 and Rudeen 2003). All five parameters relate to the repository conditions or the state of the
 5 waste at the time of intrusion. Table PA-15 lists the uncertain parameters in the DRSPALL
 6 calculations; these parameters are also listed in Table PA-19.

7 **Table PA-15. Uncertain Parameters in the DRSPALL Calculations**

Parameter	Variable	Implementation
Repository Pressure	REPIPRES	Initial repository pressure (Pa); spall calculated for values of 10, 12, 14, and 14.8 MPa. Defines initial repository pressure in Equation (PA.171) (see Section PA-4.6.2.2) and P_{ff} in Equation (PA.184).
Repository Permeability	REPIPERM	Permeability (m^2) of waste, implemented by parameter SPALLMOD/REPIPERM. Log-uniform distribution from 2.4×10 to 2.4×10^{-12} . Defines k in Equation (PA.168).
Repository Porosity	REPIPOR	Porosity (dimensionless) of waste, implemented by parameter SPALLMOD/REPIPOR. Uniform distribution from 0.35 to 0.66. Defines ϕ in Equation (PA.167).
Particle Diameter	PARTDIAM	Particle diameter of waste (m) after tensile failure, implemented by parameter SPALLMOD/PARTDIAM. Log-uniform distribution from 0.001 to 0.1 (m). Defines d_p in Equation (PA.186).
Tensile Strength	TENSLSTR	Tensile strength of waste (Pa), implemented by parameter SPALLMOD/TENSLSTR. Uniform distribution from 0.12 MPa to 0.17 MPa. Defines maximum $\bar{\sigma}_r$ for Section PA-4.6.2.3.4.

8

9 The computational requirements of DRSPALL prohibit calculation of spall volumes for all
 10 possible combinations of initial conditions and parameter values. Since repository pressure is a
 11 time-dependent value computed by the BRAGFLO model (see Section PA-4.2), DRSPALL
 12 calculations were performed for a small number of pressures. Sensitivity studies showed that
 13 spall does not occur at pressures below 10 MPa; this value was used as the lower bound on
 14 pressure. In DRSPALL, the repository pressure cannot exceed the far-field confining stress
 15 (14.8 MPa); consequently, 14.8 MPa was used as the upper bound on pressure. Computations
 16 were also performed for intermediate pressures of 12 and 14 MPa. The remaining four
 17 parameters listed in Table PA-15 are treated as subjectively uncertain. The uncertainty
 18 represented by these parameters pertains to the future state of the waste, which is modeled in PA
 19 as a homogeneous material with uncertain properties (see Section PA-5.0).

20 Spall volumes are computed for each combination of initial pressure and sample element, for a
 21 total of $4 \times 300 = 1,200$ model runs. Although repository porosity could be treated as an initial
 22 condition (using the time-dependent value computed by BRAGFLO), to reduce the number of
 23 computational cases and ensure that extreme porosity values were represented, repository
 24 porosity was included as a sampled parameter.

1 The spallings submodel of the code CUTTINGS_S uses the DRSPALL results to compute the
2 spall volume for a given initial pressure P . If $P < 10$ MPa or $P > 14.8$ MPa, the spall volume is
3 the value computed for REPIPRESS = 10 MPa or REPIPRESS = 14.8 MPa, respectively. If P
4 falls between 10 and 14.8 MPa, the spall volume is constructed by linear interpolation between
5 the DRSPALL results for pressures that bracket P .

6 **PA-4.6.5 Additional Information**

7 Additional information on DRSPALL and its use in PA to determine spallings releases can be
8 found in the DRSPALL user's manual (WIPP Performance Assessment 2003f) and in the
9 analysis package for spallings releases (Ismail 2008). Additional information on the construction
10 of spall volumes by the code CUTTINGS_S can be found in the CUTTINGS_S design document
11 (WIPP Performance Assessment 2003g).

12 **PA-4.7 DBR to Surface: BRAGFLO**

13 This section describes the model for DBR volumes, which are volumes of brine released to the
14 surface at the time of a drilling intrusion. DBR volumes are calculated by the code BRAGFLO,
15 the same code used to compute two-phase flow in and around the repository (see Section PA-
16 4.2).

17 **PA-4.7.1 Overview of Conceptual Model**

18 DBRs could occur if the pressure in the repository at the time of a drilling intrusion exceeds
19 8 MPa, which is the pressure exerted by a column of brine-saturated drilling fluid at the depth of
20 the repository (Stoelzel and O'Brien 1996). For repository pressures less than 8 MPa, no DBRs
21 are assumed to occur. However, even if the repository pressure exceeds 8 MPa at the time of a
22 drilling intrusion, a DBR is not assured, as there might not be sufficient mobile brine in the
23 repository to result in movement towards the borehole.

24 DBRs are estimated for the following cases: (1) an initial intrusion into the repository into either
25 a lower (down-dip), middle, or upper (up-dip) panel; (2) an intrusion into a waste panel preceded
26 by an E1 intrusion into either the same waste panel, an adjacent panel, or a nonadjacent panel;
27 and (3) an intrusion into a waste panel preceded by an E2 intrusion into either the same waste
28 panel, an adjacent panel, or a nonadjacent panel (see Section PA-6.7). To determine releases for
29 the above cases, the DBR calculations use a computational grid that explicitly includes all 10
30 waste panels (Figure PA-28).

31 For perspective, the following list provides a comparison of the BRAGFLO mesh for the Salado
32 flow calculations (Figure PA-15) and the DBR mesh used for the DBR calculations (Figure PA-
33 28):

- 34 1. The DBR mesh is defined in the areal plane with the z dimension (height) one element thick;
35 the BRAGFLO mesh is defined as a cross section, with multiple layers in height and the
36 thickness (y dimension) one element thick.

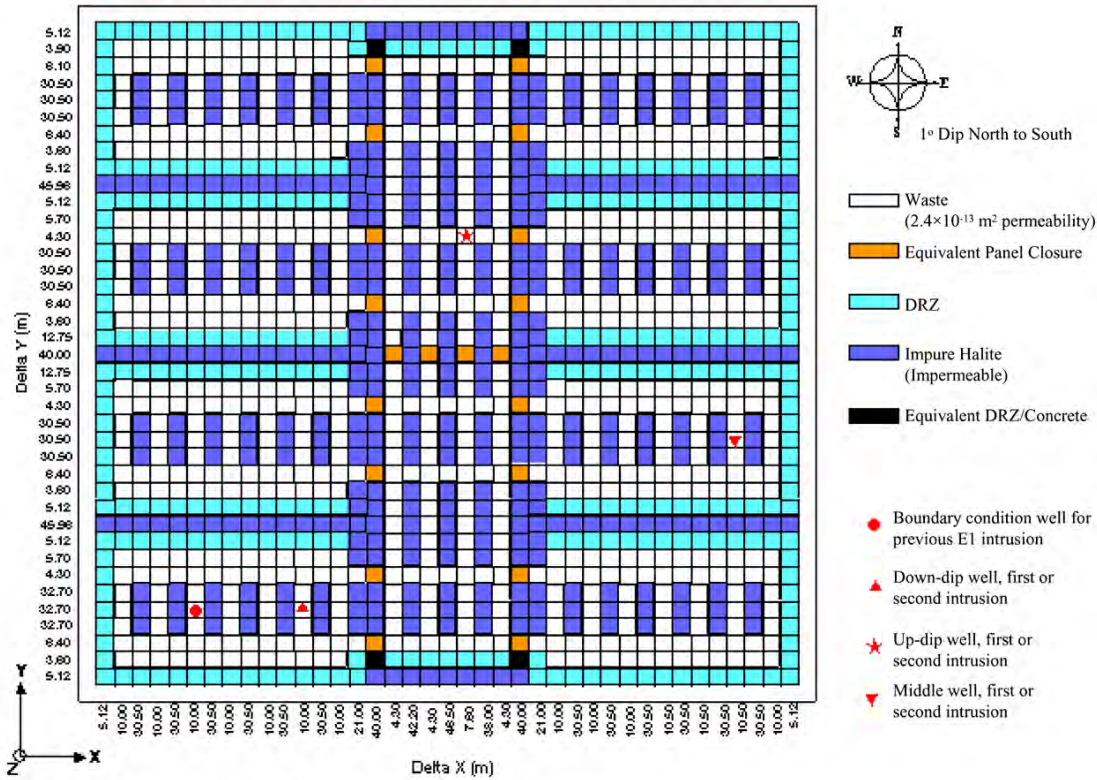


Figure PA-28. DBR Grid Used in PA

- 1
- 2
- 3 2. The DBR mesh uses constant thickness, while the BRAGFLO mesh uses rectangular flaring
- 4 to account for three-dimensional volumes in a two-dimensional grid (Figure PA-16).
- 5 3. The DBR mesh represents flow only in the waste area. The BRAGFLO model includes the
- 6 surrounding geology as well as the entire WIPP excavation (including operations,
- 7 experimental, and shaft regions).
- 8 4. Local scale heterogeneities are included in the DBR mesh, including the salt pillars, rooms,
- 9 panel closures, and passageways that contain waste. These are not fully represented in the
- 10 BRAGFLO mesh.
- 11 5. The DRZ is included in both models, but exists above and below the excavated regions in the
- 12 BRAGFLO model, whereas the DRZ surrounds the waste rooms on the sides of the DBR
- 13 mesh.
- 14 6. Both models include a one-degree formation dip through the excavated regions (Equation
- 15 (PA.33)).
- 16 The DBRs are assumed to take place over a relatively short period of time (i.e., 3 to 4.5 days; see
- 17 Section PA-4.7.8) following the drilling intrusion. The initial value conditions for determining
- 18 DBR volumes are obtained by mapping solutions of Equation (PA.24), Equation (PA.25),
- 19 Equation (PA.26), Equation (PA.27), Equation (PA.28), Equation (PA.29), and Equation (PA.30)

1 obtained from BRAGFLO with the computational grid in Figure PA-15 onto the grid in Figure
2 PA-28.

3 In concept, the DBR for a drilling intrusion has the form

$$4 \quad DBR = \int_0^{t_e} rDBR(t) dt \quad (PA.202)$$

5 where

6 DBR = DBR volume (m³) for drilling intrusion

7 $rDBR(t)$ = rate (m³) at time t at which brine flows up intruding borehole

8 t = elapsed time (s) since drilling intrusion

9 t_e = time (s) at which DBR ends

10 The definition of $rDBR(t)$ is discussed in the following sections. It is based on the two-phase
11 flow relationships in Equation (PA.24), Equation (PA.25), Equation (PA.26), Equation (PA.27),
12 Equation (PA.28), Equation (PA.29), and Equation (PA.30) and use of the Poettmann-Carpenter
13 correlation (Poettmann and Carpenter 1952) to determine a boundary pressure at the connection
14 between the intruding borehole and the repository. The time t_e is based on current drilling
15 practices in the Delaware Basin (Section PA-4.7.8).

16 PA-4.7.2 Linkage to Two-Phase Flow Calculation

17 The mesh in Figure PA-28 was linked to the mesh in Figure PA-15 by subdividing the waste
18 disposal area in the mesh in Figure PA-15 into three regions (Figure PA-29). The upper region
19 represents the northern rest of repository (North RoR) area in Figure PA-15. The middle region
20 represents the southern rest of repository (South RoR) area in Figure PA-15. The lower region
21 represents the farthest down-dip repository area (Waste Panel) in Figure PA-15 that contained
22 waste and thus corresponds to the single down-dip waste panel. The linkage between the
23 solutions to Equation (PA.24), Equation (PA.25), Equation (PA.26), Equation (PA.27), Equation
24 (PA.28), Equation (PA.29), and Equation (PA.30) and the DBR calculations was made by
25 assigning quantities calculated by BRAGFLO for each region in Figure PA-15 to the
26 corresponding waste region in Figure PA-28.

27 The height of the grid in Figure PA-28 was assigned a value that corresponded to the crushed
28 height, h (m), of the waste as predicted by the solution of Equation (PA.24) through Equation
29 (PA.30). Specifically,

$$30 \quad h = h_i \frac{1 - \phi_i}{1 - \phi} \quad (PA.203)$$

31 where h_i and ϕ_i are the initial height (m) and porosity of the waste and ϕ is the volume-averaged
32 porosity of the waste at the particular time under consideration (Section PA-4.2.3). The areas
33 designated equivalent panel closures, DRZ, and impure halite in Figure PA-28 were assigned the
34

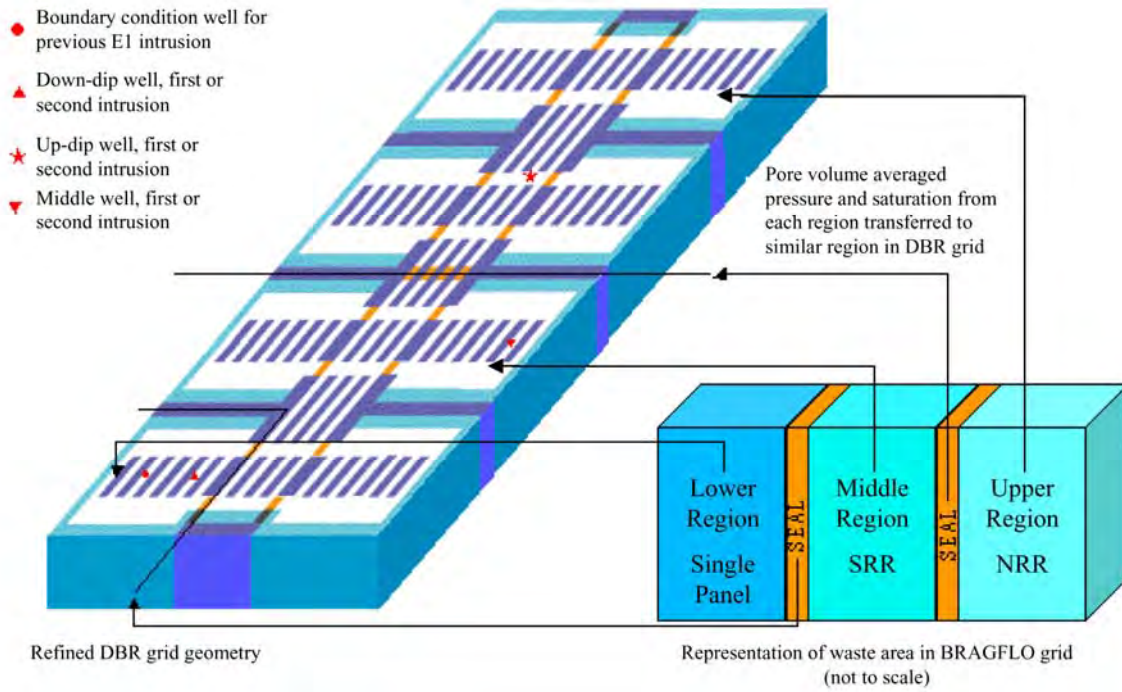


Figure PA-29. Assignment of Initial Conditions for DBR Calculation

same pressures and saturations as the corresponding grid blocks in the 10,000-year BRAGFLO calculations. The area designated equivalent DRZ/concrete (Figure PA-28) was assigned the same pressures and saturations as the DRZ. These areas were assigned porosities that resulted in a conservation of the initial pore volumes used in the solution of Equation (PA.24), Equation (PA.25), Equation (PA.26), Equation (PA.27), Equation (PA.28), Equation (PA.29), and Equation (PA.30) on the grid in Figure PA-15. Specifically, the pore volumes associated with the panel closures, DRZ, and impure halite do not change with time the constant values being given by the definitions of $\phi(x, y, 0)$ in Table PA-16.

The initial brine pressure $p_b(x, y, 0)$ and gas saturation $S_g(x, y, 0)$ in the grid in Figure PA-28 are assigned by

$$p_b(x, y, 0) = \frac{\int_R \tilde{p}_b(\tilde{x}, \tilde{y}, t_{int}) dV}{\int_R dV} \quad (\text{PA.204})$$

$$S_g(x, y, 0) = \frac{\int_R \tilde{S}_g(\tilde{x}, \tilde{y}, t_{int}) dV}{\int_R dV} \quad (\text{PA.205})$$

where (x, y) designates a point in the grid in Figure PA-28, \tilde{p}_b and \tilde{S}_g denote solutions to Equation (PA.24), Equation (PA.25), Equation (PA.26), Equation (PA.27), Equation (PA.28), Equation (PA.29), and Equation (PA.30), \tilde{x} and \tilde{y} denote the variables of integration, t_{int} is the time at which the drilling intrusion occurs, and R corresponds to the region in the BRAGFLO computational grid (Figure PA-15) that is mapped into the region in the DBR computational grid

1 (Figure PA-28) that contains the point (x, y) (Figure PA-29). Note that t_{int} defines a time in the
 2 solution of Equation (PA.24), Equation (PA.25), Equation (PA.26), Equation (PA.27), Equation
 3 (PA.28), Equation (PA.29), and Equation (PA.30); $t = 0$ defines the start time for the DBR
 4 calculation and corresponds to t_{int} in the solution of Equation (PA.24), Equation (PA.25),
 5 Equation (PA.26), Equation (PA.27), Equation (PA.28), Equation (PA.29), and Equation
 6 (PA.30).

7 The initial porosity $\phi(x, y, 0)$ in the grid in Figure PA-28 is set by the equations listed in Table
 8 PA-15. In Table PA-16, h_i is the initial height of the waste panels (3.96 m), $\phi_{WP,i}$ is the initial
 9 porosity of the waste panels (0.848), $h(t_{int})$ is the height of the repository at the time of intrusion
 10 (typically 1 to 1.5 m; corresponds to h in Equation (PA.24), Equation (PA.25), Equation (PA.26),
 11 Equation (PA.27), Equation (PA.28), Equation (PA.29), and Equation (PA.30)), $h_{DRZ,i}$ is the
 12 initial DRZ height (43.60 m) that results in the DRZ in Figure PA-28 having the same pore
 13 volume as the initial pore volume of the DRZ in Figure PA-15, A_{DRZ} is the area associated with
 14 DRZ in Figure PA-28, and $\phi_{DRZ,i}$ is the initial porosity of DRZ (see Table PA-3). The quantity
 15 $h_{DRZ,i} \times A_{DRZ} \times \phi_{DRZ,i}$ is equal to the pore volume of DRZ above and below the waste filled
 16 regions in Figure PA-15. In Table PA-16, the term ϕ_C is the porosity of the panel closure
 17 concrete material (CONC_PCS; see Table PA-3), d_1 is the length of the drift/explosion wall
 18 portion of the panel closure (32.1 m; see Figure PA-20), and d_2 is the length of the concrete
 19 portion of the panel closure (7.9 m; see Figure PA-20). The porosity of the panel closure and the
 20 equivalent DRZ/concrete materials are defined as the volume-weighted mean porosity of the
 21 component materials; this definition results in the same brine volume within the pore space in
 22 each set of panel closures in Figure PA-15 and Figure PA-28. In Table PA-16, $h_{H,i}$ is the initial
 23 height of undisturbed halite in Figure PA-28, which is arbitrarily taken to be 8.98 m. However,
 24 this value is unimportant because of the extremely low permeability of the undisturbed halite
 25 ($\sim 3.16 \times 10^{-23}$ m²); any brine in the halite could not flow into the waste over the short time
 26 period of the DBR calculation, so no effort was made to preserve halite pore volume when
 27 mapping from the computational grid in Figure PA-15 to the computational grid in Figure PA-
 28 28. The quantity $\phi_{H,i}$ is the initial porosity of halite (HALPOR, see Table PA-19).

29 **PA-4.7.3 Conceptual Representation for Flow Rate $rDBR(t)$**

30 The driving force that would give rise to the DBR is a difference between waste panel pressure,
 31 p_w (Pa), and the flowing bottomhole pressure in the borehole, p_{wf} (Pa), at the time of the
 32 intrusion. The flowing bottomhole pressure p_{wf} , defined as the dynamic pressure at the inlet of
 33 the intruding borehole to the waste panel, is less than the static pressure p_w due to friction and
 34 acceleration effects. The rate at which brine and gas are transported up the intruding borehole is
 35 determined by the difference $p_w - p_{wf}$ and a productivity index J_p for the intruded waste panel
 36 (Mattax and Dalton 1990, p. 79):

$$37 \quad q_p(t) = J_p [p_w(t) - p_{wf}] \quad (\text{PA.206})$$

38 where

1

Table PA-16. Initial Porosity in the DBR Calculation

Grid Region	Initial Porosity
Waste (ϕ_W)	$1 - h_i \frac{1 - \phi_{WP,i}}{h(t_{int})}$
Panel Closures	$\frac{d_1 \phi_W + d_2 \phi_C}{d_1 + d_2}$
DRZ	$\phi_{DRZ,i} \frac{h_{DRZ,i}}{h(t_{int})}$
Impure Halite	$\phi_{H,i} \frac{h_{H,i}}{h(t_{int})}$
Equivalent DRZ/Concrete	$\frac{d_1 \phi_C + d_2 \phi_{DRZ,i}}{d_1 + d_2}$

2

3 $q_p(t)$ = flow rate (m³/s) at time t for phase p ($p = b \sim$ brine, $p = g \sim$ gas)

4 J_p = productivity index (m³/Pa·s) for phase p

5 and p_w and p_{wf} are defined above. As indicated by the inclusion/exclusion of a dependence on t ,
 6 the terms J_p and p_{wf} are constant during the determination of $q_p(t)$ for a particular drilling
 7 intrusion in the present analysis, and $p_w(t)$ changes as a function of time. In concept, the DBR is
 8 given by

9
$$DBR = \int_0^{t_c} rDBR(t) dt = \int_0^{t_c} J_b [p_w(t) - p_{wf}] dt \quad (PA.207)$$

10 once J_b (brine), p_w , and p_{wf} are determined. Section PA-4.7.4 discusses the determination of J_p
 11 (for both gas and brine), Section PA-4.7.5 presents the numerical determination of p_w and DBR,
 12 and the determination of p_{wf} is discussed in Section PA-4.7.6. The associated gas release is
 13 given by the corresponding integral with J_g (gas) rather than J_b (brine). In the computational
 14 implementation of the analysis, DBR is determined as part of the numerical solution of the
 15 system of PDEs that defines p_w (Section PA-4.7.5).

16 **PA-4.7.4 Determination of Productivity Index J_p**

17 In a radial drainage area with uniform saturation, which is assumed to be valid throughout the
 18 DBR, the following representation for J_p can be determined from Darcy's law (Mattax and
 19 Dalton 1990, p. 79; Williamson and Chappellear 1981; Chappellear and Williamson 1981):

$$J_p = \frac{2\pi k k_{rp} h}{\mu_p \left[\ln \left(\frac{r_e}{r_w} \right) + s + c \right]} \quad (\text{PA.208})$$

2 where

- 3 k = absolute permeability (assumed to be constant through time at $2.4 \times 10^{-13} \text{ m}^2$)
 4 k_{rp} = relative permeability to phase p (calculated with modified Brooks-Corey model in
 5 Equation (PA.139), Equation (PA.140), and Equation (PA.141) and brine and gas
 6 saturations, S_b and S_g , obtained by mapping solutions of Equation (PA.24), Equation
 7 (PA.25), Equation (PA.26), Equation (PA.27), Equation (PA.28), Equation (PA.29),
 8 and Equation (PA.30) obtained with the grid in Figure PA-15 onto the grid in Figure
 9 PA-28)
 10 h = crushed panel height (Equation (PA.203))
 11 μ_p = viscosity of fluid phase (assumed to be constant through time with $\mu_b = 1.8 \times 10^{-3} \text{ Pa}\cdot\text{s}$,
 12 and $\mu_g = 8.92 \times 10^{-6} \text{ Pa}\cdot\text{s}$ [Kaufmann 1960])
 13 r_e = external drainage radius (for use with the rectangular grid blocks in Figure PA-28, r_e is
 14 taken to be the equivalent areal radius; see Equation (PA.209))
 15 r_w = wellbore radius (assumed to be constant through time at 0.1556 m (Gatlin 1960, Table
 16 14.7))
 17 c = -0.50 for pseudo-steady-state flow
 18 s = skin factor, which is used to incorporate flow stimulation caused by cavings and
 19 spallings release (see Equation (PA.210))

20 In the present analysis,

$$r_e = \sqrt{(\Delta x)(\Delta y) / \pi} \quad (\text{PA.209})$$

22 where Δx is the x dimension (m) and Δy is the y dimension (m) of the grid block containing the
 23 down-dip well in Figure PA-28 ($\Delta x = 10 \text{ m}$ and $\Delta y = 32.7 \text{ m}$).

24 The skin factor s is derived from the cavings and spallings release. Due to the uncertainty in the
 25 cavings and spallings parameters, the calculated solid release volume can vary for each
 26 realization. The skin factor is calculated for each realization, based on the calculated solid
 27 release volume, through the following petroleum engineering well testing relationship (Lee 1982,
 28 pp. 5–7):

$$s = \left(\frac{k}{k_s} - 1 \right) \ln \left(\frac{r_s}{r_w} \right) \quad (\text{PA.210})$$

30 where

1 k_s = permeability (m^2) of an open channel as a result of spillings releases (assumed to be
 2 infinite)
 3 r_s = effective radius (m) of the wellbore with the cuttings, cavings, and spillings volume
 4 removed

5 The effective radius r_s is obtained by converting the cuttings, cavings, and spillings volume
 6 removed into a cylinder of equal volume with the initial height of the waste (h_i), and then
 7 computing the radius of the cylinder:

$$8 \quad r_s = \sqrt{\frac{V_i}{h_i \pi}} \quad (\text{PA.211})$$

9 and substitution of r_s into Equation (PA.210) with $k_s = \infty$ yields

$$10 \quad s = (-1) \ln \left(\frac{\sqrt{\frac{V_i}{h_i \pi}}}{r_w} \right) \quad (\text{PA.212})$$

11 **PA-4.7.5 Determination of Waste Panel Pressure $p_w(t)$ and DBR**

12 The repository pressure $p_w(t)$ in Equation (PA.207) after a drilling intrusion is determined with
 13 the same system of nonlinear PDEs discussed in Section PA-4.2. These equations are solved
 14 numerically by the code BRAGFLO used with the computational grid in Figure PA-28 and
 15 assumptions (i.e., parameter values, initial value conditions, and boundary value conditions)
 16 appropriate for representing brine flow to an intruding borehole over a relatively short time
 17 period immediately after the intrusion (e.g., 3 to 4.5 days). Due to the short time periods under
 18 consideration, the model for DBR does not include gas generation due to either corrosion or
 19 microbial action or changes in repository height due to creep closure. Furthermore, to stabilize
 20 the calculation and thus allow longer time steps in the numerical solution, the capillary pressure
 21 was assigned a value of 0 Pa in all modeled regions (Figure PA-28); in the analysis of the full
 22 system in Section PA-4.2, capillary pressure had a value of 0 Pa in the waste regions and the
 23 DRZ, but a nonzero value in the panel closures (Table PA-4). Use of a capillary pressure of 0 Pa
 24 results in the brine pressure $p_b(x, y, t)$ and the gas pressure $p_g(x, y, t)$ being equal, with the
 25 pressure $p_w(t)$ in Equation (PA.207) given by

$$26 \quad p_w(t) = p_b(x, y, t) \quad (\text{PA.213})$$

27 Although the determination of DBR can be conceptually represented by the integral in Equation
 28 (PA.202), in the numerical implementation of the analysis, DBR is determined within the
 29 numerical solution of the system of PDEs that defines $p_b(x, y, t)$.

1 With the specific assumptions for DBR, Equation (PA.24) , Equation (PA.25), Equation (PA.26),
 2 Equation (PA.27), Equation (PA.28), Equation (PA.29), and Equation (PA.30) become

3 Gas Conservation
$$\nabla \cdot \left[\frac{\alpha \rho_g K_g k_{rg}}{\mu_g} (\nabla p_g + \rho_g g \nabla h) \right] = \alpha \frac{\partial (\phi \rho_g S_g)}{\partial t} \quad (\text{PA.214})$$

4 Brine Conservation
$$\nabla \cdot \left[\frac{\alpha \rho_b K_b k_{rb}}{\mu_b} (\nabla p_b + \rho_b g \nabla h) \right] = \alpha \frac{\partial (\phi \rho_b S_b)}{\partial t} \quad (\text{PA.215})$$

5 Saturation Constraint
$$S_g + S_b = 1 \quad (\text{PA.216})$$

6 Capillary Pressure Constraint
$$p_g - p_b = 0 \quad (\text{PA.217})$$

7 Gas Density
$$\rho_g \text{ determined by RKS equation of state (Equation (PA.54))} \quad (\text{PA.218})$$

8 Brine Density
$$\rho_b = \rho_0 \exp \left[c_b (p_b - p_{b0}) \right] \quad (\text{PA.219})$$

9 Formation Porosity
$$\phi = \phi_0 \exp \left[c_\phi (p_b - p_{b0}) \right] \quad (\text{PA.220})$$

10 with all symbols having the same definitions as in Equation (PA.24), Equation (PA.25), Equation
 11 (PA.26) Equation (PA.27), Equation (PA.28), Equation (PA.29), and Equation (PA.30).

12 The primary differences between the BRAGFLO calculations described in Section PA-4.2 and
 13 the BRAGFLO calculations described in this section are in the computational meshes (Figure
 14 PA-28 and Figure PA-15), initial values (Table PA-3 and Section PA-4.7.2), and boundary
 15 conditions (Table PA-17). In particular, brine and gas flow associated with intruding boreholes
 16 in the DBR calculations are incorporated by the assignment of appropriate boundary conditions.
 17 Specifically, brine flow up an intruding borehole is incorporated into Equation (PA.214),
 18 Equation (PA.215), Equation (PA.216), Equation (PA.217), Equation (PA.218), Equation
 19 (PA.219), and Equation (PA.220) by using the Poettmann-Carpenter wellbore model to
 20 determine the pressure at the outflow point in a waste panel (Figure PA-28), with this pressure
 21 entering the calculation as a boundary value condition (Table PA-17). The details of this
 22 determination are discussed in Section PA-4.7.6. Furthermore, for calculations that assume a
 23 prior E1 intrusion, the effects of this intrusion are also incorporated into the analysis by
 24 specifying a pressure as a boundary condition (Table PA-17). The determination of this pressure
 25 is discussed in Section PA-4.7.6.

26 **PA-4.7.6 Boundary Value Pressure p_{wf}**

27 The boundary value pressure p_{wf} at the inlet of the intruding borehole is defined by a system of
 28 equations of the following form:

1

Table PA-17. Boundary Conditions for p_b and S_g in DBR Calculations

(x, y) on Upper (Northern) or Lower (Southern) Boundary in Figure PA-28, $0 \leq t$	
$(\nabla p_g + \rho_g g \nabla h) _{(x,y,t)} \cdot \mathbf{j} = 0 \text{ Pa/m}$	No gas flow condition
$(\nabla p_b + \rho_b g \nabla h) _{(x,y,t)} \cdot \mathbf{j} = 0 \text{ Pa/m}$	No brine flow condition
(x, y) on Right (Eastern) or Left (Western) Boundary in Figure PA-28, $0 \leq t$	
$(\nabla p_g + \rho_g g \nabla h) _{(x,y,t)} \cdot \mathbf{i} = 0 \text{ Pa/m}$	No gas flow condition
$(\nabla p_b + \rho_b g \nabla h) _{(x,y,t)} \cdot \mathbf{i} = 0 \text{ Pa/m}$	No brine flow condition
(x, y) at Location of Drilling Intrusion under Consideration (see indicated points in Figure PA-28), $0 \leq t$	
$p_b(x, y, t) = p_{wf}$ (see Section PA-4.7.6)	Constant pressure condition
(x, y) at Location of Prior Drilling Intrusion into Pressurized Brine (see indicated point in Figure PA-28), $0 \leq t$	
$p_b(x, y, t) = p_{wEI}$ (see Section PA-4.7.7)	Constant pressure condition

2

3
$$\frac{dp}{dh} = G(q_b [p(0)], q_g [p(0)], p(h), h), \quad 0 \leq h \leq 655m \quad (\text{PA.221})$$

4
$$p(655) = 1.013 \times 10^5 \text{ Pa} \quad (\text{PA.222})$$

5
$$q_b [p(0)] = J_b [p_w - p(0)] \quad (\text{PA.223})$$

6
$$q_g [p(0)] = J_g [p_w - p(0)] \quad (\text{PA.224})$$

7 where $p(h)$ is pressure (Pa) at elevation h in the borehole, with $h = 0$ m corresponding to the
 8 entry point of the borehole into the waste panel and $h = 655$ m corresponding to the land surface
 9 (Figure PA-30); G is a function (Pa/m) characterizing the change of pressure with elevation in
 10 the borehole; $p(655)$ is an initial value condition requiring that pressure at the land surface (i.e.,
 11 the outlet point of the borehole) be equal to atmospheric pressure; $q_b[p(0)]$ and $q_g[p(0)]$ define
 12 brine and gas flow rates (m^3/s) into the borehole; J_b and J_g are productivity indexes ($\text{m}^3/\text{Pa s}$)
 13 (see Equation (PA.208)); and p_w is the pressure (Pa) in the repository at the time of the drilling
 14 intrusion.

15 The boundary value pressure p_{wf} is defined by

16
$$p_{wf} = p(0) \quad (\text{PA.225})$$

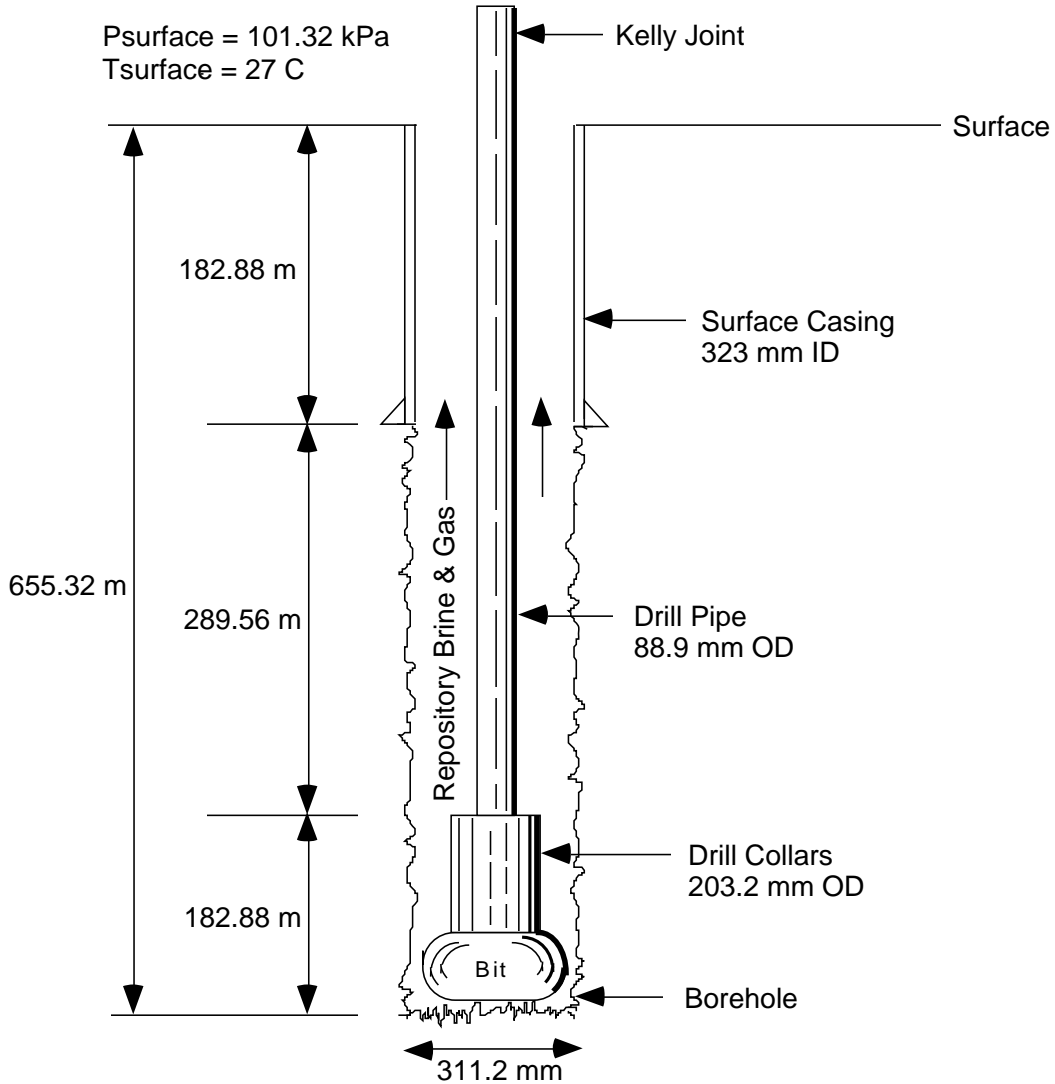


Figure PA-30. Borehole Representation Used for Poettmann-Carpenter Correlation

Thus, p_{wf} is determined by the numerical solution of Equation (PA.221) for $p(0)$ subject to the constraints in Equation (PA.222), Equation (PA.223), and Equation (PA.224).

The pressure p_w corresponds to the pressure $p_w(0)$ in Equation (PA.213) and is obtained from the solution of Equation (PA.24), Equation (PA.25), Equation (PA.26), Equation (PA.27), Equation (PA.28), Equation (PA.29), and Equation (PA.30) with the computational grid in Figure PA-15 (see Section PA-4.7.2). The production indexes J_b and J_g are defined in Equation (PA.208).

Thus, the only quantity remaining to be specified in Equation (PA.221), Equation (PA.222), Equation (PA.223), and Equation (PA.224) is the function G .

Brine and gas flow up a borehole is governed by complex physics dependent on frictional effects and two-phase fluid properties. This phenomenon has been widely studied in the petroleum industry and many modeling procedures have been developed to predict flow rates and pressures in vertical two-phase pipe flow (i.e., to define G in Equation (PA.221)) (Brill and Beggs 1986).

1 For this analysis, the Poettmann-Carpenter model (Poettmann and Carpenter 1952; Welchon,
 2 Bertuzzi, and Poettmann 1962) was used to define G because it accounts for multiphase
 3 frictional effects based on empirical (i.e., field) data from flowing wells, is one of the few
 4 modeling approaches that included annular flow data in its development, and is relatively easy to
 5 implement. Specifically, the Poettmann-Carpenter model defines G by

$$\begin{aligned}
 & G(q_b[p(0)], q_g[p(0)], p(h), h) \\
 & = gm(h) + f'(m(h), D(h), q_b[p(0)]) gm(h) F^2(h) / D^5(h)
 \end{aligned}
 \tag{PA.226}$$

8 where

9 g = acceleration due to gravity (9.8 m/s²)

10 $m(h)$ = density (kg/m³) of fluids (i.e., gas and brine) in wellbore at
 11 elevation h (Note: $m(h)$ is a function of $q_b[p(0)]$ and
 12 $q_g[p(0)]$; see Equation (PA.227) below)

13 $f'\{m(h), D(h), q_b[p(0)]\}$ = empirically defined scale factor (m/s²) (Note: f' is the scale
 14 factor in the Poettmann-Carpenter model for fluid flow in a
 15 wellbore [Poettmann and Carpenter 1952]; see discussion
 16 below)

17 $F(h)$ = flow rate (m³/s) of fluids (i.e., gas and brine) in wellbore at
 18 elevation h (Note: $F(h)$ is a function of $q_b[p(0)]$ and
 19 $q_g[p(0)]$; see Equation (PA.228))

20 $D(h)$ = effective diameter (m) of wellbore (see Equation (PA.231))

21 The first term, $gm(h)$, in Equation (PA.226) results from the contribution of elevation to
 22 pressure; the second term results from frictional effects (Poettmann and Carpenter 1952). The
 23 fluid density $m(h)$ at elevation h is given by

$$m(h) = \frac{q_b[p(0)]\rho_b[p(0)] + q_g[p(0)]\rho_g[p(0)]}{F(h)}
 \tag{PA.227}$$

25 where

$$F(h) = q_b[p(0)] + \frac{z(h)p(h)}{p(0)} q_g[p(0)]
 \tag{PA.228}$$

27 and

28 $\rho_b[p(0)]$ = density (kg/m³) of brine at pressure $p(0)$ and temperature 300.1 K, which is
 29 fixed at 1230 kg/m³

1 $\rho_g [p(0)]$ = density (kg/m³) of H₂ at pressure $p(0)$ and temperature 300.1 K (see Equation
2 (PA.229), below)

3 $z(h)$ = z-factor for compressibility of H₂ at elevation h (Note: $z(h)$ is a function of
4 $p(h)$; see Equation (PA.230), below), and $q_b[p(0)]$ and $q_g[p(0)]$ are defined in
5 Equation (PA.221), Equation (PA.222), Equation (PA.223), and Equation
6 (PA.224)

7 The gas density in Equation (PA.227) is obtained from the universal gas law, $PV = nRT$, by

$$8 \quad \rho_g [p(0)] = C_{m,kg} \frac{n}{V} = C_{m,kg} \frac{P}{RT} \quad (\text{PA.229})$$

9 where n is the amount of gas (mol) in a volume V , $C_{m,kg}$ is the conversion factor from moles to
10 kilograms for H₂ (i.e., 2.02×10^{-3} kg/mol), $P = p(0)$, $R = 8.3145$ J/mol K, and $T = 300.1$ K. The
11 z-factor is given by

$$12 \quad z(h) = 1 + (8.54 \times 10^{-8} \text{ Pa}^{-1}) p(h) \quad (\text{PA.230})$$

13 and was obtained from calculations performed with the SUPERTRAPP program (Ely and Huber
14 1992) for pure H₂ and a temperature of 300.1 K (Stoelzel and O'Brien 1996, Figure 4.7.4). The
15 preceding approximation to $z(h)$ was obtained by fitting a straight line between the results for
16 pressures of 0 psi and 3000 psi and a H₂ mole fraction of 1 in Stoelzel and O'Brien (1996, Figure
17 4.7.4); the actual calculations used the more complex, but numerically similar, regression model
18 given in Stoelzel and O'Brien (1996, Figure 4.7.4). The numerator and denominator in Equation
19 (PA.227) involve rates, with the time units canceling to give $m(h)$ in units of kg/m³.

20 The effective diameter $D(h)$ in Equation (PA.226) is defined with the hydraulic radius concept.
21 Specifically,

$$22 \quad D^5(h) = [D_o(h) + D_i(h)]^2 [D_o(h) - D_i(h)]^3 \quad (\text{PA.231})$$

23 where $D_i(h)$ and $D_o(h)$ are the inner and outer diameters (m) of the wellbore at elevation $h(m)$
24 (see Figure PA-30). The factor f' in Equation (PA.226) is a function of $m(h)$, $D(h)$, and
25 $q_b[p(0)]$.

26 Subsequent to submittal of the CCA PA, it was discovered that the factor of 2π was omitted
27 from Equation (PA.208). This error was determined to be of no consequence to the CCA PA
28 conclusions (Hadgu et al. 1999) and was corrected in the CRA-2004 PA. As a consequence of
29 the error correction, the regression models used to determine the boundary pressure p_{wf} were
30 recalculated (Hadgu et al. 1999). The corrected regression models are reported in this appendix.

31 The following iterative procedure based on the bisection method was used to approximate
32 solutions to Equation (PA.221), Equation (PA.222), Equation (PA.223), and Equation (PA.224).

1 Step 1. Estimate $p(0)$ using a bisection algorithm:

2 The initial guess for $p(0)$ is the midpoint $\frac{1}{2} p_w$ of interval $[0, p_w]$, where p_w is the
 3 pressure in the repository at the time of the drilling intrusion used in Equation (PA.221),
 4 Equation (PA.222), Equation (PA.223), and Equation (PA.224).

5 The next guess for $p(0)$ is at the midpoint of either $\left[0, \frac{1}{2} p_w\right]$ or $\left[\frac{1}{2} p_w, p_w\right]$, depending
 6 on whether the resultant approximation to $p(655)$ is above or below atmospheric
 7 pressure.

8 Subsequent guesses for $p(0)$ are made in a similar manner.

9 Step 2. Use $p(0)$, known values for J_b , J_g , and p_w , and Equation (PA.221), Equation (PA.222),
 10 Equation (PA.223), and Equation (PA.224) to determine $q_b[p(0)]$ and $q_g[p(0)]$.

11 Step 3. Use the bisection method with $\Delta h = 25 \text{ ft} = 7.62 \text{ m}$ and appropriate changes in annular
 12 diameter (Figure PA-30) to determine $p(655)$ (i.e., $p(h + \Delta h) = p(h) + G(q_b[p(0)]$,
 13 $q_g[p(0)], p(h), h), \Delta h)$).

14 Step 4. Stop if $p(655)$ is within 0.07% of atmospheric pressure (i.e., if $|1.013 \times 10^5 \text{ Pa} - p(655)| \leq$
 15 70 Pa). Otherwise, return to Step 1 and repeat process.

16 The preceding procedure is continued until the specified error tolerance (i.e., 0.07%) has been
 17 met. The computational design of the PA has the potential to require more than 23,000 separate
 18 DBR calculations (3 replicates \times 5 scenarios \times 3 drilling locations \times 100 vectors \times 5 to 6
 19 intrusion times per scenario). In concept, each of these cases requires the solution of Equation
 20 (PA.221), Equation (PA.222), Equation (PA.223), and Equation (PA.224) with the iterative
 21 procedure just presented to obtain the boundary value condition $p_{wf} = p(0)$ (Table PA-17). To
 22 help hold computational costs down, $p(0)$ was calculated for approximately 2,000 randomly
 23 generated vectors of the form

$$24 \quad \mathbf{v} = \left[p_w, h, S_{br}, S_{gr}, S_b, A_i \right] \quad (\text{PA.232})$$

25 where p_w is the repository pressure (used in definition of $q_b[p(0)]$ and $q_g[p(0)]$ in Equation
 26 (PA.221), Equation (PA.222), Equation (PA.223), and Equation (PA.224)), h is the crushed
 27 height of the repository (used in definition of J_p in Equation (PA.208)), S_{br} and S_{gr} are the
 28 residual saturations for gas and brine in the repository (used in definition of k_{rp} in Equation
 29 (PA.208)), S_b is the saturation of brine in the repository (used in definition of k_{rp} in Equation
 30 (PA.208)), and A_i is the equivalent area of material removed by cuttings, cavings, and spillings
 31 (used in definition of skin factor s in Equation (PA.212)). The outcomes of these calculations
 32 were divided into three cases:

33 1. Mobile brine only (i.e., $k_{rg} = 0$ in Equation (PA.214))

1 2. Brine-dominated flow (i.e., $k_{rb} > k_{rg}$)

2 3. Gas-dominated flow (i.e., $k_{rg} > k_{rb}$)

3 Regression procedures were then used to fit algebraic models that can be used to estimate $p(0)$.
 4 These regression models were then used to determine $p(0)$, and hence, p_{wf} . The resulting three
 5 regression models (or curve fit equations) for flowing bottomhole pressure (p_{wf}) are as follows:

6 1. For a system with only mobile brine ($k_{rg} = 0$)

7
$$p_{wf} = a + bx + cy + dx^2 + ey^2 + fxy + gx^3 + hy^3 + ixy^2 + jx^2y \quad (\text{PA.233})$$

8 where $x = \log(j_b)$ and $y = p_w$ (= repository pressure), the coefficients in Equation (PA.233)
 9 were determined to be

10 $a = 3.2279346 \times 10^{11}$

11 $b = 9.4816648 \times 10^{10}$

12 $c = -6.2002715 \times 10^3$

13 $d = 9.2450601 \times 10^9$

14 $e = 4.1464475 \times 10^{-6}$

15 $f = -1.2886068 \times 10^3$

16 $g = 2.9905582 \times 10^8$

17 $h = 1.0857041 \times 10^{-14}$

18 $i = 4.7119798 \times 10^{-7}$

19 $j = -6.690712 \times 10^{-1}$

20 with a resulting coefficient of determination $R^2 = 0.974$.

21 2. For brine-dominated flow ($k_{rb} > k_{rg}$)

22
$$p_{wf} = \frac{a + bx + cx^2 + dy}{1 + ex + fx^2 + gx^3 + hy} \quad (\text{PA.234})$$

23 where $x = \log\left(\frac{k_{rg}}{k_{rb}}\right)$ and $y = p_w$ (= repository pressure), the coefficients in Equation (PA.234)

24 were determined to be

25 $a = 1.6065077 \times 10^6$

26 $b = 2.6243397 \times 10^6$

27 $c = 2.4768899 \times 10^6$

28 $d = -5.3635476 \times 10^{-2}$

29 $e = 7.0815693 \times 10^{-1}$

30 $f = 3.8012696 \times 10^{-1}$

1 $g = 4.1916956 \times 10^{-3}$
 2 $h = -2.4887085 \times 10^{-8}$

3 with a resulting coefficient of determination $R^2 = 0.997$.

4 3. For gas-dominated flow ($k_{rg} > k_{rb}$)

5
$$p_{wf} = a + b \frac{1}{x} + cy + d \frac{1}{x^2} + ey^2 + f \frac{x}{y} + g \frac{1}{x^3} + hy^3 + i \frac{y^2}{x} + j \frac{y}{x^2} \quad (\text{PA.235})$$

6 where $x = \log(j_g)$ and $y = p_w$ (= repository pressure), the coefficients in Equation (PA.235)
 7 were determined to be

8 $a = -1.0098405 \times 10^9$
 9 $b = -2.3044622 \times 10^{10}$
 10 $c = 9.8039146$
 11 $d = -1.7426466 \times 10^{11}$
 12 $e = 1.8309137 \times 10^{-7}$
 13 $f = 1.7497064 \times 10^2$
 14 $g = -4.3698224 \times 10^{11}$
 15 $h = -1.4891198 \times 10^{-16}$
 16 $i = 1.3006196 \times 10^{-6}$
 17 $j = 7.5744833 \times 10^2$

18 with a resulting coefficient of determination $R^2 = 0.949$.

19 **PA-4.7.7 Boundary Value Pressure p_{wE1}**

20 Some of the DBR calculations are for a drilling intrusion that has been preceded by an E1
 21 intrusion in either the same waste panel, an adjacent waste panel, or a nonadjacent waste panel
 22 (Section PA-6.7.6). The effects of these prior E1 intrusions are incorporated into the solution of
 23 Equation (PA.214), Equation (PA.215), Equation (PA.216), Equation (PA.217), Equation
 24 (PA.218), Equation (PA.219), and Equation (PA.220), and hence into the DBR, by specifying a
 25 boundary pressure p_{wE1} at the location of the E1 intrusion into the repository (Table PA-17).

26 Two cases are considered for the definition of p_{wE1} : (1) an open borehole between the brine
 27 pocket and the repository and (2) a borehole filled with silty-sand-like material between the brine
 28 pocket and the repository. The first case corresponds to the situation in which the drilling
 29 intrusion occurs within 200 years of a prior drilling intrusion that penetrated the pressurized
 30 brine pocket, and the second case corresponds to the situation in which the drilling intrusion
 31 occurs more than 200 years after a prior drilling intrusion that penetrated the pressurized brine
 32 pocket.

1 **PA-4.7.7.1 Solution for Open Borehole**

2 In this case, p_{wE1} is set equal to the flowing well pressure p_{wfBP} of an open borehole between the
3 brine pocket and the repository, and is given by

4
$$Q = f_1(p_{BP}, p_{wfBP}) \quad (\text{PA.236})$$

5
$$Q = f_2(p_{wfBP}, p_{wfBI}) \quad (\text{PA.237})$$

6
$$Q = f_3(p_{wfBI}, p_{wfBO}) \quad (\text{PA.238})$$

7 where

8 p_{BP} = pressure (Pa) in brine pocket

9 p_{wfBP} = flowing well pressure (Pa) at outlet from brine pocket

10 p_{wfBI} = flowing well pressure (Pa) at inlet to repository from brine pocket

11 p_{wfBO} = flowing well pressure (Pa) at outlet from repository due to intruding borehole
12 (Note: The boreholes associated with p_{wfBI} and p_{wfBO} arise from different drilling
13 intrusions and hence are at different locations; see Figure PA-28)

14 Q = brine flow rate (m^3/s) from brine pocket to repository, through repository, and then
15 to surface

16 and f_1 , f_2 , and f_3 are linear functions of their arguments. In the development, p_{BP} and p_{wfBO} are
17 assumed to be known, with the result that Equation (PA.236), Equation (PA.237), and Equation
18 (PA.238) constitutes a system of three linear equations in three unknowns (i.e., p_{wfBP} , p_{wfBI} and
19 Q) that can be solved to obtain p_{wfBI} . In the determination of p_{wfBI} for use in a particular
20 solution of Equation (PA.214), Equation (PA.215), Equation (PA.216), Equation (PA.217),
21 Equation (PA.218), Equation (PA.219), and Equation (PA.220), p_{BP} is the pressure in the brine
22 pocket at the time of the intrusion obtained from the solution of Equation (PA.24), Equation
23 (PA.25), Equation (PA.26), Equation (PA.27), Equation (PA.28), Equation (PA.29), and
24 Equation (PA.30) with BRAGFLO, and p_{wfBO} is the flowing well pressure obtained from
25 conditions at the time of the intrusion (from the solution of Equation (PA.24), Equation (PA.25),
26 Equation (PA.26), Equation (PA.27), Equation (PA.28), Equation (PA.29), and Equation
27 (PA.30)) and the solutions of the Poettmann-Carpenter model embodied in Equation (PA.233),
28 Equation (PA.234), and Equation (PA.235) (i.e., given pressure, k_{rg} and k_{rb} at the time of the
29 intrusion, and J_p , p_{wfBO} is determined from the regression models indicated in Equation
30 (PA.233), Equation (PA.234), and Equation (PA.235)).

31 The definition of Equation (PA.236), Equation (PA.237), and Equation (PA.238) is now
32 discussed. Equation (PA.236) characterizes flow out of the brine pocket into an open borehole
33 and has the form (Williamson and Chappellear 1981, Chappellear and Williamson 1981)

$$Q = \left(\frac{2\pi k_{BP} h_{BP}}{\mu [\ln(r_{eBP} / r_w) - 0.5]} \right) (p_{BP} - p_{wfBP}) \quad (\text{PA.239})$$

2 where

- 3 k_{BP} = brine pocket permeability (m²)
 4 h_{BP} = effective brine pocket height (m)
 5 r_{eBP} = effective brine pocket radius (m)
 6 r_w = wellbore radius (m)
 7 μ = brine viscosity (Pa s)

8 In the present analysis, k_{BP} is an uncertain analysis input (see BHPRM in Table PA-19); h_{BP} =
 9 125.83 m; r_{eBP} = 114 m (Stoelzel and O'Brien 1996), which corresponds to the size of the
 10 largest brine pocket that could fit under one waste panel; r_w = (8.921 in.)/2 = 0.1133 m, which is
 11 the inside radius of a 9 5/8 in. outside diameter casing (Gatlin 1960, Table 14.7); μ = 1.8×10^{-3}
 12 Pa s; and p_{BP} is determined from the solution of Equation (PA.24), Equation (PA.25), Equation
 13 (PA.26), Equation (PA.27), Equation (PA.28), Equation (PA.29), and Equation (PA.30), as
 14 previously indicated.

15 Equation (PA.237) characterizes flow up an open borehole from the brine pocket to the
 16 repository and is based on Poiseuille's Law (Prasuhn 1980, Eqs. 7-21, 7-22). Specifically,
 17 Equation (PA.237) has the form

$$Q = \left[\frac{\pi D^4}{128\mu (y_{BP} - y_{rep})} \right] \left[(p_{wfBP} - p_{wfBI}) + g\rho (y_{rep} - y_{BP}) \right] \quad (\text{PA.240})$$

19 where

- 20 D = wellbore diameter (m)
 21 y_{rep} = elevation of repository (m) measured from surface
 22 y_{BP} = elevation of brine pocket (m) measured from surface
 23 g = acceleration due to gravity (9.8 m/s²)
 24 ρ = density of brine (kg/m³)

25 and the remaining symbols have already been defined.

26 In the present analysis, $D = 2r_w = 0.2266$ m, $\rho = 1230$ kg/m³, and $y_{BP} - y_{rep} = 247$ m. With the
 27 preceding values,

$$128\mu (y_{BP} - y_{rep}) / \pi D^4 = 6.87 \times 10^3 \text{ Pa s} / \text{m}^3 \quad (\text{PA.241})$$

1
$$g\rho(y_{rep} - y_{BP}) = 2.98 \times 10^6 \text{ Pa} \quad (\text{PA.242})$$

2 Thus,

3
$$p_{wfBI} = p_{wfBP} - 2.98 \times 10^6 \text{ Pa} \quad (\text{PA.243})$$

4 when Q is small ($\leq 0.1 \text{ m}^3/\text{s}$). When appropriate, this approximation can be used to simplify the
5 construction of solutions to Equation (PA.236), Equation (PA.237), and Equation (PA.238).

6 Equation (PA.238) characterizes flow through the repository from the lower borehole to the
7 bottom of the borehole associated with the drilling intrusion under consideration and has the
8 same form as Equation (PA.239). Specifically,

9
$$Q = \left(\frac{2\pi k_{rep} h_{rep}}{\mu [\ln(r_{e,rep} / r_w) - 0.5]} \right) (p_{wfBI} - p_{wfBO}) \quad (\text{PA.244})$$

10 where

11 k_{rep} = repository permeability (m^2)

12 h_{rep} = repository height (m)

13 $r_{e,rep}$ = effective repository radius (m)

14 and the remaining symbols have already been defined. In the present analysis, $k_{rep} = 2.4 \times 10^{-13}$
15 m^2 ; h_{rep} at the time of the drilling intrusion under consideration is obtained from the solution of
16 Equation (PA.24), Equation (PA.25), Equation (PA.26), Equation (PA.27), Equation (PA.28),
17 Equation (PA.29), and Equation (PA.30) (see Equation (PA.203)); and $r_{e,rep}$ is the same as the
18 radius r_e defined in Equation (PA.209). As previously indicated, p_{wfBO} is obtained from the
19 solutions to the Poettmann-Carpenter model summarized in Equation (PA.233), Equation
20 (PA.234), and Equation (PA.235).

21 Three equations (i.e., Equation (PA.239), Equation (PA.240), and Equation (PA.244)) with three
22 unknowns (i.e., p_{wfBP} , p_{wfBI} and Q) have now been developed. The solution for p_{wfBI} defines
23 the initial value p_{wE1} in Table PA-17. When the simplification in Equation (PA.243) is used, the
24 resultant solution for p_{wfBI} is

25
$$p_{wfBI} = \frac{p_{wfBO} + (p_{BP} - 2.98 \times 10^6) K_1}{1 + K_1} \quad (\text{PA.245})$$

26 where

1
$$K_1 = \frac{k_{BP}h_{BP} \left[\ln \left(\frac{r_{e,rep}}{r_w} \right) - \frac{1}{2} \right]}{k_{rep}h_{rep} \left[\ln \left(\frac{r_{eBP}}{r_w} \right) - \frac{1}{2} \right]} \quad (\text{PA.246})$$

2 and -2.98×10^6 comes from Equation (PA.242). The expression in Equation (PA.246) was used
 3 to define p_{wE1} in the CCA for the determination of DBRs resulting from a drilling intrusion that
 4 occurred within 200 years of a preceding E1 intrusion (see Table PA-7). The same approach was
 5 used for the CRA-2004 and the CRA-2009.

6 **PA-4.7.7.2 Solution for Sand-Filled Borehole**

7 The determination of the pressure p_{wfBI} , with the assumption that a borehole filled with silty-
 8 sand-like material connects the brine pocket and the repository, is now considered. The
 9 approach is similar to that used for the open borehole, except that Equation (PA.236) and
 10 Equation (PA.237) are replaced by a single equation based on Darcy’s Law. Specifically, flow
 11 from the brine pocket to the repository is represented by

12
$$Q = \frac{k_{BH} A_{BH} \left[(p_{wfBP} - p_{wfBI}) + g \rho \right]}{\mu (y_{BP} - y_{rep})} \quad (\text{PA.247})$$

13 where

14 k_{BH} = borehole permeability (m²)

15 A_{BH} = borehole cross-sectional area (m²)

16 and the remaining symbols have been previously defined. In the present analysis, k_{BH} is an
 17 uncertain input (see BHPRM in Table PA-19) and A_{BH} is defined by the assumption that the
 18 borehole diameter is the same as the drill bit diameter (i.e., 12.25 in. = 0.31115 m).

19 The representation for flow from the brine pocket inlet point through the repository to the outlet
 20 point associated with the drilling intrusion under consideration remains as defined in Equation
 21 (PA.244). Thus, two equations (i.e., Equation (PA.244) and Equation (PA.247)) and two
 22 unknowns (i.e., p_{wfBI} and Q) are under consideration. Solution for p_{wfBI} yields

23
$$p_{wfBI} = \frac{p_{wfBO} + K_2 p_{BP} - 2.98 \times 10^6 K_2}{1 + K_2} \quad (\text{PA.248})$$

24 where

$$K_2 = \frac{\pi k_{BH} r_w^2 \left[\ln \left(\frac{r_{eBP}}{r_w} \right) - \frac{1}{2} \right]}{2\pi h_{rep} k_{rep} (y_{BP} - y_{rep})} \quad (\text{PA.249})$$

1
2 and -2.98×10^6 comes from Equation (PA.242). The expression in Equation (PA.249) was used
3 to define p_{wE1} in the determination of DBRs for a drilling intrusion that occurred more than 200
4 years after a preceding E1 intrusion (see Table PA-7).

5 **PA-4.7.8 End of DBR**

6 The CRA-2009 PA has 23,400 cases that potentially require solution of Equation (PA.214)
7 through Equation (PA.220) to obtain the DBR volume (See Section PA-6.7.6). However, the
8 DBR was set to zero without solution of Equation (PA.214), Equation (PA.215), Equation
9 (PA.216), Equation (PA.217), Equation (PA.218), Equation (PA.219), and Equation (PA.220)
10 when there was no possibility of a release (i.e., at the time of the intrusion, the intruded waste
11 panel had either a pressure less than 8 MPa or a brine saturation below the residual brine
12 saturation S_{br}).

13 For the remaining cases, Equation (PA.214), Equation (PA.215), Equation (PA.216), Equation
14 (PA.217), Equation (PA.218), Equation (PA.219), and Equation (PA.220) were solved for a time
15 period of 50 days, although the value used for t_e was always less than 50 days. The minimum
16 value used for t_e was three days, which is an estimate of the time required to drill from the
17 repository through the Castile Formation and then cement the intermediate casing. If there is
18 little or no gas flow associated with brine inflow into the borehole during drilling in the Salado
19 Formation, the current industry practice is to allow the brine to “seep” into the drilling mud and
20 be discharged to the mud pits until the salt section is cased.

21 If there is a significant amount of gas flow, it is possible that the driller will lose control of the
22 well. In such cases, DBRs will take place until the gas flow is brought under control. Two
23 possibilities exist: (1) the driller will regain control of the well when the gas flow drops to a
24 manageable level, and (2) aggressive measures will be taken to shut off the gas flow before it
25 drops to a manageable level. In the CCA PA, the driller was assumed to regain control of the
26 well when the gas flow dropped to a “cut-off” rate of 1×10^5 standard cubic feet per day (SCF/d
27 in commonly used oil field units). Experience at the South Culebra Bluff Unit #1, which blew
28 out in January 1978, suggests that approximately 11 days may be needed to bring a well under
29 control before the gas flow drops to a manageable level (i.e., 1×10^5 SCF/d) (the CCA,
30 Appendix MASS, Attachment MASS 16-2). In particular, it took 11 days to assemble the
31 equipment and personnel needed to bring that well under control.

32 A reevaluation of the current drilling practices, including a review of the historic information and
33 interviews with current drilling personnel in the WIPP area, was conducted (Kirkes 2007). This
34 analysis found

35 1. The South Culebra Bluff #1 is not a suitable analogue for a hypothetical WIPP blowout.

- 1 2. Basing the WIPP maximum DBR parameter on the single most catastrophic blowout event in
 2 the region’s history does not reasonably represent “current drilling practice” as directed by
 3 regulations.
- 4 3. Well-known drilling procedures are sufficient to stop or *kill* a WIPP blowout under the most
 5 extreme anticipated pressures in hours, not days.
- 6 4. Using 4.5 days for a maximum DBR duration is still quite conservative, in that it assumes
 7 flow into the wellbore continues throughout the kill procedure and casing/cementing
 8 procedures, even though this assumption is not consistent with current practice.

9 Therefore, for the CRA-2009 PA, a value of 4.5 days was used for the maximum value used for
 10 t_e .

11 Given the preceding, t_e is defined by

$$12 \quad t_e = \begin{cases} \max \{ 3 \text{ d}, t_f \} & \text{if } t_f \leq 4.5 \text{ d} \\ 4.5 \text{ d} & \text{if } t_f > 4.5 \text{ d} \end{cases} \quad (\text{PA.250})$$

13 in PA, where t_f is the time at which the gas flow out of the well drops below 1×10^5 SCF/d. As
 14 a reminder, gas flow out of the repository in the intruding borehole, and hence t_e , is determined
 15 as part of the solution to Equation (PA.214), Equation (PA.215), Equation (PA.216), Equation
 16 (PA.217), Equation (PA.218), Equation (PA.219), and Equation (PA.220).

17 **PA-4.7.9 Numerical Solution**

18 As previously indicated, the BRAGFLO program is used to solve Equation (PA.214), Equation
 19 (PA.215), Equation (PA.216), Equation (PA.217), Equation (PA.218), Equation (PA.219), and
 20 Equation (PA.220) with the computational grid in Figure PA-28, the initial value conditions in
 21 Section PA-4.7.2, the boundary value conditions in Table PA-17, and parameter values
 22 appropriate for modeling DBRs. Thus, the numerical procedures in use for Equation (PA.214),
 23 Equation (PA.215), Equation (PA.216), Equation (PA.217), Equation (PA.218), Equation
 24 (PA.219), and Equation (PA.220) are the same as those described in Section PA-4.2.11 for the
 25 solution of Equation (PA.24), Equation (PA.25), Equation (PA.26), Equation (PA.27), Equation
 26 (PA.28), Equation (PA.29), and Equation (PA.30).

27 In this solution, the boundary value conditions associated with drilling intrusions (i.e., p_{wf} and
 28 p_{wE1} in Table PA-17) are implemented through the specification of fluid withdrawal terms (i.e.,
 29 q_g and q_b in Equation (PA.24), Equation (PA.25), Equation (PA.26), Equation (PA.27), Equation
 30 (PA.28), Equation (PA.29), and Equation (PA.30)), rather than as predetermined boundary value
 31 conditions. With this implementation, the representations in Equation (PA.214) and Equation
 32 (PA.215) for gas and brine conservation become

$$1 \quad \nabla \cdot \left[\frac{\alpha \rho_g K_g k_{rg}}{\mu_g} (\nabla p_g + \rho_g g \nabla h) \right] + \alpha q_g = \alpha \frac{\partial (\phi \rho_g S_g)}{\partial t} \quad (\text{PA.251})$$

$$2 \quad \nabla \cdot \left[\frac{\alpha \rho_b K_b k_{rb}}{\mu_b} (\nabla p_b + \rho_b g \nabla h) \right] + \alpha q_b = \alpha \frac{\partial (\phi \rho_b S_b)}{\partial t} \quad (\text{PA.252})$$

3 and the constraints in Equation (PA.214), Equation (PA.215), Equation (PA.216), Equation
 4 (PA.217), Equation (PA.218), Equation (PA.219), and Equation (PA.220) remain unchanged.
 5 As used in Equation (PA.251) and Equation (PA.252), q_g and q_b are independent of the
 6 computational grid in use (Figure PA-28). In practice, q_g and q_b are defined with a productivity
 7 index (see Equation (PA.208)) that is a function of the specific computational grid in use, with
 8 the result that these definitions are only meaningful in the context of the computational grid that
 9 they are intended to be used with. This specificity results because q_g and q_b as used in Equation
 10 (PA.251) and Equation (PA.252) are defined on a much smaller scale than can typically be
 11 implemented with a reasonably sized computational grid. As a result, the values used for q_g and
 12 q_b in the numerical solution of Equation (PA.251) and Equation (PA.252) must incorporate the
 13 actual size of the grid in use.

14 In the solution of Equation (PA.251) and Equation (PA.252) with the computational grid in
 15 Figure PA-28, q_g is used to incorporate gas flow out of the repository, and q_b is used to
 16 incorporate both brine inflow to the repository from a pressurized brine pocket and brine flow
 17 out of the repository. For gas flow out of the repository,

$$18 \quad q_g(x, y, t) = \frac{kk_{rg}(x, y, t)[p_g(x, y, t) - p_{wf}]}{\mu_g[\ln(r_e / r_w) + s + c]} \quad (\text{PA.253})$$

19 if (x, y) is at the center of the grid cell containing the drilling intrusion (Figure PA-28), and $q_g(x,$
 20 $y, t) = 0$ (kg/m³)/s otherwise, where k , k_{rg} , μ_g , r_e , r_w , s , and c are defined in conjunction with
 21 Equation (PA.208), p_g is gas pressure, and p_{wf} is the flowing well pressure at the outlet borehole
 22 (i.e., the boundary value condition in Table PA-17). The factor h in Equation (PA.208) is the
 23 crushed height of the repository as indicated in Equation (PA.208) and defines the factor α in
 24 Equation (PA.251) and Equation (PA.252). In the numerical solution, $q_g(x, y, t)$ defines $q_{g,i,j}^{n+1}$ in

25 Equation (PA.91), with $q_{g,i,j}^{n+1}$ having a nonzero value only when i, j correspond to the grid cell
 26 containing the borehole through which gas outflow is taking place (i.e., the grid cells containing
 27 the down-dip, middle, and up-dip wells in Figure PA-28).

28 For brine flow,

$$29 \quad q_b(x, y, t) = \frac{kk_{rb}(x, y, t)[p_b(x, y, t) - p_{wf}]}{\mu_b[\ln(r_e / r_w) + s + c]} \quad (\text{PA.254})$$

1 if (x, y) is at the center of the grid cell containing the drilling intrusion through which brine
2 outflow from the repository is taking place (Figure PA-28);

$$3 \quad q_b(x, y, t) = \frac{kk_{rb}(x, y, t)[p_{wE1} - p_b(x, y, t)]}{\mu_b[\ln(r_e / r_w) + c]} \quad (\text{PA.255})$$

4 if (x, y) is at the center of the grid cell containing a prior drilling intrusion into a pressurized
5 brine pocket (Figure PA-28), where p_{wE1} is the boundary value condition defined in Table PA-
6 17; and $q_b(x, y, t) = 0$ otherwise. In the numerical solution of Equation (PA.251), $q_g(x, y, t)$
7 defines $q_{b_{i,j}}^{n+1}$ in a discretization for Equation (PA.252) that is equivalent to the discretization for
8 Equation (PA.251) shown in Equation (PA.91), with $q_{b_{i,j}}^{n+1}$ having a nonzero value only when i, j
9 correspond to the grid cell containing the borehole through which brine outflow is taking place
10 (i.e., the grid cells containing the down-dip, middle, and up-dip wells in Figure PA-28), in which
11 case, Equation (PA.254) defines $q_{b_{i,j}}^{n+1}$, or when i, j corresponds to the grid cell containing the
12 borehole through which brine inflow to the repository from a pressurized brine pocket is taking
13 place (i.e., the grid cell containing the E1 intrusion in Figure PA-28), in which case Equation
14 (PA.255) defines $q_{b_{i,j}}^{n+1}$.

15 **PA-4.7.10 Additional Information**

16 Additional information on BRAGFLO and its use in the CRA-2009 PA to determine DBRs can
17 be found in the analysis package for DBR (Clayton 2008b) and in the BRAGFLO user's manual
18 (Nemer 2007c).

19 **PA-4.8 Groundwater Flow in the Culebra Dolomite**

20 Extensive site characterization and modeling activities conducted in the WIPP vicinity have
21 confirmed that the Culebra Dolomite Member of the Rustler Formation is the most transmissive
22 geologic unit above the Salado. Thus, the Culebra is the unit into which actinides are most likely
23 to be introduced from long-term flow up a hypothetical abandoned borehole.

24 The Culebra's regional variation in groundwater flow direction is influenced by the distribution
25 of rock types in the groundwater basin where the WIPP is located. Site characterization
26 activities have shown that the direction of groundwater flow in the Culebra varies somewhat
27 regionally, but in the area that overlies the site, flow is generally southward. Site
28 characterization activities have also demonstrated that there is no evidence of karst groundwater
29 systems in the controlled area, although groundwater flow in the Culebra is affected by the
30 presence of fractures, fracture fillings, and vuggy pore features.

31 Basin-scale regional modeling of three-dimensional groundwater flow in the units above the
32 Salado demonstrates that it is appropriate, for the purposes of estimating radionuclide transport,
33 to conceptualize the Culebra as a two-dimensional confined aquifer. Groundwater flow in the
34 Culebra is modeled as a steady-state process, but uncertainty in the flow field is incorporated in

1 the analysis by using 100 different geostatistically based T fields. The T fields are initially
 2 constructed to be consistent with available head, transmissivity, and well testing data. Each T
 3 field is subsequently modified to incorporate impacts of uncertain future processes (potash
 4 mining and climate change), as described below.

5 Potash mining in the McNutt Potash Zone (hereafter referred to as the McNutt) of the Salado,
 6 which occurs now in the Delaware Basin outside the controlled area and may continue in the
 7 future, could affect flow in the Culebra if subsidence over mined areas causes fracturing or other
 8 changes in rock properties. Consistent with regulatory criteria, mining outside the controlled
 9 area is assumed to occur in the near future, and mining within the controlled area is assumed to
 10 occur with a probability of 1 in 100 per century (adjusted for the effectiveness of AICs during
 11 the first 100 years following closure). Consistent with regulatory guidance, the effects of mine
 12 subsidence are incorporated in the PA by increasing the transmissivity of the Culebra over the
 13 areas identified as mineable by a factor sampled from a uniform distribution between 1 and 1000.
 14 T fields used in the PA are therefore adjusted to account for this and steady-state flow fields
 15 calculated accordingly, once for mining that occurs only outside the controlled area, and once for
 16 mining that occurs both inside and outside the controlled area. Mining outside the controlled
 17 area is considered in both undisturbed and disturbed performance.

18 Climatic changes during the next 10,000 years may also affect groundwater flow by altering
 19 recharge to the Culebra. The extent to which the climate will change during the next 10,000
 20 years and how such a change will affect groundwater flow in the Culebra are uncertain.
 21 However, regional three-dimensional modeling of groundwater flow in the units above the
 22 Salado indicates that flow velocities in the Culebra may increase by a factor of 1 to 2.25 for
 23 reasonably possible future climates (Corbet and Swift 1996a and 1996b). This uncertainty is
 24 incorporated in the PA by scaling the calculated steady-state specific discharge within the
 25 Culebra by a sampled parameter within this range.

26 **PA-4.8.1 Mathematical Description**

27 Groundwater flow in the Culebra is represented by the PDE

$$28 \quad S = \left(\frac{\partial h}{\partial t} \right) = \nabla \cdot (b\mathbf{K}\nabla h) - Q \quad (\text{PA.256})$$

29 where

30 S = medium storativity (dimensionless),

31 h = hydraulic head (m),

32 t = time (s),

33 b = aquifer thickness (m),

34 \mathbf{K} = hydraulic conductivity tensor (m/s),

35 Q = source/sink term expressed as the volumetric flux per unit area ((m³/m²)/s = m/s).

36 Further, the Culebra is assumed to be two-dimensional with isotropic hydraulic conductivity. As
 37 a result, \mathbf{K} is defined by

$$\mathbf{K}(x, y) = k(x, y) \begin{bmatrix} 1 & 0 \\ 0 & 1 \end{bmatrix} \quad (\text{PA.257})$$

where $k(x, y)$ is the hydraulic conductivity (m/s) at the point (x, y) . The following simplifying assumptions are also made: fluid flow in the Culebra is at steady state (i.e., $\partial h / \partial t = 0$), and source and sink effects arising from borehole intrusions and infiltration are negligible (i.e., $Q = 0$). Given these assumptions, Equation (PA.256) simplifies to

$$\nabla \cdot (b\mathbf{K}\nabla h) = 0 \quad (\text{PA.258})$$

which is the equation actually solved to obtain fluid flow in the Culebra. In PA, $b = 7.75$ m, and $k(x, y)$ in Equation (PA.257) is a function of an imprecisely known T field, as discussed in Section PA-4.8.2.

PA-4.8.2 Implementation

This section describes the salient features of the Culebra flow field calculation implementation. One should note, however, that this implementation has not been changed for the CRA-2009 PA. Instead, the flow fields generated for the CRA-2004 PABC have been reused for the CRA-2009 PA (Lowry and Kanney 2005).

The first step in the analysis of fluid flow in the Culebra is to generate T fields $T(x, y)$ (m^2/s) for the Culebra and to characterize the uncertainty in these fields. This was accomplished by generating a large number of plausible T fields. A description of the method used to construct these T fields is included in Appendix TFIELD-2009. A brief outline of the method is presented below.

The T fields used for PA are based on several types of information, including a regression model developed on WIPP-site geologic data, measured head levels in the Culebra for the year 2000, and well drawdown test results. The process that led to the final T fields used in the PA is discussed below.

Geologic data, including (1) depth to the top of the Culebra, (2) reduction in thickness of the upper Salado by dissolution, and (3) the spatial distribution of halite in the Rustler below and above the Culebra, were used to define a geologic regression model that relates transmissivity at any location to a set of geologically defined parameters.

Base T fields are defined for a modeling domain measuring 22.4 km (19 miles) east-west by 30.7 km north-south using a method of stochastic simulation. The base T fields were constructed from information on the depth to the Culebra, indicator functions defining the location of Salado dissolution, halite occurrence, and high transmissivity zones.

Seed T fields are defined by conditioning base T fields to measured values of transmissivity. This conditioning is performed with a Gaussian geostatistical simulation algorithm.

1 The seed T fields are calibrated to transient water-level data from the year 2000 in 37 wells
 2 across the region using the parameter estimation program PEST (Doherty 2002). The PEST
 3 program iteratively changes the seed T field values to minimize an objective function, using
 4 MODFLOW 2000 (Harbaugh et al. 2000) to compute the flow solution for each iteration. The
 5 objective function minimized by PEST is a combination of the weighted sum of the squared
 6 residuals between the measured and modeled heads and a second weighted sum of the squared
 7 differences in the estimated transmissivity between pairs of pilot points. The second weighted
 8 sum is designed to keep the T field as homogeneous as possible and provide numerical stability
 9 when estimating more parameters than there are data.

10 The calibrated T fields produced by PEST and MODFLOW are screened according to specific
 11 acceptance criteria (Beauheim 2003). Calibrated T fields that meet the acceptance criteria are
 12 modified for the partial and full mining scenarios. This modification increases transmissivity by
 13 a random factor between 1 and 1000 in areas identified as containing potash reserves, as
 14 described below. Steady-state flow simulations are then run using the mining-modified T fields.

15 Because radionuclide transport calculations are performed using a grid with uniform cells of $50 \times$
 16 50 m, the final step in the flow simulation is to run MODFLOW with a 50×50 m grid to
 17 calculate the flow fields required for the transport code. The hydraulic conductivities for the
 18 finer grid are obtained by dividing each 100×100 m cell used in the T field calculations into
 19 four 50×50 m cells. The conductivity assigned to each of the four cells is equal to the
 20 conductivity of the larger cell (Leigh, Beauheim, and Kanney 2003).

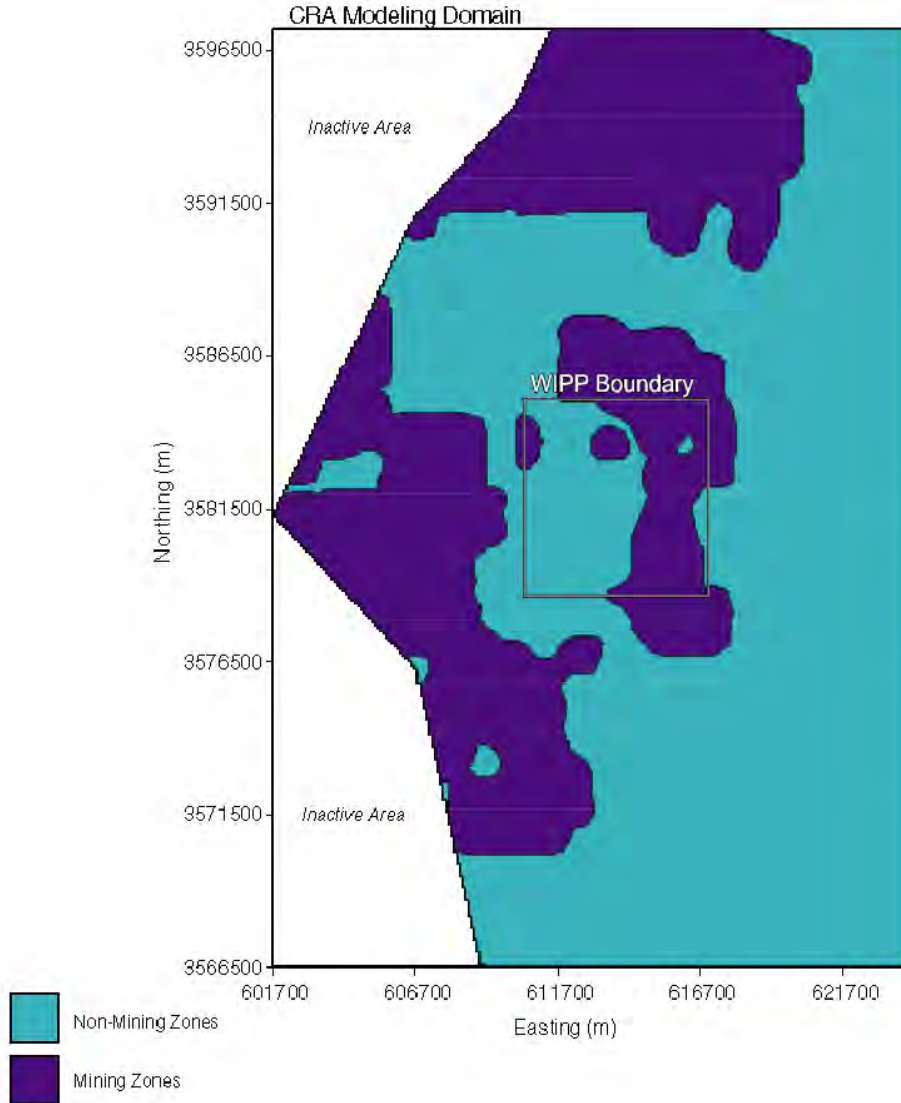
21 The hydraulic conductivity $k(x, y)$ in Equation (PA.257) is defined in terms of the T fields $T(x, y)$
 22 by

$$23 \quad k(x, y) = T(x, y) / b \quad (\text{PA.259})$$

24 Fluid flow is determined (using MODFLOW to solve Equation (PA.258)) for two different
 25 cases: (1) a partial mining case (mining of potash deposits outside the LWB), and (2) a full
 26 mining case (mining of potash deposits inside and outside the LWB) (Figure PA-31; see Lowry
 27 and Kanney 2005, Section 3.2.5 for more details). As specified by guidance in 40 CFR Part 194,
 28 potash mining increases the Culebra's hydraulic conductivity in the vicinity of such mining by an
 29 uncertain factor with a value between 1 and 1000. As specified in section 194.32 and described
 30 in Section PA-3.9, economic potash reserves outside the LWB are assumed to have been fully
 31 mined by the end of the 100-year period of AICs, after which the occurrence of potash mining
 32 within the LWB follows a Poisson process with a rate constant of $\lambda_m = 1 \times 10^{-4} \text{ yr}^{-1}$.

33 In the partial mining case, the hydraulic conductivity $k_{PM}(x, y)$ is defined by Equation (PA.259)
 34 inside the WIPP boundary and by $k_{PM}(x, y) = k(x, y) \times MF$ outside the WIPP boundary, where
 35 MF is determined by the uncertain parameter CTRANSFM (see Table PA-19). In the full
 36 mining case, the hydraulic conductivity is defined by $k_{FM}(x, y) = k(x, y) \times MF$ in all areas of the
 37 modeling domain.

38 In turn, $k_{PM}(x, y)$ and $k_{FM}(x, y)$ result in the following definition for the hydraulic conductivity
 39 tensor \mathbf{K} :



1
2 **Figure PA-31. Areas of Potash Mining in the McNutt Potash Zone**

3
$$\mathbf{K}_i(x, y) = k_i(x, y) \begin{bmatrix} 1 & 0 \\ 0 & 1 \end{bmatrix}, \quad i = PM, FM \quad (\text{PA.260})$$

4 In the analysis, Equation (PA.258) is solved with each of the preceding definitions of \mathbf{K}_i to
5 obtain characterizations of fluid flow in the Culebra for partially-mined conditions and fully
6 mined conditions.

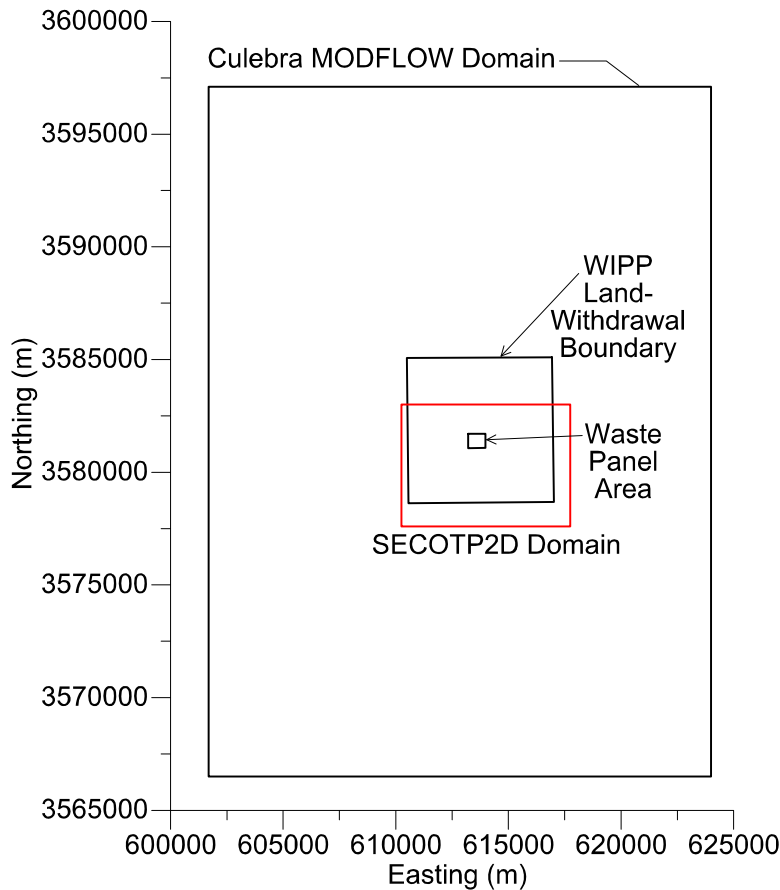
7 The determination of fluid flow in the Culebra through the solution of Equation (PA.258) does
8 not incorporate the potential effects of climate change on fluid flow. Such effects are
9 incorporated into the analysis by an uncertain scale factor to introduce the potential effects of
10 climate change into the analysis (Corbet and Swift 1996a and 1996b). Specifically, the Darcy
11 fluid velocity $v_i(x, y)$ actually used in the radionuclide transport calculations is given by

1
$$\mathbf{v}_i(x, y) = [u_i(x, y), v_i(x, y)] = SFC [\mathbf{K}_i(x, y) \nabla h_i(x, y)]^T, \quad i = PM, FM \quad (\text{PA.261})$$

2 where $u_i(x, y)$ and $v_i(x, y)$ represent Darcy fluid velocities (m/s) at the point (x, y) in the x and y
 3 directions, respectively; $\nabla h_i(x, y)$ is obtained from Equation (PA.258) with $\mathbf{K} = \mathbf{K}_i$; and SFC is a
 4 scale factor used to incorporate the uncertainty that results from possible climate changes. The
 5 scale factor SFC is determined by the uncertain parameter CCLIMSF (see Table PA-19).

6 **PA-4.8.3 Computational Grids and Boundary Value Conditions**

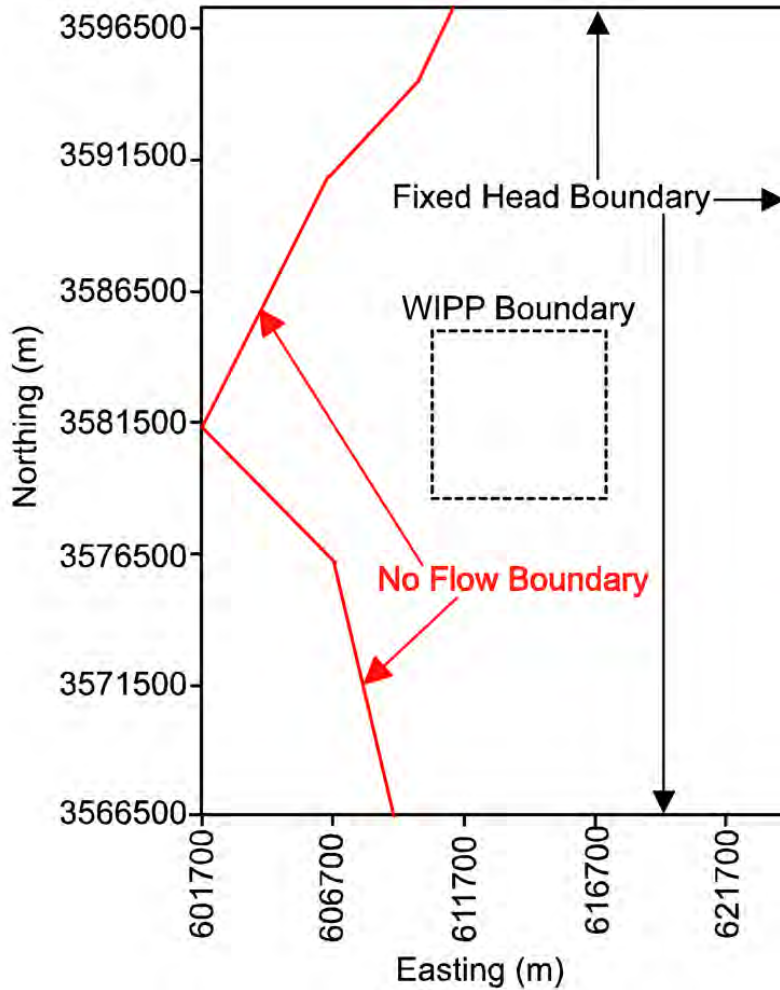
7 The representation for fluid flow in the Culebra in Equation (PA.258) is evaluated on a
 8 numerical grid 22.4 km (13 miles) east-west by 30.7 km (19 miles) north-south, aligned with the
 9 compass directions (Figure PA-32). The modeling domain is discretized into 68,768 uniform
 10 100×100 m cells. The northern model boundary is slightly north of the northern end of Nash
 11 Draw, 12 km (7.4 mi) north of the northern WIPP site boundary, and about 1 km (0.62 miles)
 12 north of Mississippi Potash Incorporated's east tailings pile. The eastern boundary lies in a low-
 13 transmissivity region that contributes little flow to the modeling domain. The southern boundary
 14



15
 16 **Figure PA-32. Modeling Domain for Groundwater Flow (MODFLOW) and Radionuclide**
 17 **Transport (SECOTP2D) in the Culebra**

1 lies 12.2 km (7.5 miles) south of the southern WIPP site boundary, far enough from the WIPP
 2 site to have little effect on transport rates on the site. The western model boundary passes
 3 through the Mosaic (formerly International Minerals and Chemicals) tailings pond (Laguna Uno;
 4 see Hunter [1985]) due west of the WIPP site in Nash Draw.

5 Two types of boundary conditions are specified: constant-head and no-flow (Figure PA-33).
 6 Constant-head conditions are assigned along the eastern boundary of the model domain, and
 7 along the central and eastern portions of the northern and southern boundaries. Values of these
 8 heads are obtained from a kriged initial head field. The western model boundary passes through
 9 the Mosaic tailings pond (Laguna Uno) due west of the WIPP site in Nash Draw. A no-flow
 10 boundary (a flow line) is specified in the model from this tailings pond up the axis of Nash Draw
 11 to the northeast, reflecting the concept that groundwater flows down the axis of Nash Draw,
 12 forming a groundwater divide. Similarly, another no-flow boundary is specified from the
 13 tailings pond down the axis of the southeastern arm of Nash Draw to the southern model
 14 boundary, coinciding with a flow line in the regional modeling of Corbet and Knupp (1996).
 15



16
 17 **Figure PA-33. Boundary Conditions Used for Simulations of Brine Flow in the Culebra**

1 Thus, the northwestern and southwestern corners of the modeling domain are specified as
2 inactive cells in MODFLOW.

3 **PA-4.8.4 Numerical Solution**

4 The flow model in Equation (PA.258) is evaluated on the computational grid described in
5 Section PA-4.8.3 using MODFLOW 2000 (Harbaugh et al. 2000). MODFLOW discretizes the
6 flow equation with a second-order difference procedure (McDonald and Harbaugh 1988, p. 126).
7 Specifically, the discretized form of Equation (PA.258) is

$$8 \quad 0 = CR_{i,j-1/2} (h_{i,j-1} - h_{i,j}) + CR_{i,j+1/2} (h_{i,j+1} - h_{i,j}) \\ 9 \quad + CC_{i-1/2,j} (h_{i-1,j} - h_{i,j}) + CC_{i+1/2,j} (h_{i+1,j} - h_{i,j}) \quad (\text{PA.262})$$

10 where CR and CC are the row and column hydraulic conductances at the cell interface between
11 node i, j and a neighboring node (m^2/s). Since the grid is uniform, the hydraulic conductance is
12 simply the harmonic mean of the hydraulic conductivity in the two neighboring cells multiplied
13 by the aquifer thickness. For example, the hydraulic conductance between cells (i, j) and $(i, j -$
14 $1)$ is given by $CR_{i,j-1/2}$, and the hydraulic conductance between cells (i, j) and $(i + 1, j)$ is given
15 by $CC_{i+1/2,j}$:

$$16 \quad CR_{i,j-1/2} = \frac{2k_{i,j}k_{i,j-1}}{k_{i,j} + k_{i,j-1}} \times b \quad \text{and} \quad CC_{i+1/2,j} = \frac{2k_{i,j}k_{i+1,j}}{k_{i,j} + k_{i+1,j}} \times b$$

17 where $k_{i,j}$ is the hydraulic conductivity in cell i, j (m/s) and b is the aquifer thickness (m).

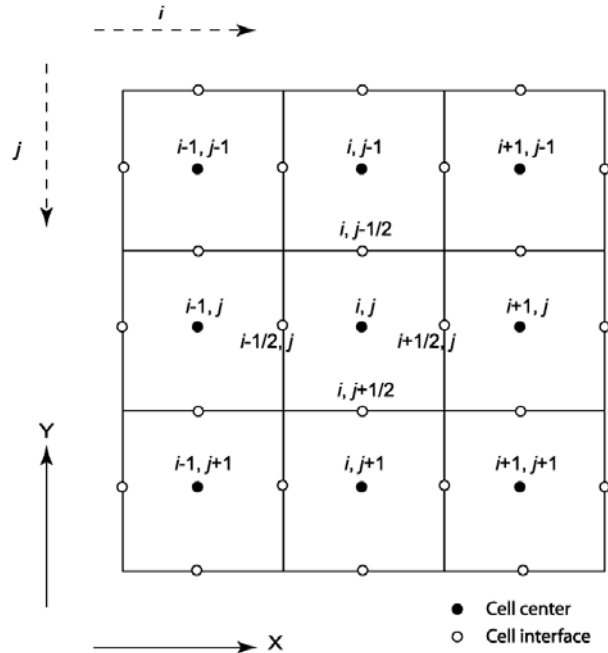
18 Figure PA-34 illustrates the cell numbering convention used in the finite-difference grid for
19 MODFLOW. The determination of h is then completed by the solution of the linear system of
20 equations in Equation (PA.262) for the unknown heads $h_{i,j}$. Fluxes at cell interfaces are
21 calculated from the values for $h_{i,j}$ internally in MODFLOW.

22 **PA-4.8.5 Additional Information**

23 Additional information on MODFLOW and its use in WIPP PA to determine fluid flow in the
24 Culebra can be found in the MODFLOW-2000 user's manual (Harbaugh et al. 2000) and in
25 McKenna and Hart (2003), Lowry (2003), and Lowry and Kanney (2005). Calculation of the
26 flow fields used in the CRA-2009 PA is presented in Lowry and Kanney (2005).

27 **PA-4.9 Radionuclide Transport in the Culebra Dolomite**

28 Extensive laboratory and field investigations have focused on the physical mechanisms
29 influencing transport in the Culebra, as well as the behavior of dissolved and colloidal actinides
30 in the Culebra. Field tests have shown that the Culebra is best characterized as a double-porosity
31



1
2 **Figure PA-34. Finite-Difference Grid Showing Cell Index Numbering Convention Used by**
3 **MODFLOW**

4 medium when estimating radionuclide transport in groundwater. Groundwater flow and
5 advective transport of dissolved or colloidal species and particles occur primarily in a small
6 fraction of the rock's total porosity corresponding to the porosity of open and interconnected
7 fractures and vugs. Diffusion and (much slower) advective flow occur in the remainder of the
8 porosity, which is associated with the low-permeability dolomite matrix. Transported species,
9 including actinides, if present, will diffuse into this porosity.

10 Diffusion from the advective porosity into the dolomite matrix will retard An transport by two
11 mechanisms. Physical retardation occurs simply because actinides that diffuse into the matrix
12 are no longer transported with the flowing groundwater, so transport is interrupted until they
13 diffuse back into the advective porosity. In situ tracer tests have been conducted to demonstrate
14 this phenomenon (Meigs, Beauheim, and Jones 2000). Chemical retardation also occurs within
15 the matrix as actinides are sorbed onto dolomite grains. The relationship between sorbed and
16 liquid concentrations is assumed to be linear and reversible. The distribution coefficients (K_{ds})
17 that characterize the extent to which actinides will sorb on dolomite are based on experimental
18 data. After their review of the CCA, the EPA required the DOE to use the same ranges, but to
19 change the distribution from uniform to loguniform. The DOE continues to use the EPA's
20 distributions in the CRA-2009 PA.

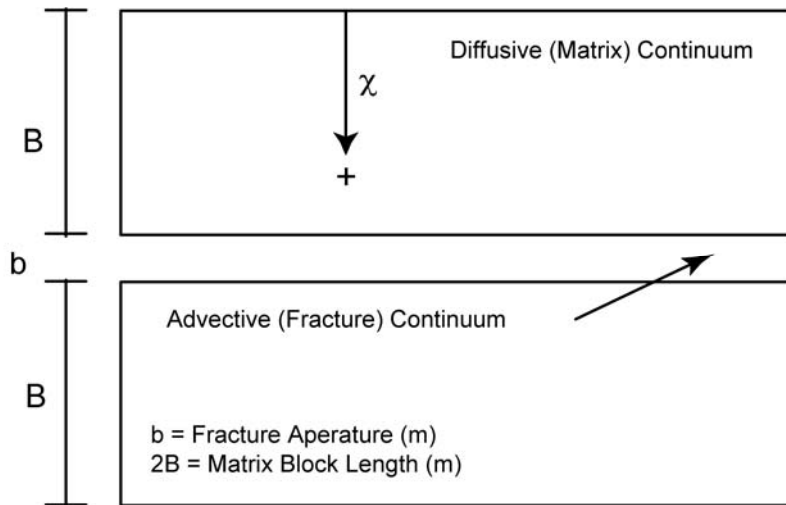
21 Modeling, supported by field tests and laboratory experiments, indicates that physical and
22 chemical retardation will be extremely effective in reducing the transport of dissolved actinides
23 in the Culebra. Experimental work has demonstrated that transport of colloidal actinides is not a
24 significant mechanism in the Culebra. As a result, An transport through the Culebra to the
25 subsurface boundary of the controlled area is not a significant pathway for releases from the
26 WIPP. As discussed in Section PA-9.0, the location of the mean CCDF that demonstrates

1 compliance with the containment requirements of section 191.13 is determined almost entirely
 2 by direct releases at the ground surface during drilling (cuttings, cavings, and spillings).

3 Radionuclide transport in the Culebra is computed using the SECOTP2D computer code (WIPP
 4 Performance Assessment 1997b). The mathematical equations solved by SECOTP2D and the
 5 numerical methods used in the code are described in the following sections.

6 **PA-4.9.1 Mathematical Description**

7 Radionuclide transport in the Culebra is described by a parallel-plate, dual-porosity model
 8 (Meigs and McCord 1996). The parallel-plate, dual-porosity conceptualization assumes that the
 9 numerous fractures within the formation are aligned in a parallel fashion and treats the fractured
 10 porous media as two overlapping continua: one representing the fractures and the other
 11 representing the surrounding porous rock matrix (see Figure PA-35). In this model, one system
 12 of PDEs is used to represent advective transport in fractures within the Culebra and another PDE
 13 system is used to represent diffusive transport and sorption in the matrix that surrounds the
 14 fractures.



15
 16 **Figure PA-35. Parallel-Plate, Dual-Porosity Conceptualization**

17 **PA-4.9.1.1 Advective Transport in Fractures**

18 The PDE system used to represent advective transport in fractures is given by (WIPP
 19 Performance Assessment 1997b)

20
$$\nabla \cdot [\phi \mathbf{D}_k \nabla C_k - \mathbf{v} C_k] = \phi R_k \left(\frac{\partial C_k}{\partial t} \right) + \phi R_k \lambda_k C_k - \phi R_{k-1} \lambda_{k-1} C_{k-1} - Q_k - \Gamma_k, \quad (\text{PA.263})$$

21 for $k = 1, 2, \dots, nR$, where

22 nR = number of radionuclides under consideration

23 C_k = concentration of radionuclide k in brine (kg/m^3)

- 1 \mathbf{D}_k = hydrodynamic dispersion tensor (m²/s)
- 2 \mathbf{v} = Darcy velocity (i.e., specific discharge) of brine (m/s = (m³/m²)/s)
- 3 ϕ = advective (i.e., fracture) porosity (dimensionless)
- 4 R_k = advective retardation coefficient (dimensionless)
- 5 λ_k = decay constant for radionuclide k (s⁻¹)
- 6 Q_k = injection rate of radionuclide k per unit bulk volume of formation ((kg/s)/m³) (Note:
- 7 $Q_k > 0$ corresponds to injection into the fractures)
- 8 Γ_k = mass transfer rate of radionuclide k per unit bulk volume of formation due to
- 9 diffusion between fractures and surrounding matrix ((kg/s)/m³) (Note: $\Gamma_k > 0$
- 10 corresponds to diffusion into fractures)

11 The Darcy velocity v is obtained from the solution of Equation (PA.258); specifically, v is
 12 defined by the relationship in Equation (PA.261). The advective porosity ϕ , defined as the ratio
 13 of the interconnected fracture pore volume to the total volume, is determined by an uncertain
 14 parameter (see CFRCPOR in Table PA-19).

15 The hydrodynamic dispersion tensor is defined by (WIPP Performance Assessment 1997b; Bear
 16 1972)

$$17 \quad \mathbf{D}_k = \frac{1}{\|\mathbf{v}\|\phi} \begin{bmatrix} u & -v \\ v & u \end{bmatrix} \begin{bmatrix} \alpha_L & 0 \\ 0 & \alpha_T \end{bmatrix} \begin{bmatrix} u & v \\ -v & u \end{bmatrix} + \tau D_k^* \begin{bmatrix} 1 & 0 \\ 0 & 1 \end{bmatrix} \quad (\text{PA.264})$$

18 where α_L and α_T are the longitudinal and transverse dispersivities (m); u and v are the x and y
 19 components of \mathbf{v} (i.e., $\mathbf{v} = [u, v]$); \mathbf{D}_k^* is the free water molecular diffusion coefficient (m² s⁻¹)
 20 for radionuclide k ; and τ is the advective tortuosity, defined as the ratio of the true length of the
 21 flow path of a fluid particle to the straight-line distance between the starting and finishing points
 22 of the particle's motion. As in the CCA PA (Helton et al. 1998), the CRA-2009 PA uses $\alpha_L = \alpha_T$
 23 = 0 m and $\tau = 1$. Thus, the definition of \mathbf{D}_k used in PA reduces to

$$24 \quad \mathbf{D}_k = \mathbf{D}_k^* \begin{bmatrix} 1 & 0 \\ 0 & 1 \end{bmatrix} \quad (\text{PA.265})$$

25 The diffusion coefficients, D^*k , for the oxidation states of the radionuclides under consideration
 26 are shown in Table PA-18 (see Fox 2008, Table 35). The existence of Pu in the (III) or (IV)
 27 oxidation state (i.e., as Pu(III) or Pu(IV)) and the existence of U in the (IV) or (VI) oxidation
 28 state (i.e., as U(IV) or U(VI)) is determined by an uncertain parameter (see WOXSTAT in Table
 29 PA-19).

30 **Table PA-18. Radionuclide Culebra Transport Diffusion Coefficients**

Oxidation State	III	IV	VI
Diffusion Coefficient (m ² /s)	3.00 × 10 ⁻¹⁰	1.53 × 10 ⁻¹⁰	4.26 × 10 ⁻¹⁰

31

1 **Table PA-19. Variables Representing Epistemic Uncertainty in the CRA-2009 PA**

Material	Property	Name	Description
AM+3	MKD_AM	CMKDAM3	Matrix distribution coefficient (m^3/kg) for Am in the III oxidation state. Defines K_{dk} in Equation (PA.271).
BH_SAND	PRMX_LOG	BHPERM	Logarithm of intrinsic permeability (m^2) of the silty-sand-filled borehole (Table PA-7). Used in regions Upper Borehole and Lower Borehole in Figure PA-15.
BOREHOLE	DOMEGA	DOMEGA	Drill string angular velocity (rad/s). Defines $\Delta\Omega$ in Equation (PA.133).
BOREHOLE	TAUFAIL	WTAUFAIL	Shear strength of waste (Pa). Defines $\tau(R, 1)$ in Equation (PA.131).
CASTILER	COMP_RCK	BPCOMP	Bulk compressibility (Pa^{-1}) of Castile brine reservoir. Defines c_{fB} in Equation (PA.35) for region CASTILER of Figure PA-15.
CASTILER	PRESSURE	BPINTPRS	Initial brine pore pressure in the Castile brine reservoir (region CASTILER in Figure PA-15).
CASTILER	PRMX_LOG	BPPRM	Logarithm of intrinsic permeability (m^2) of the Castile brine reservoir. Used in region CASTILER in Figure PA-15.
CELLULS	FBETA	FBETA	Factor beta for microbial reaction rates.
CONC_PCS	PORE_DIS	CONBCEXP	Brooks-Corey pore distribution parameter (dimensionless) for panel closure concrete (Section PA-4.2.8.1). Defines λ in Equation (PA.38), Equation (PA.39), and Equation (PA.40) for region CONC_PCS of Figure PA-15 for use with Brooks-Corey model; defines λ in $m = \lambda/(1 + \lambda)$ in Equation (PA.44), Equation (PA.45), and Equation (PA.46) for use with van Genuchten-Parker model in region CONC_PCS.
CONC_PCS	PRMX_LOG	CONPRM	Logarithm of intrinsic permeability (m^2) for the concrete portion of the panel closure (Section PA-4.2.8.1). Used in region CONC_PCS in Figure PA-15.
CONC_PCS	SAT_RBRN	CONBRSAT	Residual brine saturation (dimensionless) in panel closure concrete (Section PA-4.2.8.1). Defines S_{br} in Equation (PA.43) for use in region CONC_PCS in Figure PA-15.
CONC_PCS	SAT_RGAS	CONGSSAT	Residual gas saturation (dimensionless) in panel closure concrete (Section PA-4.2.8.1). Defines S_{gr} in Equation (PA.43) for area CONC_PCS in Figure PA-15.
CONC_PLG	PRMX_LOG	PLGPRM	Logarithm of intrinsic permeability (m^2) of the concrete borehole plugs (Table PA-7). Used in region Borehole Plugs in Figure PA-15.
CULEBRA	APOROS	CFRACPOR	Culebra fracture (i.e., advective) porosity (dimensionless). Defines ϕ in Equation (PA.263).
CULEBRA	DPOROS	CMTRXPOR	Culebra matrix (i.e., diffusive) porosity (dimensionless). Defines ϕ' in Equation (PA.270).

2
3

**Table PA-19. Variables Representing Epistemic Uncertainty in the CRA-2009 PA
(Continued)**

Material	Property	Name	Description
CULEBRA	HMBLKLT	CFRACSP	Culebra fracture spacing (m). Equal to half the distance between fractures (i.e., the Culebra half-matrix-block length). Defines B in Equation (PA.276) and Figure PA-34.
CULEBRA	MINP_FAC	CTRANSFM	Multiplier (dimensionless) applied to transmissivity of the Culebra within the LWB after mining of potash reserves. Defines MF in Equation (PA.256) (see Section PA-4.8.2).
DRZ_1	PRMX_LOG	DRZPRM	Logarithm of intrinsic permeability (m^2) of the DRZ. Used in regions Upper DRZ and Lower DRZ in Figure PA-15.
DRZ_PCS	PRMX_LOG	DRZPCPRM	Logarithm of intrinsic permeability (m^2) of the DRZ immediately above the panel closure concrete (Section PA-4.2.8.3). Used in region DRZ_PCS in Figure PA-15.
GLOBAL	CLIMITDX	CCLIMSF	Climate scale factor (dimensionless) for Culebra flow field. Defines SFC in Equation (PA.261).
GLOBAL	OXSTAT	WOXSTAT	Indicator variable for elemental oxidation states (dimensionless). $WOXSTAT \leq 0.5$ indicates radionuclides in lower oxidation states. $WOXSTAT > 0.5$ indicates radionuclides in higher oxidation states.
GLOBAL	PBRINE	BPPROB	Probability that a drilling intrusion penetrates pressurized brine in the Castile. Defines pB_1 ; see Section PA-3.6.
GLOBAL	TRANSIDX	CTRAN	Indicator variable for selecting T field. See Section PA-4.8.2.
PHUMOX3	PHUMCIM	WPHUMOX3	Ratio (dimensionless) of concentration of actinides attached to humic colloids to dissolved concentration of actinides for oxidation state III in Castile brine. Defines $SF_{Hum}(\text{Castile}, +3, \text{Am})$ and $SF_{Hum}(\text{Castile}, +3, \text{Pu})$ for Equation (PA.103).
PU(III)	MKD_PU	CMKDPU3	Matrix distribution coefficient (m^3/kg) for Pu in III oxidation state. Defines K_{dk} in Equation (PA.271).
PU(IV)	MKD_PU	CMKDPU4	Matrix distribution coefficient (m^3/kg) for Pu in IV oxidation state. Defines K_{dk} in Equation (PA.271).
S_HALITE	COMP_RCK	HALCOMP	Bulk compressibility of halite (Pa^{-1}). Defines c_r in Equation (PA.37) for Salado region of Figure PA-15.
S_HALITE	POROSITY	HALPOR	Halite porosity (dimensionless). Defines ϕ_0 in Equation (PA.30) for Salado region in Figure PA-15.
S_HALITE	PRESSURE	SALPRES	Initial brine pore pressure (Pa) in the Salado halite, applied at an elevation consistent with the intersection of MB 139. Defines $p_{b,ref}$ for Equation (PA.55) for Salado region in Figure PA-15.
S_HALITE	PRMX_LOG	HALPRM	Logarithm of intrinsic halite permeability (m^2). Used in region Salado in Figure PA-15.

**Table PA-19. Variables Representing Epistemic Uncertainty in the CRA-2009 PA
(Continued)**

Material	Property	Name	Description
S_MB139	PORE_DIS	ANHBCEXP	Brooks-Corey pore distribution parameter for anhydrite (dimensionless). Defines λ in Equation (PA.38), Equation (PA.39), and Equation (PA.40) for regions MB 138, Anhydrite AB, and MB 139 of Figure PA-15 for use with Brooks-Corey model; defines λ in $m = \lambda/(1 + \lambda)$ in Equation (PA.44), Equation (PA.45), and Equation (PA.46) for use with van Genuchten-Parker model in the same regions.
S_MB139	PRMX_LOG	ANHPRM	Logarithm of intrinsic anhydrite permeability (m^2). Used in regions MB 138, Anhydrite AB, and MB 139 in Figure PA-15.
S_MB139	RELP_MOD	ANHBCVGP	Indicator for relative permeability model (dimensionless) for regions MB 138, Anhydrite AB, and MB 139 in Figure PA-15. See Table PA-4.
S_MB139	SAT_RBRN	ANRBRSAT	Residual brine saturation in anhydrite (dimensionless). Defines S_{br} in Equation (PA.43) for regions MB 138, Anhydrite AB, and MB 139 in Figure PA-15.
SHFTL_T1	PRMX_LOG	SHLPRM2	Logarithm of intrinsic permeability (m^2) of lower shaft-seal materials for the first 200 years after closure. Used in Lower Shaft region in Figure PA-15.
SHFTL_T2	PRMX_LOG	SHLPRM3	Logarithm of intrinsic permeability (m^2) of lower shaft-seal materials from 200 years to 10,000 years after closure. Used in Lower Shaft region in Figure PA-15.
SHFTU	PRMX_LOG	SHUPRM	Logarithm of intrinsic permeability (m^2) of upper shaft-seal materials. Used in Upper Shaft region in Figure PA-15.
SHFTU	SAT_RBRN	SHURBRN	Residual brine saturation in upper shaft-seal materials (dimensionless). Defines S_{br} in Equation (PA.43) for Upper Shaft region in Figure PA-15.
SHFTU	SAT_RGAS	SHURGAS	Residual gas saturation in upper shaft-seal materials (dimensionless). Defines S_{gr} in Equation (PA.42) for Upper Shaft region in Figure PA-15.
SOLMOD3	SOLVAR	WSOLVAR3	Solubility multiplier (dimensionless) for III oxidation states. Used by ALGEBRA prior to PANEL (Section PA-4.4, Garner and Leigh 2005).
SOLMOD4	SOLVAR	WSOLVAR4	Solubility multiplier (dimensionless) for IV oxidation states. Used by ALGEBRA prior to PANEL (Section PA-4.4, Garner and Leigh 2005).
SPALLMOD	PARTDIAM	SPLPTDIA	Particle diameter of waste (m) after tensile failure, implemented by parameter SPALLMOD/PARTDIAM. Loguniform distribution from 0.001 to 0.1 (m). Defines d_p in Equation (PA.186).
SPALLMOD	REPIPERM	REPIPERM	Waste permeability of gas (m^2) local to intrusion borehole. Defines k in Equation (PA.168).
SPALLMOD	REPIPOR	SPLRPOR	Waste porosity (dimensionless) at time of drilling intrusion. Defines ϕ in Equation (PA.167).

Table PA-19. Variables Representing Epistemic Uncertainty in the CRA-2009 PA (Continued)

Material	Property	Name	Description
SPALLMOD	TENSLSTR	TENSLSTR	Tensile strength (Pa) of waste. Defines $\bar{\sigma}_r$ in Section PA-4.6.2.3.4.
STEEL	CORRMCO2	WGRCOR	Rate of anoxic steel corrosion (m/s) under brine-inundated conditions with no CO ₂ present. Defines R_{ci} in Equation (PA.68) for areas Waste Panel, South RoR, and North RoR in Figure PA-15.
TH(IV)	MKD_TH	CMKDTH4	Matrix distribution coefficient (m ³ /kg) for Th in IV oxidation state. Defines K_{dk} in Equation (PA.271).
U(IV)	MKD_U	CMKDU4	Matrix distribution coefficient (m ³ /kg) for U in IV oxidation state. Defines K_{dk} in Equation (PA.271).
U(VI)	MKD_U	CMKDU6	Matrix distribution coefficient (m ³ /kg) for U in VI oxidation state. Defines K_{dk} in Equation (PA.271).
WAS_AREA	BIOGENFC	WBIOGENF	Probability of obtaining sampled microbial gas generation rates.
WAS_AREA	GRATMICH	WGRMICH	Rate of CPR biodegradation (mol C ₆ H ₁₀ O ₅ / kg C ₆ H ₁₀ O ₅ /s) under anaerobic, humid conditions. Defines R_{mi} in Equation (PA.70) for areas Waste Panel, South RoR, and North RoR in Figure PA-15.
WAS_AREA	GRATMICI	WGRMICI	Rate of CPR biodegradation (mol C ₆ H ₁₀ O ₅ / kg C ₆ H ₁₀ O ₅ /s) under anaerobic, brine-inundated conditions. Defines R_{mi} in Equation (PA.70) for areas Waste Panel, South RoR, and North RoR in Figure PA-15.
WAS_AREA	PROBDEG	WMICDFLG	Index for model of CPR material microbial degradation (dimensionless). Used in Waste Panel, South RoR, and North RoR areas in Figure PA-15.
WAS_AREA	SAT_RBRN	WRBRNSAT	Residual brine saturation in waste (dimensionless). Defines S_{br} in Equation (PA.42) for Waste Panel, South RoR, and North RoR areas in Figure PA-15; also used in waste material in Figure PA-28 for DBR calculation; see Section PA-4.7.
WAS_AREA	SAT_RGAS	WRGSSAT	Residual gas saturation in waste (dimensionless). Defines S_{gr} in Equation (PA.43) for Waste Panel, South RoR, and North RoR areas in Figure PA-15; also used in waste material in Figure PA-28 for DBR calculation; see Section PA-4.7.
WAS_AREA	SAT_WICK	WASTWICK	Increase in brine saturation of waste due to capillary forces (dimensionless). Defines S_{wick} in Equation (PA.90) for Waste Panel, South RoR, and North RoR areas in Figure PA-15.

- 1
- 2 The advective retardation coefficient R_k is defined by
- 3
- $$R_k = 1 + (1 - \phi) \rho_A K_{Ak} / \phi \quad (\text{PA.266})$$

1 where

2 ρ_A = surface area density of fractures in Culebra ($m^2/m^3 = 1/m$) (i.e., surface area of
3 fractures (m^2) divided by volume of fractures (m^3))

4 K_{Ak} = surface area distribution coefficient ($(kg/m^2)/(kg/m^3) = m$) (i.e., concentration of
5 radionuclide k sorbed on fracture surfaces (kg/m^2) divided by concentration of
6 radionuclide k dissolved in brine within fractures (kg/m^3))

7 Following the logic used in the CCA (Helton et al. 1998), $K_{Ak} = 0$ and thus $R_k = 1$ are used in the
8 PA.

9 In concept, the term Q_k in Equation (PA.263) provides the link between the releases to the
10 Culebra calculated with NUTS and PANEL (Section PA-6.7) and transport within the Culebra.
11 In the computational implementation of PA, radionuclide transport calculations in the Culebra
12 were performed for unit radionuclide releases to the Culebra, and the outcomes of these
13 calculations were used to construct the release to the accessible environment associated with
14 time-dependent releases into the Culebra derived from NUTS and PANEL calculations (Section
15 PA-6.8.3). The definition of Q_k is discussed in more detail in Section PA-4.9.1.4.

16 The initial condition for Equation (PA.263) is

17
$$C_k(x, y, 0) = 0 \text{ kg/m}^3 \quad (\text{PA.267})$$

18 Furthermore, the boundary value conditions for Equation (PA.263) are defined at individual
19 points on the boundary of the grid in Figure PA-32 on the basis of whether the flow vector $v =$
20 $[u, v]$ defines a flow entering the grid or leaving the grid. The following Neumann boundary
21 value condition is imposed at points (x, y) where flow leaves the grid:

22
$$\nabla C_k(x, y, t) \cdot n(x, y) = 0 \text{ (kg/m}^3\text{)}/m^3 \quad (\text{PA.268})$$

23 where $n(x, y)$ is an outward-pointing unit normal vector defined at (x, y) . The following Dirichlet
24 boundary value condition is imposed at points (x, y) where flow enters the grid:

25
$$C_k(x, y, t) = 0 \text{ kg/m}^3 \quad (\text{PA.269})$$

26 **PA-4.9.1.2 Diffusive Transport in the Matrix**

27 The system of PDEs used to represent diffusive transport in the matrix surrounding the fractures
28 is given by (WIPP Performance Assessment 1997b)

29
$$\frac{\partial}{\partial \chi} \left(\phi'_k D'_k \frac{\partial C'_k}{\partial \chi} \right) = \phi'_k R'_k \left(\frac{\partial C'_k}{\partial t} \right) + \phi'_k R'_k \lambda_k C'_k - \phi'_k R'_{k-1} \lambda_{k-1} C'_{k-1} \quad (\text{PA.270})$$

30 where χ is the spatial coordinate in Figure PA-35, D'_k is the matrix diffusion coefficient (m^2/s)
31 for radionuclide k defined by $D'_k = D_k^* \tau'$, and τ' is the matrix tortuosity. The remaining terms

1 have the same meaning as those in Equation (PA.263), except that the prime denotes properties
 2 of the matrix surrounding the fractures. A constant value ($\tau' = 0.11$) for the matrix (i.e.,
 3 diffusive) tortuosity is used in PA (Meigs 1996). The matrix (i.e., diffusive) porosity ϕ' is an
 4 uncertain input to the analysis (see CMTRXPOR in Table PA-19). The matrix retardation R'_k is
 5 defined by

$$6 \quad R'_k = 1 + (1 - \phi') \rho_s K_{dk} / \phi' \quad (\text{PA.271})$$

7 where ρ_s is the particle density (kg/m^3) of the matrix and K_{dk} is the distribution coefficient
 8 ($(\text{Ci/kg})/(\text{Ci/m}^3) = \text{m}^3/\text{kg}$) for radionuclide k in the matrix. The density ρ_s is assigned a value of
 9 $2.82 \times 10^3 \text{ kg/m}^3$ (Martell 1996b). The distribution coefficients K_{dk} are uncertain inputs to the
 10 analysis and dependent on the uncertain oxidation state of the relevant element (see CMKDAM3,
 11 CMKDPU3, CMKDPU4, CMKDTH4, CMKDU4, CMKDU6, and WOXSTAT in Table PA-19).

12 The initial and boundary value conditions used in the formulation of Equation (PA.270) are

$$13 \quad C'_k(x, y, \chi, 0) = 0 \text{ kg/m}^3 \quad (\text{PA.272})$$

$$14 \quad \partial C'_k(x, y, 0, t) / \partial z = 0 \text{ kg/m}^2 \quad (\text{PA.273})$$

$$15 \quad C'_k(x, y, B, t) = C_k(x, y, t) \quad (\text{PA.274})$$

16 where (x, y) corresponds to a point in the domain on which Equation (PA.263) is solved and B is
 17 the matrix half-block length (m) in Figure PA-35 (i.e., $2B$ is the thickness of the matrix between
 18 two fractures). The initial condition in Equation (PA.272) means that no radionuclide is present
 19 in the matrix at the beginning of the calculation. The boundary value condition in Equation
 20 (PA.273) implies that no radionuclide movement can take place across the centerline of a matrix
 21 block separating two fractures. The boundary value condition in Equation (PA.274) ensures that
 22 the dissolved radionuclide concentration in the matrix at the boundary with the fracture is the
 23 same as the dissolved radionuclide concentration within the fracture. The matrix half-block
 24 length B is an uncertain input to the analysis (see CFRACSP in Table PA-19).

25 PA-4.9.1.3 Coupling Between Fracture and Matrix Equations

26 The linkage between Equation (PA.263) and Equation (PA.270) is accomplished through the
 27 term Γ_k , defining the rate at which radionuclide k diffuses across the boundary between a
 28 fracture and the adjacent matrix (see Figure PA-35). Specifically,

$$29 \quad \Gamma_k = -\frac{2\phi}{b} \left(\phi' D'_k \frac{\partial C'_k}{\partial \chi} \Big|_{z=\chi} \right) \quad (\text{PA.275})$$

30 where b is the fracture aperture (m) defined by

$$1 \qquad b = \phi B(1 - \phi) \qquad \text{(PA.276)}$$

2 **PA-4.9.1.4 Source Term**

3 As already indicated, Equation (PA.263) and Equation (PA.270) are solved for unit radionuclide
 4 releases to the Culebra. Specifically, a release of 1 kg of each of the four lumped radionuclides
 5 (^{241}Am , ^{234}U , ^{230}Th , and ^{239}Pu) under consideration was assumed to take place over a time
 6 interval from 0 to 50 years, with this release taking place into the computational cell WPAC,
 7 located at the center of the Waste Panel Area in Figure PA-32, that has dimensions of 50 m \times
 8 50 m. The volume of this cell is given by

$$9 \qquad V = (50\text{m})(50\text{m})(4\text{m}) = 1 \times 10^4 \text{ m}^3 \qquad \text{(PA.277)}$$

10 where 4 m is the assumed thickness of the Culebra Dolomite (Meigs and McCord 1996). As a
 11 result, $Q_k(x, y, t)$ has the form

$$12 \qquad Q_k(x, y, t) = \frac{1 \text{ kg}}{(1 \times 10^4 \text{ m}^3)(50 \text{ yr})(3.16 \times 10^7 \text{ s / yr})} = 6.33 \times 10^{-14} \text{ kg / m}^3 / \text{s}$$

13 \qquad \qquad \qquad \text{(PA.278)}

14 for $0 \leq t \leq 50 \text{ yr}$ and (x, y) in cell WPAC, and $Q_k(x, y, t) = 0 \text{ (kg/m}^3/\text{s)}$ otherwise.

15 **PA-4.9.1.5 Cumulative Releases**

16 If B denotes an arbitrary boundary (e.g., the LWB) in the domain of Equation (PA.263) (i.e.,
 17 Figure PA-32), then the cumulative transport of $C_k(t, B)$ of radionuclide k from time 0 to time t
 18 across B is given by

$$19 \qquad C_k(t, B) = \int_0^t \left[\int_B \{v(x, y)C_k(x, y, \tau) - \phi D_k(x, y, t) \nabla C_k(x, y, \tau)\} b \cdot n(x, y) ds \right] d\tau \quad \text{(PA.279)}$$

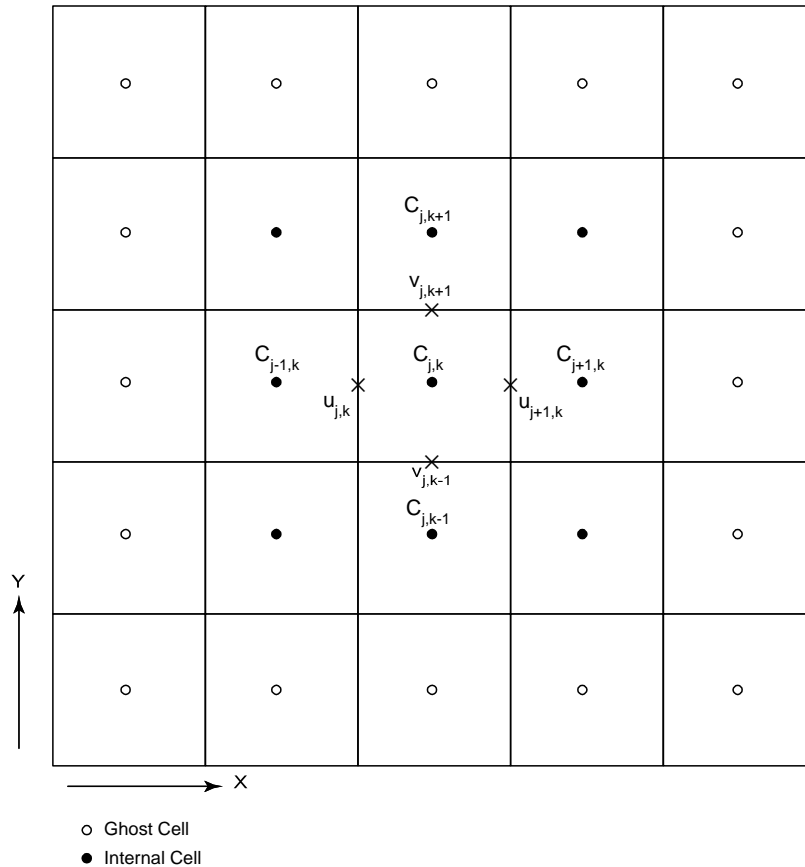
20 where h is the thickness of the Culebra (4 m), ϕ is the advective porosity in Equation (PA.263),
 21 $n(x, y)$ is an outward pointing unit normal vector, and $\int_B ds$ denotes a line integral over B .

22 **PA-4.9.2 Numerical Solution**

23 The numerical solution to the coupled PDE system represented by Equation (PA.263) and
 24 Equation (PA.270) is computed using SECOTP2D, an implicit finite-volume code for the
 25 simulation of multispecies reactive transport. A high-level description of the numerical
 26 procedures implemented in SECOTP2D follows, with more detail available in WIPP
 27 Performance Assessment (1997b).

1 **PA-4.9.2.1 Discretization of Fracture Domain**

2 The fracture domain is discretized in space using the block-centered finite-difference method
 3 indicated in Figure PA-36. In this formulation, cell concentrations are defined at grid block
 4 centers while the velocity components [u , v] are defined on grid cell faces. A uniform mesh with
 5 $50\text{ m} \times 50\text{ m}$ cells is used for the spatial discretization. Ghost cells are placed outside the
 6 problem domain for the purpose of implementing boundary conditions. The temporal
 7 discretization is accomplished using variable time step sizes.



11 The dispersive term, $\nabla \cdot (\phi D_k \nabla C_k)$, in Equation (PA.263) is approximated using a second-order
 12 central difference formula (Fletcher 1988).

13 The advective term, $\nabla \cdot \mathbf{v} C_k$, is approximated using the Total Variation Diminishing (TVD)
 14 method (Sweby 1984). The TVD method provides a way of accurately resolving advection-
 15 dominated transport problems without the occurrence of nonphysical oscillations commonly
 16 present in second-order solutions. This method invokes a weighted upstream differencing
 17 scheme that locally adjusts the weighting to prevent oscillatory behavior and maximize solution
 18 accuracy. The weighting parameters are known as the TVD flux limiters $\Phi(x, y, r)$, where r is a

1 function of the concentration gradient and direction of flow. PA uses the van Leer TVD limiter
 2 (Sweby 1984, p. 1005), which is defined as

$$3 \quad \Phi(x, y, r) = \max \left\{ 0, \min \left\{ 2r, \frac{r + |r|}{1 + |r|} \right\} \right\} \quad (\text{PA.280})$$

4 At locations where u (i.e., the Darcy velocity in the x direction) is positive, r is defined at the
 5 $j-1/2, k$ interface by

$$6 \quad r_{j-1/2,k} = \frac{\partial C / \partial x|_{j-3/2,k}}{\partial C / \partial x|_{j-1/2,k}} \quad (\text{PA.281})$$

7 and at locations where u is negative, r is defined by

$$8 \quad r_{j-1/2,k} = \frac{\partial C / \partial x|_{j+1/2,k}}{\partial C / \partial x|_{j-1/2,k}} \quad (\text{PA.282})$$

9 Similar definitions are made for r at the $j, k-1/2$ interface in the y-direction with v (i.e., the
 10 Darcy velocity in the y direction) used instead of u .

11 Because Φ_k is a function of C_k , the discretized set of equations is nonlinear. This nonlinearity is
 12 addressed by treating the flux limiters explicitly (i.e., time lagged). Explicit treatment of the
 13 limiter functions, however, can lead to oscillatory and sometimes unstable solutions when the
 14 Courant number exceeds unity ($Cr > 1$), where Cr is defined by

$$15 \quad Cr = \max \{ Cr_x, Cr_y \}, \text{ where } Cr_x = |u| \Delta t / \phi \Delta x \text{ and } Cr_y = |v| \Delta t / \phi \Delta y$$

16 (PA.283)

17 To avoid this behavior, the application of the TVD method is restricted to regions in which the
 18 Courant numbers are less than one. In regions where $Cr > 1$, a first-order full upwinding scheme
 19 is invoked, which is unconditionally stable and nonoscillatory.

20 The discretized form of Equation (PA.263) can be expressed in a delta formulation as

$$21 \quad (\mathbf{I} + \mathbf{L}_{xx} + \mathbf{L}_{yy} + \mathbf{S}) \Delta \mathbf{C}^{n+1} = \mathbf{RHS}^n \quad (\text{PA.284})$$

22 where \mathbf{I} is the identity matrix, \mathbf{L}_{xx} and \mathbf{L}_{yy} are finite-difference operators in the x and y
 23 directions, \mathbf{S} is an implicit source term that accounts for decay and mass transfer between the
 24 matrix and the fracture, \mathbf{RHS} consists of the right-hand-side known values at time level n , and
 25 $\Delta \mathbf{C}_{n+1} = \mathbf{C}_{n+1} - \mathbf{C}_n$. Direct inversion of Equation (PA.284) for a typical Culebra transport
 26 problem is very computationally intensive, requiring large amounts of memory and time. To
 27 reduce these requirements, the operator in Equation (PA.284) is factored as follows:

$$(\mathbf{I} + \mathbf{L}_{xx} + \alpha_x \mathbf{S})(\mathbf{I} + \mathbf{L}_{yy} + \alpha_y \mathbf{S})\Delta \mathbf{C}^{n+1} = \mathbf{RHS}^n \quad (\text{PA.285})$$

where α_x and α_y are constants that must sum to one (i.e., $\alpha_x + \alpha_y = 1$). The left-hand sides in Equation (PA.284) and Equation (PA.285) are not equivalent, with the result that the factorization of Equation (PA.284) and Equation (PA.285) is referred to as an approximate factorization (Fletcher 1988). The advantage of approximately factoring Equation (PA.284) is that the resulting equation consists of the product of two finite-difference operators that are easily inverted independently using a tridiagonal solver. Hence, the solution to the original problem is obtained by solving a sequence of problems in the following order:

$$(\mathbf{I} + \mathbf{L}_{xx} + \alpha_x \mathbf{S})\Delta \bar{\mathbf{C}} = \mathbf{RHS}^n \quad (\text{PA.286})$$

$$(\mathbf{I} + \mathbf{L}_{yy} + \alpha_y \mathbf{S})\Delta \mathbf{C}^{n+1} = \Delta \bar{\mathbf{C}} \quad (\text{PA.287})$$

$$\mathbf{C}^{n+1} = \mathbf{C}^n + \Delta \mathbf{C}^{n+1} \quad (\text{PA.288})$$

PA-4.9.2.2 Discretization of Matrix Equation

The nonuniform mesh used to discretize the matrix equation is shown in Figure PA-37. Straightforward application of standard finite-difference or finite-volume discretizations on nonuniform meshes results in truncation error terms that are proportional to the mesh spacing variation (Hirsch 1988). For nonuniform meshes, the discretization can be performed after a transformation from the Cartesian physical space (χ) to a stretched Cartesian computational space (ξ). The transformation is chosen so that the nonuniform grid spacing in physical space is transformed to a uniform spacing of unit length in computational space (the computational space is thus a one-dimensional domain with a uniform mesh). The transformed equations contain metric coefficients that must be discretized, introducing the mesh size influence into the difference formulas. Standard unweighted differencing schemes can then be applied to the governing equations in the computational space.

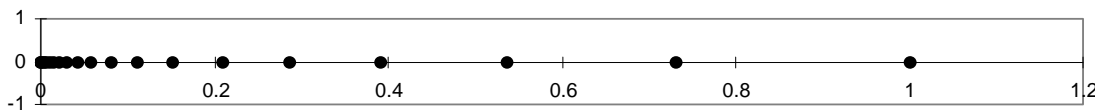


Figure PA-37. Illustration of Stretched Grid Used for Matrix Domain Discretization

The SECOTP2D code applies such a coordinate transformation to the nonuniform diffusion domain mesh, solving the transformed system of equations in the uniform computational space. The transformed matrix equation is written as

$$\phi' R'_k \frac{\partial \hat{C}'_k}{\partial t} - \frac{\partial \hat{F}'_v}{\partial \xi'} = -\phi' R'_k \lambda_k \hat{C}'_k + \phi' R'_{k-1} \lambda_{k-1} \hat{C}'_{k-1} \quad (\text{PA.289})$$

where

$$1 \quad \hat{C}'_k = \frac{C'_k}{J} \quad (\text{PA.290})$$

$$2 \quad \hat{F}'_v = D'_{\xi_x} \frac{\partial C'_k}{\partial \xi'} \quad (\text{PA.291})$$

3 In the uniform computational space, a first-order backwards difference formula is used to
 4 approximate the temporal derivative, while a second-order accurate central difference is used to
 5 approximate spatial derivatives.

6 **PA-4.9.2.3 Fracture-Matrix Coupling**

7 The equations for the fracture and the matrix are coupled through the mass transfer term, Γ_k . In
 8 the numerical solution, these equations are coupled in a fully implicit manner and solved
 9 simultaneously. A procedure outlined in Huyakorn, Lester, and Mercer (1983) was adapted and
 10 redeveloped for an approximate factorization algorithm with the delta formulation and a finite-
 11 volume grid. The coupling procedure consists of three steps:

12 Step 1. Write the mass transfer term Γ_k in a delta (Δ) form.

13 Step 2. Evaluate Δ terms that are added to the implicit part of the fracture equation. This is
 14 accomplished using the inversion process (LU factorization) in the solution of the matrix
 15 equation. After the construction of the lower tridiagonal matrix L and the intermediate
 16 solution, there is enough information to evaluate the Δ terms. This new information is
 17 fed into the fracture equation that is subsequently solved for concentrations in the
 18 fracture at the new time level ($n+1$).

19 Step 3. Construct the boundary condition for the matrix equation at the fracture-matrix interface
 20 using fracture concentrations at the ($n+1$) time level. Matrix concentrations are then
 21 obtained using the upper tridiagonal matrix U by back substitution. A detailed
 22 description of this technique and its implementation is given in the SECOTP2D user's
 23 manual (WIPP Performance Assessment 1997b).

24 **PA-4.9.2.4 Cumulative Releases**

25 The cumulative transport $C_k(t, B)$ of individual radionuclides across specified boundaries
 26 indicated in Equation (PA.279) is also accumulated during the numerical solution of Equation
 27 (PA.263) and Equation (PA.270).

28 **PA-4.9.3 Additional Information**

29 Because neither the Culebra flow fields nor the random seed used in LHS sampling have been
 30 changed from the CRA-2004 PABC, the radionuclide transport calculations from the CRA-2004
 31 PABC were used in the CRA-2009 PA. Additional information on SECOTP2D and its use to
 32 determine radionuclide transport in the Culebra can be found in the SECOTP2D user's manual

- 1 (WIPP Performance Assessment 1997b) and in the CRA-2004 PABC analysis package for
- 2 radionuclide transport in the Culebra Dolomite (Lowry and Kanney 2005).

1 PA-5.0 Probabilistic Characterization of Subjective Uncertainty

2 This section summarizes the treatment of uncertainty in the CRA-2009 PA parameters. This
3 uncertainty gives rise to the epistemic uncertainty in the CCDFs defined in Section PA-2.2.4.

4 PA-5.1 Probability Space

5 As discussed in Section PA-2.2.4, the statement of confidence in the CCDFs of releases from the
6 CRA-2009 PA is based on a probabilistic characterization of the uncertainty in important input
7 parameters to the analysis. The probability distribution for each parameter is based on all
8 available knowledge about the parameter, including measurements, and describes a degree of
9 belief as to the appropriate range of the parameter value. This degree of belief depends on the
10 numerical, spatial, and temporal resolution of the models selected for use in PA (Section PA-
11 4.0). Correlations and other dependencies between imprecisely known variables are also
12 possible. These relationships represent observed or logical dependencies between the possible
13 parameter values.

14 The probability space that characterizes epistemic uncertainty can be represented as $(\mathcal{S}_{su}, \mathbb{S}_{su},$
15 $p_{su})$. The subscript su indicates that epistemic (i.e., subjective) uncertainty is being considered;
16 the letters su are retained for historical context. The individual elements of \mathcal{S}_{su} are vectors \mathbf{v}_{su} of
17 the form

$$18 \quad \mathbf{v}_{su} = [v_1, v_2, \dots, v_{nv}] \quad (\text{PA.292})$$

19 where each v_j is an imprecisely known input to the analysis, and nv is the number of such inputs.

20 The uncertainty in the v_j , and hence in \mathbf{v}_{su} , is characterized by developing a distribution

$$21 \quad D_j, \quad j = 1, 2, \dots, nv \quad (\text{PA.293})$$

22 for each v_j . Each distribution is based on available knowledge about the corresponding variable
23 and describes a degree of belief as to the appropriate range of this variable. This degree of belief
24 depends on the numerical, spatial, and temporal resolution of the models selected for use in PA
25 (Section PA-4.0). When appropriate, correlations between imprecisely known variables are also
26 possible, indicating a dependency in the knowledge about the correlated variables. It is the
27 distributions in Equation (PA.292) and any associated correlations between the v_j that define
28 $(\mathcal{S}_{su}, \mathbb{S}_{su}, p_{su})$.

29 The uncertain parameters incorporated into the CRA-2009 PA are discussed in Section PA-5.2,
30 and the distributions and correlations assigned to these variables are described in Section PA-5.3
31 and Section PA-5.4. Finally, a discussion of the concept of a scenario is given in Section PA-
32 5.5.

1 **PA-5.2 Variables Included for Subjective Uncertainty**

2 The CRA-2009 PA identified 56 imprecisely known variables for inclusion in the analysis (Table
3 PA-19). Most of the variables listed in Table PA-19 were also treated as uncertain in the CRA
4 2004. Table PA-20 and Table PA-21 list the additions and removals between the sets of
5 uncertain parameters in the CRA-2004 PA and the CRA-2009 PA, that resulted from changes
6 made for the CRA-2004 PABC. All subjectively uncertain variables incorporated into the
7 CRA-2009 PA are used as input to the models discussed in Section PA-2.2.3 and Section PA-
8 4.0.

9 **Table PA-20. Sampled Parameters Added Since the CRA-2004 PA**

Material	Property
SOLMOD3	SOLVAR
SOLMOD4	SOLVAR
WAS_AREA	BIOGENFC

10

11 **Table PA-21. Sampled Parameters Removed Since the CRA-2004 PA**

Material	Property
SOLU4	SOLCIM
SOLTH4	SOLCIM
S_MB139	COMP_RCK
S_MB139	SAT_RGAS
SOLAM3	SOLSIM
SOLAM3	SOLCIM
SOLPU3	SOLSIM
SOLPU3	SOLCIM
SOLPU4	SOLSIM
SOLPU4	SOLCIM
SOLU4	SOLSIM
SOLU6	SOLSIM
SOLU6	SOLCIM
SOLTH4	SOLSIM
SPALLMOD	RNDSPALL

12

13 **PA-5.3 Variable Distributions**

14 Each uncertain variable is assigned a distribution that characterizes the subjective uncertainty in
15 that variable. Distributions for each parameter are described in Fox (2008), which also contains
16 documentation for each of the 56 parameters sampled by the LHS code during the PA.

1 **PA-5.4 Correlations and Dependencies**

2 Most of the variables in Table PA-19 are assumed to be uncorrelated. However, the pairs
 3 (S_HALITE:PRMX_LOG, S_HALITE:COMP_RCK), and (CASTILER:PRMX_LOG,
 4 CASTILER:COMP_RCK) are assumed to have rank correlations of -0.99 and -0.75,
 5 respectively (Figure PA-38 and Figure PA-39). These correlations result from a belief that the
 6 underlying physics imply that a large value for one variable in a pair should be associated with a
 7 small value for the other variable in the pair. The scatterplots in Figure PA-38 and Figure PA-39
 8 result from the Replicate 1 samples generated by the LHS code and described in Section PA-6.4,
 9 with the rank correlations within the pairs induced with the Iman and Conover (1982) restricted
 10 pairing technique.

11 A conditional relationship had previously been enforced between WAS_AREA:GRATMICH
 12 and WAS_AREA:GRATMICI using ALGEBRA prior to running the BRAGFLO code (Nemer
 13 and Stein 2005). This relationship was implemented by setting WAS_AREA:GRATMICH to the
 14 value of WAS_AREA:GRATMICI if WAS_AREA:GRATMICH exceeded WAS_AREA:
 15 GRATMICI in any particular sample of parameter values (vector). Changing these values in this
 16 way introduced a small error into the sensitivity analysis for WAS_AREA:GRATMICH because
 17 the regression analysis was based on the sampled values rather than the conditional values used
 18 in the code. For the CRA-2009 PA, it was assumed that WAS_AREA:GRATMICH was
 19 uniformly distributed between 0 and the minimum of either 1.02717E-9 (the upper bound of the
 20 uniform distribution specified in the parameter database for the variable) or the value selected for
 21 WAS_AREA:GRATMICI. The sampled value of WAS_AREA:GRATMICH was rescaled from
 22 the range 0 to 1.02717E-9 to the new range using the equation

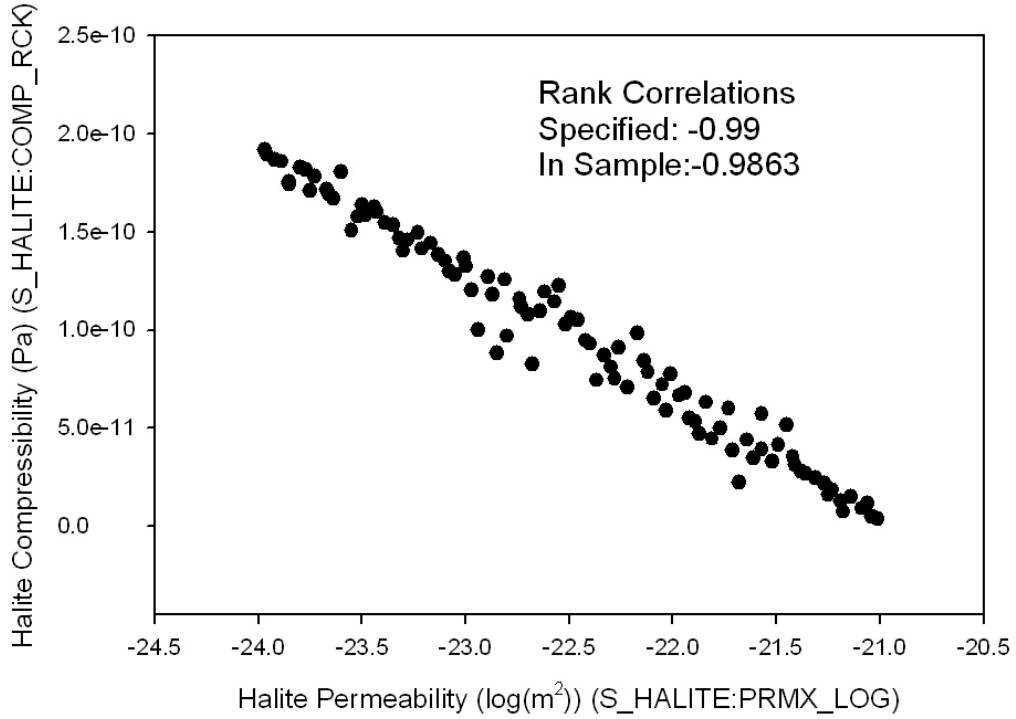
23
$$v'_i = \frac{v_i - U_{V,lower}}{U_{V,upper} - U_{V,lower}} \times (\min(x_i, U_{V,upper}) - U_{V,lower}) + U_{V,lower} \quad (PA.294)$$

24 where v'_i is the conditioned value of WAS_AREA:GRATMICH, v_i is the sampled value of
 25 WAS_AREA:GRATMICH, x_i is the sampled value of WAS_AREA:GRATMICI, and $U_{V,lower}$
 26 and $U_{V,upper}$ are the bounds of the uniform distribution assigned to WAS_AREA:GRATMICH
 27 (Figure PA-40). This method preserves the quantile associated with the value of
 28 WAS_AREA:GRATMICH. The nature of the correlation is fundamentally different than that
 29 which LHS could induce between the variables: if, instead of limiting the value of
 30 WAS_AREA:GRATMICH, a correlation had been specified between the variables in the input
 31 file to LHS, then LHS would have generated values for WAS_AREA:GRATMICH that
 32 exceeded the corresponding value for WAS_AREA:GRATMICI.

33 The distributions and associated dependencies indicated in Table PA-19 and Figure PA-38,
 34 Figure PA-39, and Figure PA-40 define the epistemic uncertainty described in Section PA-2.2.4.
 35 The set of sampled parameters constitutes a vector, \mathbf{v}_{su} , of the form

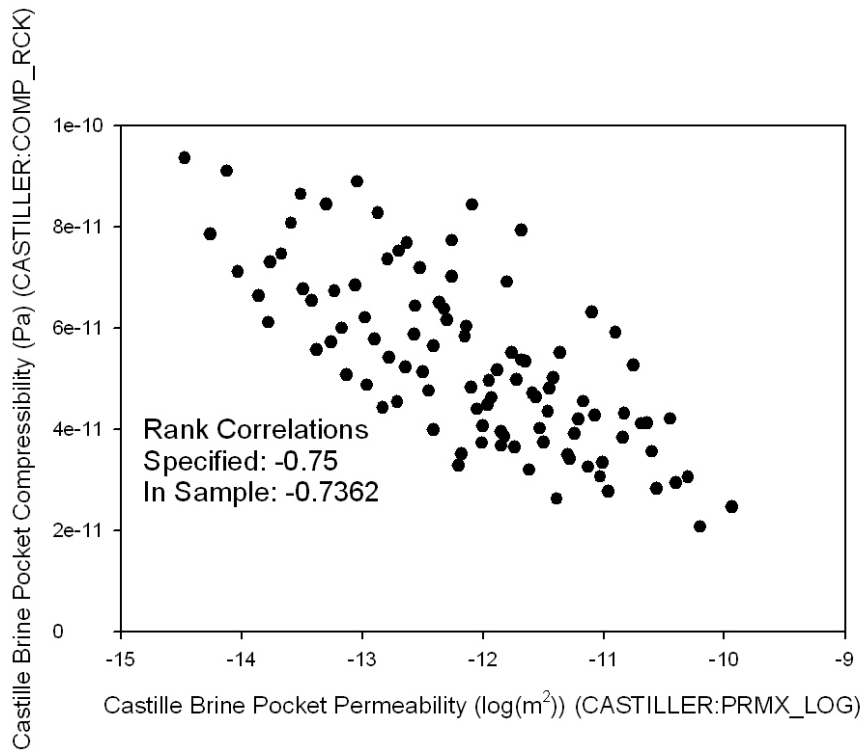
36
$$\mathbf{v}_{su} = [\text{ANHBCEXP, ANHBCVGP, ..., WTAUFAIL}] \quad (PA.295)$$

37 where the individual elements of \mathbf{v}_{su} are the subjectively uncertain variables described in Table
 38 PA-19.



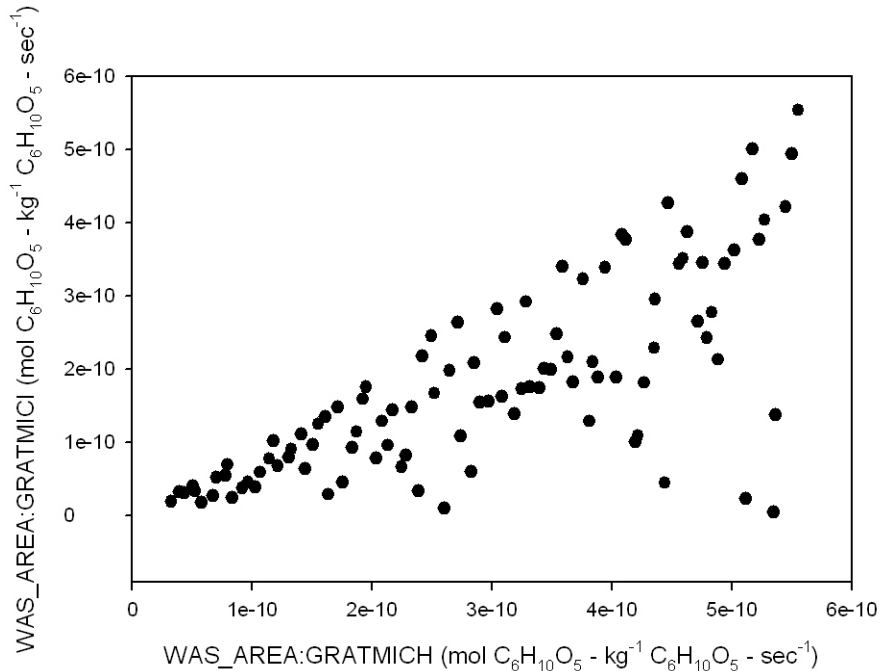
1
2
3

Figure PA-38. Correlation Between S_HALITE:PRMX_LOG and S_HALITE:COMP_RCK



4
5
6

Figure PA-39. Correlation between CASTILLER:PRMX_LOG and CASTILLER:COMP_RCK



1

2 **Figure PA-40. Dependency between WAS_AREA:GRATMICI and**
 3 **WAS_AREA:GRATMICH**

4 **PA-5.5 Separation of Aleatory and Epistemic Uncertainty**

5 PA uses the term *scenario* to refer to specific types of events within the sample space for
 6 aleatory uncertainty (E0, E1, E2, or E1E2; see Section PA-3.10). This definition is consistent
 7 with the concept that a scenario is something that could happen in the future. To maintain the
 8 important distinction between the two sample spaces, subsets of the sample space for subjective
 9 uncertainty are not referred to as scenarios. A future contains events of the form defined in
 10 Equation (PA.2) and is associated with a probability, one that characterizes the likelihood that a
 11 possible future will match the occurrences that will take place at the WIPP over the next 10,000
 12 years. In contrast, the probability associated with a specific vector \mathbf{v}_{su} , i.e., a specific set of
 13 parameter values, characterizes a degree of belief that the vector contains the appropriate values
 14 for the 56 uncertain variables in Table PA-19. This probability represents the impact that
 15 epistemic uncertainty in the parameters has on the distribution of possible futures and is used to
 16 establish confidence in the results.

1 PA-6.0 Computational Procedures

2 This section outlines the computational procedures used to execute the CRA-2009 PA. First, the
3 sampling procedures applied to evaluate performance accounting for epistemic and aleatory
4 uncertainty are outlined. The mechanistic calculations used to evaluate the function $f(\mathbf{x}_{st})$ in
5 Equation (PA.23) are tabulated, followed by a description of the algorithms used to compute
6 releases. This section concludes with a discussion of sensitivity analysis techniques used to
7 identify which uncertain parameters are primary contributors to the uncertainty in the PA results.

8 PA-6.1 Sampling Procedures

9 Extensive use is made of sampling procedures in PA. In particular, simple random sampling is
10 used to generate individual CCDFs (Section PA-2.2.3) and LHS is used to assess the effects of
11 imprecisely known model parameters (Section PA-2.2.4).

12 Using simple random sampling, a possible future, $\mathbf{x}_{st,i,k}$, is thus characterized by the collection of
13 intrusion events occurring in that future (Equation (PA.2)). The subscript st denotes that
14 intrusion is modeled as a stochastic process, the subscript i indicates that the future is one of
15 many possible futures, and the subscript k indicates that the variable set is one of many possible
16 variable sets. The nR sets of values (possible futures) are selected according to the joint
17 probability distribution for the elements of \mathcal{S}_{st} as defined by $(\mathcal{S}_{st}, \mathbb{S}_{st}, p_{st})$. In practice, the joint
18 probability distribution is defined by specifying a distribution D_j for each element x_j of \mathcal{S}_{st} .
19 Points from different regions of the sample space occur in direct relationship to the probability of
20 occurrence of these regions. Furthermore, each sample element is selected independently of all
21 other sample elements. The values selected using simple random sampling provide unbiased
22 estimates for means, variances, and distributions of the variables. The collection of nR samples
23 can be denoted as a vector $\mathbf{x}_{st,k}$:

$$24 \quad \mathbf{x}_{st,k} = \left[\mathbf{x}_{st,1,k}, \mathbf{x}_{st,2,k}, \dots, \mathbf{x}_{st,nR,k} \right] \quad (\text{PA.296})$$

25 The WIPP PA code CCDFGF is used to simulate possible futures based on the values of the
26 variables sampled. These variables control the stochastic processes defined within CCDFGF,
27 such as the time when a drilling intrusion can take place, where that drilling intrusion is located,
28 and whether the drilling intrusion encounters an excavated area. The code CCDFGF is capable
29 of generating and evaluating thousands of possible futures; PA uses a sample size (nR) of 10,000
30 to generate a distribution of possible repository releases. This sample size is sufficient to
31 estimate the 0.999 quantile for the distribution of releases to the accessible environment.

32 LHS is used to sample the parameters for which distributions of epistemic uncertainty were
33 defined to integrate over the probability space for subjective uncertainty $(\mathcal{S}_{su}, \mathbb{S}_{su}, p_{su})$. This
34 technique was first introduced by McKay, Beckman, and Conover (1979). In LHS, the range of
35 each uncertain parameter v_j is divided into $nLHS$ intervals of equal probability and one value is
36 selected at random from each interval. The $nLHS$ values thus obtained for v_1 are paired at
37 random without replacement with the $nLHS$ values obtained for v_2 . These $nLHS$ pairs are
38 combined in a random manner without replacement with the $nLHS$ values of v_3 to form $nLHS$

1 triples. This process is continued until a set of $nLHS$ nV -tuples is formed. These nV -tuples are
 2 of the form

$$3 \quad \mathbf{v}_{su,k} = [v_{k,1}, v_{k,2}, \dots, v_{k,nV}], k = 1, \dots, nLHS \quad (\text{PA.297})$$

4 and constitute the Latin hypercube sample. The individual v_{js} must be independent of each other
 5 for the preceding construction procedure to work; a method for generating Latin hypercube and
 6 random samples from correlated variables was developed by Iman and Conover (1982) and is
 7 used in WIPP PA. For more information about LHS and a comparison with other sampling
 8 techniques, see Helton and Davis (2003).

9 LHS stratifies the sampling to ensure that the sampled values cover the full range of each v_j in
 10 the $nLHS$ samples. LHS provides unbiased estimates for means and distribution functions of each
 11 sampled variable (McKay, Beckman, and Conover 1979). In particular, uncertainty and
 12 sensitivity analysis results obtained with LHS are robust even when relatively small samples
 13 (i.e., $nLHS = 50$ to 200) are used (Iman and Helton 1988 and 1991; Helton et al. 1995).

14 When sampling for both aleatory uncertainty and epistemic uncertainty are considered, the joint
 15 sample space, \mathbf{x} , consists of a vector of $nLHS$ vectors of possible futures:

$$16 \quad \mathbf{x} = [\mathbf{x}_{st,1}, \mathbf{x}_{st,2}, \dots, \mathbf{x}_{st,nLHS}] \quad (\text{PA.298})$$

17 The differences between the $nLHS$ futures are due to the uncertainty in the v_j , i.e. the epistemic
 18 uncertainty in model parameters.

19 **PA-6.2 Sample Size for Incorporation of Subjective Uncertainty**

20 40 CFR § 194.34(d) states that

21 The number of CCDFs generated shall be large enough such that, at cumulative releases of 1 and
 22 10, the maximum CCDF generated exceeds the 99th percentile of the population of CCDFs with at
 23 least a 0.95 probability.

24 For an LHS of size $nLHS$, the preceding guidance is equivalent to the inequality

$$25 \quad 1 - 0.99^{nLHS} > 0.95 \quad (\text{PA.299})$$

26 which results in a minimum value of 298 for $nLHS$. PA uses a total sample size of 300 to
 27 represent the epistemic uncertainty. As discussed in the next section, the 300 samples are
 28 divided among 3 replicates of size 100 each to demonstrate convergence of the mean for the
 29 population of CCDFs.

30 **PA-6.3 Statistical Confidence on Mean CCDF**

31 40 CFR § 194.34(f) states,

1 Any compliance assessment shall provide information which demonstrates that there is at least a
 2 95% level of statistical confidence that the mean of the population of CCDFs meets the
 3 containment requirements of § 191.13 of this chapter.

4 Given that LHS is used, the confidence intervals required by section 194.34(f) are obtained with
 5 a replicated sampling technique proposed by Iman (1982). In this technique, the sampling in
 6 Equation (PA.300) is repeated nS times with different random seeds. These samples lead to a
 7 sequence $\bar{P}_r(R)$, $r = 1, 2, \dots, nS$ of estimated mean exceedance probabilities, where $\bar{P}_r(R)$
 8 defines the mean CCDF obtained for sample r (i.e., $\bar{P}_r(R)$ is the mean probability that a
 9 normalized release of size R will be exceeded; see Section PA-2.2.4) and nS is the number of
 10 independent samples generated with different random seeds. The seed of the random number
 11 generator determines the sequence of the numbers it generates. Then,

$$\bar{P}(R) = \sum_{r=1}^{nS} \bar{P}_r(R) / nS \quad (\text{PA.300})$$

13 and

$$SE(R) = \left\{ \sum_{r=1}^{nS} [\bar{P}_r(R) - \bar{P}(R)]^2 / nS(nS-1) \right\}^{1/2} \quad (\text{PA.301})$$

15 provide an additional estimate of the mean CCDF and an estimate of the standard error ($SE(R)$)
 16 associated with the mean exceedance probabilities. The t-distribution with $nS-1$ degrees of
 17 freedom can be used to place confidence intervals around the mean exceedance probabilities for
 18 individual R values (i.e., around $\bar{P}(R)$). Specifically, the $1-\alpha$ confidence interval is given by
 19 $\bar{P}_r(R) \pm t_{1-\alpha/2} SE(R)$, where $t_{1-\alpha/2}$ is the $1-\alpha/2$ quantile of the t-distribution with $nS-1$ degrees
 20 of freedom (e.g., $t_{1-\alpha/2} = 4.303$ for $\alpha = 0.05$ and $nS = 3$). The same procedure can also be used to
 21 place pointwise confidence intervals around percentile curves. The mean and its standard error
 22 could equally well be computed from one replicate of size 300. However, the use of three
 23 replicates, each with its own random seed, minimizes the impact of any one seed used in random
 24 number generation. The three replicates have also been useful in evaluating the presence of
 25 spurious correlations among parameters and releases in the sensitivity analyses.

26 PA-6.4 Generation of Latin Hypercube Samples

27 The LHS program (WIPP Performance Assessment 1996) is used to produce three independently
 28 generated Latin hypercube samples of size $nLHS = 100$ each, for a total of 300 sample elements.
 29 Each individual replicate is a Latin hypercube sample of the form

$$\mathbf{v}_{su,k} = [v_{k,1}, v_{k,2}, \dots, v_{k,nV}] , k = 1, 2, \dots, nLHS = 100 \quad (\text{PA.302})$$

31 In the context of the replicated sampling procedure described in Section PA-6.2, $nS = 3$
 32 replicates of 100 are used. For notational convenience, the replicates are designated by R1, R2,
 33 and R3.

1 The restricted pairing technique described in Section PA-6.1 is used to induce requested
 2 correlations and also to assure that uncorrelated variables have correlations close to zero. The
 3 variable pairs (S_HALITE:PRMX_LOG, S_HALITE:COMP_RCK) and (CASTILER:
 4 PRMX_LOG, CASTILER:COMP_RCK) are assigned rank correlations of -0.99 and -0.75,
 5 respectively (Section PA-5.4). All other variable pairs are assigned rank correlations of zero.
 6 The restricted pairing technique successfully produces these correlations (Table PA-22 and Table
 7 PA-23). Specifically, the correlated variables have correlations that are close to their specified
 8 values and uncorrelated variables have correlations that are close to zero.

9 **Table PA-22. Correlation Observed Between Variables S_HALITE:PRMX_LOG and**
 10 **S_HALITE:COMP_RCK in Replicate 1. A Value of -0.99 was Specified.**

	CONC_PCS: SAT_RGAS	CONC_PCS: SAT_RBRN	CONC_PCS: PORE_DIS	S_HALITE: POROSITY	S_HALITE: PRMX_LOG
CONC_PCS: SAT_RGAS	1.0000	-	-	-	-
CONC_PCS: SAT_RBRN	-0.0156	1.0000	-	-	-
CONC_PCS: PORE_DIS	0.0547	-0.0943	1.0000	-	-
S_HALITE:POROSITY	-0.0177	-0.0160	-0.0743	1.0000	-
S_HALITE:PRMX_LOG	-0.0022	0.0287	-0.0094	-0.0409	1.0000
S_HALITE:COMP_RCK	0.0119	-0.0249	-0.0066	0.0248	-0.9863

11
 12 **Table PA-23. Correlation Observed Between Variables CASTILER:PRMX_LOG and**
 13 **CASTILER:COMP_RCK in Replicate 1. A Value of -0.75 was Specified.**

	CASTILER: PRMX_LOG	CASTILER: COMP_RCK	BH_SAND: PRMX_LOG	DRZ_1: PRMX_LOG
CASTILER: PRMX_LOG	1.0000	-	-	-
CASTILER: COMP_RCK	-0.7362	1.0000	-	-
BH_SAND: PRMX_LOG	0.0365	-0.0414	1.0000	-
DRZ_1: PRMX_LOG	-0.0292	0.0630	0.0081	1.0000

14
 15 The code LHS_EDIT (Kirchner 2008a) was used to enforce a conditional relationship between
 16 WAS_AREA:GRATMICH and WAS_AREA:GRATMICI in the LHS transfer file, thus making
 17 the conditioned values available for use in the sensitivity analysis (Section PA-5.4). This code
 18 rescaled the sampled value of WAS_AREA:GRATMICH from the range 0 to 1.02717E-9 to the
 19 new range using the equation

20
$$v'_i = \frac{v_i - U_{V,lower}}{U_{V,upper} - U_{V,lower}} \times (\min(x_i, U_{V,upper}) - U_{V,lower}) + U_{V,lower} \quad (\text{PA.303})$$

21 where v'_i is the conditioned value of WAS_AREA:GRATMICH, v_i is the sampled value of
 22 WAS_AREA:GRATMICH, x_i is the sampled value of WAS_AREA:GRATMICI, and $U_{V,lower}$

1 and $U_{V,upper}$ are the bounds of the uniform distribution assigned to WAS_AREA:GRATMICH.
 2 This method preserves the cumulative probability associated with the original sampled value of
 3 WAS_AREA:GRATMICH.

4 **PA-6.5 Generation of Individual Futures**

5 Simple random sampling (Section PA-6.1) is used to generate 10,000 possible futures that are
 6 then used to construct CCDFs of potential releases. Table PA-24 outlines the algorithm used to
 7 generate a single future in PA.

8 **Table PA-24. Algorithm to Generate a Single Future**

1.	<p>Sample $t_{i,1}$ with a time dependent λ_d given by</p> $\lambda_d(t) = \begin{cases} 0 & \text{if } 0 \leq t \leq t_A \\ \lambda_d & \text{if } t > t_A \end{cases}$ <p>where $t_A = 100$ yr (i.e., time at which administrative control ends) and $\lambda_d = 3.68 \times 10^{-3} \text{ yr}^{-1}$ (see Section PA-3.3). The index i is the number of the future and 1 represents the first intrusion event.</p>
2.	Sample $e_{i,l}$ with a probability of $p[E_0] = 0.797$ that the intrusion will be in an unexcavated area and a probability of $p[E_1] = 0.203$ that the intrusion will be in an excavated area (see Section PA-3.4).
3.	Sample $l_{i,j}$ with a probability of $p[L_j] = 6.94 \times 10^{-3}$ for each of the $j = 1, 2, \dots, 144$ nodes in Figure PA-14 (see Section PA-3.5).
4.	Sample $b_{i,l}$ with a probability of $p[B_1]$ that the intrusion will penetrate pressurized brine (see Section PA-3.6). $p[B_1]$ is sampled from a uniform distribution ranging from 0.01 to 0.60.
5.	Sample $p_{i,l}$ with probabilities of $p[PL_1] = 0.015$, $p[PL_2] = 0.696$, and $p[PL_3] = 0.289$ that plugging pattern 1, 2, or 3, respectively, will be used (see Section PA-3.7).
6.	Sample $\mathbf{a}_{i,l}$ (see Section PA-3.8).
6.1	Penetration of nonexcavated area (i.e., $e_{i,l} = 0$): $\mathbf{a}_{i,l} = a_{i,l} = 0$.
6.2	Penetration of excavated area (i.e., $e_{i,l} = 1$): Sample to determine if intrusion penetrates RH-TRU or CH-TRU waste with probabilities of $p[RH] = 0.124$ and $p[CH] = 0.876$ of penetrating RH-TRU and CH-TRU waste, respectively.
6.3	Penetration of RH-TRU waste: $\mathbf{a}_{i,l} = a_{i,l} = 1$.
6.4	Penetration of CH-TRU waste: Use probabilities $p[CH_j]$ of intersecting waste stream j , $j = 1, 2, \dots, 690$, (see Fox 2005) to independently sample three intersected waste streams iCH_{11} , iCH_{12} , iCH_{13} (i.e., each of iCH_{11} , iCH_{12} , iCH_{13} is an integer between 1 and 690). Then, $\mathbf{a}_{i,l} = [2, iCH_{11}, iCH_{12}, iCH_{13}]$.
7.	Repeat Steps 1 – 6 to determine properties (i.e., $t_{i,j}$, $e_{i,j}$, $l_{i,j}$, $b_{i,j}$, $p_{i,j}$, $\mathbf{a}_{i,j}$) of the j^{th} drilling intrusion.
8.	Continue until $t_{n+1} > 10,000$ yr; the n intrusions thusly generated define the drilling intrusions associated with $\mathbf{x}_{st,i}$.
9.	<p>Sample t_{min} with a time dependent λ_m given by</p> $\lambda_m(t) = \begin{cases} 0 & \text{if } 0 \leq t \leq t_A \\ \lambda_m & \text{if } t > t_A \end{cases}$ <p>where $t_A = 100$ yr and $\lambda_m = 1 \times 10^{-4} \text{ yr}^{-1}$ (see Section PA-3.9).</p>

9

1 For each vector of the LHS sample, a total of $nS = 10,000$ individual futures of the form

$$2 \quad \mathbf{x}_{st,i} = \left[\left(t_{i,1}, e_{i,1}, l_{i,1}, b_{i,1}, p_{i,1}, \mathbf{a}_{i,1} \right), \left(t_{i,2}, e_{i,2}, l_{i,2}, b_{i,2}, p_{i,2}, \mathbf{a}_{i,2} \right), \right. \\ \left. \dots, \left(t_{i,n}, e_{i,n}, l_{i,n}, b_{i,n}, p_{i,n}, \mathbf{a}_{i,n} \right), t_{i,min} \right], i = 1, 2, \dots, nR = 10,000 \quad (\text{PA.304})$$

3 are generated in the construction of all CCDFs for that LHS vector. As 300 LHS vectors are
4 used in the analysis and 10,000 futures are sampled for each LHS vector, the total number of
5 futures used in the analysis for CCDF construction is 3×10^6 .

6 The drilling rate λ_d is used to generate the times at which drilling intrusions occur. For a Poisson
7 process with a constant λ_d (i.e., a stationary process), the cumulative distribution function (CDF)
8 for the time Δt between the successive events is given by (Ross 1987, p. 113)

$$9 \quad \text{prob}(t \leq \Delta t) = 1 - \exp(-\lambda_d \Delta t) \quad (\text{PA.305})$$

10 A uniformly distributed random number r_1 is selected from $[0, 1]$. Then, solution of

$$11 \quad r_1 = 1 - \exp(-\lambda_d t_1) \quad (\text{PA.306})$$

12 for t_1 gives the time of the first drilling intrusion. An initial period of 100 years of administrative
13 control is assumed; thus 100 years is added to the t_1 obtained in Equation (PA.306) to obtain the
14 time of the first drilling intrusion. Selecting a second random number r_2 and solving

$$15 \quad r_2 = 1 - \exp(-\lambda_d \Delta t_1) \quad (\text{PA.307})$$

16 for Δt_1 gives the time interval between the first and second drilling intrusions, with the outcome
17 that $t_2 = t_1 + \Delta t_1$. This process continues until t_{n+1} exceeds 10,000 years. The times t_1, t_2, \dots, t_n
18 then constitute the drilling times in that possible future..

19 The mining time t_{min} is sampled in a manner similar to the drilling times. Additional uniformly
20 distributed random numbers from $[0,1]$ are used to generate the elements $e_j, l_j, b_j, p_j, \mathbf{a}_j$ of $\mathbf{x}_{st,i}$
21 from their assigned distributions (see Section PA-2.2.2).

22 PA-6.6 Construction of CCDFs

23 In PA, the sampling of individual futures (Section PA-6.5) and associated CCDF construction is
24 carried out by the CCDFGF program (WIPP Performance Assessment 2003b). The sampled
25 futures $\mathbf{x}_{st,i}$ in Equation (PA.304) are used to construct CCDFs for many different quantities
26 (e.g., cuttings and cavings releases, spallings releases, DBRs, etc.). The construction process is
27 the same for each quantity. For notational convenience, assume that the particular quantity under
28 consideration can be represented by a function $f(\mathbf{x}_{st,i})$, with the result that 10,000 values

1
$$f(\mathbf{x}_{st,i}), i = 1, 2, \dots, 10,000 \tag{PA.308}$$

2 are available for use in CCDF construction. Formally, the resultant CCDF is defined by the
 3 expression in Equation (PA.3). In practice, the desired CCDF is obtained after ordering $f(\mathbf{x}_{st,i})$
 4 from smallest to largest or largest to smallest, as described below.

5 PA uses a binning procedure in CCDF construction to simplify sorting the individual $f(\mathbf{x}_{st,i})$ and
 6 to reduce the number of plot points. Specifically, the range of $f(\mathbf{x}_{st,i})$ is divided into intervals
 7 (i.e., bins) by the specified points

8
$$f_{min} = b_0 < b_1 < b_2 < \dots < b_n = f_{max} \tag{PA.309}$$

9 where f_{min} is the minimum value of $f(\mathbf{x}_{st,i})$ to be plotted (typically 10^{-6} or 10^{-5} for an EPA-
 10 normalized release), f_{max} is the maximum value of f to be plotted (typically 100 for an EPA-
 11 normalized release), n is the number of bins in use, and the b_i are typically loguniformly
 12 distributed with 20 values per order of magnitude. A counter nB_j is used for each interval $[b_{j-1}, b_j]$.
 13 All counters are initially set to zero. Then, as individual values $f(\mathbf{x}_{st,i})$ are generated, the
 14 counter nB_j is incremented by 1 when the inequality

15
$$b_{j-1} < f(\mathbf{x}_{st,i}) \leq b_j \tag{PA.310}$$

16 is satisfied. When necessary, f_{max} is increased in value so that the inequality $f(\mathbf{x}_{st,i}) < f_{max}$ will
 17 always be satisfied. Once the 10,000 values for $f(\mathbf{x}_{st,i})$ have been generated, a value of nB_j exists
 18 for each interval $[b_{j-1}, b_j]$. The quotient

19
$$pB_j = nB_j / 10,000 \tag{PA.311}$$

20 provides an approximation to the probability that $f(\mathbf{x}_{st,i})$ will have a value that falls in the interval
 21 $[b_{j-1}, b_j]$. The resultant CCDF is then defined by the points

22
$$(b_j, prob(value > b_j)) = \left(b_j, \sum_{k=j+1}^n pB_k \right) \tag{PA.312}$$

23 for $j = 0, 1, 2, \dots, n-1$, where $prob(value > b_j)$ is the probability that a value greater than b_j will
 24 occur.

25 The binning technique produces histograms that are difficult to read when multiple CCDFs
 26 appear in a single plot. As the number of futures is increased and the bins are refined, the
 27 histogram CCDF should converge to a continuous CCDF as additional points are used in its
 28 construction. The continuous CCDF is approximated by drawing diagonal lines from the left end
 29 of one bin to the left end of the next bin.

30 When multiple CCDFs appear in a single plot, the bottom of the plot becomes very congested as
 31 the individual CCDFs drop to zero on the abscissa. For this reason, each CCDF stops at the
 32 largest observed consequence value among the 10,000 values calculated for that CCDF.

1 Stopping at the largest consequence value, rather than the left bin boundary of the bin that
 2 contains this value, permits the CCDF to explicitly show the largest observed consequence.
 3 Because a sample size of 10,000 is used in the generation of CCDFs for comparison with the
 4 EPA release limits, the probability corresponding to the largest observed consequence is
 5 typically 10^{-4} ; Figure PA-6 shows an example of CCDFs from the CRA-2009 PA.

6 **PA-6.7 Mechanistic Calculations**

7 In the CRA-2009 PA, calculations were performed with the models described in Section PA-4.0
 8 for selected elements of S_{st} (see Section PA-3.10), and the results were used to determine the
 9 releases to the accessible environment for the large number (i.e., 10,000) of randomly sampled
 10 futures used to estimate individual CCDFs. The same set of mechanistic calculations was
 11 performed for each LHS element. This section summarizes the calculations performed with each
 12 of the models described in Section PA-4.0; Section PA-6.8 outlines the algorithms used to
 13 construct releases for the randomly sampled elements $\mathbf{x}_{st,i}$ of S_{st} from the results of the
 14 mechanistic calculations. Long (2008) documents execution of the calculations and archiving of
 15 calculation results.

16 **PA-6.7.1 BRAGFLO Calculations**

17 The BRAGFLO code (Section PA-4.2) computes two-phase (brine and gas) flow in and around
 18 the repository. BRAGFLO results are used as initial conditions in the models for Salado
 19 transport (implemented in NUTS and PANEL), spillings (implemented in CUTTINGS_S), and
 20 DBR (also calculated by BRAGFLO). Thus, the BRAGFLO scenarios are used to define
 21 scenarios for other codes.

22 The four fundamental scenarios for the CRA-2009 PA (Section PA-3.10) define four categories
 23 of calculations to be performed with BRAGFLO (i.e., E0, E1, E2, and E1E2). These four
 24 fundamental scenarios were expanded into six general scenarios by specifying the time of
 25 drilling intrusions. Table PA-25 summarizes the specific scenarios used in the CRA-2009 PA.
 26 A total of 6 scenarios $\times nR \times nLHS = 6 \times 3 \times 100 = 1,800$ BRAGFLO calculations were
 27 conducted for the CRA-2009 PA.

28 **Table PA-25. BRAGFLO Scenarios in the CRA-2009 PA**

Fundamental Scenario (Section PA-3.10)	Specific Scenario	Time of Drilling Intrusion(s)
E0: no drilling intrusions.	S1	N/A
E1: single intrusion into excavated area ($e_1 = 1$), pressurized brine is penetrated ($b_1 = 1$), and Plugging Pattern 2 is used ($p_1 = 2$).	S2	350 years
	S3	1,000 years
E2: single intrusion into excavated area ($e_1 = 1$), pressurized brine is penetrated ($b_1 = 1$) and Plugging Pattern 3 is used ($p_1 = 3$), or pressurized brine is not penetrated ($b_1 = 0$).	S4	350 years
	S5	1,000 years
E1E2: two intrusions into the same waste panel ($e_1 = e_2 = 1$), the first being an E2 intrusion and the second being an E1 intrusion.	S6	1,000 years for E2 intrusion 2,000 years for E1 intrusion

29

1 Values for the activity level \mathbf{a}_1 and mining time t_{min} are not needed for the mechanistic
2 calculations; these values are used in the construction of the releases from the results of the
3 mechanistic calculations (Section PA-6.8). Although a value for drilling location l_1 is not
4 specified, a drilling location is required for the BRAGFLO calculations. If equivalent grids were
5 used in the definition of $\mathbf{x}_{st,i}$ (Figure PA-14) and in the numerical solution of the PDEs on which
6 BRAGFLO is based (Figure PA-15), the location of the drilling intrusion used in the BRAGFLO
7 calculations could be specified as a specific value for l_1 , which in turn would correspond to one
8 of the 144 locations in Figure PA-14 designated by l in the definition of $\mathbf{x}_{st,i}$. However, as these
9 grids are not the same, a unique pairing between a value for l_1 and the location of the drilling
10 intrusion used in the computational grid employed with BRAGFLO is not possible. The
11 BRAGFLO computational grid divides the repository into a lower waste panel (Waste Panel
12 area), a middle group of four waste panels (South RoR area), and an upper group of five waste
13 panels (North RoR area), with the drilling intrusion taking place through the center of the lower
14 panel (Figure PA-15). Thus, in the context of the locations in Figure PA-14 potentially indexed
15 by l_1 , the drilling intrusions in Scenarios S2-S5 occur at a location in Panel 5, which is the
16 southernmost panel. In Scenario S6, both intrusions occur at a location in Panel 5, with the
17 effects of flow between the two boreholes implemented through assumptions involving the time-
18 dependent behavior of borehole permeability (Table PA-7).

19 **PA-6.7.2 NUTS Calculations**

20 For Scenarios S1–S5, radionuclide transport through the Salado is computed by the code NUTS
21 (Section PA-4.3) using the flow fields computed by BRAGFLO. Two types of calculations are
22 performed with NUTS. First, a set of screening calculations identifies elements of the sample
23 from \mathcal{S}_{su} for which radionuclide transport through the Salado to the LWB or Culebra is possible.
24 The screening calculations identify a subset of the sample from \mathcal{S}_{su} for which transport is
25 possible and for which release calculations are performed. Screening calculations are performed
26 for BRAGFLO Scenarios S1-S5, for a total of 1,500 screening calculations with NUTS (Table
27 PA-25).

28 Table PA-26 summarizes the NUTS release calculations for the CRA-2009 PA. Based on the
29 screening calculations, a total of 1,600 release calculations are performed for the CRA-2009 PA.
30 For each vector that is retained (based on the screening calculations), release calculations are
31 performed for a set of intrusion times.

32 Table PA-26 lists five scenarios for release calculations corresponding to the five BRAGFLO
33 scenarios. Each NUTS scenario uses the flow field computed for the corresponding BRAGFLO
34 scenario. The intrusion times for the NUTS scenarios are accommodated by shifting the
35 BRAGFLO flow fields in time so that the NUTS and BRAGFLO intrusions coincide. For
36 example, the NUTS S3 scenario with an intrusion at 3,000 years requires a flow field for the time
37 interval between (3,000 years and 10,000 years); this scenario uses the BRAGFLO S3 scenario
38 flow field for the time interval between (1,000 years and 8,000 years).

1

Table PA-26. NUTS Release Calculations in the CRA-2009 PA

NUTS Scenario	Number of Vectors with Releases				Flow field	Intrusion Time (t_1)
	R1	R2	R3	Total		
S1	1	0	0	1	BRAGFLO S1 scenario	N/A
S2	70	76	77	223	BRAGFLO S2 scenario	E1 intrusion at 100 and 350 years
S3	55	58	60	173	BRAGFLO S3 scenario	E1 intrusion at 1,000, 3,000, 5,000, 7,000, or 9,000 years
S4	15	14	15	44	BRAGFLO S4 scenario	E2 intrusion at 100 and 350 years
S5	14	13	13	40	BRAGFLO S5 scenario	E2 intrusion at 1,000, 3,000, 5,000, 7,000, or 9,000 years

2

3 Values for the variables indicating intrusion into an excavated area (e_1), penetration of
 4 pressurized brine (b_1), plugging pattern (p_1), and drilling location (l_1) are the same as in the
 5 corresponding BRAGFLO scenario. Values for the activity level \mathbf{a}_1 and mining time t_{min} are not
 6 specified for the NUTS scenarios.

7 **PA-6.7.3 PANEL Calculations**

8 As outlined in Section PA-4.4, the code PANEL is used to estimate releases to the Culebra
 9 associated with E1E2 scenarios and to estimate radionuclide concentrations in brine for use in
 10 estimating DBRs. An E1E2 scenario assumes two drilling intrusions into the same waste panel:
 11 the first an E2 intrusion (Table PA-25) occurring at time t_1 and the second an E1 intrusion (Table
 12 PA-25) occurring at time t_2 . PANEL calculations are performed for $t_2 = 100, 350, 1,000, 2,000,$
 13 $4,000, 6,000,$ and $9,000$ years using the flow field produced by the single BRAGFLO calculation
 14 for Scenario S6, for a total of $7 \times nR \times nLHS = 7 \times 3 \times 100 = 2,100$ PANEL calculations. The
 15 BRAGFLO flow field is shifted forward or backward in time as appropriate so that the time of
 16 the second intrusion (t_2) coincides with the flow field. The shifting of the BRAGFLO flow field
 17 results in values for the time (t_1) of the first intrusion (E2) for the PANEL calculations given by

18
$$t_1 = \max \{100yr, t_2 - 1200yr\} \tag{PA.313}$$

19 where the restriction that t_1 cannot be less than 100 years results from the definition of $\mathbf{x}_{st,i}$,
 20 which does not allow negative intrusion times, and from the assumption of 100 years of
 21 administrative control during which there is no drilling (i.e., $\lambda_d(t) = 0 \text{ yr}^{-1}$ for $0 \leq t \leq 100 \text{ yr}$; see
 22 Equation (PA.6)). Under this convention, the definition of Scenario S6 for the BRAGFLO
 23 calculations differs from what is actually done computationally because t_1 does not always
 24 precede t_2 by 1,000 years in the PANEL calculation. Values for the other variables defining the
 25 element $\mathbf{x}_{st,i}$ of S_{st} for the PANEL E1E2 scenarios are the same as in the BRAGFLO S6
 26 scenario.

27 Calculating radionuclide concentrations is not specific to any BRAGFLO scenario. The
 28 concentration calculations compute the mobilized activity in two different brines (Castile and

1 Salado) and are performed at 100; 125; 175; 350; 1,000; 3,000; 5,000; 7,500; and 10,000 years
 2 for a total of $2 \times 9 \times nR = 54$ calculations.

3 **PA-6.7.4 DRSPALL Calculations**

4 The code DRSPALL calculates the spillings volume produced by gas buildup within the
 5 repository. Because of the computational expense associated with running the code, rather than
 6 evaluating all possible pressures for each vector, a set of four pressures is evaluated for each
 7 vector in each replicate. These values are then passed to CUTTINGS_S to act as a lookup table
 8 used by the latter code to linearly interpolate the spillings volume as a function of the repository
 9 pressure. DRSPALL does not compute releases to the environment, which is computed by the
 10 CUTTINGS_S code. A total of $4 \text{ pressures} \times nR \times nLHS = 4 \times 3 \times 100 = 1,200$ DRSPALL
 11 calculations were performed. As none of the changes implemented for the CRA-2009 PA
 12 affected the DRSPALL calculations, the results from the CRA-2004 PABC DRSPALL
 13 calculations were used in the CRA-2009 PA.

14 **PA-6.7.5 CUTTINGS_S Calculations**

15 The code CUTTINGS_S computes the volumes of solids removed from the repository by
 16 cuttings and cavings (see Section PA-4.5) and spillings (see Section PA-4.6). Table PA-27 lists
 17 the CUTTINGS_S calculations performed for the CRA-2009 PA, totaling $78 \times nR \times nLHS = 78$
 18 $\times 3 \times 100 = 23,400$ CUTTINGS_S calculations.

19 **Table PA-27. CUTTINGS_S Release Calculations in the CRA-2009 PA**

Scenario	Description
S1	Intrusion into lower, middle, or upper waste panel in undisturbed (i.e., E0 conditions) repository at 100; 350; 1,000; 3,000; 5,000; or 10,000 years: 18 combinations.
S2	Initial E1 intrusion at 350 years followed by a second intrusion into the same, adjacent, or nonadjacent waste panel at 550; 750; 2,000; 4,000; or 10,000 years: 15 combinations.
S3	Initial E1 intrusion at 1,000 years followed by a second intrusion into the same, adjacent, or nonadjacent waste panel at 1,200; 1,400; 3,000; 5,000; or 10,000 years: 15 combinations.
S4	Initial E2 intrusion at 350 years followed by a second intrusion into the same, adjacent, or nonadjacent waste panel at 550; 750; 2,000; 4,000; or 10,000 years: 15 combinations.
S5	Initial E2 intrusion at 1,000 years followed by a second intrusion into the same, adjacent, or nonadjacent waste panel at 1,200; 1,400; 3,000; 5,000; or 10,000 years: 15 combinations.

20

21 The CUTTINGS_S S1 scenario computes volumes of solid material released from the initial
 22 intrusion in the repository. Initial conditions for the CUTTINGS_S S1 scenario are taken from
 23 the results of the BRAGFLO S1 scenario during the intrusion of Waste Panel, South RoR, and
 24 North RoR areas in Figure PA-15, corresponding to the lower, middle, and upper waste panels.
 25 In this scenario, the excavated area is penetrated ($e_1 = 1$) and the drilling location (l_1) is defined
 26 as one of the nodes (Figure PA-14) in the appropriate panel of Figure PA-28. The actual
 27 locations where the intrusions are assumed to occur correspond to the points in Figure PA-28
 28 designated “Down-dip well,” “Middle well,” and “Up-dip well” for the lower, middle, and upper

1 waste panel, respectively. Values for the variables indicating penetration of pressurized brine
 2 (b_1), plugging pattern (p_1), activity level (\mathbf{a}_1), and mining time (t_{min}) are not specified for the
 3 CUTTINGS_S S1 scenario.

4 The other CUTTINGS_S scenarios (Scenarios S2-S5) compute volumes of solids released by a
 5 second or subsequent intrusion. Initial conditions are taken from the results of the corresponding
 6 BRAGFLO scenario at the time of the second intrusion. As in the BRAGFLO scenarios, the first
 7 intrusion occurs in the lower waste panel (Waste Panel area in Figure PA-15), so the drilling
 8 location (l_1) is defined as one of the nodes in Panel 5 (Figure PA-14). The second intrusion
 9 occurs in the same waste panel as the first intrusion (area Waste Panel in Figure PA-15), an
 10 adjacent waste panel (South RoR area in Figure PA-15), or a nonadjacent waste panel (North
 11 RoR area in Figure PA-15); hence the drilling location (l_2) is defined as one of the nodes (Figure
 12 PA-14) in the appropriate panel of Figure PA-28.

13 The activity level for the first intrusion a_1 takes a value that indicates CH-TRU waste penetration
 14 (i.e., $\mathbf{a}_1 = [2, CH_{11}, CH_{12}, CH_{13}]$), but the specific waste streams penetrated (i.e. $CH_{11}, CH_{12},$
 15 CH_{13}) are not specified. For the second intrusion, the excavated area is penetrated ($e_2 = 1$) and
 16 the drilling location (l_2) is defined as one of the nodes in the appropriate panel (Figure PA-14),
 17 as described above. As for the first intrusion, the activity level \mathbf{a}_2 only indicates CH-TRU waste
 18 penetration. Values for the other variables defining the first intrusion (e_1, b_1 , and p_1) are the
 19 same as in the corresponding BRAGFLO scenario. Values for the other variables defining the
 20 second intrusion (b_2 and p_2) and the mining time t_{min} are not specified for the CUTTINGS_S
 21 scenarios.

22 **PA-6.7.6 BRAGFLO Calculations for DBR Volumes**

23 Volumes of brine released to the surface during an intrusion are calculated using BRAGFLO, as
 24 described in Section PA-4.7. Calculations of DBR volumes were conducted for the same
 25 scenarios as CUTTINGS_S (Table PA-27). Thus, the elements of \mathcal{S}_{st} described in Section PA-
 26 6.7.5 also characterize the elements for which DBR volumes are computed. A total of 23,400
 27 BRAGFLO calculations were performed.

28 **PA-6.7.7 MODFLOW Calculations**

29 As described in Section PA-4.8, the MODFLOW calculations produce flow fields in the Culebra
 30 for two categories of conditions: partially mined conditions in the vicinity of the repository and
 31 fully mined conditions in the vicinity of the repository (Figure PA-31). As specified in 40 CFR
 32 § 194.32(b), partially mined conditions are assumed to exist by the end of the administrative
 33 control period (i.e., at 100 years after closure). After the time that mining occurs within the
 34 LWB (t_{min} ; see Section PA-3.9), fully mined conditions are assumed for the remainder of the
 35 10,000-year regulatory period. The flow fields for partially mined conditions are calculated by
 36 MODFLOW using the T fields for partially mined conditions (see Section PA-4.8.2). Additional
 37 MODFLOW calculations determine the flow fields for fully mined conditions and are performed
 38 using the T fields for fully mined conditions. Thus, a total of $2 \times nR \times nLHS = 2 \times 3 \times 100 = 600$
 39 MODFLOW calculations were performed (Table PA-28). As none of the changes implemented

1 for the CRA-2009 PA affected the Culebra flow and transport calculations, the results from the
 2 CRA-2004 PABC Culebra flow and transport calculations were used in the CRA-2009 PA.

3 **PA-6.7.8 SECOTP2D Calculations**

4 The SECOTP2D calculations are performed for the same elements $\mathbf{x}_{st,0}$ and $\mathbf{x}_{st,m}$ of \mathcal{S}_{st} defined
 5 in Section PA-6.7.7 for the MODFLOW calculations, giving a total of $2 \times nR \times nLHS = 2 \times 3 \times$
 6 $100 = 600$ SECOTP2D calculations (Table PA-29). As none of the changes implemented for the
 7 CRA-2009 PA affected the Culebra flow and transport calculations, the results from the
 8 CRA-2004 PABC Culebra flow and transport calculations were used in the CRA-2009 PA.

9 **Table PA-28. MODFLOW Scenarios in the CRA-2009 PA**

MODFLOW: 600 Flow-Field Calculations
PM: Partially mined conditions in vicinity of repository
FM: Fully mined conditions in vicinity of repository
Total calculations = $2 \times nR \times nLHS = 2 \times 3 \times 100 = 600$
Note: Only 100 unique T fields were constructed with PEST and MODFLOW for use in the analysis. The T fields are an input to the calculation of flow fields. In each replicate, the T field used for a particular flow field was assigned using an index value (CTAN; see Table PA-19) included in the LHS.

10

11 **Table PA-29. SECOTP2D Scenarios in the CRA-2004 PA**

SECOTP2D: 600 Calculations
PM: Partially mined conditions in vicinity of repository
FM: Fully mined conditions in vicinity of repository
Total calculations = $2 \times nR \times nLHS = 2 \times 3 \times 100 = 600$
Note: Each calculation includes a unit release for each of four radionuclides: ^{241}Am , ^{239}Pu , ^{230}Th , and ^{234}U .

12

13 **PA-6.8 Computation of Releases**

14 The mechanistic computations outlined in Section PA-6.7 are used to compute releases for each
 15 sampled element $\mathbf{x}_{st,i}$ of \mathcal{S}_{st} . Releases from the repository can be partitioned into three
 16 categories: undisturbed releases, which may occur in futures without drilling intrusions; direct
 17 releases, which occur at the time of a drilling event; and long-term releases, which occur as a
 18 consequence of a history of drilling intrusions. For a given future ($\mathbf{x}_{st,i}$ of \mathcal{S}_{st} in Equation
 19 (PA.304)) other than undisturbed conditions ($\mathbf{x}_{st,0}$), the direct and long-term releases are
 20 computed by the code CCDFGF (WIPP Performance Assessment 2003a) from the results of the
 21 mechanistic calculations summarized in Section PA-6.7, performed with the models presented in
 22 Section PA-4.0. Releases from an undisturbed repository are computed from the results of the
 23 NUTS S1 scenario (Section PA-6.7.2).

1 PA-6.8.1 Undisturbed Releases

2 Repository releases for the futures ($\mathbf{x}_{st,0}$) in which no drilling intrusions occur are computed by
 3 the NUTS release calculations for E0 conditions (Table PA-26). The NUTS model computes the
 4 activity of each radionuclide that reaches the accessible environment during the regulatory period
 5 via transport through the MBs, the Dewey Lake Red Beds and land surface due to brine flow up
 6 a plugged borehole. These releases are represented as $f_{MB}[\mathbf{x}_{st,0}, f_B(\mathbf{x}_{st,0})]$, $f_{DL}[\mathbf{x}_{st,0}, f_B(\mathbf{x}_{st,0})]$
 7 and $f_S[\mathbf{x}_{st,0}, f_B(\mathbf{x}_{st,0})]$ in Equation (PA.23). The undisturbed releases for the CRA-2009 PA are
 8 summarized in Section PA-7.2.

9 PA-6.8.2 Direct Releases

10 Direct releases include cuttings, cavings, spillings, and DBRs. The model for each direct release
 11 component computes a volume (solids or liquid) released directly to the surface for each drilling
 12 intrusion. These volumes are combined with an appropriate concentration of activity in the
 13 released waste. Summary information for the CRA-2009 PA direct releases are given in Section
 14 PA-8.5.

15 PA-6.8.2.1 Construction of Cuttings and Cavings Releases

16 Each drilling intrusion encountering waste is assumed to release a volume of solid material as
 17 cuttings, as described in Section PA-4.5.1. The uncompacted volume of waste removed by
 18 cuttings (V_{cut}) is computed by Equation (PA.124). In addition, drilling intrusions that encounter
 19 CH-TRU waste may release additional solid material as cavings, as described in Section PA-
 20 4.5.2. The uncompacted volume of material removed by cuttings and cavings combined ($V =$
 21 $V_{cut} + V_{cav}$) is computed by Equation (PA.125). For a drilling intrusion that encounters RH-
 22 TRU waste, the final eroded diameter D_f in Equation (PA.125) is equal to the bit diameter in
 23 Equation (PA.124). In PA, all drilling intrusions assume a drill bit diameter of 0.31115 m (Fox
 24 2008, Table 13).

25 The uncompacted volume of material removed is not composed entirely of waste material;
 26 rather, the uncompacted volume includes MgO and any void space initially present around the
 27 waste containers. The volume of waste removed (V_w) is determined by multiplying the
 28 uncompacted volume by the fraction of excavated repository volume (FVW) occupied by waste,
 29 thus

$$30 \quad V_w = V \times FVW \quad (\text{PA.314})$$

31 where $FVW = 0.385$ for CH-TRU waste and $FVW = 1.0$ for RH-TRU waste (Fox 2008, Table
 32 45). The activity in the material released by cuttings and cavings is determined by stochastically
 33 selecting a subset of all waste streams. The vector (\mathbf{a}_j) described in Section PA-3.8 determines
 34 which type of waste (CH-TRU or RH-TRU) and which waste streams are selected. The activity
 35 per cubic meter of waste stream volume is computed for each waste stream at a discrete set of
 36 times accounting for radioactive decay and ingrowth by the code EPAUNI (Fox 2005); the
 37 results of the EPAUNI calculations are presented in Fox (2005). Activities at other times are
 38 determined by linear interpolation. The cuttings and cavings release $f_C(\mathbf{x}_{st,i})$ is the product of the

1 average activity per cubic meter (C_r , computed as the average activity over the waste streams
 2 comprising the selected subset with the assumption that each waste stream contributes an equal
 3 volume to the release) and the volume of waste released (Equation (PA.315)):

$$4 \quad f_C(\mathbf{x}_{st,i}) = V_w \times C_r \quad (\text{PA.315})$$

5 **PA-6.8.2.2 Construction of Spallings Releases**

6 Spallings releases are calculated for all intrusions that encounter CH-TRU waste. The
 7 construction of the spallings release $f_{SP}(\mathbf{x}_{st,i})$ is nearly identical to that described in Section PA-
 8 6.8.2.3 for the calculation of DBRs, except that volumes of solid material released will be used
 9 rather than volumes of brine. These solid releases are calculated with the spallings submodel of
 10 the CUTTINGS_S program for the combinations of repository condition, distance from previous
 11 intrusions, and time between intrusions listed in Table PA-27. Linear interpolation determines
 12 the releases for other combinations of repository condition, distance, and time between intrusions
 13 (WIPP Performance Assessment 2003a).

14 The concentration of radionuclides in the spallings release volume is computed as the average
 15 activity per cubic meter in the CH-TRU waste at the time of intrusion. Activities in each waste
 16 stream are computed at a discrete set of times by the code EPAUNI (Fox 2005); activities at
 17 other times are determined by linear interpolation.

18 **PA-6.8.2.3 Construction of DBRs**

19 DBRs (also termed blowout releases) are calculated for all intrusions that encounter CH-TRU
 20 waste. DBRs $f_{DBR}(\mathbf{x}_{st,i})$ are constructed from the volume of brine released (V_{DBR}) to the surface
 21 (Equation (PA.202)) and radionuclide concentrations in brine (C_{bl} , see Equation (PA.96)). Brine
 22 volume released to the surface is computed by BRAGFLO (Section PA-4.7.3) for the times listed
 23 in Table PA-27; brine volumes released for intrusions at other times are computed by linear
 24 interpolation (WIPP Performance Assessment 2003b).

25 Calculating DBR volumes distinguishes between the first intrusion and subsequent intrusions.
 26 The release volumes for the initial intrusion (E0 repository conditions) are further distinguished
 27 by the panel group (upper, middle, and lower). As shown in Table PA-27, BRAGFLO computes
 28 release volumes for the initial intrusion at a series of intrusion times; the release volume for the
 29 initial intrusion at other times is computed by linear interpolation (WIPP Performance
 30 Assessment 2003a). Release volumes for subsequent intrusions are distinguished by the current
 31 state of the repository (E1 or E2) and the relative distance between the panel intruded by the
 32 current borehole and the panel of the initial intrusion (same, adjacent, nonadjacent). The
 33 algorithms for determining repository conditions and distance between intrusions are described
 34 in Section PA-6.7.5.

35 As indicated in Table PA-27, DBR volumes for a second intrusion are computed by BRAGFLO
 36 for combinations of repository condition, distance between intrusions, and time between
 37 intrusions. Brine release volumes for other combinations of condition, distance, and time are
 38 computed by linear interpolation (WIPP Performance Assessment 2003a). Brine releases from

1 the third and subsequent intrusions are computed as if the current intrusion was the second
2 intrusion into the repository.

3 Radionuclide concentrations in brine (C_{bl}) are calculated by PANEL (Section PA-6.7.3) for the
4 times listed in Table PA-26; concentrations at other times are computed by linear interpolation
5 (WIPP Performance Assessment 2003a). The type of intrusion (E1 or E2) determines the brine
6 (Salado or Castile brine) selected for the concentration calculation; Castile brine is used for E1
7 intrusions, and Salado brine is used for E2 intrusions.

8 The DBR is computed as the product of the release concentration and the volume, V_{DBR} .

$$9 \quad f_{DBR}(\mathbf{x}_{st,i}) = V_{DBR} \times C_{bl} \quad (\text{PA.316})$$

10 **PA-6.8.3 Radionuclide Transport Through the Culebra**

11 One potential path for radionuclides to leave the repository is through the boreholes to the
12 Culebra, then through the Culebra to the LWB (Ismail and Garner 2008). As indicated in Table
13 PA-26, the NUTS and PANEL models are used to estimate radionuclide transport through
14 boreholes to the Culebra $f_{NP}(\mathbf{x}_{st,i})$ for a fixed set of intrusion times; releases to the Culebra for
15 intrusions at other times are determined by linear interpolation (WIPP Performance Assessment
16 2003a). NUTS computes the release to the Culebra over time for E1 and E2 boreholes; PANEL
17 computes the release to the Culebra for an E1E2 borehole.

18 Each borehole may create a pathway for releases to the Culebra. The first E1 or E2 borehole in
19 each panel creates a release path, with the radionuclide release taken from the appropriate NUTS
20 data. Subsequent E2 boreholes into a panel with only E2 boreholes do not cause additional
21 releases; WIPP PA assumes that a subsequent E2 borehole into a panel having only earlier E2
22 intrusions does not provide a significant source of additional brine, and thus does not release
23 additional radionuclides to the Culebra.

24 An E1E2 borehole results from the combination of two or more intrusions into the same panel, at
25 least one of which is an E1 intrusion. A subsequent E1 borehole changes the panel's condition to
26 E1E2, as does an E2 borehole into a panel that has an earlier E1 intrusion. Once E1E2
27 conditions exist in a panel, they persist throughout the regulatory period. However, releases
28 from a panel with E1E2 conditions are restarted for each subsequent E1 intrusion into that panel,
29 since additional E1 intrusions may introduce new volumes of brine to the panel.

30 Releases to the Culebra are summed across all release pathways to the Culebra to obtain total
31 releases to the Culebra $r_k(t)$ for the k^{th} radionuclide at each time t . Releases to the Culebra
32 include both dissolved radionuclides and radionuclides sorbed to colloids. The WIPP PA
33 assumes that radionuclides sorbed to humic colloids disassociate and transport, as do dissolved
34 radionuclides; other colloid species do not transport in the Culebra (see Appendix SOTERM-
35 2009, Section SOTERM-4.7). The release to the Culebra is partitioned into dissolved and
36 colloid species by multiplying $r_k(t)$ by radionuclide-specific factors for the fraction dissolved and
37 the fraction on colloids. Dissolved radionuclides are always transported through the Culebra.

1 Radionuclide transport through the Culebra is computed by the code SECOTP2D (Section PA-
 2 4.9) for partially mined and fully mined conditions, as indicated in Table PA-29. These
 3 computations assume a 1 kg source of each radionuclide placed in the Culebra between 0 and 50
 4 years and result in the fraction of each source $f_{m,k}(t)$, where m is the mining condition and k is
 5 the index for the radionuclide, reaching the LWB at each subsequent time t . For convenience,
 6 the time-ordering of the data from SECOTP2D is reversed so that the fraction $f_{m,k}(t)$ associated
 7 with year $t = 200$, for example, represents the release at the boundary at year 10,000 for a release
 8 occurring between 150 and 200 years.

9 The total release through the Culebra $R_{Cul,k}$ is calculated for the k^{th} radionuclide by

$$10 \quad R_{Cul,k} = \sum_{t_i \leq t_m} r_k(t_i) f_{PM,k}(t_i) + \sum_{t_i > t_{min}} r_k(t_i) f_{FM,k}(t_i) \quad (PA.317)$$

11 where $r_k(t_i)$ is the release of the k^{th} radionuclide to the Culebra in kg at time t_i , and $f_{PM,k}(t_i)$ and
 12 $f_{FM,k}(t_i)$ are the fractions of a unit source placed in the Culebra in the interval (t_{i-1}, t_i) that
 13 reaches the LWB by the end of the 10,000-year regulatory period for partially mined and fully
 14 mined conditions within the LWB, respectively. The function $f_{m,k}(t)$ ($m = PM, FM$) changes
 15 when mining is assumed to occur within the LWB; hence the sum in the equation above is
 16 evaluated in two parts, where t_{min} is the time that mining occurs. The total releases through the
 17 Culebra $f_{ST}(\mathbf{x}_{st,i})$ is computed by converting the release of each radionuclide $R_{Cul,k}$ from kg to
 18 EPA units, then summing over all radionuclides.

19 PA-6.8.4 Determining Initial Conditions for Direct and Transport Releases

20 A sequence of intrusions into the repository can change the conditions in and around the
 21 repository and, hence, affect releases from subsequent intrusions. This section describes how
 22 panel and repository conditions are determined for a given intrusion.

23 PA-6.8.4.1 Determining Repository and Panel Conditions

24 Direct releases by DBR and spallings, and subsequent releases by radionuclide transport, require
 25 determining the conditions in the intruded panel and the repository at the time of the intrusion.
 26 One of three conditions is assigned to the repository:

- 27 • E0 the repository is undisturbed by drilling,
- 28 • E1 the repository has at least one E1 intrusion, or
- 29 • E2 the repository has one or more E2 intrusions, but no E1 intrusions.

30 In addition, each panel is assigned one of four conditions:

- 31 • E0 the excavated regions of the panel have not been intruded by drilling,
- 32 • E1 the panel has one previous E1 intrusions (intersecting a brine reservoir in the
 33 Castile),

- 1 • E2 the panel has one or more previous E2 intrusions (none intersect brine reservoirs),
2 or
- 3 • E1E2 the panel has at least two previous intrusions, at least one of which is an E1
4 intrusion.

5 Repository conditions are used to determine direct releases for each intrusion by DBRs and
6 spillings. Panel conditions are used to determine releases by transport through the Culebra.

7 When an intrusion into CH-TRU waste occurs, the stochastic variables in Table PA-24 are used
8 in the algorithm shown in Figure PA-41 to determine the type of the intrusion (E1 or E2). The
9 type of the intrusion is used to update the conditions for the intruded panel and the repository
10 before stepping forward in time to the next intrusion.

11 **PA-6.8.4.2 Determining Distance from Previous Intrusions**

12 Direct releases by DBR and spillings require determining the distance between the panel hit by
13 the current intrusion and the panels hit by previous intrusions. In PA, the 10 panels are divided
14 into three groups: lower, consisting of only Panel 5; middle, including Panels 3, 4, 6, and 9; and
15 upper, including Panels 1, 2, 7, 8, and 10, as shown in Figure PA-29. These divisions are
16 consistent with the repository representation in the BRAGFLO model for Salado flow (Section
17 PA-4.2) and for DBRs (Section PA-4.7).

18 The initial intrusion can occur in any of the 10 actual waste panels, so the direct releases for the
19 initial intrusion are modeled as if the initial intrusion occurred in a lower, middle, or upper waste
20 panel based on the division discussed above. Initial conditions for direct releases from
21 subsequent intrusions are modeled by one of three cases: lower, middle, and upper,
22 corresponding to the three panel groups shown in Figure PA-29 and listed in Table PA-27. The
23 lower case represents a second intrusion into a previously intruded panel. The middle case
24 represents an intrusion into an undisturbed panel that is adjacent to a previously disturbed panel.
25 The upper case represents an intrusion into an undisturbed panel that is not adjacent to a
26 previously disturbed panel. Adjacent panels share one side in common, and nonadjacent panels
27 share no sides in common.

28 The time and location of the previous intrusion is used to determine distance from the current
29 intrusion and depends on the repository condition, which is determined by the intrusion of
30 greatest consequence across all panels prior to the current intrusion. E1 intrusions are assumed
31 to be of greater consequence than E2 intrusions. The previous intrusion is selected by finding
32 the closest panel (same, adjacent, nonadjacent) whose intrusion condition, excluding the current
33 intrusion, is equal to the repository condition. The time of the previous intrusion is the time of
34 the most recent intrusion with the greatest consequence and closest distance. Likewise, the
35 condition of each panel is equal to the intrusion of greatest consequence into the panel prior to
36 the current intrusion.

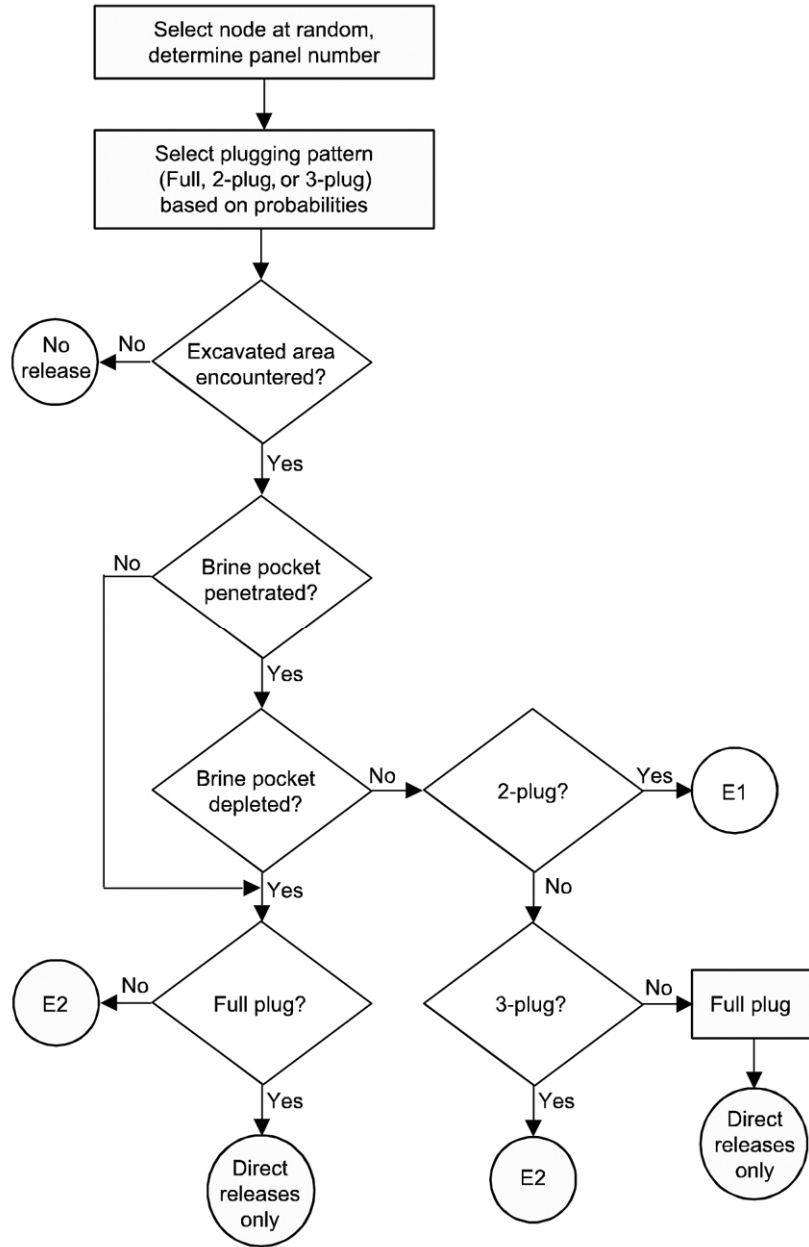


Figure PA-41. Logic Diagram for Determining the Intrusion Type

PA-6.8.5 CCDF Construction

For each vector $\mathbf{v}_{su,k}$ in the space of subjective uncertainty, the code CCDFGF samples a sequence $\mathbf{x}_{st,i}$, $i = 1, 2, \dots, nR$ of futures. In PA, $nR = 10,000$; this number of futures is sufficient to adequately estimate the mean CCDF of total releases for comparison with the boundary line specified in section 191.13, as demonstrated in Section PA-9.0. A release $f(\mathbf{x}_{st,i})$ for each future is then constructed as described in Section PA-6.8.1, Section PA-6.8.2, and Section PA-6.8.3. Once the $f(\mathbf{x}_{st,i})$ are evaluated, the CCDF can be approximated as indicated in Equation (PA.318).

$$1 \quad \text{prob}(Rel > R) = \int_{\mathcal{S}_{st}} \delta_R [f(\mathbf{x}_{st,i})] d_{st}(\mathbf{x}_{st,i}) dV_{st} \cong \sum_{i=1}^{nR} \delta_R [f(\mathbf{x}_{st,i})] / nR \quad (\text{PA.318})$$

2 A binning technique is used to construct the desired CCDF: the consequence axis is divided into
 3 a sequence of bins, and the number of values for $f(\mathbf{x}_{st,i})$ falling in each bin is accumulated. In
 4 addition, all values for $f(\mathbf{x}_{st,i})$ are saved and subsequently ordered to provide an alternative
 5 method for constructing the CCDFs. In addition to the total CCDF for all releases, it will be
 6 possible to obtain CCDFs for individual release modes (e.g., cuttings, spillings, DBRs, to
 7 Culebra, through MBs, through Culebra). The logic diagram for CCDF production is shown in
 8 Figure PA-42.

9 The CCDF construction indicated in this section is for a single sample element $\mathbf{v}_{su,k}$ of the form
 10 indicated in conjunction with Equation (PA.302). Repeated generation of CCDFs for individual
 11 sample elements $\mathbf{v}_{su,k}$, i.e. for the vectors representing epistemic uncertainty in the model results,
 12 will lead to the distribution of complete CCDFs.

13 **PA-6.9 Sensitivity Analysis**

14 Evaluating one or more of the models discussed in Section PA-4.0 with the LHS in Equation
 15 (PA.302) creates a mapping

$$16 \quad \{\mathbf{v}_{su,k}, \mathbf{y}_{su,k}\}, k = 1, 2, \dots, n\text{LHS} \quad (\text{PA.319})$$

17 from analysis inputs (i.e., $\mathbf{v}_{su,k}$) to analysis results (i.e., $y(\mathbf{v}_{su,k})$), where $\mathbf{y}_{su,k}$ denotes the results
 18 obtained with the model or models under consideration. In other words, for each vector of
 19 parameters samples, there is a corresponding CCDF of releases, $y(\mathbf{v}_{su,k})$. A vector notation is
 20 used for y because, in general, a large number of predicted results are produced by each of the
 21 models used in PA. Sensitivity analysis explores the mapping in Equation (PA.319) to determine
 22 how the uncertainty in individual elements of $\mathbf{v}_{su,k}$ affects the uncertainty in individual elements
 23 of $y(\mathbf{v}_{su,k})$. Understanding how uncertainty in analysis inputs affects analysis results aids in
 24 understanding PA and improving the models for future PAs.

25 The presentation of results from each major model in the WIPP PA is accompanied by sensitivity
 26 analyses of the most important output of the model. In some cases, sensitivity analysis results
 27 are based on pooling the results obtained for the three replicated LHSs (i.e., R1, R2, R3)
 28 discussed in Section PA-6.4. In other cases, the sensitivity analysis is based on the results for
 29 each replicate, and statistics are compared across the three replicates. Note that pooling LHS
 30 replicates that include correlated variables can introduce a small bias into the statistics, although
 31 there are methods that allow for correlated variables when pooling replicates (Sallaberry, Helton,
 32 and Hora 2006).

33 Three principal techniques are used in the sensitivity analysis: scatterplots, regression analyses to
 34 determine standardized regression coefficients and partial correlation coefficients, and stepwise
 35 regression analyses. Each technique is briefly discussed.

$$1 \quad (v_{k,j}, y_k), k = 1, 2, \dots, nLHS \quad (PA.320)$$

2 for each element v_j of \mathcal{S}_{su} . The resulting plots can reveal relationships between y and the
 3 elements of \mathcal{S}_{su} . Scatterplots can be effective at revealing nonlinear relationships or threshold
 4 values. Examining such plots when LHS is used can be particularly revealing because of the full
 5 stratification over the range of each input variable. Iman and Helton (1988) provide an example
 6 where the scatterplots revealed a rather complex pattern of variable interactions.

7 **PA-6.9.2 Regression Analysis**

8 A more formal investigation of the mapping in Equation (PA.319) can be based on regression
 9 analysis. In this approach, a model of the form

$$10 \quad y = b_0 + \sum_{j=1}^n b_j x_j \quad (PA.321)$$

11 is developed from the mapping between analysis inputs and analysis results shown in Equation
 12 (PA.319), where the x_j are the input variables under consideration and the b_j are coefficients that
 13 must be determined. The coefficients b_j and other aspects of the regression model's construction
 14 in Equation (PA.321) can indicate the importance of the individual variables x_j with respect to
 15 the uncertainty in y . The PA employs the method of least squares to determine the coefficients b_j
 16 (Myers 1986).

17 Often the regression in Equation (PA.321) is performed after the input and output variables are
 18 normalized to mean zero and standard deviation one. The resulting coefficients b_j are called
 19 standardized regression coefficients (SRCs). When the x_j are independent, the absolute value of
 20 the SRCs can provide a measure of variable importance. Specifically, the coefficients provide a
 21 measure of importance based on the effect of moving each variable away from its expected value
 22 by a fixed fraction of its standard deviation while retaining all other variables at their expected
 23 values.

24 Partial correlation coefficients (PCCs) can also measure the linear relationships between the
 25 output variable y and the individual input variables. The PCC between y and an individual
 26 variable x_p is obtained through a sequence of regression models. First, the following two
 27 regression models are constructed:

$$28 \quad \hat{y} = b_0 + \sum_{\substack{j=1 \\ j \neq p}}^n b_j x_j \quad \text{and} \quad \hat{x}_p = c_0 + \sum_{\substack{j=1 \\ j \neq p}}^n c_j x_j \quad (PA.322)$$

29 The results of the two preceding regressions are then used to define the new variables $y - \hat{y}$ and
 30 $x_p - \hat{x}_p$. By definition, the PCC between y and x_p is the correlation coefficient between $y - \hat{y}$
 31 and $x_p - \hat{x}_p$. Thus, the PCC provides a measure of the linear relationship between y and x_p with
 32 the linear effects of the other variables removed.

1 Regression and correlation analyses often perform poorly when the relationships between the
2 input and output variables are nonlinear. This is not surprising, as such analyses assume linear
3 relationships between variables. The problems associated with poor linear fits to nonlinear data
4 can be avoided by use of the rank transformation (Iman and Conover 1979). The rank
5 transformation is a simple concept: data are replaced with their corresponding ranks, and then
6 the usual regression and correlation procedures are performed on these ranks. Specifically, the
7 smallest value of each variable is assigned Rank 1, the next largest value is assigned Rank 2, and
8 so on up to the largest value, which is assigned the rank m , where m denotes the number of
9 observations. The analysis is then performed with these ranks used as the values for the input
10 and output variables. A formal development of PCCs and the relationships between PCCs and
11 SRCs is provided by Iman, Shortencarier, and Johnson (1985).

12 **PA-6.9.3 Stepwise Regression Analysis**

13 Stepwise regression analysis provides an alternative to constructing a regression model
14 containing all the input variables. With this approach, a sequence of regression models is
15 constructed. The first regression model contains the single input variable with the largest impact
16 on the uncertainty in the output variable (i.e., the input variable that has the largest correlation
17 with the output variable y). The second regression model contains the two input variables with
18 the largest impact on the output variable: the input variable from the first step, plus whichever of
19 the remaining variables has the largest impact on uncertainty not accounted for by the first
20 variable (i.e., the input variable that has the largest correlation with the uncertainty in y that
21 cannot be accounted for by the first variable). Additional models in the sequence are defined in
22 the same manner, until further models are unable to meaningfully increase the amount of
23 uncertainty that can be accounted for in the output variable.

24 Stepwise regression analysis can provide insights into the importance of the individual variables.
25 First, the order in which the variables are selected in the stepwise procedure indicates their
26 importance, with the most important variable being selected first, the next most important
27 variable being selected second, and so on. Second, the R^2 values at successive steps of the
28 analysis also measure variable importance by indicating how much of the uncertainty in the
29 dependent variable can be accounted for by all variables selected at each step. When the input
30 variables are uncorrelated, the differences in the R^2 values for the regression models constructed
31 at successive steps equals the fraction of the total uncertainty in the output variable accounted for
32 by the individual input variable added at each step. Third, the absolute values of the SRCs in the
33 individual regression models indicate variable importance. Further, the sign of an SRC indicates
34 whether the input and output variable tend to increase and decrease together (a positive
35 coefficient) or tend to move in opposite directions (a negative coefficient).

1 **PA-7.0 Results for the Undisturbed Repository**

2 The PA tabulates releases from the repository for undisturbed conditions. Releases from the
3 undisturbed repository to the accessible environment fall under two sets of protection
4 requirements. The first, as set forth in section 191.15, protects individuals from radiological
5 exposure; the second, in Part 191 Subpart C, protects groundwater resources from contamination.
6 This section shows how WIPP complies with these two requirements by presenting brine and gas
7 flow (BRAGFLO) and radionuclide transport (NUTS) results from modeling the undisturbed
8 repository. The results discussed in Section PA-7.2 show that there are no releases to the
9 accessible environment from the undisturbed repository. Section PA-7.0 is taken from Clayton
10 et al. (2008, Section 4.0).

11 **PA-7.1 Salado Flow**

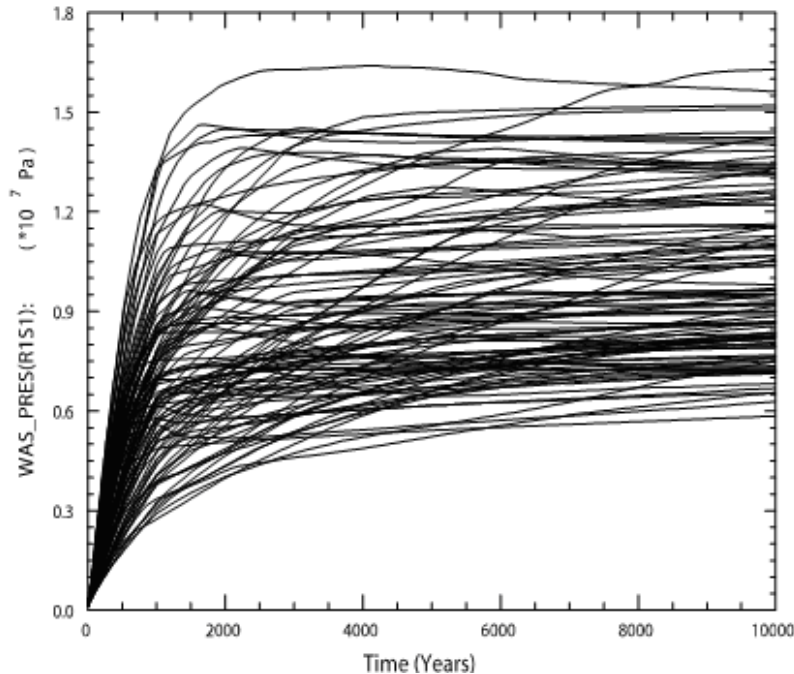
12 This section summarizes the Salado flow calculation results for the undisturbed (S1) scenario.
13 Pressure in the repository, brine saturation in the waste, and brine flow out of the repository are
14 presented, along with sensitivity analyses that identify the uncertain parameters to which these
15 results are most sensitive. The Salado flow model represents the repository as five regions in the
16 numerical grid: three waste-filled regions (the Waste Panel, South RoR, and North RoR in Figure
17 PA-15) and two excavated regions with no waste (the operations area and experimental area in
18 Figure PA-15). The analysis package for Salado flow contains a detailed presentation on the
19 BRAGFLO model, calculation results, and further sensitivity analyses (Nemer and Clayton
20 2008).

21 **PA-7.1.1 Pressure in the Repository**

22 In undisturbed conditions, pressure strongly influences the extent to which contaminated brine
23 might migrate from the repository to the accessible environment. In addition, pressure
24 developed under undisturbed conditions is an initial condition for the spillings and DBR models
25 (Section PA-8.5.2 and Section PA-8.5.3, respectively).

26 Figure PA-43 shows the pressure in the Waste Panel region for 100 vectors in replicate R1 for
27 the CRA-2009 PA. During the first 1,000 years, repository pressure may rapidly increase due to
28 several factors: rapid initial creep closure of rooms, initial inflow of brine causing gas generation
29 due to corrosion, and availability of CPR material to produce gas by microbial degradation.
30 Pressure generally approaches a steady-state value after 2,000 years as room closure ceases,
31 brine inflow slows (thereby reducing gas generation by corrosion), and CPR materials are
32 consumed.

33 In general, pressure increased for the CRA-2009 PA compared to the CRA-2004 PABC (Nemer
34 and Clayton 2008, Table 6-10). The increase was mainly caused by the correction of halite
35 porosity. The upper bound of the halite porosity distribution was increased, while the lower
36 bound and the mean remained the same. The halite porosity is positively correlated with
37 pressure, so the increase in porosity resulted in an increase in pressure (Nemer and Clayton
38 2008).



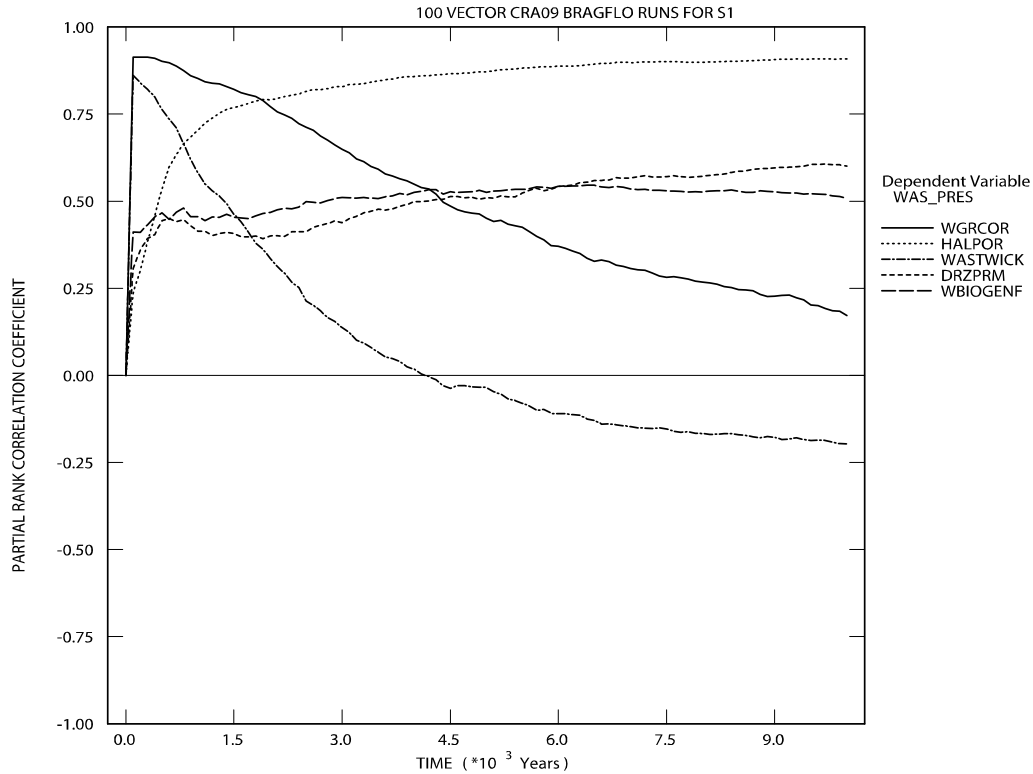
1
2 **Figure PA-43. Pressure in the Waste Panel Region, Replicate R1, Scenario S1, CRA-2009**
3 **PA**

4 Sensitivity analyses have determined the importance of parameter uncertainty to the uncertainty
5 in model results. Figure PA-44 shows partial rank correlation coefficients (PRCCs) generated by
6 the code PCCSRC (Gilkey 1995) from regression data between the pressure in the waste panel
7 (WAS_PRES) and the uncertain variables in the LHS (Section PA-5.2) for the CRA-2009 PA.
8 The figure shows that uncertain pressure in the waste panel is primarily determined by the
9 sampled halite porosity (HALPOR) (Nemer and Clayton 2008).

10 The positive correlation indicates that higher pressures result from higher values of halite
11 porosity (HALPOR). Increases in halite porosity linearly increases the DRZ porosity. This
12 increases the volume of brine available in the material overlying the waste, which, as the brine
13 flows, can then increase the amount of brine in the repository (Nemer and Clayton 2008).
14 Microbial gas generation rates are a function of the brine in the repository and increase as more
15 brine is available. Increased gas generation results in increased repository pressures. Increases
16 in the DRZ permeability (DRZPRM) accelerate brine flow into the waste, which then also
17 increases the gas generation rates, as seen by the positive correlation in Figure PA-44. The other
18 PRCCs in Figure PA-44 indicate that the uncertainty factor for microbial gas generation
19 (WBIOGENF), the corrosion rate for steel (WGRCOR), and the waste wicking parameter
20 (WASTWICK) determine the remaining variability in waste panel pressure, as they affect the gas
21 generation rate as well.

22 **PA-7.1.2 Brine Saturation in the Waste**

23 Brine saturation is an important result of the model for Salado flow because gas generation
24 processes, which tend to increase pressure, require brine. Brine saturation is also an initial
25 condition in the model for DBR (Section PA-8.5.3).

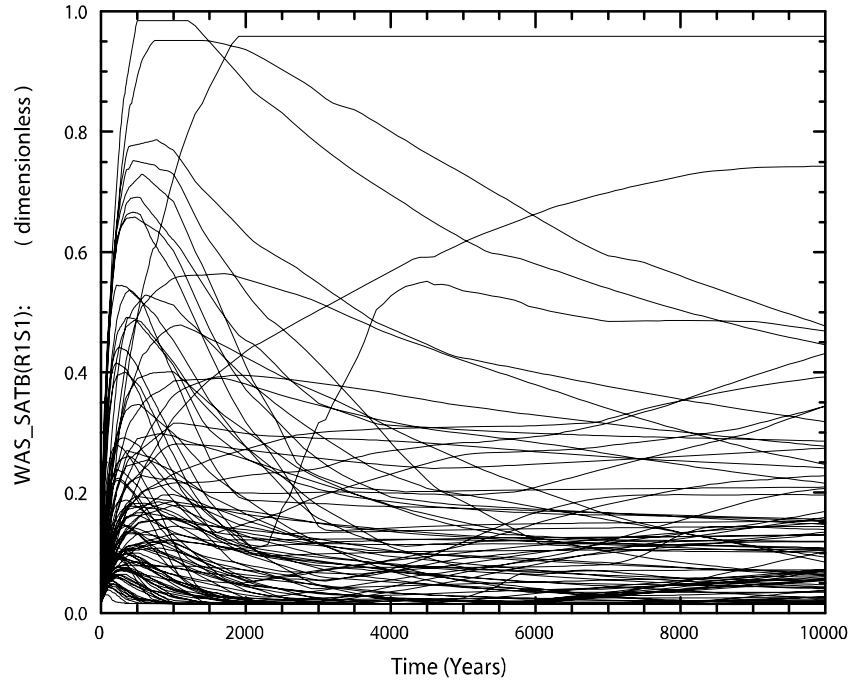


1
 2 **Figure PA-44. Primary Correlations of Pressure in the Waste Panel Region with**
 3 **Uncertain Parameters, Replicate R1, Scenario S1, CRA-2009 PA**

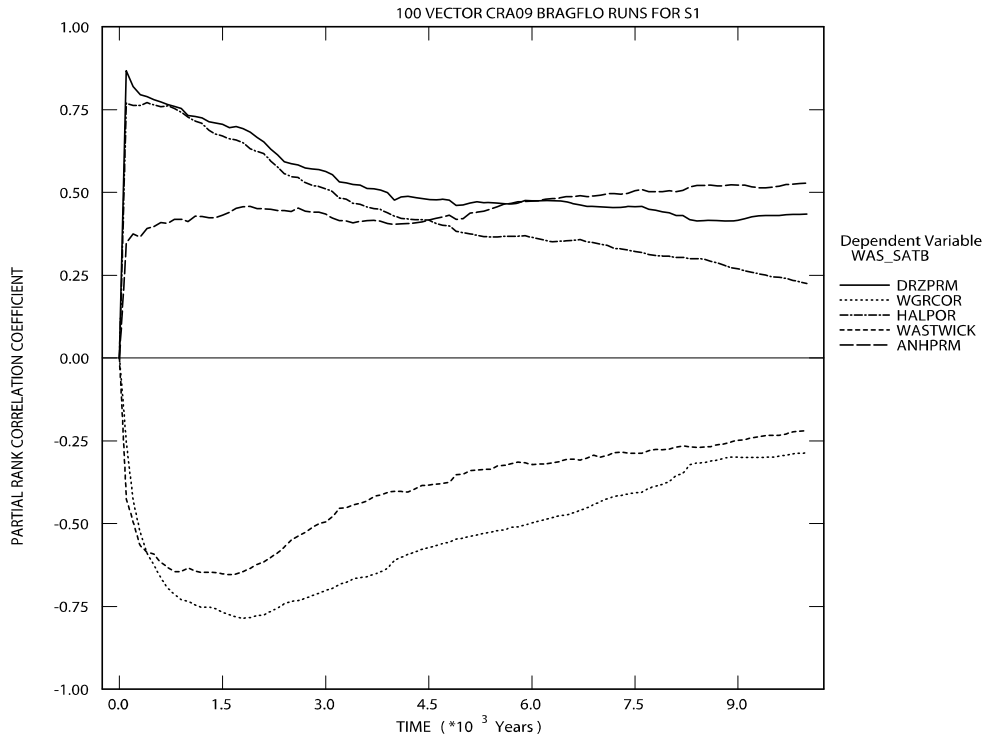
4 Figure PA-45 shows brine saturation in the Waste Panel region of the repository for the 100
 5 vectors of Replicate R1, Scenario S1 for the CRA-2009 PA. Brine saturation in the waste-filled
 6 areas is set initially to 0.015. Saturation increases very rapidly in the first 100 years in all
 7 excavated areas as brine flows toward the excavations, primarily from the DRZ above the
 8 excavation. Initially there is a large pressure differential between the DRZ and the excavated
 9 regions, and the relatively high permeability of the DRZ, compared to undisturbed halite, permits
 10 the rapid influx of brine. Brine inflow slows as the pressures equalize and as brine saturation in
 11 the DRZ decreases. Brine saturation in the waste areas decreases over time as brine is consumed
 12 by corrosion. Brine may also be driven out of the repository by high pressure.

13 The brine saturation patterns are similar, but are higher on average in the CRA-2009 PA than the
 14 CRA-2004 PABC (Nemer and Clayton 2008, Table 6-6 and Figure 6-8): there are more vectors
 15 with saturation greater than 60%. The increase in brine saturation is the result of the increased
 16 halite porosity (Nemer and Clayton 2008).

17 Computing PRCCs between the brine saturation in the waste panel (WAS_SATB) and the
 18 uncertain parameters in the LHS identifies a number of parameters that contribute to the
 19 uncertainty in brine saturation. The relative importance of these parameters varies over the
 20 10,000-year modeling period, and none of the parameters are clearly dominant. Figure PA-46
 21 shows positive correlations with anhydrite permeability (ANHPRM), DRZ permeability
 22 (DRZPRM), and halite porosity (HALPOR). Increases in halite porosity increase the volume of
 23 brine available in the material overlying the waste; increases in DRZ and anhydrite permeability
 24 accelerate brine flow into the waste. Negative correlations are found between brine saturation



1
 2 **Figure PA-45. Brine Saturation in the Waste Panel Region, Replicate R1, Scenario S1,**
 3 **CRA-2009 PA**



4
 5 **Figure PA-46. Primary Correlations of Brine Saturation in the Waste Panel Region with**
 6 **Uncertain Parameters, Replicate R1, Scenario S1, CRA-2009 PA**

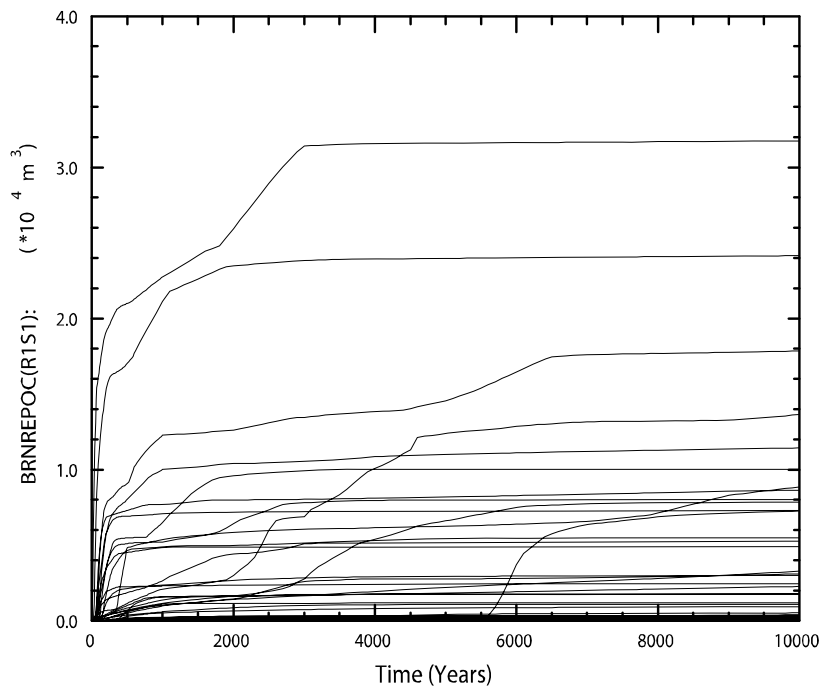
1 and the corrosion rate (WGRCOR) and the wicking factor (WASTWICK) because increases in
 2 these two variables increase the rate at which brine is consumed by corrosion, thus decreasing
 3 saturation.

4 **PA-7.1.3 Brine Flow Out of the Repository**

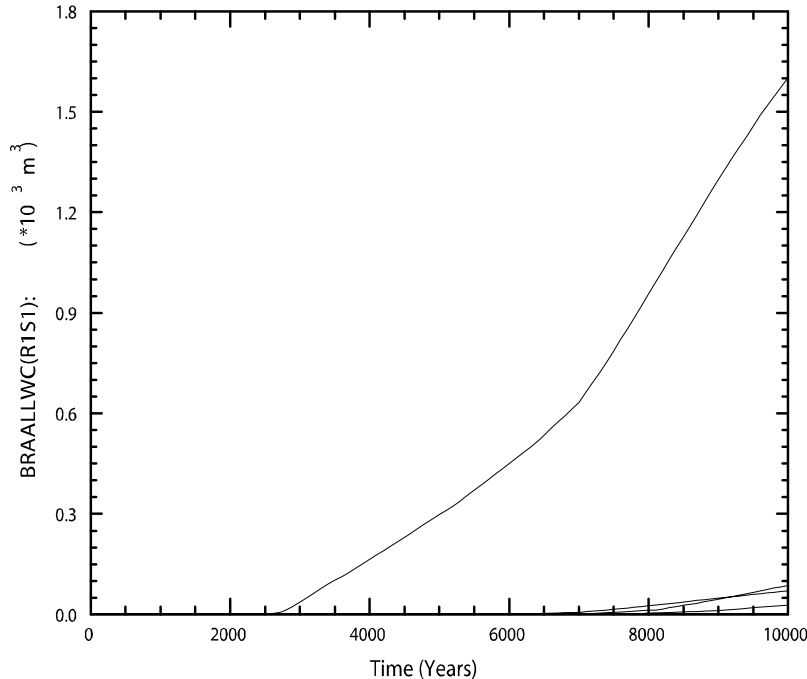
5 The anhydrite MBs and the shafts provide possible pathways for brine flow away from the
 6 repository in the undisturbed (S1) scenario. The Salado flow model only tabulates the volume of
 7 brine crossing boundaries within the model grid; it does not identify whether the brine contains
 8 radionuclides from the waste. Radionuclide transport is calculated separately from the flow and
 9 is discussed in Section PA-7.2.

10 Figure PA-47 shows cumulative brine outflow from the waste-filled regions of the repository
 11 (BRNREPOC), while Figure PA-48 shows the volumes of brine that cross the LWB through the
 12 MBs (BRAALLWC). The largest outflow across the LWB is ~1,600 m³. Brine crossing the
 13 LWB or moving up the shaft does not necessarily indicate releases from the repository, since the
 14 brine may not have been in contact with the waste; the brine may have been present in the MBs
 15 at the start of the regulatory period. Section PA-7.2 presents the results of the radionuclide
 16 transport calculations that determine the amount of radionuclides that may be released through
 17 brine transport.

18 Compared with the CRA-2004 PABC, an increase in the average and maximum cumulative brine
 19 flow away from the repository was observed for the CRA-2009 PA (see Nemer and Clayton
 20 [2008], Table 6-11). The cumulative brine flow to the LWB through the MBs also increased for



21
 22 **Figure PA-47. Brine Flow Away From the Repository, Replicate R1, Scenario S1,**
 23 **CRA-2009 PA**



1
2 **Figure PA-48. Brine Flow via All MBs Across the LWB, Replicate R1, Scenario S1,**
3 **CRA-2009 PA**

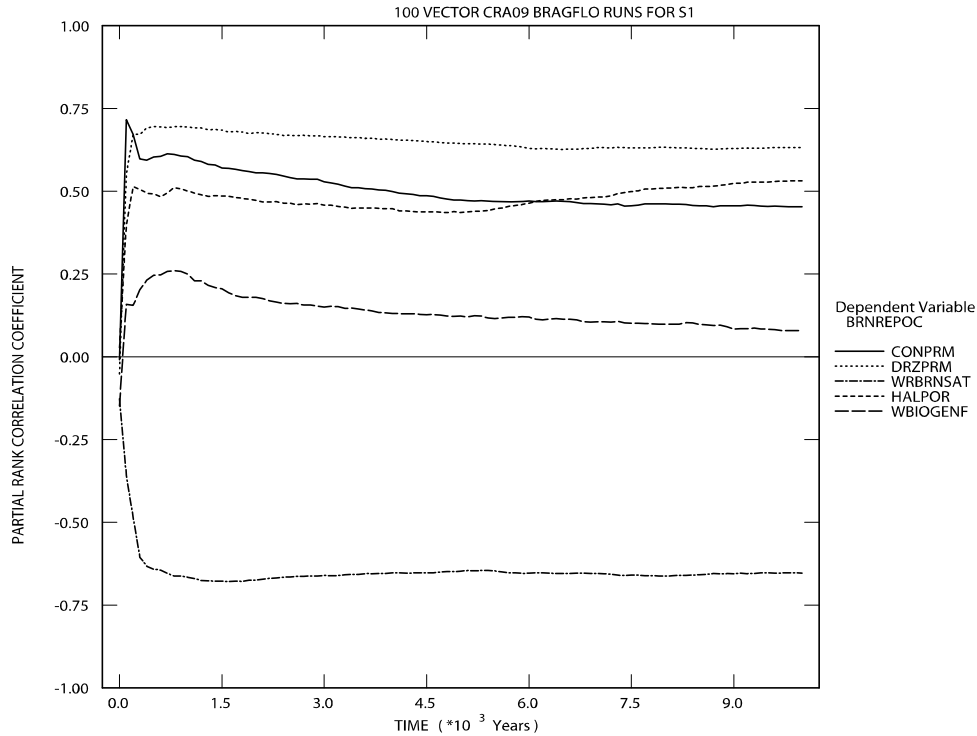
4 the CRA-2009 PA compared to the CRA-2004 PABC. These changes are the result of increased
5 repository pressure (see Section PA-7.1.1).

6 Regression analyses between total cumulative brine flow out of the waste-filled regions
7 (BRNREPOC) and the uncertain parameters are shown in Figure PA-49. The permeability of the
8 DRZ (DRZPRM) has the largest positive correlation, followed by the permeability of the
9 concrete panel seal (CONPRM) and the porosity of undisturbed halite (HALPOR). Increases in
10 the permeability of the DRZ and the concrete panel seal allow more brine to flow out of the
11 repository, as well as into the repository, which increases the gas generation and therefore the
12 pressure. The increase in the halite porosity also increases the pressure, which in turn increases
13 the amount of brine flow out of the repository. The largest negative correlation is with the waste
14 residual brine saturation (WRBRNSAT), which determines the immobile portion of the brine in
15 the waste-filled regions, and limits the amount of brine that can flow out.

16 **PA-7.2 Radionuclide Transport**

17 This section summarizes the radionuclide transport results for the undisturbed repository, both up
18 the shaft to the Culebra and through the Salado to the LWB. Ismail and Garner (2008) present a
19 detailed analysis of the NUTS results for the CRA-2009 PA.

20 Radionuclide transport in the undisturbed (S1) scenario is calculated by the code NUTS.
21 Screening runs using a conservative tracer determine which vectors have the potential to
22 transport radionuclides to the accessible environment. Full transport simulations are then
23 performed for all screened-in vectors (with the potential to transport radionuclides to the
24 accessible environment). Based upon results of the screening exercise, full radionuclide



1
 2 **Figure PA-49. Primary Correlations of Total Cumulative Brine Flow Away from the**
 3 **Repository with Uncertain Parameters, Replicate R1, Scenario S1,**
 4 **CRA-2009 PA**

5 transport simulations were performed for only one vector in the undisturbed case: Replicate R1,
 6 Vector 53. Radionuclide transport simulations were performed for other vectors in the
 7 undisturbed case to postprocess fluid-flow conditions for use in the disturbed scenario
 8 calculations.

9 **PA-7.2.1 Radionuclide Transport to the Culebra**

10 For the undisturbed repository, no vectors showed radionuclide transport through the shafts to
 11 the Culebra. Consequently, no radionuclides could be transported through the Culebra to the
 12 accessible environment under undisturbed conditions (Ismail and Garner 2008).

13 **PA-7.2.2 Radionuclide Transport to the Land Withdrawal Boundary**

14 Radionuclides can also be transported through the Salado MBs to the LWB. For the undisturbed
 15 case, only one vector was screened in. The maximum total integrated activity across the LWB at
 16 the Salado MBs for Replicate R1, Scenario S1, Vector 53 was 2.6×10^{-10} EPA units (Ismail and
 17 Garner 2008), which is the same vector with the largest outflow of brine across the LWB of
 18 $\sim 1,600 \text{ m}^3$. This is comparable to the CRA-2004 PABC results for replicate R1, Scenario S1,
 19 Vector 53 (the only screened-in vector), which had 1.3×10^{-12} EPA units at the boundary
 20 (Lowry 2005). Note that these magnitudes are smaller than the effective numerical precision of
 21 the transport calculations. As explained in Lowry (2005), this value is most likely due to
 22 numerical dispersion as a result of NUTS's finite-difference solution method. The magnitude of

- 1 the nonzero release is indicative of numerical dispersion resulting from the coarse grid spacing
2 between the repository and the LWB, rather than from actual transport of radionuclides.
- 3 Regardless of the significance attached to the numerical values reported above, the releases from
4 the undisturbed scenario are insignificant compared to releases from drilling intrusions (see
5 Section PA-8.4). Consequently, releases in the undisturbed (S1) scenario are omitted from the
6 calculation of total releases from the repository.

1 **PA-8.0 Results for a Disturbed Repository**

2 The WIPP repository might be disturbed by exploratory drilling for natural resources during the
3 10,000-year regulatory period. Drilling could create additional pathways for radionuclide
4 transport, especially in the Culebra, and could release material directly to the surface. In
5 addition, mining for potash within the LWB might alter flow in the overlying geologic units and
6 locally accelerate transport through the Culebra. The disturbed scenarios used in PA modeling
7 capture the range of possible releases resulting from drilling and mining.

8 Total releases are computed by the code CCDFGF. Total releases comprise transport releases
9 and direct releases. Transport releases generally involve movement of radionuclides up an
10 abandoned borehole into the Culebra, then through the Culebra to the LWB. Transport of
11 radionuclides to the Culebra is computed using the codes NUTS and PANEL (see Section PA-
12 6.7.2 and Section PA-6.7.3) using the brine flows computed by BRAGFLO (see Section PA-
13 6.7.1). Radionuclide transport through the Culebra is computed by the code SECOTP2D (see
14 Section PA-6.7.8) using flow fields calculated by MODFLOW (see Section PA-6.7.7).

15 Direct releases occur at the time of a drilling intrusion and include releases of solids (cuttings,
16 cavings, and spallings) computed using the code CUTTINGS_S (see Section PA-6.7.4) and
17 DBRs computed using BRAGFLO (see Section PA-6.7.6). Pressure and brine saturation within
18 the waste areas are used as initial conditions for the direct release models. Results from the
19 undisturbed repository (see Section PA-7.0) are used as the initial conditions for the first
20 intrusion. To calculate initial conditions for subsequent intrusions, and to compute the source of
21 radionuclides for transport in the Culebra, BRAGFLO uses a set of drilling scenarios to calculate
22 conditions within the repository after an intrusion (see Section PA-6.7.6).

23 This section first summarizes the scenarios used to represent drilling intrusions and the resulting
24 repository conditions calculated by BRAGFLO. Transport releases are presented next, followed
25 by cuttings, cavings, spallings, and DBRs. Section PA-8.0 is taken from Clayton et al. (2008,
26 Section 5.0).

27 **PA-8.1 Drilling Scenarios**

28 As shown in Table PA-25, the PA considers two types of drilling intrusions: E1 and E2. The E1
29 intrusion scenario represents the possibility that a borehole creates a pathway between the
30 repository and a pressurized brine reservoir located within the underlying Castile formation. The
31 E2 intrusion scenario represents a borehole that intrudes into the repository, but does not connect
32 the repository with an underlying brine reservoir. Repository conditions are calculated for the
33 E1 intrusion scenario at 350 and 1,000 years, and are referred to as the BRAGFLO S2 and S3
34 scenarios, respectively. The BRAGFLO Scenarios S4 and S5 represent E2 intrusions that occur
35 at 350 and 1,000 years, respectively. An additional BRAGFLO scenario, S6, simulates the
36 effects of an E2 intrusion at 1,000 years followed by an E1 intrusion 1,000 years later into the
37 same panel.

1 **PA-8.2 Mining Scenarios**

2 Long-term releases within the Culebra could be influenced by future mining activities that
3 remove all the known potash reserves within the LWB and cause the transmissivity within the
4 overlying Culebra to change (see Section PA-4.8). The full mining of known potash reserves
5 within the LWB in the absence of AICs and PICs is modeled as a Poisson process, with a rate of
6 10^{-4} yr^{-1} (see Section PA-3.9). For any particular future, this rate is used to determine a time at
7 which full mining has occurred. Flow fields are calculated for the Culebra for two conditions:
8 partial mining, which assumes all potash has been mined from reserves outside the LWB; and
9 full mining, which assumes all reserves have been mined both inside and outside the LWB.
10 Radionuclide transport through the Culebra uses the partial-mining flow fields prior to the time
11 at which full mining has occurred and the full-mining flow fields after that time.

12 **PA-8.3 Salado Flow**

13 This section summarizes the results of the Salado flow calculations for the disturbed scenarios.
14 Nemer and Clayton (2008) provide a detailed presentation on the BRAGFLO model, calculation
15 results, and further sensitivity analyses.

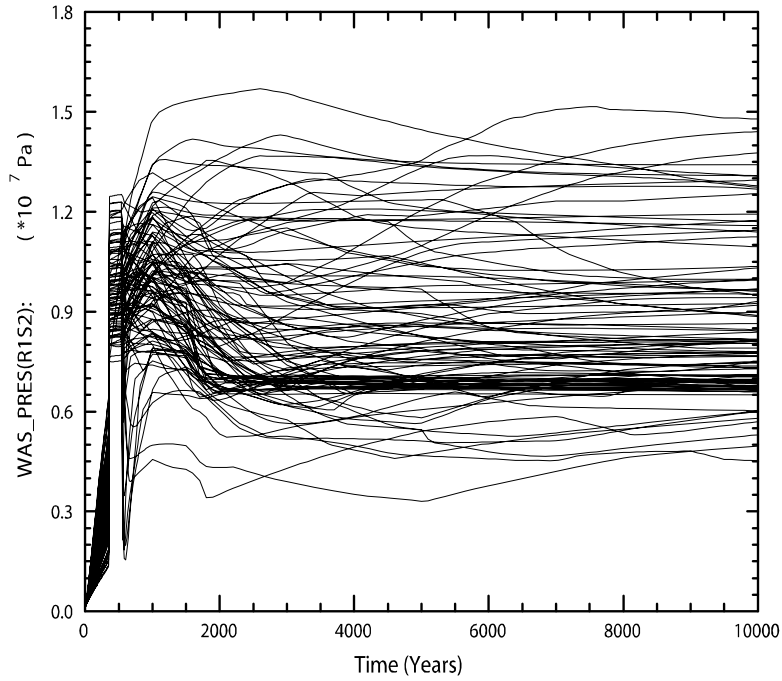
16 **PA-8.3.1 Pressure in the Repository**

17 Figure PA-50 and Figure PA-51 show pressure in the waste panel (WAS_PRES for Waste Panel
18 area in Figure PA-15) for the 100 vectors of replicate R1 for BRAGFLO Scenarios S2 and S4,
19 respectively. The pressure exhibits varying patterns depending on the type of intrusion.

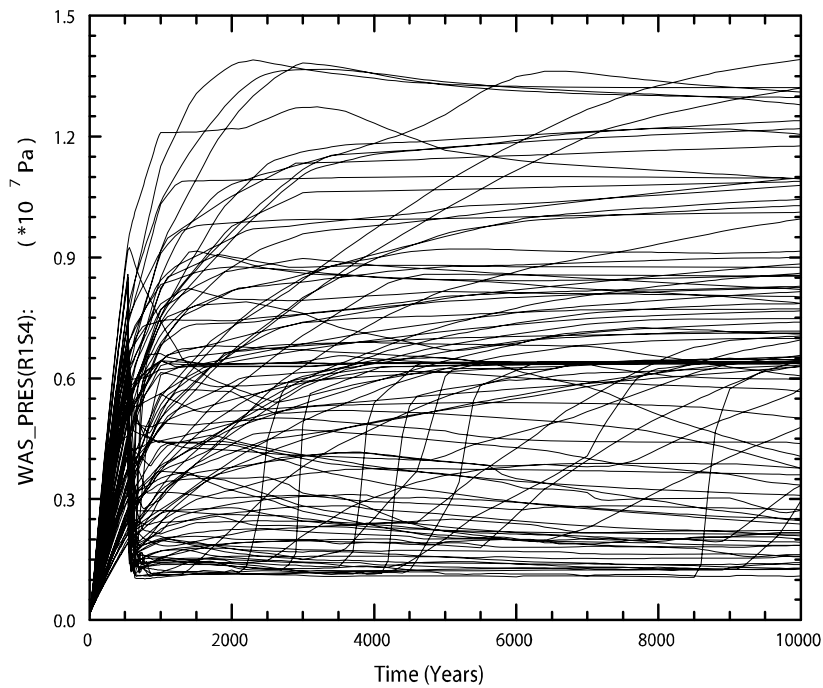
20 Scenario S2 represents an E1 intrusion at 350 years. At the time of the intrusion, brine flow from
21 the Castile brine reservoir leads to an increase in pressure (Figure PA-50). However, pressure
22 drops sharply 200 years after the intrusion, when the borehole plugs above the repository are
23 assumed to fail and the permeability of the borehole generally increases. In vectors with low
24 borehole permeability, pressure does not change noticeably as a result of the borehole plug
25 failure (Nemer and Clayton 2008).

26 Scenario S4 represents an E2 intrusion at 350 years. The borehole plugs effectively prevent any
27 change in repository pressure from the time of the intrusion until the borehole plugs fail (Figure
28 PA-51). As in the scenarios for E1 intrusions, pressure generally drops sharply when the plugs
29 fail, except for vectors with low borehole permeability after plug failure. The pressure is
30 generally lower in the E2 intrusion scenarios compared to the undisturbed and E1 intrusion
31 scenarios (Nemer and Clayton 2008).

32 The pressure trends in the disturbed scenarios for the CRA-2009 PA are similar to the results
33 obtained for the CRA-2004 PABC. The average and maximum pressures are comparable
34 between the two analyses, as well (see Table 6-16 in Nemer and Clayton [2008]). As the
35 intrusion creates a pathway for brine and gas to flow into and away from the repository, the
36 effect of the increased halite porosity is minimized (Nemer and Clayton 2008).



1
2 **Figure PA-50. Pressure in the Waste Panel Region for Replicate R1, Scenario S2,**
3 **CRA-2009 PA**



4
5 **Figure PA-51. Pressure in the Waste Panel Region for Replicate R1, Scenario S4,**
6 **CRA-2009 PA**

1 Computing PRCCs between the pressure in the waste panel (WAS_PRES) and the uncertain
2 parameters in the LHS identifies a number of parameters that contribute to the uncertainty in
3 pressure for the disturbed scenarios. The relative importance of these parameters varies over the
4 10,000-year modeling period. Figure PA-52 and Figure PA-53 show the regression analysis
5 results for pressure in the Waste Panel with uncertain parameters versus time for Scenarios S2
6 and S4, Replicate R1 from the CRA-2009 PA, respectively.

7 For both scenarios, the borehole permeability (BHPERM) has the largest negative correlation
8 with pressure after the intrusion, as this is the primary means by which pressure may escape the
9 repository in the disturbed scenarios. For Scenario S2 (Figure PA-52), the initial Castile brine
10 pocket pressure (BPINTPRS) has the largest positive correlation after the intrusion, while for
11 Scenario S4 (Figure PA-53), the largest positive correlation for the majority of the time after the
12 intrusion, results from the halite porosity (HALPOR). The negative correlation of the borehole
13 permeability is stronger than the positive correlation of the initial Castile brine pocket pressure
14 and halite porosity for either scenario.

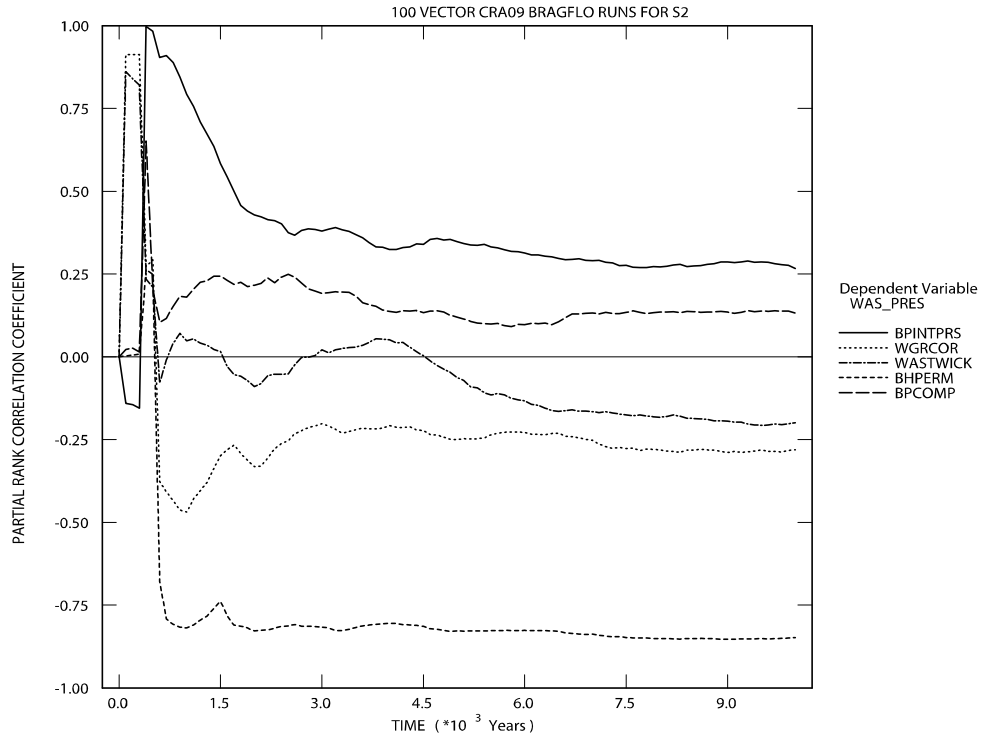
15 The higher initial Castile brine pocket pressure causes more brine at a higher pressure to flow
16 into the repository, while increasing the halite porosity increases the volume of brine available in
17 the material overlying the waste, which, as the brine flows into the waste panel, can then increase
18 the amount of brine in the repository. Microbial gas generation rates are a function of the brine
19 in the repository and increase as more brine is available. Increased gas generation results in
20 increased repository pressures.

21 The pressure in the waste panel is also controlled by the corrosion rate for steel (WGRCOR), the
22 waste wicking parameter (WASTWICK), and the index for the model of microbial degradation
23 (WMICDFLG), which all affect the gas generation rates and therefore the pressure. For Scenario
24 S2, increasing the brine pocket compressibility (BPCOMP) increases the brine inflow from the
25 brine pocket to the repository, and thus the pressure in the repository.

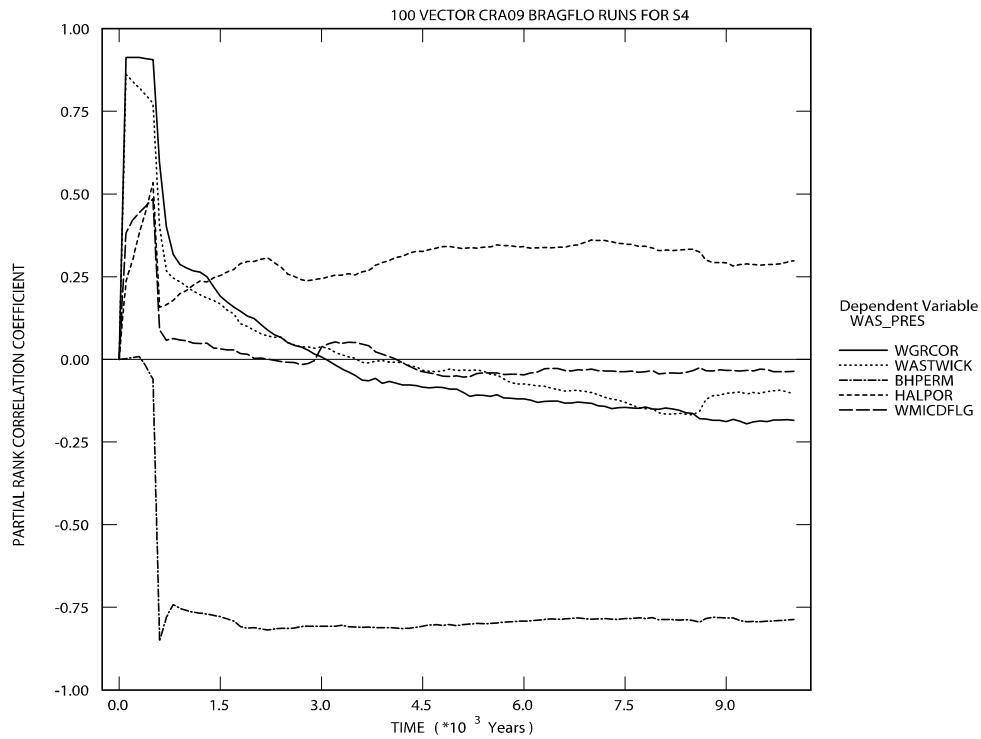
26 **PA-8.3.2 Brine Saturation**

27 Brine saturation tends to increase after a drilling intrusion. Figure PA-54 and Figure PA-55
28 show brine saturation in the waste panel (WAS_SATB for area Waste Panel in Figure PA-15) for
29 Replicate R1 for BRAGFLO Scenarios S2 and S4, respectively.

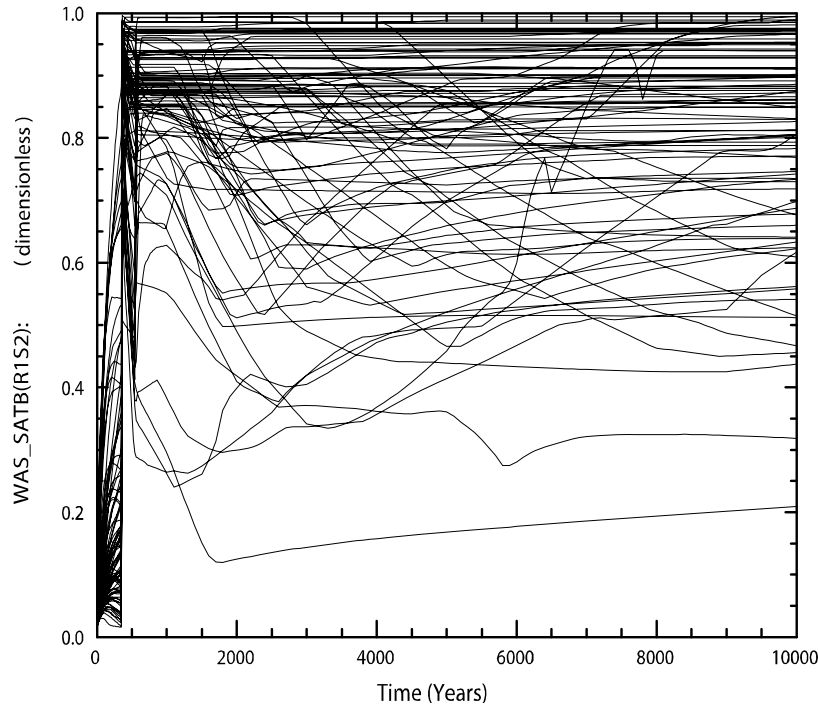
30 Scenario S2 represents an E1 intrusion at 350 years. At the time of the intrusion, brine flow from
31 the Castile brine reservoir increases saturation (Figure PA-54). However, saturation can drop
32 sharply 200 years after the intrusion when the borehole plugs above the repository are assumed
33 to fail and the permeability of the borehole generally increases. In vectors with low borehole
34 permeability, saturation does not change noticeably as a result of the borehole plug failure.
35 Twelve hundred years after the drilling intrusion, the permeability of the borehole connecting the
36 repository to the Castile is assumed to be reduced by an order of magnitude because of creep
37 closure. This material change reduces saturation in some vectors, but does not appear to have a
38 significant effect on the saturation in most vectors.



1
2 **Figure PA-52. Primary Correlations of Pressure in the Waste Panel Region with**
3 **Uncertain Parameters, Replicate R1, Scenario S2, CRA-2009 PA**



4
5 **Figure PA-53. Primary Correlations of Pressure in the Waste Panel Region with**
6 **Uncertain Parameters, Replicate R1, Scenario S4, CRA-2009 PA**



1
2 **Figure PA-54. Brine Saturation in the Waste Panel Region for Replicate R1, Scenario S2,**
3 **CRA-2009 PA**

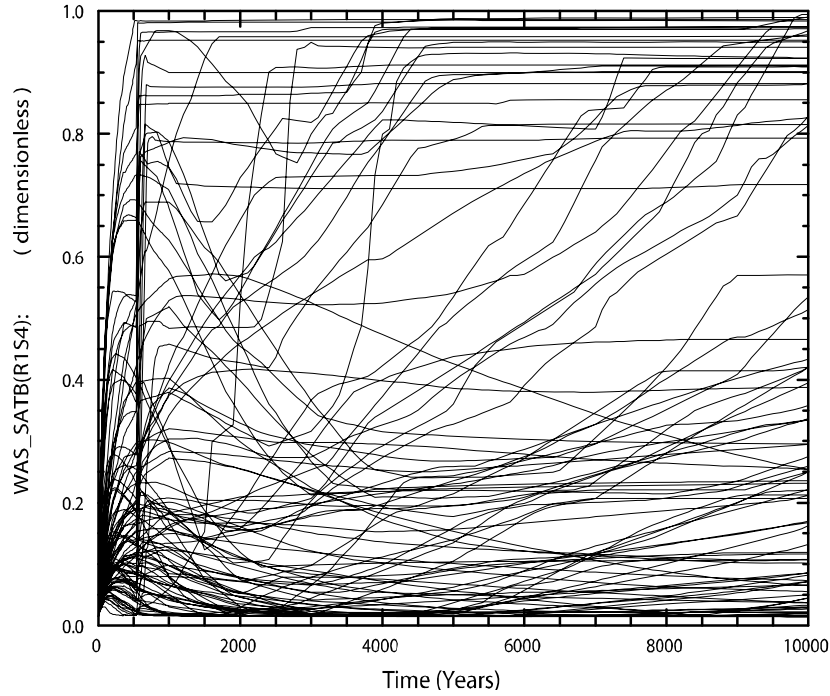
4 Scenario S4 represents an E2 intrusion at 350 years. The borehole plugs effectively prevent any
5 change in repository saturation from the time of the intrusion until the borehole plugs fail (Figure
6 PA-55). Unlike the E1 intrusions scenarios, saturation generally increases sharply when the
7 plugs fail, except for vectors with low borehole permeability after plug failure. The saturation is
8 generally lower in the E2 intrusion scenarios compared to the E1 intrusion scenarios.

9 The brine saturation trends in the disturbed scenarios for the CRA-2009 PA are similar to the
10 results obtained for the CRA-2004 PABC. The average and maximum brine saturations are
11 comparable between the two analyses, as well (see Nemer and Clayton [2008, Table 6-15]).

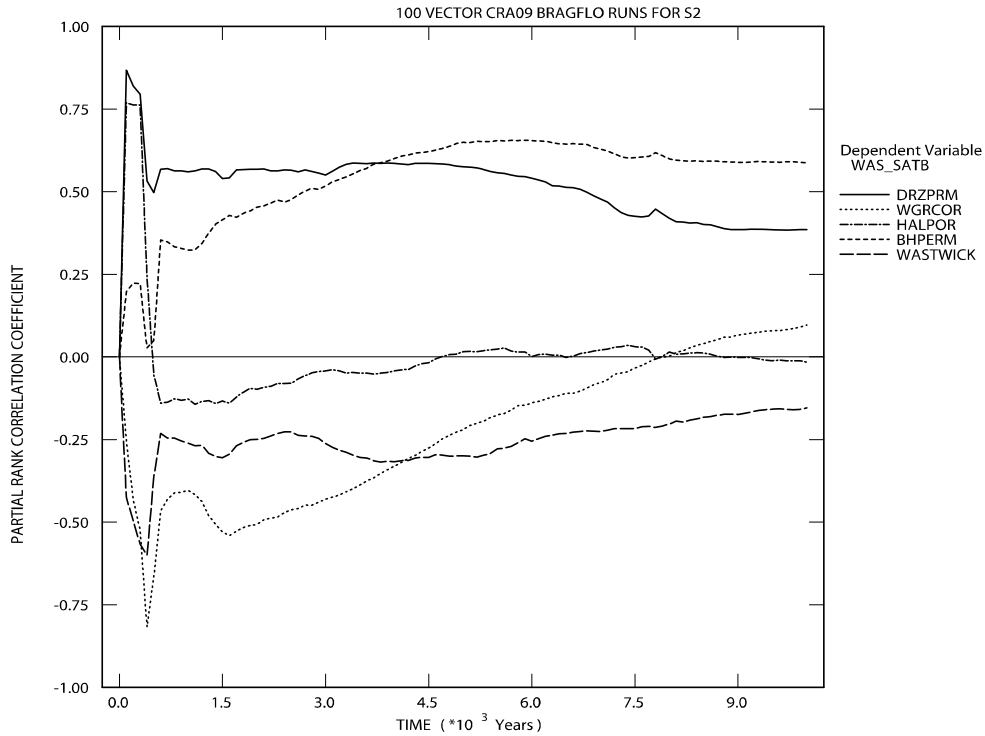
12 As the intrusion creates a pathway for brine and gas to flow into and away from the repository,
13 the effect of the increased porosity is minimized (Nemer and Clayton 2008).

14 Computing PRCCs between the saturation in the waste panel (WAS_SATB) and the uncertain
15 parameters in the LHS identifies a number of parameters that contribute to the uncertainty in
16 pressure for the disturbed scenarios. The relative importance of these parameters varies over the
17 10,000-year modeling period. Figure PA-56 and Figure PA-57 show the regression analysis
18 results for saturation in the Waste Panel with uncertain parameters versus time for Scenarios S2
19 and S4, and Replicate R1 from the CRA-2009 PA, respectively.

20 For Scenario S2 (Figure PA-56), the DRZ permeability (DRZPRM) and the borehole
21 permeability (BHPERM) have positive correlations. Increases in DRZ and borehole
22 permeability accelerate brine flow into the waste. The corrosion rate for steel (WGRCOR) and
23



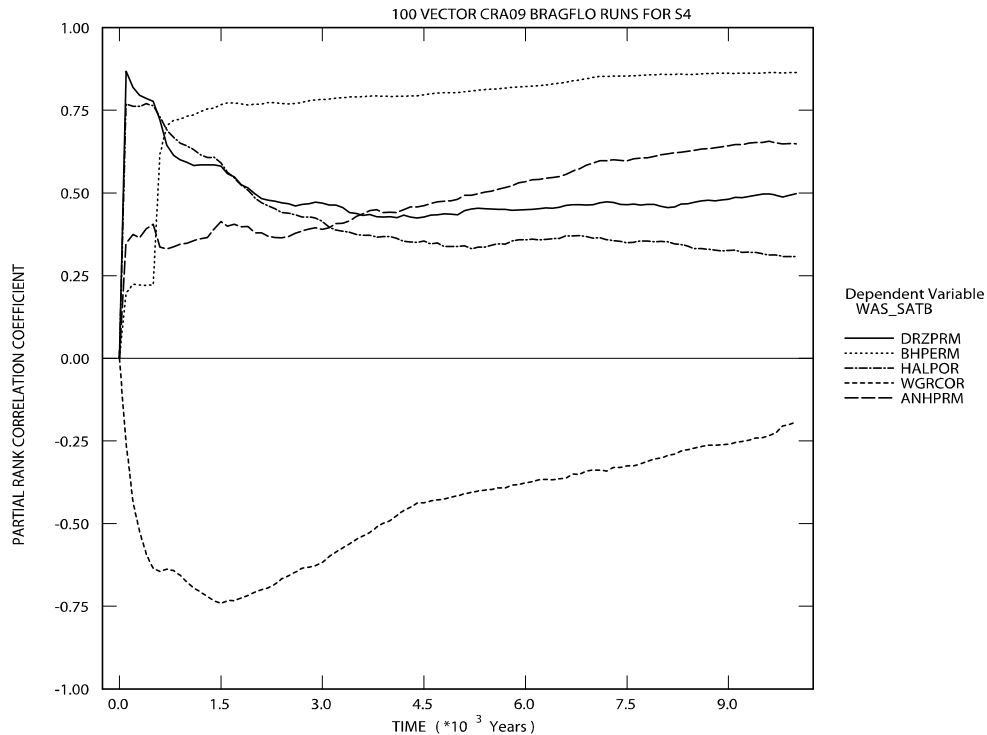
1
 2 **Figure PA-55. Brine Saturation in the Waste Panel Region for Replicate R1, Scenario S4,**
 3 **CRA-2009 PA**



4
 5 **Figure PA-56. Primary Correlations of Brine Saturation in the Waste Panel Region with**
 6 **Uncertain Parameters, Replicate R1, Scenario S2, CRA-2009 PA**

1 the waste wicking parameter (WASTWICK) are negatively correlated with the saturation, as
 2 these control the brine-consuming reactions. The halite porosity (HALPOR) has a high positive
 3 correlation before the intrusion, which then decreases.

4 For Scenario S4 (Figure PA-57), the largest positive correlation results from borehole
 5 permeability (BHPERM), with the DRZ permeability (DRZPRM), anhydrite permeability
 6 (ANHPRM), and the halite porosity (HALPOR) also showing high positive correlations.
 7 Increases in DRZ, borehole, and anhydrite permeability accelerate brine flow into the waste,
 8 while increases in halite porosity increase the volume of brine available in the material overlying
 9 the waste, all of which control the amount of brine flow into and out of the repository. The
 10 corrosion rate for steel (WGRCOR) is negatively correlated with the saturation, as this is a brine-
 11 consuming reaction.

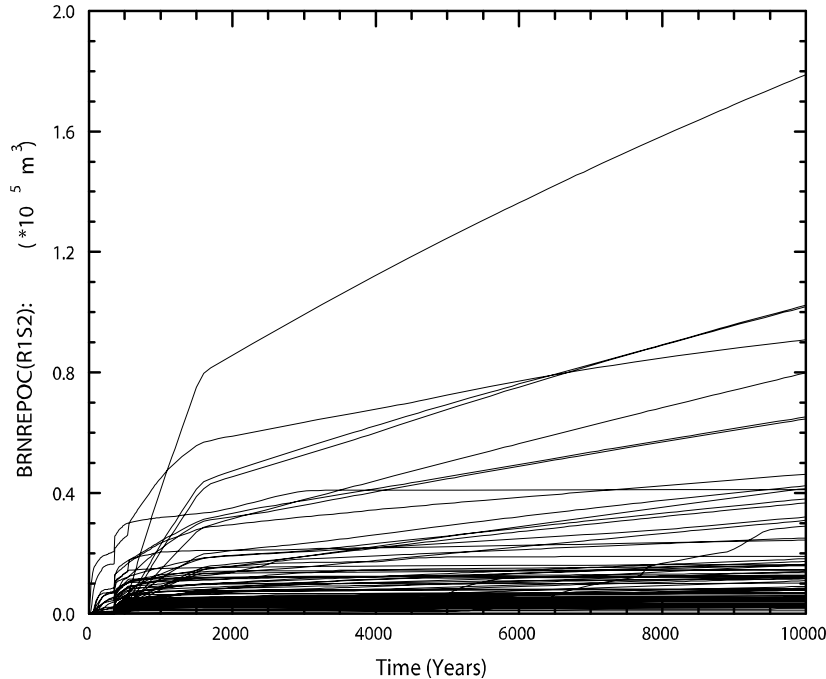


12
 13 **Figure PA-57. Primary Correlations of Brine Saturation in the Waste Panel Region with**
 14 **Uncertain Parameters, Replicate R1, Scenario S4, CRA-2009 PA**

15 **PA-8.3.3 Brine Flow out of the Repository**

16 This section describes the flow of brine up a borehole to the Culebra. Brine flow to the Culebra
 17 is important in calculating long-term releases to the Culebra. Direct brine flow up the borehole
 18 to the surface at the time of drilling is modeled separately in the DBR calculations, presented in
 19 Section PA-8.5.3.

20 Figure PA-58 shows cumulative brine flow out of the repository (BRNREPOC) for Scenario S2.
 21 Scenario S2 represents an E1 intrusion at 350 years. At the time of the intrusion, brine flow from
 22 the Castile brine reservoir fills the repository. At 200 years after the intrusion, when the
 23



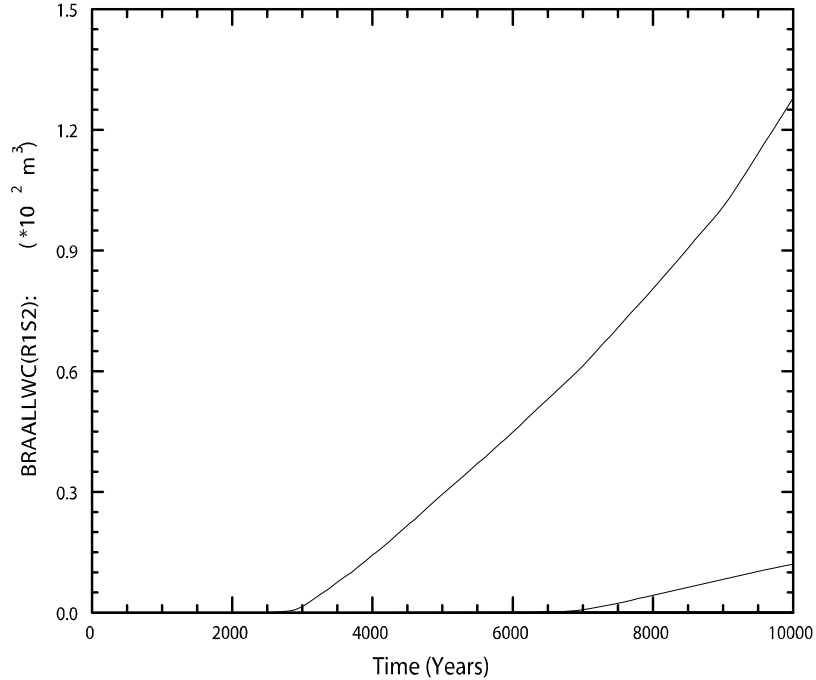
1

2 **Figure PA-58. Total Cumulative Brine Outflow in Replicate R1, Scenario S2,**
 3 **CRA-2009 PA**

4 borehole plugs above the repository are assumed to fail and the permeability of the borehole
 5 generally increases, most of the brine leaving the repository flows up the borehole to the
 6 Culebra. In vectors with low borehole permeability, the brine flow out of the repository does not
 7 noticeably change as a result of the borehole plug failure. Twelve hundred years after the
 8 drilling intrusion, the permeability of the borehole between the repository and the Castile is
 9 reduced by an order of magnitude because of creep closure, reducing brine flow into the
 10 repository and causing a corresponding decrease in brine flow out of the repository. This
 11 material change reduces brine flow out of the repository in some vectors, but does not appear to
 12 have a significant effect on the brine flow out of the repository in most vectors.

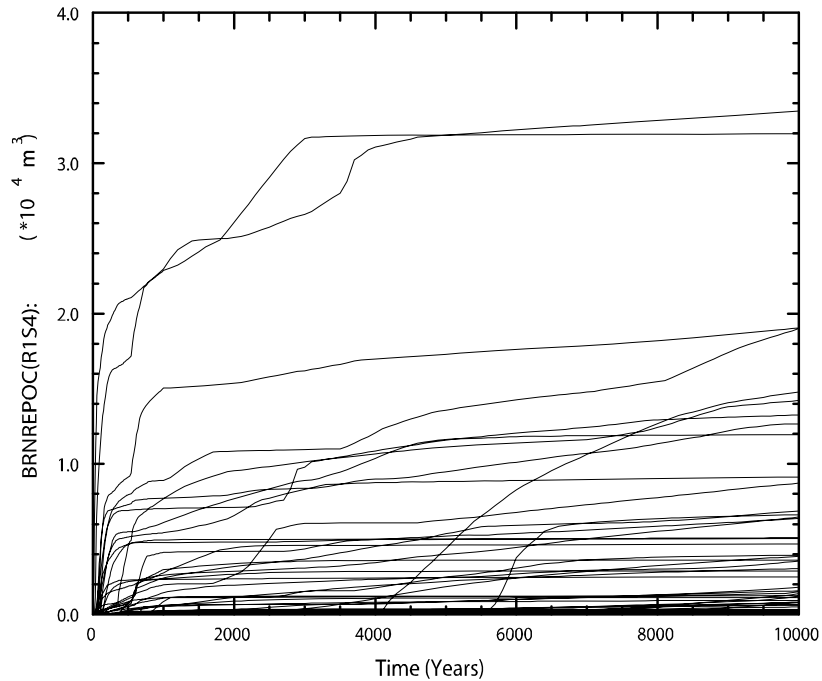
13 Figure PA-59 shows the volumes of brine that cross the LWB through the MBs for Scenario S2.
 14 The largest outflow across the LWB is $\sim 127 \text{ m}^3$, which is significantly less than the undisturbed
 15 scenario results (see Section PA-7.1.3). As the intrusion creates a pathway to the Culebra, flow
 16 to the LWB is reduced. Brine crossing the LWB or moving up the shaft does not necessarily
 17 indicate releases from the repository because the brine may not have been in contact with the
 18 waste; the brine may have been present in the MBs at the start of the regulatory period. Section
 19 PA-8.4 presents the results of the radionuclide transport calculations that determine the amount
 20 of radionuclides that may be released by transport in brine for the disturbed scenarios.

21 The total cumulative brine flow away from the repository and the brine flow across the LWB in
 22 the disturbed scenarios for the CRA-2009 PA are similar to the results obtained for the CRA-
 23 2004 PABC. The average and maximum brine flows are comparable between the two analyses
 24 as well (see Nemer and Clayton [2008, Table 6-18]). As the intrusion creates a pathway for
 25 brine and gas to flow into and away from the repository, the effect of the increased porosity is
 26 minimized (Nemer and Clayton 2008).



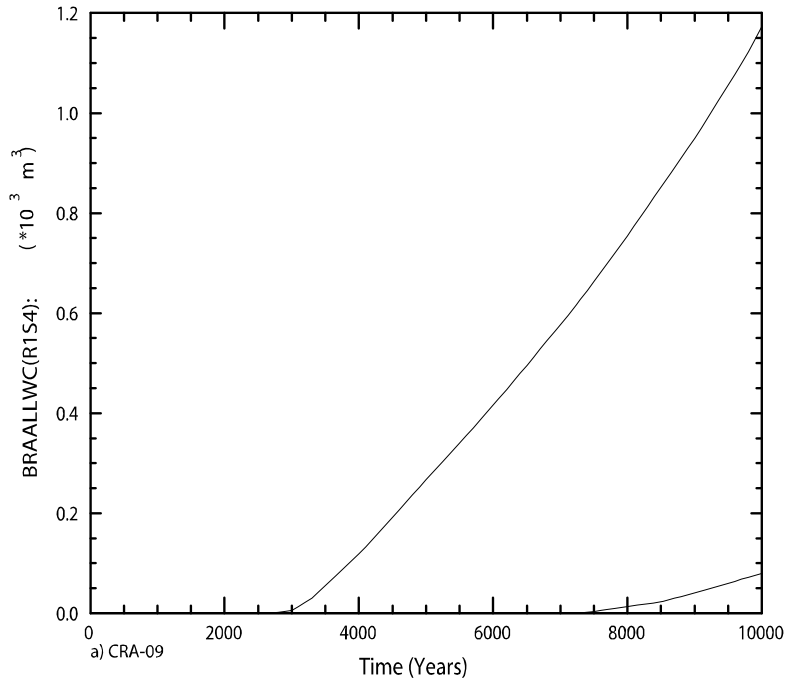
1
 2 **Figure PA-59. Brine Flow via All MBs Across the LWB in Replicate R1, Scenario S2,**
 3 **CRA-2009 PA**

4 Figure PA-60 shows cumulative brine flow out of the repository (BRNREPOC) for the
 5 BRAGFLO Scenario S4, which represents an E2 intrusion at 350 years. The results for the S4
 6 scenario are very similar to the results for the Undisturbed Scenario S1 (see Section PA-7.1.3).



7
 8 **Figure PA-60. Total Cumulative Brine Outflow in Replicate R1, Scenario S4,**
 9 **CRA-2009 PA**

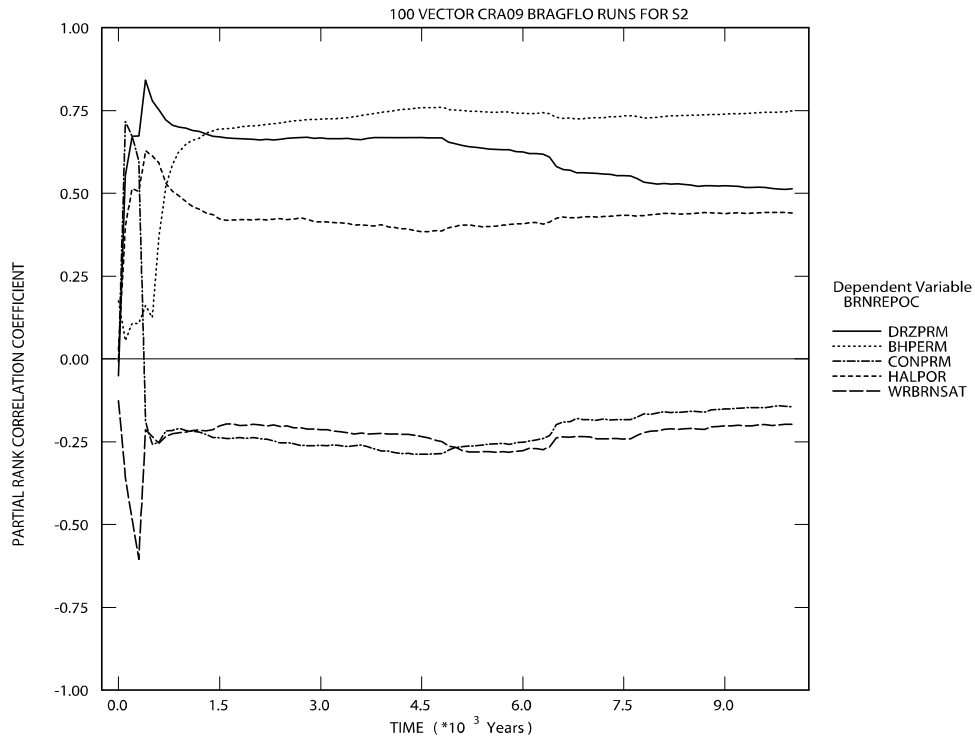
1 Figure PA-61 shows the volumes of brine that cross the LWB through the MBs for the
 2 BRAGFLO Scenario S4. The largest outflow across the LWB is ~1,200 m³, which is smaller
 3 than the undisturbed scenario results (see Section PA-7.1.3). As the intrusion creates a pathway
 4 to the Culebra, flow to the LWB is reduced. Brine crossing the LWB or moving up the shaft
 5 does not necessarily indicate releases from the repository, since the brine may not have been in
 6 contact with the waste; the brine may have been present in the MBs at the start of the regulatory
 7 period. Section PA-8.4 presents the results of the radionuclide transport calculations that
 8 determine the amount of radionuclides that may be released by transport in brine for the
 9 disturbed scenarios.



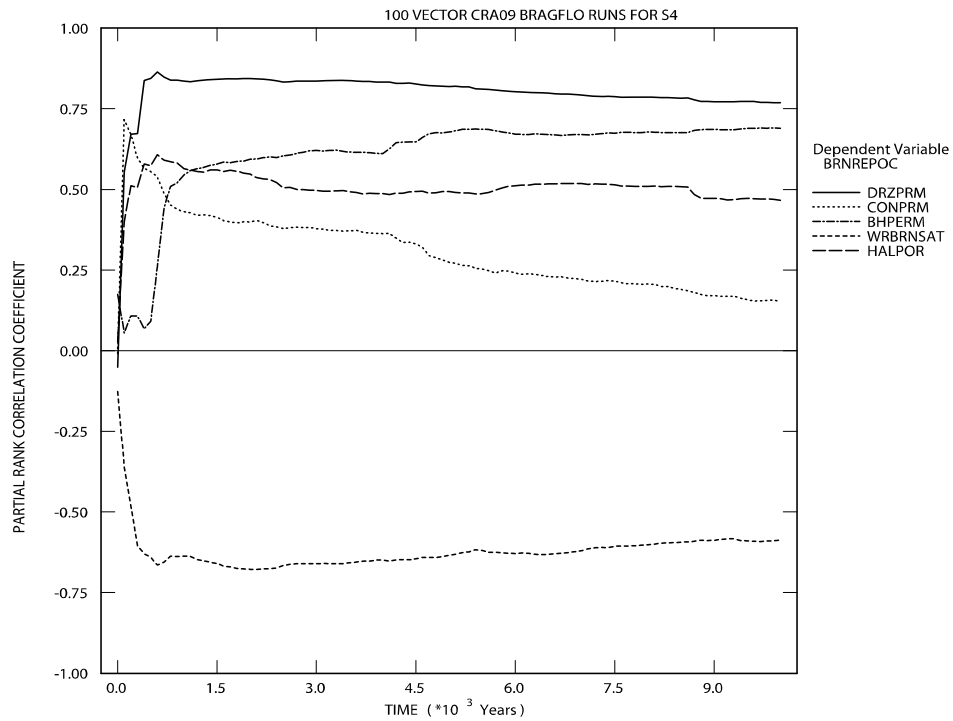
10
 11 **Figure PA-61. Brine Flow via All MBs Across the LWB in Replicate R1, Scenario S4,**
 12 **CRA-2009 PA**

13 Regression between total cumulative brine flow out of the waste-filled regions (BRNREPOC)
 14 and the uncertain parameters are shown in Figure PA-62 and Figure PA-63 for the BRAGFLO
 15 Scenarios S2 and S4, respectively. For the S2 and S4 scenarios, the permeability of the DRZ
 16 (DRZPRM), the borehole permeability (BHPERM), and the porosity of undisturbed halite
 17 (HALPOR) have positive correlations. Increases in the DRZ and borehole permeability allow
 18 more brine to flow out of the repository. The increase in the halite porosity is correlated with the
 19 increase in pressure, and an increase in pressure increases the amount of brine flow out of the
 20 repository.

21 A negative correlation with the waste residual brine saturation (WRBRNSAT) is shown for both
 22 the S2 and S4 scenarios, which determines the immobile portion of the waste brine saturation,
 23 limiting the amount of brine that can flow out of the waste-filled regions. The permeability of
 24 the concrete panel seal (CONPRM) is negatively correlated for the S2 scenario and positively
 25



1
 2 **Figure PA-62. Primary Correlations of Cumulative Brine Flow Away from the Repository**
 3 **with Uncertain Parameters, Replicate R1, Scenario S2, CRA-2009 PA**



4
 5 **Figure PA-63. Primary Correlations of Cumulative Brine Flow Away from the Repository**
 6 **with Uncertain Parameters, Replicate R1, Scenario S4, CRA-2009 PA**

1 correlated for the S4 scenario. The increased permeability of the concrete panel seal allows more
2 brine to flow from the intruded panel to the remainder of the repository (flow into another panel
3 is not considered out of the repository), reducing the higher-pressure conditions in the intruded
4 panel in the S2 scenario, and therefore the flow out of the repository through the borehole. In
5 contrast, in the S4 scenario, the increased permeability allows the brine from the remainder of
6 the repository to flow into the depressurized intruded panel, increasing the pressure and flow out
7 of the repository up the borehole.

8 **PA-8.4 Radionuclide Transport**

9 In the disturbed scenarios, radionuclide transport in the Salado is calculated by the code NUTS
10 (see Section PA-6.7.2). Radionuclide transport from the Salado to the Culebra is calculated by
11 NUTS and PANEL (see Section PA-6.7.2 and Section PA-6.7.3). Radionuclide transport within
12 the Culebra is calculated by SECOTP2D (see Section PA-6.7.8). For all radionuclide transport
13 calculations, mobilized concentrations of radionuclides in Salado and Castile brines are
14 computed by the code PANEL (see Section PA-6.7.3).

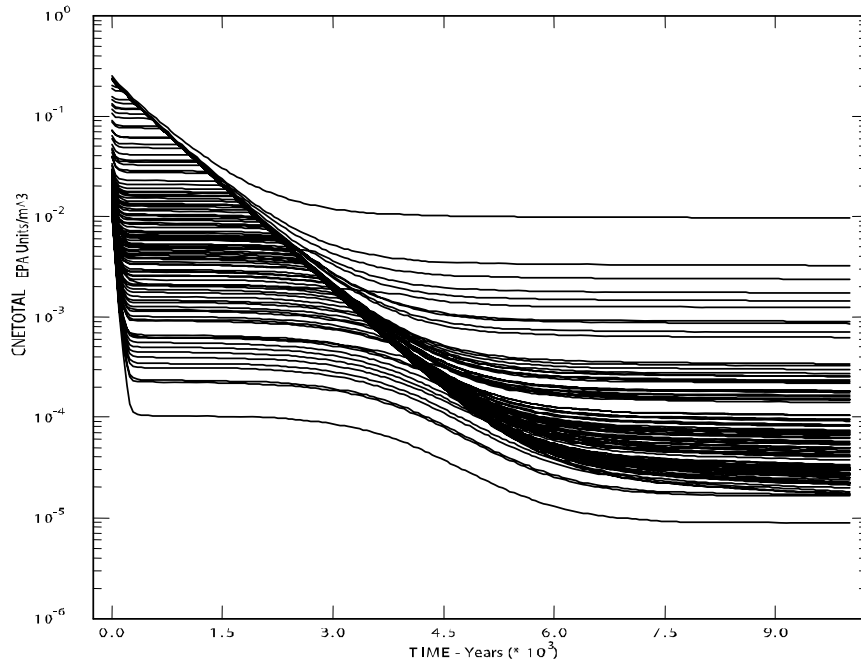
15 This section summarizes the radionuclide transport results for the disturbed scenarios. Nemer
16 and Clayton (2008) describe the brine and gas flow in the Salado. Detailed analysis of the
17 radionuclide transport in the Salado is presented in Ismail and Garner (2008). Garner and Leigh
18 (2005) provide an analysis of the mobilized concentrations of radionuclides in Salado and Castile
19 brines. Lowry and Kanney (2005) present an analysis of the flow and radionuclide transport
20 within the Culebra.

21 **PA-8.4.1 Radionuclide Source Term**

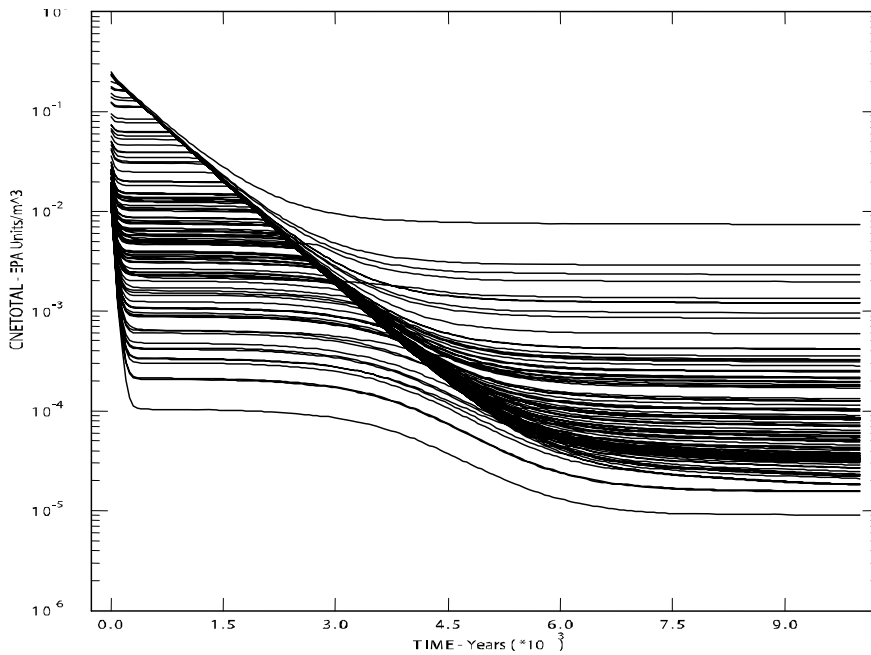
22 The code PANEL calculates the time-varying concentration of radionuclides mobilized in brine,
23 either as dissolved isotopes or as isotopes sorbed to mobile colloids (see Equation (PA.118) and
24 Equation (PA.119)). Two different brines are considered: Generic Weep Brine (GWB), a
25 magnesium-rich interstitial brine present in the Salado Formation; and ERDA-6, a sodium-rich
26 brine in the Castile. Radionuclide solubility in the two brines can be considerably different.
27 Before an E1 intrusion, PA assumes that the brine in the repository is GWB; after an E1
28 intrusion, brine in the repository is assumed to be ERDA-6.

29 Figure PA-64 and Figure PA-65 show the concentration of radioactivity mobilized in Salado and
30 Castile brines, respectively, as a function of time for all vectors in Replicate R1 for the
31 CRA-2009 PA. Because the inventory is unchanged from the CRA-2004 PABC, the results are
32 identical to the CRA-2004 PABC results. Concentrations are expressed as EPA units/m³ to
33 combine the radioactivity in different isotopes and reduce the computational time required for
34 the transport calculations.

35 Short-lived radionuclides, such as ²³⁸Pu, decay rapidly in the first few years. After this initial
36 decay, the mobilized concentration is dominated by Am (Garner and Leigh 2005); the
37 concentration of Am is limited by its solubility until all the inventory of Am is in solution. After
38 all Am is in solution, the total radionuclide concentration generally decreases as the Am decays,
39 until the mobilized concentration becomes dominated by Pu (Garner and Leigh 2005). The
40



1
2 **Figure PA-64. Total Mobilized Concentrations in Salado Brine, Replicate R1,**
3 **CRA-2009 PA**



4
5 **Figure PA-65. Total Mobilized Concentrations in Castile Brine, Replicate R1,**
6 **CRA-2009 PA**

1 horizontal lines in the figures indicate periods of time when the total radionuclide concentration
2 is limited by the solubility of Am (before about 3,000 years) or Pu (after about 6,000 years).
3 Thus, the uncertainty in total radionuclide concentration is determined by the uncertainty factors
4 used to calculate solubilities for Am and Pu.

5 **PA-8.4.2 Transport through MBs and Shaft**

6 In the disturbed scenarios, of the 300 realizations, only Vectors 53 and 59 in Replicate R1
7 resulted in transport of radionuclides through the MBs and across the LWB, with a maximum
8 total integrated activity of 3.6×10^{-10} EPA units (Ismail and Garner 2008). This is comparable
9 to the CRA-2004 PABC results for maximum integrated activity, which had 2.4×10^{-12} EPA
10 units at the boundary (Lowry 2005). The releases through the MBs and across the LWB are
11 insignificant compared to releases from drilling intrusions. In addition, no realization showed
12 transport of radionuclides through the shaft to the Culebra.

13 **PA-8.4.3 Transport to the Culebra**

14 Radionuclide transport to the Culebra via a single intrusion borehole (Disturbed Scenarios S2,
15 S3, S4, and S5) is modeled with the code NUTS (Section PA-4.3). Transport to the Culebra in
16 the multiple intrusion scenario (S6) is modeled with the code PANEL (Section PA-4.4).
17 Detailed discussion of the radionuclide transport to the Culebra calculations can be found in
18 Ismail and Garner (2008).

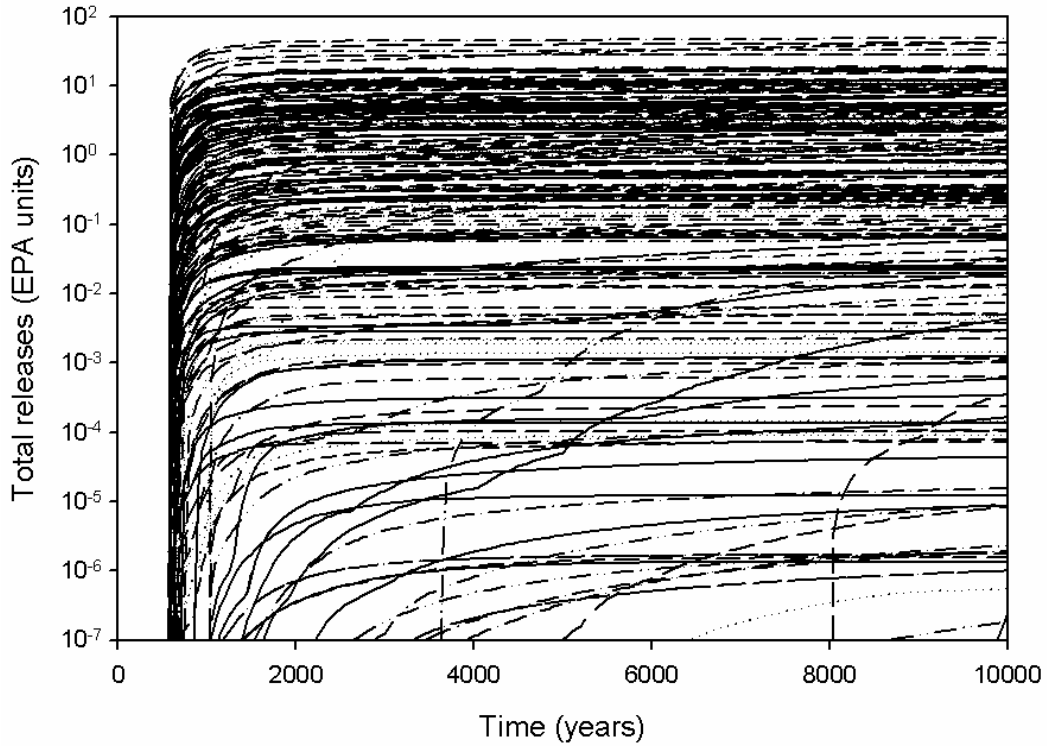
19 **PA-8.4.3.1 Single Intrusion Scenarios**

20 Figure PA-66 through Figure PA-69 show cumulative radioactivity transported up the borehole
21 to the Culebra in the single intrusion scenarios. Transport to the Culebra is larger and occurs for
22 more vectors in the S2 and S3 scenarios (E1 intrusions) than in the S4 or S5 scenarios (E2
23 intrusions). For most vectors that show significant transport, most of the transport occurs over a
24 relatively short period of time immediately after the borehole plugs fail.

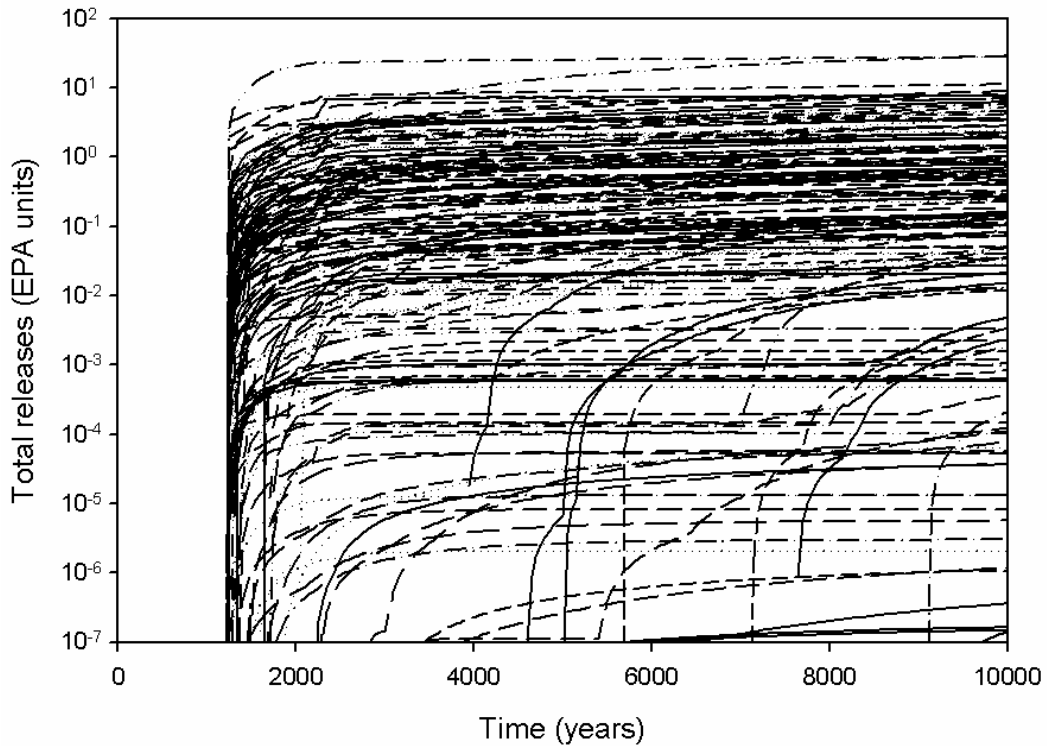
25 When compared to the results of the CRA-2004 PABC, the CRA-2009 PA showed minor
26 differences (see Ismail and Garner [2008, Section 4.2.4]). The primary changes from the CRA-
27 2004 PABC to the CRA-2009 PA that affected the calculations of transport to the Culebra are the
28 correction of the input files (Ismail 2007b) and the correction of the halite porosity (Ismail
29 2007a). Neither change significantly affected the results (Ismail and Garner 2008).

30 **PA-8.4.3.2 Multiple Intrusion Scenario**

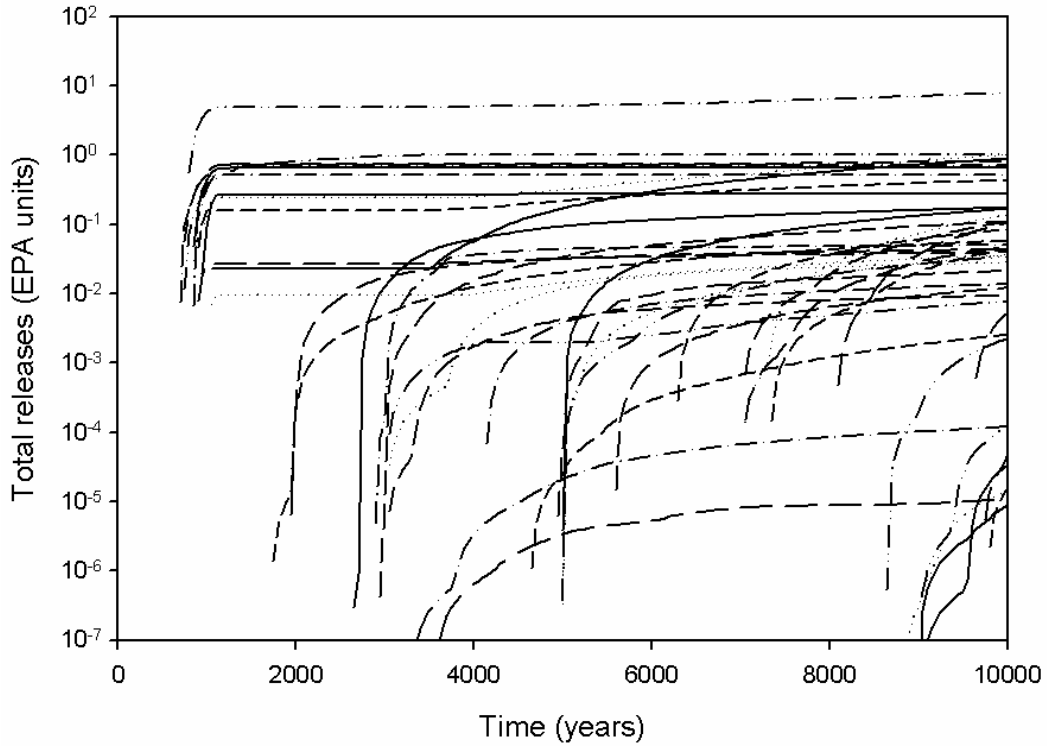
31 Figure PA-70 shows total EPA units transported to the Culebra via the borehole in the S6
32 scenario. Only two vectors show radionuclide transport after the E2 intrusion at 1,000 years;
33 most radionuclide transport occurs immediately following the E1 intrusion at 2,000 years. The
34 results from the CRA-2009 PA are almost identical to the results from the CRA-2004 PABC (see
35 Ismail and Garner [2008, Section 4.3.2]). As the disturbed results from BRAGFLO are similar
36 and the source term for the two calculations are the same, it follows that the radionuclide
37 transport to the Culebra results would be the same (Ismail and Garner 2008).



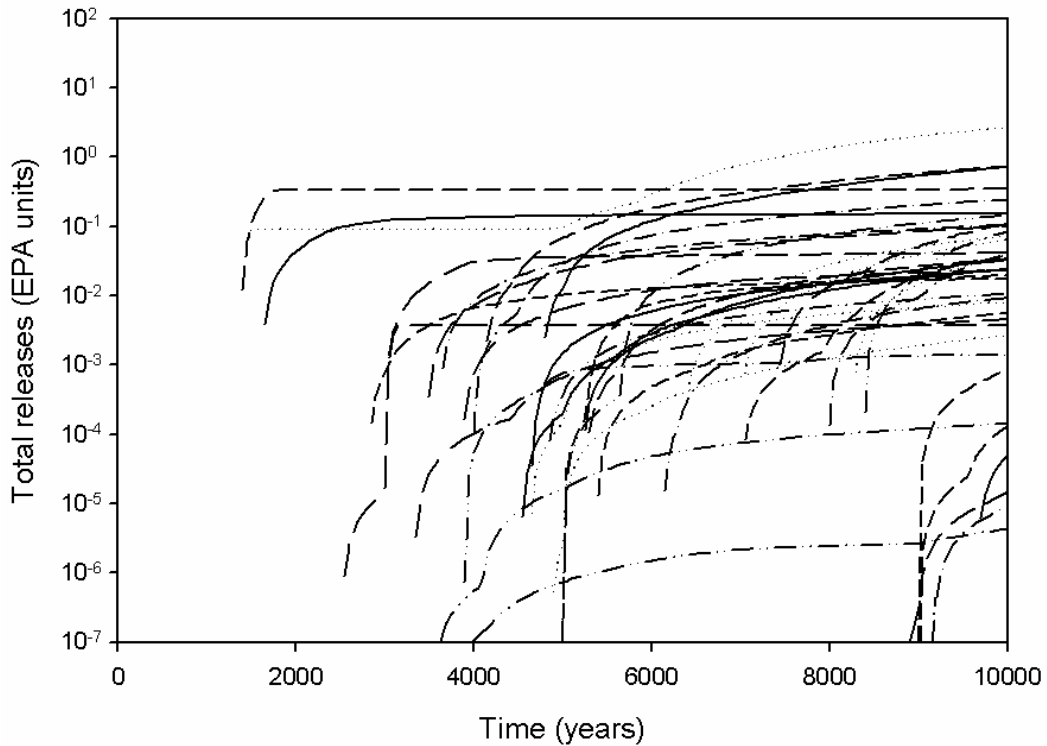
1
2 **Figure PA-66. Cumulative Normalized Release to the Culebra, Scenario S2, CRA-2009 PA**



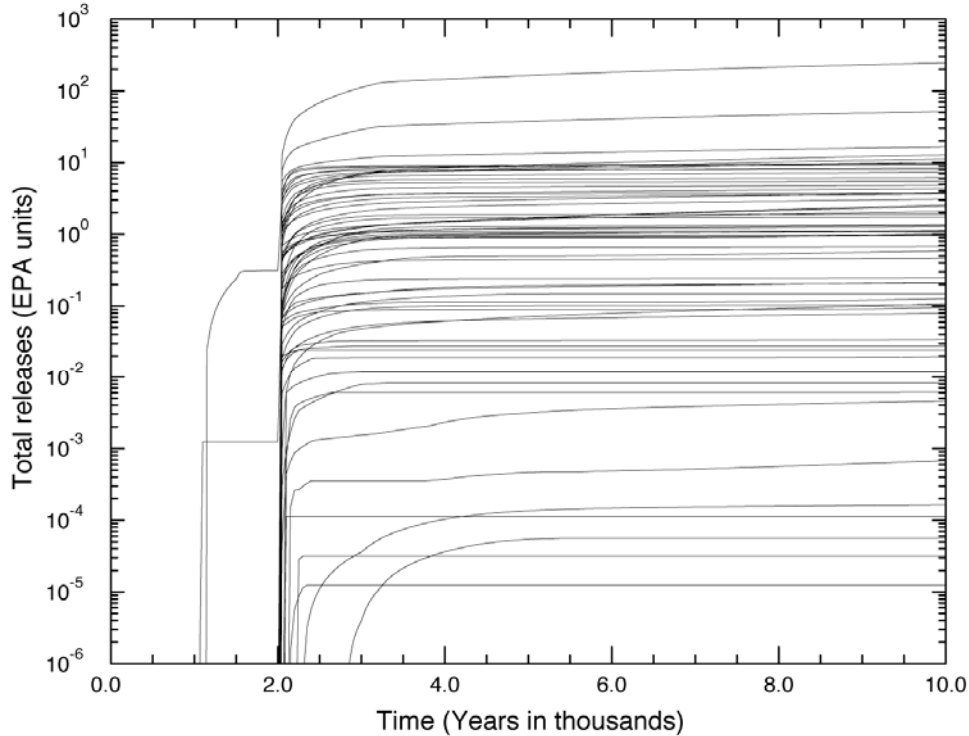
3
4 **Figure PA-67. Cumulative Normalized Release to the Culebra, Scenario S3, CRA-2009 PA**



1
2 **Figure PA-68. Cumulative Normalized Release to the Culebra, Scenario S4, CRA-2009 PA**



3
4 **Figure PA-69. Cumulative Normalized Release to the Culebra, Scenario S5, CRA-2009 PA**



1
2 **Figure PA-70. Cumulative Normalized Release to the Culebra, Replicate R1, Scenario S6,**
3 **CRA-2009 PA**

4 **PA-8.4.4 Transport Through the Culebra**

5 Radionuclide transport through the Culebra for a given set of uncertain parameters is calculated
6 with the code SECOTP2D (see Section PA-6.7.8). Note that the total release of radionuclides
7 across the LWB at the Culebra for given futures is calculated with the code CCDFGF by
8 convolving the SECOTP2D results with the radionuclide transport to the Culebra calculated by
9 NUTS and PANEL. This section discusses the SECOTP2D results; total releases through the
10 Culebra are presented in Section PA-9.4. As none of the changes implemented for the
11 CRA-2009 PA affected the Culebra flow and transport calculations, the results from the
12 CRA-2004 PABC Culebra flow and transport calculations were used in the CRA-2009 PA.

13 Culebra radionuclide transport calculations were performed for three replicates of 100 vectors
14 each for both partial-mining and full-mining scenarios (600 total simulations). Each of the 600
15 radionuclide transport simulations used a unique flow field computed separately with the code
16 MODFLOW (see Section PA-6.7.7 and Lowry and Kanney [2005]). The partial-mining scenario
17 assumes the extraction of all potash reserves outside the LWB, while the full-mining scenario
18 assumes that all potash reserves both inside and outside the LWB are exploited.

19 In each radionuclide transport simulation, 1 kg of each of four radionuclides (^{241}Am , ^{234}U ,
20 ^{230}Th , and ^{239}Pu) are released in the Culebra above the center of the waste panel area.
21 Radionuclide transport of the ^{230}Th daughter product of ^{234}U decay is calculated and tracked as
22 a separate species. In the following discussion, ^{230}Th will refer to the ^{234}U daughter product and
23 ^{230}ThA will refer to that released at the waste panel area.

1 All SECOTP2D results, regardless of magnitude, are included in the calculation of releases
 2 through the Culebra. In practice, most nonzero releases computed by SECOTP2D are
 3 vanishingly small and result from numerical dispersion (Lowry and Kanney 2005).
 4 Consequently, the analysis of SECOTP2D results focused on realizations in which at least one
 5 billionth (10^{-9}) of the 1-kg source was transported to the LWB.

6 More detailed information on the results of the Culebra radionuclide transport calculations can
 7 be found in the Analysis Package for the Culebra Flow and Transport Calculations: Compliance
 8 Recertification Application Performance Assessment Baseline Calculations (Lowry and Kanney
 9 2005).

10 **PA-8.4.4.1 Partial Mining Results**

11 Under partial-mining conditions, only the ^{234}U species and its ^{230}Th decay product were
 12 transported to the LWB in any significant amount during the course of the 10,000-year
 13 simulation (Lowry and Kanney 2005). Table PA-30 shows that no releases greater than one
 14 billionth of the 1-kg source were calculated for Replicates R1 and R3. For Replicate R2, 3
 15 vectors produced ^{234}U releases greater than 10^{-9} kg. One of the 3 vectors also resulted in a
 16 ^{230}Th release greater than 10^{-9} kg. These results are identical to the CRA-2004 PABC results.

17 **Table PA-30. Number of Realizations with Radionuclide Transport to the LWB Under**
 18 **Partial-Mining Conditions^{a,b}**

Replicate	^{241}Am	^{239}Pu	^{234}U	^{230}Th	^{230}ThA
R1	0	0	0	0	0
R2	0	0	3	1	0
R3	0	0	0	0	0

^a Number of vectors that have releases (transport to LWB) greater than one billionth of the 1-kg source released at center of waste panel.

^b ^{230}ThA refers to Th released at the waste panel area. ^{230}Th refers to thorium resulting from ^{234}U decay.

19
 20 Sensitivity analysis indicates that releases of ^{234}U in the partial-mining condition is associated
 21 with the VI oxidation state (Lowry and Kanney 2005; Kanney 2003). This result is reasonable
 22 because the matrix distribution coefficients for U in the IV state are much lower than for the VI
 23 state.

24 **PA-8.4.4.2 Full Mining Results**

25 Under full-mining conditions, only the ^{234}U species and its ^{230}Th decay product were
 26 transported to the LWB in any significant amount during the course of the 10,000-year
 27 simulation. More vectors resulted in releases greater than 10^{-9} kg for the full-mining scenario
 28 than were seen under partial-mining conditions. In addition, releases greater than 10^{-9} kg were
 29 calculated for all three replicates. Table PA-31 shows that 3 vectors in Replicate R1, 6 vectors in
 30 Replicate R2, and 3 vectors in Replicate R3 had ^{234}U releases greater than 10^{-9} kg. None of the
 31 3 vectors in Replicate R1, 3 of the 6 in Replicate R2, and 1 of the 3 in Replicate R3 showed a
 32

1 **Table PA-31. Number of Realizations with Radionuclide Transport to the LWB Under**
 2 **Full-Mining Conditions^{a,b}**

Replicate	²⁴¹ Am	²³⁹ Pu	²³⁴ U	²³⁰ Th	²³⁰ ThA
R1	0	0	3	0	0
R2	0	0	6	3	0
R3	0	0	3	1	0

^a Number of vectors that have releases (transport to LWB) greater than one billionth of the 1-kg source released at center of waste panel.

^b ²³⁰ThA refers to Th released at the waste panel area. ²³⁰Th refers to Th resulting from ²³⁴U decay.

3
 4 release of the ²³⁰Th daughter product greater than 10⁻⁹ kg. These results are identical to the
 5 CRA-2004 PABC results.

6 Sensitivity analysis indicates that releases of ²³⁴U in the full-mining condition is associated with
 7 the VI oxidation state (Lowry and Kanney 2005, Kanney 2003). This result is reasonable
 8 because the matrix distribution coefficients for U in the IV state are much lower than for the VI
 9 state.

10 **PA-8.5 Direct Releases**

11 Direct releases occur at the time of a drilling intrusion, and include cuttings and cavings,
 12 spallings, and DBRs. This section presents an analysis of the volume released by each
 13 mechanism.

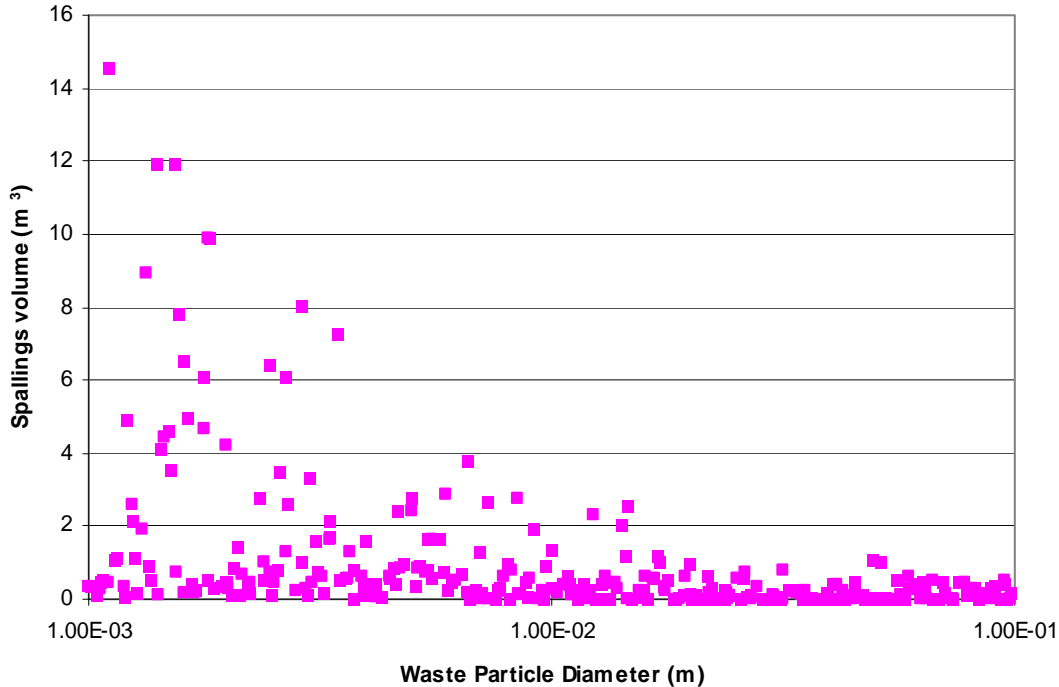
14 Ismail (2008) provides additional information about the cuttings, cavings, and spallings releases
 15 calculated for the CRA-2009 PA. Clayton (2008b) provides a detailed analysis of DBRs in the
 16 CRA-2009 PA.

17 **PA-8.5.1 Cuttings and Cavings**

18 Cuttings and cavings are the solid waste material removed from the repository and carried to the
 19 surface by the drilling fluid during borehole drilling. Cuttings are the materials removed directly
 20 by the drill bit, and cavings are the material eroded from the walls of the borehole by shear
 21 stresses from the circulating drill fluid. The volume of cuttings and cavings material removed
 22 from a single drilling intrusion into the repository is assumed to be in the shape of a cylinder.
 23 The code CUTTINGS_S calculates the area of the base of this cylinder, and cuttings and cavings
 24 results in this section are reported in terms of these areas. The volumes of cuttings and cavings
 25 removed can be calculated by multiplying these areas with the initial repository height 3.96 m
 26 (BLOWOUT:HREPO).

27 Cuttings and cavings areas calculated for the CRA-2009 PA range between 0.076 m² and
 28 0.86 m², with a mean area of 0.25 m² (Table PA-32). None of the changes implemented in the
 29 CRA-2009 PA affect the cuttings and cavings calculations, so the results are identical to the
 30 CRA-2004 PABC results (Ismail 2008).

1 Two uncertain sampled parameters affect the cavings calculations. The uncertainty in cavings
 2 areas arises primarily from the uncertainty in the shear strength of the waste (Ismail 2008).
 3 Lower shear strengths tend to result in larger cavings (Ismail 2008, Figure 1). The uncertainty in
 4 the drill string angular velocity has a smaller impact on the cavings results, but the combination
 5 of a low angular velocity and high shear strength can prohibit cavings from occurring (Figure
 6 PA-71). In fact, cavings did not occur in 10% of all vectors (Table PA-32).



7
 8 **Figure PA-71. Scatterplot of Waste Particle Diameter Versus Spallings Volume,**
 9 **CRA-2009 PA**

10 **Table PA-32. CRA-2009 PA Cuttings and Cavings Area Statistics**

Replicate	Minimum (m ²)	Maximum (m ²)	Mean (m ²)	Vectors Without Cavings
R1	0.076	0.82	0.25	9
R2	0.076	0.86	0.25	10
R3	0.076	0.83	0.25	11

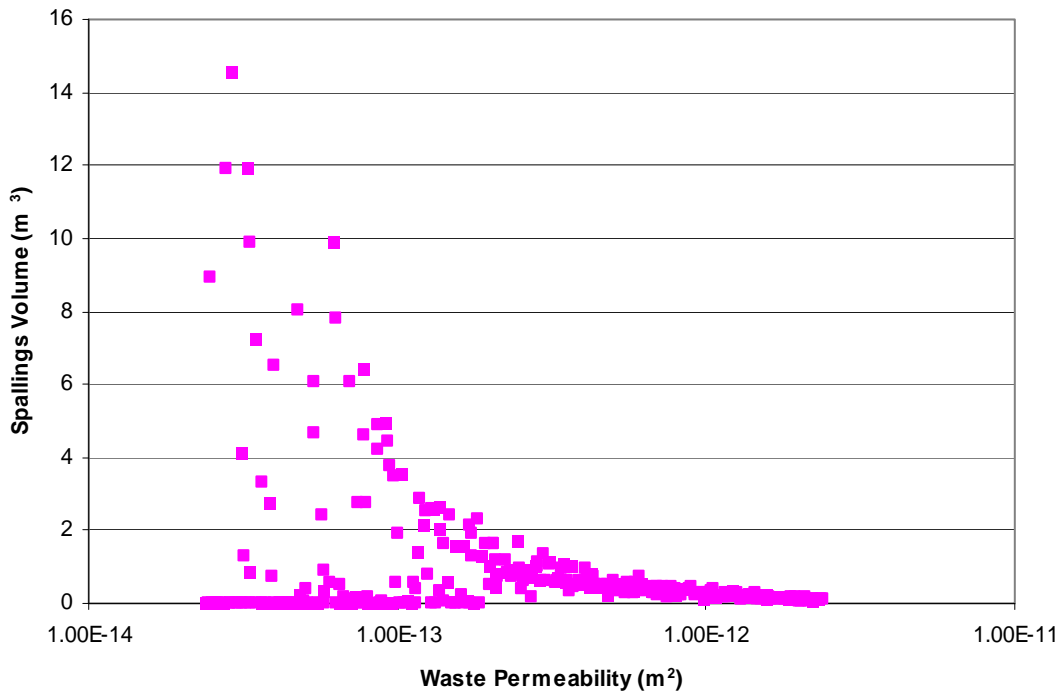
11
 12 **PA-8.5.2 Spallings**

13 Calculating the volume of solid waste material released to the surface due to spallings from a
 14 single drilling intrusion into the repository is a two-part procedure. The code DRSPALL
 15 calculates the spallings volumes from a single drilling intrusion at four values of repository
 16 pressure (10, 12, 14, and 14.8 MPa). Following this, spallings volumes from a single intrusion
 17 are calculated using the code CUTTINGS_S; this code linearly interpolates the spallings
 18 volumes calculated using DRSPALL, based on the pressure calculated by BRAGFLO. Results
 19 from both of these calculations are documented in this section.

1 **PA-8.5.2.1 DRSPALL Results**

2 None of the changes implemented in the CRA-2009 PA affect the DRSPALL calculations, so the
 3 results from the CRA-2004 PABC were used in the CRA-2009 PA. In the CRA-2004 PABC, the
 4 code DRSPALL was run for each of 100 vectors in 3 replicates and for 4 values of repository
 5 pressure (10, 12, 14, and 14.8 MPa, see Section PA-4.6.4). No spallings occurred at 10 MPa for
 6 any vector.

7 The uncertainty in the spallings volumes arises from four uncertain variables in the DRSPALL
 8 calculations: waste permeability, waste porosity, waste tensile strength, and waste particle
 9 diameter after tensile failure (Table PA-15). Figure PA-72 indicates that the largest spallings
 10 volumes occur when waste permeability is less than $1.0 \times 10^{-13} \text{ m}^2$, but larger permeability
 11 values result in a higher frequency of nonzero spallings volumes. This observation can be
 12 explained as follows: the higher permeability values sampled result in smaller tensile stresses
 13 and less tensile failure, but promote fluidization. Lower permeability leads to greater tensile
 14 stresses and tensile failure, but failed material may not be able to fluidize at this low
 15 permeability.



16
 17 **Figure PA-72. Scatterplot of Waste Permeability Versus Spallings Volume, CRA-2009 PA**

18 Smaller particle diameter values (see Figure PA-71) tend to result in larger spallings volumes
 19 and a higher frequency of nonzero spallings volumes. The uncertainty in the spallings volumes
 20 from a single intrusion is largely determined by the uncertainty in these two parameters.
 21 Obvious correlations between spallings volumes and the other two parameters could not be
 22 established.

1 **PA-8.5.2.2 CUTTINGS_S Results**

2 Two factors directly affect the CUTTINGS_S calculation of spillings volumes for the drilling
 3 scenarios: the volumes calculated by DRSPALL and the repository pressures calculated by
 4 BRAGFLO.

5 Table PA-33 summarizes the statistics for the CRA-2009 PA spillings volumes. Of the 7,800
 6 (26 intrusion time-scenario combinations × 3 drilling locations × 100 vectors) spillings volumes
 7 calculated per replicate, more than 92% of each replicate’s calculations resulted in no spillings.
 8 Only about a third of the vectors in each replicate had spillings occur in at least one of the
 9 scenarios; therefore, spillings will not contribute to the total releases calculated for the other
 10 vectors.

11 **Table PA-33. CRA-2009 PA Spallings Volume Statistics**

Scenario	# of Calculations	Maximum Volume (m ³)			Average Volume (m)			Number of Nonzero Volumes		
		R1	R2	R3	R1	R2	R3	R1	R2	R3
S1	1,800	2.52	2.52	5.33	0.10	0.10	0.17	158	177	183
S2	1,500	8.31	2.87	6.32	0.14	0.12	0.12	120	135	122
S3	1,500	7.99	2.13	3.15	0.12	0.10	0.09	129	138	133
S4	1,500	1.67	2.40	1.99	0.04	0.07	0.04	69	64	56
S5	1,500	1.67	2.20	3.00	0.07	0.09	0.06	91	93	91
All	7,800	8.31	2.87	6.32	0.09	0.10	0.10	564	607	585

12
 13 Scenarios S2 and S3 resulted in the largest maximum spillings volume, while Scenarios S1, S2,
 14 and S3 resulted in the largest average spillings volume. For the CRA-2009 PA, Scenarios S2
 15 and S3 have the highest maximum pressures because in these scenarios, the drill bit intrudes into
 16 a pressurized brine pocket (Nemer and Clayton 2008). These higher pressures lead to larger
 17 spillings volumes. Scenarios S4 and S5 resulted in the lowest maximum and average volumes
 18 as, in general, these scenarios have the lowest pressure (see Section PA-8.3.1). Scenario S1
 19 resulted in the largest number of nonzero spillings volumes per time intrusion. Without a prior
 20 intrusion creating a pathway for brine and gas flow to decrease the pressure, there are more
 21 vectors that result in pressures above 10 MPa and, hence, a nonzero spillings volume.

22 The frequency of nonzero spillings volumes increased for the CRA-2009 PA compared to the
 23 CRA-2004 PABC (see Ismail [2008, Table 8]). The maximum spillings volumes are similar
 24 between the two analyses, while the CRA-2009 PA average spillings volume increased
 25 compared with the CRA-2004 PABC results (see Ismail [2008, Table 8]). As the spillings
 26 volumes are calculated from BRAGFLO pressure and an increase in pressure was observed (see
 27 Section PA-7.1.1 and Section PA-8.3.1), an increase in the spillings releases is expected.

1 **PA-8.5.3 DBRs**

2 DBRs to the surface can occur during or shortly after a drilling intrusion. For each element of
 3 the Latin hypercube sample, the code BRAGFLO calculates volumes of brine released for a total
 4 of 78 combinations of intrusion time, intrusion location, and initial conditions (see Section PA-
 5 6.7.6). Initial conditions for the DBR calculations are obtained from the BRAGFLO Salado flow
 6 model results from Scenarios S1 through S5. Salado flow model results from the S1 scenario
 7 (Section PA-7.1) are used as initial conditions for DBR when modeling a first intrusion into the
 8 repository that may have a DBR. Salado flow model results from the S2 through S5 scenarios
 9 (Section PA-8.3) are used as initial conditions for DBR when modeling second or subsequent
 10 drilling intrusions that may have a DBR.

11 Summary statistics of the calculated DBR volumes for Replicate R1 of the CRA-2009 PA are
 12 shown in Table PA-34. As seen in Table PA-34, 1,001 of the 7,800 DBR calculations (100
 13 vectors \times 78 combinations) resulted in a nonzero DBR volume to the surface, the majority of
 14 which resulted from Scenarios S2 and S3. The maximum DBR volume is approximately 59 m³,
 15 with an average volume of 0.9 m³. Only intrusions into a lower panel (see Clayton [2008b,
 16 Section 6.2]) resulted in significant DBR volumes. In the S1 scenario, the lower panel represents
 17 an undisturbed panel at the south end of the repository. In the S2 and S3 scenarios, the lower
 18 panel represents any panel that has had a previous E1 intrusion; in the S4 and S5 scenarios, the
 19 lower panel represents any panel that has had a previous E2 intrusion. DBR volumes are larger
 20 and occur more frequently in the S2 and S3 scenarios, because the lower panel has a much higher
 21 saturation after an E1 intrusion.

22 **Table PA-34. CRA-2009 PA DBR Volume Statistics**

Scenario	Maximum Volume (m ³)	Average Volume (m ³)	Number of Nonzero Volumes
S1	19	0.1	122
S2	59	2.9	385
S3	44	1.5	317
S4	19	0.1	70
S5	21	0.1	107
All	59	0.9	1,001

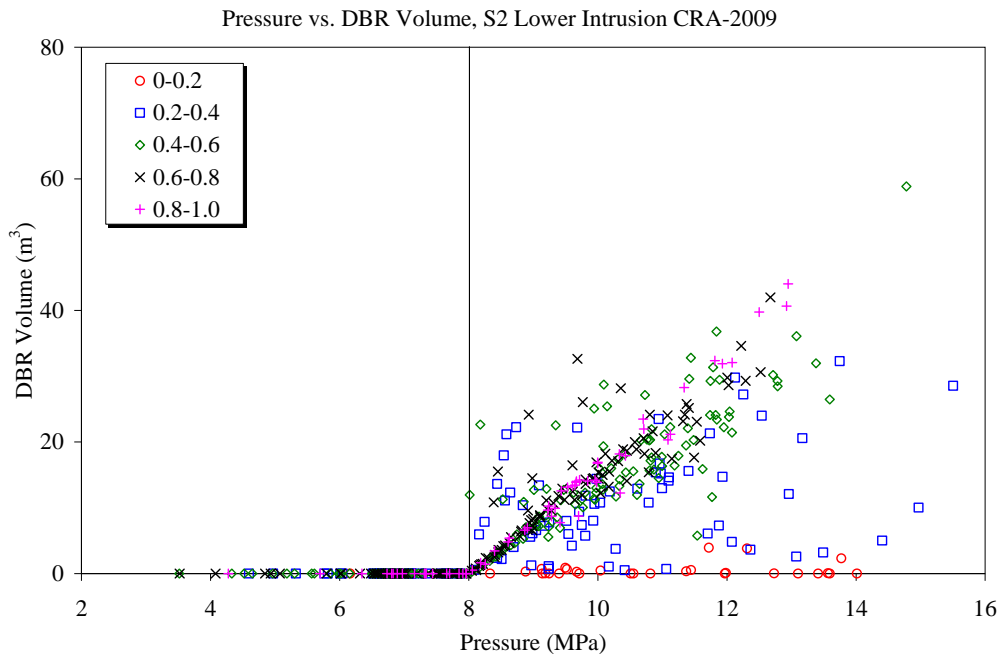
23

24 The frequency of nonzero DBR volumes increased for the CRA-2009 PA compared to the
 25 CRA-2004 PABC (see Clayton [2008b, Table 6-1]). The maximum DBR volume is lower for
 26 the CRA-2009 PA (see Clayton [2008b, Table 6-1]). The CRA-2009 PA average DBR volume
 27 increased compared to the CRA-2004 PABC results (see Clayton [2008b, Table 6-2, Table 6-3,
 28 Table 6-4, and Table 6-5]). The increase in the frequency of nonzero and average DBR volume
 29 is due to the porosity correction, while the decrease in the maximum DBR volume is from the
 30 reduction in the maximum DBR duration parameter (Clayton 2008b).

31 Previous sensitivity analyses have determined that a DBR volume from a single intrusion is most
 32 sensitive to the initial pressure and brine saturation in the intruded panel. This analysis is

1 repeated below for Scenario S2 in the CRA-2009 PA. The initial pressure and brine saturation in
 2 the DBR calculations are transferred from the Salado flow calculations, as described above.
 3 Thus, the uncertain parameters that are most influential to the uncertainty in pressure and brine
 4 saturation in the Salado flow calculations (see Section PA-7.1 and Section PA-8.3) are also most
 5 influential to the uncertainty in DBR volumes.

6 The combination of relatively high pressure and brine saturation in the intruded panel is required
 7 for DBR to the surface. Figure PA-73 shows a scatterplot of pressure in the waste panel versus
 8 DBR volumes for scenario S2, lower intrusion, with symbols indicating the value of the mobile
 9 brine saturation (defined as brine saturation minus residual brine saturation in the waste). The
 10 figure clearly shows that there are no releases until pressures exceed about 8 MPa, as indicated
 11 by the vertical line. Above 8 MPa, a significant number of vectors have zero releases, but these
 12 vectors have mobile brine saturations less than zero, and thus no brine is available to be released.
 13 When mobile brine saturation approaches one, relative permeability of the gas becomes small
 14 enough that no gas flows into the well, and in these circumstances, DBR releases end after three
 15 days. Thus, in vectors with high mobile brine saturations, DBR releases increase proportionally
 16 with increases in pressure, as evidenced by the linear relationship between DBR volume and
 17 pressure for mobile brine saturation between 0.8 and 1.0. For vectors with mobile saturations
 18 between 0.2 and 0.8, both gas and brine can flow in the well, and the rate of gas flow can be high
 19 enough that the ending time of DBR releases may be as long as 4.5 days. Although brine may be
 20 flowing at slower rates in these vectors than in vectors with high mobile saturations, brine flow
 21 may continue longer and thus result in larger DBR volumes.



22
 23 **Figure PA-73. Sensitivity of DBR Volumes to Pressure and Mobile Brine Saturation,**
 24 **Replicate R1, Scenario S2, Lower Panel, CRA-2009 PA. (Symbols Indicate**
 25 **the Range of Mobile Brine Saturation Given in the Legend.)**

1 **PA-9.0 Normalized Releases**

2 The radioactive waste disposal regulations of Part 191, Subparts B and C include containment
3 requirements for radionuclides. The containment requirements of section 191.13 specify that
4 releases from a disposal system to the accessible environment must not exceed the release limits
5 set forth in 40 CFR Part 191, Appendix A, Table 1. As set forth in section 194.34, the results of
6 PA are required to be expressed as CCDFs of total releases.

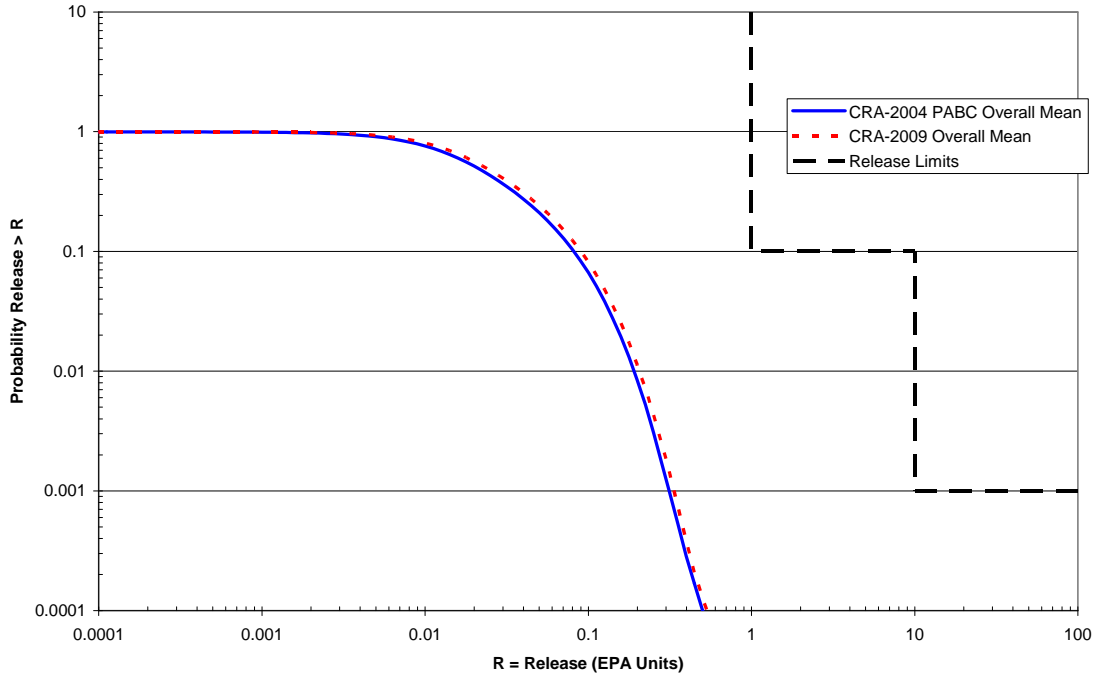
7 This section discusses each of the four categories of releases that constitute the total release:
8 cuttings and cavings, spallings, DBRs, and transport releases, followed by the total normalized
9 releases for the CRA-2009 PA. A comparison between the CRA-2009 PA and the CRA-2004
10 PABC results is also presented. In summary, despite the changes and corrections made between
11 the CRA-2004 PABC and the CRA-2009 PA, there were no major changes in the overall pattern
12 of releases. Cuttings, cavings, and DBRs remain the most significant pathways for release of
13 radioactive material to the land surface. Release by subsurface transport in the Salado or Culebra
14 continue to make essentially no contribution to total releases. Finally, the resulting CCDFs of
15 total normalized releases for the CRA-2009 PA are within the regulatory limits defined in section
16 191.13. Section PA-9.0 is taken from Clayton et al. (2008, Section 6.0).

17 Rank regression analysis was used to evaluate the sensitivity of the normalized releases to the
18 sampled parameters. Scatterplots of the dependent versus independent rank-transformed
19 variables resulting from the sensitivity analysis were examined to determine if there were any
20 obvious nonmonotonic relationships. Obvious nonmonotonic relationships were not found,
21 although there are cases where inputs are categorized as discrete variables (e.g., OXSTAT) and
22 cases where large proportions of the vectors show no release (e.g., CULREL). Application of
23 linear regression to such cases is somewhat problematic with respect to the assumptions of
24 normally distributed residuals and homogeneous variance among the residuals. However, with
25 respect to ranking the relative importance of the parameters, these issues are probably not
26 significant. Details of the analysis can be found in Kirchner (2008b).

27 **PA-9.1 Cuttings and Cavings**

28 The overall mean CCDFs for cuttings and cavings releases from the CRA-2009 PA and the
29 CRA-2004 PABC are shown in Figure PA-74. These resulting overall mean CCDFs are very
30 similar, with only a slight increase in the CRA-2009 PA mean due to the increase in the drilling
31 rate.

32 The rank regression analysis showed that the uncertainty in waste shear strength (WTAUFAIL in
33 Table PA-19) contributes about 98% of the variability in mean cuttings and cavings releases in
34 both the CRA-2009 PA and CRA-2004 PABC (Kirchner 2008b). Cuttings and caving releases
35 are primarily controlled by the volume of cuttings and cavings produced, which in turn is a
36 highly nonlinear function of the waste shear strength (Ismail 2008).



1
 2 **Figure PA-74. Overall Mean CCDFs for Cuttings and Cavings Releases: CRA-2009 PA**
 3 **and CRA-2004 PABC**

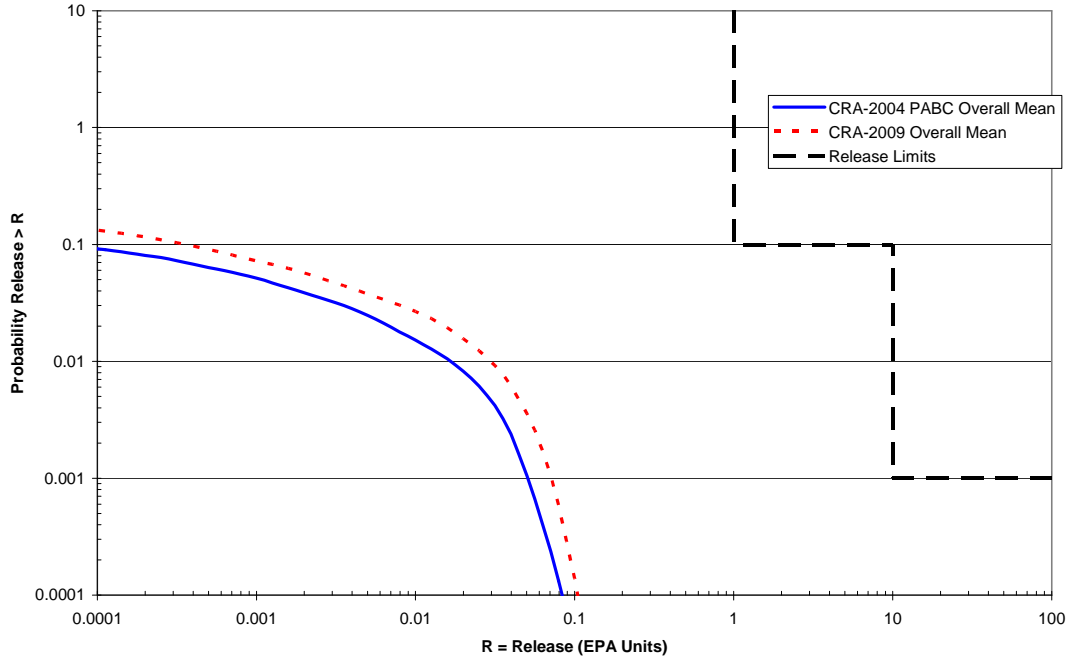
4 **PA-9.2 Spallings**

5 Figure PA-75 shows the overall mean spallings release CCDFs from the CRA-2009 PA and the
 6 CRA-2004 PABC. This increase in overall mean spallings release values can be directly
 7 attributed to an increase in overall mean spallings volumes, with a small increase due to the
 8 increase in the drilling rate. The frequency of nonzero spallings volumes calculated by
 9 CUTTINGS_S increased. CUTTINGS_S calculates the spallings volume released from a single
 10 intrusion for the WIPP PA intrusion scenarios by interpolating the volumes calculated by
 11 DRSPALL using the repository pressures calculated by BRAGFLO. These increases are largely
 12 attributable to the increase in repository pressure resulting from the larger amounts of brine
 13 available (Ismail 2008).

14 The rank regression analysis indicates that the intact halite porosity (HALPOR in Table PA-19)
 15 is the dominant uncertain parameter with regard to the uncertainty in spallings releases in the
 16 CRA-2009 PA (Kirchner 2008b). Its higher ranking in the CRA-2009 PA analysis compared to
 17 the CRA-2004 PABC analysis is due to the increase in the maximum value of its distribution
 18 (Kirchner 2008b). Increases in halite porosity lead to increases in repository pressure (see
 19 Section PA-7.1.1 and Section PA-8.3.1) and thus to increases in spallings releases.

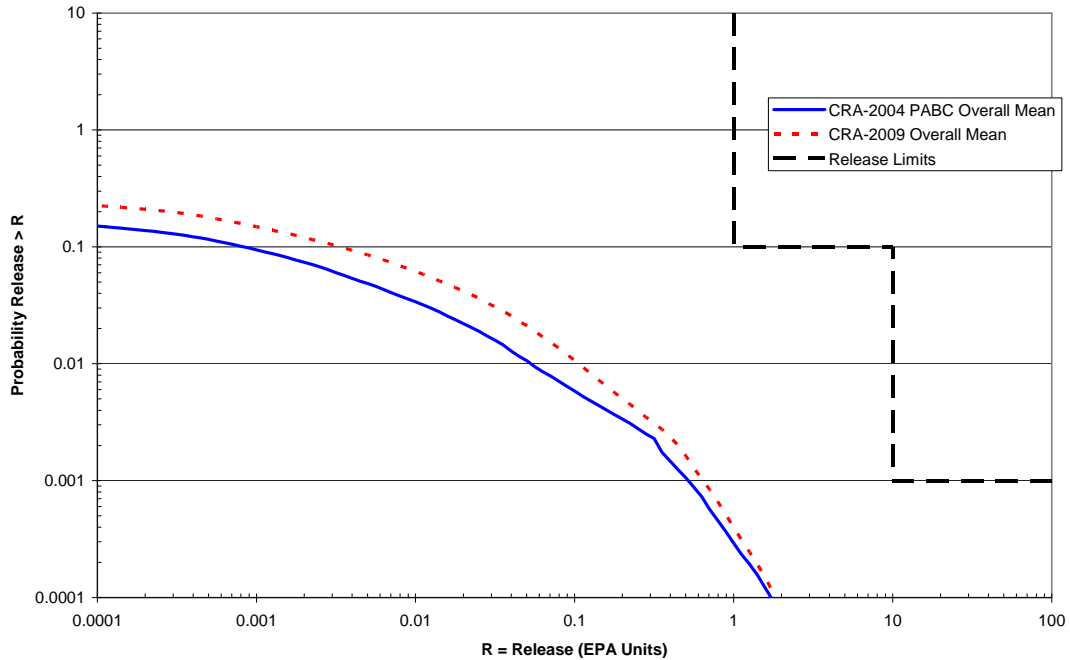
20 **PA-9.3 Direct Brine**

21 The overall mean CCDFs for DBRs from the CRA-2009 PA and the CRA-2004 PABC are
 22 shown in Figure PA-76. At all probabilities, the CRA-2009 PA mean DBRs increased from the
 23



1

2 **Figure PA-75. Overall Mean CCDFs for Spallings Releases: CRA-2009 PA and**
 3 **CRA 2004 PABC**



4

5 **Figure PA-76. Overall Mean CCDFs for DBRs: CRA-2009 PA and CRA-2004 PABC**

1 CRA-2004 PABC values, particularly at higher probabilities. In the CRA-2009 PA, at any level
2 of release, the mean probability that DBRs exceed the release level is increased from the
3 CRA-2004 PABC. This increase in the CCDFs for DBRs can be directly attributed to an
4 increase in DBR volumes (Section PA-8.5.3), with a small increase due to the increase in the
5 drilling rate (Clayton 2008a). The frequency of nonzero DBR volumes also increased (Section
6 PA-8.5.3). The frequency and volume of the DBR are strongly correlated to the repository
7 pressure. These increases are largely attributable to the increase in repository pressure resulting
8 from of the larger amounts of brine available. The increase of the brine in the repository is due
9 to higher intact halite porosities for higher probabilities and drilling rate at lower probabilities
10 (Clayton 2008b).

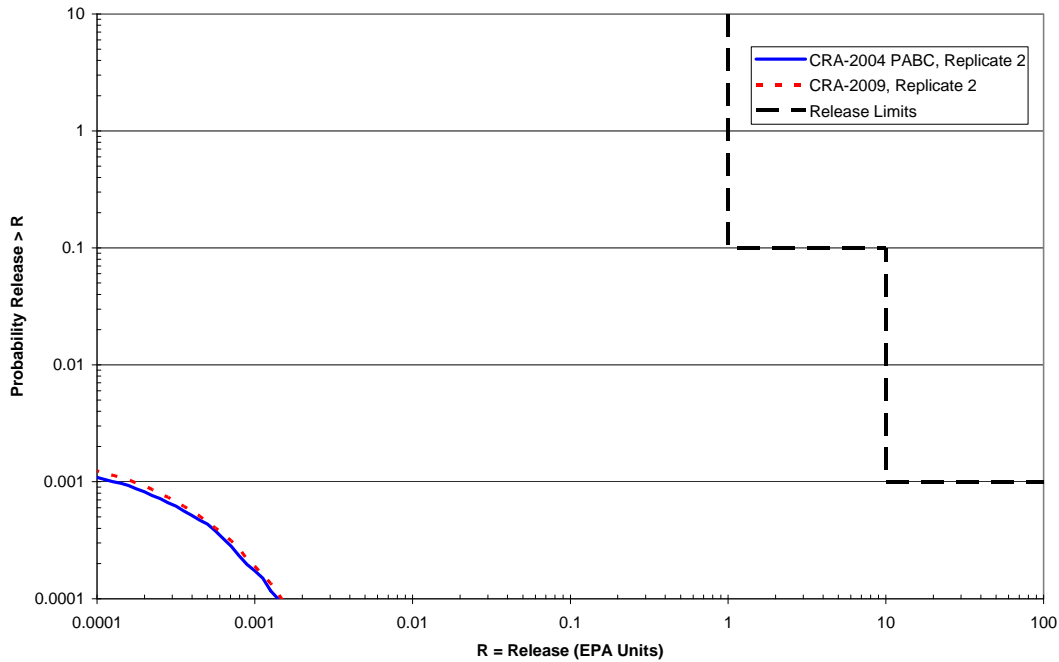
11 The rank regression analysis shows that four variables, the “solubility multiplier” representing
12 solubility uncertainty for all actinides in the III oxidation state (WSOLVAR3 in Table PA-19),
13 the initial brine pore pressure in the Castile (BPINTPRS in Table PA-19), the inundated
14 corrosion rate for steel (WGRCOR in Table PA-19), and the frequency with which Castile brine
15 intrudes the repository as a result of a drilling event (BPPROB in Table PA-19), account for
16 more than 50% of the uncertainty in DBRs for the CRA-2009 PA (Kirchner 2008b). These
17 variables are also important in the CRA-2004 PABC analysis, although the third- and fourth-
18 ranked variables are in reverse order relative to the CRA-2009 PA (Kirchner 2008b).

19 The solubility of actinides defines the concentration in DBRs. The corrosion of Fe is expected to
20 produce gas, but at the same time it consumes water. When the repository is flooded with brine
21 from the intrusion of a brine pocket, the influence on DBR would likely be positive, because the
22 production of H₂ would outweigh the minimal impact of the consumption of water. However, a
23 negative correlation is observed between the ranked variables, suggesting that the corrosion of
24 steel has its strongest influence when the repository is not saturated and DBRs are expected to be
25 small. The frequency with which Castile brine intrudes the repository as a result of a drilling
26 event and the initial pressure of that brine affect the pressure in the repository. As DBR volumes
27 are a strong function of pressure, a positive correlation is expected and shown (Kirchner 2008b).

28 **PA-9.4 Groundwater Transport**

29 Figure PA-77 shows the mean CCDFs for normalized releases due to transport through the
30 Culebra for Replicate R2 of the CRA-2009 PA and the CRA-2004 PABC. No transport releases
31 larger than 10⁻⁶ EPA units occurred in Replicates R1 and R3. Normalized transport releases for
32 the CRA-2009 PA are qualitatively similar to the CRA-2004 PABC results, in that only one
33 replicate (R2) exhibits releases that are significantly larger than the numerical error inherent in
34 the transport calculations. Overall, the mean releases for Replicate R2 of the two analyses are
35 quite similar and the numbers of vectors that had releases are identical, with only a slight
36 increase in the CRA-2009 PA due to the increase in the drilling rate (Dunagan 2008).

37 A Culebra release represents the potential release of radioactivity from the Culebra at the LWB
38 over 10,000 years. Analyzing sensitivity of Culebra releases to the input parameters using linear
39 regression is problematic (Kirchner 2008b). In the CRA-2009 PA and the CRA-2004 PABC,
40 ~83% of the vectors had Culebra releases of zero (Ismail and Garner 2008). Releases of zero are
41 found across the entire range of every parameter. This is undoubtedly due, for the most part, to
42

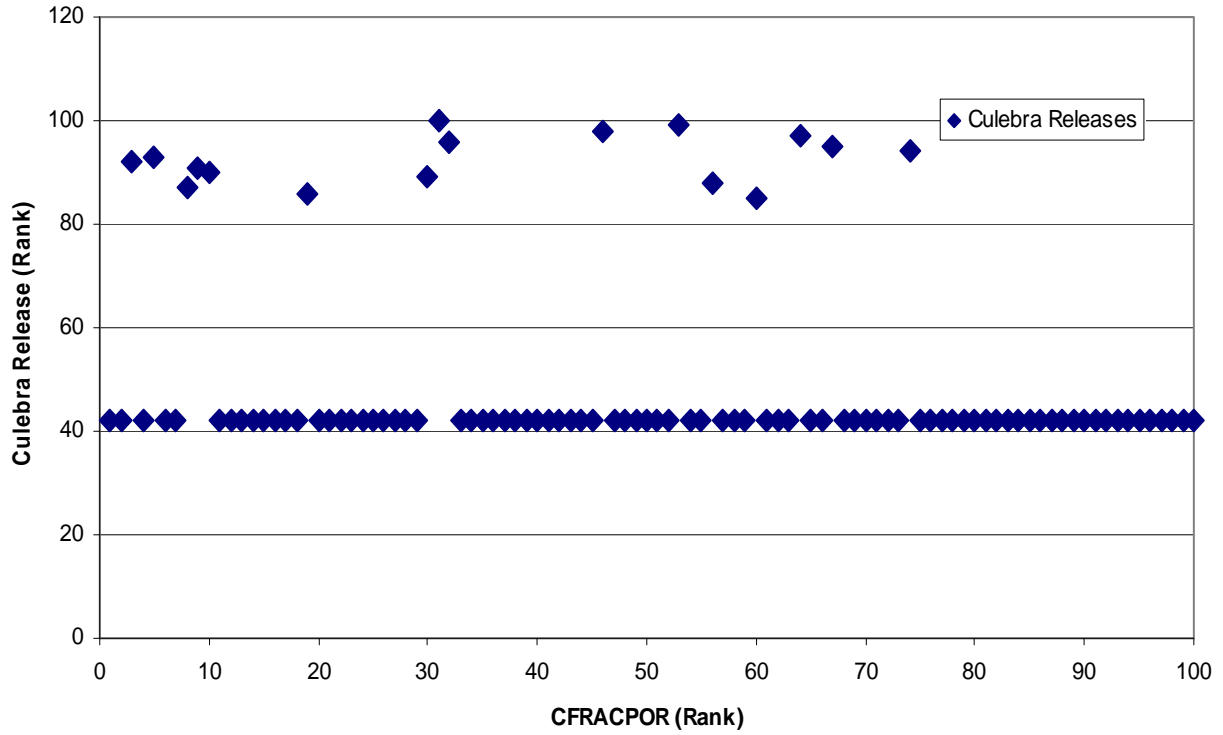


1
 2 **Figure PA-77. Mean CCDFs for Releases from the Culebra for Replicate R2: CRA-2009**
 3 **PA and CRA-2004 PABC**

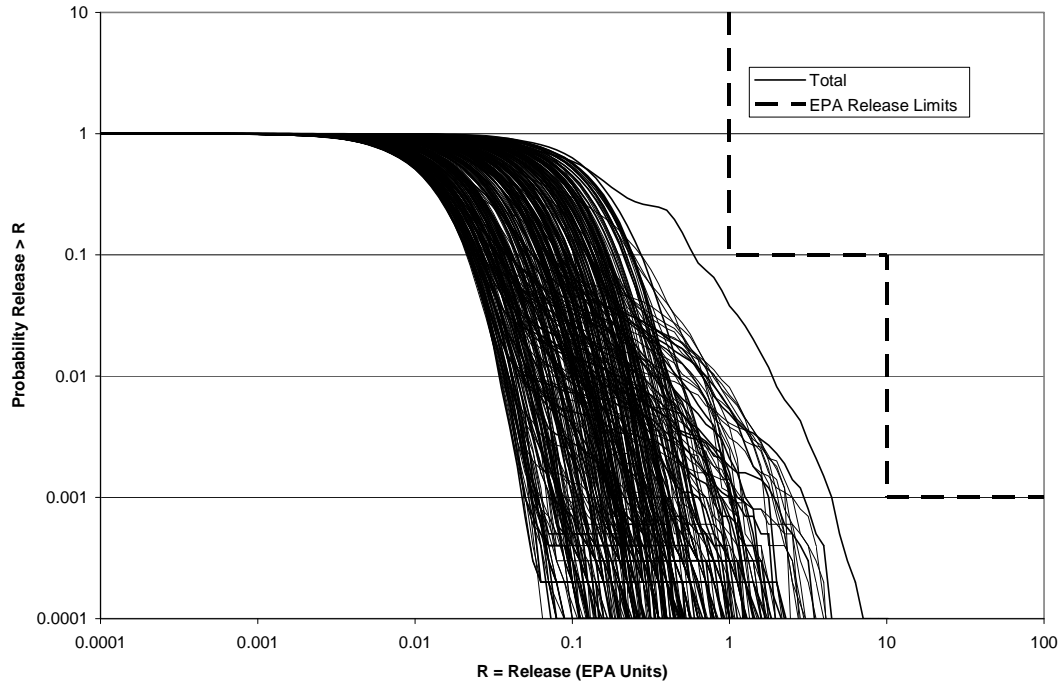
4 transport rates frequently being too small to enable contaminants to reach the boundary within
 5 the 10,000-year simulation period. Thus, the release data are strongly skewed. The times of the
 6 intrusions giving rise to flows to the Culebra are also likely to influence whether or not such
 7 releases occur. These times are not represented in the sampled input parameters, and thus cannot
 8 be associated with the releases. In addition, the preponderance of zero values tends to negate the
 9 assumption of linear regression that errors (residuals) are normally distributed. In many cases, it
 10 appears that it is the distribution of zeros along the independent axis that determines whether a
 11 positive or negative correlation is observed. For example, Figure PA-78 shows the ranks of
 12 releases from the Culebra versus the ranks of the parameter CFRACPOR(CULEBRA:APOROS)
 13 for Replicate 1. The average rank of the zero values was 42 and was assigned to all cases where
 14 no release was observed. Because releases of zero were associated with high values of
 15 CFRACPOR, as well as low values, and because there were no nonzero releases for the futures
 16 having the highest values of CFRACPOR, the arrangement of the data would lead to a negative
 17 correlation. Because of these issues, the linear ranked regression analysis is unlikely to yield a
 18 definitive identification of the sensitivity of Culebra releases to the sampled parameters, and
 19 most of the variability in Culebra releases remains unexplained by the regression model
 20 (Kirchner 2008b).

21 **PA-9.5 Total Normalized Releases**

22 Total releases are calculated by totaling the releases from each release pathway: cuttings and
 23 cavings releases, spallings releases, DBRs, and transport releases (there were no undisturbed
 24 releases to contribute to total release). Figure PA-79 shows the 300 CCDFs for total releases in
 25



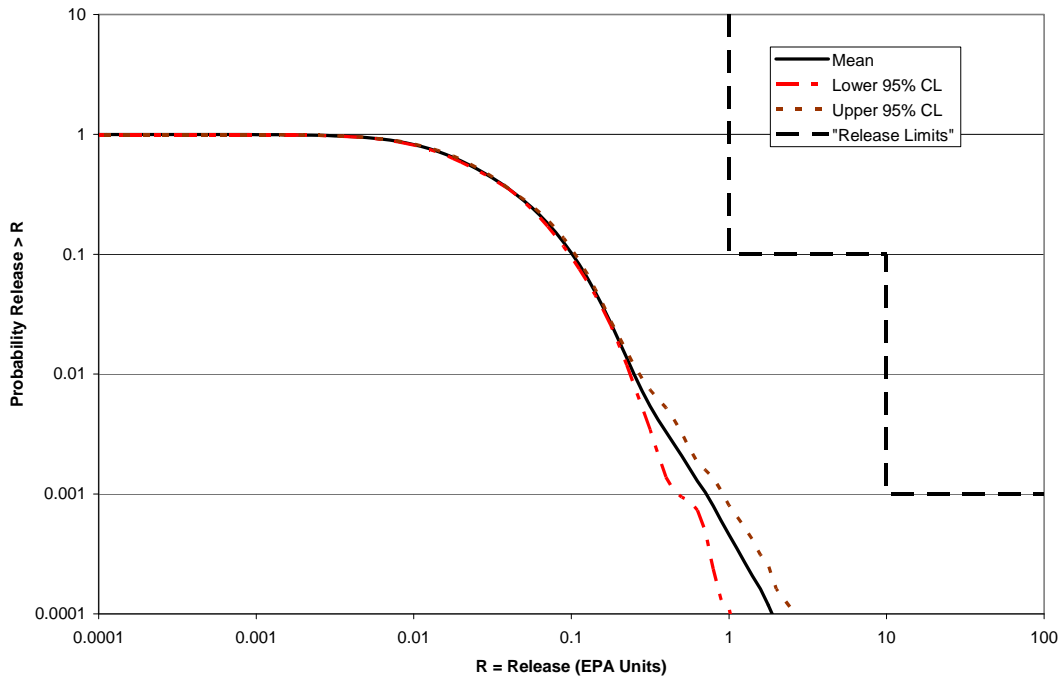
1
2 **Figure PA-78. The Preponderance and Distribution of Zeros Can Control the Regression**



3
4 **Figure PA-79. Total Normalized Releases, Replicates R1, R2, and R3, CRA-2009 PA**

1 Replicates R1, R2, and R3 of the CRA-2009 PA. As seen in Figure PA-79, all of the CCDFs lie
 2 below and to the left of the limits specified in section 191.13(a).

3 The overall mean CCDF is computed as the arithmetic mean of the mean CCDFs from each
 4 replicate. To quantitatively determine the sufficiency of the sample size, a confidence interval is
 5 computed about the overall mean CCDF using the Student's t-distribution and the mean CCDFs
 6 from each replicate. Figure PA-80 shows 95% confidence intervals about the overall mean. The
 7 CCDF and confidences intervals lie below and to the left of the limits specified in 40 CFR
 8 § 191.13(a). Thus, the WIPP continues to comply with the containment requirements of Part
 9 191.

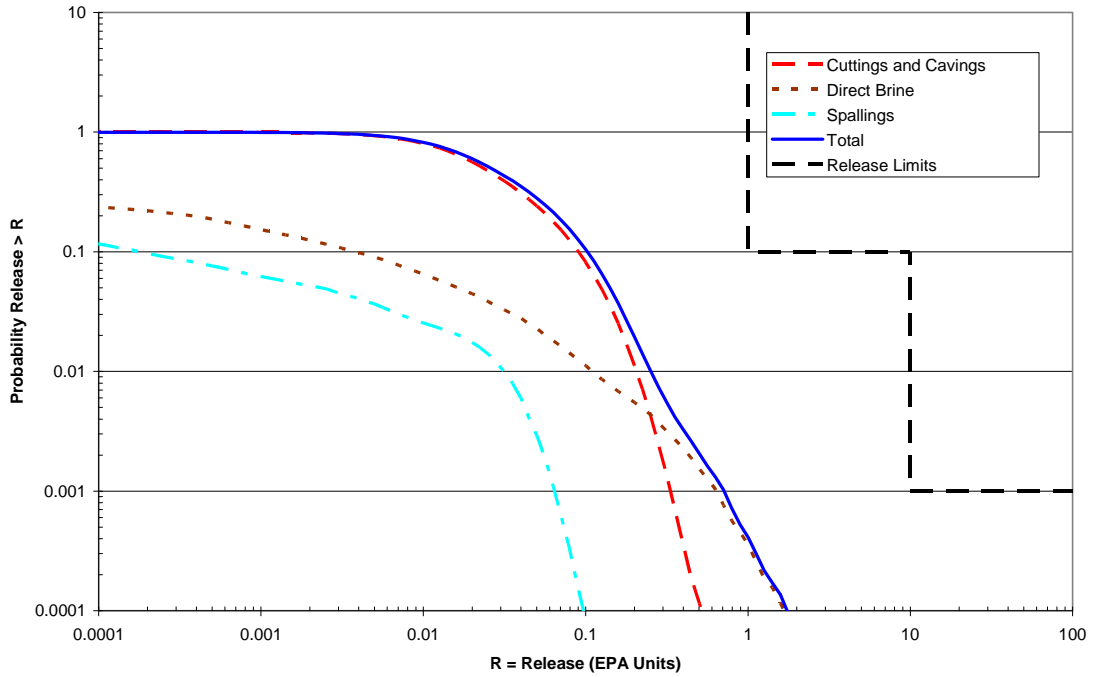


10
 11 **Figure PA-80. Confidence Interval on Overall Mean CCDF for Total Normalized**
 12 **Releases, CRA-2009 PA**

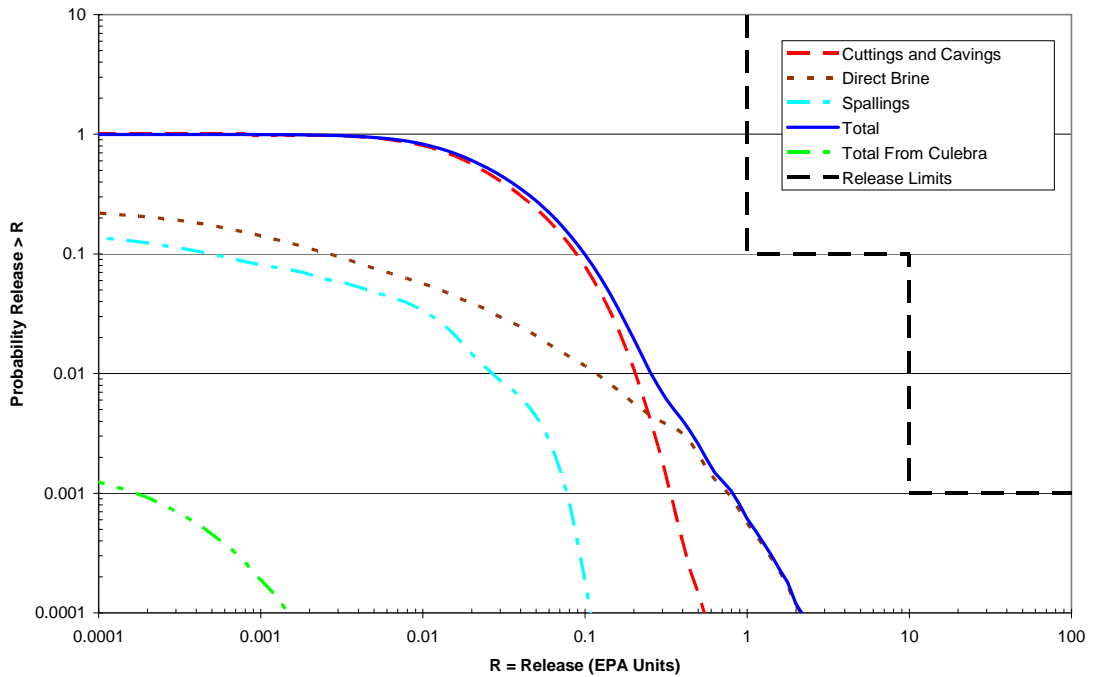
13 Figure PA-81, Figure PA-82, and Figure PA-83 show the mean CCDFs for each component of
 14 total releases for Replicates R1, R2, and R3 of the CRA-2009 PA, respectively. The
 15 contributions to total releases for each release pathway in the CRA-2009 PA are the same as
 16 those observed in the CRA-2004 PABC (Dunagan 2008).

17 Figure PA-84 provides a comparison between the CRA-2009 PA and the CRA-2004 PABC. At
 18 any level of release, the overall mean probability that total releases exceed the release level is
 19 similar between the two analyses. A small increase in the probability is mainly due to the change
 20 in the drilling rate parameter (Dunagan 2008).

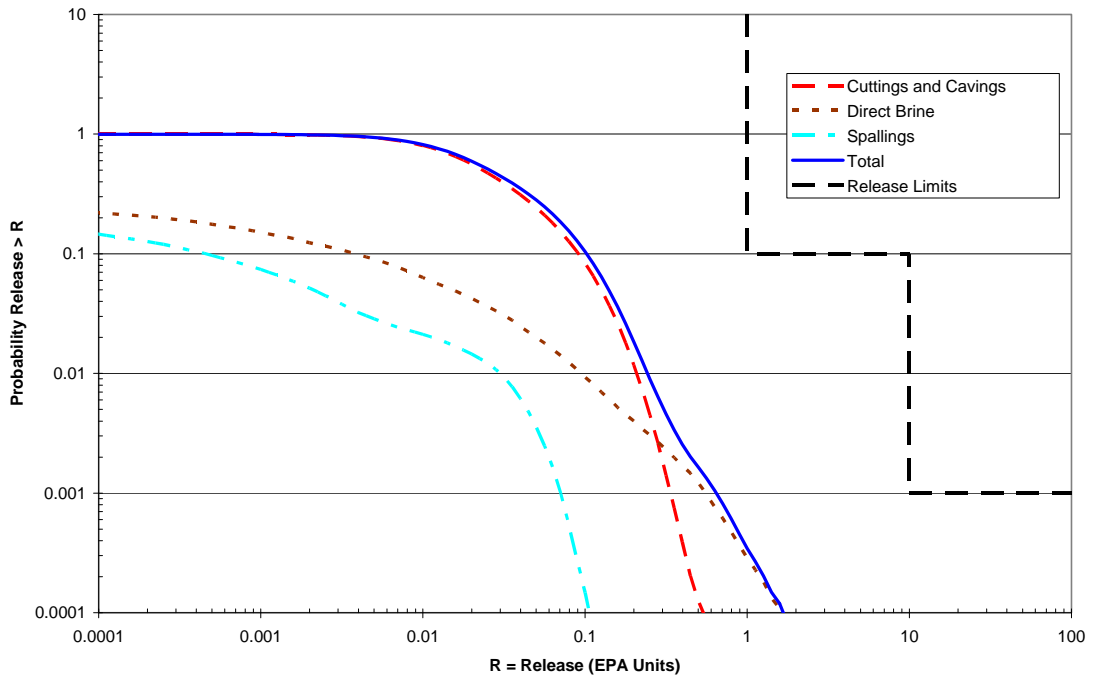
21 Table PA-35 shows the level of release at the probability of 0.1 and 0.001 from the overall mean
 22 CCDF. The CCDF value of the upper and lower 95% confidence levels on the mean CCDF at
 23



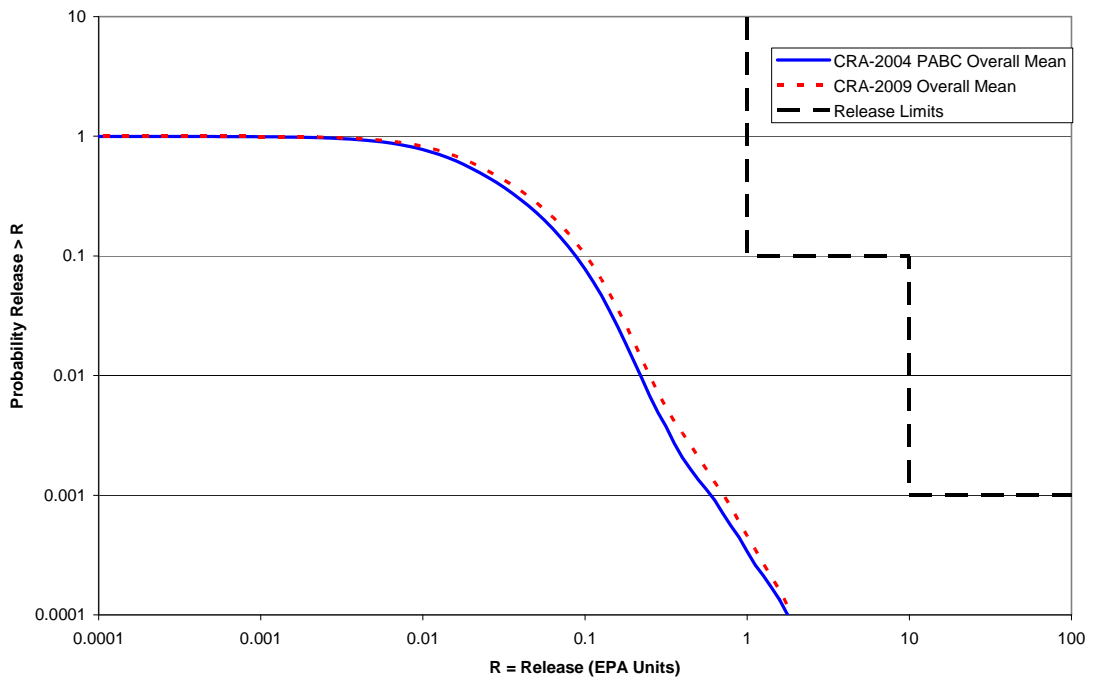
1
 2 **Figure PA-81. Mean CCDFs for Components of Total Normalized Releases, Replicate R1,**
 3 **CRA-2009 PA**



4
 5 **Figure PA-82. Mean CCDFs for Components of Total Normalized Releases, Replicate R2,**
 6 **CRA-2009 PA**



1
 2 **Figure PA-83. Mean CCDFs for Components of Total Normalized Releases, Replicate R3,**
 3 **CRA-2009 PA**



4
 5 **Figure PA-84. Overall Mean CCDFs for Total Normalized Releases: CRA-2009 PA and**
 6 **CRA-2004 PABC**

1 **Table PA-35. CRA-2009 PA and CRA-2004 PABC^a Statistics on the Overall Mean for**
 2 **Total Normalized Releases in EPA Units at Probabilities of 0.1 and 0.001**

Probability	Analysis	Mean Total Release	Lower 95% CL	Upper 95% CL	Release Limit
0.1	CRA-2004 PABC	0.09	0.08	0.09	1
	CRA-2009 PA	0.10	0.10	0.11	1
0.001	CRA-2004 PABC	0.60	0.52	0.68	10
	CRA-2009 PA	0.72	0.48	0.92	10

^a CRA-2004 PABC data was initially reported in Vugrin and Dunagan (2005).

3
 4 the 0.1 and 0.001 probability, along with the release limit, are also included. The overall mean
 5 total release CCDFs differ by ~0.01 EPA units at a probability of 0.1 and by ~0.1 EPA units at a
 6 probability of 0.001 (Table PA-35). These increases in the total releases primarily result from
 7 the increase in the drilling rate parameter.

8 There are some definite similarities between the CCDFs for the two analyses. First, for most
 9 probabilities, cuttings and cavings are the most significant pathways for release of radioactive
 10 material to the land surface. Second, release by spallings and subsurface transport in the Salado
 11 or Culebra make essentially no contribution to total releases. Finally, the resulting CCDFs of
 12 both analyses are within regulatory limits.

13 As in the CRA-2004 PABC, cuttings, cavings, and DBRs account for the majority of the total
 14 releases estimated in the CRA-2009 PA. As indicated in the rank regression analysis, in both the
 15 CRA-2009 PA and the CRA-2004 PABC, the uncertainty in waste shear strength (WTAUFAIL
 16 in Table PA-19) contributes to a large portion of the uncertainty in total normalized releases
 17 (Kirchner 2008b). The volumes of cuttings and cavings are primarily controlled by shear
 18 strength (Kirchner 2008b). The “solubility multiplier,” which represents uncertainty in
 19 solubilities for all actinides in the III oxidation state (WSOLVAR3 in Table PA-19), remained
 20 the second-most dominant parameter contributing to variability in total releases in all replicates
 21 (Kirchner 2008b). Solubility of actinides defines the concentration in DBRs. The variability in
 22 total releases explained by the waste shear strength in the CRA-2009 PA dropped from previous
 23 levels. The waste shear strength only accounts for about 81% of the total variability in total
 24 releases in the CRA-2009 PA, whereas in the CRA-2004 PABC it accounted for 88% of the
 25 variability (Kirchner 2008b). This decrease is due to the relative increase in the DBR
 26 contribution to total releases.

1 PA-10.0 References

- 2 Abdul Khader, M.H., and H.S. Rao. 1974. "Flow Through Annulus with Large Radial
3 Clearance." *American Society of Civil Engineers, Journal of the Hydraulics Division*, vol. 100,
4 no. HY1: 25–39.
- 5 Antoun, T., L. Seanman, D.R. Curran, G.I. Kanel, S.V. Razorenor, and A.V. Utkin. 2003. *Spall*
6 *Fracture*. New York: Springer-Verlag.
- 7 Aronson, D.G. 1986. "The Porous Medium Equation." *Nonlinear Diffusion Problems*. Lecture
8 Notes in Mathematics 1224. New York: Springer-Verlag.
- 9 Aziz, K., and A. Settari. 1979. *Petroleum Reservoir Simulation*. New York: Elsevier.
- 10 Barree, R.D., and M.W. Conway. 1995 "Experimental and Numerical Modeling of Convective
11 Proppant Transport." *Journal of Petroleum Technology*, vol. 47 (March): 216–22.
- 12 Bateman, H. 1910. "The Solution of a System of Differential Equations Occurring in the
13 Theory of Radio-Active Transformations." *Proceedings of the Cambridge Philosophical*
14 *Society*, vol. 15: 423–27.
- 15 Bean, J.E., M.E. Lord, D.A. McArthur, R.J. MacKinnon, J.D. Miller, and J.D. Schreiber. 1996.
16 *Analysis Package for the Salado Flow Calculations (Task 1) of the Performance Assessment*
17 *Analysis Supporting the Compliance Certification Application (CCA)*. ERMS 420238.
18 Albuquerque: Sandia National Laboratories. (EPA Air Docket A-93-02, Item II-G-08).
- 19 Bear, J. 1972. *Dynamics of Fluids in Porous Media*. New York: Dover.
- 20 Beauheim, R.L. 2003. *AP-100 Task 1: Development and Application of Acceptance Criteria*
21 *for Culebra Transmissivity (T) Fields, Analysis Report*. ERMS 531136. Carlsbad, NM: Sandia
22 National Laboratories.
- 23 Belhaj, H.A., K.R. Agha, A.M. Nouri, S.D. Butt, H.F. Vaziri, and M.R. Islam. 2003. *Numerical*
24 *Simulation of Non-Darcy Flow Utilizing the New Forchheimer's Diffusivity Equation*. SPE
25 81499. Paper presented at the SPE 13th Middle East Oil Show & Conference, Bahrain, April
26 2003.
- 27 Berglund, J.W. 1992. *Mechanisms Governing the Direct Removal of Wastes from the Waste*
28 *Isolation Pilot Plant Repository Caused by Exploratory Drilling*. SAND92-7295. Albuquerque:
29 Sandia National Laboratories.
- 30 Berglund, J.W. 1996. *Analysis Package for the Cuttings and Spallings Calculations (Task 5 and*
31 *6) of the Performance Assessment Calculation Supporting the Compliance Certification*
32 *Application (CCA), AP-015 and AP-016*. ERMS 240521. Albuquerque: Sandia National
33 Laboratories.

- 1 Bilgen, E., R. Boulos, and A.C. Akgungor. 1973. "Leakage and Frictional Characteristics of
 2 Turbulent Helical Flow In Fine Clearance." *Journal of Fluids Engineering, Transactions of the*
 3 *ASME, Series I*, vol. 95: 493–97.
- 4 Brill, J.P., and H.D. Beggs. 1986. *Two-Phase Flow in Pipes*. 5th ed. Tulsa: University of
 5 Tulsa.
- 6 Brooks, R.H., and A.T. Corey. 1964. "Hydraulic Properties of Porous Media." *Hydrology*
 7 *Paper No. 3*. Fort Collins, CO: Colorado State University. ERMS 241117.
- 8 Brush, L.H. 2005. *Results of Calculations of Actinide Solubilities for the WIPP Performance-*
 9 *Assessment Baseline Calculations* (May 18). ERMS 539800. Carlsbad, NM: Sandia National
 10 Laboratories.
- 11 Brush, L. H. and Y. Xiong. 2005. *Calculation of Organic Ligand Concentrations for the WIPP*
 12 *Performance Assessment Baseline Calculations* (May 4). ERMS 539635. Carlsbad, NM:
 13 Sandia National Laboratories.
- 14 Bynum, R.V., C. Stockman, Y. Wang, A. Peterson, J. Krumhansl, J. Nowak, J. Cotton, M.S.Y.
 15 Chu, and S.J. Patchett. 1997. "Implementation of Chemical Controls Through a Backfill System
 16 for the Waste Isolation Pilot Plant (WIPP)." SAND96-2656C. *Proceedings of the Sixth*
 17 *International Conference on Radioactive Waste Management and Environmental Remediation,*
 18 *ICEM '97, Singapore, October 12-16, 1997* (pp. 357–61). Eds. R. Baker, S. Slate, and G. Benda.
 19 New York: American Society of Mechanical Engineers.
- 20 Caporuscio, F., J. Gibbons, and E. Oswald. 2003. *Waste Isolation Pilot Plant: Salado Flow*
 21 *Conceptual Models Final Peer Review Report*. ERMS 526879. Carlsbad, NM: Carlsbad Area
 22 Office, Office of Regulatory Compliance.
- 23 Carlsbad Area Office Technical Assistance Contractor (CTAC). 1997. *Expert Elicitation on*
 24 *WIPP Waste Particle-Size Distribution(s) During the 10,000-Year Regulatory Post-Closure*
 25 *Period* (Final Report, June 3). ERMS 541365. Carlsbad, NM: U.S. Department of Energy.
- 26 Chambre Syndicale de la Recherche et de la Production du Petrole et du Gaz Naturel. 1982.
 27 *Drilling Mud and Cement Slurry Rheology Manual*. English translation. Houston: Gulf
 28 Publishing.
- 29 Chappelle, J.E., and A.S. Williamson. 1981. "Representing Wells in Numerical Reservoir
 30 Simulation: Part 2—Implementation." *Society of Petroleum Engineers Journal*, vol. 21:
 31 339–44.
- 32 Cherimisinoff, N.P., and P.N. Cherimisinoff. 1984. *Hydrodynamics of Gas-Solids Fluidization*.
 33 Houston: Gulf Publishing.
- 34 Christian-Frear, T.L. 1996. *Salado Halite Permeability from Room Q Analysis*. ERMS 414996.
 35 Albuquerque: Sandia National Laboratories.

- 1 Clayton, D.J. 2007. *Corrections to Input Files for DBR PABC Calculations*. ERMS 546311.
 2 Carlsbad, NM: Sandia National Laboratories.
- 3 Clayton, D.J. 2008a. *Analysis Plan for the Performance Assessment for the 2009 Compliance*
 4 *Recertification Application* (Revision 1). AP-137. ERMS 547905. Carlsbad, NM: Sandia
 5 National Laboratories.
- 6 Clayton, D.J. 2008b. *Analysis Package for Direct Brine Releases: Compliance Recertification*
 7 *Application–2009*. ERMS 548571. Carlsbad, NM: Sandia National Laboratories.
- 8 Clayton, D.J., S. Dunagan, J.W. Garner, A.E. Ismail, T.B. Kirchner, G.R. Kirkes, and M.B.
 9 Nemer. 2008. *Summary Report of the 2009 Compliance Recertification Application*
 10 *Performance Assessment*. ERMS 548862. Carlsbad, NM: Sandia National Laboratories.
- 11 Corbet, T.F., and P.M. Knupp. 1996. *The Role of Regional Groundwater Flow in the*
 12 *Hydrogeology of the Culebra Member of the Rustler Formation at the Waste Isolation Pilot*
 13 *Plant (WIPP), Southeastern New Mexico*. SAND96-2133. Albuquerque: Sandia National
 14 Laboratories.
- 15 Corbet, T., and P. Swift. 1996a. Memorandum to M.S. Tierney (Subject: Distribution for Non-
 16 Salado Parameter for SECOFL2D: Climate Index). 12 April 1996. ERMS 237465. U.S.
 17 Department of Energy, Sandia National Laboratories, Albuquerque, NM.
- 18 Corbet, T., and P. Swift. 1996b. *Parameters Required for SECOFL2D: Climate Index*. Record
 19 Package. ERMS 237465. Albuquerque: Sandia National Laboratories.
- 20 Cotsworth, E. 2005. Letter to U.S. Department of Energy (1 Enclosure). March 4, 2005.
 21 ERMS 538858. U.S. Environmental Protection Agency, Office of Air and Radiation,
 22 Washington, DC.
- 23 Cranwell, R.M., R.V. Guzowski, J.E. Campbell, and N.R. Ortiz. 1990. *Risk Methodology for*
 24 *Geologic Disposal of Radioactive Waste: Scenario Selection Procedure*. NUREG/CR-1667.
 25 SAND80-1429. ERMS 226750. Albuquerque: Sandia National Laboratories.
- 26 Darley, H.C.H. 1969. “A Laboratory Investigation of Borehole Stability.” *JPT Journal of*
 27 *Petroleum Technology*, July: 883–92.
- 28 Dogherty, J. 2002. *Design Document (DD) for PEST Version 5.5*. ERMS 523970. Los
 29 Alamos: Los Alamos National Laboratories.
- 30 Dunagan, S. 2007. *Parameter Problem Report (PPR), PPR-2007-001, for REFCON:FVW*.
 31 ERMS 545481. Carlsbad, NM: Sandia National Laboratories.
- 32 Dunagan, S. 2008. *Analysis Package for CCDFGF: 2009 Compliance Recertification*
 33 *Application*. ERMS 548776. Carlsbad, NM: Sandia National Laboratories.
- 34 Ely, J.F., and M.L. Huber. 1992. *NIST Thermophysical Properties of Hydrocarbon Mixtures*
 35 *Database (SUPERTRAPP), Version 1.0, User’s Guide*. Gaithersburg, MD: U.S. Department of

- 1 Commerce, National Institute of Standards and Technology, Standard Reference Data Program.
2 ERMS 242589.
- 3 Ergun, S. 1952. "Fluid Flow Through Packed Columns." *Chemical Engineering Progress*, vol.
4 48: 89–94.
- 5 Fletcher, C.A.J. 1988. *Computational Techniques for Fluid Dynamics*. 2nd ed. Vols. 1 and 2.
6 New York: Springer-Verlag.
- 7 Fox, B. 2005. *Analysis Package for EPA Unit Loading Calculations, Performance Assessment*
8 *Baseline Calculation*. ERMS 540378. Carlsbad, NM: Sandia National Laboratories.
- 9 Fox, B. 2008. *Parameter Summary Report for the CRA-2009 PA (Revision 0)*. ERMS 549747.
10 Carlsbad, NM: Sandia National Laboratories.
- 11 Fox, R.W., and A.T. McDonald. 1985. *Introduction to Fluid Mechanics*. 3rd ed. New York:
12 Wiley.
- 13 Francis, A.J., J.B. Gillow, and M.R. Giles. 1997. *Microbial Gas Generation Under Expected*
14 *Waste Isolation Pilot Plant Repository Conditions*. SAND96-2582. Albuquerque: Sandia
15 National Laboratories.
- 16 Frigaard, I.A., and N.L. Humphries. 1997. "High Penetration Rates: Hazards and Well
17 Control—A Case Study." *Proceedings, March 1997 Society of Petroleum*
18 *Engineers/International Association of Drilling Contractors Drilling Conference* (SPE paper
19 37953). Amsterdam: Society of Petroleum Engineers.
- 20 Garner, J., and C. Leigh. 2005. *Analysis Package for PANEL, CRA-2004 PA Baseline*
21 *Calculation* (Revision 0). ERMS 540572. Carlsbad, NM: Sandia National Laboratories.
- 22 Gatlin, C. 1960. *Petroleum Engineering: Drilling and Well Completions*. Englewood Cliffs,
23 NJ: Prentice-Hall.
- 24 Gilkey, A.P. 1995. *PCCSRC, Version 2.21, Software Installation and Checkout Form*. ERMS
25 227771. Carlsbad, NM: Sandia National Laboratories.
- 26 Graboski, M.S., and T.E. Daubert. 1979. "A Modified Soave Equation of State for Phase
27 Equilibrium Calculations: 3: Systems Containing Hydrogen." *Industrial and Engineering*
28 *Chemistry Process Design and Development*, vol. 18: 300–06.
- 29 Haberman, J.H., and D.J. Frydrych. 1988. "Corrosion Studies of A216 Grade WCA Steel in
30 Hydrothermal Magnesium-Containing Brines." *Materials Research Society Symposium*
31 *Proceedings: Scientific Basis for Nuclear Waste Management XI* (pp. 761–72). Eds. M.J. Apted
32 and R.E. Westerman. Pittsburgh: Materials Research Society.
- 33 Hadgu, T., P. Vaughn, J. Bean, D. Johnson, J. Johnson, K. Aragon, and J. Helton. 1999.
34 Memorandum to M. Marietta (Subject: Modifications to the 96 CCA Direct Brine Release

- 1 Calculations). 2 November 1999. ERMS 511276. U.S. Department of Energy, Sandia National
2 Laboratories, Carlsbad, NM.
- 3 Hansen, F.D., M.K. Knowles, T.W. Thompson, M. Gross, J.D. McLennan, and J.F. Schatz.
4 1997. *Description and Evaluation of a Mechanistically Based Conceptual Model for Spall*.
5 SAND97-1369. Albuquerque: Sandia National Laboratories.
- 6 Hansen, F.D., T.W. Pfeifle, and D.L. Lord. 2003. *Parameter Justification Report for DRSPALL*.
7 ERMS 531057. Carlsbad, NM: Sandia National Laboratories.
- 8 Harbaugh, A.W., E.R. Banta, M.C. Hill, and M.G. McDonald. 2000. *MODFLOW-2000: The*
9 *U.S. Geological Survey Modular Ground-Water Model—User Guide to Modularization Concepts*
10 *and the Ground-Water Flow Process*. Open File Report 00-92. Reston, VA: U.S. Geological
11 Survey.
- 12 Helton, J.C. 1993. “Drilling Intrusion Probabilities for Use in Performance Assessment for
13 Radioactive Waste Disposal.” *Reliability Engineering and System Safety*, vol. 40: 259–75.
- 14 Helton, J.C., J.D. Johnson, M.D. McKay, A.W. Shiver, and J.L. Sprung. 1995. “Robustness of
15 an Uncertainty and Sensitivity Analysis of Early Exposure Results with the MACCS Reactor
16 Accident Consequence Model.” *Reliability Engineering and System Safety*, vol. 48, no. 2:
17 129–48.
- 18 Helton, J.C., J.E. Bean, J.W. Berglund, F.J. Davis, K. Economy, J.W. Garner, J.D. Johnson, R.J.
19 MacKinnon, J. Miller, D.G. O’Brien, J.L. Ramsey, J.D. Schreiber, A. Shinta, L.N. Smith, D.M.
20 Stoelzel, C. Stockman, and P. Vaughn. 1998. *Uncertainty and Sensitivity Analysis Results*
21 *Obtained in the 1996 Performance Assessment for the Waste Isolation Pilot Plant*. SAND98-
22 0365. Albuquerque: Sandia National Laboratories.
- 23 Helton, J.C., and F.J. Davis. 2003. “Latin Hypercube Sampling and the Propagation of
24 Uncertainty in Analyses of Complex Systems.” *Reliability Engineering and System Safety*.
25 vol. 81, no. 1: 23–69.
- 26 Hirsch, C. 1988. “Numerical Computation of Internal and External Flows.” *Fundamentals of*
27 *Numerical Discretization*. Vol. 1. Chichester, UK: John Wiley & Sons.
- 28 Howard, B.A. 1996. Memorandum to Sandia National Laboratories (Subject: Performance
29 Assessment Parameter Input). 23 February 1996. ERMS 247595. Westinghouse Electric
30 Corporation, Carlsbad, NM.
- 31 Howarth, S.M., and T. Christian-Frear. 1997. *Porosity, Single-Phase Permeability, and*
32 *Capillary Pressure Data from Preliminary Laboratory Experiments on Selected Samples from*
33 *Marker Bed 139 at the Waste Isolation Pilot Plant*. SAND94-0472/1/2/3. Albuquerque: Sandia
34 National Laboratories.
- 35 Hunter, R.L. 1985. *A Regional Water Balance for the Waste Isolation Pilot Plant (WIPP) Site*
36 *and Surrounding Area*. SAND84-2233. Albuquerque: Sandia National Laboratories.

- 1 Huyakorn, P.S., B.H. Lester, and J.W. Mercer. 1983. "An Efficient Finite Element Technique
2 for Modelling Transport in Fractured Porous Media: 1. Single Species Transport." *Water*
3 *Resources Research*, vol. 19: 841–54.
- 4 Iman, R.L. 1982. "Statistical Methods for Including Uncertainties Associated with the Geologic
5 Isolation of Radioactive Waste Which Allow for a Comparison with Licensing Criteria."
6 *Proceedings of the Symposium on Uncertainties Associated with the Regulation of the Geologic*
7 *Disposal of High-Level Radioactive Waste, March 9-13, 1981* (pp. 145–57). Ed. D.C. Kocher.
8 NUREG/CP-0022, CONF-810372. Washington, DC: U.S. Nuclear Regulatory Commission,
9 Directorate of Technical Information and Document Control.
- 10 Iman, R.L., M.J. Shortencarier, and J.D. Johnson. 1985. *A FORTRAN 77 Program and User's*
11 *Guide for the Calculation of Partial Correlation and Standardized Regression Coefficients*.
12 SAND85-0044. NUREG/CR-4122. Albuquerque: Sandia National Laboratories.
- 13 Iman, R.L., and W.J. Conover. 1979. "The Use of the Rank Transform in Regression."
14 *Technometrics*, vol. 21: 499–509.
- 15 Iman, R.L., and W.J. Conover. 1982. "A Distribution-Free Approach to Inducing Rank
16 Correlation Among Input Variables." *Communications in Statistics: Simulation and*
17 *Computation*, vol. B11, no. 3: 311–34.
- 18 Iman, R.L., and J.C. Helton. 1988. "An Investigation of Uncertainty and Sensitivity Analysis
19 Techniques for Computer Models." *Risk Analysis*, vol. 8: 71–90.
- 20 Iman, R.L., and J.C. Helton. 1991. "The Repeatability of Uncertainty and Sensitivity Analyses
21 for Complex Probabilistic Risk Assessments." *Risk Analysis*, vol. 11: 591–606.
- 22 Ismail, A.E. 2007a. *Revised Porosity Estimates for the DRZ*. ERMS 545755. Carlsbad, NM:
23 Sandia National Laboratories.
- 24 Ismail, A.E. 2007b. *Errors in Input Files for NUTS for CRA-2004 PABC Calculations*. ERMS
25 546200. Carlsbad, NM: Sandia National Laboratories.
- 26 Ismail, A. E. 2008. *Analysis Package for CUTTINGS_S: Compliance Recertification*
27 *Application 2009* (Revision 1). ERMS 548618. Carlsbad, NM: Sandia National Laboratories.
- 28 Ismail, A.E., and J.W. Garner. 2008. *Analysis Package for Salado Transport Calculations:*
29 *Compliance Recertification Application 2009*. ERMS 548845. Carlsbad, NM: Sandia National
30 Laboratories.
- 31 James, S.J., and J. Stein. 2003. *Analysis Report for the Development of a Simplified Shaft Seal*
32 *Model for the WIPP Performance Assessment* (Rev 1). ERMS 525203. Carlsbad, NM: Sandia
33 National Laboratories.
- 34 Kanney, J. 2003. *Analysis Package for the Culebra Transport Calculation: Compliance*
35 *Recertification Application*. ERMS 532320. Carlsbad, NM: Sandia National Laboratories.

- 1 Kaufmann, D.W., ed. 1960. *Sodium Chloride: The Production and Properties of Salt and*
2 *Brine*. American Chemical Society Monograph 145. New York: Reinhold.
- 3 Kirchner, T. 2008a. *Generation of the LHS Samples for the AP-137 Revision 0 (CRA-09) PA*
4 *Calculations*. ERMS 547971. Carlsbad, NM: Sandia National Laboratories.
- 5 Kirchner, T. 2008b. *Sensitivity of the CRA-2009 Performance Assessment Calculation Releases*
6 *to Parameters*. ERMS 548788. Carlsbad, NM: Sandia National Laboratories.
- 7 Kirkes, R. 2007. *Evaluation of the Duration of Direct Brine Release in WIPP Performance*
8 *Assessment (Revision 0)*. ERMS 545988. Carlsbad, NM: Sandia National Laboratories.
- 9 Klinkenberg, L.J. 1941. "The Permeability of Porous Media to Liquids and Gases" (pp. 200–
10 13). *API Drilling and Production Practice*. ERMS 208556. Albuquerque: Sandia National
11 Laboratories.
- 12 Lee, J. 1982. *Well Testing*. SPE Textbook Series Vol. 1. New York: Society of Petroleum
13 Engineers of AIME.
- 14 Leigh, C.D., and J.R. Trone. 2005. *Calculation of the Waste Unit Factor For the Performance*
15 *Assessment Baseline Calculation (Rev. 0)*. ERMS 539613. Carlsbad, NM: Sandia National
16 Laboratories.
- 17 Leigh, C., R. Beauheim, and J. Kanney. 2003. *SNL WIPP Analysis Plan AP-100, Revision 0,*
18 *Analysis Plan for Calculation of Culebra Flow and Transport, Compliance Recertification*
19 *Application*. ERMS 530172. Carlsbad, NM: Sandia National Laboratories.
- 20 Leigh, C., J. Kanney, L. Brush, J. Garner, G. Kirkes, T. Lowry, M. Nemer, J. Stein, E. Vugrin, S.
21 Wagner, and T. Kirchner. 2005. *2004 Compliance Recertification Application Performance*
22 *Assessment Baseline Calculation (Revision 0)*. ERMS 541521. Carlsbad, NM: Sandia National
23 Laboratories.
- 24 Leigh, C., J. Trone, and B. Fox. 2005. *TRU Waste Inventory for the 2004 Compliance*
25 *Recertification Application Performance Assessment Baseline Calculation (Revision 0)*. ERMS
26 541118. Carlsbad, NM: Sandia National Laboratories.
- 27 Li, D., R.K. Svec, T.W. Engler, and R.B. Grigg. 2001. *Modeling and Simulation of the Wafer*
28 *Non-Darcy Flow Experiments*. SPE 68822. Paper presented at the SPE Western Regional
29 Meeting, Bakersfield, CA, March 26–30.
- 30 Lide, D.R., ed. 1991. *CRC Handbook of Chemistry and Physics*. 72nd ed. Boca Raton: CRC
31 Press.
- 32 Long, J. 2008. *SNL CPG WIPP Execution of Performance Assessment Codes for the 2009*
33 *Compliance Recertification Application Performance Assessment (Revision 0)*. ERMS 548350.
34 Carlsbad, NM: Sandia National Laboratories.

- 1 Lord, D.L., D.K. Rudeen, and C.W. Hansen. 2003. *Analysis Package for DRSPALL:*
2 *Compliance Recertification Application Part I: Calculation of Spall Volume.* ERMS 532766.
3 Carlsbad, NM: Sandia National Laboratories.
- 4 Lord, D.L., and D.K. Rudeen. 2003. *Sensitivity Analysis Report: Parts I and II: DRSPALL*
5 *Version 1.00: Report for Conceptual Model Peer Review July 7–11.* ERMS 524400. Carlsbad,
6 NM: Sandia National Laboratories.
- 7 Lowry, T. 2003. *Analysis Package for Salado Transport Calculations: Compliance*
8 *Recertification Application (Revision 0).* ERMS 530163. Carlsbad, NM: Sandia National
9 Laboratories.
- 10 Lowry, T.S. 2005. *Analysis Package for Salado Transport Calculations: CRA-2004 PA*
11 *Baseline Calculation.* ERMS 541084. Carlsbad, NM: Sandia National Laboratories.
- 12 Lowry, T.S., and J. Kanney. 2005. *Analysis Report for the CRA-2004 PABC Culebra Flow and*
13 *Transport Calculations.* ERMS 541508. Carlsbad, NM: Sandia National Laboratories.
- 14 Martell, M. 1996a. Memorandum to C. Lattier (Subject: Additional Information for the DRZ
15 [Disturbed Rock Zone] Porosity). 14 November 1996. ERMS 242257. U.S. Department of
16 Energy, Sandia National Laboratories, Albuquerque, NM.
- 17 Martell, M. 1996b. Memorandum to C. Lattier (Subject: Additional Information for the
18 Culebra Transport Parameter Id: 843, idpram: DNSGRAIN, idmtrl: CULEBRA, WIPP Data
19 Entry Form 464 at WPO # 32689). 10 December 1996. ERMS 232689. U.S. Department of
20 Energy, Sandia National Laboratories, Albuquerque, NM.
- 21 Mattax, C.C., and R.L. Dalton. 1990. *Reservoir Simulation.* SPE Monograph 13. Richardson,
22 TX: Henry L. Doherty Memorial Fund of Society of Petroleum Engineers, Inc.
- 23 McDonald, M.G., and A.W. Harbaugh. 1988. "A Modular Three-Dimensional Finite-
24 Difference Ground-Water Flow Model." *U.S. Geological Survey Techniques of Water-*
25 *Resources Investigations.* Book 6, Chap. A1. U.S. Government Printing Office.
- 26 McKay, M.D., R.J. Beckman, and W.J. Conover. 1979. "A Comparison of Three Methods for
27 Selecting Values of Input Variables in the Analysis of Output from a Computer Code."
28 *Technometrics*, vol. 21: 239–45.
- 29 McKenna, S.A., and D.B. Hart. 2003. *Analysis Report: Task 4 of AP-088 Conditioning of Base*
30 *T-Fields to Transient Heads.* ERMS 531124. Albuquerque: Sandia National Laboratories.
- 31 McTigue, D.F. 1993. *Permeability and Hydraulic Diffusivity of Waste Isolation Pilot Plant*
32 *Repository Salt Inferred from Small-Scale Brine Inflow Experiments.* SAND92-1911.
33 Albuquerque: Sandia National Laboratories.
- 34 Meigs, L. 1996. Memorandum to J. Ramsey (Subject: Non-Salado: Diffusive Tortuosity for
35 the Culebra Dolomite). 16 May 1996. ERMS 238940. U.S. Department of Energy, Sandia
36 National Laboratories, Albuquerque, NM.

- 1 Meigs, L., and J. McCord. 1996. *Physical Transport in the Culebra Dolomite*. ERMS 239167.
2 Albuquerque: Sandia National Laboratories.
- 3 Meigs, L., R.L. Beauheim, and T.L. Jones (eds). 2000. *Interpretations of Tracer Tests*
4 *Performed in the Culebra Dolomite at the Waste Isolation Pilot Plant Site*. SAND97-3109.
5 Albuquerque: Sandia National Laboratories.
- 6 Mendenhall, F.T., and W. Gerstle. 1995. *WIPP Anhydrite Fracture Modeling, Systems*
7 *Prioritization Method - Iteration 2 Baseline Position Paper: Disposal Room and Cutting*
8 *Models*. ERMS 239830. Albuquerque: Sandia National Laboratories.
- 9 Myers, R.H. 1986. *Classical and Modern Regression with Applications*. Boston: Duxbury.
- 10 Nemer, M.B. 2005. *Updated Value of WAS_AREA:PROBDEG*. ERMS 539441. Carlsbad,
11 NM: Sandia National Laboratories.
- 12 Nemer, M.B. 2007a. *Effects of Not Including Emplacement Materials in CPR Inventory on*
13 *Recent PA Results*. ERMS 545689. Carlsbad, NM: Sandia National Laboratories.
- 14 Nemer, M.B. 2007b. *Design Document for BRAGFLO Version 6.0*. ERMS 545015. Carlsbad,
15 NM: Sandia National Laboratories.
- 16 Nemer, M.B. 2007c. *Users Manual for BRAGFLO, Version 6.0*. ERMS 545016. Carlsbad,
17 NM: Sandia National Laboratories.
- 18 Nemer, M.B., and D.J. Clayton. 2008. *Analysis Package for Salado Flow Modeling, 2009*
19 *Compliance Recertification Application Calculation*. ERMS 548607. Carlsbad, NM: Sandia
20 National Laboratories.
- 21 Nemer, M.B., and J.S. Stein. 2005. *Analysis Package for BRAGFLO, 2004 Compliance*
22 *Recertification Application Performance Assessment Baseline Calculation (June 28)*. ERMS
23 540527. Carlsbad, NM: Sandia National Laboratories.
- 24 Nemer, M.B., J.S. Stein, and W. Zelinski. 2005. *Analysis Report for BRAGFLO Preliminary*
25 *Modeling Results With New Gas Generation Rates Based Upon Recent Experimental Results*.
26 ERMS 539437. Carlsbad, NM: Sandia National Laboratories.
- 27 Nemer, M.B. and W. Zelinski. 2005. *Analysis Report for BRAGFLO Modeling Results with the*
28 *removal of Methanogenesis from the Microbial-Gas-Generation Model*. ERMS 538748.
29 Carlsbad, NM: Sandia National Laboratories.
- 30 Oldroyd, J.G. 1958. "Non-Newtonian Effects in Steady Motion of Some Idealized Elastico-
31 Viscous Liquids." *Proceedings of the Royal Society of London: Series A: Mathematical and*
32 *Physical Sciences*, vol. 245, no. 1241: 278–97. ERMS 243211.
- 33 Podio, A.L., and A.P. Yang. 1986. *Well Control Simulator for IBM Personal Computer*.
34 IADC/SPE 14737. Paper presented at the International Association of Drilling
35 Engineers/Society of Petroleum Engineers Drilling Conference. Dallas, TX, February 10–12.

- 1 Poettmann, F.H., and P.G. Carpenter. 1952. "Multiphase Flow of Gas, Oil, and Water Through
2 Vertical Flow Strings with Application to the Design of Gas-lift Installations." *Drilling and*
3 *Production Practice* (1952): 257–317.
- 4 Popielak, R.S., R.L. Beauheim, S.R. Black, W.E. Coons, C.T. Ellingson, and R.L. Olsen. 1983.
5 *Brine Reservoirs in the Castile Formation Waste Isolation Pilot Plant (WIPP) Project*
6 *Southeastern New Mexico*. TME-3153. Carlsbad, NM: Westinghouse Electric Corp.
- 7 Prasuhn, A.L. 1980. *Fundamentals of Fluid Mechanics*. Englewood Cliffs, NJ: Prentice-Hall.
- 8 Prausnitz, J.M. 1969. *Molecular Thermodynamics of Fluid—Phase Equilibria*. Englewood
9 Cliffs, NJ: Prentice-Hall.
- 10 Press, W.H., B.P. Flannery, S.A. Teukolsky, and W.T. Vetterling. 1989. *Numerical Recipes in*
11 *Pascal: The Art of Scientific Computing*. Cambridge: Cambridge U P.
- 12 Rechard, R.P., H. Iuzzolino, and J.S. Sandha. 1990. *Data Used in Preliminary Performance*
13 *Assessment of the Waste Isolation Pilot Plant (1990)*. SAND89-2408. Albuquerque: Sandia
14 National Laboratories.
- 15 Roberts, R. 1996. *Salado: Brine Compressibility*. Records Package. ERMS 412842.
16 Albuquerque: Sandia National Laboratories.
- 17 Ross, S.M. 1987. *Introduction to Probability and Statistics for Engineers and Scientists*. New
18 York: John Wiley & Sons.
- 19 Ruth, D., and H. Ma. 1992. "On the Derivation of the Forchheimer Equation by Means of the
20 Averaging Theorem." *Transport in Porous Media*, vol. 7: 255–64.
- 21 Sallaberry, C.J., J.C. Helton, and S.C. Hora. 2006. *Extension of Latin Hypercube Samples with*
22 *Correlated Variables*. SAND2006-6135. Albuquerque: Sandia National Laboratories.
- 23 Sandia National Laboratories (SNL). 1992. *Preliminary Performance Assessment for the Waste*
24 *Isolation Pilot Plant, December 1992*. 5 vols. SAND92-0700/1-5. Albuquerque: Sandia
25 National Laboratories.
- 26 Sandia National Laboratories (SNL). 1997. *Summary of Uncertainty and Sensitivity Analysis*
27 *Results for the EPA-Mandated Performance Assessment Verification Test*. ERMS 420667.
28 Albuquerque: Sandia National Laboratories.
- 29 Savins, J.G., and G.C. Wallick. 1966. "Viscosity Profiles, Discharge Rates, Pressures, and
30 Torques for a Rheologically Complex Fluid in a Helical Flow." *A.I.Ch.E. Journal*, vol. 12:
31 357–63.
- 32 Stein, J.S. 2002. Memorandum to M.K. Knowles (Subject: Methodology behind the TBM
33 BRAGFLO Grid), 13 May 2002. ERMS 522373. U.S. Department of Energy, Sandia National
34 Laboratories, Carlsbad, NM.

- 1 Stein, J.S. 2005. Memorandum to L.H. Brush (Subject: Estimate of Volume of Brine in
2 Repository That Leads to a Brine Release). 19 April 2005. ERMS 539372. U.S. Department of
3 Energy, Sandia National Laboratories. Carlsbad, NM.
- 4 Stein, J.S. and W. Zelinski. 2003. *Analysis Report for: Testing of a Proposed BRAGFLO Grid*
5 *to be used for the Compliance Recertification Application Performance Assessment*
6 *Calculations*. ERMS 526868. Carlsbad, NM: Sandia National Laboratories.
- 7 Stockman, C., A. Shinta, and J. Garner, J. 1996. *Analysis Package for the Salado Transport*
8 *Calculations (Task 2) of the Performance Assessment Analysis Supporting the Compliance*
9 *Certification Application*. ERMS 422314. Carlsbad, NM: Sandia National Laboratories.
- 10 Stoelzel, D.M., and D.G. O'Brien. 1996. *Analysis Package for the BRAGFLO Direct Release*
11 *Calculations (Task 4) of the Performance Assessment Calculations Supporting the Compliance*
12 *Certification Application (CCA), AP-029, Brine Release Calculations*. ERMS 240520.
13 Albuquerque: Sandia National Laboratories.
- 14 Stone, C.M. 1997. *SANTOS—A Two-Dimensional Finite Element Program for the Quasistatic,*
15 *Large Deformation, Inelastic Response of Solids*. SAND90-0543. Albuquerque: Sandia
16 National Laboratories.
- 17 Streeter, V.L. 1958. *Fluid Mechanics*. 2nd ed. New York: McGraw-Hill.
- 18 Sweby, P.K. 1984. "High Resolution Schemes Using Flux Limiters for Hyperbolic
19 Conservation Laws." *SIAM Journal on Numerical Analysis*, vol. 21: 995–1011.
- 20 Telander, M.R., and R.E. Westerman. 1993. *Hydrogen Generation by Metal Corrosion in*
21 *Simulated Waste Isolation Pilot Plant Environments: Progress Report for the Period November*
22 *1989 Through December 1992*. SAND92-7347. Albuquerque: Sandia National Laboratories.
- 23 Telander, M.R., and R.E. Westerman. 1997. *Hydrogen Generation by Metal Corrosion in*
24 *Simulated Waste Isolation Pilot Plant Environments*. SAND96-2538. Albuquerque: Sandia
25 National Laboratories.
- 26 Thompson, T.W., W.E. Coons, J.L. Krumhansl, and F.D. Hansen. 1996. *Inadvertent Intrusion*
27 *Borehole Permeability* (July). ERMS 241131. Albuquerque: Sandia National Laboratories.
- 28 Tierney, M.S. 1990. *Constructing Probability Distributions of Uncertain Variables in Models*
29 *of the Performance of the Waste Isolation Pilot Plant: the 1990 Performance Simulations*.
30 SAND 90-2510. Albuquerque: Sandia National Laboratories.
- 31 Timoshenko, S.P., and J.N. Goodier. 1970. *Theory of Elasticity*. 3rd ed. New York: McGraw-
32 Hill.
- 33 Trovato, E.R. 1997. Letter to A. Alm (6 Enclosures). 19 March 1997. ERMS 245835. U.S.
34 Environmental Protection Agency, Office of Air and Radiation, Washington, DC.

- 1 U.S. Department of Energy (DOE). 1995. *Waste Isolation Plant Sealing System Design Report*.
2 DOE/WIPP-95-3117. Carlsbad, NM: Carlsbad Area Office.
- 3 U.S. Department of Energy (DOE). 1996. *Title 40 CFR Part 191 Compliance Certification*
4 *Application for the Waste Isolation Pilot Plant* (October). 21 vols. DOE/CAO 1996-2184.
5 Carlsbad, NM: Carlsbad Area Office.
- 6 U.S. Department of Energy (DOE). 1997. *Supplemental Summary of EPA-Mandated*
7 *Performance Assessment Verification Test (All Replicates) and Comparison with the Compliance*
8 *Certification Application Calculations* (August 8). WPO 46702. ERMS 414879. Carlsbad,
9 NM: Carlsbad Area Office.
- 10 U.S. Department of Energy (DOE). 2004. *Title 40 CFR Part 191 Compliance Recertification*
11 *Application for the Waste Isolation Pilot Plant* (March). 10 vols. DOE/WIPP 2004-3231.
12 Carlsbad, NM: Carlsbad Field Office.
- 13 U.S. Environmental Protection Agency (EPA). 1985. “40 CFR 191: Environmental Standards
14 for the Management and Disposal of Spent Nuclear Fuel, High-Level and Transuranic
15 Radioactive Wastes; Final Rule.” *Federal Register*, vol. 50 (September 19, 1985): 38066–089.
- 16 U.S. Environmental Protection Agency (EPA). 1993. “40 CFR 191: Environmental Radiation
17 Protection Standards for the Management and Disposal of Spent Nuclear Fuel, High-Level and
18 Transuranic Radioactive Wastes; Final Rule.” *Federal Register*, vol. 58 (December 20, 1993):
19 66398–416.
- 20 U.S. Environmental Protection Agency (EPA). 1996a. “40 CFR Part 194: Criteria for the
21 Certification and Recertification of the Waste Isolation Pilot Plant’s Compliance with the 40
22 CFR Part 191 Disposal Regulations; Final Rule.” *Federal Register*, vol. 61 (February 9, 1996):
23 5223–45.
- 24 U.S. Environmental Protection Agency (EPA). 1996b. *Background Information Document for*
25 *40 CFR Part 194* (January). EPA 402-R-96-002. Washington, DC: Office of Radiation and
26 Indoor Air.
- 27 U.S. Environmental Protection Agency (EPA). 1998a. “40 CFR Part 194: Criteria for the
28 Certification and Recertification of the Waste Isolation Pilot Plant’s Compliance with the
29 Disposal Regulations: Certification Decision; Final Rule.” *Federal Register*, vol. 63 (May 18,
30 1998): 27353–406.
- 31 U.S. Environmental Protection Agency (EPA). 1998b. *Technical Support Document for 194.23:*
32 *Parameter Justification Report* (May). Washington, DC: Office of Radiation and Indoor Air.
- 33 U.S. Environmental Protection Agency (EPA). 1998c. *Technical Support Document for 194.32:*
34 *Scope of Performance Assessments* (May). Washington, DC: Office of Radiation and Indoor
35 Air.

- 1 U.S. Environmental Protection Agency (EPA). 2005. Teleconference with U.S. Department of
2 Energy (DOE), Sandia National Laboratories (SNL), and Los Alamos National Laboratory
3 (LANL), Carlsbad, NM. March 2, 2005.
- 4 van Genuchten, R. 1978. *Calculating the Unsaturated Hydraulic Conductivity with a New*
5 *Closed-Form Analytical Model*. Report 78-WR-08. ERMS 249486. Princeton: Princeton
6 University, Department of Civil Engineering, Water Resources Program.
- 7 Vargaftik, N.B. 1975. *Tables on the Thermophysical Properties of Liquids and Gases in Normal*
8 *and Dissociated States*. 2nd ed. Washington, DC: Hemisphere.
- 9 Vaughn, P. 1996. Memorandum (with attachments) to M. Tierney (WAS_AREA and REPOSIT
10 SAT_RBRN Distribution). 13 February 1996. ERMS 234902. U.S. Department of Energy,
11 Sandia National Laboratories. Albuquerque, NM.
- 12 Vugrin, E.D. 2005. *Analysis Package for DRSPALL: CRA 2004 Performance Assessment*
13 *Baseline Calculation*. ERMS 540415. Carlsbad, NM: Sandia National Laboratories.
- 14 Vugrin, E.D., and S. Dunagan. 2005. *Analysis Package for CCDFGF: CRA-2004 Performance*
15 *Assessment Baseline Calculation*. ERMS 540771. Carlsbad, NM: Sandia National
16 Laboratories.
- 17 Vugrin, E.D., T.B. Kirchner, J.S. Stein, and W.P. Zelinski. 2005. *Analysis Report for Modifying*
18 *Parameter Distributions for S_MB139:COMP_RCK and S_MB139:SAT_RGAS*. ERMS 539301.
19 Carlsbad, NM: Sandia National Laboratories.
- 20 Walas, S.M. 1985. *Phase Equilibria in Chemical Engineering*. Boston: Butterworth.
- 21 Walker, R.E. 1976. "Hydraulic Limits are Set by Flow Restrictions." *Oil and Gas Journal*, vol.
22 74, no. 40: 86–90.
- 23 Walker, R.E., and W.E. Holman. 1971. "Computer Program Predicting Drilling-Fluid
24 Performance." *Oil and Gas Journal*, vol. 69, no. 13: 80–90.
- 25 Wang, Y., and L. Brush. 1996a. Memorandum to M. Tierney (Subject: Estimates of Gas-
26 Generation Parameters for the Long-Term WIPP Performance Assessment). 26 January 1996.
27 ERMS 231943. U.S. Department of Energy, Sandia National Laboratories. Albuquerque, NM.
- 28 Wang, Y., and L. Brush. 1996b. Memorandum to M. Tierney (Subject: Modify the
29 Stoichiometric Factor γ in BRAGFLO to Include the Effect of MgO Added to WIPP Repository
30 as Backfill). 23 February 1996. ERMS 232286. U.S. Department of Energy, Sandia National
31 Laboratories. Albuquerque, NM.
- 32 Weast, R.C., ed. 1969. *Handbook of Chemistry and Physics*. 50th ed. Cleveland: Chemical
33 Rubber Pub. Co.
- 34 Webb, S.W. 1992. "Appendix A: Uncertainty Estimates for Two-Phase Characteristic Curves
35 for 1992 40 CFR 191 Calculations," *Preliminary Performance Assessment for the Waste*

- 1 *Isolation Pilot Plant, December 1992* (pp. A-147 through A-155). Volume 3: Model
2 Parameters. SAND92-0700/3. Albuquerque: Sandia National Laboratories.
- 3 Welchon, J.K., A.F. Bertuzzi, and F.H. Poettmann. 1962. "Wellbore Hydraulics." *Petroleum*
4 *Production Handbook* (pp. 31-1 through 31-36). Eds. T.C. Frick and R.W. Taylor. Dallas:
5 Society of Petroleum Engineers of AIME.
- 6 Whittaker, A., ed. 1985. *Theory and Application of Drilling Fluid Hydraulics*. Boston:
7 International Human Resources Development Corporation.
- 8 Whitaker, S. 1996. "The Forchheimer Equation: A Theoretical Development." *Transport in*
9 *Porous Media*, vol. 25: 27–61.
- 10 Williamson, A.S., and J.E. Chappellear. 1981. "Representing Wells in Numerical Reservoir
11 Simulation: Part 1—Theory." *Society of Petroleum Engineers Journal*, vol. 21: 323–38.
- 12 WIPP Performance Assessment. 1996. *User's Manual for LHS, Version 2.41*. ERMS 230732.
13 Albuquerque: Sandia National Laboratories.
- 14 WIPP Performance Assessment. 1997a. *User's Manual for NUTS, Version 2.05*. ERMS
15 246002. Albuquerque: Sandia National Laboratories.
- 16 WIPP Performance Assessment. 1997b. *User's Manual for SECOTP2D, Version 1.41*. ERMS
17 245734. Albuquerque: Sandia National Laboratories.
- 18 WIPP Performance Assessment. 1998a. *User's Manual for FMT (Version 2.40)*. ERMS
19 243037. Carlsbad, NM: Sandia National Laboratories.
- 20 WIPP Performance Assessment. 1998b. *Design Document for PANEL (Version 4.00)*. ERMS
21 52169. Carlsbad, NM: Sandia National Laboratories.
- 22 WIPP Performance Assessment. 2003a. *Design Document/User's Manual for CCDFGF*
23 *(Version 5.00)*. ERMS 530471. Carlsbad, NM: Sandia National Laboratories.
- 24 WIPP Performance Assessment. 2003b. *User's Manual for PANEL Version 4.02*. ERMS
25 526652. Carlsbad, NM: Sandia National Laboratories.
- 26 WIPP Performance Assessment. 2003c. *User's Manual for CUTTINGS_S, Version 5.10*.
27 ERMS 532340. Albuquerque: Sandia National Laboratories.
- 28 WIPP Performance Assessment. 2003d. *Verification and Validation Plan and Validation*
29 *Document for DRSPALL (Version 1.00)*. ERMS 524782. Carlsbad, NM: Sandia National
30 Laboratories.
- 31 WIPP Performance Assessment. 2003e. *Design Document for DRSPALL (Version 1.00)*.
32 ERMS 529878. Carlsbad, NM: Sandia National Laboratories.

- 1 WIPP Performance Assessment. 2003f. *User's Manual for DRSPALL Version 1.00*. ERMS
- 2 524780. Carlsbad, NM: Sandia National Laboratories.
- 3 WIPP Performance Assessment. 2003g. *Design Document for CUTTINGS* (Version 5.10).